I. R. IRAN

ISSN: 1728-144X
e-ISSN: 1735-9244

International Journal of Engineering

Journal Homepage: www.ije.ir

MERC

TRANSACTIONS B: Applications

Volume 34, Number 05, May 2021

Materials and Energy Research Center

In the Name of God

INTERNATIONAL JOURNAL OF ENGINEERING
Transactions A: Basics

DISCLAIMER

The publication of papers in International Journal of Engineering does not imply that the editorial board, reviewers or publisher accept, approve or endorse the data and conclusions of authors.

International **J**ournal of **E**ngineering *Transactions A: Basics* (ISSN 1728-1431) (EISSN 1735-9244)
International **J**ournal of **E**ngineering *Transactions B: Applications* (ISSN 1728-144X) (EISSN 1735-9244)
International **J**ournal of **E**ngineering *Transactions C: Aspects* (ISSN 2423-7167) (EISSN 1735-9244)
Web Sites: www.ije.ir & www.ijeir.info E-mails: ije.editor8@gmail.com, Tel: (+9821) 88771578, Fax: (+9821) 88773352
Materials and Energy Research Center (MERC)

ISSN: 1728-144X, e-ISSN: 1735-9244

International Journal of Engineering, Volume 34, Number 5, May 2021

CONTENTS:

Civil Engineering

ISSN: 1728-144X, e-ISSN: 1735-9244

International Journal of Engineering, Volume 34, Number 5, May 2021

Electrical and Computer Engineering

Industrial Engineering

ISSN: 1728-144X, e-ISSN: 1735-9244

International Journal of Engineering, Volume 34, Number 5, May 2021

Mechanical Engineering

Mining Engineering

ISSN: 1728-144X, e-ISSN: 1735-9244

International Journal of Engineering, Volume 34, Number 5, May 2021

International Journal of Engineering

Journal Homepage: www.ije.ir

Mechanical Properties of Ultra-high Performance Concrete Reinforced by Glass Fibers under Accelerated Aging

M. Madhkhan*, P. Saeidian

Department of Civil Engineering, Isfahan University of Engineering, Isfahan, Iran

PAPER INFO

Paper history:
Received 01 January 2021
Received in revised form 14 February 2021
Accepted 13 March 2021

Keywords:
Ultra-high Performance Concrete
Glass Fibers
Accelerated Aging
Metakaolin
Mechanical Properties

ABSTRACT

Ultra-High Performance Concrete (UHPC) is a cementitious composite with fine aggregates and a homogeneous matrix with high compressive strength and excellent durability against aggressive agents. It is common to use short steel fibers in the UHPC. Besides, using steel fibers considerably increases the flexural ductility, durability and energy absorption. Using glass fibers in UHPC is a novel technique which improves its mechanical properties and it has the benefit of being lighter, and cheaper than steel fibers. Furthermore, glass fibers can be used for thin concrete plates for aesthetic purposes. However, glass fibers reinforced concrete is incompatible with the hydration reaction in the alkaline environment of concrete as it can damage glass fibers, so the mechanical properties of the concrete are decreased over long periods. The mechanical properties of UHPC containing glass fibers (GF-UHPC) was investigated under three regimes of normal curing, autoclave curing, and autoclave curing plus being in hot water for 50 days (accelerated aging). Besides, the substitution of silica fume by Metakaolin in GF-UHPC was studied to understand its mechanical properties after thermal curing. The results showed that after accelerated aging, the behavior of specimens become more brittle and the modulus of rupture and toughness indices of all prismatic specimens decreased, the modulus of rupture for samples containing glass fibers was 40% lower than autoclave curing results. However, the compressive strength under accelerated aging increased at least 4% in comparison to the normal curing. Replacement of silica fume with Metakaolin slightly increased the toughness with regard to flexural strength.

***doi**: 10.5829/ije.2021.34.05b.01*

NOMENCLATURE

I_5, I_{10}, I_{20}	Toughness Indices show the flexural strength and ductility of the specimen	δ	First-crack deflection
$R_{5,10}$, $R_{10,20}$	Residual strength factors are the strength retained after the first crack		

1. INTRODUCTION

One of the substantial achievements in concrete technology in the 20th century was the advance of ultra-high performance concrete (UHPC) or reactive powder concrete (RPC), more generally recognized as UHPC [1]. Small sand particle size (less than 0.6 mm), a high volume of cement (more than 600 kg/m^3), binder (Pozzolan, Metakaolin, Silica fume, Fly ash), and a minimum water/cement ratio (w/c $\leq$ 0.2) with high dosage of superplasticizer creates a solid matrix with high homogeneity and considerable compressive strength [2].

Plain concrete is a brittle material with low tensile strength and strain capacity; however, this troublesome property can be improved by adding short fibers to the matrix, which forestalls or controls the initiation or spreading of cracks [3]. Adding fibers to the matrix of concrete has many benefits, such as improving durability, bearing capacity, tensile capacity and toughness compared to plain concrete [4].

The reasons for using glass fibers in the matrix of concrete are higher tensile strength compared to organic fibers, cheaper compared to steel fibers, and lack of rust stains at the concrete surface [5]. Glass fibers have many other applications, for instance Glass Fiber Reinforced

*Corresponding Author Institutional Email: *madhkhan@iut.ac.ir* (M. Madhkhan)

Please cite this article as: M. Madhkhan, P. Saeidian, Mechanical Properties of Ultra-high Performance Concrete Reinforced by Glass Fibers under Accelerated Aging, International Journal of Engineering, B: Applications Vol. 34, No. 05, (2021) 1074-1084

Polymer (GFRP) can be used to enhance the bearing capacity of the pile along with concrete [6]. It can enhance the structural performance of reinforced concrete columns by coating and confine it with a layer of Glass Fibers Reinforced Polyurea (GFRPU) [7]. Due to Glass Fiber Reinforced Concrete (GFRC)'s good mechanical behavior, such as good fire resistance and mold ability, it is appropriate for cladding panels [8]. But using glass fibers in the matrix of concrete also has a disadvantage that all concrete containing glass fibers experience loss of ductility due to accelerated aging [9]. As a result, the new GFRC has higher tensile strength and ductility than aged GFRC. However, both are major drawbacks when considering GFRC as a substance for load-bearing structural parts [10]. To evaluate the long-term performance of GFRC composites, the specimens can be immersed in a hot water bath after curing regime [11]. In this paper, the long-term behavior of GF-UHPC is investigated. By putting the specimens of GF-UHPC in an autoclave and hot water to see how much the mechanical properties of GF-UHPC will be decreased.

A review of relevant papers published in the literature is given next. Rigaud et al. [9] examined the effect of volume percentage of glass fibers on the ductility and bending strength of a thin plate of GF-UHPC. They also evaluated ductility of specimens after wet aging. For this purpose, samples were placed in warm water at 50℃ for 90 days after normal curing. The results showed that ductility was nearly maintained in thin structural elements using an optimum combination of pozzolan in the mixtures. The above-mentioned concrete with 2% volumetric glass fibers absorbs more energy, but it has a lower bending yield stress compared with the specimens with 2.5% volume of fibers.

Yazici et al. [12] investigated the mechanical properties of reactive powder concrete under autoclave curing compared to the regular curing regime. Test results show that autoclave curing is more useful in improving the compressive strength of RPC compared to normal curing, and there is an optimum time, pressure, and temperature for autoclave curing to enhance the mechanical properties of RPC.

Bentur and Diamond [13] investigated the effects of substituting Silica fume with Metakaolin in the UHPC. The results illustrate that this substitution has not a significant impact on the mechanical properties of UHPC. However, Metakaolin is readily available in most countries. Therefore, this ultrafine material has an acceptable price. Moreover, due to its white color, it gives the concrete an esthetic advantage. Krahl et al. [14] investigated the cyclic response of ultra-high performance fibers reinforced concrete (UHPFRC) under cyclic loading test of tension, compression, and bending with 0%, 1%, and 2% steel fibers content. They concluded that an increment in volumetric fibers content could develop residual strength and toughness after cyclic loading.

Madhkhan and Katirai [15] investigated the influence of pozzolanic reactions in GFRC to minimize glass fibers damage with respect to aging. Different pozzolans were separately added to the matrix of GFRC, and the mechanical behavior such as toughness and compressive strength of specimens after 7, 28 and 90 days was tested. The results showed that addition of Nanosilica and Metakaolin could effectively prevent declines in concrete modulus of rupture and toughness with aging. Ali and Qureshi [16] investigated the effect of adding glass fibers to the matrix of concrete made of recycled coarse aggregate. The compressive test showed that glass fibers could compensate to some extent the loss of compressive strength due to substitution of natural aggregate with coarse aggregate. Glass fibers can increase the compressive strength of specimens by about 4-5%, and increase Flexural strength about 50%. Besides, permeability-based durability properties are adversely affected by glass fibers content.

Ryabova et al. [17] investigated long term bending strength of GFRC containing Silica fume and Metakaolin. The result showed that adding Metakaolin in an amount of 30% of Portland cement assist in keeping the long-term strength of FRC and the specific combination of Silica fume and Metakaolin added to the matrix of GFRC can even improve long-term bending strength.

Algburi et al. [18] studied the influence of glass fibers, steel fibers and a combination of both on the mechanical behavior of reactive powder concrete (RPC). Steel fibers improved comprehensive strength, tensile strength, elasticity module, and shear strength of concrete rather than no fibers RPC. However, glass and hybrid fibers increase tensile and shear strength, the comprehensive strength decreased in comparison with no fibers RPC. Liu et al. [19] studied the Mechanical Properties and durability of Glass and Polypropylene Fibers Reinforced Concrete until 28 days. To assess durability, the chloride penetration tests were carried out. The results showed that hybrid fibers reinforced concrete has the best properties rather than two other concrete. Adding polypropylene to the matrix of concrete increases the mechanical properties more than the glass fibers.

Khan et al. [20] studied the effect of substituting some portion of cement with waste glass powder in the matrix of concrete at different curing times. They compared the mechanical properties of substituted concrete with a control sample of concrete at 20MPa compressive strength. The results showed that compressive strength decreased at least 5 percent in compare to normal concrete. However, the Modulus of rupture of the prismatic specimen after 58 days curing in water achieved 2% improvement.

The novelty of this paper is investigating the mechanical behavior of RPC containing glass fibers instead of steel fibers. The effect of steel fibers on the mechanical properties and durability of the ultra-high performance concrete has been extensively investigated. Still a few reports are about GF-UHPC in the literature. Besides, mechanical properties of UHPC reinforced by glass fibers that its silica fume supplanted by Metakaolin were investigated. Also, using glass fibers in UHPC has other advantages compared to steel fibers, such as lower prices and available in the market of Iran.

2. MATERIALS

2. 1. Cement and Pozzolanic Additives The Portland cement type I produced in the Isfahan factory was used. The chemical composition and physical properties of materials are presented in Tables 1 and 2, respectively.

2. 2. Fine Aggregate Quartz sand and quartz powder were used as fine aggregates. Quartz powder is used as a filler. The diameter of the grains was between 0.01 and 0.075 millimeters. The characteristics of fine aggregate are shown in Tables 1 and 2. Quartz sand grading is given in Table 3.

TABLE 1. Chemical composition of the materials

Compound (%)	Cement	Silica fume	Metakaolin	Quartz sand
SiO_2	21.68	>91	53	98
Al_2O_3	5.9	0.9	45	1.1
Fe_2O_3	3.2	0.85	0.9	0.4
CaO	63.5	0.95	0.09	0.14
MgO	1.8	0.95	0.03	0
SO_3	1.7	-	-	-
Na_2O	0.2	-	0.1	0.01
K_2O	0.7	-	0.03	0.04
L.O.I	-	2	-	0.15

TABLE 2. Physical properties of materials

Properties	Cement	Silica fume	Metakaolin	Quartz sand
Average particle size (μm)	-	0.23	3	-
Bulk density	-	420	-	-
Specific surface (m^2/g)	0.34	22	23.5	-
Specific gravity (g/cm^3)	3.15	1.9	2.6	2.65

2. 3. Admixtures The SR340 superplasticizer was used to reduce water requirements. This product is chlorine free and it is produced in accordance with ASTM C-494-15a [21] type B, D, G. The base of this product is the polycarboxylate ether with its molecular side chains. The ratio of the weight of the superplasticizer to cement materials is recommended to be 0.2-1.5%. The superplasticizer density is 1.09 g/cm^3 [22].

2. 4. Fibers Glass fibers is a material made up of large thin fibers of glass. Glass fibers with the specifications given in Table 4 has been used. Glass fibers content was 1.5 and 2% by total volume. Due to the low workability of fresh concrete, the highest fibers content was 2.2% of concrete volume.

3. MIXTURE DETAILS

Mixed designs are obtained in the absolute volume method with an air content of 2%. Other weight parameters of the mixtures were constant (water/binder=0.2, Silica fume or Metakaolin/cement=0.3, quartz powder/cement=0.32 and quartz sand/cement=1.5) [23]. Abbreviations were used for mixtures according to usage of Silica fume or Metakaolin and glass fibers content. Three mixtures containing Silica fume were made:
- Without glass fibers (S0)
- With 1.5% volume glass fibers (S1.5)
- With 2.2% volume glass fibers (S2.2).

TABLE 3. Grading of quartz sand

Mesh size(#)	30	50	80	100	120	140	170
Sieve size(mm)	0.6	0.3	0.18	0.15	0.125	0.106	0.09
Retained(g)	0	226.1	217.8	250.8	190	100.1	15.3
Cumulative retained(g)	0	226.1	443.9	694.7	874.7	984.8	1000.1
Retained(%)	0	22.61	21.78	25.08	19	10.01	1.53
Cumulative retained (%)	0	22.61	44.39	69.47	87.47	98.48	100.01
Sand passing through	100	77.39	55.61	30.53	11.53	1.52	0

TABLE 4. Physical properties of glass fibers [24]

Type	Density (g/cm^3)	Length (mm)	ZrO_2	Failure strain	Young's modulus (MPa)	Tensile strength (MPa)
AR-Glass	2.74	10	20%	2%	74000	1480

Three reference mixtures containing Metakaolin were made:
- Without glass fibers (M0)
- With 1.5% volume glass fibers (M1.5)
- With 2.2% volume glass fibers (M2.2).

The mixture details are given in Table 5.

4. EXPERIMENTAL PROCEDURE

4. 1. Fabrication of UHPC All of the UHPCs were mixed and prepared using a mortar mixer with a nominal capacity of 10 liters. The mixer has a rotational speed of 75 rpm (round per minute) with an effective capacity of 5 liters. The mixing sequence was: dry powders included quartz sand, quartz powder, cement, and pozzolan were poured into the mixer in that order, and the mixing continues for 8 minutes or more.

While the mixer is working, half of the water is poured into the mixer; then the mixing continues for 2 minutes. Next, the water and the superplasticizer are added, and mixing continues for 3 minutes. Residual superplasticizer is added to the compound, followed by adding glass fibers and mixing at high speed for 5 minutes. It should be mentioned that a portion of the mortar was used for the ASTM C1437-13 [23] test was used to determine the flow of mortars containing cementitious materials before adding the fibers.

4. 2. Manufacturing of the Specimens The UHPC was made in cube mortar molds (75×75×75mm) and prismatic specimens (350×50×13.5mm), compacted by hand and using a vibrating table. The samples were kept in the molds for 48 hours at room temperature at about 20°C. The surface of the samples was covered with wet fabric to prevent moisture loss and surface cracking. After this period, the specimens were detached from the steel molds. The first group of samples was put in water at 20 °C for 28 days, the second group was autoclaved under (121°C, 1.25 MPa) for 24 hours, and the third group was autoclaved then kept in hot water at 50°C for 50 days.

4. 3. Mechanical Properties The mechanical behavior of the UHPC was studied by compressive and flexural strength of samples. Cube specimens were used to determine the compressive strength. This test was performed according to BS EN1881-116 [25]. For determining the flexural strength, the prismatic specimens were utilized. The flexural strength test was performed according to ASTM C78-10 [26]. The specimens were loaded at the mid-span point, as shown in Figure 1-a. The distance between simple supports was 300 mm, and electronic transducers were used to measure mid-span deflection (δ).

Furthermore, ASTM C1018-97 [27] was used for determining toughness parameters of fiber-reinforced concrete in accordance with Figure 1-b.

Toughness indices I5, I10, I20 show the flexural strength and ductility of the specimen. Calculation of the toughness indices is shown in Figure 1-b, and Equations 1 to 3. These indices show the ratio of the specific area beneath the load-deflection curve to the area under the first-crack deflection (δ).

$$I_5 = \frac{Area_{O'ACD}}{Area_{O'AB}} \tag{1}$$

$$I_{10} = \frac{Area_{O'AEF}}{Area_{O'AB}} \tag{2}$$

$$I_{20} = \frac{Area_{O'AGH}}{Area_{O'AB}} \tag{3}$$

In Equations (1), (2), and (3), $Area_{O'ACD}$, $Area_{O'AEF}$, $Area_{O'AGH}$ and $Area_{O'AB}$ are the areas under the load-deflection curve shown in Figure 1-b.

TABLE 5. Proportions of the concrete mixtures (kg/m^3)

Materials (kg/m^3)	UHPC with Silica fume			UHPC with Metakaolin		
	S0	S1.5	S2.2	M0	M1.5	M2.2
Cement	683.9	670.12	665.26	701.8	687.57	681.43
Silica fume	205.2	201	199.58	0	0	0
Metakaolin	0	0	0	210.5	206.27	204.4
Quartz powder	218.8	214.44	212.88	224.6	220	218
Quartz sand	1025.9	1005.18	997.9	1052.7	1031	1022
Super plasticizer	8	13.07	12.97	12.77	17.9	19.5
Water	177	174.23	172.97	182.5	178.8	177
Glass fibers	0	41.1	60.28	0	41.1	60.28
Super plasticizer/binder	0.9%	1.5%	1.5%	1.4%	2%	2.2%

(a)

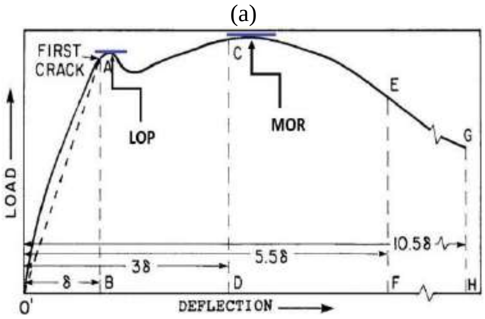

(b)

Figure 1. (a) Four-point Flexural strength test, (b) Characteristics of the load-deflection curve ASTM C1018-97 [27]

The residual strength factors $R_{5,10}$ and $R_{10,20}$ are the strength retained after the first crack. These factors are calculated by Equations (4) and (5).

$$R_{5,10} = 20(I_{10} - I_5) \tag{4}$$

$$R_{10,20} = 10(I_{20} - I_{10}) \tag{5}$$

5. EXPERIMENTAL RESULTS

Adding glass fibers in the concrete matrix plays two major roles in the mechanical properties of concrete. First, the main role is to increase the energy absorbing capacity and improve crack resistance [28]. Second, based on the experimental study, it is concluded that addition of excessive amounts of glass fibers in concrete reduces the mechanical strength. High volume of glass fibers can result in deterioration of concrete homogeneity and increases the probability of weak areas occurring in the concrete matrix [29].

Accelerated aging is defined as accelerating the formation of the hydration products, which improves the concrete strength, can affect the first role of fibers in the matrix of concrete. The chemical reactions between hydration products and pozzolans produce pozzolanic C-S-H gel, which improves the mechanical properties of concrete. Nevertheless, the interaction of hydration products, mainly calcium hydroxide, with glass fibers can have harm impact on the long-term behavior of the GFRC. Hydration products gradually bond the filaments together, which makes fibers brittle, and reducing the strain and strength capacity of the composite [30]. These effects will be used later to justify obtained results. In the next `compressive and flexural strength of specimens are presented and discussed.

5. 1. Flowability of Mortars To determine the flowability of the mortar of UHPC, ASTM C1437-13 [23] standard method was used. The results are presented in Table 6. It should be noted that in all mix designs, the water to cement ratio was 0.2.

Owing to the high binder volume and low water/binder ratio, the mixture has low workability; therefore, it needs a high amount of superplasticizer. The water/binder ratio is constant, but the superplasticizer/binder ratio may vary to keep the workability of mix designs approximately similar. Mix designs incorporating silica fume have higher flow than mix designs containing Metakaolin. In the mixtures containing fibers, the amount of superplasticizer is higher than the mixtures without fibers, because the glass fibers inhibit the flow of mortars.

5. 2. Compressive Strength The results of compressive strength for mix designs are shown in Figure 2. Under accelerated aging, each test was repeated six times, and for normal and autoclave curing methods, each test was repeated three times. The first notable result is that adding glass fibers results in higher compressive strength only in normal curing, but after autoclave curing and placing specimens in hot water (accelerated aging), specimens with lower glass fibers attain higher compressive strength.

In the next section, the effect of curing method, accelerated aging, and addition of Metakaolin are investigated.

5. 2. 1. Comparison of Normal and Autoclave Curing The compressive strength of UHPC without fibers after autoclave curing was 20 % higher than standard curing specimens, which is probably due to the accelerated rate of the hydration process and pozzolanic reaction. However, the compressive strength of specimens containing glass fibers is almost the same as or even less than strength of specimens with 2.2% (volumetric) fibers. It can be inferred that the glass fibers deteriorate the concrete homogeneity and this effect is stronger than preventing crack propagation; because

TABLE 6. Flowability of mortars

Mixtures	S0	S1.5	S2.2	M0	M1.5	M2.2
Superplasticizer/ binder	0.90%	1.50%	1.50%	1.40%	2%	2.20%
Diameter(mm)	150	185	195	155	180	195

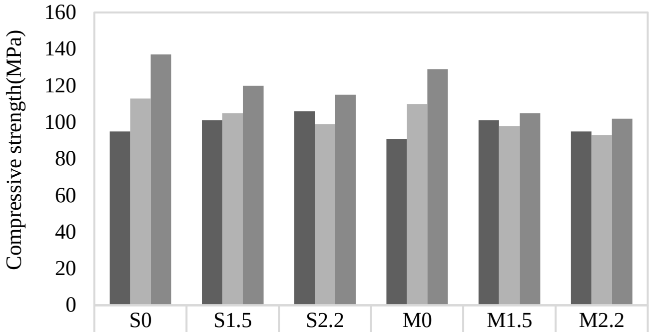

	S0	S1.5	S2.2	M0	M1.5	M2.2
Normal	95	101	106	91	101	95
Autoclave	113	105	99	110	98	93
Accelerated aging	137	120	115	129	105	102

Mixtures

Figure 2. Compressive strength of samples after curing and thermal treatment

hydration products affect the performance of glass fibers and reduce filament pull-out. As a result, the composite cured by autoclave becomes more brittle than ordinary curing.

5. 2. 2. Effect of Accelerated Aging All specimens experienced a remarkable increase in the compressive strength after accelerated aging compared with normal or autoclave curing; but specimens subject to compressive strength test fail more abruptly and explosively, particularly specimens without fibers. Hence, the specimens become more brittle. Although increasing hydration products weakens the glass fibers in the concrete matrix, the compressive strength of specimens under accelerated aging is improved. The formation of the hydration products especially C-S-H gel strengthens the concrete matrix. Therefore, after accelerated aging which increases the age of the concrete containing glass fibers, not only depressed the strength, but also the strength has been improved.

5. 2. 3. Effect of the Metakaolin Substitution of silica fume by Metakaolin led to a small decrease in compressive strength. After accelerated aging, an increase in compressive strength for specimens containing SF and MK was 16 and 11% on average. This shows that pozzolanic activity in silica fume is more complete compared to Metakaolin, and the silica fume gives a higher compressive strength in this case.

5. 3. Flexural Strength Prismatic specimens were subjected to curing or accelerating aging and then used for bending tests. Each test was repeated six times and the results (average of six tests) are presented in Tables 7 and 8. UHPC has a mean modulus of rupture (MOR) of 8.8 MPa at 28 days, and GF-UHPC has MOR 11- 14 MPa depending on fiber content. Fibers play a pivotal role in increasing ductility and flexural strength. As an example, after normal curing, The MOR of S1.5 is 18.92% higher than S0. In addition, fibers inhibit abrupt failure and control the width of

TABLE 7. Results of flexural strength test for Silica fume mixtures

Mixtures		S0			S1.5			S2.2		
Curing type		Normal curing	Autoclave curing	Accelerated aging	Normal curing	Autoclave curing	Accelerated aging	Normal curing	Autoclave curing	Accelerated aging
Limit of proportionality (MPa)		8.72	9	8.11	10.37	12.25	8.25	11.54	11	6.54
Modulus of rupture (MPa)		8.72	9	8.11	11.2	14	8.7	14.05	12.4	6.91
Index value	I_5	1	1	1	4.71	5.48	4.1	5.22	5.1	4.3
	I_{10}	1	1	1	7.22	6.68	4.6	7.57	6.37	4.87
	I_{20}	1	1	1	8.72	6.68	4.6	8.62	6.39	4.87
Residual strength factor (%)	$R_{5,10}$	0	0	0	50.23	24	10	47	25.4	11.4
	$R_{10,20}$	0	0	0	15	0	0	10.5	0.2	0

TABLE 8. Results of flexural strength test for Metakaolin mixtures

Mixtures		M0			M1.5			M2.2		
Curing type		Normal curing	Autoclave curing	Accelerated aging	Normal curing	Autoclave curing	Accelerated aging	Normal curing	Autoclave curing	Accelerated aging
Limit of proportionality (MPa)		9	11.6	10.3	10.15	13.5	8.85	10.1	11.85	7.33
Modulus of rupture (MPa)		9	11.6	10.3	12.5	14.3	9	12.8	12.8	7.8
Index value	I_5	1	1	1	5.1	4.78	3.98	5.17	5.2	4.38
	I_{10}	1	1	1	7.75	6.13	4.54	7.5	6.77	5.19
	I_{20}	1	1	1	8.99	6.13	4.54	9.1	6.77	5.19
Residual strength factor (%)	$R_{5,10}$	0	0	0	55	27	11.2	46.6	31.4	16.25
	$R_{10,20}$	0	0	0	11.46	0	0	16	0	0

cracks, therefore, the concrete has the ability to withstand more load. As a result, index values of specimens containing fibers are more than 1 and without fibers are 1, meaning that they will collapse after first crack.

Adding glass fibers to the flexural specimens increased modulus of rupture and toughness after normal curing. However, after accelerated aging and autoclave curing, MOR of specimens containing 1.5% fibers content was higher than 2.2% fibers content because the hydration products reduced filament pull-out and made them brittle. Hence, fibers' role in the deterioration of concrete homogeneity overcame the role of improving crack resistance.

Load-deflection diagrams after normal and autoclave curing are shown in Figures 3-6 shows the effect of the curing regime and percentage of glass fibers on the flexural strength better than Table 7. To be able to compare load-deflection diagrams, specimens should have the same thickness. As a result, we tried to keep the thickness and width of specimens constant, but because of low workability, the thickness of specimens was variable between 13mm to 15mm.

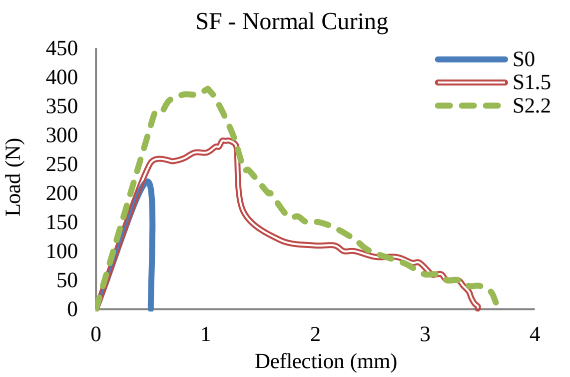

Figure 3. Load-deflection curves of SF specimens after normal curing

5. 3. 1. Comparison of Normal and Autoclave Curing Autoclave curing has consequential impacts on the properties of cement-based materials. High temperatures intensify the rate of reactions and can improve some characteristics of the specimens. Besides, the combination of pressure and high temperatures can change the chemistry of hydration products [12].

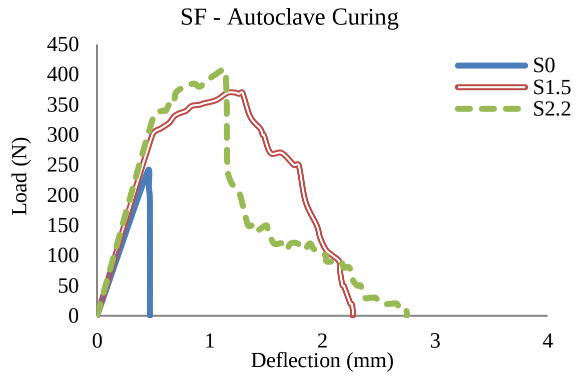

Figure 4. Load-deflection curves of SF specimens after autoclave curing

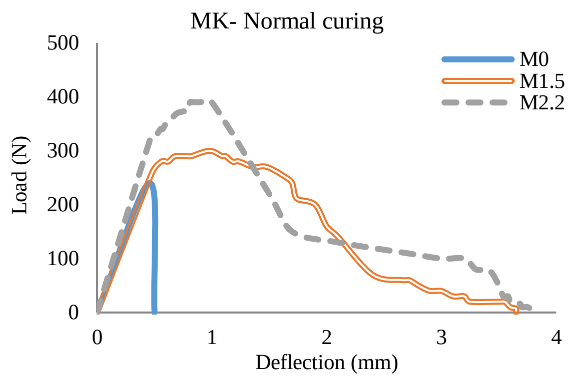

Figure 5. Load-deflection curves of MK specimens after normal curing

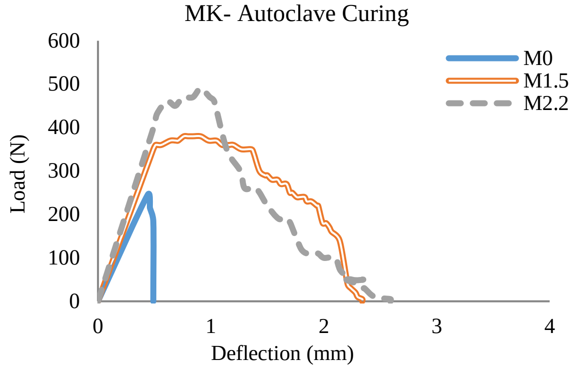

Figure 6. Load-deflection curves of MK specimens after autoclave curing

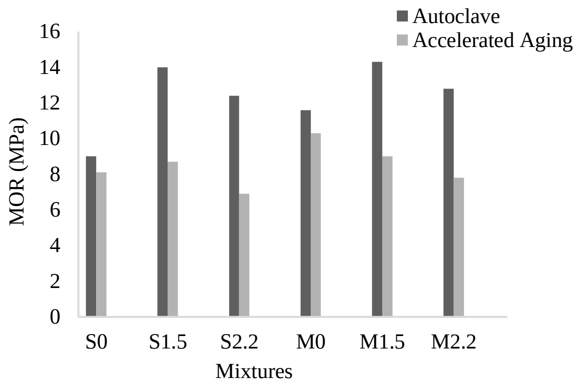

Figure 8. MOR of specimens after autoclave curing and accelerated aging

Autoclave curing increases MOR and LOP (Limit of Proportionality). However, final mid-span deflection, residual strength factor R5,10, and I10 index value decrease showing loss of ductility of specimens. High temperatures can augment porosity and deteriorate the fiber–matrix and aggregate–matrix bond. As a result, after autoclave curing, the behavior of concrete with fibers may become more brittle. Based on Figure 7, the loss of R5,10 is 40% for GF-UHPC. In other words, specimens with normal curing have more residual strength after the first crack, and they sustain more deformation and absorb more energy. After autoclave curing, specimens containing MK have a slightly higher residual strength or energy absorption than SF.

5. 3. 2. Effect of Accelerated Aging Accelerated aging can simulate the natural weathering phenomenon due to the development of hydration products that make glass fibers brittle material [9]. For this purpose, after autoclave curing, specimens were placed in hot water at 50℃ for 50 days. Placement in the hot water led to a significant reduction of flexural strength for all specimens. In Figure 8, the MOR of specimens after autoclave curing and accelerated aging are shown.

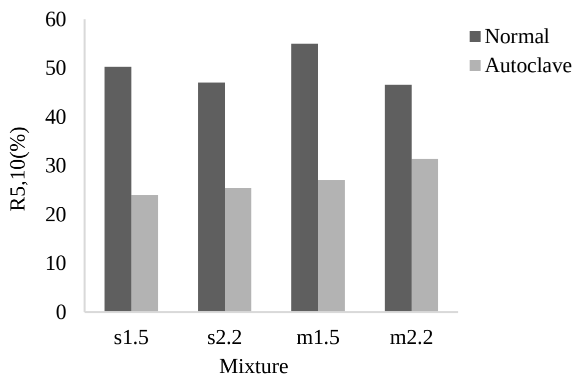

Figure 7. Residual strength factor R5,10 after normal and autoclave curing

Specimens with and without fibers lost 40% and 10% of MOR after accelerated aging. For specimens containing fibers, this can be explained by producing more hydration products, especially calcium hydroxide. They surround the thin fiber threads and connect them, and therefore the tensile strength of the fibers is reduced. In this situation, the load bearing capacity of the specimens is reduced, and the specimens show more brittle behavior.

In the specimens without fibers, the advancement of pozzolanic reaction gives us the expectation that the modulus of rupture will not drop. But the rupture modulus drop can be because of thermal treatment of UHPC, which is a complicated process. The thermal treatment improves pozzolanic reactions with cement hydration products. These chemical reactions are beneficial to some extent and if this process continues for more time, it can deteriorate the mechanical properties of concrete [1]. The loss of MOR after accelerated aging in GF-UHPC and GFRC are nearly similar. For instance, Jones et al. [31] reported that after accelerated aging of GFRC in 50°C water for 50 days, MOR was reduced by 34%. Bentur and Diamond [13] reported that after placing GFRC in 50°C water for 28 days, MOR decreased by 60%. Marikunte et al. [11] said after placing GFRC in 50°C water for 84 days, MOR was reduced by 50%.

The load-deflection diagrams in Figures 9 and 10 show the effect of accelerated aging clearly. These figures show a reduction in flexural strength, and both load capacity and mid-span deflection are diminished.

Due to the variable thickness of the specimens, for a better comparison of mixtures, index values and residual strengths are shown in Figures 11 and 12, respectively.

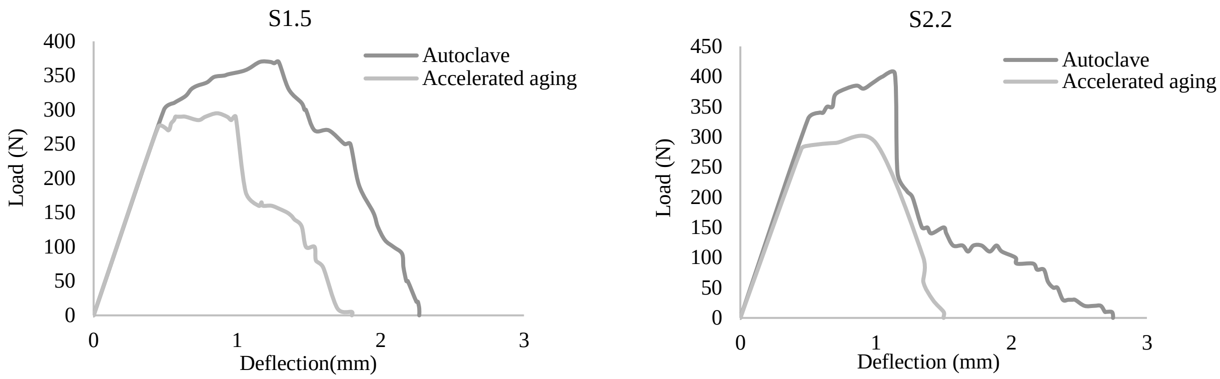

(a) (b)

Figure 9. Load-deflection diagrams of specimens with SF, (a) containing 1.5% fiber and (b) containing 2.2%

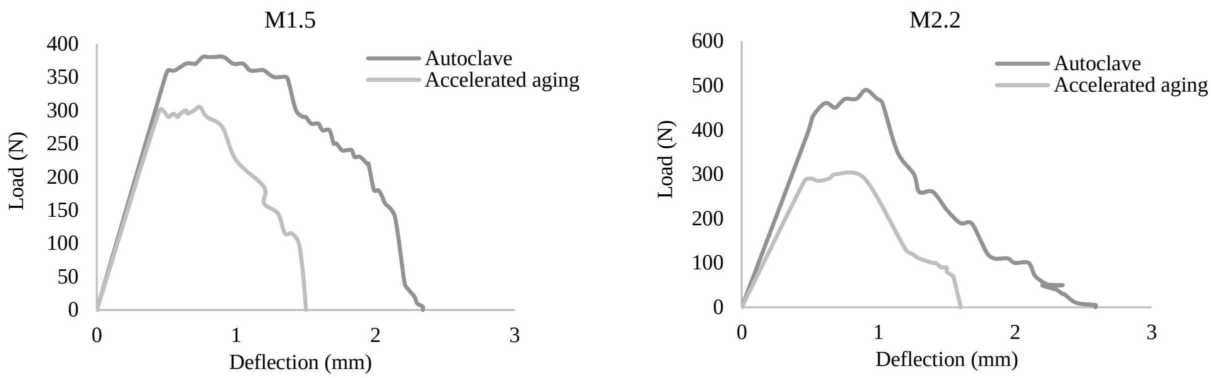

(a) (b)

Figure 10. Load-deflection diagrams of specimens with MK, (a) containing 1.5% fiber and (b) containing 2.2%

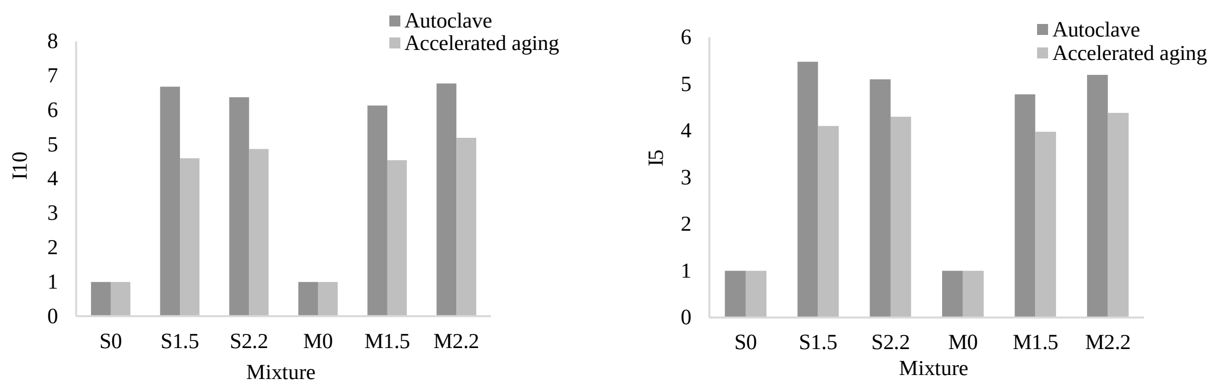

(a) (b)

Figure 11. Index values after accelerated aging, (a) index I10 and (b) index I5

Figure 11 illustrates the loss of toughness. The toughness indices of all specimens decreased as a result. The index I10 has a more severe reduction than index I5, which shows that the specimens have less deformation. Substitution of SF by MK leads to a small increase in toughness. Index values of specimens contain MK have a lower reduction after accelerated aging, particularly for M1.5. After accelerated aging, R5,10 is decreased by about 55% in all specimens.

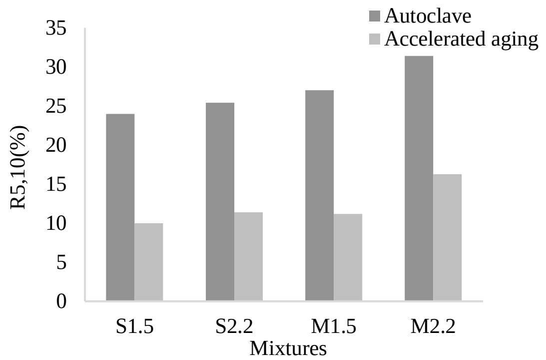

Figure 12. Residual strength factor R5, 10 after accelerated aging

6. CONCLUSIONS

In this research, the attempt is to assess the mechanical properties of Ultra-High Performance Concrete reinforced by glass fibers. The effect of using glass fibers in the matrix of UHPC is investigated with three types of curing regimes (Normal, Accelerated aging and Autoclave) and two types of pozzolans (silica fume and Metakaolin). The following results have been obtained.

Using glass fibers in the flexural specimens of UHPC highly increases the toughness and modulus of rupture.

The autoclave curing increased the limit of proportionality and modulus of proportionality compared to the normal curing; however, the specimens' toughness decreased.

After accelerated aging with hot water, which models the behavior of glass fibers reinforced concrete over long periods, the compressive strength of GF-UHPC specimens has risen. Therefore, there is no concern about losing the compressive strength of GF-UHPC by passing the time. In addition, modulus of rupture of all flexural specimens has been reduced. The decrease of the modulus of rupture in samples that contain glass fibers is about 40% compared to the autoclave curing. Also, the residual strength factor is dropped at least 48% rather than normal curing.

Substitution of silica fume with Metakoline has a positive effect on keeping resilience under accelerated aging. Using Metakaolin causes lower flowability of fresh concrete.

The finding of this research was to emphasize on the ability of substitution of glass fibers with steel ones in UHPC and to present their mechanical properties. Another research will be the study of the durability of GF-UHPC under freeze and thaw cycles, impermeability and so on.

7. REFERENCES

1. Nematollahi, B., Saifulnaz, R.M., Jaafar, M.S., and Voo, Y.L., "A review on ultra high performance 'ductile' concrete (UHPdC) technology", ***International Journal of Civil and Structural Engineering***, Vol. 2, No. 3, (2012), 1003–1018. doi:10.6088/ijcser.00202030026

2. Abbas, S., Nehdi, M. L., and Saleem, M. A., "Ultra-High Performance Concrete: Mechanical Performance, Durability, Sustainability and Implementation Challenges", ***International Journal of Concrete Structures and Materials***, Vol. 10, No. 3, (2016), 271–295. doi:10.1007/s40069-016-0157-4

3. Aydın, S., "Effects of fiber strength on fracture characteristics of normal and high strength concrete", ***Periodica Polytechnica Civil Engineering***, Vol. 57, No. 2, (2013), 191–200. doi:10.3311/PPci.7174

4. Buttignol, T. E. T., Sousa, J. L. A. O., and Bittencourt, T. N., "Ultra High-Performance Fiber-Reinforced Concrete (UHPFRC): a review of material properties and design procedures", ***IBRACON Structures and Materials Journal***, Vol. 10, No. 4, (2017), 957–971. doi:10.1590/s1983-41952017000400011

5. Chen, J., and Chanvillard, G., "UHPC composites based on glass fibers with high fluidity, ductility, and durability", Ultra-High Performance Concrete and Nanotechnology in Construction. Proceedings of Hipermat, Kassel, (2012), 265–272.

6. Farhangi, V., and Karakouzian, M., "Effect of Fiber Reinforced Polymer Tubes Filled with Recycled Materials and Concrete on Structural Capacity of Pile Foundations", ***Applied Sciences***, Vol. 10, No. 5, (2020), 1–14. doi:10.3390/app10051554

7. Song, J.-H., Lee, E.-T., and Eun, H.-C., "Shear Strength of Reinforced Concrete Columns Retrofitted by Glass Fiber Reinforced Polyurea", ***Civil Engineering Journal***, Vol. 6, No. 10, (2020), 1852–1863. doi:10.28991/cej-2020-03091587

8. Enfedaque, A., Paradela, L. S., and Sánchez-Gálvez, V., "An alternative methodology to predict aging effects on the mechanical properties of glass fiber reinforced cements (GRC)", ***Construction and Building Materials***, Vol. 27, No. 1, (2012), 425–431. doi:10.1016/j.conbuildmat.2011.07.025

9. Rigaud, S., Chanvillard, G., and Chen, J., "Characterization of Bending and Tensile Behavior of Ultra-High Performance Concrete Containing Glass Fibers", ***High Performance Fiber Reinforced Cement Composites***, Vol. 6, (2012), 373–380. doi:10.1007/978-94-007-2436-5_45

10. Purnell, P., Short, N. R., and Page, C. L., "A static fatigue model for the durability of glass fibre reinforced cement", ***Journal of Materials Science***, Vol. 36, (2001), 5385–5390. doi:https://doi.org/10.1023/A:1012496625210

11. Marikunte, S., Aldea, C., and Shah, S. P., "Durability of glass fiber reinforced cement composites: Effect of silica fume and metakaolin", ***Advanced Cement Based Materials***, Vol. 5, Nos. 3–4, (1997), 100–108. doi:10.1016/S1065-7355(97)00003-5

12. Yazıcı, H., Deniz, E., and Baradan, B., "The effect of autoclave pressure, temperature and duration time on mechanical properties of reactive powder concrete", ***Construction and Building Materials***, Vol. 42, (2013), 53–63. doi:10.1016/j.conbuildmat.2013.01.003

13. Bentur, A., and Diamond, S., "Direct incorporation of silica fume into glass fibre strands as a means for developing GFRC composites of improved durability", ***International Journal of Cement Composites and Lightweight Concrete***, Vol. 9, No. 3, (1987), 127–135. doi:10.1016/0262-5075(87)90046-7

14. Krahl, P. A., Carrazedo, R., and El Debs, M. K., "Mechanical damage evolution in UHPFRC: Experimental and numerical investigation", ***Engineering Structures***, Vol. 170, (2018), 63–77. doi:10.1016/j.engstruct.2018.05.064

15. Madhkhan, M., and Katirai, R., "Effect of pozzolanic materials on mechanical properties and aging of glass fiber reinforced concrete", ***Construction and Building Materials***, Vol. 225, (2019), 146–158. doi:10.1016/j.conbuildmat.2019.07.128

16. Ali, B., and Qureshi, L. A., "Influence of glass fibers on mechanical and durability performance of concrete with recycled aggregates", ***Construction and Building Materials***, Vol. 228, (2019), 116783. doi:10.1016/j.conbuildmat.2019.116783

17. Ryabova, A., Kharitonov, A., Matveeva, L., Shangina, N., and Belentsov, Y., "Research on Long-Term Strength of Glass-Fiber Reinforced Concrete", ***Energy Management of Municipal Transportation Facilities and Transport***, (2018), 640–646. doi:10.1007/978-3-319-70987-1_68

18. Algburi, A. H. M., Sheikh, M. N., and Hadi, M. N. S., "Mechanical properties of steel, glass, and hybrid fiber reinforced reactive powder concrete", ***Frontiers of Structural and Civil Engineering***, Vol. 13, No. 4, (2019), 998–1006. doi:10.1007/s11709-019-0533-7

19. Liu, J., Jia, Y., and Wang, J., "Experimental Study on Mechanical and Durability Properties of Glass and Polypropylene Fiber Reinforced Concrete", ***Fibers and Polymers***, Vol. 20, No. 9, (2019), 1900–1908. doi:10.1007/s12221-019-1028-9

20. Khan, F. A., Shahzada, K., Ullah, Q. S., Fahim, M., Khan, S. W., and Badrashi, Y. I., "Development of Environment-Friendly Concrete through Partial Addition of Waste Glass Powder (WGP) as Cement Replacement", ***Civil Engineering Journal***, Vol. 6, No. 12, (2020), 2332–2343. doi:10.28991/cej-2020-03091620

21. ASTM C-494-15a, "Standard specification for chemical admixtures for concrete", American Society for Testing and Materials, Annual Book of ASTM Standards, (2013).

22. Admixture properties, Performance of ADMIX SR340 in concrete", from http://white-damavand.ir/products/concrete-admixtures/admix-sr340/

23. ASTM C1437-13, "Standard test method for flow of hydraulic cement mortar", American Society for Testing and Materials, Annual Book of ASTM Standards, (2013).

24. Properties of glass fiber, Nippon Electric Glass, from http://www.arg.neg.co.jp

25. BSI EN1881-116, "Method for determination of compressive strength of concrete cubes", British Standards Institution, (1881).

26. ASTM C78-10, "Standard test method for flexural strength of concrete (using simple beam with third-point loading) ", American Society for Testing and Materials, Annual Book of ASTM Standards, (2010).

27. ASTM C1018-97, "Standard Test Method for Flexural Toughness and First-Crack Strength of Fiber-Reinforced Concrete (Using Beam With Third-Point Loading)", American Society for Testing and Materials, Annual Book of ASTM Standards, (2006).

28. Qureshi, L. A., and Ahmed, A., "An investigation on Strength properties of Glass fiber reinforced concrete", ***International Journal of Engineering Research and Technology***, Vol. 2, No. 4, (2013), 2567–2572.

29. Yazıcı, H., Yardımcı, M. Y., Aydın, S., and Karabulut, A. Ş., "Mechanical properties of reactive powder concrete containing mineral admixtures under different curing regimes", ***Construction and Building Materials***, Vol. 23, No. 3, (2009), 1223–1231. doi: https://doi.org/10.1016/j.conbuildmat.2008.08.003.

30. ASTM C1560-03, "Standard Test Method for Hot Water Accelerated Aging of Glass-Fiber Reinforced Cement-Based Composites", American Society for Testing and Materials, Annual Book of ASTM Standards, (2016).

31. Jones, J., Driver, M., and Harmon, T., "An Evaluation of the use of Finely Ground E–Glass Fiber as a Pozzolan in GFRC Composites", In 15th International GRCA Congress, Prague, (2008), 1–10.

Persian Abstract

چکیده

بتن فوق توانمند ماده‌ای متشکل از سیمان و ریزدانه است که ساختاری یکپارچه و دارای مقاومت فشاری و دوام بالایی در برابر شرایط محیطی شدید می‌باشد. استفاده از الیاف فلزی کوتاه در این بتن رایج است؛ زیرا باعث افزایش مقاومت خمشی، دوام و شکل‌پذیری این بتن می‌شود. استفاده از الیاف شیشه در این نوع بتن تکنیک جدیدی است و مزیت آن نسبت به الیاف فولادی، سبک بودن و ارزان بودن الیاف شیشه نسبت به الیاف فولادی می‌باشد. همچنین بتن مسلح شده با الیاف شیشه را می‌توان درصفحات نازک برای زیبایی و نمای سازه بکار برد. با این وجود، الیاف شیشه سازگار با فرآیند هیدراسیون در محیط قلیایی بتن نیستند و با گذر زمان، دچار آسیب می‌شوند. بنابراین با کامل شدن فرآیند هیدراسیون و گذر زمان، مقاومت مکانیکی بتن حاوی الیاف شیشه کاهش می‌یابد. برای شبیه‌سازی رفتار بلند مدت و افزایش فرآیند هیدراسیون این نوع بتن، مقاومت مکانیکی نمونه‌ها بعد از عمل‌آوری‌های معمولی، استفاده از اتوکلاو و سپس قرار گرفتن در آب گرم ۵۰ درجه سانتیگراد به مدت ۵۰ روز بررسی شدند. نتایج نشان داد بعد از عمل‌آوری‌های حرارتی، شاخص‌های شکل‌پذیری و مقاومت خمشی نمونه‌های خمشی کاهش چشمگیری می‌یابد. برای مثال، نمونه‌های قرارگرفته در آب گرم حدود ۴۰٪ مدول گسیختگی کمتر نسبت به حالت بعد از عمل‌آوری با اتوکلاو دارند؛ اگرچه مقاومت فشاری نمونه‌های فشاری حداقل به میزان ۴٪ نسبت به حالت بعد از عمل‌آوری معمولی افزایش یافته است. همچنین اثر جایگزینی متاکائولین به جای میکروسیلیس درساختار بتن جهت مطالعه رفتار بلند مدت بتن فوق توانمند بررسی شد. استفاده از متاکائولین شکل‌پذیری نمونه‌های خمشی را به مقدار کم بهبود می‌بخشد.

International Journal of Engineering

Journal Homepage: www.ije.ir

A Numerical Study of the Effect of Tunneling on Surface Settlement and Existing Buildings

A. M. Rajabi*[a], M. Mahmoudi[b], M. Taebi[b]

[a] *Engineering Geology Department, School of Geology, College of Science, University of Tehran, Tehran, Iran*
[b] *Faculty of Civil Engineering, University of Qom, Qom, Iran*

P A P E R I N F O

Paper history:
Received 10 November 2020
Received in revised form 09 February 2021
Accepted 28 February 2021

Keywords:
Ground Settlement
Tunneling
ABAQUS Finite Element
Numerical Modeling

A B S T R A C T

This study aimed to determine the effect of various influencing parameters such as tunnel diameter (D), depth (H), width (B), length (L), number of floors, and the horizontal distance of the building from the tunnel axis (X), as well as soil properties such as internal friction angle (ϕ), Poisson ratio (υ), modulus of elasticity (E), and cohesion (C) on surface settlement using ABAQUS finite element software. According to the results, the settelment increases with increasing tunnel diameter at a constant depth, while it decreases with increasing tunnel depth. Changes in the width and length of the building also affect the settlement directly; consequently, as the width and length of the building increase due to increasing the cross-sectional area of the building and its rigidity and stiffness, the settlement of the foundation becomes more uniform and resistant to displacement, leading to a decrease in the surface settlement. Also, as the distance of the building from the tunnel axis increases, the settlement decreases and follows a constant trend after a distance equal to the tunnel diameter. Based on the results of the sensitivity analysis, the depth of the tunnel has the greatest effect on the surface settlement, which can be prevented by controlling the depth of the tunnel from the ground surface. Also, among the soil geomechanical parameters, the modulus of elasticity had the greatest effect on settlement in the present study. Finally, according to the results, the effect of tunnel, building, and soil properties on surface settlement is very important, particularly in urban environments.

doi: *10.5829/ije.2021.34.05b.02*

NOMENCLATURE

E	soil modulus of elasticity	ν	the Poisson's ratio
K	earth pressure coefficient at rest	ε_L	Lateral strainsurface
Greek Symbols		β	the angular distortion
ε_P	the average maximum main strain		

1. INTRODUCTION

Tunneling affects the surface (such as buildings, bridges, etc.) and underground (urban facilities, tunnels, metro stations, etc.) structures. Therefore, such structures change the behavior of the ground around the tunnel. In urban environments, such deformations have adverse effects on surface and underground structures. Improving the design and construction of underground structures can guarantee the quality, the safety of engineering structures, and coordination between numerical calculations and actual results. The great variety in the factors influencing the surface subsidence (such as the type of soil layering, tunnel depth and dimensions, and tunneling methods) has led to numerous calculations and predictions of subsidence by researchers. All theories related to the surface subsidence calculation show a relationship between the volume of soil that is loosened by tunneling (and fills the excavated space) and the volume of the subsided surface. Given the loosened mass above the tunnel, further deformations and ground subsidence will be inevitable even if the pores between the soil particles are filled. The loosening and subsequent changes in the soil will continue during the tunneling

*Corresponding Author Institutional Email: *amrajabi@ut.ac.ir* (A. M. Rajabi)

Please cite this article as: A. M. Rajabi, M. Mahmoudi, M. Taebi, A Numerical Study of the Effect of Tunneling on Surface Settlement and Existing Buildings, International Journal of Engineering, Transactions B: Applications Vol. 34, No. 05, (2021) 1085-1093

process. In fact, it is not possible to eliminate them even with further measures taken inside the tunnel. By addressing these conditions is only possible by restoring the original soil density and level of the subsided mass. Numerous experiments on intact soil samples have shown that soil behavior is nonlinear and stress-dependent. The actual distribution of stresses in the soil requires consideration of its actual behavior. It is noteworthy that the calculation of soft soil substructure force is more accurate, and the error of deformation calculation is larger [1]. In general, studies to predict surface subsidence have focused on finite element methods [2], artificial intelligence [3], fuzzy studies [4], and cracking particle method [5, 6].

Researchers have always known that it is possible to use numerical methods indefinitely to solve engineering problems; however, given a large amount of time and money spent on programming and executing the programs by computers, the use of empirical relationships was more preferable. Nevertheless, experimental methods cannot provide accurate solutions for the problems, despite their ease of use. Obviously, the closer the model made in numerical methods is to reality, the more accurate the answer will be. Numerical methods have obtained more popularity in recent years due to the advancement of technology and related sciences such as computers and their applicability in various fields. The numerical methods are basically classified according to the type of environment used. The most important numerical methods are finite element method, finite difference method, and distinct element method.

Moorak [9] performed an extensive parametric study on the effects of tunnel construction on ground movements and near buildings constructed on clay soil. He used the discrete element method (DEM) for modeling and compared the results obtained from this modeling with the field data. He also proposed an equation for the ratio of tunnel depth to diameter (Z/D) and damage conditions as well as the ground structural destruction for different structures in the form of Equation (1) [12]:

$$\varepsilon_P = \varepsilon_L \cos\theta_{max}^2 + \beta\sin\theta_{max}\cos\theta_{max}; (\tan(2\theta_{max}) = \frac{\beta}{\varepsilon_L} \qquad (1)$$

Equation (1) was compared with field observations and the results showed it can be used for structural evaluation in the design phase of underground structures and tunnels in clay soils.

Dalong et al. [10] conducted studies on the land deformation due to tunneling in Shenzhen region of China using monitoring data analysis. They investigated the states with and without the presence of the tunnels and provided an equation to obtain the amount of ground subsidence when tunneling with a shield [10].

Selby [11] modeled tunnels in the UK using the Lagrangian finite difference method. Finally, he compared the results with experimental values and showed that the estimation of ground subsidence by the finite difference method predicted the subsidence through to be shallower and wider than the actual value, and these differences were greater in shallow tunnels. Franzius and Potts [12] conducted a study on the effect of meshing geometry on three-dimensional analysis of tunneling finite elements. They concluded that a distance of 13 times the diameter of the tunnel was sufficient to minimize the effect of boundaries on the results. Extensive studied [13-16] were conducted on the reaction of different structures due to the construction of underground tunnels and ground subsidence by finite element method. They concluded that the reaction of structures significantly depends on the type and shape of the structure as well as soil conditions. To calculate surface settlement under different types of loading, similar studies have been conducted [17-20]. In general, numerical models can provide more complete information than other methods due to their high flexibility. However, incorrect model selection, inaccurate use of parameter values, and misunderstanding of the construction process can lead to erroneous results.

Although many studies have been conducted to determine the amount of ground subsidence due to tunneling in different conditions, investigation of subsidence concerning underground structures is still one of the most challenging issues in the field of geotechnical engineering. Considering the importance of this issue, the present study has investigated the effect of soil, building, and tunnel parameters on the ground subsidence using numerical modeling with ABAQUS [16]. The importance of these parameters on the ground subsidence due to tunneling has been also examined while performing sensitivity analysis between the parameters.

2. NUMERICAL MODELING

Since practical experiments are very costly, the use of finite element simulations can be an alternative tool in the soil-structure interaction analysis. Among the software using the finite element method to analyze engineering problems, ABAQUS software is one of the most useful research and practical computer programs for finite element analysis due to its unique capabilities. Therefore, ABAQUS software was used in this study to investigate the interaction between soil and tunnel structure and examine the effect of different parameters on surface subsidence.

The characteristics of soil, tunnel, building, and configuration of the elements used in this study are described in the following. As shown in Fig. 1, a hypothetical tunnel with a diameter of D and depth of H in a soil with parameters such as internal friction angle, Poisson ratio, cohesion, and modulus of elasticity, along with a building with specified length and width is modeled in the ABAQUS software [16] environment. After making the desired geometric model, introducing the properties of the materials used, and defining the analytical methods and boundary conditions in the ABAQUS software, the environment is meshed into finite elements and then the analysis method is defined. The ABAQUS software works based on dividing the model into smaller components. Accordingly, continuous element with linear interpolation and an eight-node reduction integration (C3D8R) of regular hexagonal type has been used for soil and tunnel meshing. The continuous element with linear interpolation and a 10-node reduction integration (C3D10) of quadrilateral type has been selected for structural meshing. Also a number of 7624, 8546, and 33640 elements were considered for the building, the tunnels, and the soil, respectively. The selection of mesh dimensions in different parts of modeling has been conducted. Trial and error was applied in a way that in addition to high accuracy of results, the modeling speed was also acceptable. Investigations showed that the finer mesh dimensions have no effect on the output. Fig. 1 shows the schematic geometric drawing of tunnel of the studied models.

2. 1. Soil Properties The soil properties considered in this study were according to clayey sand soil with internal friction angle (ϕ) of 15, 20, 25, and 30 degrees, cohesion (C) of 10, 20, 30, and 40 kPa, modulus of elasticity (E) of 13, 23, 33, and 44 MPa, and Poisson's coefficient (υ) of 0.2, 0.3 and 0.4 according to Table (1). Various models have been proposed by researchers to determine the criterion of soil failure. The elastoplastic model is the best model in determining soil behavior. Soil is neither elastic nor a completely plastic material and shows a combination of the elastoplastic behavioral model. Accordingly, the Mohr-Coulomb model has been used in this study to determine soil behavior.

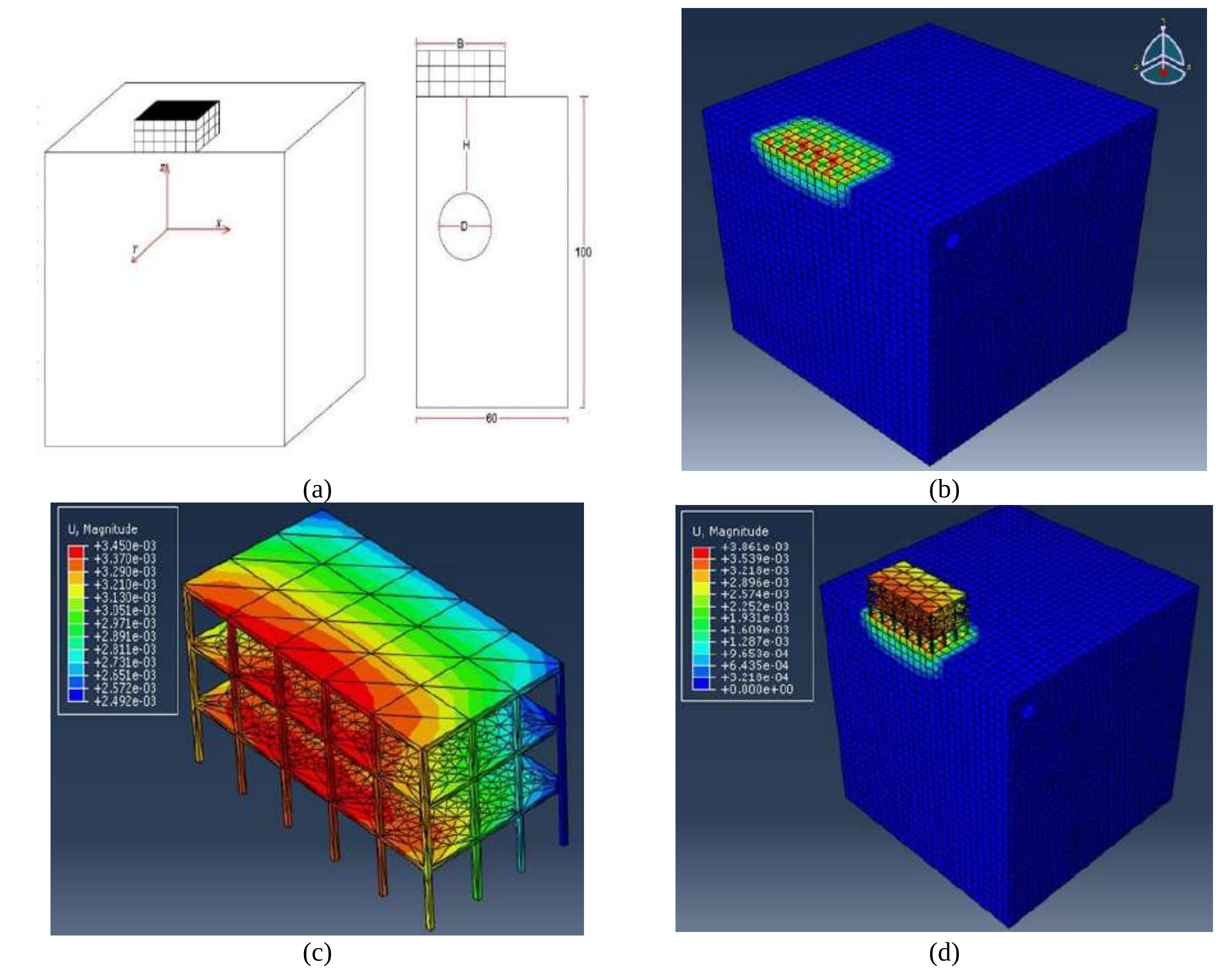

Figure 1. The geometry of the studied models a) Schematic of tunnel and building position b) deformations without building c) deformations of building; U in mm d) deformations with building; U in mm

TABLE 1. The properties of soil used in modeling

υ	E(MPa)	C(kPa)	Φ
0.2	23	20	20
0.3	33	30	25
0.4	44	40	30

2. 2. Tunnel and Buildings Properties The specifications of building and tunnel lining parameters used in modeling are given in Table 2.

The results of the present study are first compared with previous studies, after which modeling of a tunnel with different diameters and depths, and a building with specific length, width, and distance from the tunnel axis on a soil with different internal friction angle, modulus of elasticity, Poisson ratio, and cohesions were carried out and the effect of these parameters on surface settlement were investigated.

TABLE 2. Specifications of building and tunnel parameters used in this study

Building Parameters				Tunnel Lining Parameters				
No. of Stories	Distance from the tunnel axis (X)	Width of Building (B) (meters)	Length of Building (L) (meters)	Poisson ratio (υ)	Lining diameter (cm)	Modulus of elasticity (E) (MPa)	Tunnel Diameter (D) (meters)	Tunnel Depth (H) (meter)
3	10	5	10	0.2	30	37000	3	30
3	20	10	15	0.2	30	37000	5	50
3	30	15	20	0.2	30	37000	7	70
3	40	20	25	0.2	30	37000	9	90

3. RESULTS AND DISCUSSION

3. 1. Comparison of the Present Study with the Previous Research In this section, the surface settlement has been calculated for different tunnel depths (30, 50, 70, and 90 meters) using equations defined by Atkinson [7]. Then, the surface settlement has been calculated for the tunnel diameter of 9 meters and the internal friction angle (ϕ)and modulus of elasticity (E) of 30 degrees and 17 MPa, r by increasing the distance of the building from the tunnel, the impact of the tunnel on the settlement of the building decreases, resulting in the decreasing of the surface settlement. Indeed, the ground in the parts outside the tunnel acts as a suppor, .espectively along with the Poisson's coefficient (ν) equal to 0.3. Finally, the results have been compared.

According to Figure. 2, the amount of settlement calculated by ABAQUS software is greater than the experimental relationships, and the graph obtained from Atkinson [7] relationships is closer to numerical modeling. Also, at a depth of 30 meters, the amount of settlement in Atkinson [7] relation is equal to 4.6 mm, while at the same depth, the amount of settlement obtained from ABAQUS software is equal to 6 mm, which shows about 30% higher values. Fig. 3 compares the amount of surface settlement with increasing distance from the tunnel center in the analytical relationships presented by Cao et al. [13] and Bobet [8] with the numerical modeling used in the present study. In this comparison, the diameter of the tunnel is equal to 3 meters, and the tunnel burial depth is equal to 30 meters. The soil parameters include modulus of elasticity, Poisson ratio, and internal friction angle, which are 17 MPa, 0.3, and 30 degrees, respectively.

According to Figure 3, the curve obtained from the ABAQUS software is closer to the curve obtained by the Cao et al. [13] method and shows some overlap. Also, the two curves obtained from the numerical modeling and Cao et al. [13] intersect at a distance of 15 meters from the tunnel axis, which can be due to the boundary conditions defined by Cao et al. [13] method obtained from experimental observations and simple hypotheses. Besides, these relationships are just for undrained conditions.

3. 2. Numerical Study in the Present Study Generally, with increasing the horizontal distance of the building from the tunnel, the effect of the tunnel on building settlement decreases, leading to decreasing of the surface settlement. Indeed, the ground around the tunnel acts as a support. This section investigates the effect of different parameters on surface settlement.

3. 2. 1. Effect of the Tunnel Depth Relative to Diameter (H/D) and Internal Friction Angle of the Soil on Surface Settleme Figure 4 shows the results of numerical modeling for the case where a building with the width and length of 10 and 20 meters, respectively, is located above the tunnel axis and the diameter of the tunnel is equal to a constant value of 3 meters and different depths of 30, 50, 70, and 90 meters.

The internal friction angle of the soil is 15, 20, 25, and 30 degrees in this case. According to Figure 4, the maximum settlement is for the internal friction angle of 15 degrees and the tunnel depth of 30 meters.

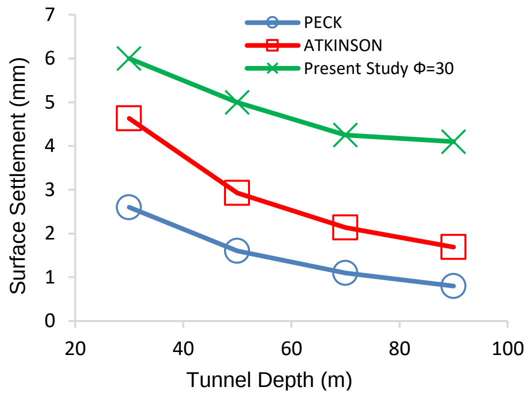

Figure 2. Comparing the amount of surface settlement in experimental and numerical relations

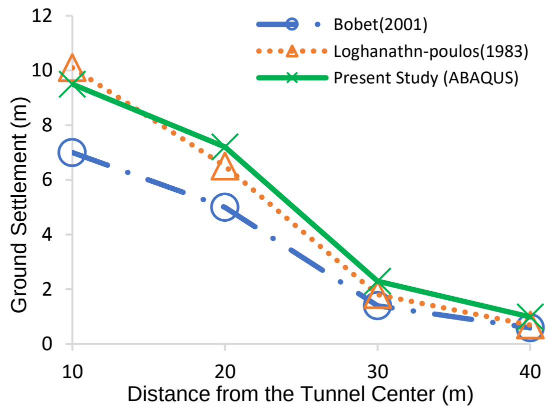

Figure 3. Comparison of the amount of settlement in analytical and numerical methods

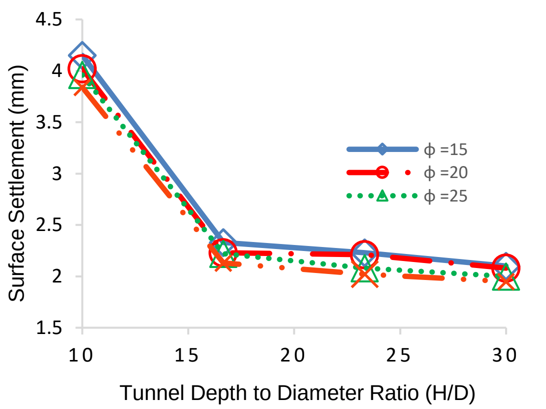

Figure 4. Surface settlement changes for the tunnel depth to diameter (H/D) ratio, where D is 3 meters

According to this figure, the settlement decreases with increasing the internal friction angle of the soil. In other words, the amount of surface settlement is more when the ratio of the tunnel depth to diameter is equal to 10 compared to when this ratio is equal to 30.

3. 2. 2. Effect of Cohesion Relative to Modulus of Elasticity (C/E) and Internal Friction Angle of the Soil on Surface Settlement

The effect of cohesion relative to the soil modulus of elasticity is investigated in this section for different values of the internal friction angle of sand-clay soils. Figure 5 shows the results of numerical modeling for the case where a building with the width and length of 10 and 20 meters, respectively, is located above the tunnel axis.

The soil modulus of elasticity is considered as 13 MPa, and its cohesion is 10, 20, 30, and 40 kPa, respectively. The tunnel burial depth and the diameter of the tunnel are 50 and 5 meters, respectively. Besides, the internal friction angles of soil are 15, 20, 25, and 30, while the Poisson's ratio has been considered to be equal to 0.3.

According to Figure 5, the maximum amount of settlement is for the internal friction angle of the soil equal to 15 degrees and the soil cohesion of 10 kPa. Based on the observations, the settlement decreases with increasing the soil internal friction angle. As can be observed, for a constant modulus of elasticity equal to 13 MPa, surface settlement decreases with the increasing ratio of the soil cohesion to modulus of elasticity.

3. 2. 3. Effect of the Building Length Relative to the Tunnel Depth (D/L) and the Soil Internal Friction Angle on the Surface Settlement

The effect of the Building length relative to the tunnel diameter is investigated for different internal friction angles in sandy-clay soils. The width and length of the building are

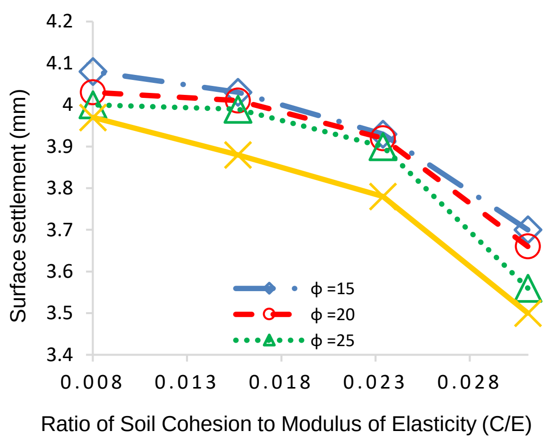

Figure 5. Changes in the surface settlement for the ratio of soil cohesion to modulus of elasticity (C/E) where modulus of elasticity is 13 Mpa

10 meters. The tunnel diameter is variable and equal to 3, 5, 7, and 9 meters with a burial depth of 50 meters. The soil internal friction angles are 15, 20, 25, and 30, while the modulus of elasticity, cohesion, and the Poisson's ratio of the soil are 17 MPa, 20, and 0.3, respectively. Figure 6 shows the results of modeling. As shown in Figure 6, the surface settlement decreases with an increase in the soil internal friction angle.

At a constant length of 10 meters for the building, the surface settlement increases with an increase in the tunnel diameter. As the diameter of the tunnel increases, the settlement increases due to the increasing excavation volume, the removal of part of the soil mass, and the occurrence of strains leading to the settlement.

3. 2. 4. Effect of the Building width Relative to its Length (B/L) and the Poisson's Ratio on the Surface Settlement Figure 7 shows the modeling results for a building with a constant length of 20 meters and variable widths of 5, 10, 15, and 20 meters. The soil Poisson Ratios were 0.1, 0.2, 0.3, and 0.4. The tunnel diameter is 5 meters with a burial depth of 50 meters, and the internal friction angle, cohesion, and modulus of elasticity were 30 degrees, 20 kPa, and 23 MPa, respectively. With increasing the width of the building, the ratio of the building width to length grows from 0.25 to 1, increasing the stiffness and rigidity of the building and decreasing the surface as well as building settlement. Similarly, by increasing the soil Poisson ratio from 0.1 to 0.4, the surface settlement also increases.

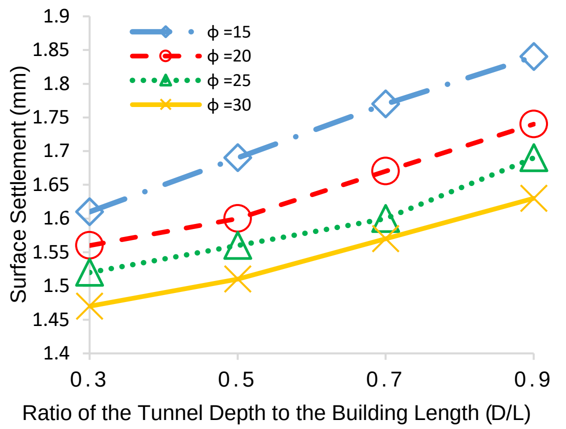

Figure 6. Changes in the surface settlement for the ratio of the tunnel depth to the building length (D/L) where the building length is 10 meters

3. 2. 5. Effect of the Building Width Relative to its Length (B/L) and the Soil Cohesion on the Surface Settlement The effect of building width on land settlement for different amounts of soil cohesion has been investigated. A building with different widths of 5, 10, 15, and 20 meters and a constant length of 10 meters is located above the tunnel axis. The tunnel diameter is 5 meters and its burial depth is 50 meters. Besides, the soil cohesion values are 10, 20, 30, and 40 kPa. According to Figure 8, the maximum settlement is for the soil cohesion of 40 kPa and the building width of 20 meters. It is also observed that with increasing soil cohesion, settlement decreases. Therefore, the soil with the cohesion of 30 kPa has less settlement than soil with cohesion of 10 kPa. As the width of the building increases at the constant building length equal to 20 meters, the stiffness of the building increases, and settlement decreases.

3. 2. 6. Effect of the Building width Relative to its Length (B/L) and the Soil Modulus of Elasticity on the Surface Settlement Figure 9 shows the numerical modeling results for a building with a length of 20 meters and different widths of 5, 10, 15, and 20, respectively. The soil modulus of elasticity is different and equal to 13, 23, 33, and 44 MPa. The tunnel burial

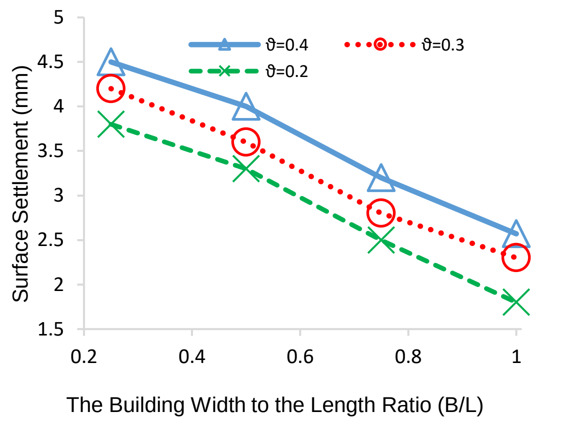

Figure 7. Changes in the surface settlement for the ratio of the building width to the length (B/L) for different Poisson ratios (L = 20 meters, ϕ =30°)

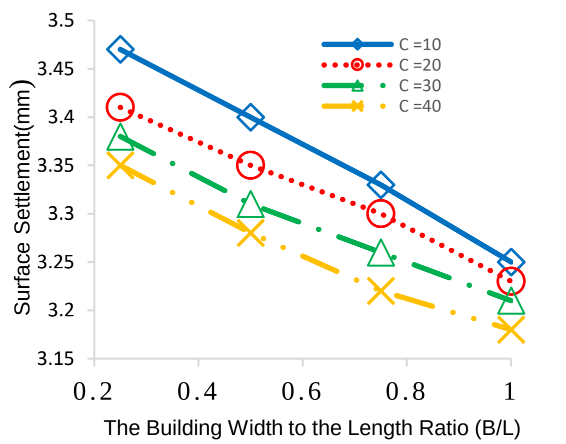

Figure 8. Changes in the surface settlement for the ratio of the building width to the length (B/L) for different soil cohesions (C) (L=20 meters, ϕ= 30°)

depth is 70 meters and its diameter is 5 meters.The maximum settlement is for the soil modulus elasticity of 13 MPa and the building width of 5 meters. It is also observed that the settlement decreases with the increasing modulus of elasticity. Accordingly, the soil with a modulus of elasticity of 44 MPa has less settlement than the case of 13 MPa. As the building width of the building, while the length is constant and equal to 20 meters, the surface settlement decreases. According to Figure 9, when the ratio of building width to length is equal to 1, the settlement is 1.9 mm for the soil with a modulus of elasticity of 13 MPa, and 1.75 mm for the modulus of elasticity of 44 MPa. This indicates that with an increase in modulus of elasticity from 13 to 44 MPa, the settlement decreased by about 8%.

3. 2. 7. Investigating the Effect of Building Weight on the Surface Settlement and Surface Building

The effect of the building weight on the surface settlement is investigated in the following. Given that with increasing the load of the building on the surface surface, the settlement also increases.

Figure 10 presents the results of modeling with and without considering the building. The tunnel diameter was 5 meters, and the buried depths were 30, 50, 70, and 90 meters, along with a 3-story building with a width of 10 m and a length of 20 meters and a load of 1600 kg/m^2 due to the weight of the building. The results show that surface settlement increases with increasing the load on the soil and the addition of the building.

3. 8. Effect of the Building Distance from the Tunnel Center Relative to the Building Length (X/L) and the Tunnel Depth on the Surface Settlement

Figure 11 shows the numerical modeling results for a building located at distances of 10, 20, 30, and 40 meters from the tunnel axis and constant

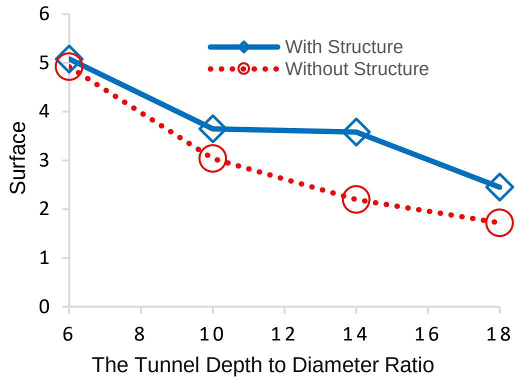

Figure 10. Changes in the surface settlement for the ratio of the tunnel depth to diameter with and without considering the building (D=5 meters)

width and length of 10 and 20 meters, respectively. The tunnel diameter is constant at 9 meters with variable depths of 30, 50, 70, and 90 meters. As the distance of the building from the tunnel axis increases, the settlement dramatically decreases; therefore, that after a certain distance, settlement decreases to almost zero. Increasing the distance between the building and the tunnel leads to reduced surface settlement, but the trend becomes constant after a distance equal to the diameter of the tunnel. The maximum increase in settlement is for the range of 0-10 meters because most changes in vertical and lateral pressure have occurred in this range.

3. 3.Sensitivity Analysis

One of the primary measures after modeling is to determine the sensitivity of the target modeled to input parameters. As a general rule, all parameters were kept constant except one parameter, which was changed to a certain percentage, to determine the impact of the input parameters on the target [15]. Table 3 presents the results obtained in this study based

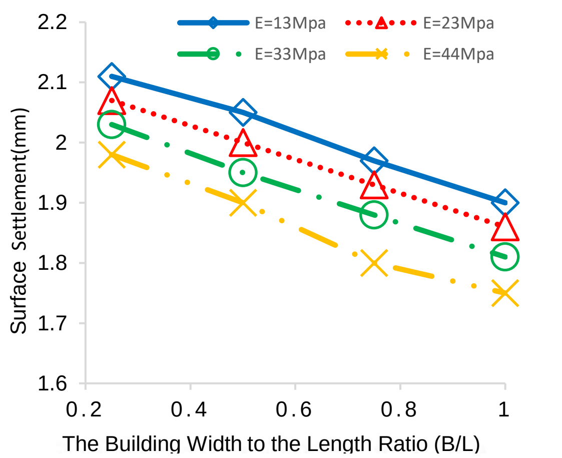

Figure 9. Changes in the surface settlement for the ratio of the building width to the length (B/L) for different soil modulus of elasticity (E) (L=20 m, ϕ= 30°)

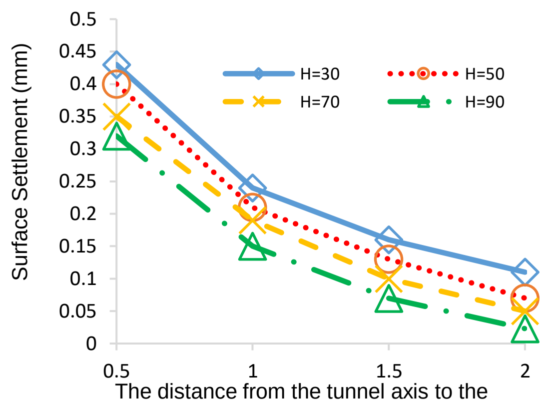

Figure 11. Changes in the surface settlement for the ratio of the distance from the tunnel axis to the building length (X/L) for different tunnel depths (H in meters) (ϕ =30°)

TABLE 3. The effect of increasing the input parameters up to 20% on the surface settlement (%)

Parameters	D	H	C	E	ν	Φ
Values Obtained from Sensitivity Analysis	0.85	1.05	0.52	0.97	0.74	0.67

*D: Tunnel Diameter; H: Tunnel Depth; C: Cohesion; E: Modulus of Elasticity; ν: Soil Poisson's Ratio; Φ: Internal friction angle

on a 20% increase in the mentioned parameters. The significant difference between the actual values indicates the greater impact of the deleted parameter on the results. Accordingly, the effect of various parameters used in modeling was investigated. Generally, values greater than 0.9 indicate a significant impact of the parameter on the output (settlement), and values less than 0.8 represent a weak effect on the output parameter [14].

According to Table 3, the depth of the tunnel had the highest effect on the surface settlement, which can be prevented by controlling the tunnel depth relative to the surface. Also, among the geomechanical parameters of the soil, the modulus of elasticity and cohesion parameters had the highest and the lowest effects on the surface settlement, respectively.

4. CONCLUSION

In this study, finite element numerical modeling aimed to predict the effect of tunneling on surface settlement in sand-clay soils. According to the obtained results and comparing the numerical modeling with the results of other researchers, the modeling performed with ABAQUS software provides acceptable results. Therefore, the use of ABAQUS software is recommended as a useful tool to model and predict the surface settlement under the influence of tunneling. According to the output of the modeling, the surface settlement increases with an increase in the tunnel diameter (D), which is related to the increase in excavation volume and the removal of part of the soil mass along with the occurrence of strains that leads to surface settlement. Also, as the depth of the tunnel (H) increases, the settlement decreases. The results of the sensitivity analysis showed that out of the tunnel parameters studied in this study, the depth of the tunnel had the most impact on the surface settlement, and it is possible to avoid surface settlement by controlling the tunnel depth. As the width (B) and length (L) of the building increase, the settlement decreases; but this decrease is more for changes in the width of the building, which can be attributed to the greater cross-section of the foundation and an increase in its stiffness so that the settlement of the foundation becomes more uniform and more resistant to displacement. As the lateral distance between the building and the tunnel (X) increases, the surface settlement increases initially, and after an approximately equal distance to the tunnel diameter, the settlement changes show a steady trend. The highest increase in settlement is between 0 and 10 meters because most vertical and lateral pressure changes occur in this range. As the internal soil friction angle (ϕ), soil cohesion (C), and the modulus of elasticity (E) increase, the surface settlement decreases. According to the results of sensitivity analysis, among the geomechanical parameters of the soil examined in this study, the modulus of elasticity and cohesion had the highest and lowest effect on the surface settlement, respectively. In general, the results of numerical modeling showed that if the exact parameters of soil and building are available, numerical modeling provides acceptable results in the estimation of surface settlement resulted in from the surface building.

5. REFERENCES

1. Zhu H., Shi L. "Application of Typical Engineering. In: Methodology of Highway Engineering Structural Design and Construction." ***Advanced Topics in Science and Technology in China***, Vol. 59. (2021), 73-231. DOI: https://doi.org/10.1007/978-981-15-6544-1_5
2. Chen I, Rabczuk T, Bordas S, Liu GR, Zeng KY, Kefriden P. "Extended finite element method with edge-based strain smoothing (esm-xfem) for linear elastic crack growth." ***Computer Methods in Applied Mechanics and Engineering***, Vol. 209, (2012), 250-265, DOI: 10.1016/j.cma.2011.08.013
3. Chen, R., Zhang, P., Wu, H., Wang, Zh., Zhong, Zh." Prediction of shield tunneling-induced ground settlement using machine learning techniques". ***Frontiers of Structural and Civil Engineering***, Vol. 13, (2019), 1363-1378. DOI: https://doi.org/10.1007/s11709-019-0561-3
4. Zhuang X, Zhou S, Sheng M, Li G. "On the hydraulic fracturing in naturally-layered porous media using the phase field method." ***Engineering Geology.*** Vol. 266, (2020), DOI:10.1016/j.enggeo.2019. 105306
5. Zhou, F., Molinari, J.F. "Dynamic crack propagation with cohesive elements: a methodology to address mesh dependence", ***International Journal of Numerical Methods in Engineering***, Vol. 59, No. 1, (2004), 1-24. DOI: https://doi.org/10.1002/nme.857
6. Rabczuk, T., Belytschko,T., "Cracking particles: a simplified meshfree method for arbitrary evolving cracks ***International Journal of Numerical Methods in Engineering,*** Vol. 61, No. 13, (2004), 2316-2343. DOI: https://doi.org/10.1002/nme.1151
7. Atkinson, J.H., Potts, D.M. "Subsidence above Shallow Circular Tunnel in Soft Ground", ***Journal of Geotechnical Engineering Division, ASCE,*** Vol. 103, G.T.4, (1977), 307-325. DOI: http://worldcat.org/oclc/3519342
8. Bobet, A. "Analytical Solutions for Shallow Tunnels in Saturated Ground", ***Journal of Engineering Mechanics***, Vol. 127, No. 12, (2001), 1258-1266. DOI: https://doi.org/10.1061/(ASCE)0733-9399(2001)127:12(1258)
9. Moorak, S. "Response analysis of nearby structures to tunneling-induced ground movements in clay soils", ***Tunneling and***

Underground Space Technology, Vol. 56, (2016), 90-104. https://doi.org/10.1016/j.tust.2016.01.032

10. Dalong, J., Dajun, Y., Xinggao L., Haotian, Z. "Analysis of the settlement of an existing tunnel induced by shield tunneling underneath", ***Tunneling and Underground Space Technology*** Vol. 81, (2018), 209-220. DOI: https://doi.org/10.1016/j.tust.2018.06.035
11. Selby, A.R. "Tunneling in Soil Ground Movement and Damage to Building in Workington, UK", ***Geotechnical and Geologocal Engineering,*** Vol. 17, (1999), 351-371. DOI: https://doi.org/10.1023/A:1008985814841
12. [12] Franzius, J.N., Potts, D.M. "Influence of mesh geometry on three-dimensional finite element analysis of tunnel excavation", ***ASCE International Journal of Geomechanics*** Vol. 5, No. 3, (2005), 256-266. DOI: https://doi.org/10.1061/(ASCE)1532-3641(2005)5:3(256)
13. Cao, L., Zhang, D., Fang, Q. "Semi-analytical prediction for tunneling-induced ground movements in multi-layered clayey soils", ***Tunneling and Underground Space Technology***, Vol. 102, (2020), DOI: https://doi.org/10.1016/j.tust.2020.103446
14. Barla, C. "Continuum and Discontinuum Modeling in Tunnel Engineering", Italian Ministry for University and Technological Research (M.U.R.S.T) as part of the Research Program, Tunneling in Difficult Condition, Vol. 12, No. 1, (2000), 45-57. DOI: https://hrcak.srce.hr/5033
15. Mahmoudi, M., Rajabi, A.M "Application of numerical back analysis for determination of soil mass specifications during tunnel construction". ***Arabian Journal of Geosciences***, Vol. 13, No. 19, (2020), 1-9. DOI: https://doi.org/10.1007/s12517-020-05935-1
16. Manual, A.: ABAQUS documentation version 6.13. Dassault Systems SIMULIA Corp., Providence, RI, USA (2013)
17. Civaleka, Ö., Öztürkb B. "Discrete singular convolution algorithm for non-linear transient response of circular plates resting on Winkler-Pasternak elastic foundations with different types of dynamic loading." ***Indian Journal of Engineering & Materials Sciences***, Vol. 16 (2009), 259-268. DOI: http://hdl.handle.net/123456789/6038
18. Cengiz, C., Guler, E. "Load bearing and settlement characteristics of Geosynthetic Encased Columns under seismic loads." ***Soil Dynamics and Earthquake Engineering***, Vol, 136, (2020), 106244. DOI: https://doi.org/10.1016/j.soildyn. 2020.106244
19. Feng, W-Q., Yin, J-H., Chen, W-B., Tan M D-Y., Wu P-Ch. "A new simplified method for calculating consolidation settlement of multi-layer soft soils with creep under multi-stage ramp loading." ***Engineering Geology***, Vol. 264, (2019), 105322. DOI: https://doi.org/10.1016/j.enggeo. 2019.105322
20. Wu, P.-Ch., Feng, W-Q., Yin, J-H. "Numerical study of creep effects on settlements and load transfer mechanisms of soft soil improved by deep cement mixed soil columns under embankment load.", ***Geotextiles and Geomembranes***, Vol. 48, (2020), 331-348. DOI: https://doi.org/10.1016/j.geotexmem. 2019.12.005

Persian Abstract

چکیده

در این مطالعه با استفاده از نرم‌افزار اجزای محدود آباکوس، تاثیر پارامترهای مختلف از جمله قطر تونل (D)، عمق تونل (H)، عرض (B)، طول (L)، تعداد طبقات و فاصله افقی ساختمان از محور تونل (X) و ویژگی‌های خاک شامل زاویه اصطکاک داخلی (ϕ) نسبت پواسون (υ)، مدول الاستیسیته (E) و چسبندگی (C) روی نشست خاک مورد بررسی قرار گرفته است. نتایج نشان می‌دهد که با افزایش زاویه اصطکاک داخلی خاک، میزان نشست کاهش یافته و با کاهش مدول الاستیسیته و چسبندگی خاک به علت سخت شدن خاک نشست افزایش می‌یابد. همچنین در یک عمق ثابت با افزایش قطر تونل نشست زمین افزایش می‌یابد در حالی که با افزایش عمق قرارگیری تونل میزان نشست کاهش می‌یابد. تغییرات عرض و طول ساختمان نیز اثر مستقیم بر روی نشست دارد؛ به طوری که با افزایش عرض و طول ساختمان به علت افزایش سطح مقطع پی ساختمان و افزایش صلبیت و سختی آن، نشست پی سازه یکنواخت‌تر و در برابر جابجایی از خود مقاومت بیشتری نشان می‌دهد و نشست زمین کاهش می‌یابد. همچنین با افزایش فاصله سازه از محور تونل نشست زمین کاهش پیدا کرده و پس از فاصله‌ای معادل با قطر تونل، روند ثابتی داشته است. نتایج آنالیز حساسیت انجام گرفته نشان می‌دهد در بین پارامترهای انتخاب شده، عمق قرارگیری تونل بیشترین تاثیر را در نشست سطح زمین دارد که با کنترل عمق قرار گیری تونل از سطح زمین می‌توان از نشست‌های سطح زمین جلوگیری نمود. همچنین دربین پارامترهای ژئومکانیکی خاک، در این مطالعه پارامتر مدول الاستیسیته بیشترین تاثیر را روی نشست سطح زمین دارد. در نهایت نتایج این مطالعه نشان می‌دهد تاثیر مشخصات تونل، سازه و خاک بر روی نشست زمین به خصوص در محیط‌های شهری بسیار حائز اهمیت است و بایستی مورد توجه طراحان قرار گیرد.

IJE TRANSACTIONS B: Applications Vol. 34, No. 05, (May 2021) 1094-1104

International Journal of Engineering

Journal Homepage: www.ije.ir

Strength Capacity Cracks Propagations Deflection and Tensile Enhancement of Reinforced Concrete Beams Warped by Glass Fiber Reinforced Polymer Strips

M. M. Abbass[a], M. K. Medhlom[b]. I. F. Ali[c]

[a] *Consultant Structural Engineering Baghdad, Iraq*
[b] *Department of Civil Engineering College of Engineering Al Mustansiriyah University, Baghdad, Iraq*
[c] *Ministry of Transport and Communications, Baghdad, Iraq*

PAPER INFO

Paper history:
Received 05 October 2020
Received in revised form12 December 2020
Accepted 29 December 2020

Keywords: Cracks
Propagations Composite
Action Tensile Strength
Glass Fiber Reinforced Polymer
Strength Capacity
ANSYS
Finite Elements

ABSTRACT

Different approaches were adapted to strength the structural elements to increase the load capacity and reduce the deformation such as deflection. The easiest and light external strengthening of reinforced concrete members are Fiber Reinforced Polymer (FRP) family such as Armed, Carbon, Glass and Basalt, respectively. This paper presents the theoretical approach to check out the experimental tests of reinforced concrete beams strengthened by glass fiber reinforced polymer (GFRP) using finite elements method by ANSYS software in which all models are simulate the tested beams. All models have the same geometry and mechanical properties but differ in GFRP layers and width. The main objectives of present work are evaluating the strength capacity, cracks propagations, deflection and tensile enhancement of reinforced concrete beams warped by GFRP strips subject to four points static load. Analysisof results indicate that the presences of GFRP sheets enhance the capacity and ductility of reinforced concrete beams in additional to delay the post crack concrete. The delay in the formation of first crack, increase in the number of cracks and ultimate loads of the models compared with the control model. There are improvements in flexural strength based on the modulus of rupture. Also, the cracks propogation become less in case of presence of GFRP and there is improvements in tensile resistance due to flexural. Analysis results inicated that the presence of GFRP at the bottom face of reinforced concrete beam in case of two layers gave increase in ultimate load 104.3% as compared with the control model. The reduction of the deflection for same models is 10.84%. Factor of the modulus of rupture range between (0.76-1.36) that is more than with ACI code suggested as 0.6. All model results were close to the experimental tests.

***doi**: 10.5829/ije.2021.34.05b.03*

NOMENCLATURE

Symbol			
A_f	GFRP area (mm^2)	M_n	nominal flexural strength (N-mm)
c	Distance from extreme compression fiber to the neutral axis (mm)	M_u	factored moment at a section (N-mm)
d	distance from extreme compression fiber to centroid of tension reinforcement (mm)	β_1	ratio of depth of equivalent rectangular stress block to depth of the neutral axis
f_{fu}	design ultimate tensile strength of GFRP (MPa)	φ	strength reduction factor
f_s	stress in steel reinforcement (MPa)	ψ_f	GFRP strength reduction factor = 0.85 for flexure (calibrated based on design material properties)
h	overall thickness or height of a member (mm)	M_n	nominal flexural strength (N-mm)

1.INTRODUCTION

Concrete as a material is very weak to resist tensile stress that developed in tension concrete zone due to applied loads. When the internal stress in the structural members increased the cracks will increase [1]. The mechanical properties of GFRP high strength to weight ratio, lightweight and giving better solution for strengthening. Hence, adopt in structural members. Strengthening reinforced concrete beam by GFRP with orientation of fiber reinforcements along the beam

*Corresponding Author Email: mohammadmakki2003@gmail.com (M. M. Abbass)

Please cite this article as: M. M. Abbass, M. K. Medhlom. I. F. Ali, Strength Capacity Cracks Propagations Deflection and Tensile Enhancement of Reinforced Concrete Beams Warped by Glass Fiber Reinforced Polymer Strips, International Journal of Engineering, Transactions B: Applications Vol. 34, No. 05, (2021) 1094-1104

increasing flexural resistance of beam, stiffness, reduce in deflection and enhance the tensile strength so that the cracks reduced [1]. Wraped of a simple reinforced concrete beams by FRP layered showed the beams were carried excessive uniform loads in flexure when the layers in the bottom face [2]. The models of simply supported concrete beams that simulated by finite elements approach gave the same behavior and failure modes the same as the reinforced concrete beams strengthened by FRP laminates but differed in capacity, deflection and stress. Applied FRP strips for concrete members increased in the strength to improve the reinforced concrete beams [3, 4]. Presence of GFRP in bottom of reinforced concrete beam showed high post crack and enhanced the strength capacity of reinforced concrete beams [5]. The relative displacements that developed in concrete surface and GFRP was proportional [6]. GFRP recover damage of reinforced concrete members with excellent durability against environment [7]. Presences of FRP lead to increase the shear strength capacity of the reinforced concrete continuous beam over than 25% as compared with the control beam [8]. Modulus of elasticity and yield strength of FRP are affected on the strength capacity of concrete beam and the global average reliability between the unstrengthening and strengthening beams with strips and full wrapped were differ in strength capacity [9]. The rehabilitated and strengthened coupling beams with FRP sheets can achieve appropriate strengths even larger than those of original beams [10]. In case of adopted flexible torsion bar in the design of trailing edge flap system showed a beneficial decreased in torsional stiffness, while increased the bending stiffness of the whole system. In addition, the worm gear drive gave a high torque to overcome aerodynamic force on the flap area and the torsional rigidity of support bar, but also plays as a brake to avoid instability due to the high torsional flexibility of the support bar [11]. The GFRP reinforcement having lower modulus of elasticity, gave in higher deflection than the steel reinforced specimens which have higher modulus of elasticity and the ultimate moment carrying capacity of the GFRP reinforced beam. That beam gave higher than the conventional steel reinforced beam [12]. Automated the printed process lead to make the use of the beam more efficient. This makes the method also attractive for expert users, who want to maximize the quality of their work [13]. The use of FRP composite jackets gave much better performance in terms of ductility as compared with the reinforced concrete refrence [14].

2. AIM AND SIGNIFICANT RESEARCH

The aims of present study to evaluate the strength capacity, cracks propagations, deflections and tensile stress enhancement performance of reinforced concrete beams warped by GFRP located at tension zone and assumed full interactions as surface bound with bottom face of the beams that subjected to four-point static loading using finite elements approach by ANSYS software. The parameters that taking into accounts are GFRP layers and widths. The actual loadings from experimental tests were applied in finite elements ANSYS software to predicate the full performance of reinforced concrete beams strengthened by GFRP and checking with experimental tests.

3. THEORETICAL ANALYSIS

Bonding of GFRP in the tension face of the simply supported reinforced concrete beam to increase the flexural resistance of the reinforced concrete beams, reducing deflection and improve the tensile resistance of concrete against internal tension stress in which the GFRP oriented along the beam span. Therefore, that works as main reinforcement and enhancing the amount of reinforcements in tension zone. Based on ACI – 440 – 2R – 2008 [15], the strength designs of the reinforced concrete beam satisfy Equation (1):

$$\varphi M_n \geq M_u \tag{1}$$

The ultimate moment capacity of the reinforced concrete (RC) beam according to ACI – 318 – 2019 [15] was calculated without presences of GFRP (control model). The mode of failure of reinforced concrete beam flexural in case of strengthening with GFRP relay on the crushing of concrete compression zone (when the concrete strain reaching 0.003), plane before the reinforcements yield, or the reinforcements yield and then followed by GFRP sheets tension zone, other case reinforcements in tension zone yield then the concrete in compression level crushing and de-bonding of the GFRP sheets.

The nominal strength as flexural for RC beam strengthening with GFRP calculated by Equation (2) [16]. The ultimate moment with and without presences of GFRP were calculated based on the mechanical properties [1].

$$M_n = A_s f_s (d \frac{\beta_1 c}{2}) + \psi_f A_f f_{fe} (h \frac{\beta_1 c}{2}) \tag{2}$$

4. MODELS GEOMETRY AND SPECIFICATIONS

Seven models are simulated with the same dimensions and geometry include control model without GFRP while other models differ in GFRP layers and width that matching the real experimental works [1]. The model dimensions that simulates by ANSYS (150x150x700 mm) in which the span beams are 620 mm with total reinforcements are located at the bottom (2ϕ8) and (2ϕ4) at top, the stirrups ϕ6@90 mm c/c as shown in Figure 1. The total length of GFRP layer is 580 mm along the beam span [1], Tables 1 and 2 lists the models details and material mechanical properties. The model mark is COMPW-N in which COMP is composite model, W is the GFRP width, N is number of layer. Stress–strain behavior reinforcement assumed that elastic–full plastic is shown in Figure 2. Figure 3 stress–strain curve for concrete and Figure 4 is devoted to GFRP. The GFRP thickness is 0.43 mm.

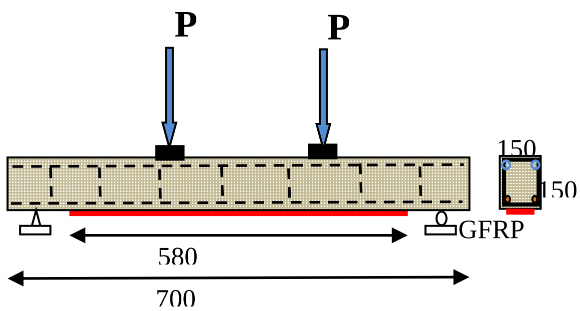

Figure 1. Model dimensions (all in mm)

TABLE 1. Beams model specification

Model mark	COMP 25-1	COMP 25-2	COMP 50-1	COMP 50-2	COMP 100-1	COMP 100-2	RC w/o GFRP
GFRP width (mm)	25	25	50	50	100	100	NA
Number of layer	1	2	1	2	1	2	NA

TABLE 2. Material mechanical properties

Concrete		Reinforcements		GFRP	
f_c (MPa)	E_c (MPa)	f_y (MPa)	E_s (MPa)	f_y (MPa)	E_s (MPa)
40	36450	420	200000	875	75900

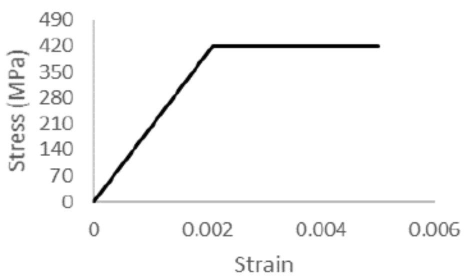

Figure 2. Stress–strain for reinforcement

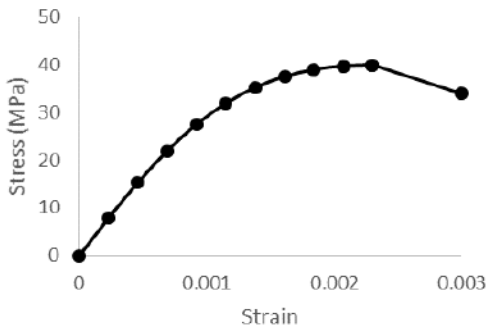

Figure 3. Stress–strain for concrete

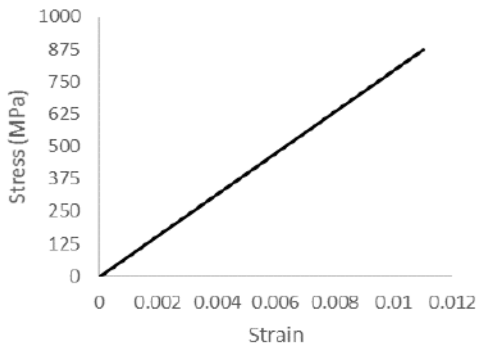

Figure 4. Stress – strain for GFRP

5. NUMERICAL APPROACH

Average load capacities were taken from the previous test [1] that adopted and applied to the models that is simulated by ANSYS [17]. The loads were applied under four points and the models were run as static analysis. The model is divided into a numbers of small elements, 70 elements longitudinal direction (each element is 10 mm), 12 elements in width and depth directions that mean each element is 12.5 mm. All lines within the beam model are divided to produce meshes, lines meshes adopted after many trails to select the mesh size to get near close solutions. The connections between rebar nodes is similar to the concrete solid nodes, so that the concrete and steel reinforcement nodes are merged (full interaction, no slip and friction). The same approach was adopted for GFRP composites. The tolerance value of 0.05 is used as displacement control during the nonlinear solution for convergence.

6. FINITE ELEMENTS MODELING

Numerical analysis using finite elements approach by ANSYS software is adopted to simulate all reinforced concrete beams strengthened by GFRP including the control model. Different elements were selected to represent the actual behavior of concrete, plate supports, plate under loads, reinforcements as main and stirrups and GFRP layer. SOLID65 element used for concrete material in which three degrees of freedom at each nodes plus translations. LINK180 element is adopted to simulate all steel reinforcement. SOLID185 is chosen to represent the steel plates that locates under the applied loads and supports. SHELL181 element is used to simulate GFRP layer due to this element having membrane (in-plane) stiffness [17]. Smeared crack is the best representation of reinforced concrete members such as adapt beam. The open and close coefficients for concrete cracks were 0.2 and 0.7 respectively. The materials nonlinearity for steel rebar's and concrete are behaved as elastic – full plastic reinforcements, concrete linear up to 0.3fc', elastic up to 0.85 fc', maximum value of concrete strain is 0.003. The main assumptions of numerical analysis for the plane section remain plane before and after applied loads, the concrete is homogeneous, full bounds between concrete and reinforcements, full interactions between the concrete and GFRP layers and the material nonlinearity of GFRP is linear up to failure and the self-weight of beam not considered in analysis that match the experimental tests. Figure 5 shows the beam model meshes. Figure 6 shows the main and stirrupd reinforcements, Figure 7 shows the wireframe model. In addition, Figures 8, 9 and 10 shows the GFRP elements of model COMP25, COMP50 and COMP100, respectively.

7. LOADING AND SUPPORTS CONDITIONS

The average of three applied load for each specimen that tested for each beam are lists in Table 3. All applied loads adopted from tested beams [1].

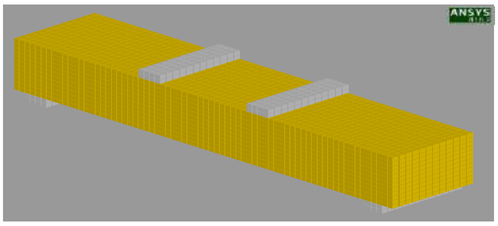
Figure 5. Beam model meshes

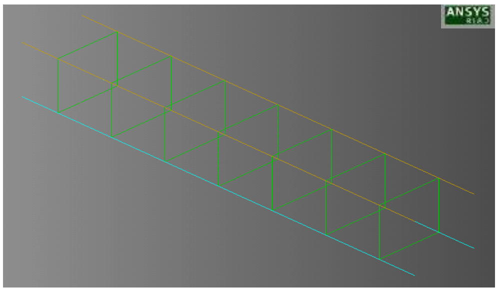
Figure 6. Main and stirrups reinforcements elements

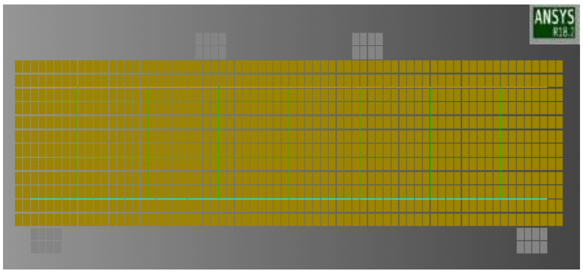
Figure 7. Model wireframe

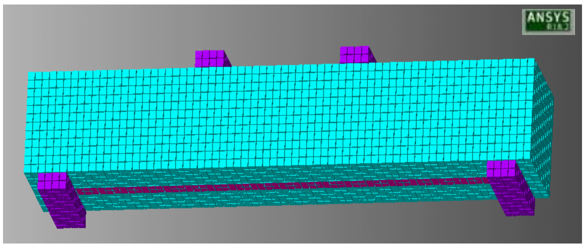
Figure 8. Model COMP25

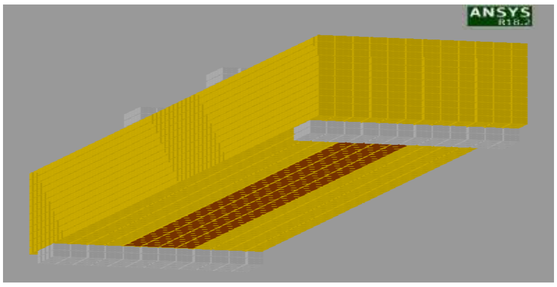
Figure 9. Model COMP50

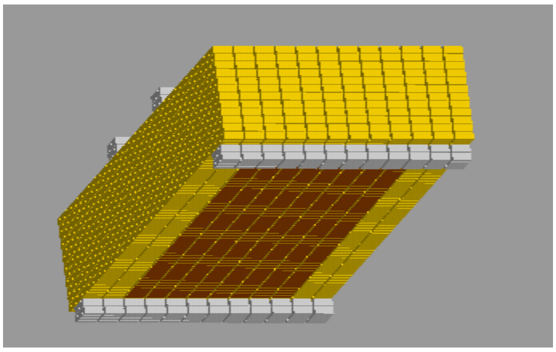
Figure 10. Model COMP100

The loads are divided into series of point loads that applied at the top center line of the upper plates. The supports conditions are simply supported in which the left support simulated as roller that zero displacement in vertical direction. The right support is pin so that restraint in longitudinal and vertical directions. The loads were applied at the central upper nodes that located at the tops of steel plates in which the loads

TABLE 3. Applied loading (average)

Spaceman mark	Specimen No.	Load (P) from tests (kN) [1]	Average loading (kN) 2P
	1	31	
COMP25-1	2	*20	68
	3	37.5	
	1	38	
COMP25-2	2	34	72
	3	32	
COMP50-1	1	33	70
	2	38	
	1	48	
COMP50-2	2	49	98.5
	3	51	
	1	46	
COMP100-1	2	53	95
	3	44.5	
COMP100-2	1	42	91
	2	49	
RC w/o GFRP-control	1	24	48

*Unexpected failure

were distributed through nodes. Figure 11 shows the loads and supports conditions.

8. ANALYSIS RESULTS

The static analysis of all models included the control model such as strength capacity, cracks propagations, deflection and tensile strength caused by flexural loadings, are discuses and compare with the test results [1].

8. 1. Crack Pattern Figure 12 represents the cracks propagations at the ultimate load stage for all models and compares the cracks intensity with

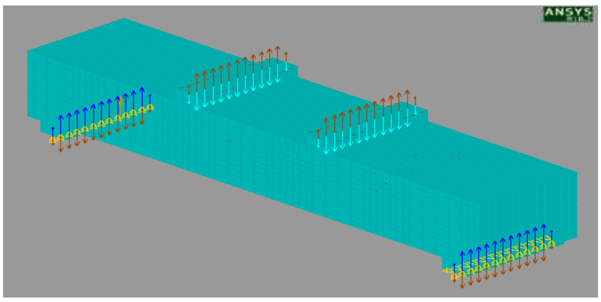

Figure 11. Loads and supports conditions

experimental tests. The circular shape that is lies in the plane represents the cracks while the crush concrete at the compression zone shown as octahedron. Comparisons of cracks patterns between reference and beam with one layer of GFRP (specimen COMP25-1) at ultimate loadings from experimental test that show same cracks propagations. The cracks concentration become less in presence of GFRP at the same loading of reference that is mean the GFRP make the reinforce concrete beam more ductile and there is improvement in elastic deformation of the reinforced concrete beams at early stage of applied loads. The modulus of rupture and splitting tensile strength fcr and fct are based on ACI-318 – 2019, respectively [16] stated as follows:

$$f_{cr}0.56(fc')^{0.5} \quad (3)$$

$$f_{ct}=0.60(fc')^{0.5} \quad (4)$$

Based on the numerical analysis the load caused first crack lists in Table 4. The factor (*k*) 0.56 and 0.6 if increased that means there is improvement in tensile resistance of concrete in tension zone due to tensile load and bending, respectively. Also, there are improvement in elastic deformation for each specimen. The new values of the factor in presence of GFRP base on the crack loadings from numerical analysis lists in Table 4 with the new values of factor (*k*).

8. 2. Load-Deflection Behavior Figures 13 to 18 represent the deflection behavior of all models at

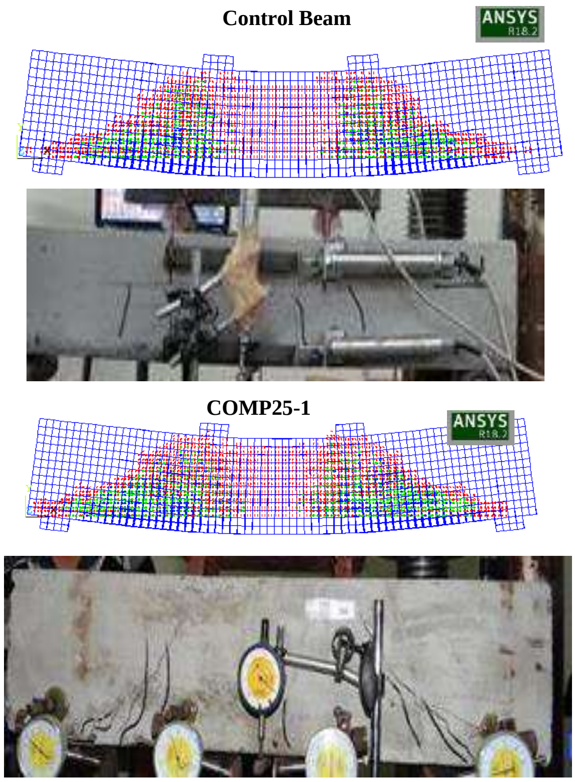

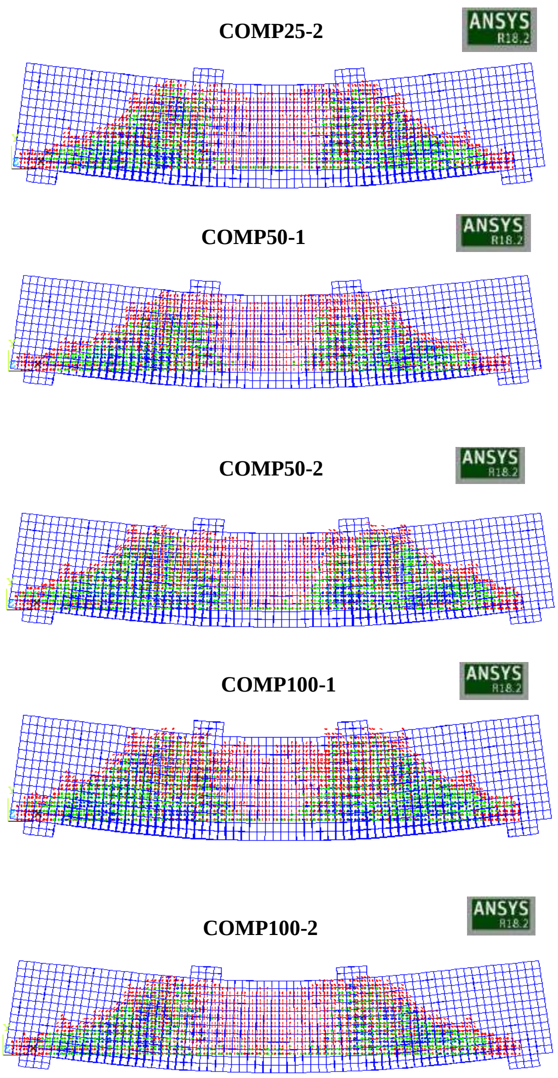

Figure 12. Cracking of the control and RC beams strengthening by GFRP Strips

TABLE 4. First crack loadings, modulus of ruptures and the factor *k*

Model mark	**COMP 25-1**	**COMP 25-2**	**COMP 50-1**	**COMP 50-2**	**COMP 100-1**	**COMP 100-2**
Crack loading (kN)	26	36	34	46	44	47
Modulus of rupture (MPa)	4.77	6.62	6.25	8.45	8.09	8.63
Factor *k*	0.76	1.05	0.99	1.33	1.28	1.36
%Enhancements of factor *k*	26.6	75.0	65.0	121	113.	126

ultimate applied load, all model results show close with that in test results. Figure 19 shows the full performance of load-deflection for all models that compare with experimental behavior. The difference between the changes in slopes at various ultimate load levels of the seven beams is a direct result of composite and non-composite behavior. When the load is applied gradually, at its initial stage, only reinforced concrete section works resisting 15-30% of the applied load. After this point, the composite section kicks in and works in full or partial interaction depending on the type of connection between RC beam and GFRP. RF represents reference beam, up 50% of maximum applied loading is linear and within elastic range and serviceability. After that around 76% become nonlinear that means in the range of elastic – plastic and first cracks developed due to increase in loading and the slop become along the longitudinal direction indicated that the material become weak. The next performance is full nonlinear and the slop become toward horizontal up to failure. COMP25-1 up to 25% of maximum applied loading is linear and within elastic range and serviceability, after that around 80% become nonlinear that means in the range of elastic – plastic and first cracks developed due to increase in loading. The behavior of composite is better than that reference beam because of in presence of GFRP delay the cracks in tension face because it is enhancement in resistance tensile strength of concrete tension zone become more resistance. After cracks developed a full nonlinear and the slop become toward horizontal up to failure due to decrease in the beam stiffness because that increase in loads that lead increase the deflections. All other beams, linear up to 22% of maximum applied loading and cracks developed around 86% because of the same reasons mentioned above. COMP25-1 to COMP100-2 are linear and after that become nonlinear according to capacity of composite beam that is really on the number of GFRP layers and scheme layout. The behavior of composite beam rely on where, width and number of layers to re-strengthening RC beam. The permissible deflection values for structural members are listed in the ACI 318-2019 code [16]. According to this reference, the maximum allowable deflection for simply supported beams under service loads should not be greater than L/360. Therefore, the maximum deflection of a beam 680 mm span becomes equal to 1.723 mm. However; if FRP is used, then the deflection ratio changes and according to ACI 440-2R [15], the maximum deflection ratio for composite beams (beams with GFRP) is L/250, which results become approximatly 2.48 mm-deflection. Table 5 lists the comparisons between the experimental and finite elements approach as maximum deflections and compare the models results with control model. Mean value founded from statistical analysis and the standard deviation, variance and coefficient of correlation as the ratio for numerical results and experimental tests showed closed. Figure 20 shows the performance of load and deflection results with number of layers of GFRP. Increase GFRP layer width that lead to increase the value of load beam capacity and reduce deflection due to increase in beam stiffness, reinforcement in tension zone and make the concrete more ductile due to presence of GFRP sheet. Deflections and crack intensity of models with GFRP strips have higher elastic modulus and moment of inertia due to composite action of reinforced concrete neams wrapped by GFRP strips are less than at the same load contrl model. Analysis results of the numerical simulations clearly showed that beam capacity, stiffness degradation and failure mode of failure are significantly influenced by the GFRP widths and thickness. GFRP makes the concrete more ductile so that reduceing in deflection and cracks become less. The reduced in deflections and cracks due to composite beam delay the formation of plastic hinge that make the deflection at first crack load to the maximum deflection less si that the ductility increase in presence of GFRP sheets.

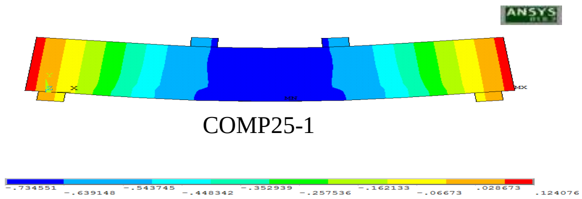

Figure 13. Deflection of COMP25-1 at ultimate load

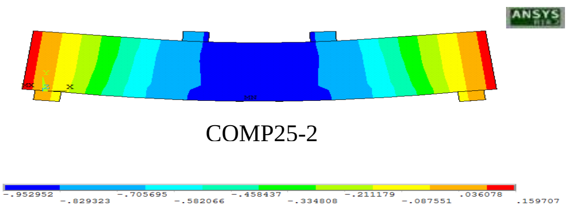

Figure 14. Deflection of COMP25-2 at ultimate load

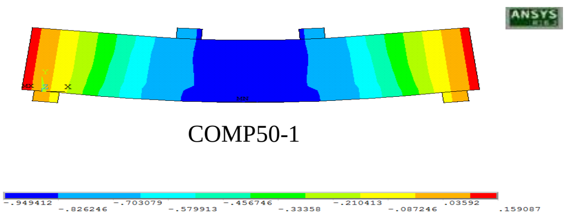

Figure 15. Deflection of COMP50-1 at ultimate load

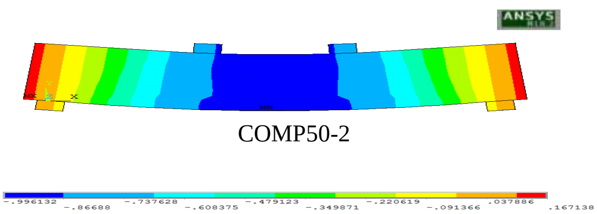

Figure 16. Deflection of COMP50-2 at ultimate load

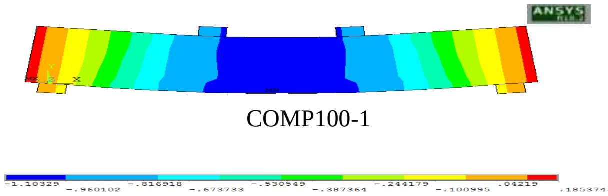

Figure 17. Deflection of COMP100-1 at ultimate load

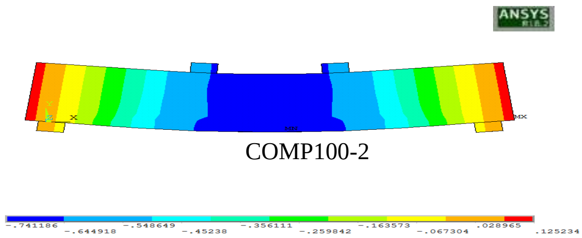

Figure 18. Deflection of COMP100-2 at ultimate load

TABLE 5. Comparison results

Spaceman mark	Specimen No.	Max.Deflection on Tests (mm) [1]	Max.Deflection on FEM (mm)	Ratio (Max. deflection-test/Max. deflection - FEM)	Deflection at loading from reference beam (mm) – FEM ANSYS
COMP25-1	1 2 3	0.78	0.73	0.94	0.73
COMP25-2	1 2 3	0.94	0.95	1.01	0.71
COMP50-1	1 2	0.78	0.95	1.01	0.69
COMP50-2	1 2 3	0.98	0.99	1.01	0.61
COMP100-1	1 2 3	1.18	1.10	0.93	0.65
COMP100-2	1 2	0.75	0.74	0.99	0.49
RC w/o GFRP- RF	1	0.88	0.83	0.94	0.83
Mean				0.98	
Standard deviation				0.037	
Variance				0.0014	
Coefficient of correlation				0.85	

8. 3. Principle Stresses and Principle Straines

The plane that make angle with the beam axis have a point that lie in this plane occur maximum normal and shearing stresses. Such plane is the principle plane that is developed principle stresses. Increases in applied load make increase in internal tension stress at the location of tension zone that creating cracks so that principle stresses with direction 45° that lead to diagonal cracking as shown in Figure 12 which is perpendicular to the planes of principle tensile strength. To prevent dangerous or decreasing the cracks within limit, GFRP strips used to enhance the tensile behavior of reinforced

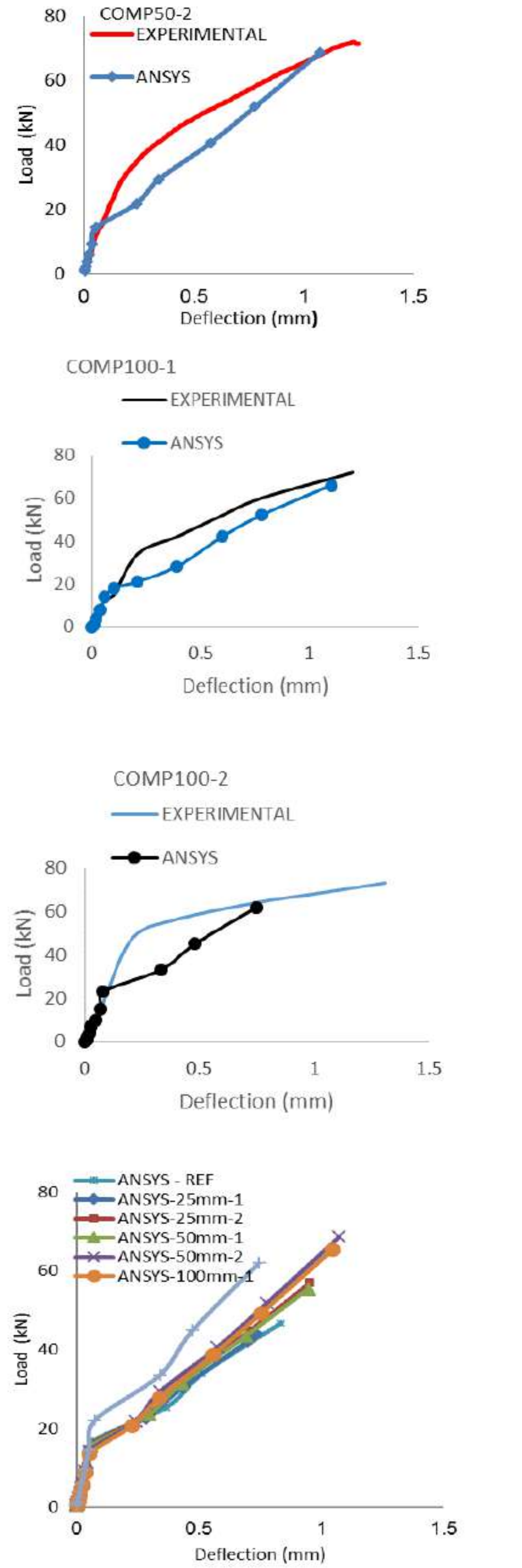

Figure 19. Load–deflection curves for all modeling that compared with test results

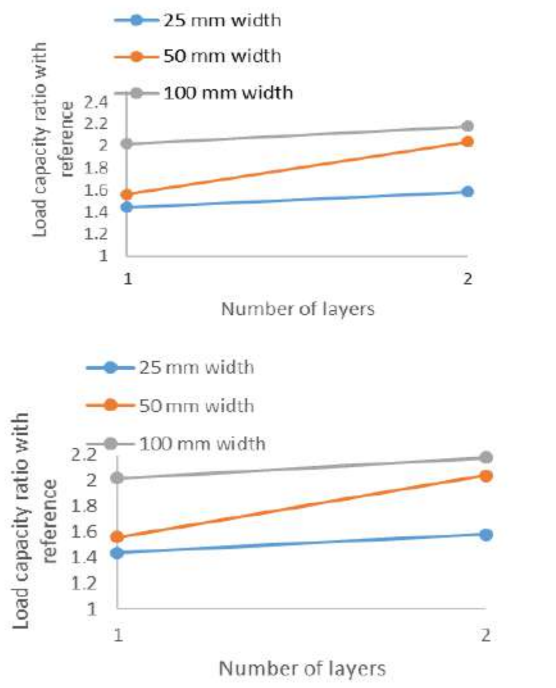

Figure 20. Behavior of load-deflection results with number of layers of GFRP

concrete beam. Figure 21 shows the principle stress for reference beam that the stresses concentrated and directed vectors toward the top. Figure 22 represents the principle stresses of beam strengthened by GFRP 2 layers, so the principle stresses vector toward the bottom and there are a concentration of stresses there. The principle strain for reference beam and strengthening beams presented in Figures 23 and 24, respectively. The principle strain at ultimate load it is more concentrated than in case of reference beam, so that presence of GFRP make the RC beam more ductile and the strain reduced, the deflection and tensile stresses reduced. The Von Misses criteria (yield criteria) which is written as follows:

$$(\sigma_1-\sigma_2)^2+(\sigma_1-\sigma_3)^2+(\sigma_2-\sigma_3)^2=2f_y^2 \tag{5}$$

In which σ_1, σ_2 and σ_3 represent first, second and third principle stress and f_y is the yield strength. The vector principle stresses represent the stress path through the model due to applied load. Principle stress shown in Figure 21 different distributions, Figure 22 for beam with GFRP100-2 due to presences of GFRP that concentrated vectors at the bottom at the location of GFRP that sustained and increase the strength capacity of the beam and increase in flexural resistance due to increase in whole beam stiffness. Based on the numerical analysis of the models, the failure criteria that adopted are flexural not shear or torsion. Failure occur for all models in concrete without spalling of GFRP due to reach the concrete ultimate experimental loads that applied from experimental tests [1]. The vector stress distributions of beam with GFRP100-2 more intensity than control beam model under the nutral axis in the zone of tension zone near tensile reinforcing and GFRP that assumed cracked that means there is concrete tension enhancement in this zobe.

9. STRENGTH CAPACITY OF REINFORCED CONCRETE BEAM BASED ON ACI-318 AND ACI-440-2R

Figure 25 shows the point's distributions around the 45° line that represent the experimental test results and the analytical analysis results for strength capacity of reinforced concrete beam with and without GFRP strips.

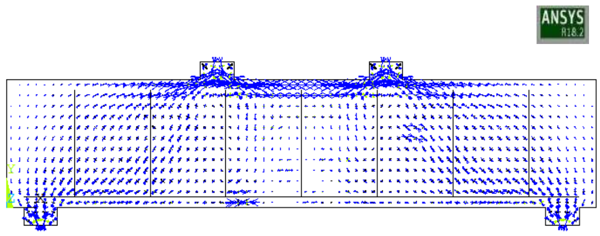

Figure 21. Principle stress vector of control beam

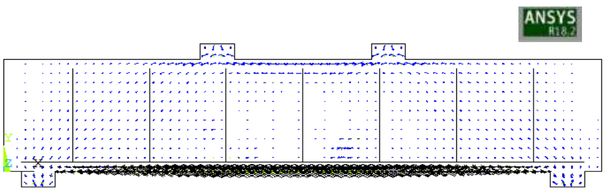

Figure 22. Principle stress vector of beam with GFRP100-2

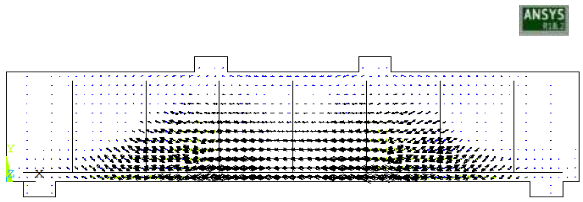

Figure 23. Principle strain vector of beam control beam

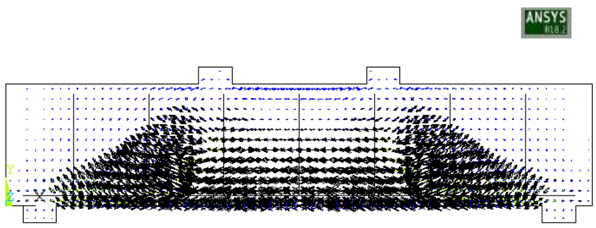

Figure 24. Principle strain vector of with GFRP100-2

Figure 26 represents the deflections at failure load. The point's lies about and close to the straight line that indicates the numerical analysis results are conservative. Table 6 lists the maximum load capacity based on ACI-318 and ACI-440-2R that compare with the experimental test results.

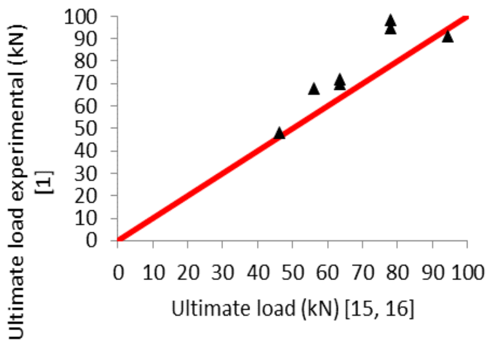

Figure 25. Comparisons between experimental and analytical analysis ultimate load capacity

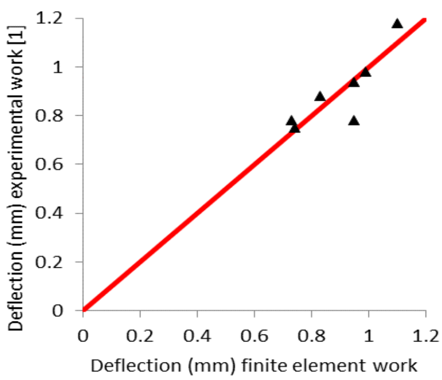

Figure 26. Comparisons between experimental and numerical analysis deflection at ultimate load

TABLE 6. Comparisons between average experimental and theoretical ultimate loads

Spaceman mark	Average loading (kN) 2P-Exp.	Loading (kN) 2P-ACI-440-2R [15]	% (Exp./ Theoretical)
COMP25-1	68	56.25	120.88
COMP25-2	72	63.65	113.11
COMP50-1	70	63.65	109.97
COMP50-2	98.5	78.15	126.04
COMP100-1	95	78.15	121.56
COMP100-2	91	94.5	96.35
RC w/o GFRP-control	48	46.25 [16]	103.78

10. DISCUSSIONS AND CONCLUSION

In this paper, numerical analysis using finite elements approach by ANSYS software and analytical solution results using formula presented in ACI-440-2R-08 [15], several conclusions may be drawn as follows:

1. Analysis results of the numerical simulations clearly showed that beam capacity, cracks intensity, deflections tensile resistance and mode of failure are significantly influenced by the GHFRP layers and widths. Results from analytical solution for ultimate load capacities showed close with that in experimental tests. Flexural strengthening of reinforced concrete beams with the GFRP sheets is effective, as significantly improved the flexural performance in which in case of two layers of GFRP gave ultimate load 94.5 kN; while, the control model gave 46.25 kN that was increased by 104.32%, the reduction of the deflection for same models as COMP100-2 with RC w/o GFRP-control the reduction is 10.84%. The delay in the formation of first crack and the increase in the number of cracks and ultimate loads of the models compared with the control model. Increasing the layer width and amount of the strengthening layers improved the flexural performance of the models compared with the control model. The model COMP100-2 compared with the model COMP50-2, an increase in ultimate strength is 20.92%.
2. Presences of GFRP layers minimized the cracks proportions due to there is enhancement in tensile resistance for reinforced concrete beam. The presence structure material like GFRP in the tension zone increase the concrete resistance against bending that lead to increase in the tension stress that developed inside concrete in the tension zone. The crack patterns at the final loads from the finite element models correspond well with the observed failure modes of the experimental beams.
3. Two layers of GFRP improve the serviceability, flexural performance and increase strength beam capacity. model COMP100-2 compare with the model COMP100-1, an increase in ultimate strength is 20.92%.
4. Increase in GFRP width become more effective to enhancement the beam performance such as reduce in deflection, increase load capacity and reduce in cracks intensity. COMP100-2 compare with the model COMP50-2, the decrease in deflection is 25.25%.
5. All strengthening beams modelling including control beam "reference beam" as compared with tests result as deflection in case of values and general behaviour listed in Table (5) showed a closed result, so the verification levels results had shown a good agreement between FE modelling procedures using ANSYS and the results from tested results published before [1]. The mean value is 0.98 that is close to unity.
6. Presence of GFRP in tension zone delay in load that cause first crack that lead to delaying earlier failure and shifting failure load to increase. The presences of GFRP plies are useful to enhance concrete member behaviour in resisting loads. In case of two layers of GFRP model COMP100-2 gave crack load 47 kN while the control model gave 25 kN that lead to 88% zone delay in load that cause first crack. Presence of GFRP delays the post cracking of reinforced concrete beam. The concrete cracks in model analysis due to the principal stress are tensile with a crack plane normal to this principal stress. Based on the first crack loadings in case of presence of GFRP that make the factor k become more that indicates there is improvement and enhancement in the tensile stress in tension zone due to flexural loadings. The increase in factor k in case of increase in width COMP100-2 with COMP50-2 and layers model COMP100-2 compare with COMP100-1 were 2.26% and 6.25%, respectively. Increase in factor k that indicate there is enhancement in elastic deformation that lead the first crack loadings become more in case of increase GFRP layer or increase in width of GFRP. Increase in factor k that make the concrete strain increase that indicate the concrete become more ductile.
7. Analysis results from finite element models has some difference as compare with test results due to in model in finite elements slightly more stiffness than the actual experimental tests and the effects of bond slips and the developed micro-cracks occurred in the actual beams were excluded in the finite element models.

11. REFERENCES

1. Abbass, M.M., "Enhancement of the tensile strength of reinforced concrete beams using gfrp", ***International Journal of Scientific Engineering and Technology***, Vol. 3, No. 12, (2014), 1424-1430. doi.
2. Ali, F.F., Shawky, R.M. And Al-Sayed, A.-T.A., "Finite element modeling of strengthened simple beams using frp techniques," a parametric study", Vol. 2, No. 2, (2011).
3. Viradiya, S.R. and Vora, T.P., "Comparative study of experimental and analytical results of frp strengthened beams in flexure", ***International Journal of Research in Engineering and Technology***, Vol. 3, No. 4, (2014), 555-561. doi: 10.15623/ijret.2014.0304097
4. Tarigan, J., Patra, F.M. and Sitorus, T., "Flexural strength using steel plate, carbon fiber reinforced polymer (CFRP) and glass fiber reinforced polymer (GFRP) on reinforced concrete beam in building technology", in IOP Conference Series: Earth and

Environmental Science, IOP Publishing. Vol. 126, No. 1, 012025.

5. Goldston, M., Remennikov, A. and Sheikh, M.N., "Experimental investigation of the behaviour of concrete beams reinforced with gfrp bars under static and impact loading", ***Engineering Structures***, Vol. 113, (2016), 220-232. doi: 10.1016/j.engstruct.2016.01.044.

6. Rashidi, M. and Takhtfirouzeh, H., "An experimental study on shear and flexural strengthening of concrete beams using gfrp composites", arXiv preprint arXiv:1808.10008, (2018). doi: https://doi.org/10.37516/global.j.civ.eng.2019.0047.

7. Siddika, A., Al Mamun, M.A., Alyousef, R. and Amran, Y.M., "Strengthening of reinforced concrete beams by using fiber-reinforced polymer composites: A review", ***Journal of Building Engineering***, Vol. 25, (2019), 100798. doi: 10.1016/j.jobe.2019.100798.

8. Elrawaff, B., Abdul Samad, A.A. and Alferjani, M., "Experimental and theoretical investigation on shear strengthening of rc precraced continuous t-beams using cfrp strips", ***International Journal of Engineering***, Vol. 28, No. 5, (2015), 671-676. doi: 10.5829/idosi.ije.2015.28.05b.04.

9. FADAEE, M.J. and Dehghani, H., "Reliabilty-based torsional design of reinforced concrete beams strengthened with cfrp laminate", ***International Journal of Engineering, Transactions A: Basics***, Vol. 26, No. 10, (2013), 1103-1110. doi: 10.5829/idosi.ije.2013.26.10a.01.

10. Mohammadi, H., Esfahani, M. and Riyazi, M., "Behavior of coupling beams strengthened with carbon fiber reinforced polymer sheets", ***International Journal of Engineering, Transactions B: Applications***, Vol. 20, No. 1, (2007), 49-58. doi.

11. Ha, K., "Innovative blade trailing edge flap design concept using flexible torsion bar and worm drive", ***HighTech and Innovation Journal***, Vol. 1, No. 3, (2020), 101-106. doi.

12. Balamuralikrishnan, R. and Saravanan, J., "Finite element modelling of rc t-beams reinforced internally with gfrp reinforcements", ***Civil Engineering Journal***, Vol. 5, No. 3, (2019), 563-575. doi: 10.28991/cej-2019-03091268.

13. Jung, S., Peetz, S. and Koch, M., "Poeam–a method for the part orientation evaluation for additive manufacturing", in Sim-AM 2019: II International Conference on Simulation for Additive Manufacturing, CIMNE., 440-443.

14. Shadmand, M., Hedayatnasab, A. and Kohnehpooshi, O., "Retrofitting of reinforced concrete beams with steel fiber reinforced composite jackets", ***International Journal of Engineering, Transactions B: Applications***, Vol. 33, No. 5, (2020), 770-783. doi: 10.5829/ije.2020.33.05b.08.

15. Kuchma, D.A., Wei, S., Sanders, D.H., Belarbi, A. and Novak, L.C., "Development of the one-way shear design provisions of aci 318-19 for reinforced concrete", ***ACI Structural Journal***, Vol. 116, No. 4, (2019).

16. Bakis, C.E., Ganjehlou, A., Kachlakev, D.I., Schupack, M., Balaguru, P., Gee, D.J., Karbhari, V.M., Scott, D.W., Ballinger, C.A. and Gentry, T.R., "Guide for the design and construction of externally bonded frp systems for strengthening concrete structures", ***Reported by ACI Committee***, Vol. 440, No. 2002, (2002). doi.

17. Ansys manual reference help version 18.2, ansys multiphasic, ansys, inc. Is a ul registered iso 9001:2000 company.

Persian Abstract

چکیده

رویکردهای مختلف برای تقویت عناصر سازه ای برای افزایش ظرفیت بار و کاهش تغییر شکل مانند انحراف ، سازگار شدند. ساده ترین و سبکترین تقویت خارجی اجزای بتن آرمه به ترتیب الیاف تقویت شده از خانواده پلیمر مانند مسلح ، کربن ، شیشه و بازالت (AFRP، CFRP، GFRP و BFRP)است. در این مقاله رویکرد نظری برای آزمایشی تیرهای بتن آرمه تقویت شده توسط GFRP با استفاده از روش عناصر محدود توسط نرم افزار ANSYS که در آن همه مدل ها تیرهای آزمایش شده را شبیه سازی می کنند ، ارائه شده است. همه مدل ها دارای هندسه و خصوصیات مکانیکی یکسانی هستند اما در لایه ها و عرض GFRP متفاوت هستند. اهداف اصلی کار حاضر ارزیابی ظرفیت مقاومت ، انتشار ترک ، انحراف و افزایش کشش تیرهای بتونی مسلح است که توسط نوارهای GFRP تحت چهار بار استاتیکی تاب خورده است. نتایج تجزیه و تحلیل نشان می دهد که وجود ورق های GFRP باعث افزایش ظرفیت و شکل پذیری تیرهای بتن مسلح می شود تا بتونی بعد از ترک خوردگی به تأخیر بیفتد. تاخیر در تشکیل اولین ترک ، افزایش تعداد ترک ها و بارهای نهایی مدل ها در مقایسه با مدل کنترل. بهبودهایی در مقاومت خمشی بر اساس مدول پارگی وجود دارد. همچنین در صورت وجود GFRP میزان انتشار ترکها کمتر می شود و در مقاومت در برابر کشش به دلیل خمش بهبودی حاصل می شود. نتایج تجزیه و تحلیل حاکی از آن است که وجود GFRP در سطح پایین تیرآهن بتن آرمه در صورت وجود دو لایه باعث افزایش بار نهایی ۱۰۴.۳٪ در مقایسه با مدل کنترل می شود و کاهش انحراف برای مدلهای مشابه ۱۰.۸۴٪ ، عامل دامنه مدول پارگی بین (۰.۷۶–۱.۳۶) که بیش از کد ACI به عنوان ۰.۶ پیشنهاد شده است. همه نتایج مدل با آزمایش های آزمایشی نشان می دهد.

International Journal of Engineering

Journal Homepage: www.ije.ir

The Effects of Mathematical Modelling of Magneto-rheological Dampers on Its Control Performance: A Comparative Study Between the Modified Bouc-Wen and the Maxwell Nonlinear Slider Hysteretic Models

R. Karami Mohammadi, H. Ghamari*

School of Civil and Environmental Engineering, KN Toosi University of technology, Tehran, Iran

PAPER INFO

Paper history:
Received 18 October 2020
Received in revised form 13 March 2021
Accepted 24 March 2021

Keywords:
Magneto-rheological Damper
Semi-active Control
Maxwell Nonlinear Slider Model
Bouc-Wen Model
Linear Quadratic Regulator Algorithm
Nonlinear Instantaneous Optimal Control

ABSTRACT

Input voltage of Magneto Rheological (MR) dampers is the only controllable parameter as a semi-active control device. Therefore, voltage selection has an important role in control procedure via MR dampers. In many of semi-active control algorithms, a mathematical modelling method is required for determining the MR damper voltage at each time instant. As a result, applying different mathematical modelling methods can lead to different voltages for the MR damper, which subsequently results in different control performance. In the present research, the effects of mathematical modelling method of an MR damper hysteretic behaviour on its control performance were investigated. The most exact and common Maxwell nonlinear slider and modified Bouc-Wen hysteretic models were employed through a nonlinear comparative numerical study. A building structure was utilized for numerical investigations. A ten-story office building steel structure is excited by seven acceleration time histories. Nonlinear instantaneous optimal control and linear quadratic regulator controllers were utilized as two active-based semi-active algorithms. Results of nonlinear investigations showed an obvious difference between the Maxwell nonlinear slider and the modified Bouc-Wen models from the control performance viewpoint. Outputs show a very slight better performance for the MNS model in reducing the nonlinear responses.

***doi**: 10.5829/ije.2021.34.05b. 04*

NOMENCLATURE

R , Q	Wheighting matrices	J	Performance index
A	open-loop plant matrix	B	Control force locating matrix
M , C , K	Mass, damping, stiffness matrices	$\ddot{x}_g$	Ground acceleration
E_h	Hysteretic energy	ζ , η	Constants of NIOC algorithm
ρ	Constant	P	solution of the Riccati equation
$\{H\}$, $\{\delta\}$	Force-adjustment vectors	u	Control input
$\{z(t)\}$	State vector	k	Optimal gain matrix
x , $\dot{x}$, $\ddot{x}$	Vector of relative displacement, velocity, and acceleration response.	$f_v(t)$, $f_x(t)$	Internal force vectors
y , z	Variables of the modified Bouc-Wen and MNS models	Δt	Lattice time step
$\alpha, c_o, k_o, k_1, c_1, n, A$	Modified Bouc-Wen parameters	c, k, a, b, n, m_o	MNS model parameters
I , O	Identity and zero matrices	Δ , Δ_R	Interstory drift and residual drift

* Corresponding Author Email: hghamari@mail.kntu.ac.ir (H. Ghamari)

Please cite this article as: R. Karami Mohammadi, H. Ghamari. The Effects of Mathematical Modelling of Magneto-rheological Dampers On Its Control Performance; A Comparative Study Between the Modified Bouc-Wen and the Maxwell Nonlinear Slider Hysteretic Models, International Journal of Engineering, Transactions B: Applications Vol. 34, No. 05, (2021) 1105-1117

1. INTRODUCTION

Vibration control of structures intends to preserve the vibration behaviour of a structure within a desired range. Ha [1] used a method for the reduction of rotor blade vibrations and noise. There are several types of motion control for a structure. In a performance viewpoint, there are three control categories: Active, passive, and semi-active manners. Passive control devices generate control force using the local response of the installation location. Characteristics of passive devices are not changeable. Active control devices generate control forces using an external source of electric power based on a pre-defined control algorithm. However, there is a deficiency: the drawback of this category is that, external power supply may disconnect during severe earthquakes. Also, the energy which is applied to the structure by active devices may lead to instability. On the other side, this control type is adaptable. Semi-active control devices produce control forces utilizing the local response of the installation location of device. Nevertheless, a semi-active device can change its characteristics during the excitation using a relatively small power supply e.g., a few batteries. Therefore, this system enjoys the positive features of both active and passive vibration control systems, namely, adaptability and stability [2-9].

There are numerous semi-active control devices such as Magneto-rheological (MR) dampers, Electro-rheological (ER) dampers, variable orifice devices, variable stiffness devices, etc. Among of all the semi-active devices, MR fluid based dampers are the most applicable type due to their valuable characteristics. MR damper includes micron-sized polarizable particles. These particles are dispersed in a carrier medium such as mineral or silicone oil (see Figure 1). MR fluid can change from a linear Newtonian fluid to a nonlinear semi-solid material. This transformation occurs in milliseconds due to change in magnetic field which is imposed on the MR damper. Thus, MR damper properties can change within a very short time when its commanding voltage and magnetic field changes. In addition, MR fluid has a high capacity of energy dissipation, due to the large value of yielding stress [10]. These dampers could be manufactured by a 3D printing technique such as Inject Binder technique which is introduced on Ntintakis et al. [11]. Input voltage of MR damper is the only directly controllable parameter of this damper [12]. Therefore, one of the most important phases of the control process is voltage determination using an appropriate control algorithm.

In some of the semi-active control algorithms such as Clipped Optimal Control (COC), a desired control force is determined using a reference active control algorithm such as LQR, NIOC, H^2/LQG, etc. Consequently, an input voltage is set to achieve this reference active control force via MR damper, [2, 3, 6, 7, 13-15]. In an active-based semi-active control method, the controller is mostly an optimal active controller. The calculated desired active control force is converted to voltage v for current driver and a current i for MR damper. Then, the MR damper produces a control force based on local responses of its installation position and current i. This produced force can be different from the desired control force. Hashemi et al. [16] employed the Bouc-Wen model and developed a wavelet neural network-based semi-active method, which converts the desired control force to the MR damper voltage. Hiramoto et al. [17] proposed a new semi-active control strategy based on a reference active control law. Parameters of the reference active control law were optimized to improve semi-active control performance. Reference active control law predicts desired control forces. Then, based on this predicted control force, the command signal of semi-active control device is determined. The effectiveness of this method is demonstrated through a numerical investigation on a 15-DOF structural system. Liu et al. [18] introduced a semi-active control method using MR damper. They utilized an active-based method for determining the reference control forces via LQR algorithm. This research showed the efficiency of their proposed approach, especially in mitigating the drift and acceleration responses. Zafarani and Halabian [19] developed a model-based semi-active control algorithm for MR dampers. They used a simplified Bouc-Wen model for modelling MR damper hysteretic behavior. They employed active-based semi-active control algorithms for controlling the nonlinear structures. Azar et al. [20] used of three MR dampers through an eleven-story structure. They investigated on optimizing the placement of dampers through the structure. Cruze et al. [21] proposed a new type of MR damper and tested this damper. They used this damper for controlling a scaled structure in a numerical investigation. They concluded this damper is an effective device for alleviating the responses of structure. Jenis et al. [22] proposed a permanent magnet which is installed on MR dampers to promote the abilities of this damper in case of power supply failure.

NIOC method can be used for controlling the nonlinear structures in active control, without the risk of instability of structure [13, 23]. In this algorithm, the control law for the (k+1)'th time step is defined as follows:

$$u_{k+1} = \frac{1}{12}\eta^{-1}R^{*^{-1}}B^{T}\left[Pz_{k+1} + q_{k+1}\right] \tag{1}$$

where B stands for a matrix which locates active control forces vector (u(t)). The NIOC method cost function J is formulated as follows:

$$J_{k+1} = z_{k+1}^{T}Qz_{k+1} + u_{k+1}^{T}Ru_{k+1} \tag{2}$$

Q has to be a positive semi-definite matrix and R must be a positive definite matrix. If Q matrix is chosen relatively large, the response reduction has more importance than the reducing control forces. The NIOC algorithm is used in nonlinear structures as well as linear structures. There is more detailed discussion about the above formulation and notations in Huang et al. [13].

The LQR method uses the subsequent quadratic performance index [6]:

$$J=\int_{\circ}^{\infty}\left[z^{T}(t)Qz(t)+u^{T}(t)Ru(t)\right]dt \tag{3}$$

The LQR control law is:

$$u=kz \tag{4}$$

k represents the optimal gain matrix which minimizes the performance index J subjected to constraint $\left\{\dot{z}(t)=[A]\{z(t)\}+\{H\}\ddot{x}_g(t)+[B]\{u(t)\}\right\}$. Notations of the LQR method are same as those equations of the NIOC. More discussions are available in Fuller et al. [6] and Pourzeynali et al. [14].

A mathematical representation is mostly required for converting a reference control force to input voltage of MR damper, especially in active-based semi-active control algorithms. Spencer et al. [24] proposed a modified Bouc-Wen model. They investigated on a phenomenological model in comparison with three other mathematical models through a set of experimental tests. They showed that the modified Bouc-Wen model can predict the MR damper behavior more accurately than Bingham, Gamota-Filisko and classic Bouc-Wen models. Cha et al. [12] utilized the modified Bouc-Wen model on their real-time hybrid tests. They identified modelling parameters of the modified Bouc-Wen model of a 200-kN MR damper through some experimental tests. They used this model for controlling a three story office building steel structure by employing active-based semi-active control algorithms. Chae et. al. [10] proposed Maxwell Nonlinear Slider (MNS) model for modelling MR dampers and tested a 300-kN MR damper. This research utilized two other mathematical models for comparison purposes: the modified Bouc-Wen, and the hyperbolic tangent models. Their research showed a good accuracy for the modified Bouc-Wen model. Also, they proved there was a better conformity between the experimental results and the MNS model predictions. Winter and Swartz [25] proposed a small scale MR-fluid extraction damper for testing the small-scale structures equipped with MR dampers. They used a Bouc-Wen model for mathematical representation of the damper. Daniel et al. [4] tested a small scale MR damper within a 3 story small scale structure. They reported that displacement response of all stories was reduced about 50% with a small MR damper which is installed in the 1st story. Rastegarian and Sharifi [26] investigated on the correlation of inter-story drift and performance levels of an RC frame. Here, inter-story drifft is considered as one of assessment criteria. Aghajanzadeh and Mirzabozorg [27] investigated on concrete fracture process which can be undertaken for a RC frame.

In previous researches the main concern of MR damper mathematical model selection was the accuracy and a better agreement between the predictions of the model and the real responses. Effects of mathematical model of MR damper on global control performance of structure are investigated in this research, whereas, no attention was paid earlier. Sapinski et al. [28] and Chae et al. [10] compared different models of MR damper considering the accuracy of modelling with respect to experimental data. Nevertheless, previous researches had not investigated the control performance of these models. Actually, MR damper voltage and resulted control performance of the mentioned models will be different due to differences between the mathematical modeling. As a result, mathematical model selection is an effective part of control of a structure which can effect on control performance and will be investigated here.

At First of all, theoritical background is presented. This section contains an introduction to the MR damper, the modified Bouc-Wen and MNS models, and state-space representation of a system. At the end of this section the applied semi-active control algorithms are described. Next, by the numerical investigations part the utilized reference active control algorithms are designed, and the characteristics of MR dampers and structure which is used for numerical investigations are deployed. In this section, the results of semi-active control of investigated structure are presented. Both the modified Bouc-Wen and MNS models are used in the present research. Finally, conclusions part are summarized.

2. THEORETICAL BACKGROUND

A schematic of a 300-kN MR damper is depicted in Figure 1. This damper, manufactured by Lord Corporation, is used here for numerical investigations. Full characteristics of this large scale MR damper and its identifying tests were deployed by Chae et al. [10]. In subsequent sections, two of the most common models of hysteretic behaviour of an MR damper are introduced, namely: the modified Bouc-Wen, and the MNS models.

2. 1. Modified Bouc-Wen Hysteretic Model

A phenomenological Bouc-Wen model is utilized here to model the MR damper. This model is illustrated in Figure 2.

The modified Bouc-Wen model is formulated as follows [12]:

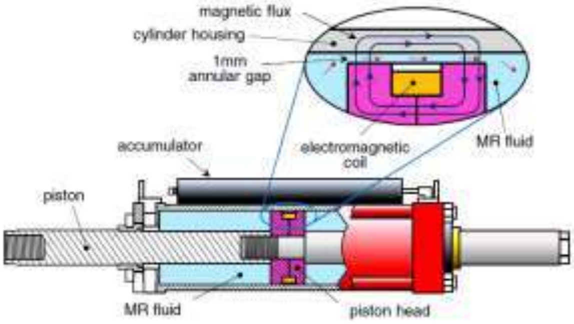

Figure 1. Schematic of the 300-kN MR damper [10]

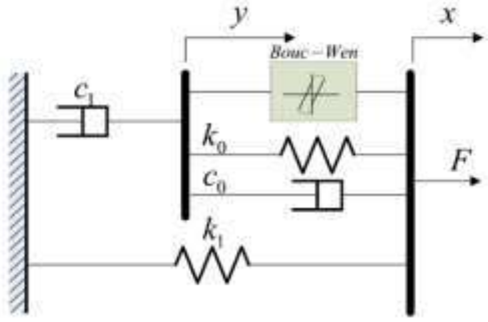

Figure 2. Schematic of mechanical model of MR damper (modified Bouc-Wen model [12, 20])

$$F = \alpha z + c_0(\dot{x} - \dot{y}) + k_0(x - y) + k_1(x - x_0) \tag{5}$$

$$c_1\dot{y} = \alpha z + c_0(\dot{x} - \dot{y}) + k_0(x - y) \tag{6}$$

$$\dot{z} = -\gamma|\dot{x} - \dot{y}|z|z|^{n-1} - \beta(\dot{x} - \dot{y})|z|^{n-1} + A(\dot{x} - \dot{y}) \tag{7}$$

where F stands for the damper force, c_1 represents the dashpot constant for behavior of MR damper at low velocities, k_1 reveals the accumulator stiffness, c_0 and k_0 denote the damping, and stiffness values at large velocities respectively, x_0 shows the initial displacement of the spring, k_1, α, β, γ, n and A are constants. These parameters have to be identified through experimental tests. The modified Bouc-Wen model was first introduced by Spencer et al. [24], and is utilized in many researches such as Sapinski et al. [28], Cha et al. [12], Chae et al. [10], etc.

2. 2. Maxwell Nonlinear Slider Model A schematic of the MNS model is shown in Figure 3. This model divides the response of an MR damper into two modes: pre-yield and post-yield modes. Pre-yield mode is represented by a Maxwell element, which includes a dashpot with coefficient c and a spring with stiffness k in series. In the pre-yield mode, the damper force f is calculated by solving the following differential equation:

$$f = k(y - z) = c\dot{z} \tag{8}$$

The responses of the pre-yield mode based on Chae et al. [10] experimental identifying tests are shown in Figure 4. They had compared the MNS and the modified Bouc-Wen models in their paper and they had concluded that the MNS model can predict the response of MR damper more accurate than the modified Bouc-Wen model. These curves were extracted at small amplitudes of harmonic loadings. Post-yield behavior can be divided into separate curves for positive and negative zones (see Figure 5). The following equation is formulated for positive curve of the post-yield mode:

$$f_{py}^{+}(\dot{x}) = \begin{cases} a^{+} + b^{+}|\dot{x}|^{n+} & \text{if } \dot{x} \geq \dot{x}_t^{+} \\ a_t^{+}(\dot{x} - \dot{x}_t^{+}) + f_t^{+} & \text{if } \dot{x} < \dot{x}_t^{+} \end{cases} \tag{9}$$

There is a similar equation for negative curve of the post-yield mode as follows:

$$f_{py}^{-}(\dot{x}) = \begin{cases} a^{-} + b^{-}|\dot{x}|^{n-} & \text{if } \dot{x} \leq \dot{x}_t^{-} \\ a_t^{-}(\dot{x} - \dot{x}_t^{-}) + f_t^{-} & \text{if } \dot{x} > \dot{x}_t^{-} \end{cases} \tag{10}$$

a, b, n and $\dot{x}_t$ are parameters of the MNS model. Also, $a_t^{\pm} = b^{\pm} \times n^{\pm} \times |\dot{x}_t^{\pm}|^{n^{\pm}-1}$ and $f_t^{\pm} = a^{\pm} + b^{\pm}|\dot{x}_t^{\pm}|^{n^{\pm}}$.

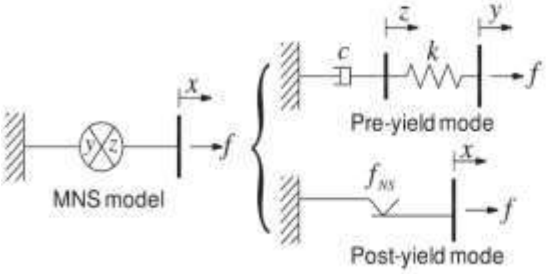

Figure 3. Schematic of mechanical model of MR damper (MNS model [10])

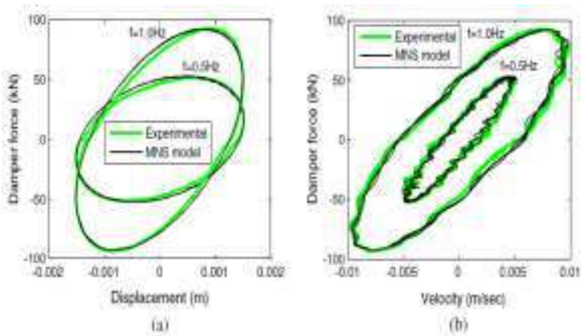

Figure 4. Pre-yield response of MR damper based on the MNS model: a) Force-displacement response. b) Force-velocity response [10]

Based on Figure 6, there is a small difference between increasing and decreasing phases on the MR damper response curves. Taking this issue into account, the subsequent equation is employed:

$$f=\begin{cases} f_{py}(\dot{x}) & \text{increasing phase} \\ f_{py}(\dot{x})+m_o(\ddot{x}) & \text{decreasing phase} \end{cases} \quad (11)$$

m_0 represents a constant. Chae et al. [10] completely introduced the MNS model at their research.

2. 3. State-Space Representation of Equation of Motion

Equation of motion of earthquake-excited structure can be written as follows:

$$[M]\{\ddot{x}\}+[C]\{\dot{x}\}+[K]\{x\}=[M]\{1\}\ddot{x}_g(t) \quad (12)$$

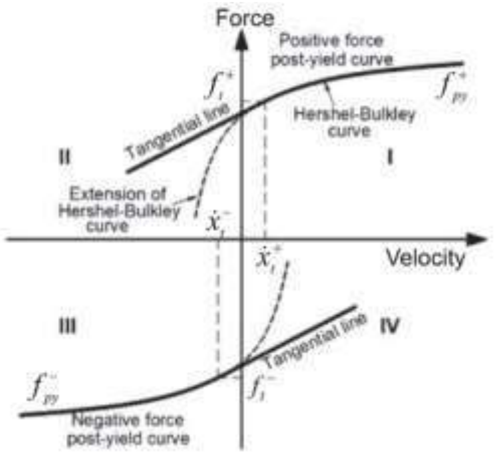

Figure 5. Post-yield curves of the MNS model [10]

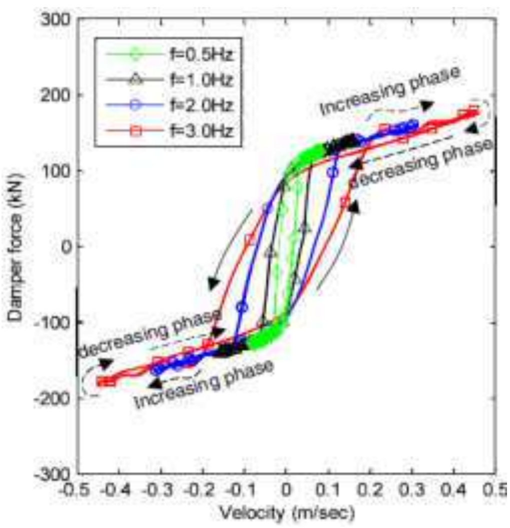

Figure 6. Force-velocity response of MR damper based on the MNS model [10]

[M], [C] and [K] represent the mass, damping, and stiffness matrices, respectively. x , $\dot{x}$ and $\ddot{x}$ denote the relative displacement vector, relative velocity vector, and relative acceleration vector of the system respectively. $\ddot{x}_g$ reveals the ground acceleration. The system can be transferred into state space as follows [6]:

$$\{\dot{z}(t)\}=[A]\{z(t)\}+\{H\}\ddot{x}_g(t) \quad (13)$$

z(t) denotes the state vector of system, [A] represents the open-loop plant matrix and {H} shows a matrix for adjustment of applying point(s) of earthquake inertia force.

$$[A]=\begin{bmatrix} [o] & [I] \\ -[M]^{-1}[K] & -[M]^{-1}[C] \end{bmatrix}_{2n\times 2n} \quad (14)$$

$$\{H\}=\begin{Bmatrix} \{o\} \\ [M]^{-1}\{\delta\} \end{Bmatrix}_{2n\times 1} \quad (15)$$

$\{\delta\}$ adjusts applying point(s) of inertia force, n stands for the number of stories, I and o denote the identity and zero matrices respectively. δ vector is defined as follows:

$$\{\delta\}=[-m_1 \quad -m_2 \quad \dots \quad -m_n]^T_{n\times 1} \quad (16)$$

Uppercase T suggests the transpose, and m_i represents the seismic mass of the i'th story. There is an introduction to the state space formulation in Fuller et al. [6].

2. 4. Semi-active Control Method

Two active-based semi-active control algorithms are employed here: an LQR-based method and an NIOC-based controller. The following steps describe an active-based semi-active control method:

1. An active control law has to be designed first. (Here, the LQR or NIOC)
2. The matrices of structural system are formed at each time step (m, c, and k matrices).
3. Reference active control force is calculated (Using formulation of the introduction part).
4. The reference active control force is converted to voltage of MR damper (Using an iterative procedure).

Based on previous researches such as Chae et al. [10] and Cha et al. [12], the parameters of an MR damper were always identified for some discrete values of currents. Therefore, there are only some discrete values of currents, which can be chosen for a specified mathematical model (e.g. modified Bouc-Wen, MNS, etc.). In the present research, the current determination will be an iterative process during every single time step. In this state, the analysis is implemented for all possible discrete currents, and the best current is selected as the current that commanded the MR damper. It results in better control performance, but at the cost of consuming more time. The above mentioned procedure is shown on the following flowchart (see Figure 7).

In the subsequent section, a ten-story office building will be used as a prototype steel structure. This structure will be studied for numerical investigation. Two reference active control algorithms are employed to control this structure.: a LQR based, and a NIOC based algorithms. Calculated control force will be converted to input voltage of MR damper. Ten MR dampers will be used for controlling the prototype ten-story structure.

3. NUMERICAL INVESTIGATIONS

A ten story office building steel structure is employed here for numerical investigations where all stories have an equal area of 22500 square feet. There are 6 bays in each direction with 25-ft width, and the height of all stories is 12.5-ft. Each primary direction is composed of eight MRF and four DBF in each primary direction. In Figure 8, MRF's are shown in blue color and DBF's depicted in yellow color, respectively. Plan of the structure is shown in Figure 7. The plan of this structure is very similar to Cha et al. [12]. In this office building, considerations and preservations of Pinheiro [29] and Burciaga [30] could be undertaken to make a green building.

This structures have a full symmetry in both primary directions of plan. In all four corners of plan, two columns are designed to maintain the full independence of two primary directions (see Figure 8). Therefore, only one-fourth of total area would be analyzed as tributary seismic area. Also, two directions will be considered independently due to symmetry principles. Cha et al. [12] used 0.6-scale model of three-story structure as shown in Figure 9a. Here, the full-scale structure is employed (see Figure 9b).

All diaphragms are supposed to be rigid. Now, two MRF of the structure will be analyzed in order to execute numerical investigations. Vertical degrees of freedom are eliminated using the static condensation method. Therefore, mass, and stiffness matrices of structure are extracted through finite element method. The damping matrix is calculated using the Rayleigh method with five percent of critical damping for the first, and the second mode of vibration.

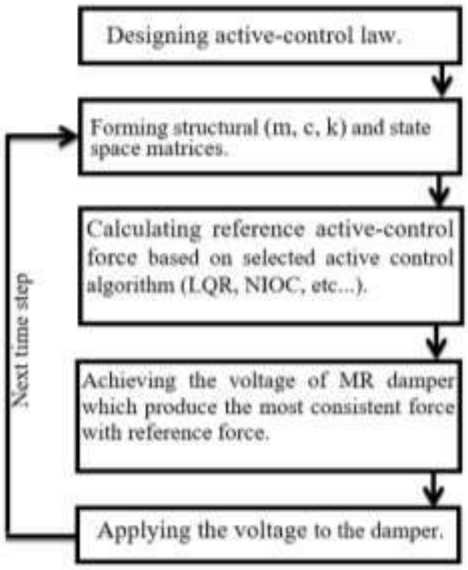

Figure 7. A schematic of the employed semi-active control algotithm

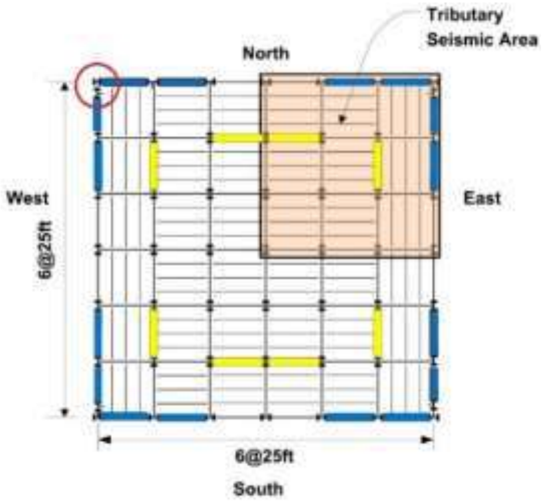

Figure 8. Structure model

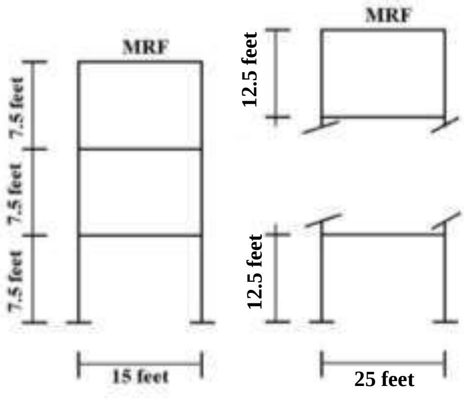

a.Three-story structure (Cha et al. [12]) b. Ten-story structure (Present study)

Figure 9. MRF frame model

The mass, damping, and initial stiffness matrices of structures are presented as follows:

[m]=

330000	0	0	0	0
0	326000	0	0	0
0	0	323000	0	0
0	0	0	322000	0
0	0	0	0	320000
0	0	0	0	0
0	0	0	0	0
0	0	0	0	0
0	0	0	0	0
0	0	0	0	0
0	0	0	0	0
0	0	0	0	0
0	0	0	0	0
0	0	0	0	0
0	0	0	0	0
319000	0	0	0	0
0	318000	0	0	0
0	0	316000	0	0
0	0	0	313000	0
0	0	0	0	301000

[C] =

1.15E+07	-5246889	971737.6	-165530	40224.73
-5246891	6520370	-3413867	673343.8	-78075
971737.9	-3413867	4945671	-2787034	506984.9
-165530	673343.5	-2787035	4282808	-2413674
40224.44	-78075.3	506984.6	-2413674	3682740
-8833.97	25294.38	-60835.9	438292	-2023057
1574.682	-5093.4	15474.84	-43469.3	372554.2
399.4307	1389.553	-2183.21	11366.06	-33629.4
-216.537	-175.655	44.15915	-2047.97	6975.204
932.3492	942.9214	1941.575	1528.17	-1051.23
-8833.88	1574.8	399.9862	-216.754	933.1585
25294.48	-5093.28	1390.091	-175.864	943.7005
-60835.8	15474.94	-2182.69	43.95329	1942.332
438292.1	-43469.1	11366.6	-2048.17	1528.935
-2023057	372554.3	-33628.9	6974.999	-1050.49
3160785	-1772419	299773.9	-16448.1	4307.57
-1772420	2722533	-1411131	180816.5	-11936.3
299773.6	-1411132	1935697	-875542	121494.1
-16447.9	180816.6	-875542	1364456	-609938
4306.851	-11937	121493.5	-609939	536925.5

[k] =

8.95E+08	-4.10E+08	7.60E+07	-1.29E+07	3.15E+06
-4.10E+08	5.06E+08	-2.67E+08	5.27E+07	-6.11E+06
7.60E+07	-2.67E+08	3.83E+08	-2.18E+08	3.96E+07
-1.29E+07	5.27E+07	-2.18E+08	3.31E+08	-1.89E+08
3.15E+06	-6.11E+06	3.96E+07	-1.89E+08	2.84E+08
-6.91E+05	1.98E+06	-4.76E+06	3.43E+07	-1.58E+08
1.23E+05	-3.98E+05	1.21E+06	-3.40E+06	2.91E+07
3.12E+04	1.09E+05	-1.71E+05	8.89E+05	-2.63E+06
-1.69E+04	-1.37E+04	3.45E+03	-1.60E+05	5.46E+05
7.29E+04	7.37E+04	1.52E+05	1.20E+05	-8.22E+04
-6.91E+05	1.23E+05	3.13E+04	-1.70E+04	7.30E+04
1.98E+06	-3.98E+05	1.09E+05	-1.38E+04	7.38E+04
-4.76E+06	1.21E+06	-1.71E+05	3.44E+03	1.52E+05
3.43E+07	-3.40E+06	8.89E+05	-1.60E+05	1.20E+05
-1.58E+08	2.91E+07	-2.63E+06	5.45E+05	-8.22E+04
2.43E+08	-1.39E+08	2.34E+07	-1.29E+06	3.37E+05
-1.39E+08	2.09E+08	-1.10E+08	1.41E+07	-9.33E+05
2.34E+07	-1.10E+08	1.48E+08	-6.85E+07	9.50E+06
-1.29E+06	1.41E+07	-6.85E+07	1.03E+08	-4.77E+07
3.37E+05	-9.34E+05	9.50E+06	-4.77E+07	3.84E+07

All matrices are presented in S.I. units. One can calculate the period of vibration modes utilizing an eigen analysis using the [k] and [m] matrices. It leads to 3.02, 1.09 and 0.62 s for the first three modes of vibration respectively. On the other hand, the analysis results of 3d model in the OpenSees™ finite element software show these periods as 3.05, 1.09 and 0.61 s respectively. These are very coincident.

Seven acceleration time histories are used here. Each record has a different value of PGA. Four records are scaled based on ASCE/SEI7-10 [31] method and three records are originally used as unscaled records. NORT, Kobe, Elcent and IMP records are scaled records. These are listed in the following Table 1. Large values of PGA, make the structure behave nonlinearly during analysis. Also, response spectrum of seven acceleration time histories are shown in Figure 10.

300-kN MR dampers are used here for numerical investigations. One MR damper will be installed in each single story. Therefore, there will be ten MR dampers for the ten-story structure. Parameters of these dampers were identified in Chae et al. [10] during experimental tests and used in the present paper. These parameters were given for discrete values of currents: 0, 0.5, 1.0, 1.5, 2.0 and 2.5 A.

Q and R matrices of LQR-based, and NIOC-based semi-active control methods are considered as Equation (17) and Equation (18).

$$Q = \rho \times \begin{bmatrix} 1 & \cdots & \circ \\ \vdots & \ddots & \vdots \\ \circ & \cdots & 1 \end{bmatrix}_{2n\times 2n} \tag{17}$$

TABLE 1. Acceleration time histories

Record Name	Earthquake	Year	Station Name	PGA
SAN	San Fernando	1971	Old Ridge Root	0.32g
Elcent	Elcentro	1940	Elcentro Array 9	0.50g
NORT	Northridge	1994	Alhambra 90	0.50g
VICT	Victoria Mexico	1980	Cerro Prieto	0.63g
Tabas	Tabas	1978	Tabas	0.86g
Kobe	Kobe	1995	Kobe University	1.00g
IMP	Imperial Valley	1979	Elcentro Array	1.50g

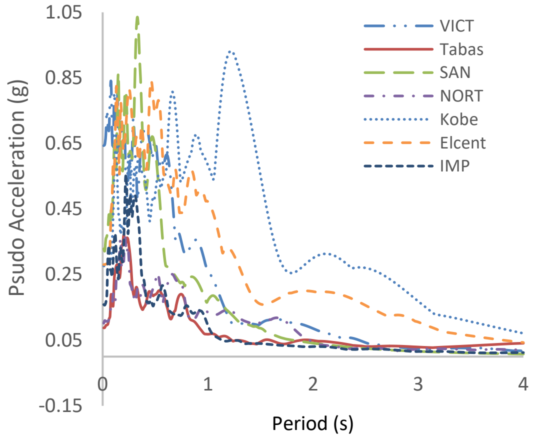

Figure 10. Response spectrum of the used acceleration time histories

$$R = \begin{bmatrix} 1 & \cdots & \circ \\ \vdots & \ddots & \vdots \\ \circ & \cdots & 1 \end{bmatrix}_{n\times n} \tag{18}$$

Coefficient of Q weighting matrix (ρ) is adjusted based on a set of pre-analysis results. When Q is selected relatively large, reducing the responses has more importance than reducing the control forces, and vice versa. Here, the allowable values for the maximum of control forces is set to 10% of the structural total seismic weight. On the contrary, if Q matrix is selected relatively small, then, the control performance would not be acceptable. Therefore, an optimum value has to be chosen. Two levels of control are introduced: cheap control and expensive control. In the cheap mode of control, small value of the maximum of control forces will be achieved, and the expensive mode of control tries to achieve the best control performance with a larger value of maximum of control forces. The ρ coefficient is adjusted for different control algorithms and different control modes based on previous comments. The results are listed in Table 2.

Three comparative criteria are introduced. The first is drift criterion, the second criterion belongs to residual drift, and the third one denotes hysteretic energy.

$$J_1 = \left\{ \frac{\max_{t,i} |\Delta_i(t)|}{\max_{t,i} |\Delta_{iU}(t)|} \right\} \tag{19}$$

$\Delta_i(t)$ represents the interstory drift of *i*'th story at time t and $\Delta_{iU}(t)$ shows the interstory drift of the uncontrolled structure at time t. J_2 criterion is defined as follows:

$$J_2 = \left\{ \frac{\max_i |\Delta_{iR}|}{\max_i |\Delta_{iRU}|} \right\} \tag{20}$$

TABLE 2. Coefficient of Q weighting matrix (ρ).

ρ Coefficient	cheap control	expensive control
LQR	1.0 e +11	3.0 e +11
NIOC	6.0 e +13	1.5 e +14

Δ_{iR} represents the residual drift of *i*'th story at the end of analysis, and Δ_{iRU} shows the residual drift of *i*'th story of the uncontrolled structure at the end of analysis.

$$J_3 = \left\{ \frac{\max_i E_{hi}}{\max_i E_{hUi}} \right\} \tag{21}$$

E_{hi} represents the total hysteretic energy of *i*'th story and E_{hUi} stands for the total hysteretic energy of i'th story of the uncontrolled structure. It should be noted that the hysteretic energy is calculated for moment-rotation curve of both ends of each beam.

UI Sim-Cor™ is implemented for analyzing the structure. This hybrid simulation code employs the OpenSees™, and Matlab™ softwares simultaneously. Implicit Newmark integration method with alpha equal to 0.25 and beta equal to 0.1667 is used. Results of analysis based on prementioned notes are calculated and listed in Table 3. In this table, the average values of the modified Bouc-Wen model and the MNS model are calculated for each mode of control. The ratio of average values of these two mathematical models are calculated in the Bouc/MNS rows. In addition to three defined criteria, the maximum of control forces among all stories are listed in the table.

TABLE 3. Results of evaluation criteria for ten-story structure

	LQR Based		NIOC Based	
	Cheap	**Expensive**	**Cheap**	**Expensive**
J1				
SAN Bouc	0.971	0.904	0.976	0.876
SAN MNS	0.952	0.828	0.957	0.761
Elcent Bouc	0.967	0.793	0.894	0.826
Elcent MNS	0.968	0.773	0.869	0.833
NORT Bouc	1.011	0.948	0.856	0.908
NORT MNS	1.009	0.945	0.848	0.896
VICT Bouc	0.954	0.849	0.911	0.737
VICT MNS	0.947	0.829	0.891	0.707
Tabas Bouc	0.881	0.739	0.883	0.823
Tabas MNS	0.875	0.732	0.88	0.82
Kobe Bouc	0.973	1.008	0.979	0.979
Kobe MNS	0.973	1.015	0.974	0.982
IMP Bouc	0.956	0.845	0.883	0.762
IMP MNS	0.945	0.848	0.85	0.768

Average Bouc	0.959	0.869	0.912	0.844
Average MNS	0.953	0.853	0.896	0.824
Bouc/MNS	1.007	1.019	1.018	1.025
J2				
SAN Bouc	0	0	0	0
SAN MNS	0	0	0	0
Elcent Bouc	0.8215	0.5531	0.8582	0.7140
Elcent MNS	0.8113	0.5334	0.7998	0.7183
NORT Bouc	0.9335	1.1168	0.9687	1.6330
NORT MNS	1.0008	1.1254	0.9090	1.6561
VICT Bouc	0	0	0	0
VICT MNS	0	0	0	0
Tabas Bouc	0.9640	0.9036	0.7460	0.5495
Tabas MNS	0.9837	0.8464	0.7371	0.5210
Kobe Bouc	1.0204	1.1593	1.0360	1.0688
Kobe MNS	1.0248	1.1721	1.0277	1.0937
IMP Bouc	0.9148	0.9069	1.0109	0.8535
IMP MNS	0.8912	0.9298	0.9678	0.9336
Average Bouc	0.6649	0.6628	0.6600	0.6884
Average MNS	0.6731	0.6581	0.6345	0.7032
Bouc/MNS	0.9878	1.0071	1.0401	0.9789
J3 (HE)				
SAN Bouc	0.961	0.955	0.988	0.928
SAN MNS	0.935	0.899	0.935	0.858
Elcent Bouc	0.801	0.566	0.904	0.711
Elcent MNS	0.772	0.558	0.902	0.706
NORT Bouc	0.773	0.524	0.564	0.424
NORT MNS	0.776	0.509	0.545	0.4
VICT Bouc	0.948	0.902	1.094	0.947
VICT MNS	0.929	0.885	0.945	0.854
Tabas Bouc	0.771	0.545	0.764	0.606
Tabas MNS	0.765	0.537	0.766	0.6
Kobe Bouc	0.909	0.851	0.942	0.874
Kobe MNS	0.904	0.85	0.938	0.871
IMP Bouc	0.73	0.459	0.778	0.579
IMP MNS	0.713	0.459	0.835	0.54
Average Bouc	0.842	0.686	0.862	0.724
Average MNS	0.828	0.671	0.838	0.69
Bouc/MNS	1.017	1.022	1.028	1.05
Control Force				
SAN Bouc	31	84	30	128
SAN MNS	44	84	84	131
Elcent Bouc	155	246	145	254
Elcent MNS	157	242	137	246
NORT Bouc	129	240	239	236
NORT MNS	122	238	237	235
VICT Bouc	49	92	96	135
VICT MNS	46	93	97	138
Tabas Bouc	142	232	266	264
Tabas MNS	145	232	252	250
Kobe Bouc	310	310	244	308
Kobe MNS	274	273	229	272
IMP Bouc	169	276	187	274
IMP MNS	168	261	180	259
Average Bouc	141	211	173	228
Average MNS	136	203	174	219
Bouc/MNS	1.03	1.04	0.99	1.04

Figures 11 to 15 illustrate some of analysis results. Figures 11 and 12 show average of drifts and average of residual drifts through the height of structure, respectively. Figures 13 and 14 display force-displacement and force-velocity response of MR damper where attached to the 3^{rd} story, respectively. Finally, Figure 15 illustrates time history of maximum of drifts under Elcentro record. These figures prove that there are differences between the modified Bouc-Wen model and the MNS model in control performance of an MR damper. It means, using each mathematical MR damper model can lead to different control forces.

Based on Figure 11 to Figure 15 and Table 3, some notes on control algorithms and mathematical modelling methods are remarkable:

a. The MNS model performs better than the modified Bouc-Wen model in J_3 criterion. In other words, the MNS model has outperformed the other model in reducing the maximum of hysteretic energy. This observation is correct for the averages of all the control algorithms, and all the control modes.
b. There is no pronounced difference between these two models in reducing the drift response, and residual drift.
c. The NIOC-based semi-active control algorithm has outperformed the LQR-based algorithm in reducing the drift response for all modes of control.
d. The LQR-based control algorithm has outperformed the NIOC-based algorithm in reducing the maximum of hysteretic energy for all modes of control.
e. The NIOC-based control algorithm has reduced the residual drift more than the LQR-based algorithm for the cheap mode of control.

f. The LQR-based control algorithm has reduced the residual drift more than the NIOC-based algorithm for the expensive mode of control.
g. The maximum of control forces of these two algorithms for the expensive mode of control is the same.
h. The maximum of required control forces for the MNS model is slightly less than modified Bouc-Wen model.
i. The MNS model requires a smaller capacity of MR damper for all modes of control, while it performs better than the modified Bouc-Wen model especially in J_1, and J_3 criteria. In other words, the MNS model would be an appropriate choice when reducing the drift and hysteretic energy are considered.
j. Choosing the LQR-based algorithm for all modes of control leads to a smaller capacity of MR damper.
k. Figures 11, 12, and 15 display the effectiveness of all control modes and algorithms in controlling the structure in comparison with uncontrolled structure. This advantage occurs in drift and residual drift.

There is another point; Figure 12 shows a more uniformity in residual drifts for controlled structure. This concept may lead to damage reduction in a structure. Residual drift and hysteretic energy are distributed more uniform through the entire structure. As a result, the MNS model has a higher performance than the modified Bouc-Wen model. Using the MNS model the acceleration responses and the maximum of hysteretic energy of the ten-story structure is more reduced with smaller control forces. Therefore, as the MNS model is a more accurate model, it has outperformed the modified Bouc-Wen model from the control performance point of view.

It should be noted that there is no considerable difference between the two investigated models in time cost of analysis.

4. SUMMARY AND CONCLUSION

A comparative study on two mathematical models of MR damper has been implemented in this research: the modified Bouc-Wen model and the MNS model. These models are employed in this research through two active-based semi-active control algorithms on a nonlinear ten story office building structure: an LQR based and a NIOC based semi-active control algorithms. Ten 300-kN MR dampers utilized, are each installed on a single story. analysis. For better contrast, two control modes are set: the cheap mode of control with smaller Q weighting matrix and the expensive mode of control with larger values of Q matrix.

The drift of the 3rd floor and the 9th floor of the ten-story structure is more than other stories, based on Figure 11. On the other side, the residual drift of the 9th floor is larger, based on Figure 12. As a result, control of the 9th floor responses is more important than other floors. The MNS model has reduced the maximum drift and the residual drift of the 9th floor better than the modified Bouc-Wen model based on Figures 11 and 12 for both control algorithms. Therefore, the MNS model can control the maximum damage of structure, more than the modified Bouc-Wen model, if damage index is supposed as a combination of maximum drift and residual drift of each story.

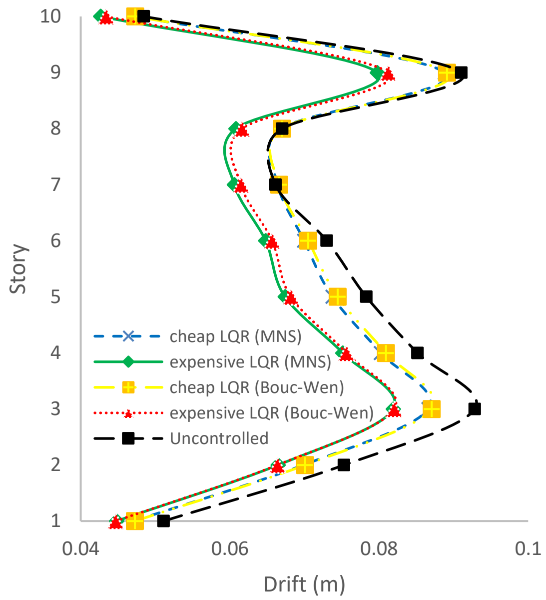

(a) LQR method vs. uncontrolled

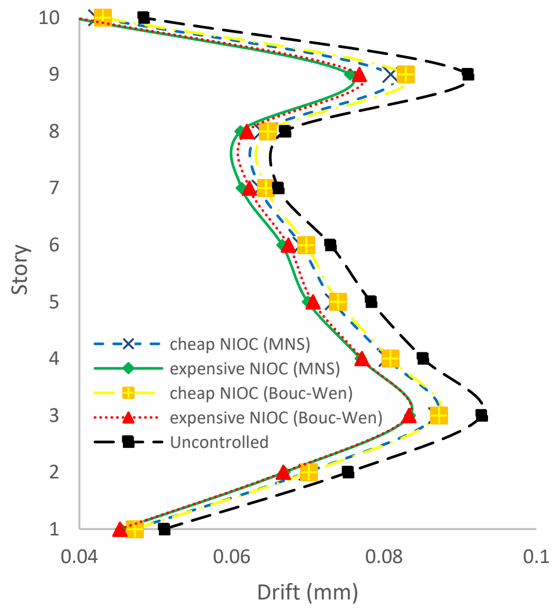

(b) NIOC method vs. uncontrolled

Figure 11. Diagram of the average of maximum story drifts

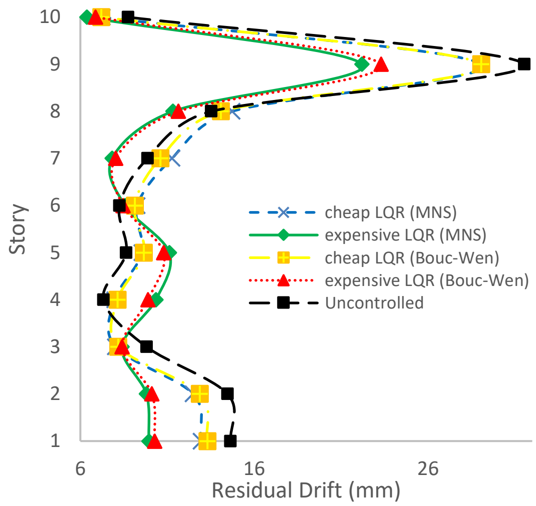

(a) LQR method vs. uncontrolled

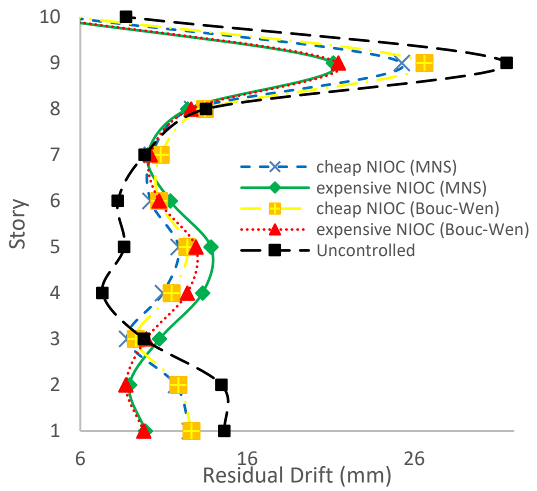

(b) NIOC method vs. uncontrolled

Figure 12. Diagram of the average of residual drifts for Elcentro, Tabas and IMP records

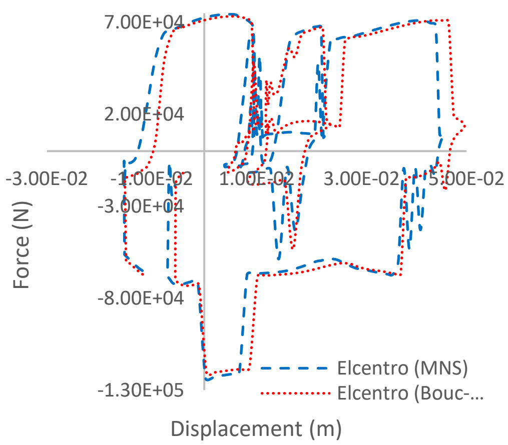

The 3rd story

Figure 13. Diagram of the force–displacement of the MR damper of the 3rd floor (control algorithm: LQR-based semi-active)

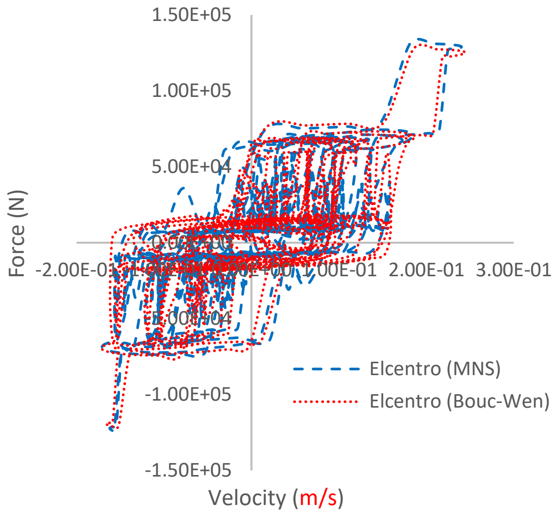

The 3rd story

Figure 14. Diagram of the force – velocity of the MR damper of the 3rd floor (control algorithm: LQR-based semi-active)

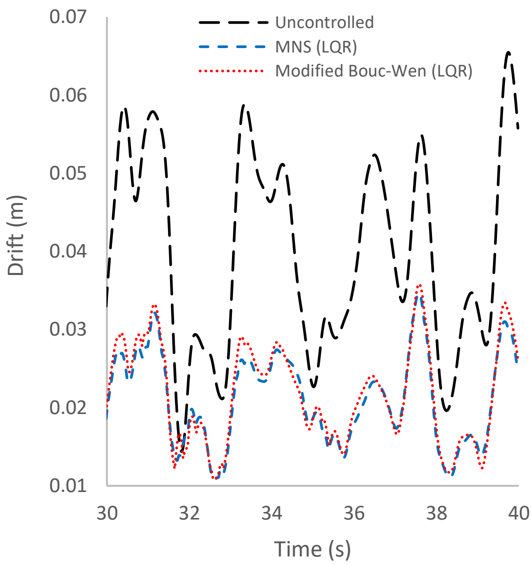

Figure 15. Time history of the maximum of drifts (expensive mode of control of the Elcentro record)

Final results show a slight superiority for the MNS model in reducing the hysteretic energy, and maximum of drifts while this model requires smaller capacity of MR dampers in comparison with the modified Bouc-Wen model. This point can be used for mathematical model selection in a control practic. Based on Cha et al. [12], the MNS model has also more accuracy. Then, the MNS hysteretic model looks more appropriate for using in semi-active control via MR dampers, especially in mid-rise building structures.

The LQR-based algorithm, results in a higher control performance for reducing the maximum of hysteretic energy, and residual drifts. Also, the NIOC-based algorithm requires a larger capacity of MR dampers. Nevertheless, it reduces the maximum of drifts responses more than the LQR-based algorithm. Finally, it can be extracted that the NIOC-based control algorithm containing the MNS hysteretic model is more prefered for control of building structures via MR dampers.

Time delay and measurement noise probable effects on the control performance of two investigated algorithms should be studied. Also, more researches are required for evaluating the impacts of structural height on the results and conclusions. Other mathematical hysteretic models of MR damper such as standard Bouc-Wen model, bilinear model etc. can be used for a better outcome.

5. REFERENCES

1. Ha, Kwangtae, "Innovative Blade Trailing Edge Flap Design Concept Using Flexible Torsion Bar and Worm Drive", ***HighTech and Innovation Journal,*** Vol. 1, No. 3, (2020). https://dx.doi.org/10.28991/HIJ-2020-01-03-01.
2. Cheng, Y. F., Jiang, H., Lou, K., SMART STRUCTURES, Innovative systems for Seismic Response Control, CRC Press, 2008. doi:https://doi.org/10.1201/9781420008173
3. Connor, J. J., Introduction to Structural Motion Control. Pearson Education Ltd., 2003. doi:978-3-319-06281-5
4. Daniel, C., Hemalatha, G., Sarala, L., Tensing, D., & Sundar Manoharan, S., "Seismic Mitigation of Building Frames using Magnetorheological Damper", ***International Journal of Engineering Transactions A: Basics,*** (2019), 1543-1547. doi:10.5829/ije.2019.32.11b.05
5. Dyke, S. J., Spencer Jr., B. F., Sain, M. K., Carlson, J. D., "Experimental Verification of Semi-Active Structural Control Strategies Using Acceleration Feedback", Proceedings of the 3rd International Conference on Motion and Vibration Control, (1996), 291-296, Chiba, Japan.
6. Fuller, C. R., Elliott, S. J., Nelson, P. A., Active Control of Vibration. Academic Press, 1996.
7. Jansen, L. M., Dyke, S. J., "Semi-Active Control Strategies for MR Dampers: A Comparative Study", ***Journal of Engineering Mechanics***, (2000), 795-803. doi:10.1061/(ASCE)0733-9399(2000)126:8(795)
8. Soong, T. T., Active Structural Control: Theory and Practice. NY: Longman Group. Retrieved from, 1990. https://doi.org/10.1061/(ASCE)0733-9399(1992)118:6(1282)
9. Soong, T. T., Dargush, G. F., Passive Energy Dissipation Systems in Structural Engineering. John Wiley & Sons, Ltd. (UK), 1997.
10. Chae, Y., Ricles, J. M., Sause, R., "Modeling of a large-scale magneto-rheological damper for seismic hazard mitigation. Part I: Passive mode", ***Earthquake Engineering & Structural Dynamics,*** Vol. 42, (2013), 669-685. doi:10.1002/eqe.2237
11. Ntintakis, I., Stavroulakis, G., E., Plakia, N., "Topology Optimization by the Use of 3D Printing Technology in the Product Design Process", ***HighTech and Innovation Journal***, Vol. 1, No. 4, (2020). https://dx.doi.org/10.28991/HIJ-2020-01-04-03.
12. Cha, Y.J., Zhang, J., Agrawal, A. K., Dong, B., Friedman, A., Dyke, S. J., Ricles, J., "Comparative Studies of Semiactive Control Strategies for MR Dampers: Pure Simulation and Real-Time Hybrid Tests", ***Journal of Structural Engineering***, (2013), 1237-1248. doi:10.1061/(ASCE)ST.1943-541X.0000639
13. Huang, K., Betti, R., Ettouney, M. M., "Instantaneous Optimal Control for Seismic Analysis of Non-Linear Structures", ***Journal of Earthquake Engineering,*** Vol. 3, No. 1, (1999), 83-106. doi:10.1002/eqe.322
14. Pourzeynali, S., Jooei, P., "Semi-active Control of Building Structures using Variable Stiffness Device and Fuzzy Logic", ***International Journal of Engineering, Transactions A: Basics***, (2013), 1169-1182. doi:10.5829/idosi.ije.2013.26.10a.07
15. Pourzeynali, S., Malekzadeh, M., Esmaeilian, F., "Multi-objective Optimization of Semi-active Control of Seismically Exited Buildings Using Variable Damper and Genetic Algorithms", ***International Journal of Engineering Transactions A: Basics***, (2012), 265-276. doi:10.5829/idosi.ije.2012.25.03a.08
16. Hashemi, S., Haji Kazemi, H., Karamodin, A., "Localized genetically optimized wavelet neural network for semiactive control of buildings subjected to earthquake", ***Structural Control and Health Monitoring***, (2016). doi:10.1002/stc.1823
17. Hiramoto, K., Matsuoka, T., Sunakoda, K., "Semi-active vibration control of structural systems based on a reference active control law: output emulation approach", ***Structural Control and Health Monitoring***, Vol. 23, (2016), 423-445. doi:10.1002/stc.1770
18. Liu, Y.-F., Lin, T.-K., Chang, K.-C., "Analytical and experimental studies on building mass damper system with semi-active control device", ***Structural Control and Health Monitoring***, (2018). doi:https://doi.org/10.1023/A:1004442832316
19. Zafarani, M., Halabian, A., "Supervisory adaptive nonlinear control for seismic alleviation of inelastic asymmetric buildings equipped with MR dampers", ***Engineering Structures,*** Vol. 176, (2018), 849-858. doi:10.1016/j.engstruct.2018.09.045
20. Azar, B. F., Veladi, H., Talatahari, S., Raeesi, F., "Optimal design of magnetorheological damper based on tuning Bouc-Wen model parameters using hybrid algorithms", ***KSCE Journal of Civil Engineering***, (2020), 867-878. doi:10.1007/s12205-020-0988-z
21. Cruze, D., Gladston, H., Farsangi, E., Loganathan, S., Dharmaraj, T., Solomon, S., "Development of a Multiple Coil Magneto-Rheological Smart Damper to Improve the Seismic Resilience of Building Structures", ***The Open Civil Engineering Journal,*** (2020). doi:10.2174/1874149502014010078
22. Jeniš, F., Kubík, M., Macháček, O., Šebesta, K., Strecker, Z.,"Insight into the response time of fail-safe magnetorheological damper", ***Smart Materials and Structures***, (2020).
23. Yang, J. N., Long, F. X., Wong, D., "Optimal Control of Nonlinear Structures", ***Journal of Applied Mechanics***, (1988), 931-938. doi:https://doi.org/10.1115/1.3173744
24. Spencer Jr., B. F., Dyke, S. J., Sain, M. K., Carlson, J. D., "Phenomenological Model For Magnetorheological Dampers", ***Journal of Engineering Mechanics***, (1997), 230-238. doi:10.1061/(ASCE)0733-9399(1997)123:3(230)
25. Winter, B. D., Swartz, R. A., "Low-force magneto-rheological damper design for small-scale structural control", ***Structural Control and Health Monitoring***, (2017). https://doi.org/10.1016/j.tafmec.2019.03.0122
26. Rastegarian, S., Sharifi, A., "An Investigation on the Correlation of Inter-Story drift and Performance Objectives in Conventional RC Frames", ***Emerging Science Journal***, Vol. 2, No. 3, (2018). https://dx.doi.org/10.28991/esj-2018-01137.

27. Aghajanzadeh, S.M. Mirzabozorg, H., "Concrete Fracture Process Modeling by Combination of Extended Finite Element Method and Smeared Crack Approach", ***Theoritical and Applied Fracture Mechanics***, (2019).

28. Sapinski, B., Filus, J., "Analysis of Parametric Models of MR Linear Damper", ***Journal of Theoretical and Applied Mechanics***, Vol. 41, No. 2, (2002), 215-240. doi: 10.1.1.453.2815

29. Pinheiro, Ana Paula, "Architectural Rehabilitation and Sustainability of Green Buildings in Historic Preservation", ***HighTech and Innovation Journal,*** Vol. 1, No. 4, (2020). https://dx.doi.org/10.28991/HIJ-2020-01-04-04.

30. Burciaga, Ulises Mercado, "Sustainability Assessment in Housing Building Organizations for the Design of Strategies against Climate Change", ***HighTech and Innovation Journal,*** Vol. 1, No. 4, (2020). https://dx.doi.org/10.28991/HIJ-2020-01-04-01.

30. American Society of Civil Engineers, & Structural Engineering Institute, "Minimum Design Loads for Buildings and Other Structures", *ASCE/SEI*., 2010.

Persian Abstract

چکیده

موضوع مقاله حاضر مقایسه دو روش مختلف مدل‌سازی رفتار چرخه‌ای میراگر نیمه‌فعال MR می‌باشد. این مقایسه با تاکید بر تاثیر این مدل‌ها بر کیفیت اثر کنترلی میراگر بر سازه‌های غیرخطی صورت پذیرفته است. در مقاله حاضر از دو مدل بوک- ون اصلاح شده و لغزنده غیرخطی ماکسول به جهت مدل‌سازی رفتار چرخه‌ای میراگر استفاده شده است. نیز دو الگوریتم کنترلی شناخته‌شده‌ی LQR و NIOC به جهت تعیین نیروهای کنترلی مورد استفاده قرار گرفته‌اند. در بخشی از روند تعیین نیروهای کنترلی میراگر MR ، استفاده از روش مدل‌سازی رفتار چرخه‌ای میراگر ضروری می‌باشد. بر این اساس مقایسه ای بین میزان کاهش برخی پاسخ‌های سازه مانند جابه‌جایی نسبی بین طبقات، انرژی چرخه‌ای تیرهای طبقات و جابه‌جایی مانده در طبقات با بهره‌گیری از هر کدام از روش‌های مدل‌سازی ذکرشده صورت پذیرفته است. یک سازه ده طبقه اسکلت فلزی با کاربری اداری به جهت بررسی موضوع مقاله حاضر مورد بررسی قرار گرفته است. تحلیل‌های تاریخچه زمانی غیرخطی بر روی این سازه با استفاده از هفت شتاب نگاشت زلزله با بزرگا و خصوصیات مختلف انجام شده است. نتایج تحلیل‌ها، نشان از تفاوت نسبی پاسخ‌های سازه در استفاده از هر یک از دو روش مدل‌سازی یادشده دارد.

International Journal of Engineering

Journal Homepage: www.ije.ir

Effect of Super Absorbent Polymer on Workability, Strength and Durability of Self Consolidating Concrete

K. Venkateswarlu*, S. V. Deo, M. Murmu

Department of Civil Engineering, NIT Raipur, CG, India

P A P E R I N F O

Paper history:
Received 05 January 2021
Received in revised form 01 March 2021
Accepted 03 March 2021

Keywords:
Internal curing
Super absorbent Polymer
Workability
Compressive strength
Electrical resistivity

A B S T R A C T

This study presents the effect of super absorbent polymer (SAP) as internal curing agent on workability, durability and compressive strength of self-consolidating concrete (SCC). In order to estimate the internal curing efficiency of SAP in different curing conditions and curing ages, compressive strength and electrical resistivity tests have been performed. Homogenous and denser microstructure was formed by gradual release of water from SAP into pores created by SAP. Further pozzolanic reaction of fly ash has enhanced the strength and durability properties. High desorption rate of water from SAP in air curing condition resulted in an increased electrical resistivity and compressive strength. Compressive strength of internal cured SCC mixtures increased to 15-25% at 7 days and 10-19% at 28 days. Electrical resistivity values were increased 11-30% in water curing condition and 16-53% in air curing condition. The costs for 0.35w/b and 0.40 w/b at optimum internal cured SCC mixtures compared to control SCC mixtures were reduced to 9.39 and 9.70%, respectively.

***doi**: 10.5829/ije.2021.34.05b.05*

NOMENCLATURE

W/C	Water cement ratio	**Greek Symbols**		
V_{water}	Volume of water (m^3/m^3)	$\propto_{max}$	The expected maximum hydration degree of hydration	
C	Quantity of cement in the mixture (kg/m^3)	ρ_{water}	Unit weight of water (kg/m^3).	
CS	Chemical shrinkage of cement paste (ml/g)	M_{SAP}	Mass of super absorbent polymer	

1. INTRODUCTION

Presently self-consolidating concrete (SCC) has become high performable concrete by introducing concrete additives. SCC is high flowable concrete which can flow through every corner of heavy reinforced concrete sections with its own weight without external vibration [1]. In recent years construction industry is using significant amount of SCC in pre-cast elements due to many advantages [2, 3]. Past studies states that mineral admixtures can be used as fines which are required to achieve self compactability of SCC. Especially fly ash can enhance workability, durability and mechanical properties of SCC [4]. Higher requirement of cementitious material in SCC needs sufficient curing to complete the hydration especially at high temperature climatic regions. External curing is not adequate to achieve 100% hydration in practical conditions of site. Authors reviewed that internal curing by super absorbent polymers (SAP) can achieve full hydration which further increase the durability and reduce the shrinkage [5]. SAPs are cross linking chain polymers which can absorb the moisture 100 to 1000 times of their own mass. At the time of mixing, dry SAPs will absorb the moisture and becomes stable during placing, consolidation of concrete [6]. SAP addition affects the SCC in different manner in different properties which has shown by the following studies. Snoeck et al. [7] investigated that shrinkage can be eliminated by internal curing with SAP. They also reported that workability decreases when the dry SAP is

*Corresponding Author Email: venkateswar154@gmail.com (K. Venkateswarlu)

Please cite this article as: K. Venkateswarlu, S. V. Deo, M. Murmu, Robust Effect of Super Absorbent Polymer on Workability, Strength and Durability of Self Consolidating Concrete, International Journal of Engineering, Transactions B: Applications Vol. 34, No. 05, (2021) 1118-1123

added to concrete without additional water. However, additional water reduces the compressive strength of concrete. But, Pourjavadi et al. [8] reported that air curing results increase in compressive strength of concrete than reference concrete. Whereas workability decreases due to initial water absorption. Other studies shown that electrical resistivity values can assess the resistance to corrosion [9, 10]. Most of the researchers focused on reduction of shrinkage by using higher dosage of SAP [11, 12]. But lower amounts of SAP especially less than 0.2% of mass of cement can decrease the shrinkage and also enhance the mechanical and durability properties of concrete [13]. Hence in this study effect of SAP on self consolidating concrete was assessed by testing workability, compressive strength, and electrical resistivity of concrete. Pinheiro [14] found the importance of green and sustainable buildings and less CO_2 materials should introduce instead of cement. Rubberized concrete with waste rubber would also lead to sustainable and environmental friendly concrete [15]. Rath et al. [16] have confirmed the use of fly ash to reduce the corrosion of concrete by electrical resistivity values. Even in the fly ash and rice husk ash combination mixes also fly ash removed the difficulties of workability and particle packing of binding materials [17] where rice husk ash act internal curing agent. Joel [18] suggested that 30% fly ash replacement gives optimum compressive strength results. But, Kanthe et al. [19] specially conducted strength and durability experiments on fly ash from Bhilai steel Plant, India and quoted that 15% fly ash can give optimum results than higher fly ash percentages. Hence in the present investigation the mixtures having 85% cement in binder remaining 15% is fly ash which is from Bhilai steel plant, India. From the literature it was concluded that to eliminate the shrinkage higher SAP dosage has been used and SAP effect on SCC less literature is available. Hence lower dosages of SAP (0.05% to 0.15%) could enhance the strength and durability with addition to shrinkage reduction. Hot weather concretes present in India leads to increase the water demand and permeability. However, internal curing can be the best possible way to resolve this problem.

2. EXPERIMENTAL PROGRAM

2. 1. Materials In the present investigation chemical oxide compositions of OPC-43 grade cement and fly are given in Table 1. The specific gravities of cement and fly were 3.05 and 2.20, respectively. Super plasticiser from BASF Company which is poly carboxylate ether based water reducing admixture used to achieve self-compactability. Specific gravity, pH, and chloride ion percentage of super plasticiser are 1.08, ≥6, <0.2%, respectively. Aggregates used in this project are confirming to IS: 383-2016. Zone-II locally available river sand and 10mm coarse aggregates with 2.6 and 2.7 specific gravities, respectively [20] was used. Commercially available sodium based poly acrylate was used as super absorbent polymer. Water absorption capacities of SAP is 36g/g in cement solution (solution prepared with W/C=5.0) and 170g/g in water calculated by Tea bag method which was given by Schröfl et al. [21]. Higher ionic concentration of Ca^{+2}, Na^{+} present in cement solution may decrease the water absorption of SAP. Even significant percentage of SiO_2 present in cement and fly ash but most of SiO_2 are immobile [22]. Hence SiO_2 ions cannot affect the water absorption of SAP.

2. 2. Required Amount of IC Water To achieve maximum degree of hydration of concrete mixes, previous studies has given following equations to calculate the volume of water required for internal curing and to calculate the mass of SAP [23, 24].

$$Vwater * \rho water = C \times CS \times \propto max \quad (1)$$

$$M_{SAP} = \frac{C \times CS \times \propto \max}{S \times \emptyset SAP} \quad (2)$$

Volume of water required to get maximum degree of hydration is 32 kg/m^3 as per equation (2). However water supplied by SAP to SCC mixtures are 0, 38.86, 77.71, and 116.60 kg/m^3 for SAP0, SAP0.05, SAP0.10, and SAP0.15 respectively. But, these quantities were decreased to 0, 8.23, 16.44, 24.68 kg/m^3 in cement solution. Generally in practice W/C ratios would be in the range of 0.1-0.7. Hence SAP dosages has fixed according to absorption of SAP in pure water as shown in Table 2.

3. RESULTS AND DISCUSSIONS

3. 1. Workability As shown in Figures 1 and 2 the flowability of SCC was decreased with increasing

TABLE 1. Chemical oxide composition of binders

Chemical Oxides	Cement (%)	Fly ash (%)
CaO	68.5	1.23
SiO_2	16.5	64.5
Al_2O_3	4.5	24.5
Fe_2O_3	3.7	5.01
MgO	1.68	0.55
SO_3	-	-
K_2O	2.36	2.51
Na_2O	0.4	0.10

TABLE 2. Mixture proportion of SCC in kg/m^3

Mix	Cement	Fly ash	W/B ratio	Water	Sand	Coarse aggregate	SAP	SP
35S0	389	69	0.35	160	928	840	0	6.9
35S5	389	69	0.35	160	928	840	0.23	6.9
35S10	389	69	0.35	160	928	840	0.46	6.9
35S15	389	69	0.35	160	928	840	0.69	6.9
40S0	372	66	0.4	175	912	821	0	6.6
40S5	372	66	0.4	175	912	821	0.22	6.6
40S10	372	66	0.4	175	912	821	0.44	6.6
40S15	372	66	0.4	175	912	821	0.66	6.6

SAP dosage but it is in limits. As comprared to control SCC mix internal cured SCC mixes were reduced the slump flow diameters 1-2% from Figure 2. It may be because of dry SAPs absorb the water initially from the SCC mix. These results are compatible with other researchers with the same fly ash additions [25, 26]. In this experimentation super plasticiser was restricted to1.5% of binder beyond these dose it could shows bleeding and reduction of strength. These super plasticiser dose leads to 610 to 640mm slump flow diameter. This range of slump flow classified SCC as SF1 as per IS 10262:2019 [27].

With increase in dosage of SAP from 0 to 0.15% both V-Funnel and T500 values were increased with increasing w/b ratio independent of SAP dose, as shown in Figure 3. The workability of SCC was decreased with increasing SAP dose from 0 to 0.15% as slump flow diameters decreased.

From flowability tests the relationship between viscosity and yield stress has been introduced based on T500 and V-Funnel time. As shown in Figure 4 T500 and V-Funnel times had R^2 value of 0.955 which shows strong correlation as other researchers observed [28].

3. 2. Compressive Strength Internal curing affects compressive strength results in different curing conditions. As shown in Figure 5 as increase in SAP dose, almost similar compressive strength values have been observe in water curing condition. This lower compressive strength results due to early absorption of water by dry SAP from the specimen. It leads to permeable and porous structure in the concrete specimen [29]. However, internal curing with recycled aggregates lost their compressive strength by 7-19% compared to control concrete [30]. While in this research, an increase

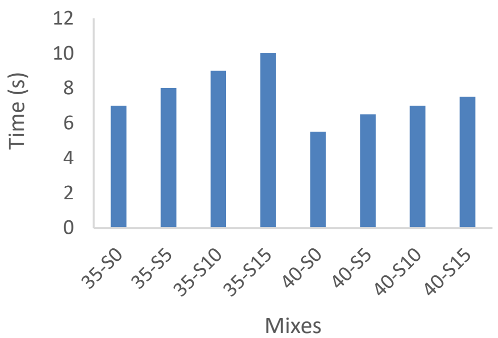

Figure 1. Slump flow time (T500) time of SCC

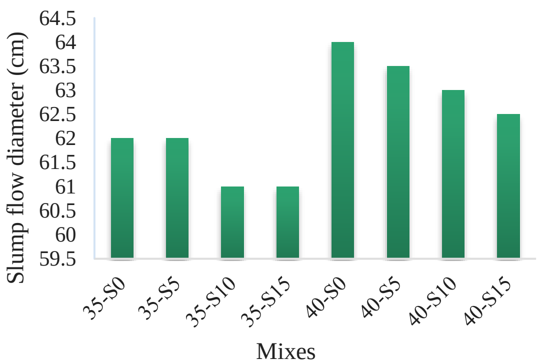

Figure 2. Max Slump flow diameters of SCC

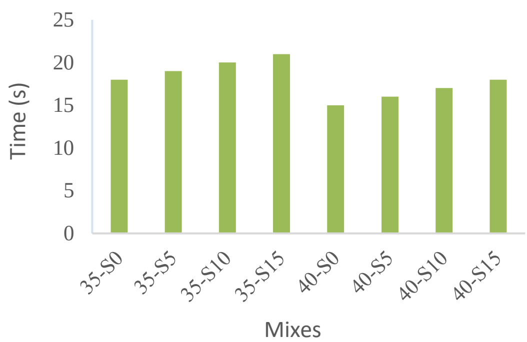

Figure 3. V-Funnel time of SCC mixtures

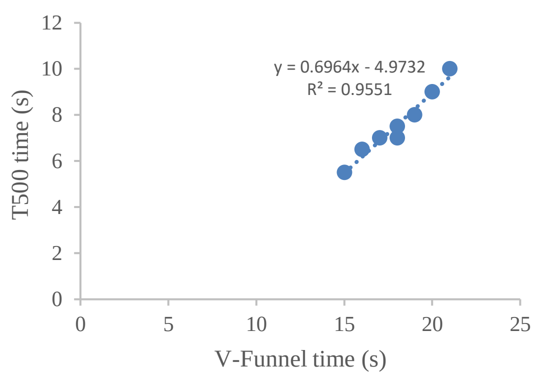

Figure 4. Relationship between T500 and V-funnel time for SCC

in the SAP dose increases the compressive strength of SCC in air curing condition. This increment was high at high w/b ratio at 7 days in air curing condition. From Figure 5 in air curing at 7 days, the compressive strength has increased by 21-26% and 15-25% for 0.4w/b, 0.35 w/b ratios, respectively. But at 28 days this enhancement of compressive strength higher in low w/b ratio in air curing. The compressive strength with respect control mixture at 28 days of air curing has increased by 6.75-13.5% and 10-19% for 0.4w/b and 0.35w/b ratios, respectively. This is due to increased hydration of binder material due to higher availability of moisture from SAP at 28 days as compared to 7 days curing. It leads to better hydration denser interfacial transition zone (ITZ) and concrete matrix. Hence further it gives higher compressive strength. Other researchers also stated that when relative humidity of concrete drops SAP can supply the water in air curing effectively [8]. Other studies shown that LWA could increase the compressive strength with 2-5% only while SAP has increased compressive strength 10-25% in air curing condition [31]. In case of water curing condition reduction in compressive strength observed compared to control SCC at 7 days but it was slightly improved at 28 days as shown in Figure 5. At 0.35w/b and 0.40 w/b ratio concretes at 28 days a slight improvement in compressive strength with 2-4% was observed while at 7 days slight reduction of compressive strength with 1-6% was observed. This is due to initially SAP pores at early age causes the reduction of compressive strength after that improvement of hydration has filled the pores which are created by SAP [32, 33].

3. 3. Electrical Resistivity Possible rate of corrosion of reinforcement can be interpret by electrical resistivity test of concrete [34]. In both curing conditions electrical resistivity values at 7 and 28 days were similar increasing rate with compressive strength values. From Figure 6, at 28 days in water curing, the electrical resistivity was increased by 11 to 30% and 19 to 53% for 0.35w/b and 0.4w/b ratio, respectively. By increasing SAP dose from 0 to 0.15%, this increment higher in air curing specimens as 16-53% and 25-70% for 0.35 w/b and 0.40 w/b ratio concretes, respectively. Ramezanianpour et al. [35] showed higher the electrical resistivity concretes would show the higher resistance of corrosion of resistance due to discharging of electrons from anodic region to cathodic region. For 0.4W/C ratio the electrical resistivity values of SAP and fly ash combination given 16% higher than the rice husk ash and fly ash combination [17] and other researchers also confirmed that electrical resistivity in air curing increased by nearly 12% in 0.35 to 0.4w/b internal curing mixtures. Hence, the SAP can perform better than the other internal curing agents. As shown in Figure 6 electrical values were more than 20 kΩ-cm for 0.1% and 0.15% SAP dose which are in corrosion free zone.

Table 3 shows that risk of corrosion is having correlation with electrical resistivity values [9]. At 28 days for the above 0.1% of SAP dose electrical resistivity values were more than 20 kΩ-cm for 0.35w/b ratio concretes and for 0.15% of SAP dose electrical resistivity values were more than 20 kΩ-cm.

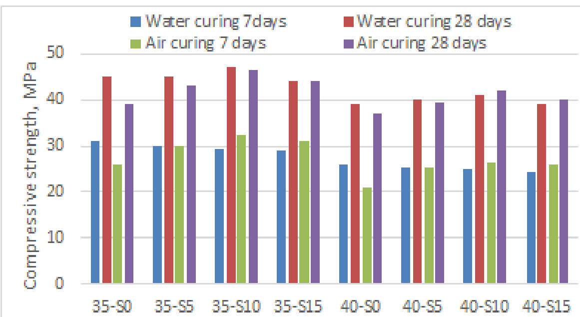

Figure 5. Compressive strength of SCC mixes under water and air curing at 7 and 28 days

4. COST ANALYSIS OF CONCRETE

The cost analysis of control Self-consolidating concrete and internal cured self-consolidating concrete were worked out as per current market rate. Initially cost of control and internal cured concrete were the same. In curing stage cost would decreased for internal cured concrete due to spray curing or pond curing in the site. The cost was reduced to 9.39% and 9.70%, respectively for 0.35w/b and 0.40 w/b internal cured SCC mixtures

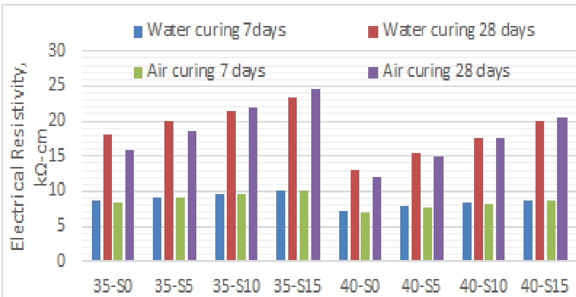

Figure 6. Electrical resistivity of SCC mixes under water and air curing at 7 and 28 days

TABLE 3. Corrosion risk range for different electrical resistivity values

Electrical Resistivity (kΩ -cm)	Corrosion risk
More than 20	Negligible
10 to 20	Low
5 to 10	High
Less than 5	Very high

compared to control SCC mixtures. Above internal curing SCC mixtures (SAP= 0.1% of mass of binder) were given optimum results of compressive strength and electrical resistivity.

5. CONCLUSIONS

1. Workability of SCC mixtures were decreased to 1-2% due to initial absorption of water from mix by dry SAP particles. However, these values were in permissible limits. Slump flow time and V-funnel time shows the same pattern and both have perfect correlation with R^2 of 0.95.
2. Compressive strength values were increased under air curing condition by 15-25% at 7 days and 10-19% at 28 days with internal effect by SAP while small decreasing of compressive strength results 1-2% was observed in water curing condition. In both the curing conditions 0.1% SAP dosage has given higher strength than other mixtures.
3. Electrical resistivity values were increased 11-30% in water curing condition and 16-53% in air curing condition. For 0.1% SAP dosage and above the electrical resistivity values were observed more than 20 kΩ-cm at 28 days in air curing and water curing. Hence SCC mixtures above 0.1% SAP dose could not subject to corrosion.
4. Based on test results of workability, compressive strength and electrical resistivity 0.10% dose of SAP is optimum for both w/b ratios.
5. The costs for 0.35w/b and 0.40 w/b for optimum internal cured SCC mixtures compared to control SCC mixtures were reduced to 9.39 and 9.70%, respectively.

6. REFERENCES

1. EFNARC, "Specification and Guidelines for Self-Compacting Concrete," (2002), 1-32.
2. M. F. Nuruddin, K. Y. Chang, and N. M. Azmee, "Workability and compressive strength of ductile self compacting concrete (DSCC) with various cement replacement materials," ***Construction and Building Materials***, Vol. 55, (2014), 153-157, doi.org/10.1016/j.conbuildmat.2013.12.094.
3. M. Tuyan, R. Saleh, T. Kemal, Ö. Andiç, and K. Ramyar, "Influence of thixotropy determined by different test methods on formwork pressure of self-consolidating concrete," ***Construction and Building Materials.***, Vol. 173, 189-200, (2018), doi.org/10.1016/j.conbuildmat.2018.04.046.
4. R. Siddique, "Properties of self-compacting concrete containing class F fly ash," ***Materials and Design,*** Vol. 32, No. 3, (2011), 1501-1507, doi:10.1016/j.matdes.2010.08.043
5. K. Venkateswarlu, S. V Deo, and M. Murmu, "Overview of effects of internal curing agents on low water to binder concretes," ***Materials Today Proceedings***, Vol. 32, (2020), 752-759, doi.org/10.1016/j.matpr.2020.03.479.
6. V. Mechtcherine, E. Secrieru, and C. Schröfl, "Effect of superabsorbent polymers (SAPs) on rheological properties of fresh cement-based mortars - Development of yield stress and plastic viscosity over time," ***Cement Concrete Research,*** Vol. 67, (2015), 52-65, doi.org/10.1016/j.cemconres.2014.07.003.
7. D. Snoeck, D. Schaubroeck, P. Dubruel, and N. De Belie, "Effect of high amounts of superabsorbent polymers and additional water on the workability, microstructure and strength of mortars with a water-to-cement ratio of 0.50," ***Construction and Building Materials,*** Vol. 72, (2014), 148-157, doi.org/10.1016/j.conbuildmat.2014.09.012.
8. A. Pourjavadi, S. Mahmoud, A. Khaloo, and P. Hosseini, "Improving the performance of cement-based composites containing superabsorbent polymers by utilization of nano-SiO_2 particles," ***Materials and Design,*** Vol. 42, (2012), 94-101, doi.org/10.1016/j.matdes.2012.05.030.
9. O. Sengul and O. E. Gjørv, "Electrical Resistivity Measurements for Quality Control during Concrete Construction," ***ACI Materials Journal,*** Vol. 105, (2008), 541-547.
10. K. Farzanian, K. Pimenta Teixeira, I. Perdigão Rocha, L. De Sa Carneiro, and A. Ghahremaninezhad, "The mechanical strength, degree of hydration, and electrical resistivity of cement pastes modified with superabsorbent polymers," ***Construction Building Materials,*** Vol. 109, (2016), 156-165, doi.org/10.1016/j.conbuildmat.2015.12.082.
11. [11] B. J. Olawuyi and W. P. Boshoff, "Influence of SAP content and curing age on air void distribution of high performance concrete using 3D volume analysis," ***Construction Building Materials,*** Vol. 135, (2017), 580-589, doi.org/10.1016/j.conbuildmat.2016.12.128.
12. V. N. Kanthe, S. V Deo, and M. Murmu, "Early Age Shrinkage Behavior of Triple Blend Concrete," ***International Journal of Engineering, Transactions B: Applications***, Vol. 33, No. 8, (2020), 1459-1464, doi: 10.5829/ije.2020.33.08b.03.
13. D. Shen, X. Wang, D. Cheng, J. Zhang, and G. Jiang, "Effect of internal curing with super absorbent polymers on autogenous shrinkage of concrete at early age," ***Construction and Building Materials***, Vol. 106, No. 1, (2016), 512-522, doi.org/10.1016/j.conbuildmat.2016.05.048 .
14. A. P. Pinheiro, "Architectural Rehabilitation and Sustainability of Green Buildings in Historic Preservation," ***HighTech Innovation Journal***, Vol. 1, No. 4, (2020), 172-178, doi.org/10.28991/HIJ-2020-01-04-04.
15. A. Abdulameer and H. M. K. Al-mutairee, "An Experimental Study on Behavior of Sustainable Rubberized Concrete Mixes," ***Civil Engineering Journal***, Vol. 6, No. 7, (2020), 1273-1285, doi.org/10.28991/cej-2020-03091547.
16. B. Rath, S. Deo, and G. Ramtekkar, "Durable Glass Fiber Reinforced Concrete with Supplimentary Cementitious Materials," ***International Jounal of Engineering, Transactions A: Basics,*** Vol. 30, No. 7, (2017), 964-971, doi: 10.5829/ije.2017.30.07a.05.
17. V. Kanthe, S. Deo, and M. Murmu, "Combine Use of Fly Ash and Rice Husk Ash in Concrete to Improve its Properties," ***International Jounal of Engineering Transactions A: Basics,*** Vol. 31, No. 7, (2018), 1012-1019, doi: 10.5829/ije.2018.31.07a.02.
18. S. Joel, "Compressive Strength of Concrete using Fly Ash and Rice Husk Ash : A Review," ***Civil Engineering Journal,*** Vol. 6, No. 7, (2020), 1400-1410, doi.org/10.28991/cej-2020-03091556.
19. V. N. Kanthe, S. V Deo, and M. Murmu, "Effect of fly ash and rice husk ash on strength and durability of binary and ternary blend cement mortar," ***Asian Journal of Civil Engineering,*** Vol. 6, (2018), doi.org/10.1007/s42107-018-0076-6.
20. Indian and Standard, "Coarse and Fine Aggregate for Concrete - Specification (Third Revision)," (2016).

21. C. Schröfl, V. Mechtcherine, and M. Gorges, "Relation between the molecular structure and the ef fi ciency of superabsorbent polymers (SAP) as concrete admixture to mitigate autogenous shrinkage," ***Cement Concrete Research,*** Vol. 42, (2012), 865-873, doi:10.1016/j.cemconres.2012.03.011.
22. G. T. T. Trang, N. H. Linh, N. T. T. Linh, and P. H. Kien, "The Study of Dynamics Heterogeneity in SiO_2 Liquid," ***HighTech Innovation Journal,*** Vol. 1, No. 1, (2020), 1-7, doi.org/10.28991/HIJ-2020-01-01-01
23. D. Shen, H. Shi, X. Tang, Y. Ji, and G. Jiang, "Effect of internal curing with super absorbent polymers on residual stress development and stress relaxation in restrained concrete ring specimens," **C*onstruction and Building Materials*,** Vol. 120, 309-320, (2016), doi.org/10.1016/j.conbuildmat.2016.05.048.
24. B. Y. D. P. Bentz, P. Lura, and J. W. Roberts, "Mixture Proportioning for Internal Curing," ***Concrete international*** 27, No. 2, (2005), 35-40.
25. P. Dinakar, M. Karthik Reddy, and M. Sharma, "Behaviour of self compacting concrete using Portland pozzolana cement with different levels of fly ash," ***Materials and Design***, Vol. 46, (2013), 609-616.
26. A. Pourjavadi, S. M. Fakoorpoor, P. Hosseini, and A. Khaloo, "Interactions between superabsorbent polymers and cement-based composites incorporating colloidal silica nanoparticles," ***Cement Concrete Composites***, Vol. 37, No. 1, 196-204, (2013), doi.org/10.1016/j.cemconcomp.2012.10.005.
27. Bureau of Indian standards, "Concrete Mix Proportioning-Guidelines (Second Revision)-IS 10262:2019," (2019).
28. H. Azarijafari, A. Kazemian, M. Rahimi, and A. Yahia, "Effects of pre-soaked super absorbent polymers on fresh and hardened properties of self-consolidating lightweight concrete," **C*onstruction and Building Materials***., Vol. 113, (2016), 215-220, doi.org/10.1016/j.conbuildmat.2016.03.010.
29. B. Fazelabdolabadi and M. Hossein, "Towards Bayesian Quantification of Permeability in Micro-scale Porous Structures - The Database of Micro Networks," ***HighTech Innovation Journal,*** Vol. 1, No. 4, (2020), 148-160, doi.org/10.28991/HIJ-2020-01-04-02.
30. N. Yadav, D. S. V. Deo, and D. G. D. Ramtekkar, "Workable and robust concrete using high volume," ***International Journal Technology***, Vol. 3, (2018), 537-548, doi.org/10.14716/ijtech.v9i3.1126.
31. J. Hyung, S. Woo, K. Myong, and Y. Cheol, "Influence of internal curing on the pore size distribution of high strength concrete," **C*onstruction and Building Material*s.**, Vol. 192, (2018), 50-57, doi.org/10.1016/j.conbuildmat.2018.10.130.
32. A. J. Klemm and K. S. Sikora, "The effect of Superabsorbent Polymers (SAP) on microstructure and mechanical properties of fly ash cementitious mortars," ***Construction and Building Materials,*** Vol. 49, (2013), 134-143, doi.org/10.1016/j.conbuildmat.2019.01.206.
33. F. C. R. Almeida and A. J. Klemm, "Efficiency of internal curing by superabsorbent polymers (SAP) in PC-GGBS mortars," ***Cement Concrete Composites,*** Vol. 88, (2018), 41-51. doi.org/10.1016/j.cemconcomp. 2018.01.002.
34. A. A. Ramezanianpour, A. Kazemian, M. A. Moghaddam, F. Moodi, and A. M. Ramezanianpour, "Studying effects of low-reactivity GGBFS on chloride resistance of conventional and high strength concretes Studying effects of low-reactivity GGBFS on chloride resistance of conventional and high strength concretes," ***Material sand Structures***, Vol. 49, (2015), 2597-2609, DOI: 10.1617/s11527-015-0670-y.
35. A. A. Ramezanianpour, A. Kazemian, M. Sarvari, and B. Ahmadi, "Use of Natural Zeolite to Produce Self-Consolidating Concrete with Low Portland Cement Content and High Durability," ***Jounal of Materials in Civil Engineering***, Vol. 25, (2013), 589-596, DOI: 10.1061/(ASCE)MT.1943-5533.0000621 .

Persian Abstract

چکیده

این مطالعه اثر پلیمر فوق جاذب (SAP)به عنوان عامل بعمل آوری داخلی بر کارایی ، دوام و مقاومت فشاری بتن خودتراکمی (SCC)را ارائه می دهد. به منظور برآورد بازده ترمیم داخلی SAP در شرایط مختلف و مدت بعمل آوری ، آزمون مقاومت فشاری و مقاومت الکتریکی انجام شده است. ریزساختار همگن و متراکم تر با انتشار تدریجی آب از SAP به منافذ ایجاد شده توسط SAP تشکیل شد. واکنش پوزولانی بیشتر خاکستر باعث افزایش خواص مقاومت و دوام می شود. میزان بالای جذب آب از SAP در شرایط پخت هوا منجر به افزایش مقاومت الکتریکی و مقاومت فشاری می شود. مقاومت فشاری مخلوط های درمان شده SCC داخلی در ۱۵ روز به ۲۵-۲۵ درصد و در ۲۸ روز به ۱۰-۱۹ درصد افزایش یافت. مقادیر مقاومت الکتریکی در شرایط پخت آب ۱۱-۳۰٪ و در شرایط پخت هوا ۱۶-۵۳٪ افزایش یافته است. هزینه های w / b۰.۳۵ و w / b ۰.۴۰ در بهینه مخلوط SCC پخته شده داخلی در مقایسه با مخلوط SCC شاهد به ترتیب به ۹/۳۹ و ۹/۷۰ درصد کاهش یافت.

International Journal of Engineering

Journal Homepage: www.ije.ir

Experimental Investigations on Strengthened Reinforced Concrete Columns under Monotonic Axial Loading

S. Sirimontree[a], S. Keawsawasvong[a], C. Thongchom[a], P. Jongvivatsakul[b], E. Noroozinejad Farsangi*[c]

[a] Department of Civil Engineering, Thammasat School of Engineering, Thammasat University, Pathumthani, Thailand
[b] Innovative Construction Materials Research Unit, Department of Civil Engineering, Faculty of Engineering, Chulalongkorn University, Bangkok, Thailand
[c] Faculty of Civil and Surveying Engineering, Graduate University of Advanced Technology, Kerman, Iran

P A P E R I N F O

Paper history:
Received 5 February 2021
Received in revised form 22 March 2021
Accepted 27 March 2021

Keywords:
RC Column
Steel Jacketing
Steel Strap
Ferro-cement
Reinforced Concrete
Strengthening

A B S T R A C T

Strengthening of the existing reinforced concrete (RC) column is nessesary to enhance their axial load-carrying capacity or ductility. This paper presents the results of an experimental study relating to the performance of reinforced concrete columns strengthened with different techniques such as the steel angle, steel straps, and ferro-cement under pure axial load. A total of six square short reinforced concrete columns were constructed. The cross-section and height of tested columns are 150×150 mm and 1.2 m, respectively. Two specimens were set as the control columns (without strengthening). The other four reinforced concrete columns were strengthened with different techniques. Two columns are strengthened with four steel angles at each corner of the column confined with prestressed steel straps. Another two columns are also strengthened with four steel angles confined with prestressed steel straps and ferro-cement. The experimental results are reported in terms of the load-deformation curves as well as the failure modes. A significant enhancement of the maximum axial load-carrying capacity and the ductility is observed for the strengthened reinforced concrete columns. Finally, the discussion of the use of different strengthening techniques is also carried out in this paper.

doi: *10.5829/ije.2021.34.05b.06*

1. INTRODUCTION

There are several effective approaches that can be used to enhance the axial load-carrying capacity and the ductility of RC structures. For instance, many researchers in the past have employed ferro-cement [1-5], fiber-reinforced materials [6-12], or steel angle/strips [13-15], to strengthen the reinforced concrete structures. Previous works by Mourad and Shannag [1], Kaish et al. [2], and Sirimontree et al. [3] employed the ferro-cement jacketing to strengthen RC column. The ferro-cement jacketing was utilized to repair concrete beams by Jongvivatsakul et al. [4-5]. In addition to ferro-cement jacketing, the fiber-reinforced materials is one of the strengthening composites widely used to increase the capacity of several RC structures (e.g., Kianoush and Esfahani [7], Maghsoudi et al. [8], Nateghi and Khazaei-Poul [9], Rahmanzadeh and Tariverdilo [10], Al-Akhras [11], Shadmand et al. [12]). The use of steel jackets is also a simple procedure to strengthen various types of RC structures, where its good performance was demonstrated by Abdel-Hay and Fawzy [13], Ma et al. [14], and Tarabia and Albakry [15].

The main elements supporting a building structure are the columns. The failure in columns can lead to the progressive collapse of the whole building. Thus, column strengthening is an essential issue in the seismic retrofitting of a building structure. To enhance the axial load-carrying capacity, the stiffness, or the ductility of the reinforced concrete columns, several researchers have used steel angles, steel jackets, or ferro-cement jackets to experimentally investigate the strengthening of

*Corresponding Author Institutional Email: noroozinejad@kgut.ac.ir (E. Noroozinejad Farsangi)

Please cite this article as: S. Sirimontree, S. Keawsawasvong, C. Thongchom, P. Jongvivatsakul, E. Noroozinejad Farsangi, Experimental Investigations on Strengthened Reinforced Concrete Columns under Monotonic Axial Loading, International Journal of Engineering, Transactions B: Applications Vol. 34, No. 05, (2021) 1124-1131

reinforced concrete columns by employing these composites. For previous works considering steel angles, Adam et al. [16] performed the laboratory tests of RC columns retrofitted with steel angles and steel strips under axial static loading. These results of laboratory tests were then used to develop numerical models, the nonlinearity of the materials between different materials is taken into account. Tarabia and Albakry [15] carried out a study on the performance of the reinforced concrete square columns strengthened with steel angles and steel strips. They found that the confinement effects significantly dependent on several factors such as the strip spacing, the size of the steel angles, and the connection between the steel angles and steel strips to the head of the specimen. Campione [17] also proposed a design procedure for designing RC columns strengthened with steel angles and battens. The proposed procedure was validated with the experimental results to ensure the performance of the design process. The behaviors of reinforced concrete columns strengthened with steel jackets were also studied by Belal et al. [18] and Abdel-Hay and Fawzy [19]. For previous studies relating the use of ferro-cement jackets to strengthen reinforced concrete columns, Takiguchi [20] demonstrated that the use of external confinement to cover the entire length of the reinforced concrete columns can significantly increase the ductility of the reinforced concrete columns. By using a nonlinear finite element software, Elsayed and Elsayed [21] investigated the performance of the reinforced concrete columns wrapped by ferro-cement jackets under biaxial loading. More details on the performance of steel angles, steel jackets, and ferro-cement jackets can be found in the state-of-the-art review by Raza et al. [22] and Kaish et al. [23]. Recently, the uses of fibrous jackets, textile-reinforced concrete jackets, and prestressed steel jackets to strengthen RC structures were demonstrated by Jassim and Chassib [24], Ngo et al. [25], and Sirimontree et al. [26], respectively, The performance of RC circular and square columns under cyclic loading were examined by Ahmed et. al. [27]. The information of the framework to quantify the absolute permeability of water in a porous structure can be found in literature [28]. Besides, more information on the sustainability assessment in housing buildings can be found in literature [29].

This paper studies the behavior of strengthened reinforced concrete columns subjected to axial load. A total of six reinforced concrete square columns were investigated. Different techniques for strengthening the existing reinforced concrete columns were used such as the steel angle, steel straps, and ferro-cement. All columns are tested under static load. The load-displacement relationship and the failure modes of tested columns are presented and discussed in this paper.

The following is the structure of the paper. The details of all test specimens as well as the preparation processes are first presented to give the information of all considered factors in this study. The test setup and instrumentations are later shown in the same section. The experimental results of all columns are presented in the form of load-displacement curves to demonstrate the performance of all tested columns. The modes of failures showing the column collapses are also presented to portray the failure patterns of all columns. The conclusion of this paper is given lastly to summarize this work.

The innovation of this paper is to investigate the increasing axial load-carrying capacity and ductility of columns strengthened with steel angles confined with prestressed steel straps. Besides, a similar investigation on the use of ferro-cement confined around the reinforced concrete column is also carried out in this study.

2. EXPERIMENTAL PROGRAM

2. 1. Tested Specimens In the present study, a total of six reinforced concrete columns were cast. The cross-section of all columns was 150×150 mm and the height was 1.20 m. The ratio between column height and width was eight which was a short column. The columns were reinforced with four longitudinal bars with a diameter of 12 mm (DB12) and transverse bars with a diameter of 6 mm (RB6) that had a spacing of 150 mm. The area of longitudinal bars was 2.0 percent of cross-sectional area. The clear concrete covering was considered as 20 mm. Two columns were set as the control specimens (Columns CC-1 and CC-2), as shown in Figure 1(a). The other four reinforced concrete columns were strengthened with different techniques.

For strengthened reinforced concrete columns, two columns (CSA-1 and CSA-2) were strengthened with four steel angles at each corner of the columns and then confined with prestressed steel straps that had a spacing of 150 mm, as shown in Figure 1(b). The cross-section and thickness of steel angle were 30×30 mm and 3.0 mm, respectively. An injection plaster was employed in order to fill the gap between the steel jacket and concrete for the strengthened columns.

Another two columns (CSAF-1 and CSAF-2) were also strengthened with four steel angles at each corner of the columns and then confined with prestressed steel straps that had a spacing of 150 mm. After that, the ferro-cement was used to confine the columns at the last step. The square welded wire mesh was used to wrap around the existing column and the cement mortar was applied. A cross-dimension of 250×250 mm was controlled. Figure 1(c) shows the detail of columns CSAF-1 and CSAF-2.

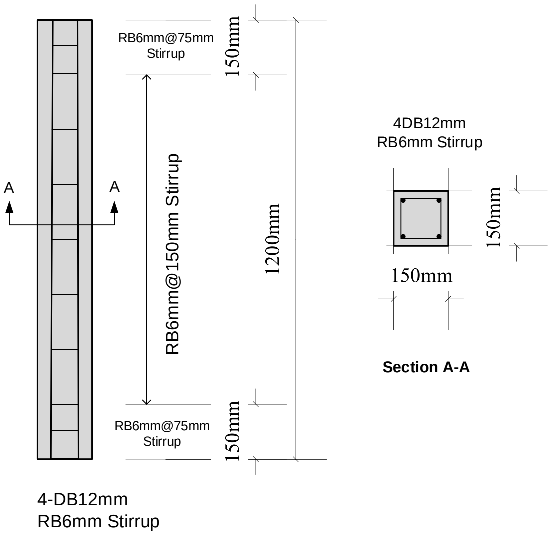

(a) Columns CC-1 and CC-2 (References)

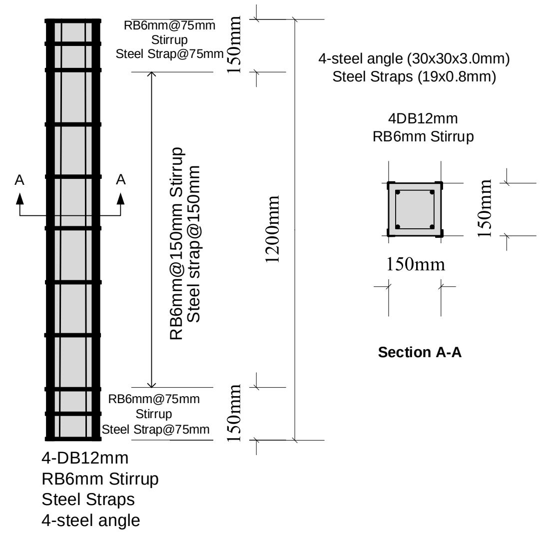

(b) Columns CAS-1 and CAS-2

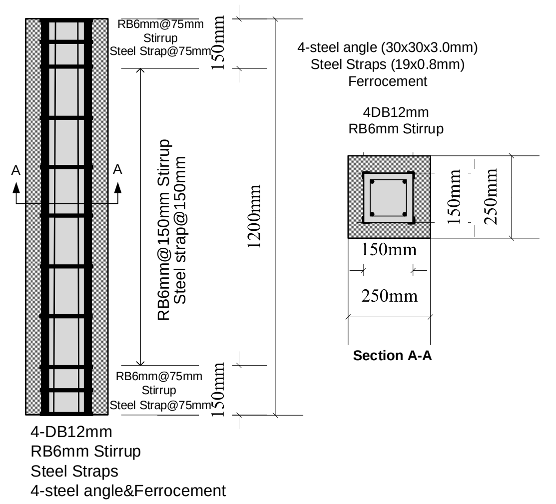

(c) Columns CASF-1 and CASF-2

Figure 1. Details of tested specimens

2. 2. Specimens Descriptions In this experimental work, ordinary Portland cement was used for both mortar and concrete. The water-to-cement ratio (w/c) was set to 0.45. The average compressive strength of mortar and concrete obtained from the test of three samples (Ø150×300 mm) at 28 days was 23 MPa.

Two diameters of steel reinforcement were used. The average yield strength and the ultimate strength of 12-mm diameter (deformed bar, DB) obtained from the test of three samples were 586 and 717 MPa, respectively. The average yield strength and ultimate strength of 6-mm diameter (round bar, RB) obtained from the test of three samples were 423 and 538 MPa, respectively. The steel with equal angle was used. The cross-section and thickness of steel angle were 30×30 mm and 3.0 mm, respectively. The norminal yeild strength was 240 MPa.

For the steel strap, the width and the thickness were 19 and 0.8 mm, respectively. The average yield and ultimate strengths obtained from the test of three samples of the steel straps were 466 and 520 MPa, respectively.

2. 3. Specimens Preparation Figure 2 presents the flowchart of the experimental program. All specimens were cast from the same concrete batch. All columns were remolded after 24 hours and then were cured using plastic wrap. After 28 days, the columns (CSA-1, CSA-2, CSAF-1, and CSAF-2) were strengthened with four steel angles at each corner of the column and then confined with prestressed steel straps with a spacing of 150 mm. A steel strap was prestressed using a steel strap hand tool, as shown in Figure 3. The elongation of steel straps was controlled to be 2.0 mm or 4.2 kN. After that, the steel strap was locked by the steel grip. An injection plaster was carried out in order to fill the gap between the concrete surface and the steel jacket. The ferro-cement was applied for columns CSAF-1 and CSAF-2. The square welded wire mesh was used to wrap around the column and the cement mortar was installed. The controlled cross-dimension was 250×250 mm. After ferro-cement was applied, the plastic wrap was used to cure for another 28 days. Figure 4. shows the plastic curing for column CSAF-1 and CSAF-2.

2. 4. Test Setup and Instrumentations A typical test setup for all tested specimens is demonstrated in Figure 5. The static load was gradually applied in the vertical direction at the top of the tested columns by using a hydraulic jack. The load cell with a capacity of 5000 kN was set-up on top of tested columns. Two linear variable differential transformers (LVDT-1 and LVDT-2) were also set-up at two opposite sides of the columns to measure the vertical displacements. To ensure a uniform loading taking place at the top and bottom of the specimens, capping was used. during the specimens testing procedure, the load and displacements were automatically recorded by using the data logger. The failure modes of the tested columns were observed.

3. EXPERIMENTAL RESULTS AND DISCUSSION

3. 1. Load and Displacement Curve The relationships between axial load and displacement for all tested columns are represented in Figure 6. Table 1 summarizes the maximum axial load carrying capacity and the corresponding displacements of all tested columns in this research work.

For unstrengthened columns, the maximum axial load-carrying capacity of columns CC-1 and CC-2 were

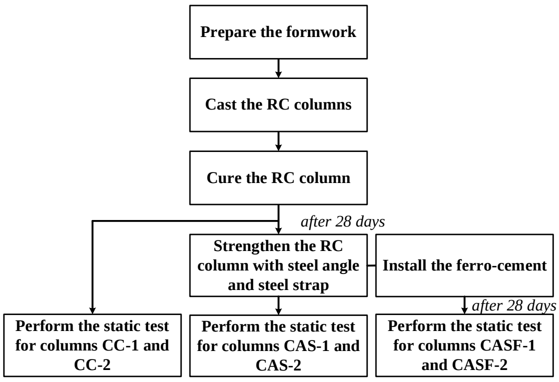

Figure 2. Flow chart of the experimental program

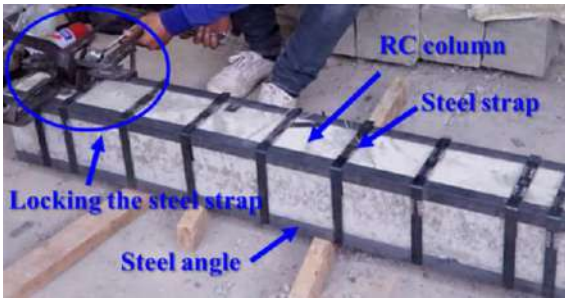

Figure 3. Strengthened column

Figure 4. Plastic curing for column CSAF

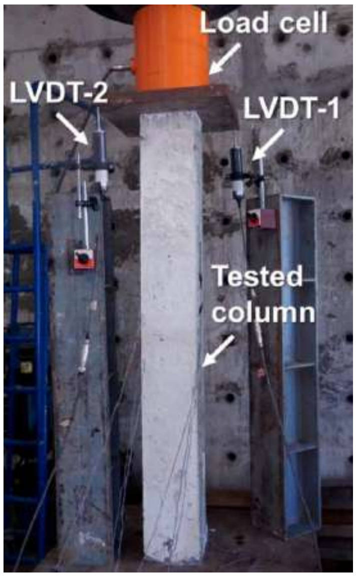

Figure 5. Test setup of a tested column

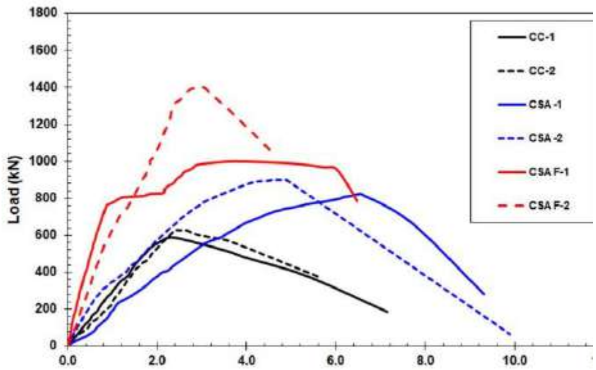

Figure 6. Load-displacement curves of tested columns

TABLE 1. The experimental results of all columns

Specimen Model	Steel Strap	Steel Angle	Ferro-Cement	Maximum Load (kN)	The Displacement* (mm)
CC-1	No	No	No	600	2.22
CC-2	No	No	No	630	2.46
CSA-1	Yes	Yes	No	825	6.55
CSA-2	Yes	Yes	No	900	4.89
CSAF-1	Yes	Yes	Yes	1000	3.97
CSAF-2	Yes	Yes	Yes	1400	3.04

* The displacement corresponding to the maximum load

600 and 630 kN, respectively, which yield an average of 615 kN. The axial displacements correspond to the maximum axial load-carrying capacity of columns CC-1 and CC-2 were 2.22 and 2.46 mm, respectively, which reach an average of 2.34 mm.

For columns CSA-1 and CSA-2, the maximum axial load-carrying capacities were 825 and 900 kN, respectively, which yield an average of 863 kN. The axial displacements corresponding to the maximum axial load carrying capacity of columns CSA-1 and CSA-2 were 6.55 and 4.89 mm, respectively, which yield an average of 5.72mm.

For columns CSAF-1 and CSAF-2 (larger cross-section area), the maximum axial load-carrying capacities were 1000 and 1400 kN, respectively, which reach an average of 1200 kN. The axial displacements corresponding to the maximum axial load carrying capacity of columns CSAF-1 and CSAF-2 were 3.97 and 3.04 mm, respectively, which reach an average of 3.51 mm.

Based on these observed results, the maximum axial load capacity and corresponding displacement of reinforced concrete columns strengthened with steel angle confined by prestressed steel straps (Column CSA) increased by 40% and 144%, respectively, compared to the control columns (Column CC). Using the ferro-cement as the confinement, the maximum axial load capacity and corresponding displacement of column CSAF increased by 95% and 50%, respectively, compared to the control column. In addition to the strength and ductility enhancement, the ferro-cement can improve the stiffness due to the cross-sectional expansion compared to the control column as depicted in Figure 6. All strengthened columns have more ductile behavior compared to the control specimen.

3. 2. Modes of Failure The modes of failure of tested columns are demonstrated hereafter in Figures 7 to 9. For the unstrengthened columns (Columns CC-1 and CC-2), the concrete crushing near the top of the columns was observed for the case of Columns CC-1 (see Figure 7a) and the propagated crushing towards the middle position of the column was observed for the case of Columns CC-2 (see Figure 7b). The buckling of the longitudinal steel bar was found after the concrete cover spalled off, which can be observed in Figure 7.

In the case of the reinforced concrete columns strengthened by steel angles (Columns CSA-1 and CSA-2), the failure has been the steel angles bucking followed by the steel strap rupture. The failure at the connected steel straps was not observed. After that, the concrete was crushed at one end of the column. Figures 8(a) and 8(b) depict the failure modes for columns CSA-1 and CSA-2, respectively. By comparing with the previous work by Sirimontree et al. [26], we found that the mode of failure is in the similar way as presented in the work by Sirimontree et al. [26].

In the case of the reinforced concrete columns strengthened by steel angles and then confined with

(a) Column CC-1

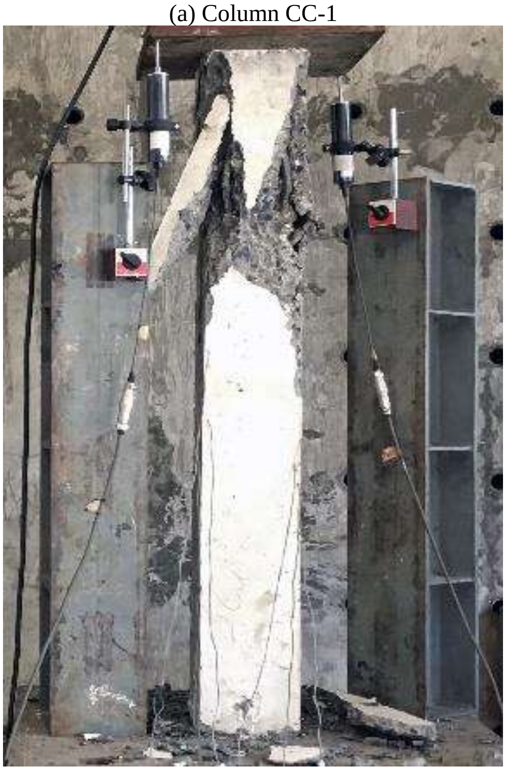

(b) Column CC-2

Figure 7. Failure modes of Columns CC

(a) Column CSA-1

(b) Column CSA-2

Figure 8. Failure modes of Columns CSA

ferro-cement (Columns CSAF-1 and CSAF-2), the crack initiated at the top of the column. A large vertical crack of the concrete was observed for column CSAF-2. Figures 9(a) and 9(b) show the failure modes for columns CSAF-1 and CSAF-2, respectively.

(a) Column CSAF-1

(b) Column CSAF-2

Figure 9. Failure modes of Columns CSAF

4. CONCLUSION

This paper demonstrates the performance of strengthened reinforced concrete columns that were evaluated under the axial load test. A total of six square RC columns were investigated. The original cross-section has been 150×150 mm with a height of 1.2 m. The main objective of this research is to investigate the axial behavior of RC columns strengthened with steel angles with and without ferro-cement. The following conclusions based on the experimental works can be reported:

- The reinforced concrete columns strengthened with steel angles confined with prestressed steel straps enhanced the maximum axial load-carrying capacity and the ductility up to 40% and 144%, respectively, compared to the un-strengthened reinforced concrete columns.
- Using ferro-cement confined around the reinforced concrete column strengthened with steel angle confined with prestressed steel straps, the maximum axial load carrying capacity and ductility increased by 95% and 50%, respectively, compared to the un-strengthened reinforced concrete columns.

5. ACKNOWLEDGMENTS

This research was supported by the Faculty of Engineering Research Fund, Thammasat University. Also, the authors would like to thank Mr. Ittipon Pasityothin for the experiments.

7. REFERENCES

1. Mourad, S. M., and Shannag, M. J., "Repair and strengthening of reinforced concrete square columns using ferro-cement jackets", ***Cement and Concrete Composites***, Vol. 34, No. 2, (2012), 288-294. DOI: 10.1016/j.cemconcomp.2011.09.010
2. Kaish, A. B. M. A., Alam, M. R., Jamil, M., Zain, M. F. M., and Wahed, M. A., "Improved ferro-cement jacketing for restrengthening of square RC short column", ***Construction and Building Materials***, Vol. 36, No. 11, (2012), 228–237. DOI: 10.1016/j.conbuildmat.2012.04.083
3. Sirimontree, S., Witchayangkoon, B., and Lertpocasombut, K., "Strengthening of reinforced concrete column via ferro-cement jacketing", ***American Transactions on Engineering and Applied Sciences***, Vol. 4, No. 1, (2015), 39-47.
4. Jongvivatsakul, P., Bui, L. V. H., Koyekaewphring, T., Kunawisarut, A., Hemstapat, N., and Stitmannaithum, B., "Using steel fiber-reinforced concrete precast panels for strengthening in shear of beams: an experimental and analytical investigation", ***Advances in Civil Engineering***, Vol. 2019, (2019), 4098505. DOI: 10.1155/2019/4098505
5. Jongvivatsakul, P., Thi, C. N., Tanapornraweekit, G., and Bui, L. V. H., "Mechanical properties of aramid fiber-reinforced composites and performance on repairing concrete beams damaged by corrosion", ***Songklanakarin Journal of Science & Technology***, Vol. 42, No. 3, (2020), 637-644. DOI: 10.14456/sjst-psu.2020.81
6. Lenwari, A., Rungamornrat, J., and Woonprasert, S., "Axial compression behavior of fire-damaged concrete cylinders confined with CFRP sheets", ***Journal of Composites for Construction***, Vol. 20, No. 5, (2016), 04016027. DOI: 10.1061/(ASCE)CC.1943-5614.0000683
7. Kianoush M. R., and Esfahani M. R., "Axial compressive strength of reinforced concrete columns wrapped with fiber reinforced polymers (FRP)", ***International Journal of Engineering, Transactions B: Applications***, Vol. 18, No. 1, (2005), 9-19.
8. Maghsoudi, A. A., Rahgozar, R., and Hashemi, S. H., "Flexural testing of high strength reinforced concrete beams strengthened with CFRP sheets", ***International Journal of Engineering, Transactions B: Applications***, Vol. 22, No. 2, (2009), 131-146.
9. Nateghi, F., and Khazaei-Poul, M., "Theoretical and numerical study on the strengthened steel plate shear walls by FRP laminates", ***International Journal of Engineering, Transactions C: Aspects***, Vol. 25, No. 1, (2012), 25-37.
10. Rahmanzadeh, S., and Tariverdilo, S., "Evaluating applicability of ASTM C 928 approach in assessing adequacy of patch repair of bridge piers", ***International Journal of Engineering, Transactions C: Aspects***, Vol. 33, No. 12, (2020), 2455-2463. DOI: 10.5829/ije.2020.33.12c.04
11. Al-Akhras, N., and Al-Mashraqi, M., "Repair of corroded self-compacted reinforced concrete columns loaded eccentrically using carbon fiber reinforced polymer", ***Case Studies in Construction Materials***, Vol. 14, (2021), e00476. DOI: 10.1016/j.cscm.2020.e00476
12. Shadmand, M., Hedayatnasab, A., and Kohnehpooshi, O., "Retrofitting of reinforced concrete beams with steel fiber reinforced composite jackets", ***International Journal of Engineering, Transactions A: Basics***, Vol. 33, No. 5, (2020), 770-783. DOI: 10.5829/ije.2020.33.05b.08
13. Abdel-Hay, A. S., and Fawzy, Y. A. G., "Behavior of partially defected RC columns strengthened using steel jackets", ***HBRC Journal***, Vol. 11, No. 2, (2015), 194-200. DOI: 10.1016/j.hbrcj.2014.06.003
14. Ma, C. K., Yung, S. C. S., Apandi, N., Awang, A. Z., and Omar, W., "Innovative concrete repairing technique using post tensioning steel straps", ***MATEC Web of Conferences***, Vol. 103, (2017), 02011. DOI: 10.1051/matecconf/201710302011
15. Tarabia, A. M., and Albakry, H. F., "Strengthening of RC columns by steel angles and strips", ***Alexandria Engineering Journal***, Vol. 53, No. 3, (2014), 615-626. DOI: 10.1016/j.aej.2014.04.005
16. Adam, J. M., Ivorra, S., Giménez, E., Moragues, J. J., Miguel, P., Miragall, C., and Calderón, P. A., "Behaviour of axially loaded RC columns strengthened by steel angles and strips", ***Steel and Composite Structures***, Vol. 7, No. 5, (2007), 405. DOI: 10.12989/scs.2007.7.5.405
17. Campione, G., "RC columns strengthened with steel angles and battens: experimental results and design procedure", ***Practice Periodical on Structural Design and Construction***, Vol. 18, No. 1, (2013), 1-11. DOI: 10.1061/(ASCE)SC.1943-5576.0000125
18. Belal, M. F., Mohamed, H. M., and Morad, S. A., "Behavior of reinforced concrete columns strengthened by steel jacket", ***HBRC Journal***, Vol. 11, No. 2, (2015), 201-212. DOI: 10.1016/j.hbrcj.2014.05.002
19. Abdel-Hay, A. S., and Fawzy, Y. A. G., "Behavior of partially defected RC columns strengthened using steel jackets", ***HBRC Journal***, Vol. 11, No. 2, (2015), 194-200. DOI: 10.1016/j.hbrcj.2014.06.003
20. Takiguchi, K., "An investigation into the behavior and strength of reinforced concrete columns strengthened with ferro-cement jackets", ***Cement and Concrete Composites***, Vol. 25, No. 2, (2003), 233-242. DOI: 10.1016/S0958-9465(02)00005-7

21. Elsayed, M., and Elsayed, A., "Behaviour of Biaxially loaded RC Columns Retrofitted by Ferro-cement jacketing", ***International Research Journal of Engineering and Technology***, Vol. 5, No. 5, (2018), 55-65.

22. Raza, S., Khan, M. K., Menegon, S. J., Tsang, H. H., and Wilson, J. L., "Strengthening and repair of reinforced concrete columns by jacketing: state-of-the-art review", ***Sustainability***, Vol. 11, No. 11, (2019), 3208. DOI: 10.3390/su11113208

23. Kaish, A. B. M. A., Jamil, M., Raman, S. N., Zain, M. F. M., and Nahar, L., "Ferro-cement composites for strengthening of concrete columns: A review", ***Construction and Building Materials***, Vol. 160, (2018). 326-340. DOI: 10.1016/j.conbuildmat.2017.11.054

24. Jassim, W., and Chassib, S. M., "Effect of fibrous jacket on behavior of RC columns", ***Civil Engineering Journal***, Vol. 6, No. 10, (2020), 1876-1894.

25. Ngo, D. Q., Nguyen, H. C., and Mai, D. L., "Experimental and numerical evaluation of concentrically loaded RC columns strengthening by textile reinforced concrete jacketing", ***Civil Engineering Journal***, Vol. 6, No. 8, (2020), 1428-1442.

26. Sirimontree, S., Keawsawasvong, S., and Thongchom, C., "Reinforced concrete columns confined with prestressed steel straps under axial loading", ***Journal of Applied Science and Engineering***, Vol. 24, No. 3, (2021), 401-406. DOI: 10.6180/jase.202106_24(3).0015

27. Ahmed, A., Mohammed, A. M. Y., and Maekawa, K. "Performance comparison of high strength reinforced concrete circular and square columns subjected to flexural controlled cyclic loading", ***Civil Engineering Journal***, Vol. 7, No. 1, (2021), 83-97.

28. Fazelabdolabadi, B., and Golestan, M. H., "Towards Bayesian quantification of permeability in micro-scale porous structures – The database of micro networks", ***HighTech and Innovation Journal***, Vol. 1, No. 4 (2020), 148-160. Doi: 10.28991/HIJ-2020-01-04-02.

29. Burciaga, U. M., "Sustainability assessment in housing building organizations for the design of strategies against climate change", ***HighTech and Innovation Journal***, Vol. 1, No. 4 (2020), 136-147. DOI: 10.28991/HIJ-2020-01-04-01.

Persian Abstract

چکیده

مقاوم سازی ستون های بتن مسلح موجود به منظور بالابردن ظرفیت باربری محوری و همچنین شکل پذیری آنها ضروری به نظر می رسد. در این مطالعه روش های مختلف مقاوم سازی ستونهای بتن مسلح با کمک نبشی، تسمه فلزی و *ferrocement* به صورت آزمایشگاهی مورد بررسی قرار گرفته است. در کل ۶ نمونه ستون بتن مسلح برای آزمایش ها ساخته شد. مقطع تمامی ستونها ۱۵۰ در ۱۵۰ میلی متر و ارتفاع همه ۱/۲ متر در نظر گرفته شد. دو نمونه به عنوان نمونه مرجع در نظر گرفته شد و سایر نمونه ها با روشهای پیشنهادی در این مطالعه مقاوم سازی گردیدند. دو نمونه با کمک نبشی و تسمه فلزی و دو نمونه دیگر با کمک نبشی و تسمه فلزی و *ferrocement* مقاوم سازی گردیدند. نتایج مطالعات آزمایشگاهی در قالب دیاگرام های نیرو-تغییرمکان و مدهای خرابی ارائه و با یکدیگر مقایسه گردیدند. نتایج بیانگر ارتقا قابل توجه عملکرد سازه ای ستونهای تقویت شده بوده است. در نهایت بحث بر روی روشهای پیشنهادی صورت گرفت.

IJE TRANSACTIONS B: Applications Vol. 34, No. 05, (May 2021) 1132-1144

International Journal of Engineering

Journal Homepage: www.ije.ir

Multi-stage Performance Upgrade of Steel Moment Frames by Post-tension Connections

A. M. Heydari T., M. Gerami*

Department of Civil Engineering, Semnan University, Semnan, Iran

P A P E R I N F O

Paper history:
Received 01 February 2021
Received in revised form 29March 2021
Accepted 04 April 2021

Keywords:
Posttensioned Energy Dissipating Connection
Performance Upgrading Factor
Performance Efficiency Factor
Time History Analysis

A B S T R A C T

Numerous studies have been conducted on self-centering seismic lateral force resisting systems, the consequences of which have resulted in removing many ambiguities regarding the use of such systems in retrofitting the existing frames. The present study evaluated the new approach of improvement of multi-stage performance using such systems. Due to the significant costs of running the whole retrofit project in one stage, as well as some issues such as the impossibility of stopping the use of all floors in some of the existing buildings, multi-stage improvement can be considered as a good suggestion. In this regard, a part of the floors are retrofitted in the first stage and the next stage of improvement are then implemented by spending less budget and time. Accordingly, the execution of the first stage leads to an enhancement in the frame performance to an appropriate extent. In addition, the measuremets taken in the stage are a part of final retrofit project. In the present study, PUF and PEF coefficients were introduced and utilized to select the most appropriate pattern for applying post-tensioned connections in different floors. After analyzing frames, a model was proposed for the multi-stage improvement of each frame by selecting the appropriate pattern using post-tensioned connections in the floors. In the first stage of the suggested plan, for 3-, 6-, and 10-story frames the performance improvements were 15.3, 11.4, and 8.5%, respectively.

***doi**: 10.5829/ije.2021.34.05b.07*

NOMENCLATURE

PUF		A_{ED}(cm^2)	The ED element area
PEF	Performance Efficiency Factor	L_{ED}(cm)	The ED element unbonded length
RPI	Performance Upgrading Factor	$F_{int,PT}$(%FU)	The PT initial prestress force
PT	Post-Tensioned Element	M_w	The moment magnitude scale
ED	Energy Dissipator	t_d(s)	The time duration of earthquake
PTED	Posttensioned Energy Dissipating Connection	RJB(km)	Joyner-Boore distance
SLV	The slaving constrains	PGA(g)	Peak ground acceleration
K_{PT}(Tonf/Cm)	The PT element stiffness	PGV(cm/s)	Peak ground velocity

1. INTRODUCTION

The use of post-tensioning method is considered as one of the solutions to reduce or eliminate residual deformations in the main members of the structure. Applying such systems was examined by researchers in concrete structures [1-3] and then by those specilized in steel ones [4-6], all of whom reported a decrease in permanent drifs by utlizing the system. Additionally, some studies focued on the effect of the changes in each of the effective parameters in such connections [7, 8], and some others highlihted the effect of such systems on retrofitting weak connections, as well as seismic sequencing [9,10].

Post-tension connection with energy dissipating elements (PTED) is one of the modes of reversible systems in steel bending frames that has been introduced and evaluated by researchers [11]. PTED connection includes high strength steel (PT) rebars parallel to the beam axis, and the energy dissipating (ED) bars at the top and bottom of the beam on both the

*Corresponding Author Institutional Email: mgerami@semnan.ac.ir (M. Gerami)

Please cite this article as: A. M. Heydari T., M. Gerami, Multi-stage Performance Upgrade of Steel Moment Frames by Post-tension Connections, International Journal of Engineering, Transactions B: Applications Vol. 34, No. 05, (2021) 1132-1144

left and right sides of the web (Figure 1). The PT bars provide a restoring force which the frame to its initial state after an earthquake. The ED bars embedded in steel cylinders, can be yield under the axial force, leading to energy dissipation. Energy dissipation in the PTED structure is limited to the ED element only and no significant nonlinear deformation occurs in the beam and column elements [12].

Generally, a significant development was made in the field of self-centering reversible seismic systems due to their ability to reduce post-earthquake structural repair costs in recent years [13]. In this regard, different modes of the self-centering moment frame systems were suggested by some researchers [14-16]. In all of the proposed cases, the damage to the main elements of the structure reduced through the gap opening mechanism

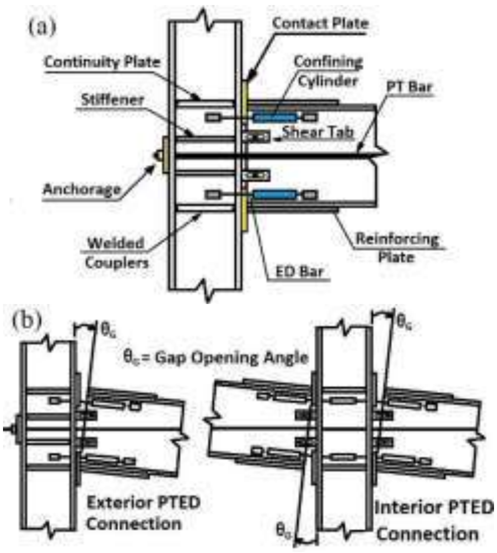

Figure 1. The schematic representation of the posttensioned connection with the energy dissipating elements (a) and gap opening on external and intermediate connection (b) [11]

between the beam and column. In general, after experiencing a major earthquake, it is only necessary to replace the energy dissipating elements in self-centering systems [17].

The novelty of this study is to proposal that in improving a steel moment frame using post-tension connections, instead of all the floors being improved in one stage, only a few floors should be reinforced in the first stage with post-tension connections. Then, in the next stages, the final improvement plan will be implemented, which can lead to economic savings. In other words, after completing some stages of the improvement operation, some floors will have conventional welded joints and some floors will have self-centered connections. In this research, PTED connection was selected and modeled for evaluations among the types of self-centering steel moment systems.

In order to retrofit the frame with welded connections the load on the frame is removed by installing the jacks under the beam element in the first step. In the next step, the top, seat, and shear plates of the beam-column connection are removed. Then the contact plates are welded to the column flange and new shear plates with horizontal slot holes are added to the beam-column connection. Then the columns are drilled to pass the PT elements and the contact elements are welded to the outer flange of the perimeter columns to resist the punching stress caused by the post-tensioning force. Finally, PT elements are post-tensioned and the jacks are removed (Figure 2).

2. VALIDATION

Various approaches have been proposed to model the PT connection-based moment frame structures. These solutions include finite element modeling [18- 20] and modeling with introducing post-tension members by

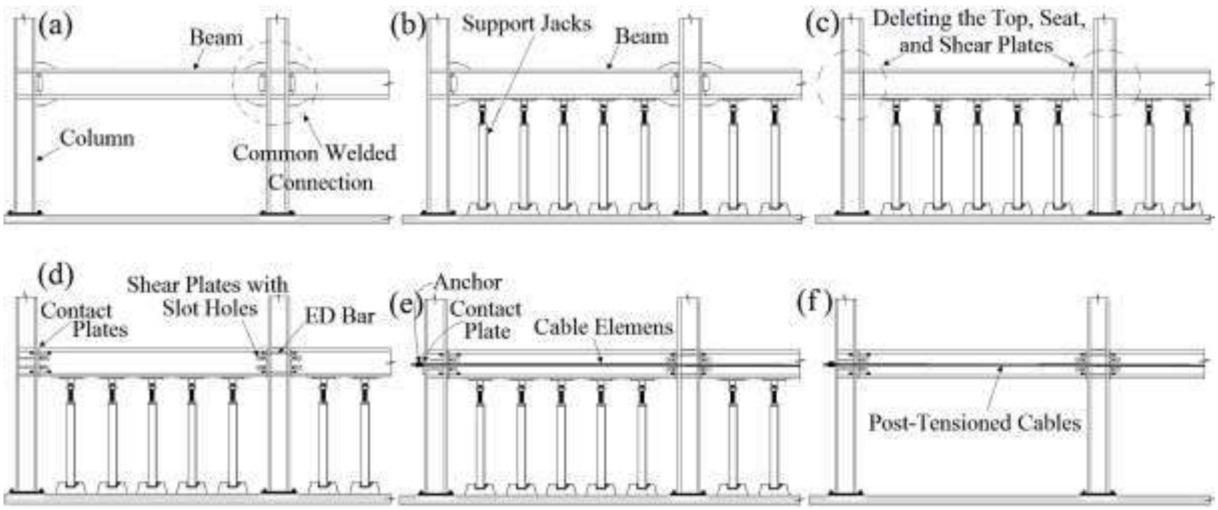

Figure 2. Erection details of retrofitting moment frame with welded connections using post-tensioned elements

the spring element [21]. Prolonged analysis and lack of direct external reflection of the behavior of the connection members leads to the abandonment of the use of finite element and spring modeling, respectively. Finally, separate modeling of the connection elements is considered in Perform-3d [22] software to increase the applicability, as well as reducing the analysis time.

The experimental study of Christopoulos et al. [11] is intended to assess the accuracy of the modeling procedure (Figure 3). A PTED beam-column connection under cyclic loading is evaluated based on the SAC loading protocol. Then, as shown in Figure 4, the elements of beam, column, rigid, connection, ED and PT are modeled in Perform-3d software. The displacement of all nodes is restricted to H_2 to provide two-dimensional frame performance. According to experimental research, the beam and column sections are assigned to W24 × 76 and W14 211, respectively.

Modeling the PT and ED elements is performed as steel bar. The tension-only and none-buckling nonlinear steel materials were used to introduce PT and ED, respectively. The experimental study indicates that a cross-section of 3.8 cm^2 (each cable diameter is 46 mm) and 16.9 cm^2 is provided for the cable and PT elements, respectively. The specifications of DSI high strength bars with elasticity modulus, the final stress and the yield stress are 1.9×10^6, 10500 and 8500 kg/cm^2, respectively, which assigned to the cables and the DSI threaded bars specifications with elasticity modulus, the final stress and the yield stress are 2.038×10^6, 6000 and 4200 kg/cm^2, respectively, which assigned to the ED element. An initial strain equivalent to 0.0028 was applied to the cables to provide posttension until the axial force of 655 KN is created similar to the experimental work in the beam element. The contact element is nonlinear elastic gap hook bar with a low tensile stiffness to provide gap opening which is modeled with a compressive stiffness of 4.62×10^7 Kg_f/cm. The rigid element is defined from non-standard zero-dimensional sections with high axial, shear and moment resistances with high inertia to ensure its rigid performance. Finally, as shown in Figure 4, the elements of beam, column, rigid, PT, ED and contact are modeled. Some constraints between different nodes to ensure system performance are also presented in Table 1.

Then the cyclic load simulation is performed by introducing 30 cycles as gravity load, with positive coefficients for positive and negative coefficients to and fro loads, respectively, as well as applying drift constraints in each cycle to stop the analysis and subsequent cumulative application of these weight loads. In addition, the output end of each cycle is extracted separately and added to the output end of the previous cycles with a negative coefficient. Finally, the structural response under cyclic loading is illustrated in Figure 5, which is in line with the results of the experimental study.

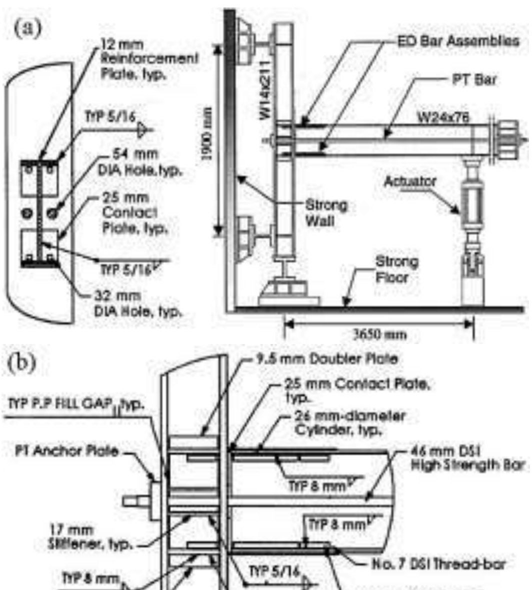

Figure 3. Overview of the experimental model of connection after stress with energy dissipating elements (a) and display of its connection details (b) [11]

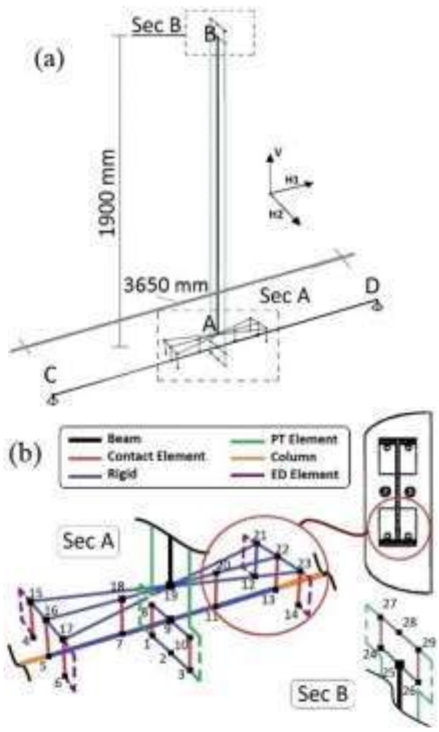

Figure 4. Overview of beam-column modeling with PTED connection (a) and details of the A and B sections (b)

TABLE 1. The constraints applied between nodes

	Node Number									
SLV	**1-3**	**4-5 6-8 10-12 13-14**	**2-9-19**	**4-5-6-8 10-12 13-14**	**15-16-17**	**15-16 17-18 20-21 21-23**	**21-22-23**	**24-25 26-27 28-29**	**5-9-13**	**24-25 26-27 28-29**
H1	✓	✓	✓			✓		✓		
V			✓	✓	✓		✓			✓
R2					✓		✓		✓	
RV	✓	✓				✓		✓		

SLV: Terms H1 and V are displacement in H1 and V direction and R2 and RV rotation around H2 and V axis respectively.

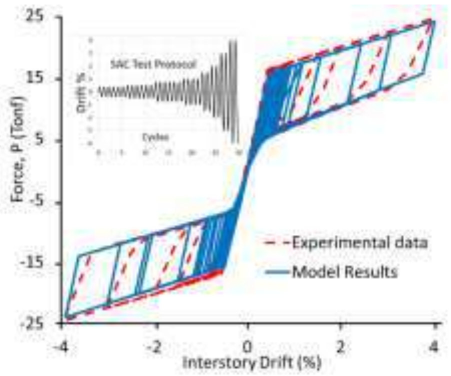

Figure 5. Experimental and numerical force interstory drift

3. MODELING

In this study, three-, six-, and ten-story structures were evaluated. The perimeter frames are in the east-west direction of the special moment frame and the north-south direction of the braced frame. Internal frames tolerate the gravity load while perimeter frames tolerate the lateral loads. The plan of all three structures is similar, as shown in Figure 6.

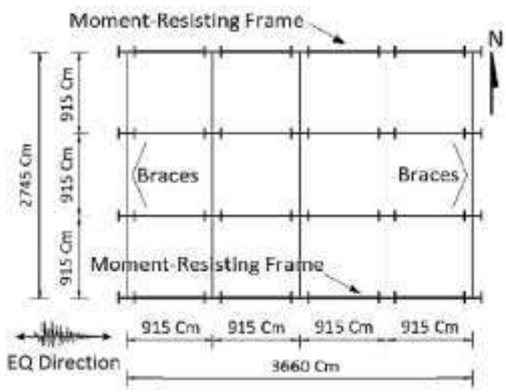

Figure 6. Plane view of structures evaluated in this study

The three-story structure used in the present study was first designed by Shen et al. [23], and then re-designed and evaluated by Apostolakis et al. [24] (Figure 7a). Then PTED connection is used to provide moment resistance of the frame by Apostolakis et al. [25]. The frame with similar specifications as the PTED connections frame designed by Apostolakis et al. [25] was modeled and the result of the push-over analysis is shown in Figure 7b. In addition, the results shown in Figure 7b confirm the validity of the modeling procedure performed in this study.

The six- and ten-story structure was designed in both cases with the welded (Figures 8a and 8b) and PTED connections across all stories based on Apostolakis et al. [25] proposed procedure through plans, loading, codes and the specifications similar to the mentioned three-story structure. The modeling parameters of PTED

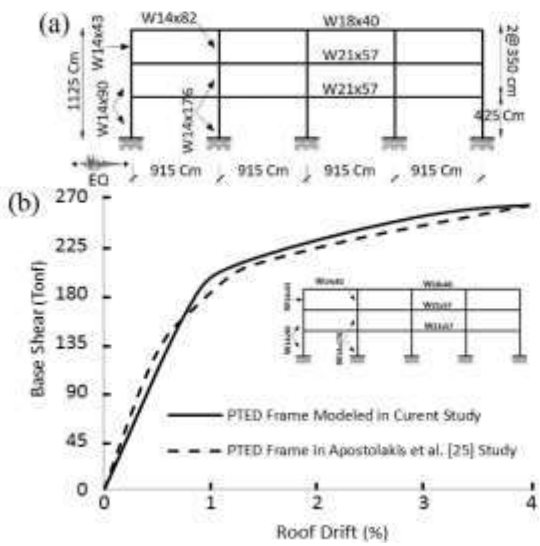

Figure 7. Elevation view (a) and structural pushover curves (b) of three-story frame in Apostolakis et al. [25] and current research

connections in all three-, six- and ten-story structures are shown in Table 2.

Seven states for the three-story frame, ten states for the six-story frame and fourteen states for the ten-story frame were evaluated based on the engineering judgment to evaluate the different states of the post-tensioned distribution in the floors. The different statuses and the nomenclature of the frames are shown in Table 3. For example, the frame with the abbreviation s-1 is a six-story frame which the PTED connections is used in the first and second floors.

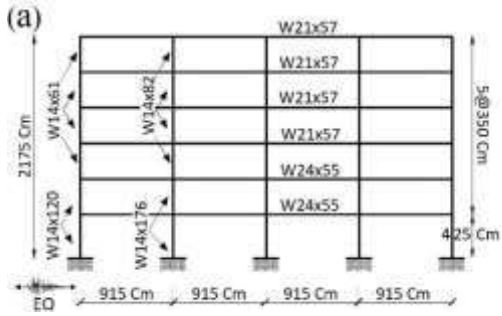

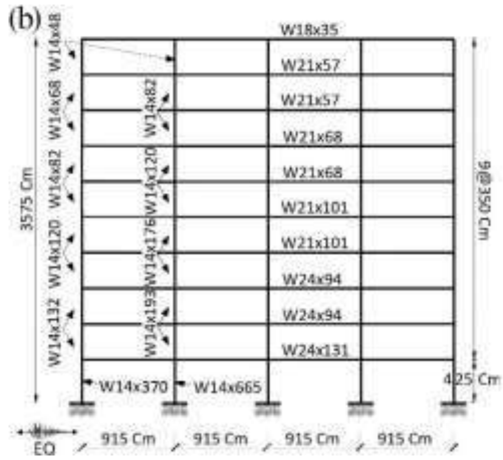

Figure 8. Elevation view of six-story (a) and ten-story (b) frames that are examined in this research

4. ANALYSIS

The time history analysis was performed on eight three-story frames, eleven six-story frames and fifteen ten-story frames (presented in Table 3). In the time history

TABLE 2. The PTED parameters of 3-, 6- and 10-story frames

	Story	Three- and six-story				Story	Ten story			
		K_{PT}(tonf/ Cm)	A_{ED} (Cm^2)	L_{ED} (Cm)	$F_{init,PT}$ (%FU)		K_{PT}(tonf/ Cm)	A_{ED} (Cm^2)	L_{ED} (Cm)	$F_{init,PT}$ (%FU)
3-story	St1	6	7	58.4	0.3	St1	9	9.5	64.3	0.32
	St2	6	7	38.1	0.36	St2	9	9.5	64.3	0.32
	St3	9	5.8	58.1	0.26	St3	9	8.5	58.4	0.36
						St4	6	8.5	58.4	0.36
6-story	St1	9	8.5	58.4	0.3	St5	6	8.5	58.4	0.36
	St2	9	8.5	58.4	0.3	St6	6	7	38.1	0.3
	St3	6	7	58.4	0.36	St7	6	7	38.1	0.3
	St4	6	7	38.1	0.36	St8	9	7	38.1	0.3
	St5	9	5.8	38.1	0.26	St9	9	5.8	37	0.26
	St6	9	5.8	38.1	0.26	St10	9	5.8	37	0.26

TABLE 3. Distribution of PT connections in floors

3-story		6-story		10-story	
Frame	**PT Stories**	**Frame**	**PT Stories**	**Frame**	**PT Stories**
3st-MRF	No story	6st-MRF	No story	10st-MRF	No story
3st-PTED	All stories	6st-PTED	All stories	10st-PTED	All stories
t-1	1	s-1	1,2	Te-1	1,2
t-2	2	s-2	3,4	Te-2	1,2,5,6
t-3	3	s-3	5,6	Te-3	1,2,6,7
t-4	1,2	s-4	1,2,3	Te-4	1,2,7,8
t-5	1,3	s-5	2,3,4	Te-5	1,2,6,7,8
t-6	2,3	s-6	3,4,5	Te-6	1,2,5,6,7,8
		s-7	4,5,6	Te-7	1,2,3
		s-8	2,3,4,5	Te-8	1,2,3,5,6
		s-9	1,2,3,4	Te-9	1,2,3,6,7
				Te-10	1,2,3,7,8
				Te-11	1,2,3,6,7,8
				Te-12	1,2,3,5,6,7,8
				Te-13	1,2,3,4,5,6

analyses of this study, the record to record variability is considered by employing a set of 15 ground motion records representative of different intensities, durations and frequency contents, adopted from the FEMA P-695 [26]. The characteristics of the selected ground motion records are provided in Table 4.

Similar to Apostolakis et al. [25] study, maximum and residual drift, and maximum and RMS acceleration were considered as performance evaluation of the structural parameters. RMS parameter demonstrates root mean square floor acceleration, which is calculated based on Equation (1):

$$\mathrm{RMSAcc} = \max\left\{\sqrt{\frac{\sum_{j=1}^{N}\left[Acc_i\left(t_j\right)\right]^2}{N}}\right\} \quad \text{for} \quad \mathrm{i}=1,\ldots,\mathrm{N}_{\mathrm{story}} \qquad (1)$$

where N and Acc_i (t_j) are the number of time steps within the actual duration of an earthquake (t_d in Table 4) and the absolute acceleration of the story i at the time step j, respectively. Figure 9 displays the values of the above-mentioned parameters for three-, six-, and ten-story frames with conventional welding connections (3st-MRF, 6st-MRF and 10st-MRF).

5. ASSESSING THE COMPETENCY OF EACH FRAME

The overall upgrading effect associated with retrofitting by post-tension connections was quantified by a relative performance index (RPI), which combines several single-parameter indices (SPIs), including peak interstory drift ratios, residual interstory drift ratios, peak floor accelerations, and root mean square floor accelerations [27, 28] (Equation (2)). In this regard, the mentioned parameters were evaluated for each frame and then only a single numerical parameter is assigned to the relative performance of each frame using RPI, which has led to the use of this evaluation procedure instead of other evaluation methods such as incremental dynamic analysis.

$$\begin{gathered}\mathrm{RPI} = \alpha\times\mathrm{MDR} + \beta\times\mathrm{RDR} + \gamma\times\mathrm{RMSAR} + \delta\times\mathrm{MAR} \\ \mathrm{MDR} = \frac{\mathrm{MaxDrift}_{\mathrm{Frame}}}{\mathrm{MaxDrift}_{\mathrm{MRF}}} \;;\; \mathrm{RDR} = \frac{\mathrm{ResDrift}_{\mathrm{Frame}}}{\mathrm{ResDrift}_{\mathrm{MRF}}} \\ \mathrm{RMSAR} = \frac{\mathrm{RMSAcc}_{\mathrm{Frame}}}{\mathrm{RMSAcc}_{\mathrm{MRF}}} \;;\; \mathrm{MAR} = \frac{\mathrm{MaxAcc}_{\mathrm{Frame}}}{\mathrm{MaxAcc}_{\mathrm{MRF}}}\end{gathered} \qquad (2)$$

In Equation (2), the parameters MaxDrift, ResDrift, RMSAcc and MaxAcc are Maximum interstory drift, residual interstory drift, root mean square floor acceleration and max floor absolute acceleration, respectively, and root mean square floor acceleration values are calculated based on Equation (1). The coefficients α, β, γ and δ in Equation (2) are weighting coefficients, the sum of which is equal to one and can have values ranging from 0 to 1.

Based on Table 5, 15 various states for the values of weighting coefficients were considered in the present study to select the optimal frame with more accuracy.

In addition, each frame was first analyzed by applying 15 earthquake records (presented in Table 4). Further, the mean of 15 frame responses was extracted and their maximum was computed and used in the calculations of Equation (2). Furthermore, the weight coefficients corresponding to each scenario (Table 4) were replaced in Equations (2) and (15) values were calculated for RPI.

TABLE 4. The ground motion characteristics

Name	Earthquake event	Year	Station	M_W	t_d (s)	RJB (km)	PGA (g)	PGV (Cm/s)
EQ1	Northridge	1994	Beverly Hills-Mulhol	6.7	30	9.4	0.488	63
EQ2	Northridge	1994	Canyon Country-WLC	6.7	20	11.39	0.471	45
EQ3	Duzce, Turkey	1999	Bolu	7.1	56	12	0.805	62
EQ4	Hector Mine	1999	Hector	7.1	45	10.3	0.328	42
EQ5	Imperial Valley	1979	Delta	6.5	100	22	0.349	33
EQ6	Imperial Valley	1979	El Centro Array #11	6.5	39	12.5	0.379	42
EQ7	Kobe, Japan	1995	Nishi-Akashi	6.9	41	7	0.483	37
EQ8	Kobe, Japan	1995	Shin-Osaka	6.9	41	19.1	0.233	38
EQ9	Kocaeli, Turkey	1999	Duzce	7.5	27	13.6	0.364	59
EQ10	Kocaeli, Turkey	1999	Arcelik	7.5	30	10.5	0.21	40
EQ11	Landers	1992	Yermo Fire Station	7.3	44	23.6	0.244	52
EQ12	Landers	1992	Coolwater	7.3	28	19.7	0.417	42
EQ13	Loma prieta,USA	1989	Capitola	6.9	40	8.6	0.511	35
EQ14	Loma prieta,USA	1989	Gilroy Array #3	6.9	40	12.2	0.559	45
EQ15	Manjil, Iran	1990	Abbar	7.3	53	12.5	0.514	54

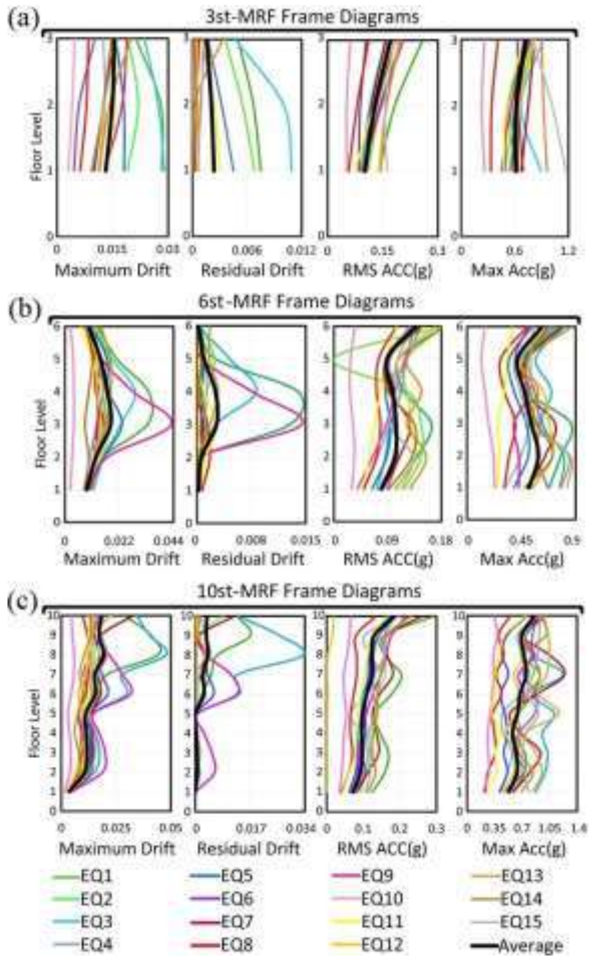

Figure 9. Schematic Diagrams of 3st-MRF (a), 6st-MRF (b) and 10st-MRF (c) frame responses (Maximum drift, Residual drift, RMS acceleration and Maximum acceleration) under earthquakes mentioned in Table 4

TABLE 5. The values considered for α, β, γ and δ

Weight Factor	Different scenarios for RPI														
	RPI_1	RPI_2	RPI_3	RPI_4	RPI_5	RPI_6	RPI_7	RPI_8	RPI_9	RPI_{10}	RPI_{11}	RPI_{12}	RPI_{13}	RPI_{14}	RPI_{15}
α	1	0	0	0	$\frac{1}{4}$	0	$\frac{1}{3}$	$\frac{1}{3}$	$\frac{1}{3}$	$\frac{1}{3}$	$\frac{1}{6}$	$\frac{1}{6}$	$\frac{1}{6}$	$\frac{1}{3}$	$\frac{1}{3}$
β	0	1	0	0	$\frac{1}{4}$	$\frac{1}{3}$	0	$\frac{1}{3}$	$\frac{1}{3}$	$\frac{1}{3}$	$\frac{1}{6}$	$\frac{1}{3}$	$\frac{1}{3}$	$\frac{1}{6}$	$\frac{1}{6}$
γ	0	0	1	0	$\frac{1}{4}$	$\frac{1}{3}$	$\frac{1}{3}$	0	$\frac{1}{3}$	$\frac{1}{6}$	$\frac{1}{3}$	$\frac{1}{6}$	$\frac{1}{3}$	$\frac{1}{6}$	$\frac{1}{3}$
δ	0	0	0	1	$\frac{1}{4}$	$\frac{1}{3}$	$\frac{1}{3}$	$\frac{1}{3}$	0	$\frac{1}{6}$	$\frac{1}{3}$	$\frac{1}{3}$	$\frac{1}{6}$	$\frac{1}{3}$	$\frac{1}{6}$

Finally, the RPIs were averaged and the final value of the performance index related to each frame was determined.

5. 1. Upgrade and Effectiveness of Each Frame

The inverse of RPI can be utilized to determine the degree of improving or reducing the frame performance relative to moment frame so that RPI greater than one reflects upgrading performance vice versa. Accordingly, performance upgrade factor (PUF) was introduced based on Equation (3) for the first time in this study to calculate the degree of increasing the performance of each frame in relation to the moment frame.

$$PUF = \frac{1}{RPI} - 1 \tag{3}$$

Additionally, performance efficiency factor (PEF) was provided and used based on the Equation (4) in order to examine the efficiency of utilizing PT connections in each floor. In fact, the coefficient allows to calculate the effect of using PT connection per story so that the state with the highest PEF indictaes obtaining the maximum performance improvement by using PT connections in the lowest number of floors. Accordingly, considering PEF during suggesting a retrofitting plan for an existing structure is important when requiring more cost-effective PT systems.

$$PEF = \frac{PUF}{n} \tag{4}$$

where n illustrates the number of the stories in which PT connections are applied. It is worth noting that PEF values less than zero represent the negative efficiency of utilizing PT connection in each floor.

Tables 5, 6, and 7 summarize the RPI, PUF, and PEF values of each frame. As demonstrated, the normalized PUF values are presented as NPUF parameter in the fifth column, which are considered as the ratio of the PUF related to each frame to the maximum PUF of frames with similar floors.

Based on the results in Table 6, the least RPI was observed in 3st-PTED (0.829) and t-4 frames (0.829), while the highest was related to t-2 (0.968) and t-3 frames (0.964).

The PUF and PEF values of three-story frames are represented in Figure 10. As shown, all states result in

TABLE 6. Competency assessment values for 3-story frames

Frame	PT Stories	RPI	PUF	NPUF	n	PEF
3st-PTED	All Stories	0.825	0.233	100 %	3	0.078
t-1	1	0.875	0.153	65.9 %	1	0.153
t-2	2	0.968	0.035	14.9 %	1	0.035
t-3	3	0.964	0.039	16.6 %	1	0.039
t-4	1,2	0.829	0.232	99.5 %	2	0.116
t-5	1,3	0.857	0.177	75.9 %	2	0.088
t-6	2,3	0.940	0.066	28.4 %	2	0.033

enhancing the performance of the frame compared to that of frame with conventional welded connections (PUF>1). Further, 3st-PTED (0.233) and t-4 frames (0.232) attain the maximum PUF, while t-1 (0.153) and t-4 frames (0.116) achieve the highest PEF .

In order to increase the performance of three-story frames during multi-stage, two scenarios were proposed based on the values presented in Figure 10 and Table 6. The first scenario includes upgrading the frame to t-5 one in the first stage and 3st-PTED one during the next stages. Due to the low value of PEF in t-5 and 3st-PTED frames, the scenario failed to provide the economic savings intended in the study. Therefore, the second scenario was proposed, upon which the frame is upgraded to t-1 in the first stage (65.9% of the final performance improvement), t-4 in the second stage (99.5% of the final improvement), and finally, 3st-PTED frame in the third step if an upgrade to 23.3% is considered (Figure 11).

According to the proposed improvement scenario, the response diagrams of t-1 and t-4 frames are represented in Figures 12a and 12b. Furthermore, Figure 12c demonstrates the mean response of t-1, t-4, 3st-PTED, and 3st-MRF frame diagrams for easifying comparison. As displayed, the t-1, t-4, and 3st-PTED

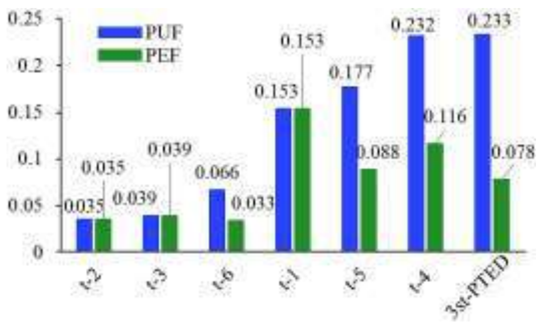

Figure 10. PUF and PEF values of 3-Story frames

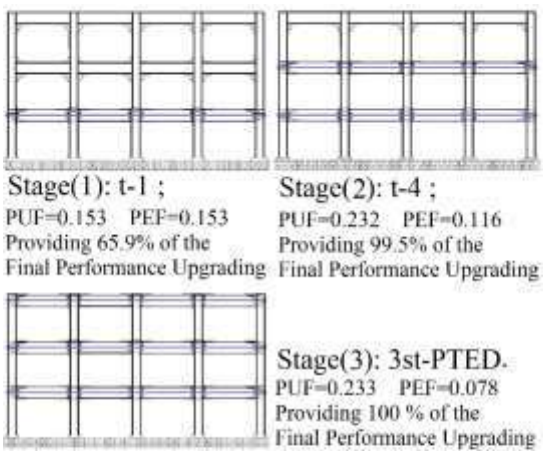

Figure 11. Proposed scenario for multi-stage retrofitting of three-story frame

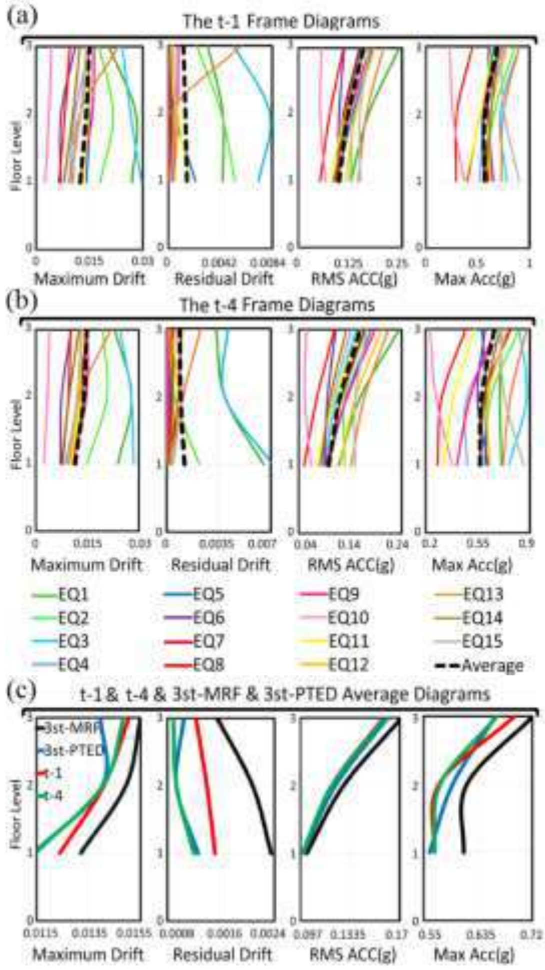

Figure 12. Schematic Diagrams of t-1 (a), t-4 (b) and average of t-1, t-4, 3st-MRF and 3st-PTED (c) frame responses under earthquakes mentioned in Table 4

frames provide a more appropriate response compared to the 3st-MRF one. The response of 3st-PTED frame at maximum dirift, and that of t-4 frame at residual dirift and maximum acceleration are better than that of other frames, while the RMSAcc response of frames t-1, t-4, and 3st-PTED are almost identical.

Considering the values of RPI, PUF, NPUF, n, and PEF of six-story frames (Table 7), the RPI coefficients of the frames s-3, s-6, and s-7 are higher than one. This issue reflects that the conversion of the frame with conventional welded connections to the intended frames in all floors results in decreasing the performance of the frame instead of enhancing the performance.

Figure 13 depicts the PUF and PEF for six-story frames, which are sorted based on the largest values. As shown, the highest PUF is obtained in s-9 (0.301) and 6st-PTED frames (0.239), while the maximum PEF is achieved in s-9 (0.075) and s-1 frames (0.057).

Based on the PUF and PEF values in Table 7 and Figure 13, two scenarios were proposed to enhance the

TABLE 7. Competency assessment values for 6-story frames

Frame	PT Stories	RPI	PUF	NPUF	n	PEF
6st-PTED	All stories	0.83	0.239	79.4 %	6	0.040
s-1	1,2	0.90	0.113	37.8 %	2	0.057
s-2	3,4	0.96	0.045	14.9 %	2	0.023
s-3	5,6	1.63	-0.334	---	2	-0.167
s-4	1,2,3	0.90	0.122	40.5 %	3	0.041
s-5	2,3,4	0.88	0.153	51 %	3	0.051
s-6	3,4,5	1.09	-0.077	---	3	-0.025
s-7	4,5,6	1.39	-0.247	---	3	-0.082
s-8	2,3,4,5	0.998	0.002	0.5 %	4	0.0004
s-9	1,2,3,4	0.802	0.301	100 %	4	0.0753

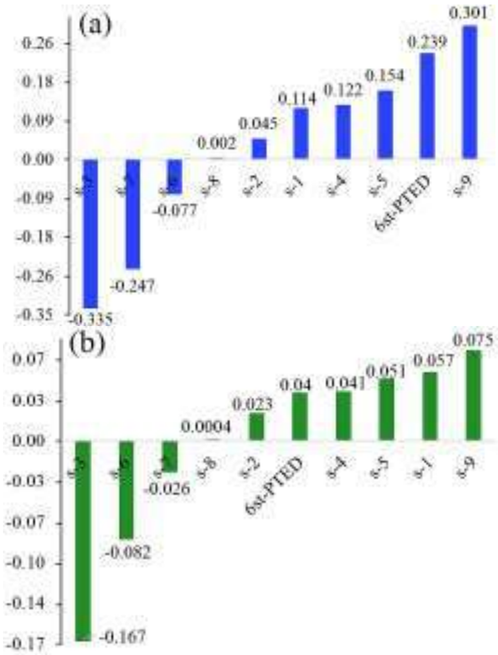

Figure 13. PUF (a) and PEF (b) values of 6-Story frames

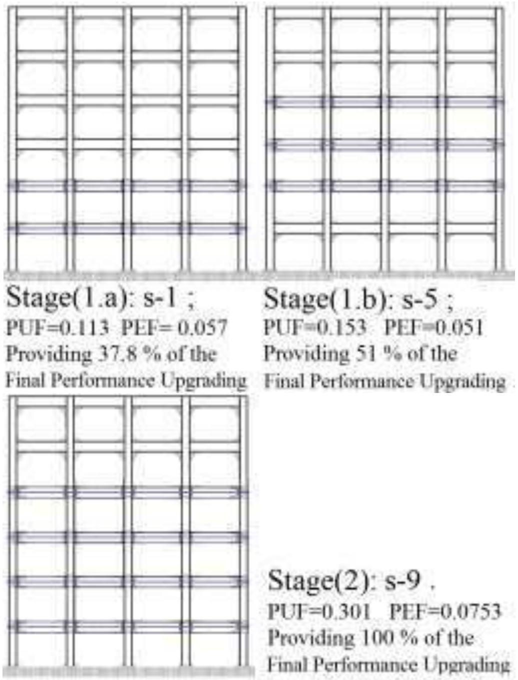

Figure 14. Proposed scenario for multi-stage retrofitting of six-story frame

frame performance during multi-stages (Figure 14). Regarding the first scenario, the frame was upgraded to s-1 in the first step and finally to s-9. The second scenario was suggested if an enhancement in performance by 37.8% of the final performance upgrade (performance improvement provided by s-1 frame) was insufficient for the first stage. In the second scenario, the frame was upgraded to s-5 in the first stage (leading to 51% of final performance improvement) and s-9 in the final stage. In the first scenario, an enahncement in performance was low in the first stage although it was more economical due to the larger PEF value of s-1 frame compared to that of s-5 one.

Figures 15a and 15b display the response diagrams of frames s-1 and s-9. In order to compare better, Figure 15c depicts the mean response of the s-1 and s-9 frame diagrams providing the highest PEF values, as well as that of 6st-PTED and 6st-MRF frames. As demonstrated, the maximum response values of drift and residual drift in the s-1, s-9 and 6st-PTED frames reduce relative to those of the frame with welded connections in all floors, while the MaxAcc and RMSAcc diagrams of all four frames are almost identical.

In addition, ten-story frames were evaluated, the RPI, PUF, NPUF, n, and PEF of which are summarized in Table 8. Based on the results in Table 8, RPI was minimized and maximized in 10st-PTED (0.882) and Te-7 frames (0.984), respectively.

Figure 16 presents the PUF and PEF values for ten-story frames, which are sorted by largest values, which indicates the highest PUF in 10st-PTED (0.14) and Te-2 frames (0.09), as well as the maximum PEF in Te-2 (0.021) and Te-4 ones (0.016).

Considering the PUF and PEF in Table 8 and Figure 16, two scenarios were suggested for increasing the frame performance in multi-stages (Figure 17). The first scenario includeed improving the frame to Te-2 in the first stage and finally upgrading to 10st-PTED. Given that the PEF value of Te-2 frame was maximum among that of all ten-story frames, the use of the scenario was the most economical mode of improvement. The second scenario was proposed for the cases in which the start of

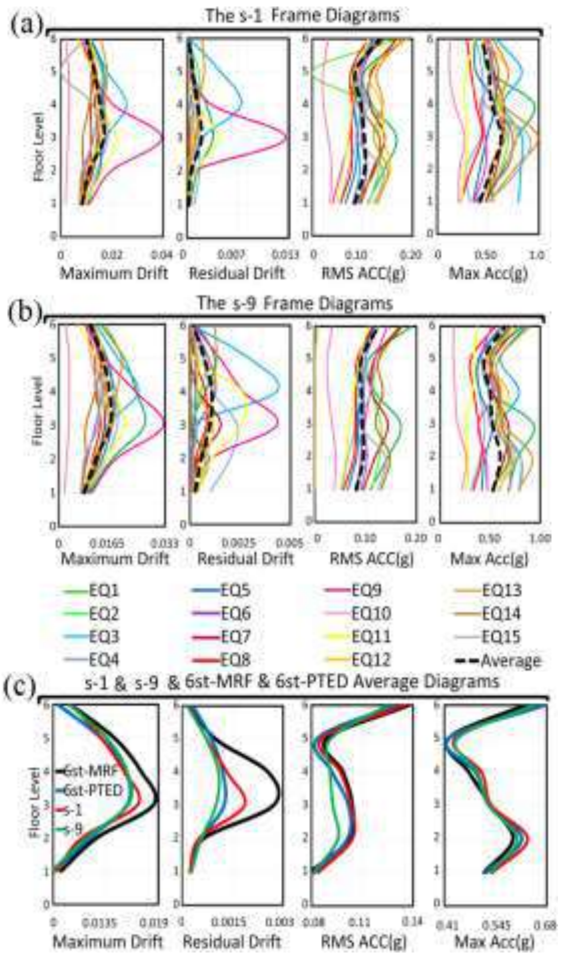

Figure 15. Schematic Diagrams of s-1 (a), s-9 (b) and average of s-1, s-9, 6st-MRF and 6st-PED (c) frame responses

TABLE 8. Competency assessment values for 10-story frames

Frame	PT Stories	RPI	PUF	NPUF	n	PEF
10st-PTED	All Stories	0.882	0.142	100 %	10	0.0142
Te-1	1,2	0.979	0.022	15.7 %	2	0.0111
Te-2	1,2,5,6	0.923	0.085	60.1 %	4	0.0213
Te-3	1,2,6,7	0.957	0.046	32.7 %	4	0.0116
Te-4	1,2,7,8	0.943	0.063	44.7 %	4	0.0159
Te-5	1,2,6,7,8	0.933	0.074	52 %	5	0.0147
Te-6	1,2,5,6,7,8	0.929	0.078	55.3 %	6	0.0131
Te-7	1,2,3	0.984	0.016	11.4 %	3	0.0054
Te-8	1,2,3,5,6	0.928	0.078	55.4 %	5	0.0157
Te-9	1,2,3,6,7	0.980	0.021	14.5 %	5	0.0041
Te-10	1,2,3,7,8	0.949	0.056	39.7 %	5	0.0112
Te-11	1,2,3,6,7,8	0.941	0.064	45.1 %	6	0.0107
Te-12	1,2,3,5,6,7,8	0.943	0.061	43.2 %	7	0.0087
Te-13	1,2,3,4,5,6	0.935	0.069	48.7 %	6	0.0115

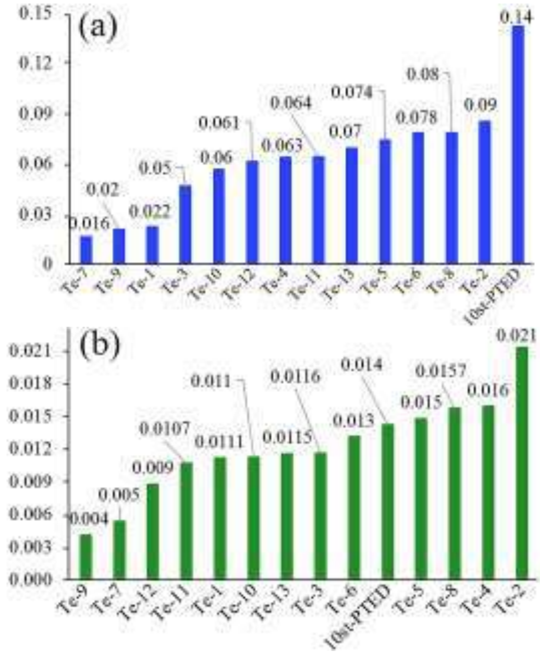

Figure 16. PUF (a) and PEF (b) values of 10-Story frames

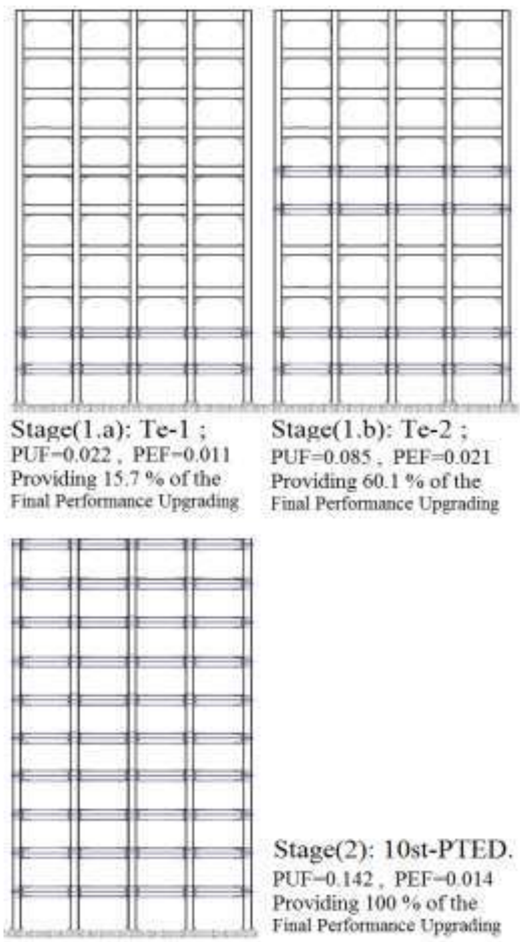

Figure 17. Proposed scenario for multi-stage retrofitting of ten-story frame

upgrade by using PT connections in four floors is impossible due to the lack of retrofit budget or similar cases. In the scenario, the frame was upgraded to the Te-1 by improving only two floors in the first stage. Then, it was respectively upgraded to Te-2 and 10st-PTED frames in the second and third stages. The scenario led to 15.7 and 60.1% of the final performance improvement in the first and second stages, respectively.

Figures 18a and 18b represent the response diagrams of the Te-2 and 10st-PTED frames providing the highest PUF. Finally, the mean response diagrams of Te-2, 10st- PTED, and 10st-MRF are displayed in Figure 18c for better comparison, which demonstrtaes a decrease in the response values of the maximum and residual drift, RMSAcc, and MaxAcc in Te-2 and 10st-PTED frames relative to that of frame with conventional welded connections in all Floors.

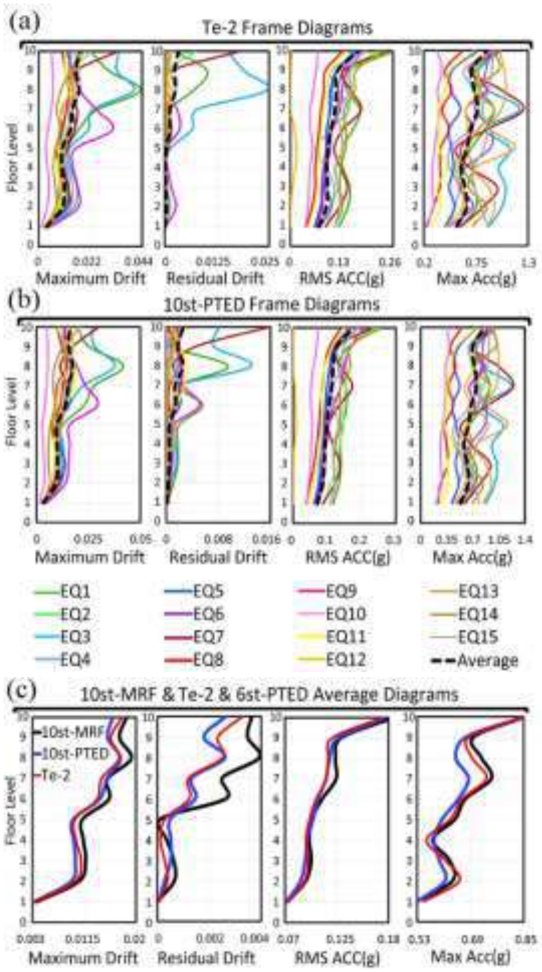

Figure 18. Schematic Diagrams of Te-2 (a), 10st-PTED (b) and average of Te-2, 10st-PTED and 10st-MRF (c) responses

6. CONCLUSION

The present study sought to evaluate the efficiency of the multi-stage improvement's new aproach of moment frames with conventional welded connections using reversible system. In this regard, 6, 10, and 14 post-tensioning states in the 3-, 6-, and 10-story frame were respectively selected in order to assess the feasibility of the suggestion. Additionally, RPI, PUF, and PEF coefficients were applied to examine the intended frames in different states. It should be noted that the PUF coefficient is presented and used for the first time in this paper. Based on the results, the use of PT connections in the lower floors of the frames under study, as the first stage of retrofitting, is a good suggestion.

Among the three-story frames, 3st-PTED frame with a 23.3% performance improvement compared to the MRF one was determined as the most suitable state for attaining the final purpose of upgrading.

Further, the t-1 frame using PT connections in only one floor led to a 15.3% improvement in frame performance (65.9% of the final frame upgrade), and was selected as an option proposed for the first stage of improvement among three-story frames.

Regarding the six-story frames, the s-9 frame using PT connections in the first four floors resulted in enahncing performance by 30.1% compared to that of 6st-MRF, which was even higher than the performance upgrade in the 6st-PTED.

Accordingly, the s-9 frame was selected as the final improvement plan in the study, which represents that finding the situations which can provide the highest performance upgrade without retrofitting all floors is possible if the location of PT connectiotns is evaluated in different floors. Furthermore, the performance of s-1 frame enhanced by 11.4% by using PT connections in two floors (37.8% of the final frame upgrade) and was adopted as an option suggested for the first stage of improvement among 6-story frames.

Based on the results of assessing the ten-story frames, the 10-PTED frame was obtained as the most suitable state for achieving the final goal of improvement. In addition, it increased performance by 14.2% compared to that of 10st-MRF frame. Further, the Te-2 frame using PT connections in four floors enhanced performance as 8.5% (60.1% of the final frame upgrade) and was selected as an option proposed for the first stage of improvement among the ten-story frames.

Finally, upgrading frame performance using PT connections during multi-stagecan lead to a good performance in each stage, along with economic savings.

7. REFERENCES

1. Cheok, G.S. and Lew, H.S. "Performance of Precast Concrete Beam-to-column Connections Subject to Cyclic Loading." ***PCI Journal,*** Vol. 36, No. 3, (1991), 56-67. DOI: 10.15554/pcij.05011991.56.67
2. Priestley, M.N. and Tao, J.R. "Seismic Response of Precast Prestressed Concrete Frames with Partially Debonded Tendons." ***PCI Journal,*** Vol. 38, No. 1, (1993), 58-69. DOI: 10.15554/pcij.01011993.58.69
3. Kurama, Y., Pessiki, S., Sause, R. and Lu, L.W. "Seismic Behavior and Design of Unbonded Post-tensioned Precast Concrete Walls." ***PCI Journal,*** Vol. 44, No. 3, (1999), 72-89. DOI: 10.15554/pcij.05011999.72.89
4. Ricles, J.M., Sause, R., Garlock, M.M. and Zhao, C. "Posttensioned Seismic-resistant Connections for Steel Frames." ***Journal of Structural Engineering,*** Vol. 127, No. 2, (2001), 113-121. DOI: 10.1061/(ASCE)0733-9445(2001)127:2(113)
5. Ricles, J.M., Sause, R., Peng, S.W. and Lu, L.W. "Experimental Evaluation of Earthquake Resistant Posttensioned Steel Connections." ***Journal of Structural Engineering,*** Vol. 128, No. 7, (2002), 850-859. DOI: 10.1061/(ASCE)0733-9445(2002)128:7(850)
6. Garlock, M.M., Ricles, J.M. and Sause, R. "Experimental Studies of Full-scale Posttensioned Steel Connections." ***Journal of Structural Engineering,*** Vol. 131, No. 3, (2005), 438-448. DOI: 10.1061/(ASCE)0733-9445(2005)131:3(438)
7. Gerami, M. and Khatami, M. "The Effects of Initial Post Tensioning Force on Seismic Behavior of Steel Moment Resisting Frames by Post-tensioned Connections." ***Sharif Journal of Civil Engineering,*** Vol. 33, No. 1, (2017), 107-115(In Persian). DOI: 10.24200/j30.2017.1101
8. Azizi, M. and Siahpolo, N. "Evaluating the Effect of Strength and Geometry Parameters of Angle on Behavior of Post-Tensioned Steel Connection with Top and Bottom Angles." ***Journal of Structural and Cunstruction Engineering,*** Vol. 24, No. 2, (2019), 193-210, DOI: 10.22065/JSCE.2018.97060.1311
9. Saberi, V., Gerami, M. and Kheyroddin, A. "Seismic rehabilitation of bolted end plate connections using post-tensioned tendons" ***Engineering Structures,*** Vol. 129, (2016), 18-30. DOI: 10.1016/j.engstruct.2016.08.037
10. Akhavan Salmassi, M., Gerami, M. and Heidari Tafreshi, A. "Evaluation of Flexible Steel Frame Structures with Post Tensioned Cables to Sequences Far From Fault." ***Journal of Structural and Construction Engineering,*** Vol. 6, Special Issue 3, (2019), 221-234, DOI: 10.22065/JSCE.2018.101782.1350
11. Christopoulos, C., Filiatrault, A., Uang, C.M. and Folz, B. "Posttensioned Energy Dissipating Connections for Moment-resisting Steel Frames." ***Journal of Structural Engineering,*** Vol. 128, No. 9, (2002), 1111-1120. DOI: 10.1061/(ASCE)0733-9445(2002)128:9(1111)
12. Wang, D.Numerical and experimental studies of self-centering post-tensioned steel frames. State University of New York at Buffalo, 2007.
13. Chancellor, N.B., Eatherton, M.R., Roke, D.A. and Akbaş, T. "Self-centering Seismic Lateral Force Resisting Systems: High Performance Structures for the City of Tomorrow." ***Buildings,*** Vol. 4, No. 3, (2014), 520-548. DOI: 10.3390/buildings4030520
14. Kim, H.J. and Christopoulos, C. "Friction Damped Posttensioned Self-centering Steel Moment-resisting Frames." ***Journal of Structural Engineering,*** Vol. 134, No. 11, (2008), 1768-1779. DOI: 10.1061/(ASCE)0733-9445(2008)134:11(1768)
15. Naghipour, M. Nemati, M. Doostdar, HM. "Experimental Study and Modeling of Reinforced Concrete Beams Strengthened by Post-Tensioned External Reinforcing Bars." ***International Journal of Engineering, Transactions A: Basics,*** Vol. 23, No. 2, (2010), 127-144.
16. Sarvestani, H.A. "Cyclic Behavior of Hexagonal Castellated Beams in Steel Moment-resisting Frames with Post-tensioned Connections." ***Journal of Structures,*** Vol. 11, (2017), 121-134. DOI: 10.1016/j.istruc.2017.05.001
17. Zhao, Z., Jian, X., Liang, B. and Liu, H. "Progressive Collapse Assessment of Friction Damped Post-tensioned Steel Frames Based on a Simplified Model." ***Journal of Structures,*** Vol. 23, (2020), 447-458. DOI: 10.1016/j.istruc.2019.09.005
18. Al Kajbaf, A., Fanaie, N. and Najarkolaie, K.F. "Numerical Simulation of Failure in Steel Posttensioned Connections Under Cyclic Loading." ***Engineering Failure Analysis,*** Vol. 91, (2018), 35-57. DOI: 10.1016/j.engfailanal.2018.04.024
19. Nateghi, F. Vatandoost, A."Seismic Retrofitting RC Structures With Precast Prestressed Concrete Braces-ABAQUS FEA Modeling." ***International Journal of Engineering, Transactions C: Aspects,*** Vol. 31, No. 3, (2018), 394-404. DOI:10.5829/ije.2018.31.03c.01
20. Sharbati, R., Hayati, Y. and Hadianfard, M.A. "Numerical Investigation on the Cyclic Behavior of Post-tensioned Steel Moment Connections with Bolted Angles." ***International Journal of Steel Structures,*** Vol. 19, No. 6, (2019), 1840-1853. DOI: 10.1007/s13296-019-00247-x
21. Guan, X., Burton, H. and Moradi, S. "Seismic Performance of a Self-centering Steel Moment Frame Building: From Component-level Modeling to Economic Loss Assessment." ***Journal of Constructional Steel Research,*** Vol. 150, (2018), 129-140. DOI: 10.1016/j.jcsr.2018.07.026
22. CSI PERFORM-3D.Nonlinear Analysis and Performance Assessment for 3D Structures, Version4. Computers and Structures, Inc., Berkeley, California, 2006.
23. Shen, J. and Akbaş, B. "Seismic Energy Demand in Steel Moment Frames." ***Journal of Earthquake Engineering,*** Vol. 3, No. 04, (1999), 519-559. DOI: 10.1080/13632469909350358
24. Apostolakis, G. Evolutionary aseismic design of self-centering post-tensioned energy dissipating steel frames. State University of New York at Buffalo, 2006.
25. Apostolakis, G., Dargush, G.F. and Filiatrault, A. "Computational Framework for Automated Seismic Design of Steel Frames With Self-centering Connections." ***Journal of Computing in Civil Engineering,*** Vol. 28, No. 2, (2014), 170-181. DOI: 10.1061/(ASCE)CP.1943-5487.0000226
26. Applied Technology Council, Quantification of building seismic performance factors. US Department of Homeland Security, FEMA, 2009.
27. Tafreshi, A.M.H. and Gerami, M. "Implementing posttensioned connections only in some floors of steel moment frames." ***Journal of Structures,*** Vol. 31, (2021), 98-110. DOI: 10.1016/j.istruc.2021.01.080
28. Qiu, C., Zhao, X., & Zhu, S. "Seismic upgrading of multistory steel moment-resisting frames by installing shape memory alloy braces: Design method and performance evaluation." ***Structural Control and Health Monitoring,*** Vol. 27, No. 9, (2020), e2596. DOI: 10.1002/stc.2596

Persian Abstract

چکیده

در سال‌های اخیر مطالعات گسترده‌ای در زمینهٔ سیستم‌های خودمرکزگرای فولادی توسّط محققین صورت پذیرفته که بسیاری از ابهامات در زمینه استفاده از چنین سیستم‌هایی در بهسازی قابهای موجود را برطرف نموده‌است. با توجه به هزینه‌های اجرای کل پروژه بهسازی در یک مرحله و همچنین مواردی نظیر عدم امکان توقف کاربری تمامی طبقات در برخی از ساختمان‌های موجود، روش چند مرحله‌ای بهسازی با استفاده از سیستم‌های خودمرکزگرا در این تحقیق پیشنهاد و بررسی گردیده‌است. در این راستا در مرحله اول با صرف بودجه و زمان اجرای بهسازی کمتر، اقدام به بهسازی بخشی از طبقات صورت می‌پذیرد و در ادامه، مرحله بعدی بهسازی اجرا میگردد. بر این اساس با اجرای مرحله اول بهسازی عملکرد قاب تا حدود مناسبی ارتقا پیدا میکند و همچنین اقدامات صورت پذیرفته در مرحله اولیه بخشی از طرح نهایی بهسازی می‌باشد. در این تحقیق ضرایب PUF و PEF به منظور انتخاب مناسب ترین الگوی بکارگیری اتصالات پس‌کشیده در طبقات مختلف، معرّفی و مورداستفاده قرارگرفته‌شده‌است. پس از انجام تحلیل‌های‌تاریخچه زمانی بر قاب‌های سه، شش و ده طبقه، الگویی برای بهسازی چند مرحله‌ای هر قاب با انتخاب الگوی مناسب استفاده از اتصالات پس‌کشیده در طبقات، پیشنهاد گردیده بنحویکه در مرحله اول طرح پیشنهادی در قاب سه طبقه ۱۵/۳ درصد، قاب شش طبقه ۱۱/۴ درصد و قاب ده طبقه ۸/۵ درصد ارتقای عملکردی ایجاد گردیده است.

International Journal of Engineering

Journal Homepage: www.ije.ir

Large-scale Experimental Study on Collapsible Soil Improvement using Encased Stone Columns

M. Bahrami*, S. M. Marandi

Department of Civil Engineering, Shahid Bahonar University of Kerman, Kerman, Iran

PAPER INFO

Paper history:
Received 24 December 2020
Received in revised form 06 April 2021
Accepted 12 April 2021

Keywords:
Collapsible Soil
Large-scale Specimens
Stone Columns
Geogrid-encased
Aspect Ratio
Soil Improvement

ABSTRACT

The aim of this study was to improve the characteristics of natural collapsible soils using the geogrid-encased stone column technique. For this purpose, 20 large-scale specimens of stone columns were prepared using rigid metal cylinders with a diameter of 308 mm and a height of 97 to 154 mm according to the unit cell theory. The aspect ratio was 10 to 25%. For the occurrence of bulging failure, the height of the stone columns was considered six times the diameter. The stone columns were encased with geogrids of varying stiffness from 80 to 200 kN/m. The soil around the stone column inside the unit cell was compacted to similar site conditions. Loading was applied similar to the test, which determines the soil collapsibility potential while the specimens were being inundated from the bottom of the metal cylinder by a water feeding system. During loading, the vertical displacements of the stone columns were measured at two locations on the loading plate. The results showed that the columns settlement due to inundation diminished by increasing the stiffness of the encased stone columns and aspect ratio. The optimum aspect ratio was approximately 15%. Encasement of the stone columns increased the lateral pressure in the collapsible soil and prevented the collapse of the stone column. The settlement values of stone columns were compared with a settlement prediction model and showed a good agreement. The data obtained in this study can be used as a practical method to improve natural collapsible soils during inundation.

***doi**: 10.5829/ije.2021.34.05b.08*

1. INTRODUCTION

Collapsible soils are partially saturated deposits whose void ratio drastically diminishes by an unexpected increase in moisture content with or without additional loading. Such types of soils are problematic to practice in geotechnical engineering. They are usually found in silty clay deposits, sedimentary loess soils, sand dunes, and gypsum silt in both arid and semi-arid regions. If the collapsible soil underneath the any structural foundations is saturated, it will encounter a large settlement. The collapsibility settlement of soil is caused by the reduction of lateral support of the surrounding soil while it collapses. Thus, the identification and modification of these types of soils is necessary prior to construction of structures.

Researchers who have addressed the methods to identify collapsible soils or predicting their settlement during inundation have provided many reports [1-3]. A complex theoretical and practical mathematical model created in order to test how the operating system works after heavy and long rains when the soil moisture is greatly increase [4]. A research was carried out to quantify the permeability in micro-scale porous structures [5].

Other researchers have proposed different methods for improving the performance of collapsible soils. Engineered compacted fills may possess collapsible behavior [6, 7]. Soils compacted within certain specifications might experience considerable collapse as well [8].

Attempts have been made to stabilize problematic soils by means of chemical additives. For example, the

*Corresponding Author Institutional Email: bahrami@eng.uk.ac.ir (M.Bahrami)

Please cite this article as: M. Bahrami, S. M. Marandi, Large-scale Experimental Study on Collapsible Soil Improvement using Encased Stone Columns, International Journal of Engineering, Transactions B: Applications Vol. 34, No. 05, (2021) 1145-1155

effect of aerobic microorganisms on grain soil improvement in Garmsar industrial town was evaluated experimentally in order to investigate the effects of these phenomena on soil shear strength and stiffness [9]. The results showed that the unconfined compressive strength and stiffness of the soil increased by adding the microbial solution. Hosseini et al. [10] used electrokinetics and nanomaterials to stimulate the additives to move through soil pores, as an in-situ remedial measure. The results revealed that the collapse potential significantly improved by using 3% lime and 5% nanomaterial. A study explored the effect of three kinds of nanomaterial, including nano-silica (NS), nano-clay (NC) and nano-calcium carbonate (NCC) on the properties of a loessial collapsible soil [11]. The results showed that a small amount of nanomaterial (less than 1% of the total dry weight of the soil) could significantly improve the mechanical behavior of the loessial collapsible soil. An experimental study was performed to understand the effect of improving collapsible soil using polyethylene / Nano-lime mixture [12]. The results indicated that the improvement produced a significant change in the collapse potential, permeability, compressibility, and shear strength.

Houston and Houston [13] used pre-wetting as an improvement technique for the collapsible soil. Rollins and Rogers [14] performed the pre-wetting technique in conducting full-scale tests on wetted collapsible soil with 2% sodium silicate solution.

Use of geotextile and geogrid as reinforcement to improve bearing capacity and to reduce settlement for foundation on layered soils has also been examined. Ayadat [15] designed a physical model (390 mm inside diameter, 520 mm depth and 17.5 mm wall thickness) and implemented a geotextile-encased sand column. The collapsible soil used in this investigation was made in the laboratory by a mixture gap-graded soil. The mixture was made of 78% concrete sand, 10% Leighton buzzard sand (less than 90 µm), and 12% kaolin clay. Hanna and Solyman [16] designed an experimental prototype for testing rigid strips foundation on collapsible soils subjected to inundation due to raise of the groundwater table. Collapsible soils have been partially replaced with cohesionless materials with and without a geotextile reinforcing layer. They found a significant improvement in reducing the collapse settlement in the case of a combining of partially replaced collapsible soil with geotextile layer at the interface.

Several numerical studies have also examined the parametric effect of encased geotextile stiffness [17, 18]. Marandi et al. [19] as well as Alonso and Jimenez [20] analyzed the uncertainty and reliability of using stone columns. Demir and Sarici [21] in a laboratory work and numerical analysis explored the behavior of stone column with or without geogrid in clayey soil. Alkhorshid et al. [22] tested the performance of encased columns constructed on a very soft soil using three woven geotextiles and different column fill materials. The results showed that breakage of column filling materials would affect the load-settlement behavior of gravel and recycled waste columns.

A review of the existing literature showed that extensive numerical and experimental works have been performed on collapsible soil improvement; however, few studies have been reported on improving the use of natural collapsible soils with stone column techniques. Most researchers have prepared the collapsed soil in the laboratory by mixing sand and clay [15]. Preparation of artificial soil in the laboratory can affect soil cementation that exists in the natural soil deposition in the field. However, these studies did not lead to preparation of guidelines on the foundation analysis and design on collapsible soils. Thus, professional engineers are not sufficiently confident to design conventional foundations on collapsible soils. In addition, the majority of researchers have artificially produced collapsible soils in the laboratory by mixing sand and clay soils in their respective studies. On the other hand, one of the important reasons for the occurrence of collapse during inundation is the reduction of lateral pressure in the soil, so the technique of encased stone column is one of the most effective solutions.

Since the results of laboratory methods should be used in the field, it seems that the scale of the experimental study is of particular importance. This study sought to develop the stone column technique by conducting large-scale experiments near the field scale to find a solution to improve the collapsible soil. In this case, the results of large-scale experiments can be easily generalized to the field. Further, by setting up large-scale experiments, it is possible to provide the conditions under which materials can be used on a real scale.Thus, in the present work; large-scale experimental program was designed and implemented to improve the natural collapsible soils using encased stone columns with geogrid and crushed aggregate in order to develop new data for engineering earthworks.

2. MATERIALS AND METHODS

2. 1. Soil Properties and Characteristics

The soil samples used in this research were collected from the southern part of a vast collapsible zone located in Kerman, Iran. To characterize the in-situ collapsible soil, 15 boreholes were drilled with depths of 10 to 30 m in the sampling region. The disturbed and undisturbed samples were prepared at varying depths of boreholes. The Standard Penetration Test (SPT), in-situ soil unit weight, natural water content, and soil electrical resistance tests were performed on the site. The results are shown in Table 1.

TABLE 1. In-situ soil characteristics

Characteristic	Value
SPT	19-26 blows/30 cm
Dry unit weight	13.10-14.40 kN/m^3
Natural water content	7.1-16.5 %
Electrical Resistance	1-5 Ω-m

In the laboratory, the analysis of the particle size, plasticity indices, specific gravity of solids, conventional undrained and drained triaxial, collapsibility potential, and soil chemical tests was carried out according to the standard methods of ASTM D422, ASTM D421, ASTM D854, BS 1377, ASTM D5333, and ASTM D1411, respectively. According to the Unified Soil Classification System (USCS), the soil classification in the site was generally in the CL soil group to the end of the depth of 30 m. The soil grading curves used in this study are shown in Figure 1. The physical, mechanical, and chemical properties of the soil are presented in Table 2.

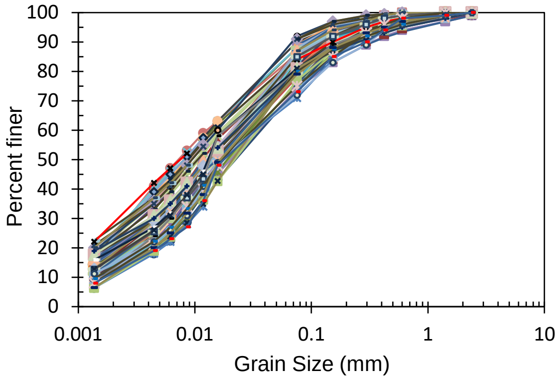

Figure 1. Grain size distribution of in-situ soil

TABLE 2. Soil physical, mechanical, and chemical properties

Property	Value
PI	8-12%
Activity Index	0.15-0.31%
Liquidity Index	-1.38 to -0.24
CP (Collapsibility potential)	2.0-5.7%
e_0 (initial void ratio)	0.790-0.910
Specific gravity of solids (GS)	2.529-2.548
Saturation Degree (S)	27-39%
c_u	30-60 kPa
c'	3.1-6.2 kPa
φ'	24-31 deg.
pH	8.2
SiO2	47%
CaO	17%
Sulphates in term of Ca SO4	1.6%
Chlorides in term of Cl-	0.03%

By considering the plasticity indices and the particle size finer than 2 microns, it was determined that the collected soil was inactive. The liquidity index shows that the soil was slightly over consolidated clay. Although the amount of collapsibility potential was low to moderate (2-5.7%), significant damage was observed at the site due to collapsibility. Further, the soil dispersive potential was investigated by determining sodium, potassium, calcium and magnesium ions. (Table 3). Based on the results of the chemical analysis, the dispersive potential of the soil used in this study is negligible.

In order to determine the effect of specimen disturbance factor on collapsibility potential (CP), the collapsibility potential tests were performed on a number of specimens consisting of remolded and undisturbed specimens. The results are presented in Table 4. The results revealed that the CP for the undisturbed specimens was slightly higher than that for the undisturbed specimens. This difference is due to the voids in remolded specimens, which have more uniform distribution than in the undisturbed specimens. Thus, more voids are exposed to soak during inundation.

2. 2. Characteristics of Crushed Aggregate

The uniform aggregates used to construct the stone columns were prepared from angular limestone chips with a nominal size ranging from 9 to 25 mm. The sieve analysis of crushed aggregate is demonstrated in Figure 2. The scale of the unit cell was so large that these crushed materials were used inside the stone column on their actual scale.

The minimum and maximum densities of the crushed stone were determined using standard tests of ASTM D4253 and ASTM D4254, respectively. Based on ASTM D3080, the internal friction angle of crushed stone was measured by a large direct shear box under vertical stresses of 100, 200, and 300 kPa. The specimens were prepared with the maximum unit weight of crushed aggregate. The characteristics of crushed aggregate are presented in Table 5.

TABLE 3. Soil chemical analysis for dispersive potential

EC (ms/cm)	Na^+ (meq/L)	K^+ (meq/L)	Ca^{++} (meq/L)	Mg^{++} (meq/L)
3-6	8.5-15.5	0.18-0.41	5.1-11.6	0.4-4.3

TABLE 4. CP of remolded and undisturbed specimens

Types of specimen	γ_d (kN/m^3)	Water content (%)	S (%)	e_0	CP (%)
Un-disturbed	14.1-14.3	6.8-8.5	22-28	0.781-0.797	3.8-4.4
Remolded	13.9-14.2	7.1-9.2	26-30	0.792-.818	5.1-5.9

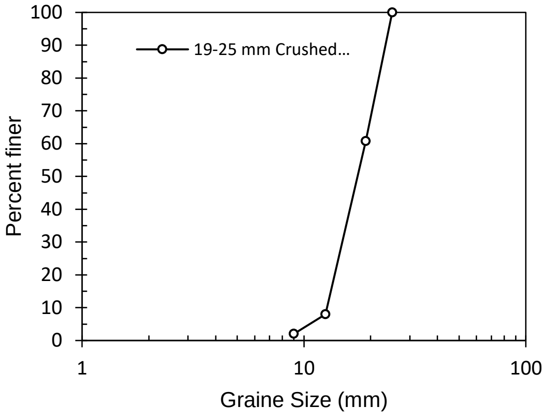

Figure 2. Grain size distribution of crushed stone

TABLE 5. Crushed aggregate characteristics

Characteristic	Value
USCS	GP
Maximum unit weight	15.3 kN/m^3
Minimum unit weight	13.5 kN/m^3
φ′	44 deg.

2. 3. Geogrid Characteristics

In the present research, three types of commercial named For Tex uni-axial geogrid were used to encase the stone columns. The geogrids were manufactured by weaving polyester micro yarns in a rectangular format and were coated with PVC. According to the manufacturer, the technical specifications of geogrids, adapted from Istanbul Teknik Corporation, are shown in Table 6. MD and CMD stand for machine direction cross machine direction, respectively.

2. 4. Design of Laboratory Testing Program for Stone Column Models

For designing the stone columns models, the experimental program was considered the unit cell concept with 308 mm in diameter and triangular pattern in the field. The diameters of the stone columns were calculated with respect to the desired aspect ratios (Ar.) in the designed program. The testing program for the stone column model is shown in Table 7. Further, two models were designed for individual soil (S0) and soil with non-encased stone column (SC).

The L/D ratio (length to diameter of the stone column) was used five for the single stone column in the experimental studies. Ghazavi and Nazari Afshar [23] showed that at least L/D = 4 is required to control the bulging failure mode. In this study, in order to overcome the bulging failure mode of the stone columns, the height of each specimen was chosen to be six times greater than its diameter.

2. 5. Design and Manufacturing Accessories

The loading device and accessories were designed to model the implementation of the stone column replacement method. The loading system capable of stress control method was made of steel. The device rig included a hydraulic jack with capacity of 600 kN by installing a 100 kN load measurement dial gauge. The front and planar views of the large-scale loading frame are shown in Figure 3.

To manufacture the unit cell tanks, a seamless Mannesmann metal tube was prepared with 12 m in length, 305 mm internal diameter, and 10 mm in thickness. Four tanks with heights of 900 to 1200 mm were cut from the Mannesmann metal tube. After turning and polishing, the inner tanks' diameter was 308 mm. The base plates with 450 mm in diameter and 25 mm in thickness were welded to the bottom of these tanks. At the central of the base plate, a threaded metal rod with a height of 50 mm was installed to provide space for filter materials. A brass lattice plate was designed to be screwed to the metal rod in the base plate at the height of the filter material. Around the perimeter of the brass plate, a semicircular groove was designed to sit an O-ring, which could seal the tank wall entirely. Three water ducts of 10 mm in diameter were created across the base plate to allow water to seep into the tank from its outside. To control the flow rate, three faucets measuring 6 mm in diameters were placed on the water pipe paths in the tank exterior.

TABLE 6. Technical characteristics of the geogrids

Type of geogrid	Tensile Strength (kN/m)		Elongation in Nominal Strength (%)	
	MD	CMD	MD	CMD
ForTex GG 80/30 P	80	30	12(±2)	12(±2)
ForTex GG 120/30 P	120	30	12(±2)	12(±2)
ForTex GG 200/50 P	200	50	12(±2)	12(±2)

TABLE 7. Testing program for the stone column models

Model type		SC1	SC2	SC3	SC4
Ar (%)	Aspect ratio	10	15	20	25
D_e (mm)	Unit cell diameter	308	308	308	308
$D = D_e\sqrt{A_r}$ (mm)	Stone column diameter	97.4	119.3	137.7	154.0
L (mm)	Stone column height	584	716	826	924

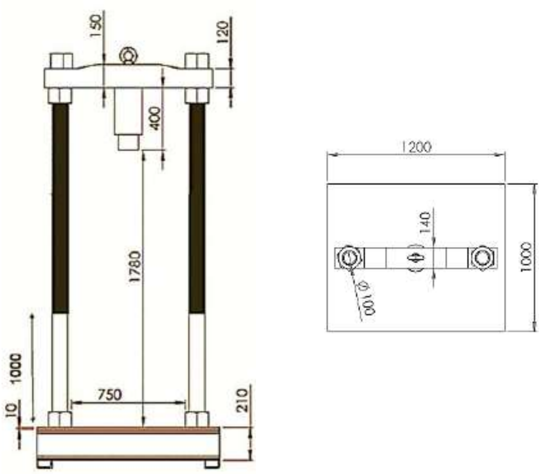

(a) (b)

Figure 3. Large-scale loading frame (a) Front, (b) Planar view

Four steel thin-walled tubes with 800 mm in height, 2 mm in thickness, and the outer diameters equal to the diameters of the stone columns were designed for developing the stone columns model. At the bottom of the drainage brass plate, four circular grooves (2 mm wide) were made to place the stone columns vertically inside the unit cell tank.

To compact the soil around the stone column, two light compaction hammers were welded to each other at a distance proportional to the diameter of the unit cell.

To inundate the specimens, a water-flow system was selected from the bottom to the top of the tank. An 80-L water barrel was placed on a four-legged metal base at altitude of 2 m above the laboratory floor. A glass box was prepared with dimensions of 20 cm × 20 cm × 30 cm for creating a laminar and steady state flow of water. At the upper side of this box, two valves with 19 and 6 mm in diameters were embedded for water inlet and air outlet, respectively. Three valves with 6 mm in diameters were installed on three vertical sides of the glass box. Silicone hoses were installed to allow water to flow from the glass box to the valves mounted in the outer part of the tank base plate. Figure 4 illustrates the test rig set up of the large-scale experimental model.

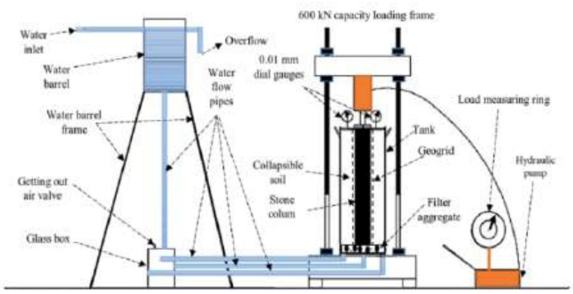

Figure 4. The test rig setup

2. 6. Test Procedure To minimize the skin friction, the inner wall of the unit cell tank was covered with a thin layer of grease. The filtering material was placed in the tank bottom up to a height of 50 mm. The drainage brass plate was screwed about 5 mm to the metal rod of the tank bottom. The geogrid was wrapped around the stone column models and fixed by sewing with polymer yarn. The geogrid-encased tube was placed inside the tank in the prepared groove at the bottom of the brass lattice plate. The tank was prepared to place the soil around the stone columns.

For each tank, about 80 kg of dried soil, passed through a 4.75 mm sieve, and was mixed with water (8.5% by weight of water content) as a homogeneous mixture. The soil mixture was stored for 24 h in a container with no change in its moisture content. Then, the required quantity of wet soil was weighed according to the wet unit weight of the soil with respect to 50 mm height of the tank. The soil was slowly placed around the stone column model tube inside the tank. The compacting device was inserted into the tank. In this way, the compaction hammers was placed on the top of the hollow plate. Then the compaction hammers were pulled up with a rope where impact energy was introduced for attaining the predicted value of the height of the soil within the tank.

The weighed crushed aggregate to build a height of 50 mm of the stone column was placed into the tube and vibrated by an electrical vibrator hose until the desired height was attained. Finally, the sand between 8 and 16 mesh sieves was used to smooth and level the surface of the stone column. In this way, specimens were prepared. Figure 5 shows the tank setup and prepared specimens SC1 and SC4, respectively.

The specimens were transferred to the loading device lifted using ceiling crane and forklift. The specimen was adjusted at its place in the center of the loading device. Three hoses from the outlet valves of the dividing glass box were connected to the three valves inlets at the bottom base plate of the tank. Then, all valves were closed. A 15 mm thick steel plate with the same

Figure 5. Prepared specimens SC1 and SC4

diameter of stone column was placed on top of the specimens. The specimen was prepared for loading. In order to apply the load axially, a special metallic connector was used between the loading piston and the loading plate. Two vertical displacement gauges were connected and aligned to the loading plate using the magnetic connector (Figure 6).

Loading was carried out according to the collapsibility potential test standard. Stresses of 25, 50, 100, and 200 kPa were applied in conditions where the specimen had a natural moisture content. A constant stress of 200 kPa was applied for 24 h. After this period, the three water valves were opened to allow the water to flow into the drainage system and inundate the specimen. During the experiment, the water head was kept constant. Then 400, 800, 1600 and 3200 kPa stresses were applied to the inundated specimen. The loading steps were carried out according to the stress control method and the vertical displacement gauge readings were recorded until they stopped. At the end of the experiments, the inundated specimens were taken from the laboratory and disposed of in a suitable place away from any contamination in the environment.

2. 7. Repeatability of Tests After preparing the collapsible soils and assembling the rig, a number of preliminary tests were conducted to verify the repeatability of the tests. Equation 1 was used to determine the repeatability based on the BS 812 standard.

$$r_1 = 2.8\sqrt{V_r} \tag{1}$$

where V_r represents the repeatability variance and r_1 denotes the value of repeatability, below which the absolute difference of the results of two single test may be expected to lie with a probability of 95%. The displacement values above the stone column for the three iterations with Ar. = 15 % under 200 kPa stress were 11.23, 12.01, and 11.83 mm, respectively. The repeatability variance was 0.17 and $r_1 = 1.14$. The maximum absolute difference value between 12.01 and 11.23 was 0.78, which was smaller than the previous repeatability value; thus, the test results have been acceptable when it comes to repeatability.

Figure 6. Prepared specimen for loading

3. RESULTS AND DISCUSIONS

3. 1. Results The stress-settlement tests results are shown in Figure 7 which are related to soil settlement alone (S0, the specimen without stone column and geogrid) and non-encased stone columns (SC, stone column without geogrid) specimens. Comparison between two series of the settlement curves shows that the non-encased stone column has not significantly reduced the settlement caused by the inundation in the collapsible soil. When water enters the specimen, the soil structure collapses, and the crushed aggregate particles of the stone column, which are not lateral protected, also collapse. Thus, the presence of a stone column without lateral support does not have the ability to improve collapsible soil behavior and reduce the collapsibility settlement.

Figure 8 displays the variations of stress versus settlement of stone columns without geogrid and encased geogrids with various stiffness. It can be observed that there is a significant difference between the vertical displacements of the non-encased and geogrid-encased stone columns. Further, the collapsible soil volume decreases suddenly and the lateral pressure is induced when the soil is inundated. However, if the stone column is encased with reinforcing elements, the lack of lateral pressure surrounding the stone column is prevented. Thus, the geogrid-encased stone column has more load-bearing capacity and reduces suddenly settlement of surrounding soil.

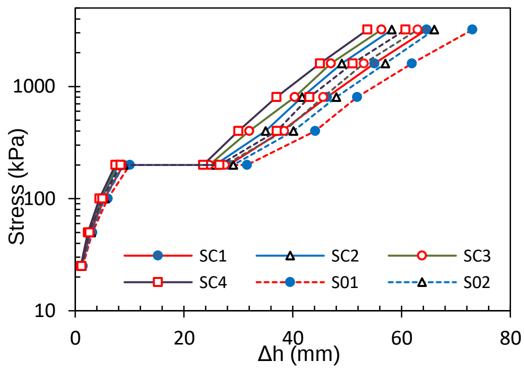

Figure 7. Variations of stress versus vertical displacement of soil alone and uncased stone columns

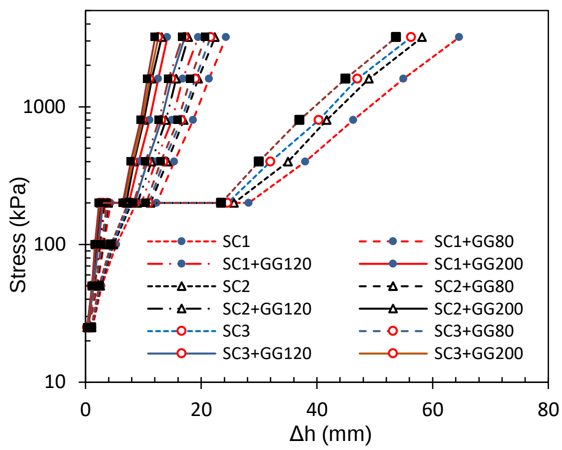

Figure 8. Stress versus vertical displacement with different conditions of stone columns

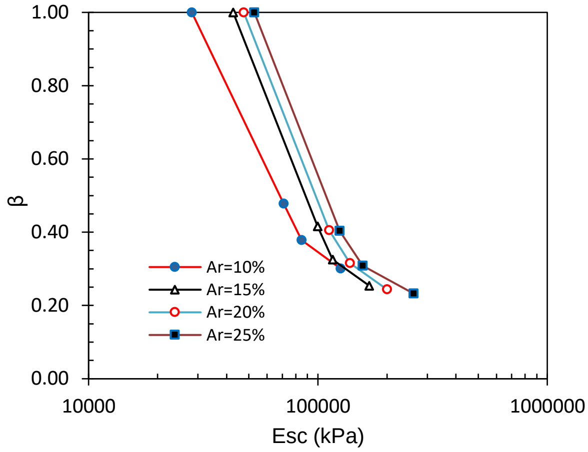

Figure 9. Changes of β versus Esc

3. 2. Data Analysis To analyze the settlement reduction factor for various experimental models, the variations in settlement reduction factor versus deformation modulus of the stone columns are used for different aspect ratios. The factor of reduction (β), presented by Ayadat and Hanna [35], was introduced in accordance with Equation (2):

$$\beta = \frac{S_i}{S_0} \tag{2}$$

where, Si denotes the stone column settlement and S0 represents the settlement of uncased column.

After inundating the specimens, the slope of stress-displacement curves for encased stone column was slightly higher than the slope of stone column without encasement. This is due to an increase in lateral pressure by the geogrid. There was no obvious difference between slopes of stress-displacement curves with increase in geogrid stiffness. Thus, increasing the geogrid stiffness as a constraining factor did not play a significant role in the settlement reduction factor.

As shown in Figure 9, the settlement reduction factor, β, has decreased following the increased stiffness of the stone column (Esc) or increased aspect ratio, Ar. The elastic modulus of the stone columns was calculated from the slope of the straight-line stress-deformation curves beyond inundation. With increase in the aspect ratio and the stiffness of the stone column, the vertical settlement diminished after inundation and the factor of β dropped in respect to Equation (2). Interestingly, the vertical settlement of the stone column was greatly influenced by the settlement brought about through its lateral displacement.

An increase in the elastic modulus of the stone column, the settlement caused by the lateral deformation can be increased to a certain value. The gentle slope at the end of the curves occurs frequently in the modulus of elasticity, with the rate of settlement reduction factor being low.

Figure 10 manifests the variations of settlement reduction factor against geogrid stiffness for various stone column aspect ratios. The results revealed that the settlement reduction factor diminished with all aspect ratios. With increasing aspect ratio, the crushed aggregate has replaced instead of soil. In this case, the elasticity modulus of the stone column increased and as a result, the stone column settlement diminished. Further, the results showed that the curve of Ar. = 15% was significantly different from the other curves, which were not significantly different among each other. Thus, the optimal aspect ratio was about 15%. This conclusion is in agreement with what was found in Figure 10 with a significant difference in the vertical settlement between the SC1 and SC2 curves.

The stone column technique can easily generalize the laboratory results to the practical scale in the field. Using the optimal aspect ratio Ar. =15% and the relationships (Equations 3 to 6) between the elements of the stone column [24], the actual diameter in the field can be calculated for triangular and square patterns of stone columns.

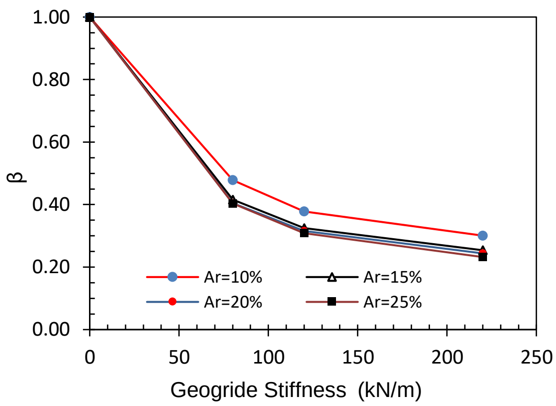

Figure 10. Variations of β versus geogrid stiffness

$$\mathrm{D_e} = 1.05 \times \mathrm{S} \tag{3}$$

$$\mathrm{D_e} = 1.13 \times \mathrm{S} \tag{4}$$

$$\mathrm{A_r} = \frac{\mathrm{A_s}}{\mathrm{A}} \tag{5}$$

$$\mathrm{D} = \mathrm{D_e} \times \sqrt{\mathrm{A_r}} \tag{6}$$

where, Equations (3) and (4) belong to triangular and square patterns, respectively; S is axis-to-axis distance between two adjacent rows of the stone columns; $\mathrm{A_s}$ is the area of stone column; A represents the unit cell area.

Typically, the diameter of the column is selected and the distance between two rows of columns in the desired pattern is calculated based on the optimal aspect ratio. In nature, there are thick layers of collapsible soil that have considerable resistance, but if they get too wet, they lose their strength, whereby extensive settlement and lateral deformation occur. By significantly reducing the vertical displacement of stone columns encased with geogrids in the collapsible soil as a modifier, this system can provide the conditions for safe transfer of the structure loads to the ground at depth

Based on Equation (7) the ratio of the stone column settlement to the collapsible layer thickness determines the collapsibility potential (CP).

$$CP = \frac{\Delta H}{H_0} \tag{7}$$

where, ΔH denotes the soil settlement with or without the stone column; and H_0 represents the collapsible soil thickness. Figure 11 shows the variations of collapsibility potential versus stone column stiffness under various Ar. and full inundation. The results also show that with increase in the aspect ratio and the stone column stiffness the CP drops significantly. The major decline in the CP reflects the role of the confinement of stone columns. From Figure 11, it can be calculated that at the 15% aspect ratio, the amount of collapsibility potential is reduced by about 82%.

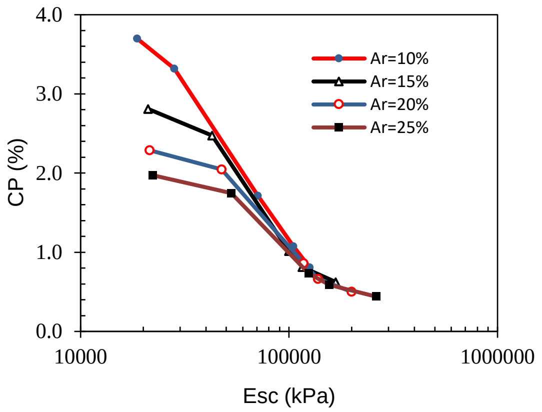

Figure 11. Changes of collapsibility potential versus Esc

3. 3. Analytical Model for Settlement Analysis

Since the settlement of stone columns was the most widely discussed matter, the intention of the analytical model was considered to predict the settlement. The settlement of the inundated stone column, which is completely penetrated into the collapsible soil and is subjected to the external axial stress of σ_a, consists of three constituents.

$$\Delta = \sum_1^3 \delta_i \tag{8}$$

where, Δ is the sum of settlement caused by the stone column inundation forced by the external load of P; δ_1 is the stone column elastic displacement brought by the stress leading to inundation; δ_2 represents the settlement caused by the downward pulling force due to the consolidated surrounding soil of the stone column; δ_3 denotes the vertical settlement caused by the stone column lateral movement.

$$\delta_1 = \frac{\sigma_a L}{E_{sc}} \tag{9}$$

$$\delta_2 = \frac{2\sigma_a L^2}{E_{sc} d}\left[C' + K_0 tan\varphi'(\frac{\gamma L}{3\sigma_a} + 1)\right] \mathrm{Q}_R \mathrm{Q}_T \tag{10}$$

where, σ_a is the stress at which inundation occurs, E_{sc} shows the elastic modulus, L denotes the height, d indicates the stone column diameter ($d = 2r_0$), C' shows the soil adhesion under drainage conditions, φ' shows the internal friction angle of the soil under drained condition, δ_2 is the axial displacement of the stone column during failure. Q_R and Q_T are correction factors for cases when full stone column–soil skid does not occur, and the delayed effects in the installation stone column, respectively [25].

The resistance of stone column against lateral pressure is boosted by adding of the geogrid materials in comparison with the soil alone. When the geogrid is subjected to tensile stress, it applies an additional pressure onto the column, and further aids the reinforcement. Using the tensile strength of the geogrid materials (τ) this pressure can be calculated. Figure 12 reveals the cylindrical specimen of geogrid associated with the lateral pressure Δσ.

The third component of Δ is presented as follows [26]:

$$\delta_3 = 2\Delta P \frac{r_0 L}{Et} \tag{11}$$

where E is the elastic modulus of the cylinder encasing the column, and

$$\Delta P = \sigma_V' K_{as} - \sigma_r' \tag{12}$$

$$K_{as} = tan^2(\frac{\pi}{4} - \frac{\varphi'}{2}) \tag{13}$$

where, σ'_v is the vertical stress exerted on the column and σ'_r denotes the effective lateral pressure applied on the column peripherally. Thus, the total settlement is defined as follows:

$$\Delta = \frac{\sigma_a L}{E_{sc}} + \frac{2\sigma_a L^2}{E_{sc} d}\left[C' + K_0 tan\varphi'\left(\frac{\gamma L}{3\sigma_a} + 1\right)\right] Q_R Q_T + 2\Delta P \frac{r_0 L}{Et} \quad (14)$$

The comparison of the measured values in the large-scale experimental study and predicted models for β, on top of the stone column due to column inundated under a given condition of stress (200 kPa) is as shown in Figure 13. It can be observed that there is a sufficient correlation between the values, especially as regards to the percentages that are lower than the aspect ratio between the predicted and measured experimental values. The results of the present study showed that the new experimental data and model behavior are in agreement with what was found by other researchers such as Ayadat and Hanna [26].

The obtained data in this study may be used as an applied method for improving the natural collapsible soil during inundation using encased stone columns.

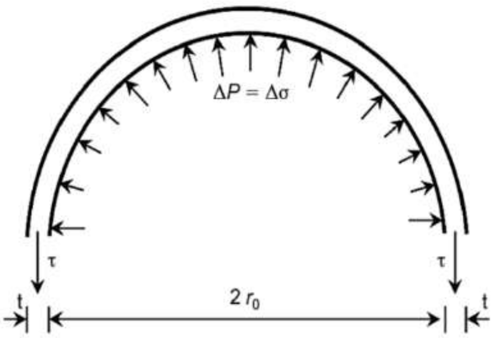

Figure 12. Cylindrical specimen of geogrid against the lateral pressure Δσ

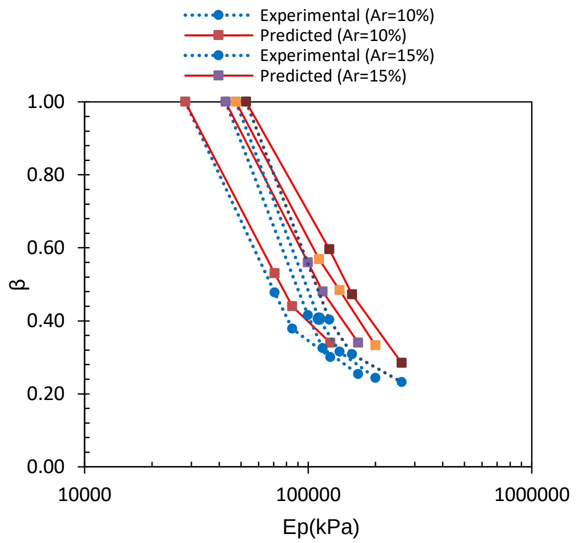

Figure 13. Variations of the settlement reduction factor along with the Esc

4. COCLUSIONS

A Large-scale experimental study was performed on collapsible soil improvement using geogrid-encased stone columns and the following results were achieved:

1. The implementation of the stone column without geogrid had no effect on the settlement reduction factor in collapsible soil under inundation conditions. The use of stone columns without lateral support in the collapsible soil during inundation caused premature failure of the stone column.
2. The optimal aspect ratio in encased stone column with geogrid was obtained as approximately 15%. In this case, the collapsibility potential was reduced by 82%.
3. The stone column technique can easily generalize the laboratory results to the practical scale in the field. Using the geometric relationships between the elements of the stone columns in different patterns and the optimal aspect ratio obtained from this study, the large-scale laboratory results could be easily generalized to the scale in the field.
4. The encasement of the stone column with geogrid increased the lateral pressure in the collapsible soil where the settlement due to the collapsibility was drastically reduced.
5. By significantly reducing the vertical displacement of stone columns encased with geogrids in the collapsible soil, this system can provide the conditions for safe transfer of the structure loads to the depth.
6. Increasing the geogrid stiffness as a confining support did not play a significant role in the settlement reduction factor in collapsible soil.
7. The experimental results on encapsulated stone columns were predicted well using the theoretical approach for settlement calculation.

By setting up large-scale experiments, it is possible to provide the conditions under which materials can be used on a real scale. The scale of the unit cell was so large that the crushed materials were used inside the stone column in their actual scale. In this case, the actual behavior and performance of the materials were demonstrated. It is necessary to implement the stone column technique in collapsible soil with an aspect ratio of 15% in the field to gain feedback on the behavior of the system on full scale.

5. REFERENCES

1. Pereira, J. F.H., and Fredlund, D.G., "Volume change behavior of collapsible compacted gneiss soil", ***Journal Geotechnical and Geoenvironmental Engineering***, Vol. 126, No. 10, (2000), 907-916. doi: 10.1061/(ASCE)1090-0241(2000)126:10(907).
2. Gaaver, Kh. E., "Geotechnical properties of Egyptian collapsible soils", ***Alexandria Engineering Journal***, Vol. 51, No. 3, (2012), 205-210. doi:10.1016/j.aej.2012.05.002.
3. Ayadat, T. and Hanna, A. M., "Assessment of soil collapse prediction methods", ***International Journal of Engineering,***

Transactions B: Applications, Vol. 25, No. 1, (2012), 19-26. doi:10.5829/idosi.ije.2012.25.01b.03.

4. Mihajlovic, G., Zivkovic, M., "Sieving Extremely Wet Earth Mass by Means of Oscillatory Transporting Platform ", ***Emerging Science Journal,*** Vol. 4, No. 3, (2020), 172-182. doi: 10.28991/esj-2020-01221.

5. Fazelabdolabadi, B., Golestan, M. H., "Towards Bayesian Quantification of Permeability in Micro-scale Porous Structures – The Database of Micro Networks", ***HighTech and Innovation Journal,*** Vol. 1, No. 4, (2020), 148-160. doi: 10.28991/HIJ-2020-01-04-02.

6. Ishihara, K., and Harada, K, "Cyclic behavior of partially saturated collapsible soils subjected to water permeation" ***Ground failures under seismic***, No. 44, (1994), 34-50.

7. Houston, S. L., Houston, W. N., Zapata, C. E., and Lawrence, C., "Geotechnical engineering practice for collapsible soils" ***Journal of Geotechnical and Geological Engineering***, No. 19, (2001), 333-355. doi: 10.1023/ A: 1013178 226615.

8. Lim, Y.Y. and Miller, G. A., "Wetting-induced compression of compacted Oklahoma soils" ***Geotechnical and Geoenvironmental Engineering***, Vol. 130, No. 10, (2004), 1014-1023. doi: 10.1061/(ASCE) 1090-0241(2004) 130:10 (1014).

9. Jalili, M., Ghasemi, M. R., Pifloush, A. R., "Stiffness and Strength of Granular Soils Improved by Biological Treatment Bacteria Microbial Cements", ***Emerging Science Journal***, Vol. 2, No. 4, (2018), 219-227. doi: 10.28991/esj-2018-01146.

10. Hosseini, A., Haeri, S. M., Siavash Mahvelati, S., Fathi, A., "Feasibility of using electrokinetics and nanomaterials to stabilize and improve collapsible soils", ***Journal of Rock Mechanics and Geotechnical Engineering***, Vol. 11, No. 5, (2019), 1055-1065. doi: 10.1016/j.jrmge. 2019.06.004.

11. Haeri, M., Valishzadeh, A., "Evaluation of Using Different Nanomaterials to Stabilize the Collapsible Loessial Soil", ***International Journal of Civil Engineering***, No. 156, (2020). doi: 10.1007/s40999-020-00583-9.

12. Margherita, Z., Laura, E., Chiara, M. M., Roberto, S., Bartolomeo, M., "Collapsible intact soil stabilisation using non-aqueous polymeric vehicle", ***Engineering Geology***, Vol. 264, (2020), 105334. doi: 10.1016/j.enggeo. 2019.105334

13. Houston, W. N. and Houston, S. L., "State of the practice: Mitigation measures for collapsible soil sites", ***Foundation Engineering***, Current Principles and Practices, Evanston, IL, USA, (1989), 161-175.

14. Rollins, K. M. and Rogers, G. W., "Mitigation measures for small structures on collapsible alluvial soils" ***Journal of Geotechnical Engineering***, Vol. 120, No. 9, (1994), 1533-1553. doi: 10.1061/(ASCE)0733-9410(1994)120:9(1533).

15. Ayadat, T., "Collapse of stone column foundations due to inundation", Ph.D. Thesis, Sheffield University, Sheffield, United Kingdom, (1990).

16. Hanna, A., Soliman, S., "Experimental Investigation of Foundation on Collapsible Soils", ***Journal of Geotechnical and Geoenvironmental Engineering***, Vol. 143, No. 11, (2017), 1-12. doi: 10.1061/(ASCE)GT.1943-5606.0001750.

17. Almeida, M.S.S., Hosseinpour, I., Riccio, M., "Performance of a geosynthetic encased column (GEC) in soft ground: numerical and analytical studies", ***Geosynthetics International***, Vol. 20, No. 4, (2013), 252-262. doi: 10.1680/gein. 13.00015.

18. Murugesan, S., Rajagopal, K., "Geosynthetic-encased stone columns: numerical evaluation", ***Geotextiles and Geomembranes***, Vol. 24, No. 6, (2007), 349-358. doi: 10.1016 /j.geotexmem.2006.05.001.

19. Marandi, S.M., Anvar, M. and Bahrami, M., "Uncertainty analysis of safety factor of embankment built on stone column improved soft soil using fuzzy logic α cut technique", ***Computers and Geotechnics***, Vol. 75, No. 5, (2016), 135-144. doi: 10.1016/ j.compgeo.2016.01.014.

20. Alonso, J., Jimenez, R., "Reliability-based design of stone columns for ground improvement considering two settlement failure modes" The XVI European Conference on Soil Mechanics and Geotechnical Engineering: Geotechnical Engineering for Infrastructure and Development, Edinburgh, Scotland, November, (2015).

21. Demir, A., Sarici. T., "Bearing capacity of footing supported by geogrid encased stone columns on soft soil", ***Geomechanics and Engineering***, Vol. 12, No. 3, (2017), 417-439. doi:10.12989/gae.2017.12.3.417.

22. Alkhorshid, N.R., Araujo, P.L.S., Palmeira, E.M., Zornberg, J.G., "Large-scale load capacity tests on a geosynthetic encased column", ***Geotextiles and Geomembranes***, Vol. 47, No. 5, (2019), 632-641. doi:10.1016/j.geotexmem. 2019.103458.

23. Ghazavi, M., Nazariafshar, J., "Bearing Capacity of Geosynthetic Encased Stone Columns, ***Geotextiles and Geomembranes***, Vol. 38, No. 6, (2013), 26-36. doi: 10.1016/j.geotexmem. 2013.04.003.

24. Barksdale, R.D., Bachus, R. C., "Design and construction of stone columns, Federal High way administration Office of Engineering and Highway Operations Research and Development, FHWA/RD-83/029", School of Civil Engineering, Georgia, Georgia, UAS, (1983).

25. Poulos, H. G., Davis, E. R., *Pile Foundation Analysis and Design*, John Wiley & Sons, New York. N.Y., USA, (1980).

26. Ayadat, T., Hanna, A. M., "Encapsulated stone columns as a soil improvement technique for collapsible soil", ***Ground Improvement***, Vol. 9, No. 4, (2005), 137-147. doi: 10.1980/grim. 2005.9.4.137.

Persian Abstract

چکیده

هدف از این مطالعه، بهبود خصوصیات خاک‌های فروریزشی طبیعی با استفاده از تکنیک ستون‌سنگی دورپیچی‌شده با ژئوگرید بود. برای این منظور ۲۰ نمونه بزرگ مقیاس از ستون سنگی بر اساس نظریه سلول واحد با استفاده استوانه‌های فلزی صلب به قطر ۳۰۸ میلی‌متر و ارتفاع ۹۷ تا ۱۵۴ میلی‌متر ساخته‌شدند. نسبت سطح ستون سنگی به سلول واحد از ۱۰٪ تا ۲۵٪ تغییرداده‌شد. برای رخداد شکست شکم‌دادگی، ارتفاع ستون‌های سنگی شش برابر قطر درنظرگرفته‌شد. لوله‌های فلزی مدل ستون‌های سنگی با ژئوگریدهایی دارای سختی‌های متفاوت از ۸۰ تا ۲۰۰ کیلونیوتن بر متر دورپیچی و درون استوانه‌های سلول واحد قرارداده‌شدند. در داخل این لوله‌ها مصالح سنگی شکسته و اطراف آن خاک رمبنده با شرایط محل اجراشد. بارگذاری شبیه به روش آزمایش تعیین قابلیت فروریزشی خاک، در حالی اعمال‌شد که نمونه از پایین استوانه فلزی به وسیله یک سیستم بالاآوردن سطح آب در حال غرقاب‌شدن بود. در اثنای بارگذاری، جابجایی‌های قائم ستون‌ها در دو محل روی صفحه بارگذاری اندازه‌گیری‌گردید. نتایج نشان‌داد که با افزایش سختی ستون‌های سنگی محصورشده و نسبت سطح، باعث کاهش نشست آن‌ها در اثر غرقاب‌شدگی شد. بهینه نسبت سطح ستون‌های سنگی تقریباً ۱۵٪ بدست‌آمد. دورپیچی ستون‌های سنگی باعث افزایش فشارجانبی در خاک شد و از فروریختن ناگهانی ستون سنگی جلوگیری‌کرد. مقادیر نشست اندازه‌گیری‌شده از نتایج آزمایشگاهی با خروجی نتایج یک مدل تحلیلی محاسبه‌شد. مقایسه نتایج اندازه‌گیری‌شده و مدل محاسباتی، مطابقت خوبی را نشان‌داد. داده‌های به دست‌آمده در این مطالعه می‌تواند به عنوان یک روش کاربردی برای بهبود خاک فروریزشی طبیعی در هنگام غرقاب‌شدگی مورد استفاده عملی قرارگیرند.

IJE TRANSACTIONS B: Applications Vol. 34, No. 05, (May 2021) 1156-1166

International Journal of Engineering

Journal Homepage: www.ije.ir

Experimental and Nonlinear Analysis of Cracking in Concrete Arch Dams Due to Seismic Uplift Pressure Variations

M. J. Kadhim[a], T. J. M. Alfatlawi[a], M. N. Hussein*[a,b]

[a] *Civil Engineering Department, University of Babylon, Babylon, Iraq*
[b] *Civil Engineering Department, Iraq University College, Basrah, Iraq*

PAPER INFO

Paper history:
Received 21 November 2020
Received in revised form 19 March 2021
Accepted 25 March 2021

Keywords:
Arch Dams
Degree of Curvature
Earthquake
Extended Finite Element
Shake Table

ABSTRACT

Cracked concrete arch dam's behavior due to moderate earthquake magnitude and water pressure variation was investigated. Plain concrete was used to cast the dam's models with 45 Mpa design strength. A shake table has been planned, manufactured, and built to create a dynamic testing facility. The experimental work was included testing of four scaled-down concrete arch dams' models, which is divided into two groups, each group contains two different degrees of curvature models. An artificial crack was made at the center of the dam's body. The extended finite element method (XFEM) is outlined in order to address the numerical predicate for the propagation of a crack. The results showed a good behavior of all arch dams under moderate earthquake intensity. The arch dam with a higher degree of curvature recorded 17.8% and 16.2% lower displacement at Z and X-direction, respectively. The stress evaluation and crack propagation in comparison with the arch dam owns the lowest degree of curvature. Hence, increasing the degree of curvature led to raising the stability of the dam, earthquake resistance, less displacement, and less growth of tensile cracks.

***doi**: 10.5829/ije.2021.34.05b.09*

1. INTRODUCTION

A dam is a hydraulic structure of nearly impermeable material created over a river to create a reservoir on its upstream side to impound water for different purposes. This may include drainage, water management, flood control, navigation, agriculture, tourism, and the most important purpose is hydropower. At first, dams were initially designed by humans to deal with the needs of small settlements for agriculture [1, 2]. Dams have begun to be used not only for irrigation but for water storage and hydroelectric power [3] depending on the location of the dam. Hydropower produces 19% of the world 's overall energy supply and is widely used in more than 150 countries and water-rich countries like Canada, Norway and Brazil that almost solely use dams for hydropower output [4].

Dams can be classified according to construction design [5] or the structures used to endure tension due to water pressure [6] in the reservoir into two types as gravity and arch dams. The most popular type of concrete dam is a concrete gravity dam that is shown in Figure 1. In this type of dam, the concrete and friction mass weight resist the water pressure of the reservoir and is made of non-reinforced vertical concrete blocks with flexible seals in the joints between the blocks. In cross-section, concrete arch dams are usually very small, as shown in Figure 2. The water forces of the reservoir acting on an arch dam are brought onto the abutments laterally, formed from a series of thin vertical blocks connected together, with water stopping between the blocks [7, 8].

Arch dams are subjected to assortment types of loads, most of the time it is static caused by water pressure, dam's self-weight, temperature variation [9, 10], and ice loads. In some cases, subjected to dynamic loads such as traffic loads, wind loads and seismic loads which is the most dangerous case. The seismic loads can play an important role in its effect to the arch dams especially if

*Corresponding Author Institutional Email: *mohammed.alhashimi@iuc.edu.iq* (M. N. Hussein)

Please cite this article as: M. J. Kadhim, T. J. M. Alfatlawi, M. N. Hussein, Experimental and Nonlinear Analysis of Cracking in Concrete Arch Dams Due to Seismic Uplift Pressure Variations, International Journal of Engineering, B: Applications Vol. 34, No. 05, (2021) 1156-1166

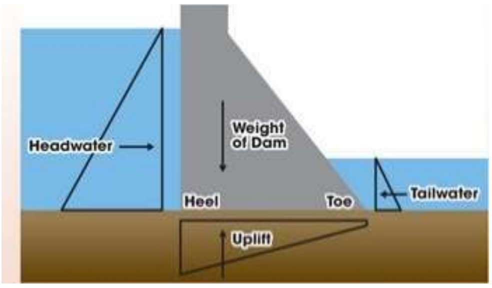

Figure 1. Concrete gravity dam

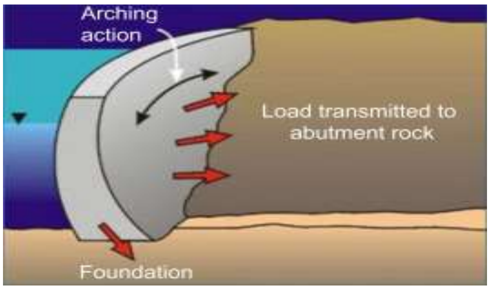

Figure 2. Concrete arch dam

these dams are subjected to prior deformations, such as cracks. The importance of studying the risk of seismic loads on arched dams lies in the extent of their impact on the stability of the dam and the response of the dam to it, which preserves its structure and prevents the development of cracks on it.

A variety of earthquake research studies on concrete arch dams have previously stated that complex impacts on arch dams should be taken into account in the ground motions. It also presents an arch dam's three-dimensional linear earthquake response. In the finite element analysis, various soil motion results are taken into account and, in addition to rigid and elastic base conditions [11].

Researchers have recently studied the impact of earthquakes on concrete arch dams and found that most of the modern dams in regions exposed to seismic activities have been built utilizing techniques that are now becoming simplistic and unreliable. The damage sustained by the few dams that have been exposed to extreme ground movements, such as Hsinfengkiang Dam in China, the Pacoima Dam in the U.S. and Koyna Dam in India, along with the increasing concern about the earthquake protection of sensitive infrastructure, has driven substantial interest in modern study and exploration of existing dams. The seismic protection of several dams has been tested over the past 20 years, and some of them have been improved to enhance their seismic tolerance [12, 13].

Concrete failure is a crack forming and development process [14]. In recent years, there has been an increasing interest in the study of the relationship between seismic effects and cracks developed in arch dams. One of the main obstacles is the process of representing the arch dam and conducting practical experiments on it, which requires equipment and high costs. The main objectives of this paper can be listed as follows;

- Make an experimental investigation to examine the behavior of arch dam under seismic loads and uplift pressure variations.
- Investigate the propagation of crack of the arch dam under seismic loads and uplift pressure variations.
- Use the extended finite element method (XFEM) for analysis of the arch dams and to predict the crack propagation and the development of other cracks under water pressure and seismic loads.

2. ARCH DAM CLASSIFICATION

Arch dams are classified according to the ratio of their thickness to their height into three sections:

1. Thin if $(\frac{b}{h}) \leq 0.2$.
2. Medium-thick $(\frac{b}{h})$ = (0.2-0.4).
3. Thick $(\frac{b}{h}) \geq 0.4$.

According to the new classification if $(\frac{b}{h}) > 0.65$. then there will be a fourth type called (Arch gravity dam). Also, arch dams are classified according to their height as :

1. Low arch dam if h ≤ 30m
2. Medium if h = (31m - 90m)
3. Large if h ≥ 91m.

Only thin arch dams need reinforcement which is not needed for other forms of dams because it greatly raises the cost [15–19].

3. SHAKING TABLE DESIGN

A uniaxial shake table with a rotating platform capability (2DOF; axial and rotational degrees of freedom) was planned, manufactured and built to create a dynamic testing facility, which is servo-electrically controlled and powered by low-friction ball bushing bearings. To ensure an effective reproduction of input motion by the shake table method, a system has been assembled with caution. In the time and frequency domain, arbitrary comparisons of input signal verses shake-table response have been used to calculate the simulator's abilities to replicate earthquake movements scaled according to similarity rules.

The electrical shake table is shown in Figure 3. It was completely manufactured locally under the direct supervision of the researcher and his supervisors uniaxially with an ability of a rotating platform in two horizontal directions.

Figure 3. Shaking table developed as experimental rig

4. EXPERIMENTAL PROGRAM

4. 1. Dimension Analysis A dimensional analysis was conducted with the aid of Buckingham (π) theorem to establish similarity relationships between systems [20, 21]. Scale factors obtained by dimensional analysis is reflected in the relation between prototype and model. The real dam that was chosen for the purpose of taking on the climatic conditions and the real loads that it is exposed to, and applied to the proposed models for the purpose of conducting the present study on the Dinas Arch Dam located in Wales City in the UK [22] with 14m height. The similitude necessities for dynamic relationships between the model and prototype rely on the geometric, material properties of the structure and on the sort of force applied to the structure. Whether we need to obtain dynamic similitude we should have geometric similarity jointly with kinematic and dynamic similarities [23, 24]. Because of the calamitous nature of earthquakes, this kind of force wants to be taken industriously into consideration in the design of structures. Replica models for shake table testing ought to satisfy both the Froude and Cauchy scaling requirements as aforesaid in Equations (1) and (2), respectively; which implies the simultaneous replication of inertia, restoring and gravitational forces [25].

$$Fr = \frac{V^2}{l.g} \tag{1}$$

$$Ca = \frac{\rho.v^2}{E} \tag{2}$$

Since the value of gravitational acceleration (g) must be equal to one, and from the dimensional analysis we get the dimensionless product of Sa/Sg =1 (a is the imposed acceleration), the following scaling law is derived:

$$SE/_{\rho} = SL \tag{3}$$

This is hard to understand because it requires that the model material has a massive mass density or small modulus or even both. A better alternative is to raise the density [15], of the structure with extra non-structural material. Similitude requirements for earthquake modelling is detailed in Table 1. Geometric dimensions of the model were obtained by directly scaling the prototype dimensions by the scale factor S_L = 15.6.

TABLE 1. Similitude requirements for earthquake modelling [21]

Parameter	Dimension	Scale Factor
Modulus E	FL^{-2}	S_E
Force Q	F	$S_E S_L^2$
Pressure q	FL^{-2}	S_E
Linear Dimensions	L	S_L
Density ρ	$FL^{-4}T^2$	$\frac{S_E}{S_L}$
Time t	T	$S_L^{0.5}$
Frequency ω	T^{-1}	$S_L^{0.5}$
Gravity Acceleration G	LT^{-2}	1

4. 2. Criteria for Arch Dam and Material Properties Such structures are designed primarily to carry only gravity, uplift pressure, and hydrostatic loads. Therefore, seismic resistance is not regarded. In this study, a single curvature scaled-down arch dams were simulated with two different curvatures to assess stress distribution over the dam, displacement of the concrete arch dam, and follow-up to the spread of crack underwater pressure and intensity of the earthquake. The dams in this investigation are depending on optional information brought by Manual-EM 1110-2-2201 [18]. However, the model used in this study is a typical model and the crack is created artificially to the model to assess the crack propagation at the center of the dam. The site, water reservoir information, the weather, and other significant details for dam plan and design were given. Typical values have been chosen to understand the properties of the materials. Experimentally, two solid 3D plain concrete medium-thick arch dam models with two different curvatures (1 model for each curvature) used in this study are shown in Figures 4 and 5; fixed from the bottom with dimensions and properties as the detail is summarized in Table 2. An artificial crack made at the center back of the dam's body is shown in Figures 6 and 7 with its dimensions as 200 mm length, 20 mm height, and 20 mm depth.

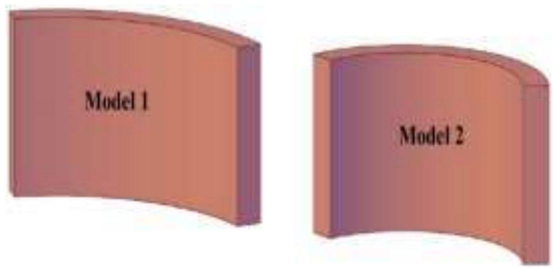

Figure 4. Arch dam models

Figure 5. Concrete arch dam models

Figure 7. Concrete arch dam with artificial crack

TABLE 2. Dimensions and properties

Dimensions		
Dimension	**Model 1**	**Model 2**
Outer length (mm)	1700	1700
Inner length (mm)	1500	1380
Radius (mm)	1188	650
Height (mm)	900	900
Thickness (mm)	180	180
°: Degree of curvature, L/r = 0.017° [26]	74°	124°
Materials Properties		
Property	**Model 1**	**Model 1**
Compressive strength, f_{cc}	44.45 Mpa	44.55 Mpa
Density of Concrete	2400 (Kg/m^3)	2400 (Kg/m^3)
Poison's ratio	0.2	0.2
Modulus of elasticity, E_c = 4700 $\sqrt{f_{cc}}$ [27]	31370 (Mpa)	31370(Mpa)
Fracture Energy, G_F = 1041 (1- $e^{-0.07 f_{cc}}$) [28]	951.2 (N/m)	951.2 (N/m)

4. 3. Experimental Tests

The model is installed as shown in Figure 8 with fixed the bottom by concrete. The shake table operated to apply a two-dimensional earthquake intensity. Moderate magnitude (5.7M) of actual earthquake records are selected from the Pacific Earthquake Engineering Research Center (PEER) ground motion database [29–31]. The acceleration of (Mammoth Lakes-04) earthquake is presented in Figure 9. A water pressure was applied to the surface of the crack using a pressure compressor with a capacity of 10 bars, as shown in Figure 10a. A 5% ratio of damping in the system of damping was considered. Up to the full reservoirs, the water level is assumed to be 14 m. A combination of multiple loads will be applied to the dam models consisting of static loads (water pressure + dam's self-weight) and dynamic loads (earthquake + hydrodynamics). Due to dam's gravity, the static solutions of the dam weight and hydrostatic loads in the initial situations are taken as the system's diverse evaluations. The Westergaard's [32, 33] virtual mass is employed to provide the influence of hydrodynamics. The importance of the simulated mass of Westergaard [34] is M_i^1 at node i on the upstream of the dam's surface is:

$$M_i^1 = \frac{7}{8}\,\rho_w\,\frac{b_{i1}+b_{i2}}{2}\sqrt{hy_i} \tag{4}$$

where (h) refers to the water's depth, (ρ_w) refers to the mass density of water, (y_i) represents the distance between the surface of the water and node (i), and (b_{i1}) and (b_{i2}) refer to the lengths of the edges of quadrilateral constant-strain elements next to node (i) on the dam's upstream surface. It is worth emphasizing that the analysis does not include consideration of seismic water pressure effects within the cracks. It is important to investigate in greater depth the impact of seismic water pressure on crack propagation, as well as the dam's dynamic response.

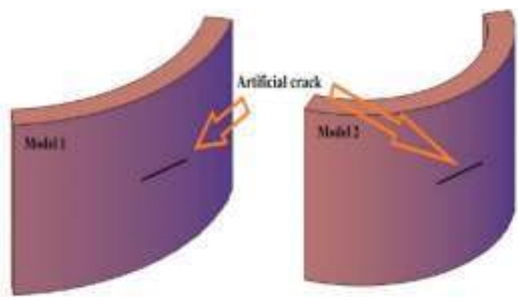

Figure 6. Arch dam model with artificial crack

Figure 8. Concrete arch dam model with fixed support

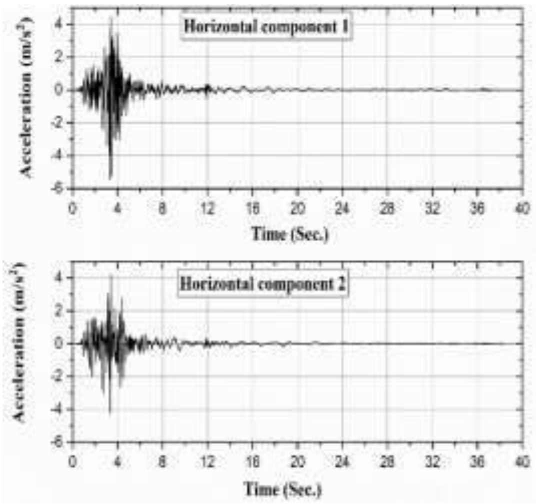

Figure 9. Acceleration components

Figure 10. (a: applied water pressure, b: measurement of displacements. c: concrete strain gauge)

Linear displacement sonic transducers were used to measure the absolute response displacements in the longitudinal (horizontal) direction during the shaking table tests fixed as shown in Figure 10b. The LVDT fixed at coordinates mesured from the center of the dam as (0,-0.15,0) for LVDT in Z-direction and (-0.75,-0.15,-0.5) for LVDT in X-direction and (-0.75,-0.15,-0.5) in Y-direction? The displacement transducer has a stroke of ±100 mm. There is a variety of mechanical and electrical methods of measuring strain, but owing to their superior measurement properties, the vast majority of stress measurements are conducted using strain gauges. Form (PL-60-11-3LJC-F) concrete strain gauges were used in the experimental method, with the following characteristics: wire form, with the stiffness of 119±0.5 percent, a gauge factor of 2.08±1 percent, a gauge length of 60 mm, and a gauge width of 2.5 mm with a maximum strain of 2 percent as shown in Figure 10c.

4. 4. Selection of the Ground (Shaking Table) Excitation Ground Motion for the Accelerogram Portion of Mammoth Lakes-04 (Figure 9) was implemented at a moderate amplitude to determine the output of the model structure under seismic excitation. The initial accelerogram has a complete duration of 40 seconds of the ground excitation period with peak acceleration 4.4 $\frac{m}{s^2}$. To satisfy the criteria for consistency, the used record was time-compressed by a factor of $S_T = \sqrt{S_L}$. While, there were around 10.3 seconds of active seismic excitation time after time compression as shown in Figure 11.

5. NONLINEAR ANALYSIS

As part of the research, the same concrete arch dam models are established and the numerical solutions are correlated with the experimental results. The models are created and analyzed by using the (XFEM) method. A strong and robust process program is compulsory for the analysis. ABAQUS/CAE 6.13 (2017) software was used to specify the nonlinear dynamic analysis in this study. The numerical models have the same geometry, dimensions, and boundary conditions of the prototype of the tested arch dam models.

5. 1. Dam Modeling by XFEM Belytschko and Black's [35] extended finite element technique encompasses substantial advantages in relation to crack propagation numerical modeling. Moreover, this method does not require the finite element mesh to correspond to the presence of cracks. Likewise, there is no requirement for the remeshing for crack growth. This is a consequence of the displacement vector function approximation which is appended to model the crack's existence. When the crack is modelled using XFEM, the classical displacement is predicated on the finite element approximation in conjunction with the partition of unity method (PUM) paradigm, as per Melenk and Babuška [10, 36, 37]. This permits easy incorporation of local

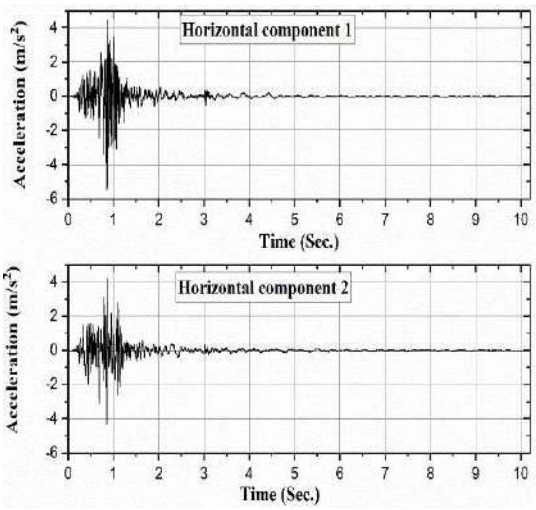

Figure 11. Scaled Down Mammoth Lakes-04 Components

enrichment functions into the finite element approximation. Specifically, enrichment functions generally comprise near-tip asymptotic functions which apprehend the uniqueness encircling the crack tip and an intermittent function that signifies the displacement leap across the surfaces of cracks. Currently, the XFEM method is employed to represent the crack initiation and proliferation manifest in concrete gravidynamics, as per ABAQUS/CAE for brittle or ductile materials, such as the concrete gravity dams modeled in the current work [38, 39]. This process is described in more detail in the ensuing sections of this paper.

The (XFEM) emerged from the cohesive segments method [40, 41]. When it is employed in unison with the phantom node technique [42–44], it is possible to replicate crack initiation and proliferation in an indiscriminate direction. This is because the crack propagation is not bound to mesh-based element peripheries. The crack tip position does not need to be specified with this method. Rather, it is only necessary to indicate a region of reference in which the crack will proliferate. Furthermore, no near-tip asymptotic singularity is required. It is merely necessary to contemplate the displacement jump across a cracked element. This means that the crack is obliged to proliferate across a complete element in an instant in order to obviate the necessity of modelling stress singularity. The phantom node approach superimposes the phantom elements, rather than incorporating further elements of freedom. In this way, this method is able to describe discontinuity and can be readily encompassed within traditional finite element codes. XFEM can be employed in relation to 2D [38, 42, 45, 46], 3D problems [45, 47–49], and dynamic problems [50–52].

5. 2. Three Dimensional Modeling and Mesh Distribution In order to model the concrete members, a 3D first order diminutive integration continuum elements (C3D8R-Brick) are applied. These components are flexible and can be used in models for basic linear analysis or for complex nonlinear interaction [53, 54], plasticity, and large deformation analyses. A normal concrete discretization mesh is presented in Figure 12.

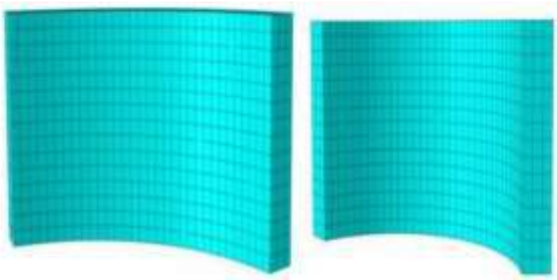

Figure 12. Concrete members discretized using brick elements

5. 3. The Model Calibration and Evaluation It cannot describe how the content changes due to damage by determining damage initiation. The damage is modelled within ABAQUS employing a scalar damage criterion (D) .This can vary from 0 which means (no - damage) to 1 which means (complete - failure). To measure the stress, including damage, the stress that would have been there without damage is multiplied by $(1-D)$. This contributes to the undamaged reaction without damage $(D=0)$, the stress is 0 with complete failure $(D=1)$ and persists in between a fraction of the stress (see Figure 13) [39, 55].

It is important to determine either the maximum displacement or the fracturing energy that is the field under the curve in traction versus the separation graph. The softening behavior can be defined by various options: how the traction-separation graph goes from the point at the beginning of damage to the fully failed state. In this case, linear softening is used, which in the traction-separation graph refers to a straight line. Mode mixing may be taken into consideration, with the BK law, power-law, or tabular data defined. Alternatively, it is possible to indicate model-independent behavior. Owing to the softening of the material model, simulations like damage evolution frequently lead to convergence difficulties. ABAQUS facilitates the use of viscous regularization during damage to stabilize the reaction. The tangent stiffness matrix will then be positive definite for sufficiently small-time measures. As a sub-option for Maxps impact, a viscosity coefficient may be defined. It should be selected in such a way that the effect on the final outcome of the stabilization is negligible. The ALLVD (viscous dissipation) production can be compared to ALLSE (strain energy) to verify this. In contrast with ALLSE, if ALLVD is not thin, viscous stabilization is likely to affect outcomes. Playing around with the coefficient of viscosity will help produce a fair outcome in a reasonable period of time [39, 55]. Apart

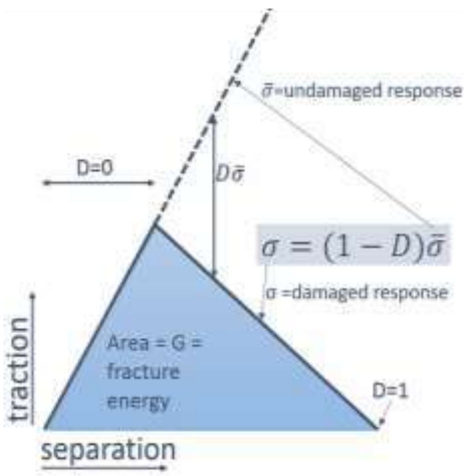

Figure 13. Damage evaluation

from determining when the material will be damaged and how it will respond after the damage is started, it is important to define the area where a crack can occur. This is the area where the words for enrichment can be applied. To permit the crack to spread, the 'allow crack growth' box should be checked. XFEM may also be used for stationary splits, which enables the measurement of contour integrals with less meshing effort. It is possible to insert a different component reflecting the crack (without property or mesh) into the assembly and move it to the correct location. The crack is described by selecting this portion as a crack position. The crack does not have to be around the edges of the part. In fact, if the crack crosses through the part, the XFEM method functions better. For interaction between both sides of the crack, frictionless small-sliding interaction can be described. The solution controls can be changed to help in achieving a converged solution. It is possible to verify discontinuous analysis in the time incrementation column. This makes it possible for ABAQUS to do further iterations before seeing whether the answer goes somewhere. The parameter (I−A) can be increased from the default (5) in the first More tab, to make ABAQUS more attempts before the simulation is aborted. Increasing the number of attempts is helpful if major cut-backs are needed. ABAQUS immediately produces an iso-surface view cut based on this performance if PHILSM is required, which displays the position of the break. The crack will not be noticeable when it is not requested, and the effects displayed will be counterintuitive. STATUxSXFEM is also XFEM-specific. It gives the position of the enriched elements, if the element is undamaged it is (0.0), if the element is absolutely cut through (no traction forces exist), and if the element is weakened but certain traction forces exist, it is a value in between. Of course, natural outputs are also available, such as stress and pressure.

6. EXPERIMIANTAL RESULTS

Two model arch dams were tested using the time-compressed Mammoth Lakes-04 1980 earthquake in two horizontal directions of excitations. one model (M1) with 74˚ degree of curvature and one model (M2) with 124˚ degree of curvature. Traces of the dam displacement, stresses, crack propagation, and table motion was recorded during each test. The test program was thus selected so that the models were exposed to 14 m maximum reservoir water level. The time-history of the dam displacements, stress distribution (see Figure 14), and crack propagation during Mammoth Lakes-04 are extracted from the experimental test as will present in this section.

6. 1. Time History Results during Moderate Seismic Excitation with Water Pressure

During the moderate magnitude, both models show a good response to the applied ground motion excitation without any damage evaluation. The results, as shown in Figures 15 and 16, indicate that M2 provides a good response

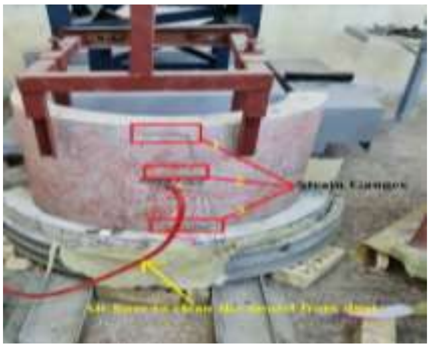

Figure 14. Strain gauges fixed in three points all over the model to verify the stress development during the test

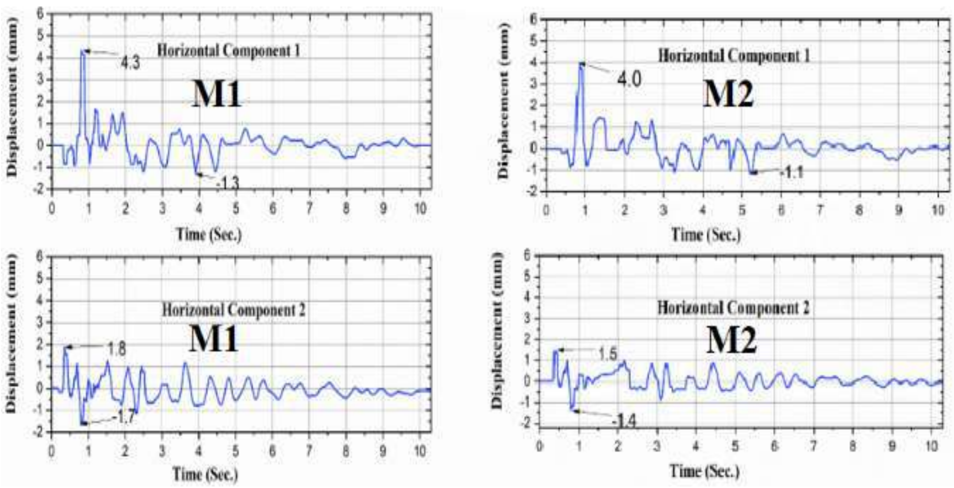

Figure 15. The response of M1 and M2 in Z, X direction, moderate magnitude 5.7M

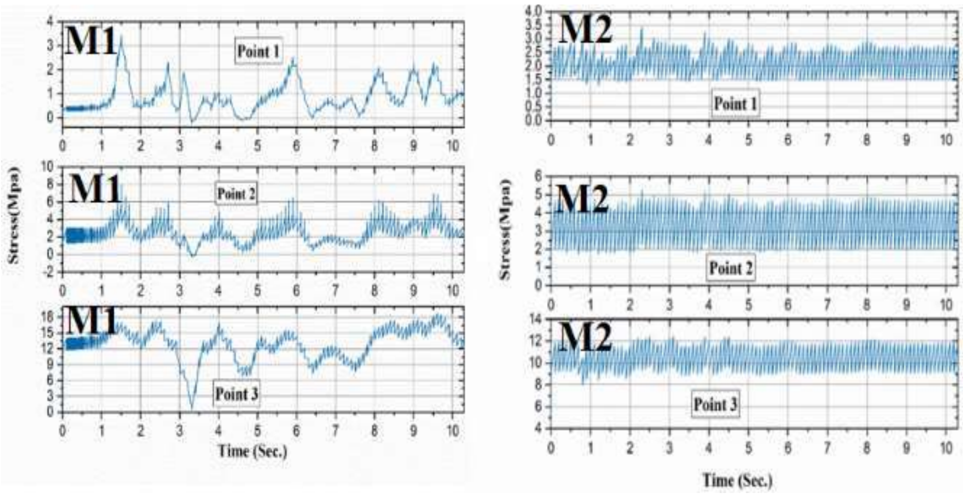

Figure 16. The-maximum principal stresses occurred in points 1, 2 and 3 for M1 and M2, moderate magnitude

compared to M1. The horizontal component 1 (Z-Direction) records the max displacement response compared to the horizontal component 2 (X-Direction) for models M1 and M2 while the max stress recorded during the test was observed at point 3 near the dam's support. Model M1 shows a slight crack propagation while there is no crack propagation is observed for M2 as shown in Figure 17.

7. NUMERICAL TIME HISTORY OF THE DAMS DURING MODERATE MAGNITUDE WITH WATER PRESSURE

The time-history of the dam displacements, stress distribution, and crack propagation during Mammoth Lakes-04 moderate excitation is presented. Figures 18 to 20 provide an overview of the analytical and experimental results, indicating a satisfactory level of agreement between the two sets of results. Numerical and experiment analysis showed a slight crack propagation in model M1. For model M2, no damages were observed during run Mammoth Lakes-04 5.7M.

Figure 17. Deformation and crack propagation patterns for (M1&M2)

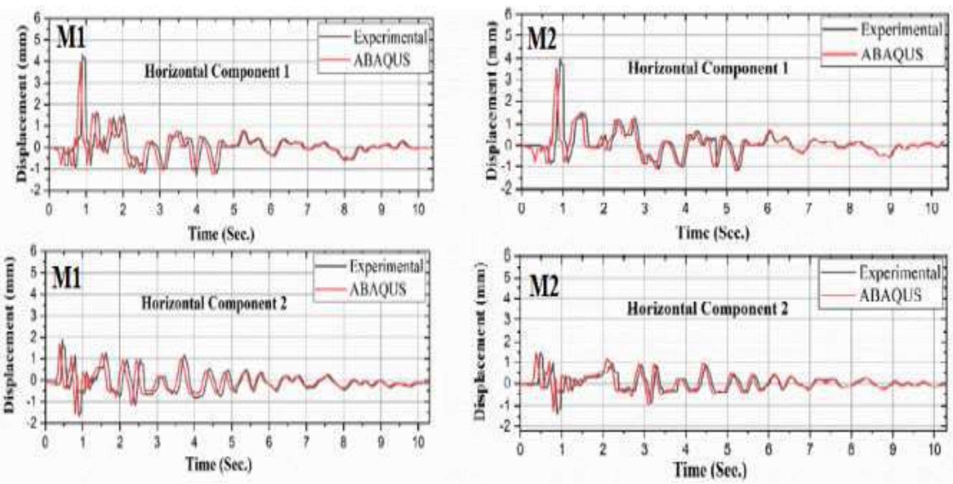

Figure 18. Displacement-time response in horizontal directions of M1and M2 model

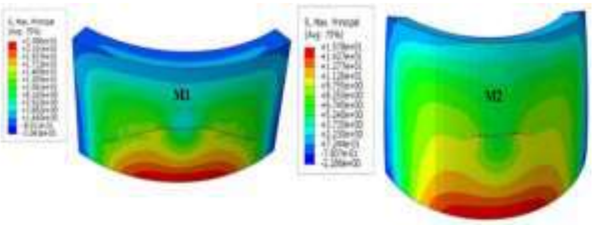

Figure 19. Stress distribution, (S in Mpa)

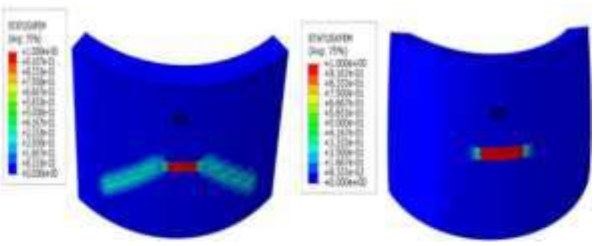

Figure 20. Plastic deformation (STATUSXFE is unitless 0 non-cracked to 1 fully cracked.)

With successive increases in earthquake time until reach to 10.3 second, in model 1, a crack at the middle has propagated from the center into the left and right sides and the max stresses distributed all over the body. Interestingly, model 2 was observed less affected by an increase in earthquake time.

8. CONCLUSION

In the current study, the conclusion can summarize as follow:

1. The curved shape of the dam provides the dam the capability to accommodate the applied loads and increase its stability.
2. For moderate earthquakes, the arch dams may withstand the earthquake even if it contains initial cracks.
3. Non-seismically reinforcement details in medium concrete arch dams do not form a potential source of damage.
4. Most of the deformation and damage development occurred due to the existence of an initial crack.
5. As a method that relies on generalized FEM and the partition of unity method, XFEM is effective for the analysis of discontinuous crack growth in a way that does not rely on the internal geometry and physical interfaces. Consequently, meshing and re-meshing complexities associated with discontinuous problems can be addressed.
6. The degree of curvature is related to the dam's stability. Increasing the degree of curvature make the dam more stable, more responsive to ground motion, less displacement, and less tensile crack development.

9. REFERENCES

1. Marche, C., and Robert, B., "Dam Failure Risk: Its Definition and Impact on Safety Assessment of Dam Structures", ***Journal of Decision Systems***, Vol. 11, Nos. 3–4, (2002), 513–534. doi:10.3166/jds.11.513-534
2. Hartford, D. N. D., and Baecher, G. B., Risk and Uncertainty in Dam Safety, (2004) Thomas Telford Publishing. doi:10.1680/rauids.32705
3. Patsialis, T., Kougias, I., Kazakis, N., Theodossiou, N., and Droege, P., "Supporting Renewables' Penetration in Remote Areas through the Transformation of Non-Powered Dams", ***Energies***, Vol. 9, No. 12, (2016), 1–14. doi:10.3390/en9121054
4. Jabbar Mizhir Alfatlawi, T., Jawad Kadhim, M., and Noori Hussein, M., "Relation between cracks behavior and curvature in cracked concrete arch dam under earthquake", ***Materials Today: Proceedings***, (In Press), (2021). doi:10.1016/j.matpr.2021.02.248
5. Chen, Q., Zou, Y. H., Tang, M., and He, C. R., "Modelling the construction of a high embankment dam", ***KSCE Journal of Civil Engineering***, Vol. 18, No. 1, (2014), 93–102. doi:10.1007/s12205-014-0180-4
6. McManamay, R. A., Oigbokie, C. O., Kao, S.-C., and Bevelhimer, M. S., "Classification of US Hydropower Dams by their Modes of Operation", ***River Research and Applications***, Vol. 32, No. 7, (2016), 1450–1468. doi:10.1002/rra.3004
7. Lin, P., Guan, J., Peng, H., and Shi, J., "Horizontal cracking and crack repair analysis of a super high arch dam based on fracture toughness", ***Engineering Failure Analysis***, Vol. 97, (2019), 72–90. doi:10.1016/j.engfailanal.2019.01.036
8. Javanmard, M., Amiri, F., and Safavi, S., "Instrumentation Readings versus Numerical Analysis of Taham Dam", ***International Journal of Engineering, Transaction A: Basics***, Vol. 32, No. 1, (2019), 28–35. doi:10.5829/ije.2019.32.01a.04
9. Malm, R., Hellgren, R., and Enzell, J., "Lessons Learned Regarding Cracking of a Concrete Arch Dam Due to Seasonal Temperature Variations", ***Infrastructures***, Vol. 5, No. 2, (2020), 1–18. doi:10.3390/infrastructures5020019
10. Mohammadi, M., Samani, H., and Monadi, M., "Optimal Design and Benefit/Cost Analysis of Reservoir Dams by Genetic Algorithms Case Study: Sonateh Dam, Kordistan Province, Iran", ***International Journal of Engineering, Transaction A: Basics***, Vol. 29, No. 4, (2016), 482–489. doi:10.5829/idosi.ije.2016.29.04a.06
11. Karabulut, M., Kartal, M. E., Capar, O. F., and Cavusli, M., "Earthquake analysis of concrete arch dams considering elastic foundation effects", ***Disaster Science and Engineering***, Vol. 2, No. 2, (2016), 46–52
12. Alves, S. W., and Hall, J. F., "Generation of spatially nonuniform ground motion for nonlinear analysis of a concrete arch dam", ***Earthquake Engineering & Structural Dynamics***, Vol. 35, No. 11, (2006), 1339–1357. doi:10.1002/eqe.576
13. Chopra, A. K., "Earthquake Analysis of Arch Dams: Factors to Be Considered", ***Journal of Structural Engineering***, Vol. 138, No. 2, (2012), 205–214. doi:10.1061/(ASCE)ST.1943-541X.0000431
14. Atici, U., Ersoy, A., and Ozturk, B., "Application of destruction specific energy for characterisation of concrete paving blocks", ***Magazine of Concrete Research***, Vol. 61, No. 3, (2009), 193–199. doi:10.1680/macr.2007.00113
15. Boggs, H. L., Tarbox, G. S., and Jansen, R. B., "Arch Dam Design and Analysis", ***Advanced Dam Engineering for Design, Construction, and Rehabilitation***, (1988), 493–539. doi:10.1007/978-1-4613-0857-7_17

16. Xu, Q., Zhang, T., Chen, J., Li, J., and Li, C., "The influence of reinforcement strengthening on seismic response and index correlation for high arch dams by endurance time analysis method", ***Structures***, Vol. 32, (2021), 355–379. doi:10.1016/j.istruc.2021.03.007

17. Jonker, M., and Espandar, R., "Evaluation of Existing Arch Dam Design Criteria in Lieu of ANCOLD Guidelines", ANCOLD 2008 Conference, Australia, (2014), 1–15.

18. US Army Corps of Engineers, ENGINEER MANUAL, No. 1110-2-2200Engineering and Design: Gravity Dam Design, (1995)

19. Ghafoori, Y., Design and Static Analysis of Arch Dam Using Software SAP2000, Master Thesis No.: 33/II.GR, University of Ljubljana, Slovenia, (2016).

20. Shokrieh, M. M., and Askari, A., "Similitude Study of Impacted Composite Laminates under Buckling Loading", ***Journal of Engineering Mechanics***, Vol. 139, No. 10, (2013), 1334–1340. doi:10.1061/(ASCE)EM.1943-7889.0000560

21. Altunisik, A. C., Kalkan, E., and Basaga, H. B., "Structural behavior of arch dams considering experimentally validated prototype model using similitude and scaling laws", ***Computers and Concrete***, Vol. 22, No. 1, (2018), 101–116. doi:https://doi.org/10.12989/cac.2018.22.1.101

22. Federal Energy Regulatory Commission, Engineering guidelines for the evaluation of hydropower projects. Chapter 11-Arch Dams. Washington DC, 20426, (1999), 11–18.

23. Kenan, H., and Azeloğlu, O., "Design of scaled down model of a tower crane mast by using similitude theory", ***Engineering Structures***, Vol. 220, (2020), 110985. doi:10.1016/j.engstruct.2020.110985

24. Xie, W., and Sun, L., "Experimental and numerical verification on effects of inelastic tower links on transverse seismic response of tower of bridge full model", ***Engineering Structures***, Vol. 182, (2019), 344–362. doi:10.1016/j.engstruct.2018.12.046

25. Harris, H., "Use of Structural Models as an Alternative to Full-Scale Testing", Full-Scale Load Testing of Structures, ASTM International, (2009) 25–44. doi:10.1520/STP27137S

26. Kutz, M., Handbook of Transportation Engineering, Vol. 768, McGraw-Hill New York, NY, USA, (2004).

27. Burhan, L., Ghafor, K., and Mohammed, A., "Quantification the effect of microsand on the compressive, tensile, flexural strengths, and modulus of elasticity of normal strength concrete", ***Geomechanics and Geoengineering***, (2019), 1–19. doi:10.1080/17486025.2019.1680884

28. Jin, A.-Y., Pan, J.-W., Wang, J.-T., and Du, X.-L., "A spectrum-based earthquake record truncation method for nonlinear dynamic analysis of arch dams", ***Soil Dynamics and Earthquake Engineering***, Vol. 132, (2020), 106104. doi:10.1016/j.soildyn.2020.106104

29. CAPEER (Pacific Earthquake Engineering Research Center), PEER Ground Motion Database, Pacific Earthquake Engineering Research Center, University of California, Berkeley, US, (2010).

30. Rezaee Manesh, M., and Saffari, H., "Empirical equations for the prediction of the bracketed and uniform duration of earthquake ground motion using the Iran database", ***Soil Dynamics and Earthquake Engineering***, Vol. 137, (2020), 106306. doi:10.1016/j.soildyn.2020.106306

31. Biswas, R., "Evaluating Seismic Effects on a Water Supply Network and Quantifying Post-Earthquake Recovery", ***International Journal of Engineering, Transaction B: Applications***, Vol. 32, No. 5, (2019), 654–660. doi:10.5829/ije.2019.32.05b.05

32. Wang, P., Zhao, M., Du, X., and Cheng, X., "A finite element solution of earthquake-induced hydrodynamic forces and wave forces on multiple circular cylinders", ***Ocean Engineering***, Vol. 189, (2019), 106336. doi:10.1016/j.oceaneng.2019.106336

33. Shahmardani, M., Mirzapour, J., and Tariverdilo, S., "Dynamic Response of Submerged Vertical Cylinder with Lumped Mass under Seismic Excitation", ***International Journal of Engineering, Transaction A: Basics***, Vol. 27, No. 10, (2014), 1547–1556. doi:10.5829/idosi.ije.2014.27.10a.08

34. Wang, M., Chen, J., Wu, L., and Song, B., "Hydrodynamic Pressure on Gravity Dams with Different Heights and the Westergaard Correction Formula", ***International Journal of Geomechanics***, Vol. 18, No. 10, (2018), 04018134. doi:10.1061/(ASCE)GM.1943-5622.0001257

35. Belytschko, T., and Black, T., "Elastic crack growth in finite elements with minimal remeshing", ***International Journal for Numerical Methods in Engineering***, Vol. 45, No. 5, (1999), 601–620. doi:10.1002/(SICI)1097-0207(19990620)45:5<601::AID-NME598>3.0.CO;2-S

36. Geelen, R., Plews, J., Tupek, M., and Dolbow, J., "An extended/generalized phase-field finite element method for crack growth with global-local enrichment", ***International Journal for Numerical Methods in Engineering***, Vol. 121, No. 11, (2020), 2534–2557. doi:10.1002/nme.6318

37. Okodi, A., Li, Y., Cheng, R., Kainat, M., Yoosef-Ghodsi, N., and Adeeb, S., "Crack Propagation and Burst Pressure of Pipeline with Restrained and Unrestrained Concentric Dent-Crack Defects Using Extended Finite Element Method", ***Applied Sciences***, Vol. 10, No. 21, (2020), 7554. doi:10.3390/app10217554

38. Moes, N., Dolbow, J., and Belytschko, T., "A finite element method for crack growth without remeshing", ***International Journal for Numerical Methods in Engineering***, Vol. 46, No. 1, (1999), 131–150. doi:10.1002/(SICI)1097-0207(19990910)46:1<131::AID-NME726>3.0.CO;2-J

39. ABAQUS User Manual, V. 6.12. Providence RI, USA: DS SIMULIA Corp, (2012).

40. REMMERS, J., DEBORST, R., and NEEDLEMAN, A., "The simulation of dynamic crack propagation using the cohesive segments method", ***Journal of the Mechanics and Physics of Solids***, Vol. 56, No. 1, (2008), 70–92. doi:10.1016/j.jmps.2007.08.003

41. Zeng, Q., and Yao, J., "Numerical Simulation of Fluid-Solid Coupling in Fractured Porous Media with Discrete Fracture Model and Extended Finite Element Method", ***Computation***, Vol. 3, No. 4, (2015), 541–557. doi:10.3390/computation3040541

42. Hansbo, A., and Hansbo, P., "A finite element method for the simulation of strong and weak discontinuities in solid mechanics", ***Computer Methods in Applied Mechanics and Engineering***, Vol. 193, Nos. 33–35, (2004), 3523–3540. doi:10.1016/j.cma.2003.12.041

43. Song, J.-H., Areias, P. M. A., and Belytschko, T., "A method for dynamic crack and shear band propagation with phantom nodes", ***International Journal for Numerical Methods in Engineering***, Vol. 67, No. 6, (2006), 868–893. doi:10.1002/nme.1652

44. Chen, Z., Liu, J., and Qiu, H., "Solidification Crack Evolution in High-Strength Steel Welding Using the Extended Finite Element Method", ***Materials***, Vol. 13, No. 2, (2020), 483. doi:10.3390/ma13020483

45. Moës, N., and Belytschko, T., "Extended finite element method for cohesive crack growth", ***Engineering Fracture Mechanics***, Vol. 69, No. 7, (2002), 813–833. doi:10.1016/S0013-7944(01)00128-X

46. Fallah, N., "A Development in the Finite Volume Method for the Crack Growth Analysis without Global Remeshing", ***International Journal of Engineering, Transaction A: Basics***, Vol. 29, No. 7, (2016), 898–908. doi:10.5829/idosi.ije.2016.29.07a.03

47. Sukumar, N., Moes, N., Moran, B., and Belytschko, T., "Extended finite element method for three-dimensional crack modelling", ***International Journal for Numerical Methods in Engineering***,

Vol. 48, No. 11, (2000), 1549–1570. doi:10.1002/1097-0207(20000820)48:11<1549::AID-NME955>3.0.CO;2-A

48. Gravouil, A., Moës, N., and Belytschko, T., "Non-planar 3D crack growth by the extended finite element and level sets-Part II: Level set update", ***International Journal for Numerical Methods in Engineering***, Vol. 53, No. 11, (2002), 2569–2586. doi:10.1002/nme.430

49. Duan, Q., Song, J.-H., Menouillard, T., and Belytschko, T., "Element-local level set method for three-dimensional dynamic crack growth", ***International Journal for Numerical Methods in Engineering***, Vol. 80, No. 12, (2009), 1520–1543. doi:10.1002/nme.2665

50. Nistor, I., Pantalé, O., and Caperaa, S., "Numerical implementation of the eXtended Finite Element Method for dynamic crack analysis", ***Advances in Engineering Software***, Vol. 39, No. 7, (2008), 573–587. doi:10.1016/j.advengsoft.2007.06.003

51. Motamedi, D., and Mohammadi, S., "Dynamic analysis of fixed cracks in composites by the extended finite element method", ***Engineering Fracture Mechanics***, Vol. 77, No. 17, (2010), 3373–3393. doi:10.1016/j.engfracmech.2010.08.011

52. Khademhosseini Beheshti, H., Haji Aboutalebi, F., and Najimi, M., "Stress Intensity Factor Determination in Functionally Graded Materials, Considering Continuously Varying of Material Properties", ***International Journal of Engineering, Transaction C: Aspects***, Vol. 29, No. 12, (2016), 1741–1746. doi:10.5829/idosi.ije.2016.29.12c.13

53. Rong, B., Rui, X., Tao, L., and Wang, G., "Theoretical modeling and numerical solution methods for flexible multibody system dynamics", ***Nonlinear Dynamics***, Vol. 98, No. 2, (2019), 1519–1553. doi:10.1007/s11071-019-05191-3

54. Sadripour, S., Estajloo, M., Hashemi, S., and Adibi, M., "Experimental and Numerical Investigation of Two Different Traditional Hand-Baking Flatbread Bakery Units in Kashan, Iran", ***International Journal of Engineering, Transaction B: Applications***, Vol. 31, No. 8, (2018), 1292–1301. doi:10.5829/ije.2018.31.08b.18

55. Gustafsson, A., Khayyeri, H., Wallin, M., and Isaksson, H., "An interface damage model that captures crack propagation at the microscale in cortical bone using XFEM", ***Journal of the Mechanical Behavior of Biomedical Materials***, Vol. 90, (2019), 556–565. doi:10.1016/j.jmbbm.2018.09.045

Persian Abstract

چکیده

رفتار سد قوس بتونی ترک خورده به دلیل شدت زمین لرزه و تغییر فشار آب مورد بررسی قرار گرفت. برای طراحی مدل‌های سد با مقاومت طراحی ۴۵ مگاپاسکال از بتن ساده استفاده شده است. یک جدول لرزش برای ایجاد یک مرکز آزمایش پویا برنامه‌ریزی، تولید و ساخته شده است. کار آزمایشی شامل آزمایش چهار مدل سد بتونی مقیاس‌پذیر بود که به دو گروه تقسیم شده است، هر گروه شامل دو درجه مختلف مدل انحنا است. یک شکاف مصنوعی در مرکز بدنه سد ایجاد شد. روش المان محدود توسعه یافته (XFEM) به منظور پرداختن به محمول عددی برای انتشار یک ترک، بیان شده است. نتایج نشان داد که رفتار خوب تمام سدهای قوسی تحت شدت متوسط زلزله وجود دارد. سد قوسی با درجه انحنای بالاتر به ترتیب ۱۷/۸ ٪ و ۱۶/۲ ٪ جابجایی کمتری را در جهت Z و X ثبت کرد. ارزیابی تنش و انتشار ترک در مقایسه با سد قوسی دارای کمترین درجه انحنا است. از این رو، افزایش درجه انحنا منجر به افزایش پایداری سد، مقاومت در برابر زلزله، جابجایی کمتر و رشد کمتر ترک‌های کششی شد.

International Journal of Engineering

Journal Homepage: www.ije.ir

Seismic Vulnerability Studies of a G+17 storey building in Abu Dhabi - UAE using Fragility Curves

S. S. Nair[a], G. Hemalatha*[b], R. Raja S.[c], E. A. Stephen[d]

[a] Buildings and Communities, Structures, Nine Cube Consultants L.L.C, United Arab Emirates
[b] Department of Civil Engineering, Karunya Institute of Technology and Sciences, India
[c] M.Tech Structural Engineering, Karunya Institute of Technology and Sciences,, India
[d] Department of Mathematics, Karunya Institute of Technology and Science, India

P A P E R I N F O

Paper history:
Received 09 January 2021
Received in revised form 17 March 2021
Accepted 26 March 2021

Keywords:
Seismic Vulnerability
Fragility Curves
Time History Analysis
Shear Walls
Multi-storey

A B S T R A C T

The growth of tall buildings in the United Arab Emirates (UAE) has paved the way for a surge in interest in the country's seismic vulnerability investigation. The case study building comprises of shear walls and RC columns as its lateral force-resisting system. It is a newly constructed G+17 storey building and is about 78 meters high. The non-linear dynamic seismic analysis which is the time history modal analysis, also known as Fast Non-linear analysis was performed on the study building with about 45 earthquakes in 3 sets of hazard levels (2%, 5%, and 10% Probability of Exceedance [PE]) to generate the inter-story drift values. Based on the Performance-based approach given by FEMA 356, the Fragility curves are developed by creating the Probabilistic Seismic Design Modal. The resultant fragility curves are given in terms of 3 probabilities i.e., (1) Immediate Occupancy, (2) Life Safety, and (3) Collapse Prevention. The whole study depends on the idea that comparative sort of structures will have a similar likelihood of a given harm state for a given seismic force.

***doi**: 10.5829/ije.2021.34.05b.10*

NOMENCLATURE

a, b	Regression Coefficients	PGA	Peak Ground Acceleration
ACI	American Concrete Institute	PSDM	Probability Seismic Design Model
ASCE	American Society for Civil Engineers	R	Response Modification Factor
DL	Dead Load	R_JB	Joyner Boore Distance
C	Capacity of Structure	RSN	Record Sequence Number
Cd	Deflection Amplificaton	Sa	Spectral Acceleration
CP	Collapse Prevention	Ss	0.2 sec Spectral Acceleration
Cp_w	Windward Coefficient	S1	1 sec Spectral Acceleration
Cp1	Leeward Coefficient	SDL	Superimposed Dead Load
D	Seismic Demand which is considered as Θ_{max}	SLS	Serviceability Limit State
FNA	Fast Non-Linear Analysis	SRSS	Square Root of Sum of the Squares
G	Ground	T1	Fundamental Time Period
GCC	Gulf Cooperation Council	UAE	United Arab Emirates
GM	Ground Motion	UHS	Uniform Hazard Spectrum
GMPE	Ground Motion Prediction Equations	ULS	Ultimate Limit State
I	Occupancy Importance	Vs30	Shear Wave velocity
IM	Intensity Measure	**Greek Symbols**	
IO	Immediate Occupancy	Θ_{max}	Maximum Interstory Drift Ratio
ISDR	Interstory Drift Ratio	Φ	Standard Normal Cumulative Function
LL	Live Load	$\hat{C}$	Median structural drift capacity
LS	Life Safety	β_c	Aleatoric Uncertainty in Capacity
NGA	Next Generation of GM Attenuation Models	β_M	Epistemic Uncertainty in modelling
PE	Probability of Exceedance	**Subscripts**	
PEER	Pacific Earthquake Engineering Research Centre	C	Capacity
		M	Modelling

*Corresponding Author Institutional Email: hemalathag@karunya.edu (G. Hemalatha)

Please cite this article as: S. S. Nair, G. Hemalatha, R. Raja S., E. A. Stephen, Seismic Vulnerability Studies of a G+17 storey building in Abu Dhabi - UAE using Fragility Curves, International Journal of Engineering, Transactions B: Applications Vol. 34, No. 05, (2021) 1167-1175

1. INTRODUCTION

The contextual analysis building is a G+17 story building newly constructed structure in Abu Dhabi, UAE [1, 2] with flat slabs and shear walls, designed for response spectrum analysis. This chosen building could represent the modern constructions in GCC countries. Thereby the research on the Earthquake Reliability Assessment [3] of this structure would lay the foundation for the proper seismic design for similar kind of structures in GCC countries. The geology, tectonics and seismic source modal for UAE especially Abu Dhabi, were referred from various studies [4-8]. Based on the geological studies on UAE performed by various eminent researchers [9-17] who have provided the results in terms of Peak Ground Acceleration, Uniform Hazard Spectra and Deaggregation [18-21]; the relevant parameters (such as the PGA, Shear wave velocity (Vs30), Joyner Boore distance (R_JB), magnitude) required for the selection of the most appropriate earthquake for the vulnerability studies were obtained from Pacific Earthquake Engineering Research Centre [2,5]. The guidelines provided by NIST GCR 11-917-15 [22, 23] were followed to formulate the significant methodology to be adopted for the vulnerability studies. In accordance to this, a total of 45 ground motions [24] under 3 sets of hazard levels as 2, 5 and 10% [25, 26] Probability of Exceedance, were chosen to perform the Non-linear Dynamic Seismic Analysis which is Time History Modal Analysis, also known as Fast Non-Linear Analysis (www.csiamerica.com) on the case study building and hence to obtain the Interstory Drift Values.

The fragility curves gives the damage level as probabilities for a structure that tends to reach over the deformation limit for a given state of ground movement [27-29]. Depending upon the performance based probabilistic Approach given by FEMA 356 [30], the results were provided in terms of Immediate Occupancy (IO), Life Safety (LS) and Collapse Prevention (CP).

The novelty of this research is that there has been no fragility curves derived so far for this newly constructed building in Abu Dhabi and not much seismic vulnerability studies is available for the GCC countries.

The objective is to study the seismic vulnerability of an existing high rise building, located in Abu Dhabi, UAE through fragility curves, thereby producing results that helps in suggesting seismic design protocols that could be adopted for similar High Rise Buildings with shear walls and columns as its lateral force resisting system.

2. CASE STUDY BUILDING

A newly constructed G+17 story building located in Abu Dhabi, UAE was selected as the case study building on which the vulnerability analysis is performed. This building is designed with Shear walls and Flat slabs.

2. 1. Structural Details The structural details of the case study building are elaborated in Table 1.

2. 2. Structural System Table 2 describes the four structural systems of the case study building. 3 D model of the building is developed in ETABS software as shown in Figure 1 and the typical floor plan is represented in Figure 2.

2. 3. Materials Used–Concrete Equation (1) gives the cylinder to cube strength relationship. Table 3 gives the conversed concrete strength (of cube & cylinder) and

TABLE 1. Structural System of G+17 storey (case study) building

Floors	Approximate Area
5 Basements (Parking)	5 x 1320 m^2
Podium 1	1320 m^2
Podium 2 (retail)	1275 m^2
1 office floor	1 x 830 m^2
2 - 17 typical floors	16 x 845 m^2
Roof	845 m^2
Upper roof	620 m^2

Height (excluding Basements) 78 m

The basement and typical floor heights are 3.3 m and 3.5 m respectively

RC Structures – Conventional Reinforced Concrete In Situ Construction

TABLE 2. Structural system of the case study building

Gravity System	• RC Flat slabs @ typical floors and basement floors • Transfer Beams @ Basement floors • Stair Flights and landings
Lateral system	• Shear walls and columns in both orthogonal directions – Building frame system • Lateral load is transferred to the shear walls by means of a horizontal diaphragm, i.e. the floor slabs • Thickness of walls – 300 mm to 400 mm • Core walls in basement levels – 300 mm to 400 mm
Raft Foundation	• Raft footing of 1.5m depth accompanied by few tension piles as per the foundation analysis. For the design of foundation, worst load combinations of earthquake forces as well as uplift water pressures are considered.
Typical Floor	• RC Flat slabs of Approximately 240 mm thick with local thickening of 280 mm rests on RC columns and walls

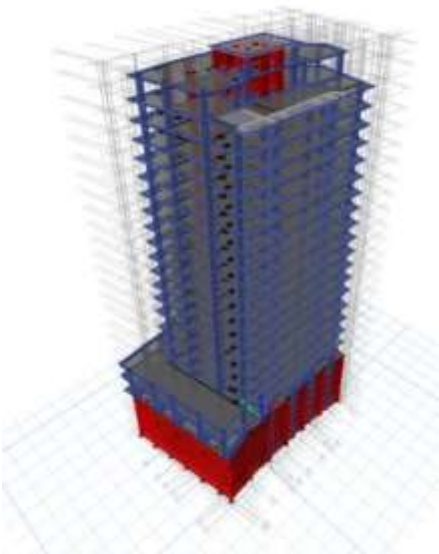

Figure 1. 3D model of the building in ETABs

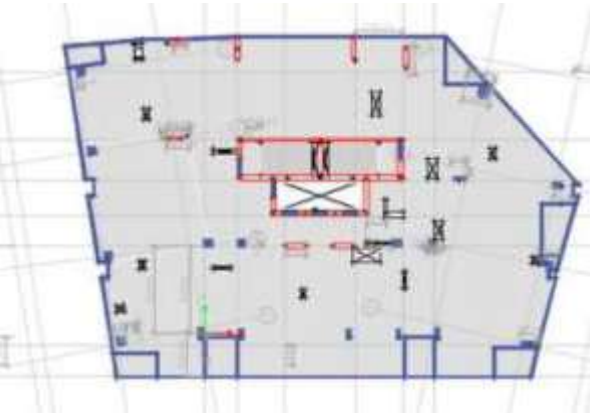

Figure 2. Typical floor model in ETABs

Young's modulus adopted in the design of the case study building.

$$\text{Cylinder strength} = 0.85 \times \text{Cube strength} \quad (1)$$

TABLE 3. Concrete Strength of cube and cylinder, and Young's modulus

Applicable	Cube Strength, f_{cu} (N/mm^2)	Cylinder Strength f_{ck} (N/mm^2)	Young's Modulus (kN/mm^2)
Foundations	60	51	38385
Slabs/ Beams/ Retaining Walls	45	38	33133
Foundations	60	51	38385
Slabs/ Beams/ Retaining Walls	45	38	33133

2. 4. Special Design Incorporated The special design specifications are as follows:

Second Order Analysis (P - Δ): 1.2DL + 0.5LL

Construction Sequence Analysis : 1.0DL + 1.0SDL

Floor Diaphragm: Semi-rigid diaphragms

Stiffness Modifiers: Based on ACI 318 10.10.4.1 (The values are compiled in Table 4)

2. 5. Wind Load (As per ASCE7-05)

Wind Speed= 90 mph

Exposure type= B

Importance Factor= 1

Cpw= 0.8

Cp1= 0.5

2. 6. Static Earthquake Load (As per ASCE7-05)

R= 5

System Overstrength, Omega= 2.5

Cd= 4.5

I= 1

Ss= 0.6

S1= 0.18

Long-Period Transition Period= 8 sec

Site Class= C

Eccentricity Ratio= 0.05

2. 7. Response Spectrum Seismic loads are considered in the analysis for both, equivalent static method and response spectrum method. As the considered case study building falls under the category of tall and irregular builing, the fundamental mode of vibration is not dominating the response. Hence dynamic analysis using Response Spectrum method is adopted. This building was designed based on Response Spectrum method as per ASCE 7-05 parameters which is indicated in Figure 3.

2. 8. Analysis Modal analysis is performed to compute modal responses and they are combined using SRSS method to get maximum responses. For design of vertical elements (columns and shear walls), forces from response spectrum method are considered.

TABLE 4. Stiffness Modifiers incorporated in the design software model

Element	ULS	SLS
Columns	0.7	1.0
Walls (uncracked)	0.7	1.0
Beams	0.35	0.5
Slabs	0.25	0.35

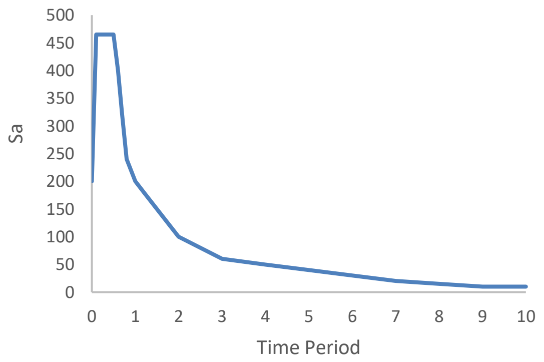

Figure 3. Response Spectrum Function as per ASCE 7-05

3. GROUND MOTION DATA

Three sets of earthquake data for 2, 5 and 10% probability of Exceedance (PE) of 50 years earthquakes which has the effective return periods of 475 years, 975 years and 2475 years respectively were selected for vulnerability studies [23, 31-33]. The target response spectrum for Abu Dhabi, U.A.E were taken from the paper [1] who have performed the seismic hazard assessment for UAE based on 7 GMPE's inclusive of 3 NGA. The interpolated values for the target spectrum of 5% PE was calculated. The three target RS for the three hazard levels are exhibited in Table 5 and its graphical representation is expressed by Figure 4. The ground motions required are selected, scaled and downloaded from PEER centre – NGA West 2 database.

The significant parameters required for the selection of most relevant earthquake data from PEER are sorted in Table 6. From Table 6, the time period for which the ground motions are to be scaled are set by the guidelines given by NIST GCR 11-917-15 [22], which is the period within $0.2T_1$ and $1.5T_1$, where T_1 is the Fundamental Time period of the Case Study Building. The value of T_1 is 4.99 s.

In total 45 ground motions (GMs) are obtained from PEER database in terms of 3 sets as 15 GMs under each

TABLE 5. Target response spectrum of Abu Dhabi for 2, 5 and 10% PE

Time (s)	PGA of Abu Dhabi, UAE		
	475 years (2% PE)	975 years (5% PE)	2475 years (10% PE)
0	0.035	0.059	0.073
0.2	0.071	0.138	0.178
1	0.040	0.062	0.075
2	0.033	0.041	0.045
3	0.016	0.022	0.025
4	0.009	0.014	0.017

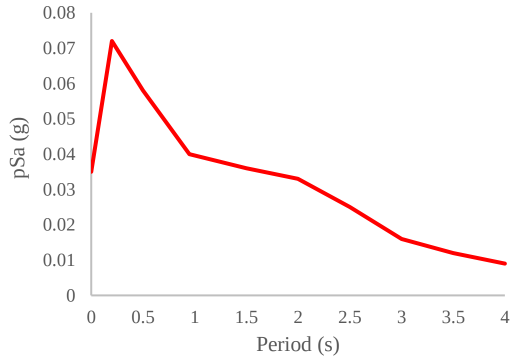

Figure 4a. Design target spectrum for 2% PE given in PEER database

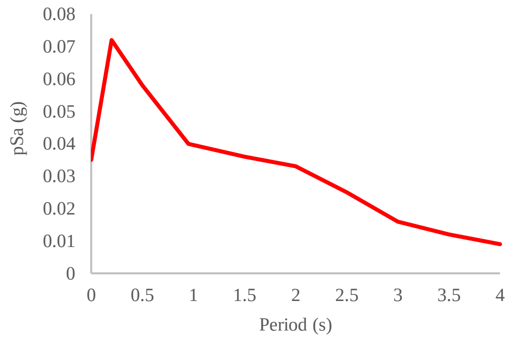

Figure 4b. Design target spectrum for 5% PE given in PEER database

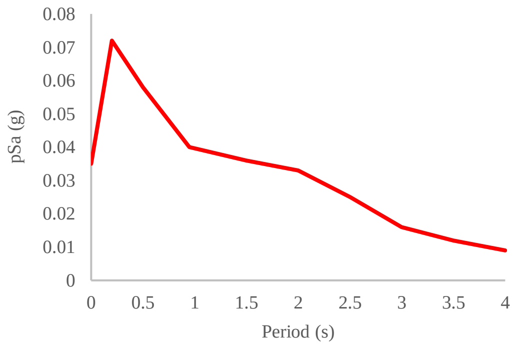

Figure 4c. Design target spectrum for 10% PE given in PEER database

set. The ground motions have approxiamtely the same magnitude but different mechanism, distance and velocity. The GM data comprises of Acceleration, Displacement and velocity files in Horizontal-1, Horizontal-2 and Vertical direction. Among which the acceleration files in Horizontal-1, Horizontal-2 are required for the non-linear dynamic analysis. The scale factor generated from PEER database (Figure 5) for each ground motion after scaling was used for the time history analysis. Earthquake data obtained from PEER databaseand the scaled ground motions are represented in Tables 7and 8, respectively.

TABLE 6. Search Parameters in PEER

Parameter	Value	Source
Fault type	SS (Strike Slip) + Reverse	[12]
Magnitude (min, max)	4, 7	[1]
R_JB (Joyner Boore distance) [min, max]	60, 300 (Km)	
Rrup (Rupture Plane distance) [min, max]	60, 300 (Km)	Assumption
Shear Wave Velocity (Vs30) –for site class C [min, max]	366, 762 (m/s)	IBC 2012 [1]
Pulse	No Pulse-like Records	Assumption
Initial Scale factor [min, max]	0.5, 3	
Spectral Ordinate	SRSS (Square Root of Sum of Squares)	[19]
Damping Ratio	5%	
Scaling Method	Minimize MSE	
Period Ratio	1, 7.5	

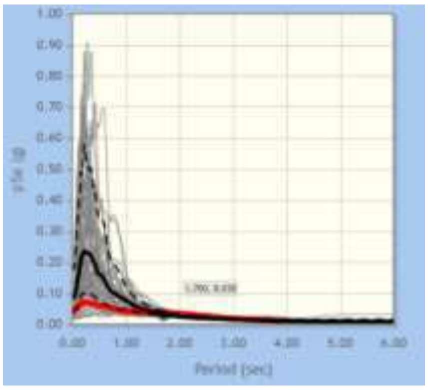

Figure 5a. Scaled spectra with Target spectrum for 2%

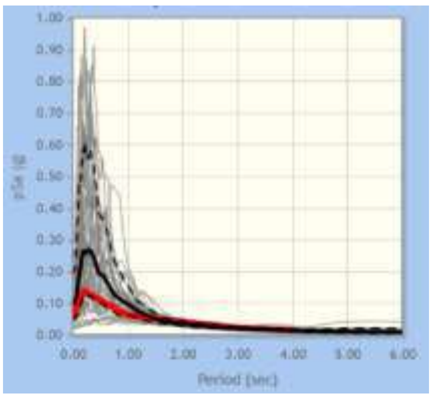

Figure 5b. Scaled spectra with Target spectrum for 5%

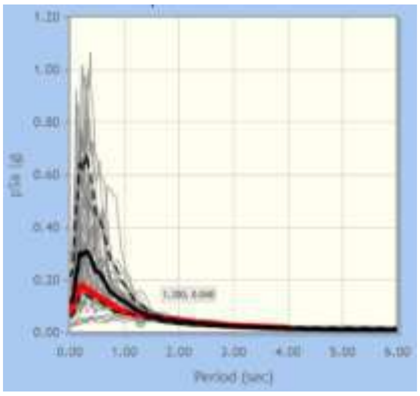

Figure 5c. Scaled spectra with Target spectrum for 10%

4. NONLINEAR DYNAMIC ANALYSIS & ISDR

A non-linear dynamic analysis – Time History Modal Analysis also known as Fast Non-Linear Analysis (FNA) was performed on the case study building for all 45 ground motions (GMs) using the commercially available software ETABS 2017. FNA method was chosen to be the most appropriate dynamic analysis since the newly constructed case study building was designed primarily as linear-elastic and consists of fairly limited predefined non-linear behaviours such as P-Δ ratio, torsional irregularities (geometric nonlinearities). The significant cases to be incorporated during the time history analysis in ETABS 2017 as per the guidelines given by Computers and Structures, Inc. (www.csiamerica.com) includes,

i. Mass Source Data: 25% Live Load + 100% Dead Load (ASCE 7-16)
ii. Modal Case Data: Ritz vector

Total Mass Participation Ratio (MPR) should be > 90% (ASCE 7-05 [12.9.1]). The sufficient number of modes required for the FNA method to attain 99% MPR is achieved by trial and error method.

The maximum Inter Story Drift Ratio (ISDR) was calculated from the resultant displacements from the analysis and the spectral acceleration at the fundamental time period (T_1 = 4.99 s) for each time history for 5% damping were tabulated in Table 9.

5. MODELLING OF FRAGILITIES

Fragility curve is a compelling device for weakness evaluation of basic frameworks. It gives gauges regarding probabilities of a structure to reach or surpass the restriction of deformation at given degrees of ground shaking [34-36]. At the end of the day, Fragility bends gives the probability of surpassing a recommended degree of harm for a wide scope of ground motion intensities. The modelling and derivation of fragility curve explained by Rajeev et al. [28, 29] was followed in this paper.

TABLE 7. Earthquake data obtained from PEER

Sl. No.	GMs (from PEER)	Year	Station Name	Magnitude	Mechanism	Rjb (Km)	Rrup (Km)	Vs30 (m/sec)
1	RSN17 Scalif	1952	San Luis Obispo	6	Strike slip	73.41	73.41	493.5
2	RSN39 Borrego	1968	Pasadena – CIT Athenaeum	6.63	Strike slip	207.14	207.14	415.13
3	RSN40 Boreggo	1968	San Onofre – So Cal Edison	6.63	Strike slip	129.11	129.11	442.88
4	RSN85 Sfern	1971	"San Juan Capistrano"	6.61	Reverse	108.01	108.01	459.37
5	RSN86 Sfern	1971	"San Onofre - So Cal Edison"	6.61	Reverse	124.79	124.79	442.88
6	RSN609 Whittier	1987	"Castaic - Hasley Canyon"	5.99	Reverse Obliq	64.56	64.96	421.05
7	RSN905 Big Bear	1992	"Featherly Park - Maint"	6.46	Strike slip	78.81	78.91	367.54
8	RSN911 Big Bear	1992	"LA - 1955 1/2 Purdue Ave. Bsmt"	6.46	Strike slip	140.22	140.28	379
9	RSN972 Northr	1994	"Featherly Park - Maint"	6.69	Reverse	82.01	82.32	367.54
10	RSN1037 Northr	1994	"Mojave - Oak Creek Canyon"	6.69	Reverse	75.54	75.8	422.73
11	RSN1109 Kobe	1995	"MZH"	6.9	Strike slip	69.04	70.26	609
12	RSN1112 Kobe	1995	"OKA"	6.9	Strike slip	86.93	86.94	609
13	RSN1630 Upland	1990	"Ocean Floor SEMS III"	5.63	Strike slip	71.72	71.73	659.6
14	RSN2078 Nenana	2002	"Anchorage - K2-18"	6.7	Strike slip	216.47	216.47	435.21
15	RSN2083 Nenana	2002	"Anchorage - NOAA Weather Fac."	6.7	Strike slip	275.47	275.47	390.32

TABLE 8. Scaled GMs for 2%, 5% and 10% PE

RSN	Earthquake Name	Scale Factor		
		2% PE	5%PE	10%PE
17	"Southern Calif"	1.91	1.6463	1.1985
39	"Borrego Mtn"	1.872	1.6135	1.1746
40	"Borrego Mtn"	1.3123	1.1311	0.8235
85	"San Fernando"	1.3674	1.1786	0.858
86	"San Fernando"	2.3585	2.0329	1.4799
609	"Whittier Narrows-01"	2.8532	2.4593	1.7903
905	"Big Bear-01"	1.8934	1.632	1.188
911	"Big Bear-01"	1.5696	1.3529	0.9849
972	"Northridge-01"	2.0657	1.7805	1.2962
1037	"Northridge-01"	2.6927	2.321	1.6896
1109	"Kobe_ Japan"	1.5064	1.2985	0.9452
1112	"Kobe_ Japan"	2.6419	2.2771	1.6577
1630	"Upland"	2.0608	1.7763	1.2931
2078	"Nenana Mountain_ Alaska"	2.1257	1.8322	1.3338
2083	"Nenana Mountain_ Alaska"	1.6706	1.44	1.0483

$$\text{Fragility} = P(D > C \mid IM) \quad (2)$$

The above fragility equation (2) depicts, the probability that the D set on the structure is more noteworthy than

TABLE 9. The maximum ISDR and pSa (@ T_1) for 2%, 5% and 10% PE in 50 years which is equivalent to 475 years, 975 years and 2475 years return periods respectively for 5% damping

G+17 Story	Period (T_1) = 4.99 sec					
Ground Motion (PEER)	2% PE		5% PE		10% PE	
	Sa (T_1)	ISDR (%)	Sa (T_1)	ISDR (%)	Sa (T_1)	ISDR (%)
RSN17 Scalif	0.007	0.116	0.006	0.100	0.005	0.073
RSN39 Borrego	0.005	0.128	0.004	0.110	0.003	0.080
RSN40 Boreggo	0.011	0.216	0.009	0.186	0.007	0.136
RSN85 Sfern	0.010	0.203	0.009	0.175	0.006	0.127
RSN86 Sfern	0.011	0.185	0.009	0.160	0.007	0.116
RSN609 Whittier	0.003	0.075	0.003	0.065	0.002	0.047
RSN905 Big Bear	0.003	0.106	0.002	0.092	0.002	0.067
RSN911 Big Bear	0.003	0.092	0.003	0.080	0.002	0.058
RSN972 Northr	0.003	0.178	0.002	0.153	0.002	0.111

RSN1037 Northr	0.004	0.111	0.003	0.095	0.002	0.069
RSN1109 Kobe	0.007	0.249	0.006	0.161	0.005	0.117
RSN1112 Kobe	0.018	0.323	0.006	0.198	0.011	0.202
RSN1630 Upland	0.010	0.210	0.008	0.181	0.006	0.132
RSN2078 Nenana	0.006	0.076	0.005	0.108	0.004	0.079
RSN2083 Nenana	0.006	0.163	0.007	0.140	0.005	0.102

the limit C of the structure. This is administered by a picked IM which means the degree of seismic stacking and it depicts the spectral acceleration as intensity measure

A proposed conceivable approach to survey the fragility function is by creating a probabilistic distribution for the demand moulded on the IM, which is known as seismic demand model PSDM and convolving it with an appropriation for the limit. The demand on the structure is measured utilizing not many chose metric(s) (say inter story drift, ductility,). Cornell et al. [8] recommended that the estimate for the median demand can be spoken by a power model as Equation (3):

$$\hat{D} = aIM^{b} \tag{3}$$

Where IM is the seismic intensity measure of choice, and both a & b are regression coefficients.

In this research both Θ_{max} and Sa are obtained for 5% damping.

5. 1. Structural Performance As briefly explained by Aiswarya et al. [30], as per FEMA 356 in the global-level seismic evaluation, the performance of the structure is quantified by the Interstory drift. The seismic evaluation approach as recommended by FEMA 356 uses three performance level which are Immediate Occupancy, Life Safety and Collapse Prevention. The global level Interstory drift limits for the three performance levels for RC building elements in FEMA 356 (ASCE 2000) is as mentioned in Table 10.

The expected damage states for the three performance levels [31, 32] are:

TABLE 10. Drift limits for the performance levels (FEMA365)

Structural Performance Level	Drift (%)
IO	1
LS	2
CP	4

- The IO level is characterized by the cut-off under which the structure can be securely occupied with no huge fix. It is portrayed by the estimation of Θ_{max} at which the casing enters the plastic range.
- The SD level (Significant Damage) creates at a mishappening at which huge harm is continued, yet a generous edge stays against nascent breakdown.
- The CP level is given by the purpose of nascent breakdown of the casing because of either extreme debasement in strength and associations or huge P-Δ impacts coming about because of exorbitant lateral deformations.

5. 2. Deriving Fragility Curves To construct the PSDM, nonlinear dynamic analysis shall be used. One of the method, "Cloud analysis" [30, 27], is a suitable method (although not the most precise). The advantage of this strategy is that it depends on the GM as they are recorded. By performing a simple linear regression of the logarithm of D against the logarithm of IM ($\hat{D} = aIM^{b}$), the PSDM parameters (a, b) could be obtained. The best power law equation was determined and is shown in Figure 6.

The appropriation of the demand about its median is regularly accepted to follow a two-boundary lognormal probability distribution. Accordingly, in the wake of assessing the scattering of the demand about its median, which is moulded upon the IM, the fragility can be given as shwn in Equation (4) and indicates the damage measure.

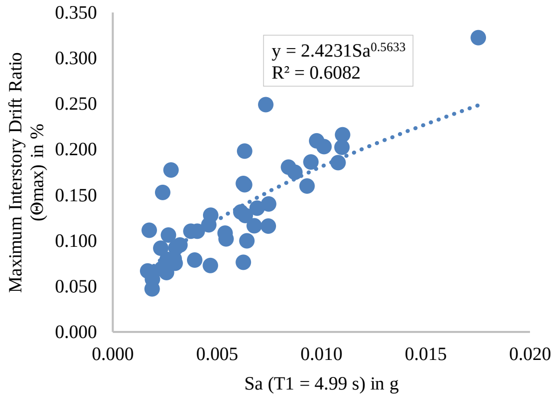

Figure 6. Probabilistic Seismic Demand Model (PSDM)

TABLE 11. PSDM parameters

PSDM PARAMETERS	
A	2.4231
b	0.5633
$\beta_{D\mid IM}$	0.271

$$P(D > C\,|\,IM) = 1 - \Phi\left(\frac{\ln(\hat{C}) - \ln(a \cdot IM^{b})}{\sqrt{\beta^2_{D|IM} + \beta^2_C + \beta^2_M}}\right) \quad (4)$$

β_C - is taken as 0.2 for this study
β_M - is taken as 0.2 for this study

5. 3. Seismic Fragility Curve The seismic fragility curves of the case study building (G+17 story) is given by Figure 7. As per the Median Structural Capacity mentioned in Table 12, in contrast to Figure 7, interprets that the non linearity of the case study building does not overwhelm the general structural reaction.

TABLE 12. Median Structural Capacity for IO, LS & CP

	$\hat{C}$
IO	1
LS	2
CP	4

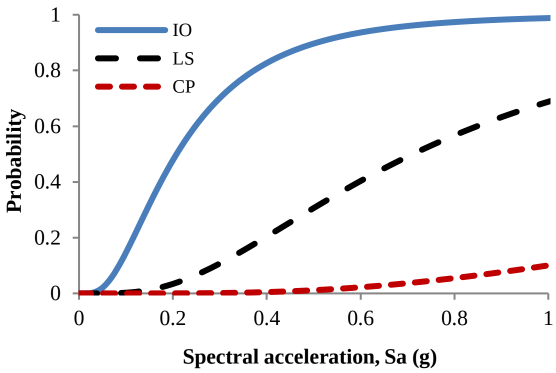

Figure 7. Fragility curve for the case study RC building

6. CONCLUSION

Seismic fragility curves were developed for the case study building. Vulnerability assessment of the building is executed using the developed fragility curves.

The vulnerability assessment of RCC multistorey building in this research is a useful tool for seismic retrofitting decisions, disaster response planning and evaluation of loss of functionality of the structures in GCC countries. Using the analytical approach, the seismic fragility curve was developed for the proposed case study building for which no fragility curves were developed before. This building was identified as a typical High Rise Building (G+17 storey) in Abu Dhabi, United Arab Emirates, in the region with Shear walls as the basic lateral load resisting system. The predictive tool for PSDM parameters (a, b, β) using response spectrum technique was created. As a result of analytical method fragility curves, the uncertainty in the ground motion does not dominate the overall structural response. The whole study is based on the idea that comparative sort of structures will have a similar likelihood of a given harm state for given seismic force.

7. REFERENCES

1. Nair, S., Hemalatha, G. and Muthupriya, P., "Response spectrum analysis and design of case study building", ***International Journal of Civil Engineering and Technology***, Vol. 8, No. 8, (2017), 1227-1238.
2. Nair, S., Hemalatha, G. and Muthupriya, P., "Vulnerability assessment using fragility curves", ***International Journal of Applied Engineering Research***, Vol. 12, No. 9, (2017), 1867-1873.
3. Kibboua, A., Kehila, F., Bechtoula, H., Mehant, Y. and Remki, M., "Development of fragility curves for seismic evaluaiton of reinforced concrete bridge", in Second European Conference on Earthquake Engineering and Seismology, Istanbul. (2014), 25-29.
4. Abdalla, J., A., Khan, Z., Eleman, M. and Irfan, M., "", (16WCEE), "Seismic hazard assessment and local site effects on uae major cities and their environs: An overview", in 16th World Conference on Earthquake Engineering, Santiago Chile., (2017), 4785.
5. Aldama-Bustos, G., J.J., B., Fenton, C., H. and Stafford P., J., "Probabilistic seismic hazard analysis for rock sites in the cities of abu dhabi, dubai and ra's al khymah", Vol. 3, No. 1, (2009), 1-29. doi: 10.1080/17499510802331363.
6. Jalayer, F., Franchin, P. and Pinto, P.E., "A scalar damage measure for seismic reliability analysis of rc frames", ***Earthquake Engineering and Structural Dynamics***, Vol. 36, No. 13, (2007), 2059-2079. doi: https://doi.org/10.1002/eqe.704.
7. Irfan, M., Khan, Z.H., El-Emam, M. and Abdalla, J., "", , (). , "Seismic hazard assessment and spectral accelerations for united arab emirates", in 15 WCEE, American University of Sharjah, United Arab Emirates, (2012).
8. Al-Dogom, D., Schuckma, K. and Al-Ruzouq, R., "Geostatistical seismic analysis and hazard assessment, uae", in The International archives of Photogrammetry, Remote Sensing and Spatial Information Sciences, Gioinformation for Disaster Management, Istanbul, Turkey. Vol. XLII-2/W4, (2018), 18-21.
9. Muhammed Irfan, "Seismic site response, analysis and characterization of major cities in uae", Thesis submitted to American University of Sharjah, (2009),
10. Aly, N., AlHamaydeh, M. and Galal, K., "Quantification of the impact of detailing on the performance and cost of rc shear wall buildings in regions with high uncertainty in seismicity hazards", ***Journal of Earthquake Engineering***, Vol. 24, No. 3, (2018), 421-446. doi: 10.1080/13632469.2018.1453406.
11. AlHamaydeh, M., Galal, K. and Sherif Yehia, "Impact of lateral force-resisting system and design/construction practicecs on seismic performance and cost of tall buildings in dubai, uae", ***Earthquake Engineering and Engineering Vibration***, Vol. 12, (2013), 385-397. doi: 10.1007/s11803-013-0180-2.
12. Halchuk, S. and John Adams, "Deaggregation of seismic hazard for selected canadian cities", in 13th World Conference on Earthquake Engineering, Vancouver, BC, Canada. (2004).
13. Oztürk, B.M., "Seismic drift response of building structures in seismically active and near-fault regions", Purdue University, Dept. of Civil Engineering, (2003),

14. Baki Ozturk, "Dynamic analysis and the resulting nonlinear response of building structures located in seismically active regions in turkey", in ICEE 2006: 4th International Conference on Earthquake Engineering, Taipei, (2006).
15. Ozturk, B., Sahin, H.E. and C Yildiz, "Seismic performance assessment of industrial structures in turkey using the fragility curves", in 15th World Conference on Earthquake Engineering, Lisbon, Portugal, (2012).
16. Abdalla, J.A. and Azm Al-Homound, "Earthquake hazard zonation of eastern arabia", in 13th World Conference on Earthquake Engineering., (2004).
17. Jamal A. Abdalla and Azm S. Al-Homoud, "Seismic hazard assessment of united arab emirates and its surroundings", ***Journal of Earthquake Engineering***, Vol. 8, No. 6, (2008), 817-837. doi: 10.1080/13632460409350510.
18. Kassem, M.M., Nazri, F.M. and Farsangi, E.N., "On the quantification of collapse margin of a retrofitted university building in beirut using a probabilistic approach", ***Engineering Science and Technology, an International Journal***, Vol. 23, No. 2, (2020), 373-381.
19. Kassem, M.M., Nazri, F.M., Wei, L.J., Tan, C.G., Shahidan, S. and Zuki, S.S.M., "Seismic fragility assessment for moment-resisting concrete frame with setback under repeated earthquakes", ***Asian Journal of Civil Engineering***, Vol. 20, No. 3, (2019), 465-477.
20. Mohamed Nazri, F., Kian Yern, C., Moffed Kassem, M. and Noroozinejad Farsangi, E., "Assessment of structure-specific fragility curves for soft storey buildings implementing ida and spo approaches", ***International Journal of Engineering, Transactions C: Aspects***, Vol. 31, No. 12, (2018), 2016-2021.
21. Kassem, M.M., Nazri, F.M. and Farsangi, E.N., "The efficiency of an improved seismic vulnerability index under strong ground motions", in Structures, Elsevier. Vol. 23, 366-382.
22. NIST, N., *Selecting and scaling earthquake ground motions for performing response-history analyses*. 2011.
23. Mwafy, A., Elnashai, A., Sigbjörnsson, R. and Salama, A., "Significance of severe distant and moderate close earthquakes on design and behavior of tall buildings", ***The Structural Design of Tall and Special Buildings***, Vol. 15, No. 4, (2006), 391-416. doi.
24. Kamaludin, P.N.C., Kassem, M.M., Farsangi, E.N., Tan, C.G. and Nazri, F.M., "Assessment of seismic scenario-structure based limit state criteria for a reinforced concrete high-rise building", in IOP Conference Series: Materials Science and Engineering, IOP Publishing. Vol. 920, No. 1, 012012.
25. Baker, J.W., "An introduction to probabilistic seismic hazard analysis", ***White Paper Version***, Vol. 2, No. 1, (2013), 79. doi.
26. Kassem, M.M., Nazri, F.M. and Farsangi, E.N., "The seismic vulnerability assessment methodologies: A state-of-the-art review", ***Ain Shams Engineering Journal***, Vol. 11, No. 4, (2020), 849-864, DOI.org/10.1016/j.asej.2020.04.001.
27. Ibrahim, Y.E., Shallan, O., El-Shihy, A. and Selim, M., "Assessment of seismic damage of multistory structures using fragility curves", ***International Journal of Engineering Research and Applications***, Vol. 6, No. 1, (2016), 63-72.
28. Rajeev, P. and Tesfamariam, S., "Seismic fragilities for reinforced concrete buildings with consideration of irregularities", ***Structural Safety***, Vol. 39, (2012), 1-13. doi.
29. Rajeev, P. and Tesfamariam, S., "Seismic fragilities of non-ductile reinforced concrete frames with consideration of soil structure interaction", ***Soil Dynamics and Earthquake Engineering***, Vol. 40, (2012), 78-86.
30. Aiswarya, S. and Mohan, N., "Vulnerability analysis by the development of fragility curves", ***IOSR Journal of Mechanical and Civil Engineering (IOSR-JMCE)***, Vol. 11, No. 2, (2014), 33-40.
31. Tesfamariam, S. and Saatcioglu, M., "Risk-based seismic evaluation of reinforced concrete buildings", ***Earthquake Spectra***, Vol. 24, No. 3, (2008), 795-821.
32. Tesfamariam, S. and Saatcioglu, M., "Seismic vulnerability assessment of reinforced concrete buildings using hierarchical fuzzy rule base modeling", ***Earthquake Spectra***, Vol. 26, No. 1, (2010), 235-256.
33. Youngs, R.R. and Coppersmith, K.J., "Implications of fault slip rates and earthquake recurrence models to probabilistic seismic hazard estimates", ***Bulletin of the Seismological society of America***, Vol. 75, No. 4, (1985), 939-964.
34. Vamvatsikos, D. and Cornell, C.A., "Incremental dynamic analysis", ***Earthquake Engineering & Structural Dynamics***, Vol. 31, No. 3, (2002), 491-514. doi.
35. Dumova-Jovanoska, E., "Fragility curves for reinforced concrete structures in skopje (macedonia) region", ***Soil Dynamics and Earthquake Engineering***, Vol. 19, No. 6, (2000), 455-466. doi.
36. LI, S., Yu, T. and Jia, J., "Empirical seismic vulnerability and damage of bottom frame seismic wall masonry structure: A case study in dujiangyan (china) region", ***International Journal of Engineering, Transactions C: Aspects***, Vol. 32, No. 9, (2019), 1260-1268. doi: 10.5829/ije.2019.32.09c.05.

Persian Abstract

چکیده

بهبود سریع توسعه ساختمانهای بلند در امارات متحده عربی (امارات متحده عربی) ، زمینه را برای افزایش علاقه به تحقیقات خطر لرزه ای کشور فراهم کرده است. ساختمان مورد مطالعه شامل ستونهای دیوار برشی و RC به عنوان سیستم مقاومت در برابر نیروی جانبی آن است. این یک ساختمان داستانی G + 17 است که به تازگی ساخته شده و حدود ۷۸ متر ارتفاع دارد. تجزیه و تحلیل لرزه ای دینامیکی غیر خطی که همان تجزیه و تحلیل مد تاریخ است ، همچنین به عنوان تجزیه و تحلیل سریع غیر خطی سریع در حدود ۴۵ زلزله در ۳ مجموعه سطح خطر (۲ ، ۵ و ۱۰٪ احتمال افزایش [PE]) انجام می شود در ساختمان مطالعه برای تولید مقادیر رانش Interstory. بر اساس رویکرد مبتنی بر عملکرد ارائه شده توسط FEMA 356 ، منحنی های شکنندگی با ایجاد مدل طراحی لرزه ای احتمالی ایجاد می شوند. منحنی های شکنندگی حاصل از نظر ۳ احتمال ، به عنوان مثال ، (۱) اشغال فوری ، (۲) ایمنی زندگی و (۳) پیشگیری از سقوط. این بستگی به ایده ای دارد که نوع سازه های مقایسه ای احتمال مشابهی را برای یک حالت آسیب دیده برای نیروی لرزه ای معین داشته باشند.

International Journal of Engineering

Journal Homepage: www.ije.ir

Effect of Hydrodynamic Pressure on Saturated Sand Supporting Liquid Storage Tank During the Earthquake

A. A. Hussein*, M. A. Al-Neami, F. H. Rahil

Civil Engineering Department, University of Technology, Baghdad, Iraq

PAPER INFO

Paper history:
Received 10 February 2020
Received in revised form 10 April 2021
Accepted 12 April 2021

Keywords:
Hydrodynamic Pressure
Liquid Storage Tank
Earthquake
Acceleration Range

A B S T R A C T

This paper aims to illuminate the influence of hydrodynamic pressure generated in a water storage tank on the behavior of saturated sand that its support. Experimental tests were performed on two cylindrical water tank models using a fabricated shaking table which consists of a flexible laminar shear box. The first model is a water storage tank partially full of water, and the second one is a tank model with an equivalent load of water pressure to simulate the water storage tank without hydrodynamic pressure. Three earthquake histories (Kobe, El-Centro, and Ali Al Gharbi) were implemented on models to study a varied range of acceleration. It was found that the settlement and lateral displacement directions in the water storage tank were significantly increased compared to the equivalent load resulted in the second model in all cases of the acceleration histories. Also, it was monitored the pore water pressure during the testing period, and it was noticed that the excess pore pressures were affected by the hydrodynamic pressure and increased compared to the results recorded at the condition of no hydrodynamic pressure.

doi:*10.5829/ije.2021.34.05b.11*

1. INTRODUCTION

The soil-structure interaction and fluid-structure interaction are independently composite occurrences for structures. Indeed, the dynamic characteristics of transient excitations and response of liquid storage tanks are directed by several features: the interaction among the fluid and the structure, earthquake characteristics, and the structure-soil interaction along with their boundaries. Kianoush and Ghaemmaghami [1] considered the soil structure-interaction influence on a storage tank for six types of soil. In dynamic behavior, the liquid tank-soil system was found to be associated with earthquake frequency. Chaduvulaa et al. [2] carried out shake table tests on the cylindrical storage steel elevated water tank with a scale model of 1:4. They found that the moment and base shear for impulsive value were increased with the increasing acceleration of the earthquake and decreased by increasing the angle of motion. Chaithra et al. [3] modeled the soil, tank, and fluid using finite elements to consider the soil flexibility influence with three types of soil with various flexibility on a tank wall filled with fluid to consider the structure-soil interaction influence. It was determined that soil flexibility considerably influences the reaction of the storage tank. Kotrasová [4] made a theoretical experience for the analytical calculation of hydrodynamic pressures and circular frequencies developed in rectangular liquid tanks during an earthquake. Analytical investigations of natural frequencies are compared with experimental ones. Chougule et al. [5] considered the earthquake implement of the base held a storage tank sitting on the soil having the tank wall mass, the roof mass, the base slab mass, and the water mass. It was concluded that under the effect of seismic forces with raising relation of maximum water depth to the tank diameter, the further water mass would motivate in the mode of impulsive while reducing water depth to tank diameter; further, the water mass will motivate in the mode of convective. Sadek et al. [6] considered a shallow rectangular storage tank's performance during an earthquake was taking into account fluid soil-structure

*Corresponding Author Institutional Email: 42080@student.uotechnology.edu.iq (A. A. Hussein)

Please cite this article as: A. A. Hussein, M. A. Al-Neami, F. H. Rahil, Effect of Hydrodynamic Pressure on Saturated Sand Supporting Liquid Storage Tank During the Earthquake, International Journal of Engineering, Transactions B: Applications Vol. 34, No. 05, (2021) 1176-1183

interaction that was modeled using 3D finite elements. It was determined that the dynamic's attitude on the storage tank is related to the frequency field of the soil movement. Hussein et al. [7] studied a cylindrical storage tank on medium and dense sand with different relative densities. It was found that the characteristic of soil and hydrodynamic pressure have a significant influence on the tank settlement, lateral displacement in (X and Z)-direction, and lateral soil stresses that are initialized due to the movement of the storage tank. Besides, the tank displacements have a considerable impact on the frequency field and frequency value.

Waghmare et al. [8] considered a numerical investigation in a multi-real earthquake for reinforced concrete elevated tanks in viscous dampers. They found that viscous dampers' nonlinearity and low damping constant contributed a comparable reduction to those viscous dampers with linear and high damping constant. Pan and Jiang [9] investigated the change in the reflection and distribution of earthquake waves at the surface interaction of layers. It proposed an enhanced method of the same input load usual viscous-spring simulated boundary model. Considered by the three approaches are variable, which illustrate that the uniform model of footing and the conventional corresponding input load of the earthquake wave can not represent the earthquake force correctly. Dram et al. [10] investigated the possible ability to use recycled tyre pieces as a compressible insertion right back retaining walls during dynamic load; it estimated the influence of thickness in a cushion that compressible angle of friction in the backfill on the seismic enactment of retaining walls. The results presented that the seismic load contrary to the retaining wall could be significantly reduced among the presented technique.

Most of the studies related to the liquid storage tanks that consider the soil effect is focused on fluid-structure-soil interaction and the effect of tank fixity conditions to the ground, while it was not found that any study dealt with the effect of hydrodynamic pressure on the soil behavior and soil parameters. Besides, the knowledge is insufficient about the influence of hydrodynamic pressure on saturated sand soil and its effect on the different sand relative densities. Due to these reasons, this study is devoted to considering the effect of hydrodynamic pressure in a liquid storage tank using different experimental methods for saturated sand density.

In this paper, the response of saturated soil supporting cylindrical water storage ground tanks under the hydrodynamic pressure is considered. The work targets specifically: (i) to investigate the influence of acceleration characteristics on the saturated sand has different relative densities; (ii) to investigate the potential settlement and lateral displacement of water tank under the influence of hydrodynamic pressure; and (iii) to investigate the excess pore pressure variation during an earthquake.

This paper has the following structure. Section 1 gives the previous studies related to the storage tank and hydrodynamic pressure. Section 2 describes the methodology and experimental investigation, including the shake table and soil properties. Section 3 describes the test preparation for controlling sand density. Section 4 illustrates the test program and flowchart for the shake table test. Section 5 implements earthquake data used in the tests. Section 6 introduces and discusses experimental test results. Finally, the conclusion of the work is presented in section 7. Figure 1 presents a flowchart of the research methodology used in this study.

2. EXPERIMENTAL INVESTIGATION

2. 1. Soil Properties Diyala Black Sand is used in the experimental work, and several tests are performed with two relative densities (medium with Dr = 50% and dense with 75%). The conducted soil tests are carried out according to ASTM standards. According to USCS, the sand was poorly graded, and the properties resulting from the implemented tests with the used standard methods on the sand are summarized in Table 1.

2. 2. Shake Table The shake table used in this study was fabricated according to instructions given by Al-Omari et al. [11]. The shake table simulates the earthquake condition to investigate the model's performance with high quality, reliability, and cost-efficiency, as shown in Figure 2. In the current study, due to the huge dimensions of the full-scale model for liquid storage tank with height of 10m and diameter of 14m, and the available container of the shear box with

Figure 1. flowchart of research methodology

TABLE 1. physical properties and tests carried out on soils with standards

Soil Property	Medium Sand	Dense Sand	Standard
Relative density Dr(%)	50	75	
Max. γ_d (kN/m^3)	19.25		ASTM D4253
Min. γ_d (kN/m^3)	16.41		ASTM D4254
γ_d (kN/m^3)	17.72	18.64	
γ_{Total} (kN/m^3)	22.68	23.3	
Wc (%)	28	25	ASTM D2216
G.s	2.66		ASTM D854
Effective size D_{10}	0.145		
Effective size D_{30}	0.277		
Effective size D_{60}	1.675		ASTM D422
uniform Coefficient, Cu	11.5		
curvature Coefficient, Cc	0.315		
Soil classification USCS	Poorly graded sand		ASTM D2487
Soil color	Pale black		
Friction angle, deg.	30	34	ASTM D2434

dimensions of 600×600×800 mm, the maximum dimension used in the container is 150mm to verify the stress bulb zone's size. The tank model with a diameter of 140mm and a height of 100mm, which means the (1:100) scale factor has been used. The cylindrical storage tank model was filled with water up to 80 mm was placed at the center of the soil surface. However, a flexible laminar shear box has been used to reduce the reflection of seismic energy.

3. TEST PREPARATION

Several methods controlling sand density were attempted to prepared air-dried sand. Dry tamping was the preferred method since it ensured an extensive range of relative densities, on the antithesis of air pluvial or vibration methods which their results were limited to the (very loose-loose) range for the utilized sand. Two relative densities (50 and 75) % were performed to consider the influence of sand density on liquefaction potential. The calibration for both relative densities was performed utilizing maximum/minimum density mold with the volume of 0.0027 m^3; the sand layer was tamped utilizing a hammer with the weight of 86 N and released freely from a height of 75 mm. Table 2 summarizes the calibration of the density for each density required and the resultant energy of tamping for mold that was considered in Equation (1).

Figure 2. Fixable laminar shear box installed on the table

Energy/Volume=(hammer weight× drop height of hammer× blows number per layer× layer number)/ (Mold volume) (1)

In order to obtain tamping energy for the test model similar to that of the calibration mold, the sand layer was divided into layers of equal thickness of 100 mm for each layer then tamped to achieve the required relative density (50% and 75%). Similarly, the hammer with an area of 0.0179 m^2 was utilized that covers mostly 100% of the calibration mold area. Thus to tamp about 100% of the model sand area that was 0.36 m^2 which is 20.1 times, the hammer area of about 20 blows is needed to ensure that the tamping is covered most of the sand area. Two different layouts of 20 blow tamping passes were selected to ensure that the tamping effort was equally distributed through each layer. The energy of tamping for the test model was calculated again by utilizing Equation (1) and the values are reported in Table 3 that presents evidence for equivalents tamping energy for calibration mold and test model.

Finally, a relation between the tamping energy for controlling density against a relative density for both the test model and calibrated model were plotted in Figure 3.

The sand was air-dried and poured inside the storage barrel; after that, tamped in layers to obtain the required density. To study the influence of liquid storage tanks on soil density, three cases of soil layer configurations

TABLE 2. The studied cases of acceleration history

Relative density (%)	50	75
Count of blows per layer	1	3
Thickness of layer (mm)	50	50
Number of layers	3	3
Hammer weight (N)	86	86
Drop Height of hammer (mm)	75	75
Mold volume (m^3)	0.002686	0.002686
Energy (N.m)	19.35	58.05
Energy per volume (kN.m/m^3)	7.204	21.61

TABLE 3. The studied cases of acceleration history

Relative density (%)	**50**	**75**
blows number per layer	40	120
Thickness of layer (mm)	100	100
Number of layers	6	6
Hammer weight (N)	86	86
Drop Height of hammer (mm)	75	75
Mold volume (m^3)	0.216	0.216
Energy (N.m)	1548	4644
Energy per volume ($kN.m/m^3$)	7.16	21.5

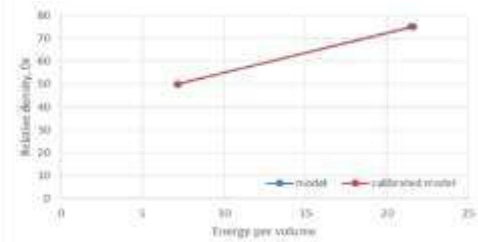

Figure 3. The relation between tamping energy against relative density for test model and calibrated model

are selected. These cases of the soil profile, as illustrated in Figure 4 are consist of the single medium layer of sand with a relative density of (50%) and 600 mm thickness, a dense layer with a relative density of (75%) and a third one consists of two layers of the sand, the top layer is medium sand (50% Dr.), and the lower layer is dense sand (75% Dr.) with a thickness of 300 mm for each layer.

The pore pressure transducers and accelerometers were embedded during the preparation of sand layers at three depths (140, 280, and 560) mm; the test model layout l is shown in Figure 5. After the soil profile was formed, the storage tank was placed at the center of the soil surface, and three displacement transducers were linked to the center of the storage tank across a screw nut.

4. TESTING PROGRAM FOR SHAKE TABLE TESTS

Six shake table tests were conducted on different soil densities. For more clarification, the testing program

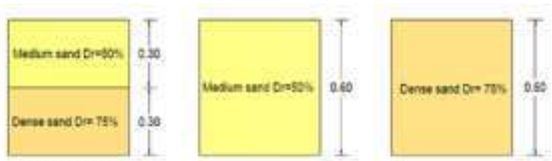

Figure 4. Cases of study of a soil profile

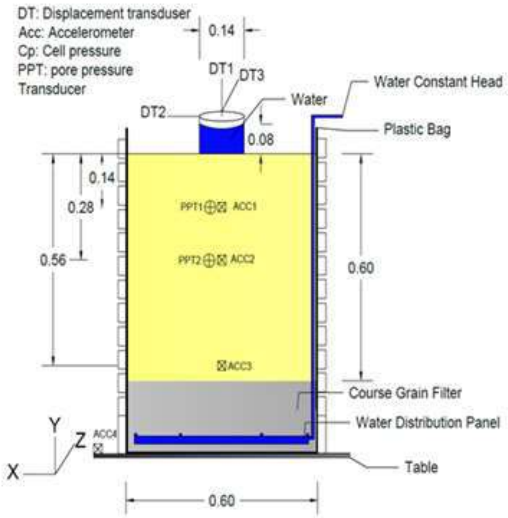

Figure 5. Test model layout

was illustrated in a flowchart in Figure 6. The test program was divided into two major parts; the first one used a water storage tank with a water height of (80mm) to represent the storage tank in case of hydrodynamic pressure. Furthermore, the other tank was filled with an equivalent load to represent the tank without hydrodynamic pressure.

5. IMPLEMENTATION OF EARTHQUAKE DATA

To study the effects of a wide range of acceleration characteristics on the saturated sandy soil, various real earthquake acceleration history data were implemented on models. The real acceleration histories for Ali Al-Gharbi, El-Centro, and Kobe were utilized. The calibration for the shake table was performed for these earthquakes by comparing the input acceleration by considering the full weight of the container and output acceleration during the earthquake, which presented very good compatibility. Table 4 summarizes information for earthquake data. Furthermore, due to the

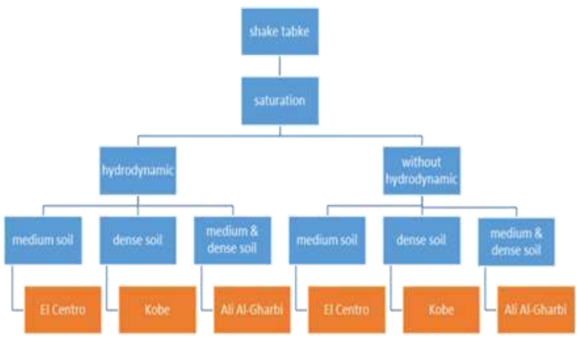

Figure 6. Flowchart for shake table test

TABLE 4. The studied cases of acceleration history

Acceleration History	Duration (s)	Acceleration Factor	Max. acceleration (g)
Ali Al-Gharbi	90	4.0	0.4
El-Centro	35	1.0	0.35
Kobe	30	1.0	0.82

small value of the maximum acceleration of the Ali Al-Gharbi earthquake (0.1g) and the significant scale factor (1:100), this acceleration has been amplified by multiplying it with four acceleration factors to impact the results in all studied cases.

6. RESULTS AND DISCUSSIONS

Test results have presented as relationships form between the various parameters studied against the time, including the acceleration, tank settlement, lateral displacement, and excess pore pressure distributed within three depths in the soil layer (140mm, 280mm, and 560mm) as illustrated in Figure 5. These parameters were obtained using the earthquake shake table accelerometer, displacement transducer, and pore water pressure transducer. Besides, the values of the settlement, the lateral displacement in (X and Z)-directions (where the X in the direction corresponding to the input acceleration direction and the Z is the direction perpendicular to the X) were presented in Figures 7 to 12.

6. 1. Influence of Earthquake History The results of these tests were presented in Figures 7 and 8. Generally, the earthquake acceleration inside the soil is less than the input acceleration at the table level. The acceleration at the bottom-depth of the soil column is

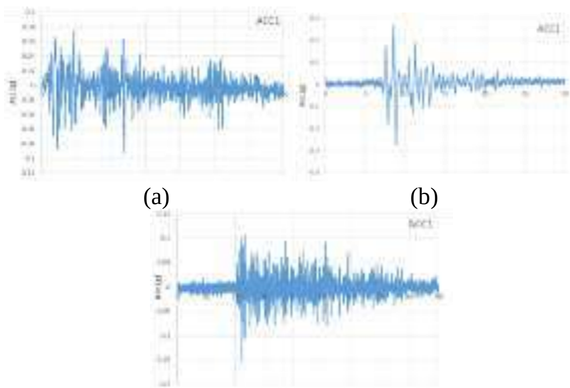

Figure 7. Results of Acceleration in depth (140mm) in case of Hydrodynamic pressure for (a) El-Centro, (b) Kobe, and (c) Ali Al-Gharbi earthquake

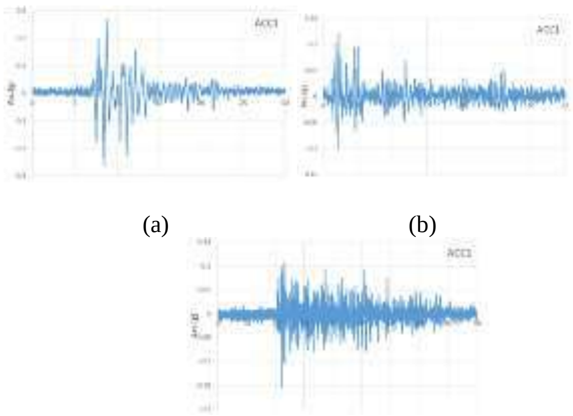

Figure 8. Results of Acceleration in depth (140mm) in case of without Hydrodynamic pressure for (a) El-Centro, (b) Kobe, and (c) Ali Al-Gharbi earthquake

slightly higher than at the mid-depth, while in the top portion of the soil column, the acceleration is comparatively less than that at the mid-depth due to saturated soil damping and acceleration spread out throughout the soil matrix. Figure 9 presents the variation of maximum acceleration with a depth in hydrodynamic pressure for all earthquakes. This finding seems to be consistent with Su et al. [13]. Earthquake frequencies significantly increased in the bottom depth and reduction in the top depth near the soil surface.

6. 2. Influence of Settlement and Lateral Displacement In all acceleration history cases, the settlement in the hydrodynamic pressure of the liquid storage tank was significantly increased compared to results of without-hydrodynamic pressure influenced by the hydrodynamic pressure onto the tank wall that is turned to the tank base applying additional forces. As a result, an additional settlement has occurred, as is presented in Figure 10. The storage tank settlement for the Ali Al-Gharbi earthquake was started at 22 seconds and increased as the pore water pressure

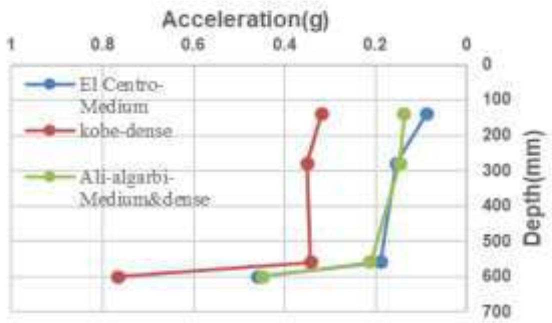

Figure 9. Variation of maximum acceleration with depth for El-Centro, Kobe, and Al Al-Gharbi in case of a liquid storage tank

generated, continued to increase, after 75 seconds, the storage tank settlement diminished at 0.063D and 0.059D (where D is the diameter of the storage tank) in case of with and without hydrodynamic pressure, respectively. In the El-Centro earthquake, it is observed that the storage tank settlement is about 0.025D and 0.024D in the case of with and without hydrodynamic pressure, respectively. The storage tank settlement in the Kobe earthquake is 0.091D and 0.08D in case of with and without hydrodynamic pressure, respectively; which they take place between 8 second and 30 seconds of earthquake duration as the generation of excess pore water pressure started that showed a noticeable effect of liquefaction.

Figure 11 displays the influence of hydrodynamic pressure on the soil settlement for cases of (El-Centro, Ali Al-Gharbi, and Kobe), it can be concluded that the increment in settlement for hydrodynamic pressure of saturated sand in the case of El-Centro is 3.2%, and 6.2% is the increment in Ali Al-Gharbi. In comparison, an increase in Kobe was 13.2% from the case without hydrodynamic pressure. Also, it was noticed that the effect of hydrodynamic pressure in the Kobe earthquake was higher than El-Centro and Ali Al-Gharbi acceleration earthquakes.

In addition, the final displacement in x- and y-directions was calculated in both cases as illustrated in Table 5. It was found that the lateral displacement of hydrodynamic pressure in Kobe was increased by 121%, 11.5% for Ali Al-Gharbi, and 101% for the El-Centro earthquake in the case of without hydrodynamic pressure. The lateral displacement in z-direction for three earthquakes of with and without hydrodynamic pressure exhibited an increment with 297%, 214%, and 143% in El-Centro, Kobe, and Ali Al-Gharbi earthquakes acceleration, respectively. Also, it was

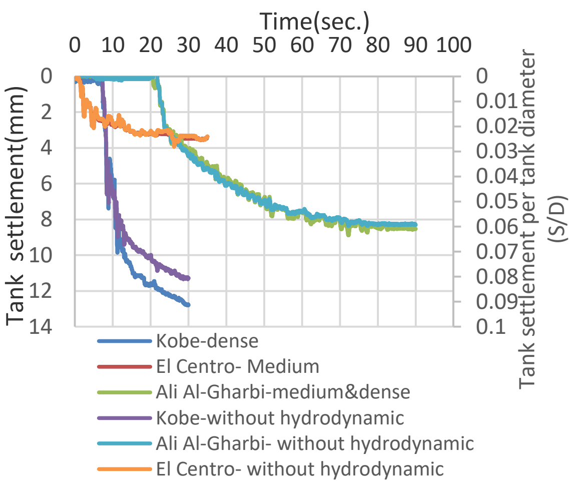

Figure 10. Results of settlement for all cases with hydrodynamic pressure and without Hydrodynamic pressure

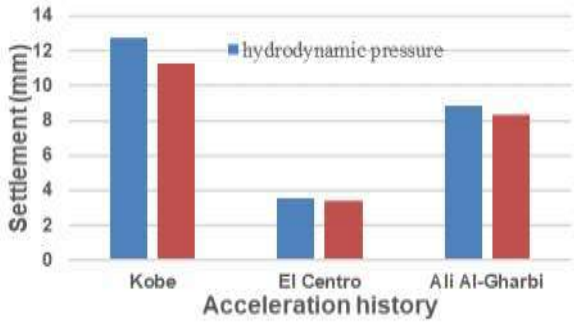

Figure 11. Variation of maximum settlement in hydrodynamic pressure and without hydrodynamic pressure for three earthquake histories

TABLE 5. Final lateral displacement in the x-direction for hydrodynamic pressure and without hydrodynamic pressure in three earthquake histories

Acceleration History	El-Centro	Kobe	Ali Al-Gharbi
x-displacement (hydrodynamic pressure)	1.05	4.2	2.9
x-displacement (without hydrodynamic pressure)	0.52	1.9	2.6
z-displacement (hydrodynamic pressure)	3.3	2.2	2.17
z-displacement (without hydrodynamic pressure)	0.83	0.7	0.89

found that the soil density affects the hydrodynamic pressure value, which later influences the displacement results. In all soil densities, the settlement and lateral displacement in the z-direction increase with an increase of the acceleration amplitude and shaking duration.

6. 3. Influence of Excess Pore Pressure

When the earthquake hits saturated sand, the pore pressure was suddenly raised to a high value within a short time that disables drainage immediately, no matter how high the permeability of sand is. Sand particles cannot withstand this increase in pore pressure; hence, their contacts are lost, and the shear strength is significantly reduced; this is known as a liquefying stage. Following that, as it is known, the fluid flows across high pressures into low-pressure areas; therefore, accumulated pore water pressure flows upward towards the low-pressure region at the surface to neutralize the fluid pressure; this stage is known as a dissipation stage. During this stage, the soil particles are relatively moved downward due to the action of shaking to fill the voids of the dissipated water and recover strength as the contact between particles was re-established; thus, densification of sand occurred at the end of the shaking duration. In particular, the influences of the relative density of the soil have been considered. It controls the soil's tendency to contract or dilate upon shear, and therefore the nature of excess pore pressure may develop in the soil. In the Ali Al- Gharbi earthquake, the initial liquefaction does not occur in both depths; the pore water pressure starts to generate rapidly at 22 seconds of acceleration duration, at both soil layers (top and bottom) in the case of hydrodynamic pressure (Excess Pore pressure Ratio) EPR reaches to (0.55, and 0.49), respectively.

In the same way, EPR reaches (0.55,0.37) at the top and bottom soil layer in the case without hydrodynamic pressure. In the El-Centro earthquake, pore water pressure generation shows no significant liquefaction effects on the tested soil and start to initiate after approximately 3 seconds, EPR in case of hydrodynamic pressure reaches (0.49, 0.39) at the upper and lower of the soil layer, respectively; while EPR reaches (0.61, 0.48) in case of without hydrodynamic pressure at top and bottom of soil layer, respectively. In the Kobe earthquake, the pore pressure increases sharply after 7 seconds, and EPR reaches the initial liquefaction at the top of the soil layer in both cases of hydrodynamic and without hydrodynamic pressure, while EPR reaches (0.95, 0.91) at the bottom depth of soil in both cases hydrodynamic and without hydrodynamic pressure, respectively. The idea of Keefer [13] and Rodriguez et al. [14], which is the shaking threshold that is needed to produce liquefaction are earthquake acceleration magnitude larger than M=5, supports these findings. Figure 12 illustrates the difference between the maximum (EPR) in the case of hydrodynamic pressure and without hydrodynamic pressure in the top and bottom states for three earthquake acceleration histories. In the case of the Kobe earthquake, liquefaction occurred at the top in both cases, and the EPR2 in hydrodynamic pressure was increased by 4% without hydrodynamic pressure. EPR1 in the Ali Al Gharbi earthquake was presented similar results and an increment in hydrodynamic pressure with 32% in EPR2 compared to the case without hydrodynamic pressure. On the contrary, the El-Centro earthquake (EPR1) and (EPR2) were decreased by (24%) and (23%), respectively in the case of hydrodynamic pressure.

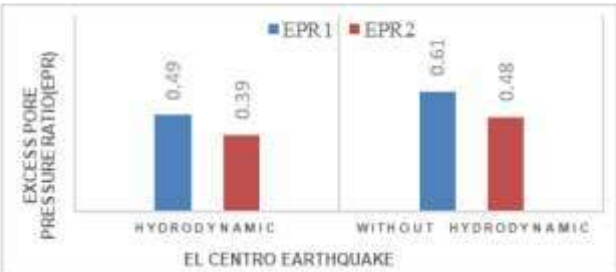

(a)

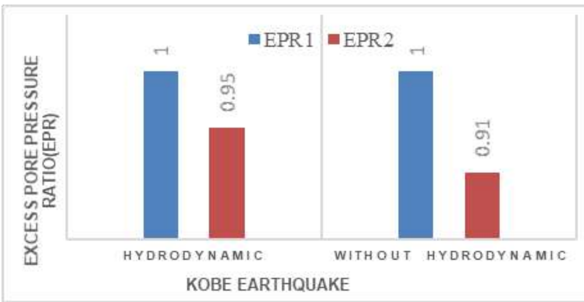

(b)

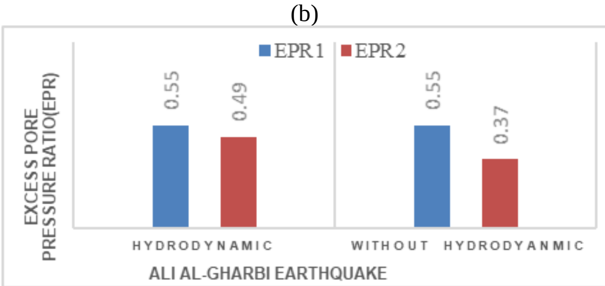

(c)

Figure 12. Variation of maximum excess pore pressure ratio (EPR) in hydrodynamic pressure and without hydrodynamic pressure for (a) El-Centro, (b) Kobe, and (c) Ali Al-Gharbi earthquake

7. CONCLUSIONS

In this paper, experimental shake table tests consider the influence of hydrodynamic pressure performed on saturated sandy soil loaded by cylindrical storage tanks during three earthquake histories. From the analysis of the results, the hydrodynamic pressure was concluded to significantly influence the saturated soil settlement and increased with (3.2%, 6.2%, and 13.2%) for El-Centro, Ali Al Gharbi, and Kobe respectively of without hydrodynamic pressure state. A lateral displacement was also influenced by the hydrodynamic pressure; in the x-direction, the increment in the hydrodynamic pressure state's displacement was (121%, 101%, and 11.5%) in Kobe, El-Centro, and Ali Al-Gharbi, respectively of without hydrodynamic pressure state. Likewise, in the hydrodynamic pressure state, the z-direction displacement was increased, 214%, 297%, and 143% in Kobe, El-Centro, and Ali Al Gharbi, respectively of without a hydrodynamic pressure state. Excess pore pressure was monitored and exhibited an increment in the Kobe earthquake, the liquefaction occurred at the EPR1 in both cases, and the EPR2 in hydrodynamic pressure was increased 4% in the case of without hydrodynamic pressure. EPR1 in the Ali Al-Gharbi earthquake is the same in results, and the increment in hydrodynamic pressure is 32% in EPR2 compared to the case without hydrodynamic pressure. On the contrary, the hydrodynamic pressure state of El-

Centro earthquake (EPR1) and (EPR2) were decreased by (24%) and (23%), respectively.

8. REFERENCES

1. Kianoush, M. and Ghaemmaghami, A. "The effect of earthquake frequency content on the seismic behavior of concrete rectangular liquid tanks using the finite element method incorporating soil–structure interaction". ***Engineering Structures***, Vol. 33, No. 7, (2011), 2186-2200, https://doi.org/10.1016/j.engstruct.2011.03.009
2. Chaduvula, U., Patel, D., and Gopalakrishnan, N. "Fluid-structure-soil interaction effects on seismic behaviour of elevated water tanks". ***Procedia Engineering***. Vol. 51, (2013), 84-91. https://doi.org/10.1016/j.proeng.2013.01.014.
3. Chaithra, M., Krishnamoorthy, A., and PM, N. N. "Analysis of soil-structure Interaction on response of tanks Filled with fluid". ***International Journal of Civil Engineering and Technology***, Vol. 8, No. 7, (2017), 813-819. http://www.iaeme.com/IJCIET/issues.asp?JType=IJCIET&VType=8&IType=7
4. Kotrasová, K. "Sloshing of liquid in rectangular tank". ***Advanced Materials Research***, Vol. 969, (2014), 320-323. https://doi.org/10.4028/www.scientific.net/AMR.969.320
5. Chougule, A. and Patil, P. "Study of seismic analysis of water tank at ground level". ***International Research Journal of Engineering and Technology,*** Vol. 4, No. 7, (2017), 2895-2900.
6. Sadek, E. S. A., Gomaa, M. S., and El Ghazaly, H. A. "Seismic behavior of ground rested rectangular RC tank considering fluid-structure-soil interaction", (2019), DOI: 10.9790/1684-1601010115.
7. Hussein, A. A., Al-Neami, M. A., and Rahil, F. H. "Hydrodynamic Pressure Effect of the Tank Wall on Soil–Structure Interaction". ***Modern Applications of Geotechnical Engineering and Construction***, (2021), 173-184. https://doi.org/10.1007/978-98115-4-9399.
8. Waghmare, M. V., Madhekar, S. N., and Matsagar, V. A. "Influence of Nonlinear Fluid Viscous Dampers on Seismic Response of RC Elevated Storage Tanks". ***Civil Engineering Journal***, Vol. 6, (2020), 98-118. DOI: 10.28991/cej-2020-SP(EMCE)-09.
9. Pan, H. and Jiang, X. "On the Characteristics of Ground Motion and the Improvement of the Input Mode of Complex Layered Sites". ***Civil Engineering Journal***. Vol. 6, No. 5, (2020), 848-859. DOI: 10.28991/cej-2020-03091512.
10. Dram, A., Benmebarek, S., and Balunaini, U" .Performance of Retaining Walls with Compressible Inclusions under Seismic Loading". ***Civil Engineering Journal***, Vol. 6, No. 12, (2020), 2474-2488. DOI: 10.28991/cej-2020-03091631.
11. Al-Omari, R. R., Al-Kifae, A. A., & Al-Tameemi, S. M. "Earthquake effect on single pile behavior with various factor of safety and depth to diameter ratio in liqufiable sand" ***International Journal of Civil Engineering and Technology***, Vol. 9, No. 4, (2018), 1253-1262. http://www.iaeme.com/IJCIET/issues.asp?JType=IJCIET&VType=9&IType=4
12. Su, D., Ming, H., and Li, X. "Effect of shaking strength on the seismic response of liquefiable level ground". ***Engineering Geology***, Vol. 166, (2013), 262-271. https://doi.org/10.1016/j.enggeo.2013.09.013.
13. Keefer, D. K. "Landslides caused by earthquakes". ***Geological Society of America Bulletin***, Vol. 95, No. 4, (1984), 406-421. https://doi.org/10.1130/0016-7606(1984)95<406:LCBE>2.0.CO;2.
14. Rodrıguez, C., Bommer, J., and Chandler, R. "Earthquake-induced landslides: 1980-1997". ***Soil Dynamics and Earthquake Engineering***. Vol. 18, No. 5, (1999), 325-346. https://doi.org/10.1016/S0267-7261(99)00012-3.

Persian Abstract

چکیده

این مقاله با هدف روشن کردن تأثیر فشار هیدرودینامیکی تولید شده در یک مخزن ذخیره آب بر رفتار شن اشباع شده از آن پشتیبانی می کند. آزمایشات بر روی دو مدل مخزن استوانه ای مخزن آب با استفاده از یک میز تکان دهنده ساخته شده که از یک جعبه برشی لایه ای انعطاف پذیر تشکیل شده است ، انجام شد. مدل اول یک مخزن ذخیره آب است که تا حدی پر از آب است و مدل دوم یک مخزن با بار معادل فشار آب برای شبیه سازی مخزن ذخیره آب بدون فشار هیدرودینامیکی است. سه تاریخ زلزله (کوبه ، ال-سانترو و علی الغربی) بر روی مدل ها برای بررسی دامنه متنوع شتاب اجرا شد. مشخص شد که جهت حل و فصل و جابجایی جانبی در مخزن ذخیره آب به طور قابل توجهی افزایش یافته است در مقایسه با بار معادل منجر به مدل دوم در تمام موارد از تاریخ شتاب است. همچنین ، فشار آب منافذ در طول دوره آزمایش کنترل شد ، و متوجه شدیم که فشار منفذی بیش از حد تحت تأثیر فشار هیدرودینامیکی قرار گرفته است که در مقایسه با نتایج ثبت شده در شرایط عدم فشار هیدرودینامیکی افزایش می یابد.

IJE TRANSACTIONS B: Applications Vol. 34, No. 05, (May 2021) 1184-1194

International Journal of Engineering

Journal Homepage: www.ije.ir

Location Allocation of Earthquake Relief Centers in Yazd City Based on Whale Optimization Algorithm

A. Zarepor Ashkezari[a], H. Mosalman Yazdi*[b]

[a] *Department of Civil Engineering, Yazd Branch, Islamic Azad University, Yazd, Iran*
[b] *Department of Civil Engineering, Maybod Branch, Islamic Azad University, Maybod, Iran*

P A P E R I N F O

Paper history:
Received 14 December 2020
Received in revised form 31 December 2020
Accepted 16 February 2021

Keywords:
Disaster Management
Earthquake
Heuristic Algorithms
Relief Center
Whale Optimization Algorithm

A B S T R A C T

Despite the fact that many governments try to set rules that guarantee having resistant buildings, there are many vulnerable structures in the world. Hence, establishing earthquake relief centers is an important issue in order to control the effect of an earthquake. Iran is a country in middle east which is severely vulnerable against earthquake. Yazd is a central city in Iran. Since there is no such a study for Yazd city, this city is considered in this study. The parcels' layer of the GIS map of Yazd city has been used as the input of the problem. Since the location allocation of relief centers is a problem with huge complexity and cannot be solved in polynomial time, Whale Optimization Algorithm (WOA) has been used to solve the problem. The Whale Optimization Algorithm or The WOA is a particle based heuristic algorithm which is suitable for solving hard problems. The main contributions of the research are modifying WOA function for the problem and designing a new method for creating whales. In order to reduce the time of reaching to the reasonable solution an innovative whale generating method has been designed. The results show that average distance of each parcel from its relief center is 1541 meters and the standard deviation of 114.

***doi**: 10.5829/ije.2021.34.05b.12*

1. INTRODUCTION

In order to mitigate the effects of natural disasters, governments and authorities must make plans and decisions in advance [1, 2]. Natural disasters, such as earthquake and flood, are inherently unpredictable and catastrophic. Lack of comprehensive plans along with low precautionary measures can have disastrous consequences for the region. Some of the serious consequences would be loss of properties, death tolls and injuries, contagious diseases and homeless people. Reducing these harsh events is the main mission in each relief and response process [3, 4]. The stronger logistic plans you have, the easier you can fulfill these goals [5]. In other words, the main part of a rescue mission is its logistic plans. At the time of any disaster, the level of our success is at the heart of decisions that we have already made [6, 7]. Moreover, when there is a detailed plan for logistics in advance, it would be easier to coordinate communication and commuting process with the delivery of commodities [8, 9]. As a result, we will have a better response time. With increasing the speed of delivery, we will be closer to our goals in rescue mission [10, 11]. Pre-locating of the relief centers is one of the most important initiatives in order to reduce the delivery time [12, 13]. This approach was used in WWII as a military strategy in order to increase the possibility of victory and also reduce the number of wounded soldiers [14]. The whole point of logistic strategy is proper location allocation of relief centers. Location of relief centers has a profound effect on rescuing process. There are many parcels on the map of a region which need to be rescued [15, 16]. If we have a closer relief center to each parcel we will deliver the food and medicine and other necessities in more reasonable time. Out of proportion distance between the parcels and the centers would decrease the quality of helping process. Helping injured people, delivering food and making a shelter for people in need would be

*Corresponding Author Email: *HAMosalmanYazdi@gmail.com* (H. Mosalman Yazdi)

Please cite this article as: A. Zarepor Ashkezari, H. Mosalman Yazdi, Location Allocation of Earthquake Relief Centers in Yazd City Based on Whale Optimization Algorithm, International Journal of Engineering, Transactions B: Applications Vol. 34, No. 05, (2021) 1184-1194

accelerated if they are in short distance from the relief centers. Therefore, the ultimate vision of the decision makers is the relief centers to be in all people's fingertip [17, 18]. The size of the region which is affected by a natural disaster has direct effect on the complexity of the problem. When it comes to a metropolis there are many bottlenecks and congested areas on the map which can complicate the rescue process. Therefore, big cities with huge populations are exposed to more hazards and in order to decrease the risk we should have a more accurate plan and strategy [19, 20].

The logistic strategy in Yazd city in center of Iran has been addressed in this paper. This big city, like many parts of Iran, is vulnerable to earthquakes and should have an accurate plan to mitigate the effects of a possible disaster. Finding the best location for each relief center is the main goal of this research. Through decreasing the distance between centers and parcels and also balancing the load of work on each center, this research is aiming to present a solution for delivering the best service in shortest time for each person in need in Yazd city.

There is a classic problem named location allocation problem or LA which is referred to any kind of problem involved in finding suitable locations for bunch of entities. It is proved that LA is a NP-hard problem which does not have any polynomial solution. In a situation that we have a large number of objects, it is almost impossible to find the optimum solution in a reasonable time. In other words, it is true to say that solving this problem in general is not plausible [21, 22]. The most effective way to tackle this problem is using optimization methods. In this method we try to come up with an algorithm that can find a sensible solution which in close enough to the best solution to be accepted by the users. Despite the fact that these methods cannot find the optimal solution, they are useful because of their reasonable execution time. In fact, we sacrifice the best answer in order to reach a useful solution in a relatively short time [23]. One of the most famous optimization methods are particle based algorithms. These algorithms try to solve the problem by simulation of particle movements which has drawn the inspiration from natural phenomena [24, 25]. Recently a new particle based algorithm has been designed which optimize the problems by inspiration from whale's hunting process. This innovative algorithm which is called WOA (or Whale Optimization Algorithm) has added new characteristics to previous algorithms which seems to be promising to solve different types of NP-hard problems [26, 27].

There is no a comprehensive research about Location Allocation problem for Yazd city in center of Iran. Therefore, in this research a new heuristic algorithm based method has been proposed in order to tackle the problem. The WOA has been adjusted to solve the LA problem in Yazd city of Iran. The proposed method has been executed on GIS information of Yazd map in order to locate relief centers in the best places. The main aim of the paper is finding the best locations for earthquake relief centers by redesigning WOA.

To analyze the algorithm, all parcels are pulled out from a GIS map of Yazd city. In proposed algorithm, all of the locations in Yazd city could convert to a relief center. When we have some pre-defined candidate locations, the solution space will become smaller and solving the problem would be easier. The WOA has been redesigned and tuned to solve the Location Allocation problem in Yazd city. The proposed method has some parameters which are calibrated by means of a simple map. After that, the problem in Yazd city has been solved by means of proposed algorithm.

The rest of the paper is structured as follows. The second section reviews previous studies in this problem. In the third section, the proposed method has been presented completely and all of its phases have been clarified. In the fourth section, the proposed algorithm has been simulated and assessed thoroughly. In the fifth section, there is a summary, conclusion and some suggestions for future works.

2. PREVIOUS STUDIES

The Location Allocation problem or LA is a general problem which is involved in many aspects of human life. To some extent, improving the quality of life lays on solving different problems which can be boiled down to a LA problem. Therefore, in this section some solutions for various LA problems have been reviewed.

2. 1. Mathematical Model Approaches One of the most famous and effective approaches to solve the location allocation problem is designing a mathematical model for the environment which the LA problem is supposed to be solved for it. All the parameters and their constraints can be embedded in the model. In order to reach the solution this model can be solved and optimized by different methods. Some of the recent papers which used this approach will be reviewed following.

Rahmani [28] proposed a new method for blood supply chain management. Their method is an accurate algorithm which tries to reduce the delivery time and avoid shortages in blood. The approach is locating blood supply centers in appropriate point that causes delivery process to be conducted in time. Therefore, the objective function is minimizing the distance between blood centers and people in need. The algorithm behind the model is Lagrangian Relaxation. The results show that the cost of the system is in direct proportion with the level of demand. Salehi et al. [29] designed another method for blood delivery. In this paper authors considered the situation of after earthquake. They presented a sophisticated model which takes to account some important issues about the blood, such as compatibility of the blood group. Two important variables can be optimized in this model. First the location of each relief center and second the amount of blood which should be saved in each center. The simulation results for Tehran city prove the effectiveness of the proposed model. Fazli-Khalaf et al. [30] have presented a new model for relief management. This model has three different objective functions. Many involved parts in after earthquake rescue mission have been attached to the model. This research was aiming to find the best locations for permanent and temporary relief centers in order to reduce the delivery delay. The simulation results on Tehran city showed the positive effects of the proposed model.

Boonmee et al. [31] solved the LA problem for relief facilities before and after a disaster. In order to evaluate the method, different conditions have been tested (deterministic, stochastic, dynamic, robust). Before the disaster, location allocation of shelters and warehouses was carried out and after that, location allocation of healthcare and distribution centers was focused. The proposed method has been tested in all conditions through a case study. Mahootchi and Golmohammadi [32] designed a stochastic mathematical model which has two levels. This model is executed in two phases before and after disaster. The location allocation of relief centers and assigning each parcel to a single center are conducted in the first and second phases, respectively. The level of storage in each center and the total amount of goods are also specified. The simulation results showed that the cost of relief mission and the number of needed centers are in the direct proportion to intensity of the earthquake. The proposed method was tested on Tehran city in Iran. Sebatli et al. [33] proposed a new method which can allocate necessary goods to areas in need. Their algorithm is based on a mathematical model which has two phases. Their aim was reducing the distance and the cost of delivering necessary supplies. The Yildirim region of Turkey was used in order to evaluate and validate the model. Chu et al. [34] proposed an integer nonlinear programming in order to optimize the process of assigning medical and healthcare teams to each group in the rescue mission. Their innovation was taking to account the stochastic transition probability of triage levels. In order to find a solution, the stochastic Markov chain was used. Their main goal was increasing the number of wounded which have received emergency medical care. The results show that assigning the medical teams to the closest and worst affected areas causes more lives to be saved.

2. 2. Heuristic Approaches

The papers which are reviewed so far were all based on mathematical models. There is another approach to address the location allocation problem. Since the LA problem is NP-hard one, the optimization algorithms which are based on heuristic methods are very useful to find a reasonable solution in a sensible time. The particle based algorithms and the genetic based algorithms are the famous heuristic methods which have been widely used to tackle the LA problem. Here some of the recent papers with this approach will be reviewed.

Golabi et al. [35] tried to find the optimal location of distribution centers in the large-scale disasters. They assumed that it was possible there would be a problem to reach to the intended points. For optimization phase they adjusted three different heuristic algorithms to be applied to the model. The GA or genetic algorithm was the first one. Another algorithm they used was Simulated annealing, and the third one was Memetic algorithm. They tested their method through a case study in Tehran. In another paper, authors designed a stochastic mathematical model in order to minimize the effects of natural disasters. Their new algorithm, which was designed for pre-disaster time, was capable of finding the best location for each center and finding the optimal capacity for each center. They also designed an objective function in order to minimize the rate of causality. They adjusted a particle based algorithm to optimize the solution [36]. In another research authors put forward a new method which tried to compare the effectiveness of the Genetic Algorithm (GA) and Bees Algorithm (BA) in location allocation of relief centers and assigning the parcels to them. The GIS data was used as the input of the algorithm. Then, each algorithm applied to the data separately for finding nine center location between the candidates and assigning the parcels to them. Before the main testing phase the algorithm was calibrated with a simple synthetic data. The simulation results indicated that the convergence of the BA was gradual to some extent, while the behavior GA was step by step. In terms of stability both algorithms were acceptable [37]. Saeidian et al. proposed a method in which the location allocation of relief centers is specified. They used Geospatial Information System (GIS), the Technique for Order of Preference by Similarity to Ideal Solution (TOPSIS) decision model, a simple clustering method and the two meta-heuristic algorithms of Particle Swarm Optimization (PSO) and Ant Colony Optimization (ACO). The authors compared PSO and ACO in different conditions. The simulation results indicate the efficiency of TOPSIS, the clustering method, and the particle based algorithms [38]. In another paper, the capacitated location-allocation problem with stochastic demand was addressed. They designed a mathematical model to find the best locations of the relief centers. A local search method was combined with genetic algorithm to tackle the problem [39]. In another research, various parameters including demand and flow of relief commodities, capacity of centers, transportation of injured people, capacity of vehicles for commodities and injured people, and back up centers were taken into account in different parts of planning. A real data from Tehran city in Iran was used to test the method. The modified multiple-objective particle swarm optimization (MMOPSO) and Non-Dominated Sorting Genetic Algorithm-II (NSGA-II) were the heuristic algorithms which were adjusted for the problem. The simulation results show that the MMOPSO has the best effectiveness [40].

Ghasemi et al. proposed a robust simulation-optimization method for planning before the disaster. Moreover, the amount of needed goods was one of the important parameters in this method. One of the stochastic parameters of the model was the demand pattern in the problem. Robust optimization approach was used to handle uncertainty. The proposed model could specify the location of each relief center and its parcels. The genetic algorithm has been modified and used in order to optimize the solution [41].

A multi-level facility location problem (FLP) is formulated to find the best number of relief centers and their locations in literature [42]. The authors assumed that the demand pattern was based on Poisson distribution. All demands are satisfied by the closest relief center. A hybrid genetic algorithm is developed to optimize the proposed model. The effectiveness of the proposed method is tested by means of a case study. The simulation results show that there was an increase in effectiveness of relief centers and also a significant decrease in response time [42]. Table 1. summorizes some of the most important reviewed papers.

3. PROPOSED METHOD

In this article a new method has been proposed based on Whale Optimization Algorithm (WOA) in order to optimize earthquake relief centers' location in Yazd city. Since the WOA is suitable for continuous problems, it has been adjusted for solving location allocation problem. All functions have been designed from scratch. Moreover, an innovative method has been proposed to speed up the convergence of the evolutionary algorithm. In this method first generation of whales is produced in a way that is more likely to be near the optimal solution. If the first generation whales are close to the best solution, the convergence of the algorithm will be faster. Figure 1 demonstrates the steps of the proposed method.

According to Figure 1 the input of the algorithm is the polygon data, extracted from GIS of Yazd city. At the beginning of the algorithm, first random solutions are produced. As it mentioned above, first whales creating is taken place by an innovative function. After this phase, there are some functions to move the whales. After each movement, the algorithm must update the fitness values. This steps will continue until we reach to exit criteria. Reporting optimal solution is the last phase of the proposed algorithm. In following, each step of the algorithm has been explained in detail.

3. 1. Whales' Structure

Each whale represents a random solution for the problem. In other word in each solution, location of relief centers in Yazd city can be found. Random whales are not optimal but they are supposed to be improved by moving functions. Every single whale is shown by an array. The length of the array is equal to number of relief centers. Each index of array represents a particular relief center and the value inside this index demonstrates the location of this relief center. Each location is determined by a couple of values (x and y). Table 2 shows an example of a whale that includes six relief centers.

TABLE 1. Previos works

Ref.	Problem	Method	Pros & cons
[28]	Blood supply	Math model	-Reasonable solution -Low scalabiity
[29]	Blood supply	Math model	-Low running time -Low scalability
[30]	Relief Management	Math model	-Multi objective -Complicated model
[31]	Location Allocation	Math model	-Optimal solution -Low scalability
[32]	Location Allocation	Heuristic	-Scalable -Computational overhead
[37]	Location Allocation	Heuristic	-Using GIS data -Computational overhead
[38]	Location Allocation	Heuristic	-Clustering -Using GIS data
[40]	Relief management	Heuristic	-Multi objective -Using GIS data

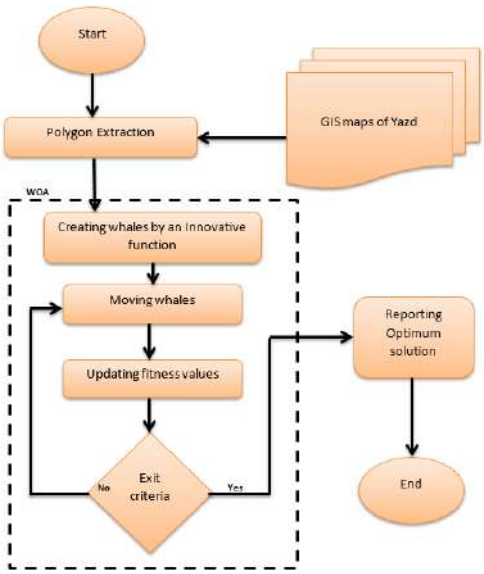

Figure 1. Steps in proposed algorithm

TABLE 2. A whale with 6 centers (meter)

Whale	$Center_1$	$Center_2$	$Center_3$	$Center_4$	$Center_5$	$Center_6$
(x , y)	(21,45)	(83,79)	(18,31)	(50,65)	(13,90)	(37,40)

3. 2. Creating Whales In order to achieve better solution and as an aim to speed up the algorithm, initial whales are produced by an innovative function. This function has been designed in a way that tries to spread the first location of centers uniformly. Relief centers should be able to serve all parts of the region and this service should be fair. So if we spread the centers among the region it is more likely to have uniform services, however population distribution and more congested points of the map should be considered. For achieving this goal, a partitioning function has been proposed in Algorithm 1.

Algorithm1 : partition

Input : points of the map as (x,y)
output : lines

$lineNum = \lfloor \sqrt{n} \rfloor$
$pointNum = length(points)/lineNum;$
$Vline = 1;$
$for\ i = 1\ to\ max(x)$
    $if\ (number\ of\ points\ with\ x \geq Vline * pointNum)\ or\ (i = \max(x))$
        $add\ a\ vertical\ line\ in\ this\ i\ position\ to\ lines;$
        $Vline = Vline + 1;$
$Hline = 1;$
$for\ j = 1\ to\ max(y)$
    $if\ (number\ of\ points\ with\ y \geq Hline * pointNum)\ or\ (i = \max(y))$
        $add\ a\ horizontal\ line\ in\ this\ j\ position\ to\ lines;$
        $Hline = Hline + 1;$
return lines

In Algorithm 1 *points* is an array that contains all points of the map. *LineNum* is a variable that determines the number of vertical and horizontal lines to partition the map. The number of vertical and horizontal lines are qual. *pointNum* is the number of points between each two lines. *Length(points)* is the number of points in the map. The output of the algorithm is an array, which is called *lines*, that contains all vertical and horizontal lines. The map could easily be partitioned by means of these lines. The partitioned map contains many rectangles that each one shows a particular partition of the map. Figure 2 shows output of this algorithm for two different maps. Comparing these two solutions shows that the proposed function not only considers the area of the map but brings the distribution of the points to play. In other word this algorithm tries to partition the map in a way that each part contains roughly equal number of points.
After partitioning it is time to create whales. In this step, for each whale we should select candidate points from different rectangles. Selecting candidate points from different rectangles helps us to distribute the centers among the map and make the random whales close to best solution. when number of rectangles are less than number of centers it is not a big problem to select multiple points from a single rectangle. Anyway, the number of selected points should be equal to number of centers.

3. 3. Fitness Function A new fitness function has been designed in order to achieve the best locations of relief centers in Yazd city. Two important issues have taken into account in calculating fitness value. Since the fitness function represents the objectives of the designers, this article has concentrated on two different aspects of the problem that are important for decision makers. The first aspect is they want to reduce the distance between centers and point as much as possible. And the second aspect is they want centers not to be over loaded. For the first goal, average distance between centers and points has been considered. The fitness function tries to reduce this value. For the second goal a penalty function has been designed. In the penalty function, finding a center that is responsible for more than average induces a negative effect on fitness value. Equation (1) shows the penalty function. The total penalty for a whale is equal the sum of the center penalties in the whale.

$$penalty(center_i) = \begin{cases} 1 & parcels_i > \dfrac{n}{k} \\ 0 & O.W. \end{cases} \tag{1}$$

Equation (2) shows the fitness function. The penalty value is in the denominator in order to have negative effect on the fitness value. The fitness function creates a value that represents the closeness of centers to the points and balancing of the centers' load simultaneously.

$$fitness(whale) = \frac{\sum_{i=1}^{n} distance(parcel_i, center_i)}{\sum_{j=1}^{k} penalty(center_j)} \tag{2}$$

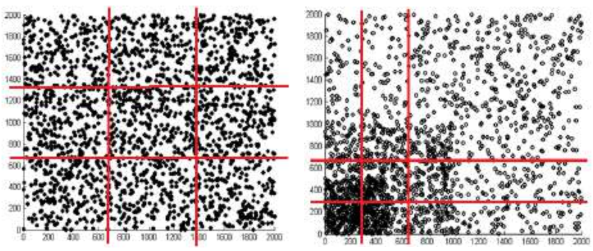

a. Even map b. Uneven map

Figure 2. Partitioning example (meter)

3. 4. Move Functions The WOA has two functions to move the whales. These functions are Shrinking and Spiral respectively. Classic move functions of WOA are not useful in this problem, hence they should be redefined to meet constraints of the problem. Both of move functions use a particular concept which is called Distance. Distance value shows the difference between two given whale. In this article Distance of two whales is in the form of an array that contains the distance between nearest centers in two whales. Therefore, the length of Distance array is equal to Whale array. In following the detail of each move function has been presented.

3. 4. 1. Spiral The Spiral function tries to go toward the best answer (prey) through a spiral path. In other word in this function each whale tries to go near the best whale conservatively. So the whale spirals around the prey and approaching it. Figure 3 illustrates the rotation angle and moving toward the best answer. W wants to spiral around the Best. The rotation angle is $2\pi l$ where l is a random value in $[-1\ +1]$. The imaginary line between W and Best must be calculated by Distance function.

Algorithm 2 shows the details of Spiral. The direction of rotation is clockwise. The inputs of the function are W and Best. W is the whale that is supposed to be spiraled and Best is the prey location (best answer).

```
Algorithm2: Spiral
Input: w1: a whale for spiral , best: the best whale
Output: w: spiraled whale
l = a random number in [-1,+1];
θ = 2πl; // rotation angle
for i = 1 to len(w)
    point = a random location on line(w1, best);
    destination = θ sized roundClock rotation centered by best;
    w(i) = destination;
end
```

3. 4. 2. Shrinking The second move function is Shrinking. In Shrinking a random whale moves directly toward the prey (best answer). In this function, there is not any rotation, so in comparison with Spiral, the whales go faster toward the prey. Algorithm 3 shows the pseudo code of the Shrinking. The inputs of the function are W and Best. W is a random whale and Best is the prey.

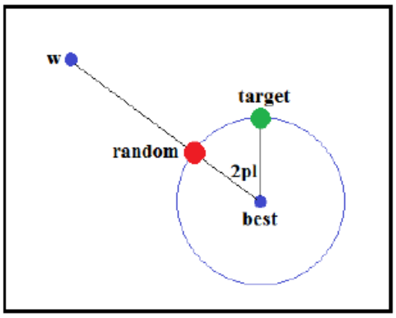

Figure 3. An example of Spiral

```
Algorithm3: Shrinking
Input: w1: a whale for spiral , best: the best whale
Output: w: shrinked whale
for i = 1 to len(w)
    destination = a random location on line(w1, best);
    w(i) = destination;
end
```

3. 4. 3. Search Apart from Shrinking and Spiral there is another useful function in proposed method which is called Search. The search function consist of three different functions. One of them is shrinking function that is used with different parameters. Instead of moving a whale toward the best, here, the shrinking function tries to move a whale toward another whale which is selected randomly. Join and random walk are two another function that are used in the search. These two functions in some extent act like crossover and mutation operators in Genetic Algorithm. All in all, the search function is used for exploring problem space. Algorithm 4 shows the pseudo code of this function.

```
Algorithm4: search
Input: w1: a whale for shrinking , w2: a randomly selected whale
Output: w: a new whale
distance = whaleDistance(w1, w2);
tmp = a random number in [0,1];
if tmp < 0.25
    w = shrinking(w1, w2);
elseif tmp < 0.25
    w = join(w1, w2);
else
    w = randomwalk(w1);
end
```

3. 5. Contributions Given the details of the proposed method which has been explained in this section, the following contributions can be considered as the novelties of this work:

- Using the WOA for the first time to solve the LA problem in Yazd city.
- Modifying the WOA functions in order to solve a discrete problem.
- Introducing an innovative Whale generating algorithm which can improve the method's efficiency.

4. EXPERIMENTAL RESULTS

After presenting the proposed method, it is time to implement and evaluate it. In order to analyze the effect of the algorithm on the Yazd maps, it has been implemented in Matlab software. The first step is calculating best parameters for the method and after that we can use the algorithm for solving the problem in Yazd city maps.

4. 1. Best Parameters of the Algorithm The proposed method has some parameters which determine its performance. In order to achieve better solutions, these parameters have to be calculated. Using a simple regular map is the best way to calculate these parameters. Since the optimal solution of this map is predefined, the effect of various parameters could easily be assessed. The number of whales and the number of movements are the parameters that must be calculated.

The outputs of the proposed method with different parameters have been listed in Table 3. According to the results it could be easily understood that the best parameters is the row number nine. So in the next sections all of the results are based on 40 whales and 100 movements. the pattern of parcel assignment has been shown in Figure 4 which is completely sensible and true.

To be more specific, the proposed method has been applied to a uniform map. The optimal parameters have been used to solve the problem. This hypothetical map has 2000 parcels which are distributed on the map uniformly. It is supposed to have six relief centers on the map. The size of the map is 2000 in 2000. The map has been shown in Figure 5.

In such a map, the sensible solution should be an assignment where number of parcels are equal in all centers. Figure 6 demonstrates the assignment pattern of the solution. As it could be seen the distance between centers are almost equal. The number of parcels for each center is roughly equal 330. Given the fact that the map has 2000 parcels and six centers, 330 parcel for each center is satisfactory (2000/6=333.33). In this problem, it has been assumed that relief centers can be located in each place of the map. If we have the limitation of locating centers just in pre-specified locations, there will no problem for the algorithm because we only have the problem space smaller, in other word, solving the problem will be easier.

4. 2. Yazd City In this section the proposed method has been applied to parcels of Yazd city in order to achieve the best locations of relief centers in the city. In this city there are roughly 8500 parcels. The parcels have been extracted from parcel layer of GIS maps. The GIS maps of the city has been acquired from the Ministry of Roads and Urban Development. According to optimal parameters, the algorithm has been executed with 40

TABLE 3. Results of the proposed method with different parameters (meter)

Row#	Whale#	Move#	Center1	Center2	Center3	Center4	Fitness	Time(minute)
1	20	60	512	580	669	739	21	2.5
2	20	80	643	599	572	686	19.5	4
3	20	100	602	535	711	652	19	5
4	30	60	699	605	614	582	19	6
5	30	80	615	641	610	634	18	7
6	30	100	637	620	618	625	16.5	8
7	40	60	621	625	630	624	16	5.5
8	40	80	621	625	630	624	16	7
9	40	100	625	625	625	625	12	9.5

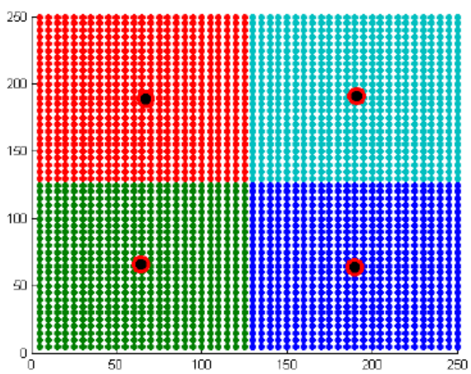

Figure 4. Optimal solution (meter)

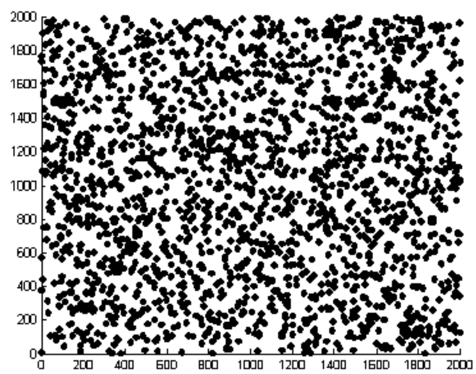

Figure 5. Sample map with 2000 parcels (meter)

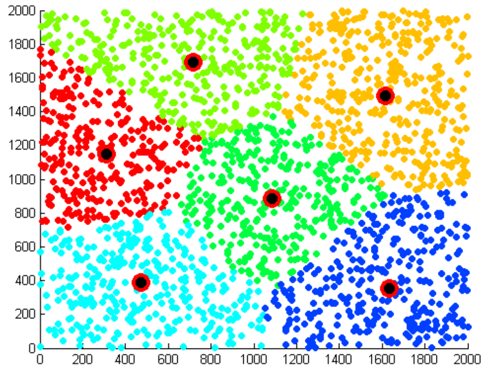

Figure 6. Location of relief centers on the map (meter)

whales and 100 movements. Figure 7 shows the results for Yazd city. In order to eliminate the mantissa, the numbers of the chart are 10000 times bigger than the real map. Figure 8 shows the process of optimization. The X axis shows the round of execution and the Y axis shows the fitness value.

4. 3. Effectiveness of Whale Creating Method

In this article a new method has been proposed in order to create effective whales at the beginning of the algorithm (section 3.2). The effectiveness of this algorithm has been analyzed in this section. For analyzing this method, map of Yazd city has been used. The best solutions, with and without whale creating method, have been compared. Three important metrics can indicate the effectiveness of the method. The first metric is convergence speed which should be shown with a chart. The second metric is average distance that shows the average distance between each parcel and its center. Finally, the third metric is standard deviation which shows that each parcel how fair could be rescued. Figure 9, demonstrates the optimization of objective function. The red line in Figure 8 shows the execution of the algorithm with random whales and blue line shows it with whales which created with proposed method. The speed of convergence and the final value in blue line in better than red line. Better solution in blue line is because of having better whales at the beginning of the algorithm. In fact, when we use the innovative whale generating method, due to having better whales at the begging of the algorithm, the final solution is slightly more optimized.

Table 4 shows the value of average distance and standard deviation for two executions. The first line shows the results for random whales and the second line shows them for whales which created by proposed method. The results show that by using whale creating method, both of metrics have more optimal values.

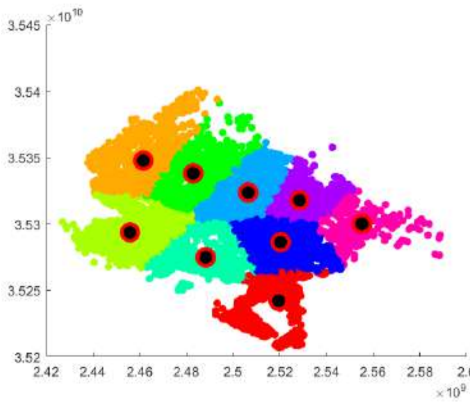

Figure 7. Location of relief centers in Yazd (meter*10000)

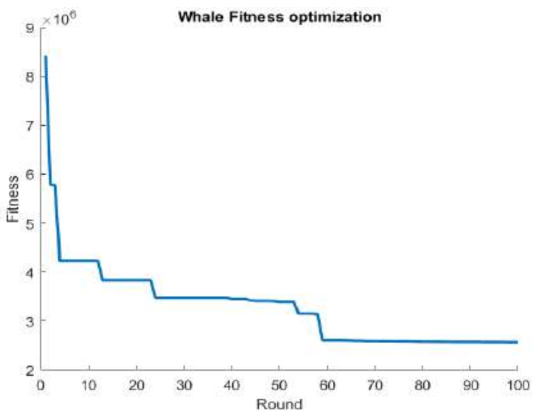

Figure 8. Optimization process for Yazd

4. 4. Stability of the Proposed Algorithm

The proposed algorithm tries to solve the problem by means of whale optimization algorithm. WOA is a kind of

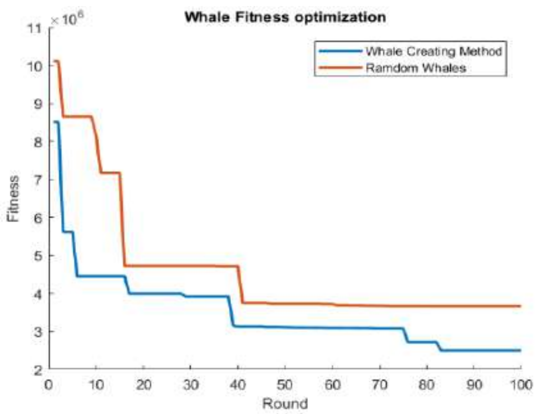

Figure 9. Effect of whale creating method

TABLE 4. Value of average distance and standard deviation for two executions

Whale creating method	Avg_dis (meter)	Standard Deviation
random	1590	155
proposed	1541	114

algorithm that solves problem heuristically. These kind of algorithms produce a different solution in each execution. Hence, the proposed method should be analyzed in terms of stability. In order to assess the stability of the algorithm it has been executed 35 times for Yazd city. The results show that the average distance is equal 1580 and the standard deviation is 20, whereas the best solution is 1541. For better assessment, the proposed algorithm has been applied to a hypothetical map as well. The results for 35 execution show that the average distance is equal 933 and the standard deviation is 13, whereas the best solution is 918. For both maps the results are satisfactory. Figure 10 shows the details of the results. Figure 10(a) is for Yazd city and Figure 10(b) is for hypothetical map.

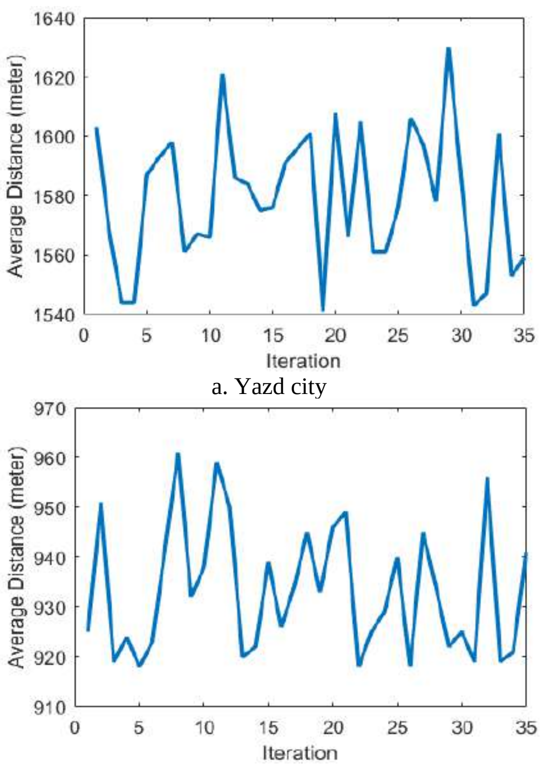

a. Yazd city

b. Hypothetical map

Figure 10. Stability of the proposed method (by 35 executions)

5. CONCLUSION

In this paper, a new algorithm has been proposed in order to find the best locations for earthquake relief centres in Yazd city. The Whale optimization algorithm or WOA has been modified for using in this problem. Redesigning functions of WOA by means of some innovative concepts is one of the most important contributions in this article. Another contribution is introducing a new method for creating better whales at the beginning of the algorithm. By means of better whales the algorithm could be converged faster and produce better solutions. Some hypothetical maps have been used to calculate the best parameters of the algorithm. Moreover, results of the problem for Yazd city has been reported thoroughly. The best average distance for each relief centre is 1541m and the standard deviation is 114. After evaluating the stability of the algorithm it can be understood that the results of the algorithm are reliable. For future works, parameters like vulnerability of the buildings in Yazd city, Level of relief centres can be considered in designing algorithm.

6. REFERENCES

1. Bozorgi-Amiri, A., Jabalameli, M. S., Alinaghian, M., and Heydari, M., "A modified particle swarm optimization for disaster relief logistics under uncertain environment", ***The International Journal of Advanced Manufacturing Technology***, Vol. 60, Nos. 1–4, (2012), 357–371. doi:10.1007/s00170-011-3596-8
2. Beiki, H., Seyedhosseini, S. M., Ghezavati, V. R., and Seyedaliakbar, S. M., "Multi-objective optimization of multi-vehicle relief logistics considering satisfaction levels under uncertainty", ***International Journal of Engineering, Transactions B: Applications***, Vol. 33, No. 5, (2020), 814–824. doi:10.5829/IJE.2020.33.05B.13
3. Every, D., and Richardson, J., "A framework for disaster resilience education with homeless communities", ***Disaster Prevention and Management: An International Journal***, Vol. 27, No. 2, (2018), 146–158. doi:10.1108/DPM-08-2017-0196
4. Beiki, H., Seyedhosseini, S. M., Ghezavati, V. R., and Seyedaliakbar, S. M., "A location-routing model for assessment of the injured people and relief distribution under uncertainty", ***International Journal of Engineering, Transactions A: Basics***, Vol. 33, No. 7, (2020), 1274–1284. doi:10.5829/ije.2020.33.07a.14
5. Liberatore, F., Pizarro, C., de Blas, C. S., Ortuño, M. T., and Vitoriano, B., "Uncertainty in Humanitarian Logistics for Disaster Management. A Review", ***Decision Aid Models for Disaster Management and Emergencies***, (2013), 45–74 Atlantis Press, Paris. doi:10.2991/978-94-91216-74-9_3
6. Maharjan, R., and Hanaoka, S., "A multi-actor multi-objective optimization approach for locating temporary logistics hubs during disaster response", ***Journal of Humanitarian Logistics and Supply Chain Management***, Vol. 8, No. 1, (2018), 2–21. doi:10.1108/JHLSCM-08-2017-0040
7. Kaviyani-Charati, M., Souraki, F. H., and Hajiaghaei-Keshteli, M., "A Robust Optimization Methodology for Multi-objective Location-transportation Problem in Disaster Response Phase under Uncertainty", ***International Journal of Engineering, Transactions B: Applications***, Vol. 31, No. 11, (2018), 1953–1961. doi:10.5829/ije.2018.31.11b.20
8. Fazelabdolabadi, B., and Golestan, M. H., "Towards Bayesian Quantification of Permeability in Micro-scale Porous Structures – The Database of Micro Networks", ***HighTech and Innovation Journal***, Vol. 1, No. 4, (2020), 148–160. doi:10.28991/HIJ-2020-01-04-02
9. Bozorgi-Amiri, A., Jabalameli, M. S., and Mirzapour Al-e-Hashem, S. M. J., "A multi-objective robust stochastic programming model for disaster relief logistics under uncertainty", ***OR Spectrum***, Vol. 35, No. 4, (2013), 905–933. doi:10.1007/s00291-011-0268-x

10. Kılcı, F., Kara, B. Y., and Bozkaya, B., "Locating temporary shelter areas after an earthquake: A case for Turkey", ***European Journal of Operational Research***, Vol. 243, No. 1, (2015), 323–332. doi:10.1016/j.ejor.2014.11.035

11. Karimi, B., Bashiri, M., and Nikzad, E., "Multi-commodity Multimodal Splittable Logistics Hub Location Problem with Stochastic Demands", ***International Journal of Engineering, Transactions B: Applications***, Vol. 31, No. 11, (2018), 1935–1942

12. Vahdani, B., Veysmoradi, D., Noori, F., and Mansour, F., "Two-stage multi-objective location-routing-inventory model for humanitarian logistics network design under uncertainty", ***International Journal of Disaster Risk Reduction***, Vol. 27, (2018), 290–306. doi:10.1016/j.ijdrr.2017.10.015

13. Borowski, P. F., "New Technologies and Innovative Solutions in the Development Strategies of Energy Enterprises", ***HighTech and Innovation Journal***, Vol. 1, No. 2, (2020), 39–58. doi:10.28991/HIJ-2020-01-02-01

14. Das, R., "Disaster preparedness for better response: Logistics perspectives", ***International Journal of Disaster Risk Reduction***, Vol. 31, (2018), 153–159. doi:10.1016/j.ijdrr.2018.05.005

15. Sadidi, J., Fakourirad, E., and Zeaieanfirouzabadi, P., "Designing a spatial cloud computing system for disaster (earthquake) management, a case study for Tehran", ***Applied Geomatics***, Vol. 10, No. 2, (2018), 99–111. doi:10.1007/s12518-018-0203-9

16. Haji Gholam Saryazdi, A., and Poursarrajian, D., "Qualitative System Dynamics Model for Analyzing of Behavior Patterns of SMEs", ***HighTech and Innovation Journal***, Vol. 2, No. 1, (2021), 9–19. doi:10.28991/HIJ-2021-02-01-02

17. Tavana, M., Abtahi, A.-R., Di Caprio, D., Hashemi, R., and Yousefi-Zenouz, R., "An integrated location-inventory-routing humanitarian supply chain network with pre- and post-disaster management considerations", ***Socio-Economic Planning Sciences***, Vol. 64, (2018), 21–37. doi:10.1016/j.seps.2017.12.004

18. Wedawatta, G., Kulatunga, U., Amaratunga, D., and Parvez, A., "Disaster risk reduction infrastructure requirements for South-Western Bangladesh", ***Built Environment Project and Asset Management***, Vol. 6, No. 4, (2016), 379–390. doi:10.1108/BEPAM-06-2015-0022

19. Noyan, N., and Kahvecioğlu, G., "Stochastic last mile relief network design with resource reallocation", ***OR Spectrum***, Vol. 40, No. 1, (2018), 187–231. doi:10.1007/s00291-017-0498-7

20. Baylan, E. B., "A Novel Project Risk Assessment Method Development via AHP-TOPSIS Hybrid Algorithm", ***Emerging Science Journal***, Vol. 4, No. 5, (2020), 390–410. doi:10.28991/esj-2020-01239

21. Allahbakhsh, M., Arbabi, S., Galavii, M., Daniel, F., and Benatallah, B., "Crowdsourcing planar facility location allocation problems", ***Computing***, Vol. 101, No. 3, (2019), 237–261. doi:10.1007/s00607-018-0670-1

22. Mihajlović, G., and Živković, M., "Sieving Extremely Wet Earth Mass by Means of Oscillatory Transporting Platform", ***Emerging Science Journal***, Vol. 4, No. 3, (2020), 172–182. doi:10.28991/esj-2020-01221

23. Babicz, D., Tihanyi, A., Koller, M., Rekeczky, C., and Horvath, A., "Simulation of an Analogue Circuit Solving NP-Hard Optimization Problems", In 2019 IEEE International Symposium on Circuits and Systems (ISCAS), (2019), 1–5. doi:10.1109/ISCAS.2019.8702694

24. Ozturk, B., "Preliminary seismic microzonation and seismic vulnerability assessment of existing buildings at the city of nigde, turkey", In 14th World Conference on Earthquake Engineering, Beijing, China, (2008), 1–7.

25. Ozturk, B., "Application of preliminary microzonation and seismic vulnerability assessment in a city of medium seismic risk in turkey", In 5th International Conference on Earthquake Geotechnical Engineering, Santiago, Chile, (2011), 1–11.

26. Mirjalili, S., and Lewis, A., "The Whale Optimization Algorithm", ***Advances in Engineering Software***, Vol. 95, (2016), 51–67. doi:10.1016/j.advengsoft.2016.01.008

27. Mehranfar, N., Hajiaghaei-Keshteli, M., and Fathollahi-Fard, A. M., "A Novel Hybrid Whale Optimization Algorithm to Solve a Production-Distribution Network Problem Considering Carbon Emissions", ***International Journal of Engineering, Transactions C: Aspects***, Vol. 32, No. 12, (2019), 1781–1789. doi:10.5829/ije.2019.32.12c.11

28. Rahmani, D., "Designing a robust and dynamic network for the emergency blood supply chain with the risk of disruptions", ***Annals of Operations Research***, Vol. 283, Nos. 1–2, (2019), 613–641. doi:10.1007/s10479-018-2960-6

29. Salehi, F., Mahootchi, M., and Husseini, S. M. M., "Developing a robust stochastic model for designing a blood supply chain network in a crisis: a possible earthquake in Tehran", ***Annals of Operations Research***, Vol. 283, Nos. 1–2, (2019), 679–703. doi:10.1007/s10479-017-2533-0

30. Fazli-Khalaf, M., Khalilpourazari, S., and Mohammadi, M., "Mixed robust possibilistic flexible chance constraint optimization model for emergency blood supply chain network design", ***Annals of Operations Research***, Vol. 283, Nos. 1–2, (2019), 1079–1109. doi:10.1007/s10479-017-2729-3

31. Boonmee, C., Arimura, M., and Asada, T., "Facility location optimization model for emergency humanitarian logistics", ***International Journal of Disaster Risk Reduction***, Vol. 24, (2017), 485–498. doi:10.1016/j.ijdrr.2017.01.017

32. Mahootchi, M., and Golmohammadi, S., "Developing a new stochastic model considering bi-directional relations in a natural disaster: a possible earthquake in Tehran (the Capital of Islamic Republic of Iran)", ***Annals of Operations Research***, Vol. 269, Nos. 1–2, (2018), 439–473. doi:10.1007/s10479-017-2596-y

33. Sebatli, A., Cavdur, F., and Kose-Kucuk, M., "Determination of relief supplies demands and allocation of temporary disaster response facilities", ***Transportation Research Procedia***, Vol. 22, (2017), 245–254. doi:10.1016/j.trpro.2017.03.031

34. Chu, X., and Zhong, Q., "Post-earthquake allocation approach of medical rescue teams", ***Natural Hazards***, Vol. 79, No. 3, (2015), 1809–1824. doi:10.1007/s11069-015-1928-y

35. Golabi, M., Shavarani, S. M., and Izbirak, G., "An edge-based stochastic facility location problem in UAV-supported humanitarian relief logistics: a case study of Tehran earthquake", ***Natural Hazards***, Vol. 87, No. 3, (2017), 1545–1565. doi:10.1007/s11069-017-2832-4

36. Paul, J. A., and MacDonald, L., "Location and capacity allocations decisions to mitigate the impacts of unexpected disasters", ***European Journal of Operational Research***, Vol. 251, No. 1, (2016), 252–263. doi:10.1016/j.ejor.2015.10.028

37. Saeidian, B., Mesgari, M. S., and Ghodousi, M., "Evaluation and comparison of Genetic Algorithm and Bees Algorithm for location–allocation of earthquake relief centers", ***International Journal of Disaster Risk Reduction***, Vol. 15, (2016), 94–107. doi:10.1016/j.ijdrr.2016.01.002

38. Saeidian, B., Mesgari, M., Pradhan, B., and Ghodousi, M., "Optimized Location-Allocation of Earthquake Relief Centers Using PSO and ACO, Complemented by GIS, Clustering, and TOPSIS", ***ISPRS International Journal of Geo-Information***, Vol. 7, No. 292, (2018), 1–25. doi:10.3390/ijgi7080292

39. Thumronglaohapun, S., "Heuristic Methods for the Capacitated Location- Allocation Problem with Stochastic Demand", ***International Journal of Industrial and Systems Engineering***, Vol. 14, No. 6, (2020), 452–457

40. Ghasemi, P., Khalili-Damghani, K., Hafezalkotob, A., and Raissi,

S., "Uncertain multi-objective multi-commodity multi-period multi-vehicle location-allocation model for earthquake evacuation planning", ***Applied Mathematics and Computation***, Vol. 350, (2019), 105–132. doi:10.1016/j.amc.2018.12.061

41. Ghasemi, P., and Khalili-Damghani, K., "A robust simulation-optimization approach for pre-disaster multi-period location–allocation–inventory planning", ***Mathematics and Computers in Simulation***, Vol. 179, (2021), 69–95. doi:10.1016/j.matcom.2020.07.022

42. Shavarani, S. M., "Multi-level facility location-allocation problem for post-disaster humanitarian relief distribution", ***Journal of Humanitarian Logistics and Supply Chain Management***, Vol. 9, No. 1, (2019), 70–81. doi:10.1108/JHLSCM-05-2018-0036

Persian Abstract

چکیده

علیرغم اینکه دولت‌ها قوانین سختگیرانه¬ای را برای تضمین استحکام ساختمان¬ها وضع می¬کنند؛ همچنان ساختمان¬های زیادی وجود دارد که در برابر زلزله آسیب¬پذیر است. ازاین رو ایجاد مراکز امداد زلزله جهت کنترل اثرات آن بسیار ضروری است. ایران یکی از کشورهای خاورمیانه است که آسیب¬پذیری زیادی در برابر زلزله دارد. شهر یزد در مرکز ایران قرار گرفته است. از آنجایی که چنین تحقیقی برای شهر یزد وجود ندارد، این شهر در این تحقیق مورد بررسی قرار گرفته است. لایه پارسل از نقشه جی آی اس شهر یزد بعنوان ورودی مساله در نظر گرفته شده است. از آنجایی که مکان¬یابی مراکز زلزله یک مساله پیچیده بوده و در زمان چندجمله¬ای قابل حل نیست؛ از الگوریتم اکتشافی بهینه¬سازی نهنگ برای حل مساله استفاده شده است. الگوریتم بهینه¬سازی نهنگ یک روش مبتنی بر ذره است که کاربرد زیادی در حل مسائل سخت دارد. نوآوری اصلی این مقاله تنظیم توابع نهنگ برای استفاده در مساله مکان¬یابی و همچنین معرفی روش جدیدی برای ایجاد نهنگ است. جهت رسیدن سریع‌تر به جواب منطقی یک روش مبتکرانه برای تولید نهنگ طراحی شده است. بررسی نتایج الگوریتم نشان می¬دهد که میانگین فاصله هر ذره تا نزدیکترین مرکز ۱۸۵۰ متر و انحراف از معیار اجراهای مختلف نیز برابر ۲۰ است.

IJE TRANSACTIONS B: Applications Vol. 34, No. 05, (May 2021) 1195-1212

International Journal of Engineering

Journal Homepage: www.ije.ir

Retrofitting of RC Beams using Reinforced Self-compacting Concrete Jackets Containing Aluminum Oxide Nanoparticles

A. Faez, A. Sayari*, S. Manie

Civil Engineering Department, Sanandaj Branch, Islamic Azad University, Sanandaj, Iran

P A P E R I N F O

Paper history:
Received 27 December 2020
Received in revised form 14 March 2021
Accepted 15 March 2021

Keywords:
Aluminum Oxide Nanoparticles
Finite Element Method
Reinforced Concrete Jacket
Retrofitting

A B S T R A C T

The purpose of this study was to introduce a proposed method to retrofit RC beams. For this purpose self-compacting concrete containing aluminium oxide nanoparticles (ANPs) and silica fume (SF) was used in RC jackets. The laboratory experiment and numerical simulation were used to investigate the behavior of the beams. The experimental variables were included the amount of ANPs used in the jackets (0 and 2.5% by weight of cement) and the surface interaction between beam and jacket (75% and 100% of the side and bottom surfaces of the beam). Five RC beams with a length of 1.4 m and the same dimensions were made and subjected to four-point loading. After completing the laboratory steps, RC beams were simulated according to laboratory conditions using the finite element method and ABAQUS software. After verifying the used method, parametric analysis was performed and parameters such as beam span length (1.5, 3, 4.5 m), concrete jacket thickness (4, 8, and 12 cm), and the diameter of the bars used in the jacket (8, 10 and 12 mm) were examined. The results showed that the use of RC jackets containing ANPs, depending on the jacket thickness, the diameter of the bars used in the jacket, and the length of the beam span increased the beams flexural strength by 155 to 447%. It was observed that the crushing of concrete without nanoparticles compared to concrete contain nanoparticles is more severe because nanoparticles affected the concrete matrix and reduced its crushing in RC jackets.

***doi**: 10.5829/ije.2021.34.05b.13*

1. INTRODUCTION

In recent years, following the deterioration of building structures and the need for retrofitting structures to satisfy the strict design requirements, much emphasis has been placed on repairing buildings [1–3]. One of the methods that can prevent the loss of materials as much as possible and reduce construction debris is retrofitting of buildings [4–6]. Increasing the strength of the structure is very important during the retrofitting because this will increase the useful life of the structure and residents will feel more secure [7–9]. Various studies have been conducted on retrofitting of RC beams. Sangi et al. [10] made 35 self-compacting concrete beams and retrofitted them with CFRP sheets in the tensile zone (bottom surface of the beam). Also, numerical simulation was used to investigate the fracture mode and cracks distribution in the samples. It was indicated that the retrofitted beam with CFRP angle 0° has more capacity in comparison to other specimens [10]. Shadmand et al. [11] introduced a proposed method for retrofitting RC beams in which steel-concrete composite jackets containing steel fibers were used. For this purpose, 75% of the peripheral surface of RC beams was initially reinforced using steel plates and bolts. Then steel fiber reinforced concrete was used between the steel plates and the perimeter of the beam. The results showed that steel fiber-reinforced composite jackets delay the formation of the first crack in the concrete and the energy absorption capacity of the beams increased by 89 to 129% depending on the amount of steel fiber [11]. Rahmani et al. [12] investigated the response of retrofitted RC beams with RC jackets containing steel fiber. For this purpose, 25 RC beams with different concrete jackets were made and their bearing capacity was evaluated. The result showed that the use of RC jacket containing steel fiber can increase the bearing capacity of the beams by about 7.4 times in compare to the control beam [12].

*Corresponding Author Email: *Sayari_arash@yahoo.com* (A. Sayari)

Please cite this article as: A. Faez, A. Sayari, S. Manie, Retrofitting of RC Beams using Reinforced Self-compacting Concrete Jackets Containing Aluminum Oxide Nanoparticles, International Journal of Engineering, B: Applications Vol. 34, No. 05, (2021) 1195-1212

On the other hand, nanotechnology development in engineering sciences has been studied by other researchers [13, 14]. The disadvantages of increasing cement production have led to use of nanoparticles in concrete. Nanoparticles can improve the concrete properties and reduce cement consumption in different countries [15–17]. The nanoparticles are usually used in concrete in powder form or distributed in solution [18–20]. The most important used nanoparticles are titanium nanoparticles (TiO_2), aluminium nanoparticles (Al_2O_3), silica nanoparticles (SiO_2), iron nanoparticles (Fe_2O_3), and clay nanoparticles (Nano-Clay) [21–23]. Among the mentioned particles, aluminum oxide nanoparticles (ANPs) are one of the important ceramic materials that have various applications in various fields [24–26]. Li et al. [27] investigated the effect of ANPs in cement mortar. The results showed that by adding 5% ANPs, the concrete elasticity modulus increased by 143% [27]. Oltulu and Sahin [28] investigated the effect of Nano silica, ANPs, and iron oxide nanoparticles separately and in combination with fly ash and silica fume. The results showed that the best performance in terms of compressive strength and permeability was obtained in the presence of 1.25% ANPs [10]. Behfarnia and Salemi [29] investigated the effects of nano silica particles and ANPs on the resistance of ordinary concrete to freezing. The results showed that the freezing resistance of concrete containing nanoparticles is significantly improved due to the dense structural creation [29]. Ismael et al. [30] investigated the effect of nano silica and ANPs additives on the adhesion between steel and concrete. The results indicated that nanoparticles increased the adhesion between steel and concrete [30]. Niewiadomski et al. [31] investigated the properties of self-compacted concrete (SCC) modified with nanoparticles. The results showed that the fluidity of concrete decreases with increasing amounts of ANPs and silica nanoparticles. Also, the hardness values and elasticity modulus of the samples containing nanoparticles were higher compared to the samples without nanoparticles [31]. Ghazanlou et al. [32] investigated the mechanical properties of cementations composites containing iron nano oxide. Cement paste samples were tested with 0.2% iron nano oxide. The results indicated that the use of nanoparticles can increase the tensile strength, flexural strength, and compressive strength of specimens by about 15-19%, 17-25%, and 23-32%, respectively [32]. Heidarzad Moghaddam et al. [33] investigated the effects of ANPs on the mechanical and durability properties of fiber SCC. The results showed that the combined use of 2% ANPs and 1% glass fibers increased the compressive and tensile strengths of SCCs by 59 and 119.2%, respectively [33]. Zeinolabedini et al. [34] investigated ultra–high–performance concrete containing polypropylene fibers and aluminum oxide, nano-lime, and nanosilica. The results showed that the effect of increasing the amount of cement on increasing the flexural strength is much less than increasing the amount of nanomaterials [34]. Muzenski et al. [35] investigated the properties of concrete containing fiber and aluminum oxide nanofibers. The results showed that the combined use of aluminum oxide nanoparticles and fibers can be a good option to improve compressive strength [35].

As mentioned, studies about retrofitting of RC structural elements show that concrete jackets and FRP sheets are the common methods that have been used. Although the FRP method can increase the bearing capacity of the beams, the separation of FRP sheets from concrete surfaces, the weakness against fire, and its different properties from concrete are among the disadvantages that can affect its performance. On the other hand, the concrete used in ordinary RC jackets is weak against tensile stresses and the performance role of the jackets can be improved by using various additives. One of these additives is ANPs. The adhesion between the steel rebars and the used binder in the RC jacket can play a very important role. Studies about the use of ANPs in the concrete show that the use of these materials in concrete increase the adhesion between concrete and rebar, so due to the relatively limited space between the formwork and the old concrete, the use of nanoparticles increase the adhesion between the rebars in the jackets and the surrounding concrete compared to ordinary concrete, and thus the bearing capacity of the RC beam will be higher. ANPs can also improve the heat resistance of concrete due to fire. These materials also affect the durability properties of concrete. Considering the advantages of ANPs in concrete, in the present study, ANPs were used in the concrete jacket to retrofit of RC beam. The study was conducted in two parts: laboratory and software simulation. Improving the performance and increasing the bearing capacity of RC beams using reinforced self-compacting concrete jackets containing ANPs are among the objectives of the present study. Thus, according to the characteristics of nanoparticles, in addition to increasing the energy absorption capacity of RC beams, the use of nanoparticles is effective in reducing the consumption of natural resources and raw materials used in cement production. Also, self-compacting of the concrete used in concrete jackets is another case that causes concrete to be poured completely into the space between the rebars.

2. STUDY PROCESS

Studies were performed in two stages: laboratory and software simulation. In the laboratory part, concrete specimens containing ANPs and SF were made for different percentages, and tests such as slump flow, T50, V-funnel, L-box, compressive strength, splitting tensile strength, and water absorption were performed and the most optimal mixture design selected. Fresh concrete tests were performed to check the self-compaction properties of the concrete specimens. Rheological, durability, and mechanical properties were investigated in a study conducted by the authors [36]. The mixture design and results of the mentioned study are presented in Tables 1 and 2, receptively. Fresh concrete tests were performed according to EFNARC [37] and compressive and splitting tensile strengths, and water absorption tests were performed according to ASTM C39 [38], ASTM C496 [39], and ASTM C642-13 [40], respectively. After reviewing the results related to determining the mechanical and rheological properties of concretes containing ANPs and SF, five RC beams with the same dimensions and specifications steel reinforcement were made and subjected to four-point loading in the center of the span in conditions with and without retrofitting. The bearing capacity, mid-span deflection, and energy absorption capacity were determined. The studied beams had hinged support and in the state without retrofitting and retrofitted with two different arrangements of the concrete jacket after 28 days were subjected to 4-point loading. The concrete used in the jacket was once conventional and once retrofitted with concrete containing ANPs. After completing the laboratory steps, retrofitted concrete beams with a concrete jacket containing ANPs were simulated using the finite element method (FEM) and ABAQUS software [41] and were subjected to loading according to laboratory conditions, and load-deflection curves were determined. After ensuring the accuracy of the simulation method, which was performed using laboratory studies, the behavior of RC beams retrofitted with the proposed jacket was evaluated by numerical simulation and variables such as beam span length, the jacket thickness, and the diameter of the reinforcement bars used in the jacket were examined.

3. LABORATORY PROGRAM

3. 1. Materials Materials include coarse aggregates, fine aggregates, cement, water, ANPs, SF, and superplasticizers. River sand and crushed gravel were

TABLE 1. Mix design (kg/m^3) [36]

Mix	C	W	SF	S	G	NP	SP
NA0	350	168	35	960	920	0	2.76
NA0.25	314.125	168	35	960	920	0.875	2.86
NA0.50	313.25	168	35	960	920	1.75	2.93
NA0.75	312.375	168	35	960	920	2.625	3.03
NA1	311.5	168	35	960	920	3.5	3.35
NA1.25	310.625	168	35	960	920	4.375	3.46
NA1.50	309.75	168	35	960	920	5.25	3.89
NA1.75	308.875	168	35	960	920	6.125	4.03
NA2	308	168	35	960	920	7	4.12
NA2.25	307.125	168	35	960	920	7.875	4.45
NA2.50	306.25	168	35	960	920	8.75	4.89
NA2.75	375.305	168	35	960	920	9.625	4.92
NA3	304.5	168	35	960	920	10.5	4.65

C: Cement W: Water SF: Silica fume S: Sand
G: Gravel NP: Nanoparticles SP: Superplasticizer

TABLE 2. Results of slump flow, T50, V-funnel, L-box, compressive strength, splitting tensile strength, and water absorption [36]

Mix	Slump flow (mm)	T50 (s)	V-funnel (s)	L-Box (H_2/H_1)	Compressive strength (MPa)			Splitting tensile strength (MPa)			Water absorption (%)
					Days			Days			Days
					7	28	90	7	28	90	28
NA0	749	2.41	6.3	0.97	21.12	26.1	29.31	2.78	2.9	3.6	5.73
NA0.25	746	2.67	6.4	0.94	22.33	28.12	30.92	2.86	2.95	3.79	5.61
NA0.50	737	2.77	6.9	0.91	24.24	33.22	34.11	2.89	3.31	3.85	5.41
NA0.75	733	2.89	7.4	0.88	25.11	35.11	37.11	2.9	3.34	3.92	5.35
NA1	721	3.53	7.7	0.86	26.14	36.21	39.22	2.91	3.41	3.95	5.15
NA1.25	701	3.57	8.3	0.86	26.32	40.12	43.13	2.92	3.41	3.98	4.81
NA1.50	691	3.78	9.19	0.85	27.22	45.11	46.21	2.98	3.43	4.11	4.41
NA1.75	687	4.41	7.971	0.85	28.13	46.21	48.12	3.19	3.86	4.33	3.76
NA2	684	4.51	10.41	0.84	29.22	47.12	50.12	3.39	4.29	5.04	3.12
NA2.25	671	4.57	10.49	0.83	29.91	48.13	51.23	3.41	4.3	5.05	2.85
NA2.50	665	4.59	11.12	0.83	30.91	49.14	54.34	3.6	4.5	5.31	2.83
NA2.75	665	4.68	11.37	0.82	30.12	48.22	53.11	3.5	4.41	5.27	2.79
NA3	663	4.91	11.82	0.82	30.01	47.34	52.12	3.4	4.4	5.21	2.77

used. The density of sand and gravel were 2600 and 2650 kg/m^3, respectively. Sand and gravel grading were conducted according to ASTM C33/C33M-18 [42]. Cement type II was used. The water used in this study is drinking water. ANPs is one of the chemical compounds with the chemical formula Al_2O_3, which has various brands such as alumina, corundum, etc. This material has a very high melting temperature about 2054 degrees Celsius and is very stable chemically. This property allows this material to be used in applications that need high temperatures. Hardness, strength, and abrasion resistance of ANPs are the highest among oxides. The ANPs used in this research have a small size and high activity, in powder form and almost spherical. These nanoparticles have a specific surface area of 138 m^2/g and a density of 3890 kg/m^3 and an average particle size of 20 nm. Also. they are white. The compounds of the used ANPs are presented in literature [36]. The SF is produced by Iran Ferrosilicon factory with a specific weight of 2200 kg/m^3 and a blaine of 20.2 g/m^2, which is added with a dry form to the concrete mix in the amount of 10% by weight of cement. The SF and cement chemical properties are presented in literature [36]. The brand of superplasticizer used is "Zhikaplast" and its specific gravity is 1.10 g/cm^3. Concrete was made using a concrete mixer. First, the coarse aggregates and fine aggregates were mixed in a concrete mixer, half of the mixing water was added and the mixing was continued. At this stage, cement, SF, and 10% water were added to the mixture, and mixing was continued in a concrete mixer. Finally, ANPs and then residual water were added. After mixing, the superplasticizer was gradually to visually feel the fresh self-compacting concrete has achieved the necessary efficiency and homogeneity.

3. 2. Retrofitting of RC Beams using SCC Jacket Containing ANPs and SF

After examining the rheological and mechanical properties of concretes containing ANPs and SF, it was concluded that the concrete specimen containing 2.5% ANPs and 10% SF has a better performance compared to other specimens according to tensile and compressive strengths.

The increase in compressive and tensile strengths of NA2.5 compared to the control sample was 88% and 55%, respectively. Also, in terms of workability, the mentioned sample has met all the criteria related to SCCs. Therefore, it was selected as the most optimal mixture design and used in the concrete jackets. The beams had hinged support. Two different arrangements were considered for the proposed jacket. A four-point bending test was used for beam specimens. Mid-span deflection and the corresponding load were recorded. Concretes containing ANPs and without ANPs were used in the jackets in different cases. The geometric characteristics and reinforcement bars details of the beams are present in Figure 1.

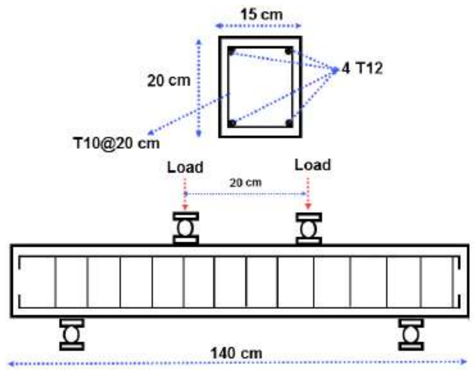

Figure 1. Geometric specifications and steel reinforcement details of the investigated beams

The beam's span length is 120 cm. The schematic arrangement of the investigated jackets is shown in Figure 2. Three sides of the beam were retrofitted due to the typical floor-to-beam connection. The proposed jacket was once placed on 75% of the perimeter and bottom of the beams and once again on 100% perimeter and bottom of beams. A beam was also constructed as a control beam to evaluate the effectiveness of the proposed method. The tested beams are presented in Table 3. According to Figure 2, the thickness of the concrete jacket (t_j) at the sides and bottom of the beam was considered 4 cm. The diameter of the reinforcement bars and the distances between them were considered 10 mm and 50 mm, receptively. The selection of studied beams dimensions and geometric characteristics has been done according to similar studies in which the beams retrofitting have been evaluated. Beam stirrups were made with a stirrup machine. To make and install concrete jacket, voids were made on the beams at intervals of about 20 cm from each other. After removing the dust inside the voids, L-shaped reinforcement bars were placed inside the voids and attached to the beam surfaces using epoxy glue. After that, the reinforcement bar mesh of the jacket was connected to L-shaped reinforcement bar using wire. The jacket reinforcement bar mesh consisted of 10 mm diameter reinforcement bar spaced approximately 5 cm apart. The construction stages of retrofitted beams are shown in Figure 3.

A fully automatic flexural jack with a load capacity of 2000 kN was used to apply loads to the beams. This

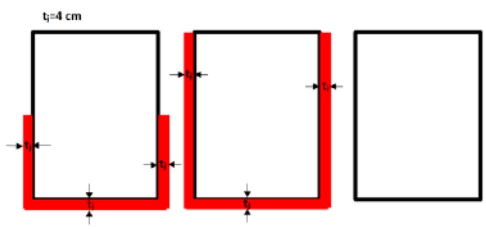

Figure 2. The arrangement of the investigated jackets

TABLE 3. Introducing the tested beams

No.	Name	Additives used in jacket	Description
1	CB	-	Control beam
2	R75	SF	75% of the perimeter surface and the lower part of the beam
3	R100	SF	100 % of the perimeter surface and the lower part of the beam
4	R75N	ANPs and SF	75% of the perimeter surface and the lower part of the beam
5	R100N	ANPs and SF	100 % of the perimeter surface and the lower part of the beam

jack is capable of recording displacement up to 50 mm. The support distance from center to center was considered 130 cm and the distance between the two loading jaws was set at 20 cm. Loading the sample is shown in Figure 4. A displacement gauge with an accuracy of 0.01 mm was placed in the middle point of the beam to record the deformation of the mid-span at the same time as applying the load. The laboratory output diagram results show the force applied values to the beam versus the displacement values in the middle of the span. LVDT was used in the testing process, and this sensor is located just below the mid-span of the beam.

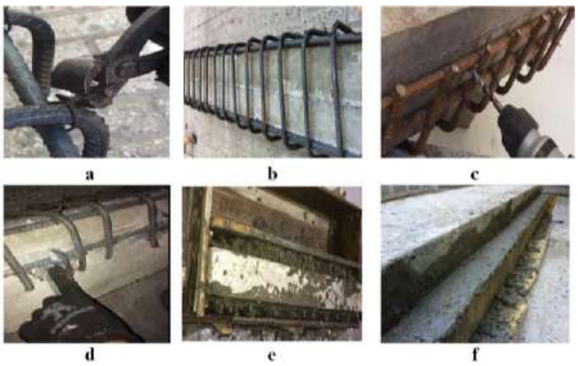

Figure 3. Steps of making and installing concrete jackets a: Making the steel reinforcement rebar b: Placing the steel rebar mesh on the beam c: Creating cavities on the surfaces of the main beams D: Installing L-shaped rebars using epoxy adhesive inside the cavities e: Concreting of jackets f: beam after concreting

Figure 4. Four-point bending flexural test

4. EXPERIMENTAL RESULTS OF RETROFITTED BEAMS

Interpretation of the beams results in the conditions with and without retrofitting was performed by examining the crack distribution and load-deflection diagrams. Crack, yield, and maximum loads as well as their corresponding deflection are considered as criteria to study the behavior of the beams. The load corresponding to the first crack is called the crack load and the displacement created in this case is called the crack deflection. The yield load is also called the load at which the steel reinforcement bars yield and the corresponding deflection is called the yield deflection. Also, the peak load is the maximum load that the beam can withstand. The deflection corresponding to the ultimate load is also defined as the ultimate deflection. According to the study conducted by Hosen et al. [43], the load-deflection curve of RC beams is divided into three distinct linear areas. The first stage is before the concrete cracks. The second stage is the cracking stage. The beam behavior at this stage is inelastic due to the creation of cracks in the cross-section and the crack expands on the peripheral surface of the beam with increasing load. The third stage is the post-cracking stage. At this stage, the concrete part is completely cracked and the steel reinforcement bars enter this stage with their strain hardness and participate in withstanding the loads.

The load-deflection curves are shown in Figure 5. Also, the failure and crack distribution of the beams at the end of loading are shown in Figure 6. In the CB beam, the first cracks were formed in the tensile region and central areas of the beam. As the load increased, the cracks extended to the beam center (near to the neutral axis) and finally, the beam failed. In the CB beam, the first crack was created in a load corresponding to 39 kN and the corresponding deflection was equal to 0.32 mm. The yield load and corresponding deflection are 99 kN and 2.4 mm, receptively.

Also, the maximum bearing load and corresponding deflection are 114 kN and 3.4 mm, receptively. The beam

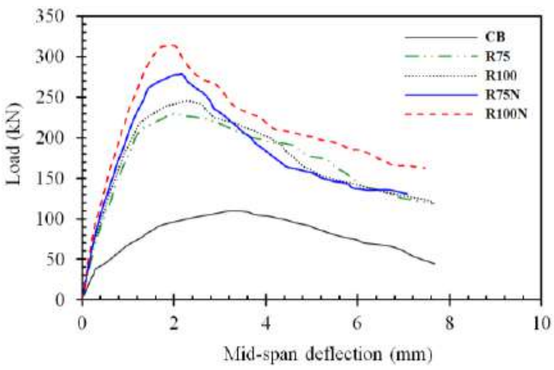

Figure 5. Comparison of the load-deflection curves (Laboratory study)

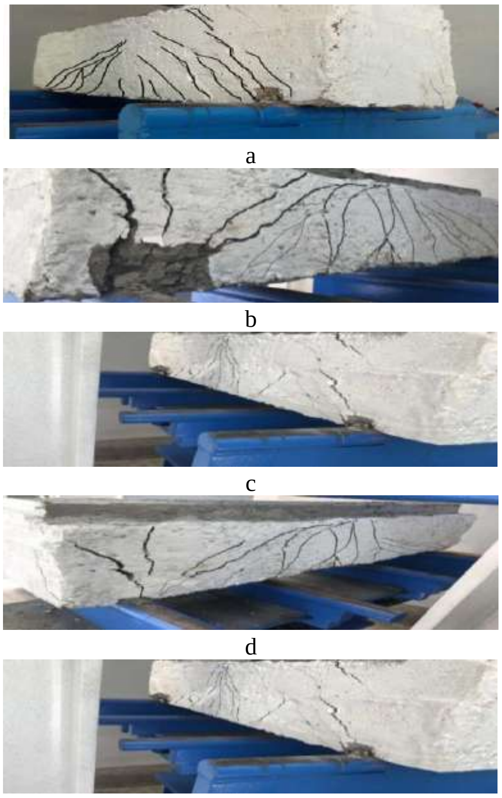

a b c d e

Figure 6. Beams failure and cracks distribute a: CB b: R75 c: R100 d: R75N e: R100N

ultimate displacement is 7.6 mm. In R75 beam, the crack load and crack deflection are 76 kN and 0.39 mm, respectively. The yield deflection and load are 1.21 mm and 205 kN, respectively. The maximum bearing load and the corresponding deflection are 229 kN and 1.87 mm, respectively. Also, the ultimate deflection of the beam is 7.65 mm. In R100 beam the load and crack deflection are equal to 81 kN and 0.32 mm, respectively. The yield deflection and load are 1.19 mm and 212 kN, respectively.

The beam maximum bearing load and corresponding deflection are 244 kN and 2.42 mm. Also, the beam ultimate deflection is 7.66 mm. In the R75N beam, load and crack deflection are 84 kN and 0.3 mm, respectively. Yield and load-deflection are 1.47 mm and 261 kN, respectively. The beam maximum bearing load and corresponding deflection are 277 kN and 2.19 mm, respectively. The beam ultimate deflection is 7.07 mm. In R100N beam, the crack load and displacement are 96 kN and 0.29 mm, respectively, and the yield load and deflection are 273 kN and 1.47 mm, respectively. The maximum bearing load and corresponding deflection are 314 kN and 1.9 mm, respectively. The beam ultimate deflection is 7.46 mm. The 4-point loading results that were examined in the laboratory study are presented in Table 4. This table shows the crack, yield, maximum and ultimate loads of the beams. Also, the corresponding deflection, ductility, and energy absorption capacity are calculated. The numbers in parentheses indicate the increased ratio in each of the quantities compared to the control beam specimen.

To investigate more, various comparative diagrams are presented. At the points where cracks are created, the maximum tensile stress is created in the farthest thread of the section and the concrete has lost its tensile strength. The load at which cross-sectional cracking occurs is called the "cracking load" (P_{cr}). The crack load of all the beams is presented in Figure 7. In all cases, the use of the proposed concrete jackets has increased the crack load. The crack load of the retrofitted beams with RC jackets without ANPs was 95 and 107% higher than the crack load, respectively.

The crack load of the retrofitted beams with RC jackets containing ANPs was 115 and 146% higher than the crack load, respectively. ANPs fill the cement and silica fume voids and increase the beam resistance against cracking by creating more adhesion. Concrete crushing is one of the common problems in the concrete structural elements. In this study, it has been observed that the crushing in concrete without ANPs is stronger than the concrete contains ANPs because ANPs affect the concrete matrix and reduce its crushing. Reducing the crushing of concrete by using ANPs and SF in RC beams can reduce the cost of retrofitting and maintenance after low to medium magnitude earthquakes. The yield loads of the beams are compared in Figure 7. The use of RC jackets containing ANPs has increased the yield load by about 164 to 176%, depending on the type of jacket arrangement. Also, the yield load of retrofitted beams with jackets in which normal concrete was used has increased by about 107 to 114%. According to the mentioned values, it can be stated that the use of ANPs has caused the reinforcement bars to yield later and the beams yield-bearing capacity has increased.

The maximum load of the beams is the bearing capacity of the beams. The beams bearing capacity are compared in Figure 7. The results show that the use of concrete jackets without and containing ANPs, depending on their arrangement, can increase the bearing capacity of RC beams by about 107 to 175%. Concrete jackets increase the flexural stiffness of the beams by enclosing them around the beam and increase the moment of inertia, making the beams able to withstand more loads.

As expected, in cases where the jacket covers the entire perimeter of the beams, the beam bearing capacity is greater than in cases where the jacket covers 75% of the peripheral surface. The difference between the RC beams bearing capacity with R100 jackets without and containing ANPs compared to their corresponding values in retrofitting beams with R75 jackets is 2.8 and 22.3%, respectively. This means that the change in the

TABLE 4. Comparison of the results of laboratory study and finite element study

Beam name	Crack load			Yield load			Maximum Load			Ultimate Load			Flexural toughness (J)		
	P_{cr} (kN)			P_y (kN)			P_{max} (kN)			P_u (kN)					
	EXP	FEM	Error (%)	EXP	FEM	Error (%)	EXP	FEM	Error (%)	EXP	FEM	Error (%)	EXP	FEM	Error (%)
CB	39	38	2.6	99	98	1	114	112	1.8	49	48	2	616	591	1.4
R75	76	74	2.6	205	180	12.2	229	228	0.4	119	123	3.4	1310	1271	3
R100	81	80	1.2	212	227	1.4	244	249	2	120	125	4.2	1331	1355	1.8
R75N	84	75	10.7	261	250	4.2	277	278	0.4	131	148	13	1294	1385	7
R100N	96	98	2.1	273	275	0.7	314	320	1.9	163	175	7.4	1587	1549	2.4

arrangement of jackets containing nanoparticles has a greater effect on changing the bearing capacity of the beams.

The percentage increase in the crack, yield, and maximum loads in beams retrofitted with a jacket containing ANPs compared to their corresponding values in beams retrofitted with jackets without nanoparticles are shown in Figure 8. In R75 beams, crack, yield and maximum loads have increased by 10.5, 27.3, and 21%, respectively. Also, in R100, the crack, yield, and maximum loads have increased by 18.5, 28.8 and 28.7%, respectively. The mentioned values indicate that ANPs have an effective role in improving the RC beams retrofitted with concrete jackets response. The reason for improving the bearing capacity in reinforced specimens of jackets containing ANPs compared to specimens without ANPs is that nanoparticles increase the beam resistance against incoming loads by increasing the tensile strength of concrete and inhibiting cracks produced on the concrete surface.

Energy absorption capacity or flexural strength is one of the parameters examined to analyze the reinforced concrete member's performance. The higher energy absorption capacity is shown the better member performance. The beam's energy absorption capacity was calculated by determining the area under the load-deflection curve. The energy absorption capacity of the beams is shown in Figure 9. The flexural toughness of all RC beams was increased compared to the reference beam. The energy absorption capacity of beams R75, R100, R75N, and R100N compared to the reference beam has increased by 112, 116, 110, and 157%, respectively. The use of ANPs in concrete jackets has been effective and has caused the RC beam to have a higher energy absorption capacity.

According to Figure 9, it is observed that in retrofitted beams with concrete jackets containing ANPs, more collision of beam surfaces with jacket surfaces leads to

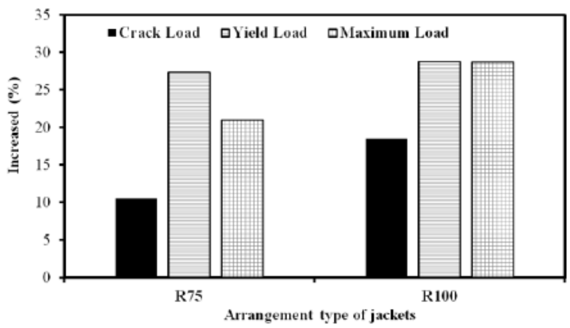

Figure 8. The percentage increase of crack, yield, and maximum loads in retrofitted beams with jackets containing ANPs compared to control beams

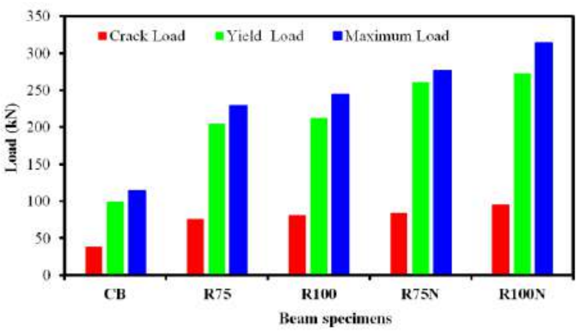

Figure 7. Comparison of crack, yield, and maximum loads

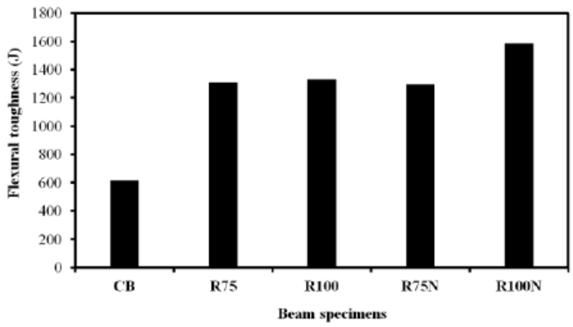

Figure 9. Comparison of flexural toughness (energy absorption capacity)

the further increase of energy absorption capacity. However, in retrofitted beams with concrete jackets without nanoparticles, the change in the type of jacket arrangement has little effect on increasing the energy absorption capacity.

Ductility capacity or ductility coefficient is defined based on the ultimate deflection ratio (Δ_u) to yield deflection (Δ_y) and is calculated using Equation (1) [11]. In Figure 10, the ductility coefficient of the studied beams was compared with each other.

$$\mu = \frac{\Delta_u}{\Delta_y} \tag{1}$$

The use of concrete jackets has caused the beams to be more ductile compared to the control beam. According to the considered variables, the beams ductility has increased by about 56 to 85%. RC jackets without nanoparticle performed much better in terms of ductility than the RC jackets containing nanoparticles; however, the nanoparticles used in the jacket have increased the yield, compressive and tensile strengths, but the deformation corresponding to the yield load is much higher compared to RC jackets without nanoparticle, which reduces the ductility. Also, Figure 10 shows that the greater the involvement of the proposed concrete jacket with the surrounding surface of the beam leads to more ductility. This is true for both jackets with and without nanoparticles; the ductility coefficient of RC beams with jackets without nanoparticles and with R100 arrangement has increased by 2 and 19%, respectively, compared to the corresponding values in RC beams with R75 arrangement.

5. FINITE ELEMENT SIMULATION

After completing the laboratory steps, RC beams retrofitted with concrete jacket containing ANPs were simulated and subjected to loading according to laboratory conditions, and their load-deflection curves were determined. After ensuring the accuracy of the method used in the simulation, which was performed using laboratory studies, variables such as the beam span length (1.5, 3, 4.5 m), the concrete jacket thickness (4, 8, and 12 cm), and the diameter of reinforcement bar used in the jacket (8, 10 and 12 mm) for retrofitting were investigated. The main beam strength is constant and equal to 21 MPa. According to the laboratory results, it was generally concluded that the use of 2.5% ANPs has a greater effect on improving the concrete mechanical properties and strength; therefore, this type of concrete characteristics have been used to simulate all concrete jackets. According to the load-deflection curves, it was concluded that when the concrete jackets are placed on 100% of the perimeter and the bottom of the beam, the response of the beam is much better than the cases where the jacket is on 75% of the perimeter and beam bottom. Therefore, the R100 model was selected in finite elements simulating the beams. The models are presented in Table 5. In this table, the letter L and the number after it represent the word length and the beam length,

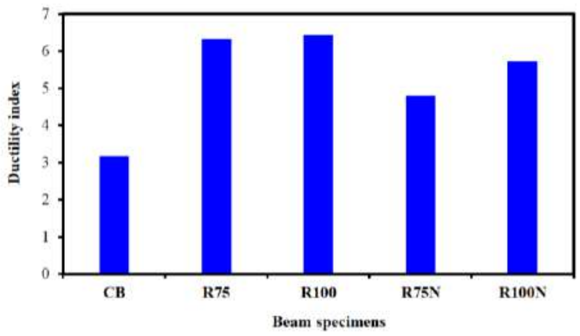

Figure 10. Comparison of ductility index

TABLE 5. Finite element models of the investigated beams

Case	Beam name	Jacket thickness (mm)	The rebar diameter used in RC Jacket	Beam span (mm)
1	L1.5	----	----	
2	L1.5-d8-t4	4		
3	L1.5-d8-t8	8	8	
4	L1.5-d8-t12	12		
5	L1.5-d10-t4	4		
6	L1.5-d10-t8	8	10	1500
7	L1.5-d10-t12	12		
8	L1.5-d12-t4	4		
9	L1.5-d12-t8	8	12	
10	L1.5-d12-t12	12		
11	L3	----	----	
12	L3-d8-t4	4		
13	L3-d8-t8	8	8	
14	L3-d8-t12	12		
15	L3-d10-t4	4		
16	L3-d10-t8	8	10	3000
17	L3-d10-t12	12		
18	L3-d12-t4	4		
19	L3-d12-t8	8	12	
20	L3-d12-t12	12		
21	L4.5	----	----	
22	L4.5-d8-t4	4		
23	L4.5-d8-t8	8	8	
24	L4.5-d8-t12	12		
25	L4.5-d10-t4	4		
26	L4.5-d10-t8	8	10	4500
27	L4.5-d10-t12	12		
28	L4.5-d12-t4	4		
29	L4.5-d12-t8	8	12	
30	L4.5-d12-t12	12		

respectively. The letter d indicates the diameter and the number after it is the diameter of the reinforcement bars used in the jacket. The letter t and the number after representing the thickness and the jacket thickness. For example, the term L1.5-d10-t12 describes a condition in which a 1.5 m long concrete beam is retrofitted by a 12 mm thickness concrete jacket and the reinforcement bars diameter used in the jacket is 10 mm. The desired outputs include damage distribution and load-deflection curve, respectively. The results are interpreted using load-deflection curves and energy absorption capacity. The effect of each studied variables and determining the most optimal states has been done by calculating the area under the load-deflection curve (energy absorption capacity), crack, yield and maximum loads and the corresponding deflections as well as ductility. The geometric and reinforcement bars characteristics of the main beams are shown in Figure 11.

The beam length and dimensions are 1500 mm and 150×200 mm, respectively. Two reinforcement bars with a diameter of 12 mm at the bottom of the beam and two reinforcement bars with a diameter of 12 mm at the top of the beam were used. Also, the shear reinforcement bars diameter was 10 mm, and their space was considered about 200 mm apart. The support conditions and how the load is applied to the beams models are shown in Figure 12. In all cases, mid-span deflection and the corresponding load are extracted as output. A schematic image of retrofitted beams is shown in Figure 13. They used reinforcement bar mesh in the jacket consists of a reinforcement bar with a diameter of 10 mm. The spaces between reinforcement bars were considered 50 mm. Finite element analysis of RC beams was performed using ABAQUS software [41].

ABAQUS can simulate numerical models of concrete for the nonlinear response. The model's dimensions are similar to the tested beams in the laboratory program. The simulation structural elements include beam rectangular cross-section, U-section jacket, the longitudinal reinforcement bars used in the beam, the transverse reinforcement bars (stirrup) used in the beam, and the jacket reinforcement bar mesh. These elements are deformable. The solid element was used to simulate concrete and the wire element was used to simulate reinforcement bars. The C3D8R element was used to simulate the concrete.

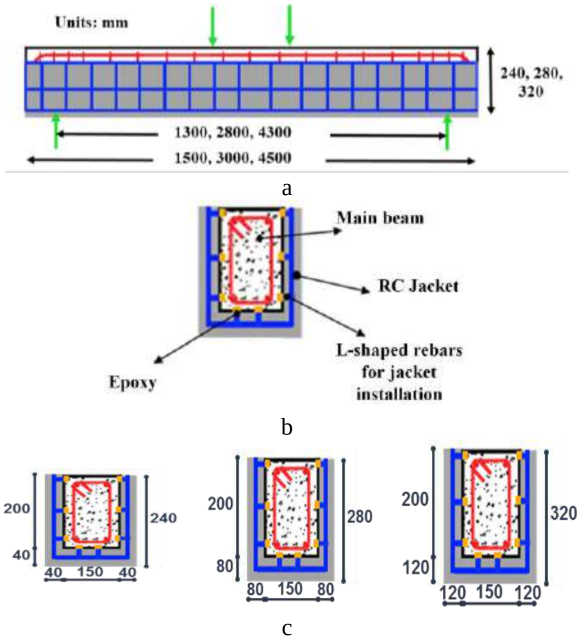

Figure 13. Schematic of retrofitted beams a: Overview of the RC beams b: Different parts of RC jacket c: The sections of retrofitted beams

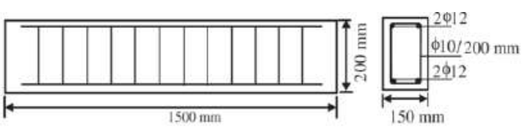

Figure 11. Geometric specifications and steel reinforcement details of beams (FEM beams)

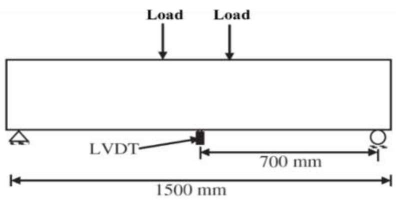

Figure 12. Support conditions of the beams

The stress-strain ideal elastic-plastic curve of reinforcement bars are applied by measuring the yield stress values. The materials behavior provided with ABAQUS (using PLASTIC settings) allows the use of a nonlinear stress-strain curve. The Von Mises yield criterion is used to define the yield isotropic of steel materials. The compressive strength of the main beam concrete was 21 MPa. Compressive and tensile strengths of the concrete used in the jacket were considered 49.14 and 3.4 MPa, respectively. According to Table 2, the concrete used in the jacket is the same as NA2.5 concrete, in which 2.5% of ANPs are used in combination with cement and SF. Based on results of the reinforcement bar tensile test, yield stress and reinforcement bars elasticity modulus is 200 (GPa) and 420 MPa, respectively. The materials used specifications are presented in Table 6. The interaction between steel reinforcement bras and concrete was defined using the embedded method. The meshing step is one of the most important steps in finite element simulations. In finite element problems, the optimal meshing method should be used, to achieve appropriate responses. For this purpose, the stress created at a specific point of the beams was considered and in the next step, the elements were doubled (the element's dimensions were halved) and the model was analyzed

TABLE 6. Specifications of materials defined in the finite element models

	f_c (MPa)	f_t (MPa)	υ
Concrete of the main beams	21	2.9	0.2
Concrete of the RC jacket	49.14	3.4	
	E_s (GPa)	f_y (MPa)	υ
Steel reinforcement rebar	200	420	0.3

again to measure the effect of this fine-tuning on the stress. This must continue until a compromise between time and the number of elements; In other words, by increasing the number of the elements, there is no significant change in the obtained response. In such a case, it can be said that the responses are converged, and increasing the number of the elements has no effect on increasing the accuracy of the response. The sweep technique was used for meshing. This method is suitable for modeling with complex surfaces. The concrete behavior is defined using concrete damaged plasticity. This model is based on the hypothesis of isotropic damage and is designed for situations where the concrete is under arbitrary loads. This model considers the effect of stiffness recovery as the result of a plastic strain, both in tension and in pressure. In RC, the post-failure behavior properties are generally determined by giving the fracture stress as a function of the crack $\tilde{\varepsilon}_t^{cr}$. Crack strain is the total strain minus the elastic strain corresponding to the non-damaged material (Equations (2) and (3)).

$$\varepsilon_c^{in} = \varepsilon_c - \varepsilon_c^{el} \tag{2}$$

$$\varepsilon_c^{in} = \frac{\sigma_c}{E_0} \tag{3}$$

$$\varepsilon_c^{\sim pl} = \varepsilon_c^{\sim in} - \frac{d_c}{(1-d_c)}\frac{\sigma_c}{E_0} \tag{4}$$

Tensile stiffening data are entered by the crack strain. When loading data is available, the data is prepared to be given as a tensile damage curve to the ABAQUS program [41]. The program automatically converts the cracking strain values to the plastic strain values using Equations (6) and (7) (Figure 14).

$$\varepsilon_t^{cr} = \varepsilon_t - \varepsilon_t^{el} \tag{5}$$

$$\varepsilon_t^{el} = \frac{\sigma_t}{E_0} \tag{6}$$

$$\varepsilon_t^{\sim pl} = \varepsilon_t^{\sim ck} - \frac{d_t}{(1-d_t)}\frac{\sigma_t}{E_0} \tag{7}$$

The compressive inelastic strain is the total strain minus the elastic strain corresponding to the material being

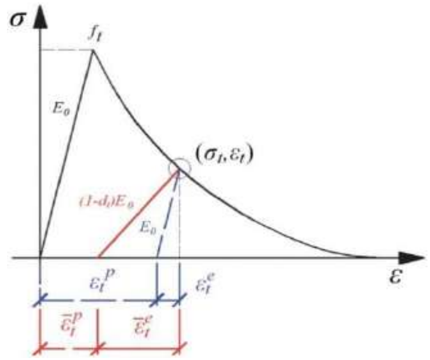

Figure 14. Cracking strain used to define tensile stiffness data [41]

damaged. The program automatically converts the inelastic strain values into plastic strain values using the following illustration (Figure 15).

6. VALIDATION

In numerical and software simulations, performing the validation process is one of the steps that lead to ensuring the analysis results. In the present study, the accuracy of the method and behavioral models used in the modeling of RC beams was evaluated and the results are presented in this section. All of the five beams were simulated using the methods and behavioral models presented in section 5 and the load-deflection and crack distribution (failure) diagrams are presented in Figures 16 and 17. Figures 16-a and 17-a compare the CB laboratory results and the finite element analysis. The failure range and the cracks created in the finite element model (FEM) and the experimental (Exp.) specimen are very close to each other. The crack angle created relative to the horizon is about 45 degrees and most of the cracks are created in the area between the support and the span center.

The crack, yield, maximum and ultimate loads of the FEM of CB are 38, 98, 112, and 48 kN, respectively, and the crack, yield, maximum and ultimate loads of the experimental specimen of the control beam are 39, 99,

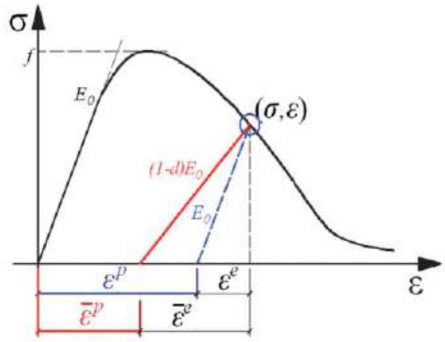

Figure 15. Inelastic compressive strain to define compressive stiffness data [41]

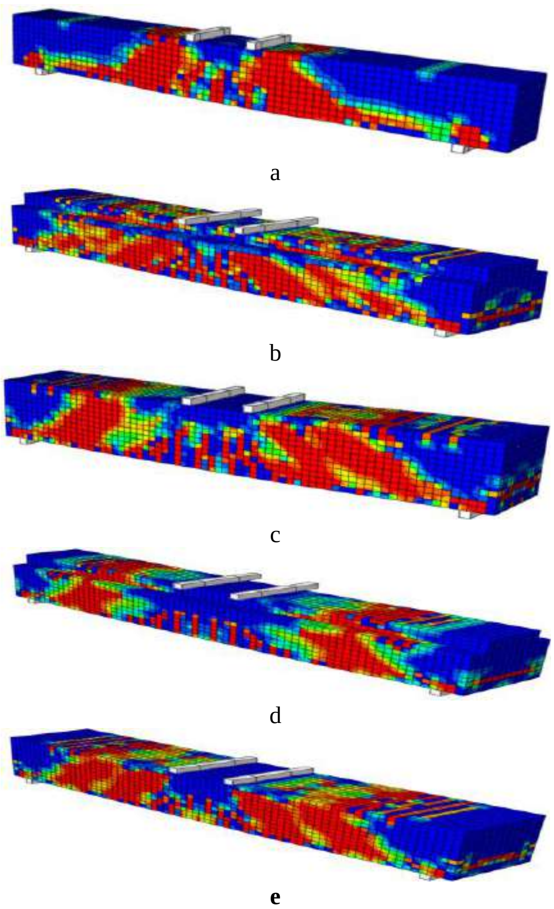

Figure 16. Damage distribution of FEMs of beams a: CB b: R75 c: R100 d: R75N e: R100N

114 and 49 kN, respectively. The difference between crack, yield, maximum and ultimate loads of FEM and Exp. of CB is 2.6, 1, 1.8, and 2%, respectively. The energy absorption capacity of FEM and Exp. of CB beam are 616 and 591, respectively and the difference between them is about 4%.

The FEM and Exp. specimen of R75 are presented in Figures 16-a and 20-b. According to the load-deflection curve, the difference between crack, yield, maximum and ultimate loads is 2.6, 12.2, 0.4, and 3.4%, respectively. Also, the energy absorption capacity of FEM and Exp. specimen of R75 is equal to 1310 and 1271 kJ, respectively and the difference between them is about 3%.

The failure distribution and load-deflection curve of FEM and Exp. specimen of R100 are presented in Figures 16-a and 17-c. This beam is retrofitted using concrete jacket without nanoparticles. These jackets were covered 100% of the beams perimeter. According to the load-deflection curve, crack, yield, maximum and ultimate loads of R100 FEM are 80, 227, 249, 125 kN, respectively. Also, the crack, yield, maximum and ultimate loads of R100 Exp. specimen are 81, 212, 244, 120 kN, respectively and the difference between them is 1.2, 1.4, 2, and 4.2 percent, respectively. Also, the energy absorption capacity of FEM and Exp. Specimen of R100 is equal to 1355 and 1331 kJ, respectively and the difference between them is about 1.8%. The crack pattern distribution in both FEM and Exp. specimen is very close to each other; in both cases, cracks have been created in the area between the center and the supports.

The failure distribution and load-deflection curves of the R75N beam obtained from FEM analysis and laboratory study are shown in Figures 16-b and 17-d. This beam is retrofitted with concrete jacket containing ANPs and SF. These jackets cover 75% of the beams perimeter. According to the load-deflection curve, the crack, yield, maximum and ultimate loads of the R75N FEM are 75, 250, 278, and 148 kN, respectively. Also, the crack, yield, maximum and ultimate loads of the R75N beam laboratory sample are 84, 261, 277, and 131 kN, respectively. The difference between the values of crack, yield, maximum and ultimate loads of the FEM and Exp. specimen of R75N is 10.7, 4.2, 0.4, and 13%, respectively. Also, the energy absorption capacity obtained from finite element analysis and laboratory study of R75N beam is 1385 and 1294 kJ, respectively.

The finite element analysis and laboratory study results of the R100N beam are shown in Figures 16-b and 17-e. This beam is retrofitted with concrete jacket containing ANPs and SF, and the concrete jacket covers

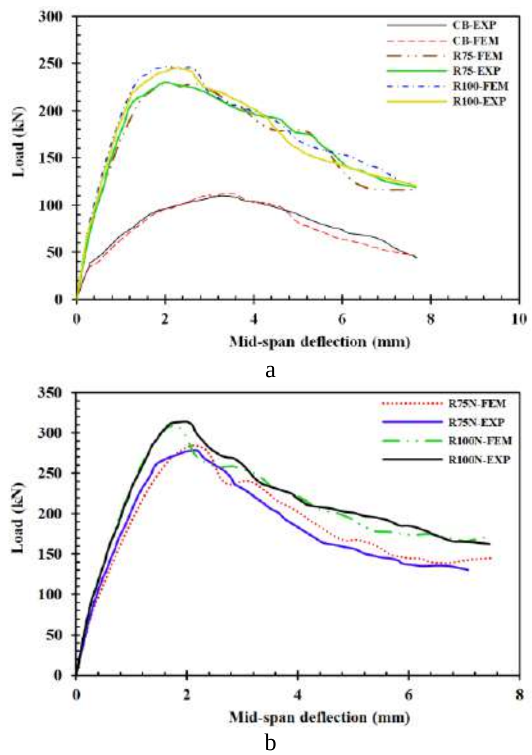

Figure 17. Load-deflection curves of the beams a: CB, R75, and R100 b: R75N and R100N

all sides and bottom of the beam. According to the load-deflection curves, the crack, yield and maximum, and ultimate loads of R100N FEM are 98, 275, 320, and 175 kN, respectively. Also, the crack, yield, maximum and ultimate loads of R100N Exp. specimen are 96, 273, 314 and 163 kN, respectively. The difference between crack, yield, maximum and ultimate loads obtained from the FEM and laboratory study are 2.1, 0.7, 1.9, and 7.4%, respectively. Crack distribution of R100N beam shows that the use of ANPs affects reducing crack distribution in beams.

Energy absorption capacity, crack, yield, maximum and ultimate loads are presented in Table 7. In this table, the percentage difference of load values obtained from finite element analysis (FEM) to the corresponding values in the laboratory study (EXP) is obtained. The difference of crack load, yield load, maximum load, ultimate load and, energy absorption capacity is about 2.1 to 10.7%, 0.7 to 12.2 %,.4 to 1.9%, 2 to 13 %, and 1.4 to 7%, respectively. According to the load-deflection curves and the comparison of laboratory specimens and numerical models simulated by ABAQUS software, it is observed that the maximum load and deflection values of experimental specimens and finite elements are close to each other; therefore, the results of the method used in this study, which is performed using ABAQUS software, have a relatively good agreement with the laboratory results.

7. FINITE ELEMENT ANALYSIS RESULTS

7. 1. Energy Absorption Capacity The flexural strength (energy absorption capacity) and its percentage increase compared to the control beams are shown in Figure 18. The use of reinforcement concrete jacket containing ANPs, depending on the jacket thickness, the number of reinforcement bars used in the jacket, and the length of the beam span, increased the flexural strength of the beams about 2.55 to 5.55 times compared to control specimens. The increase of flexural strength in beams retrofitted with RC jacket containing ANPs that have longer spans is much higher than beams with shorter spans. For example, the increase in flexural strength of the L4.5-d12-t12 beam is 5.47 times compared to the control specimen; this is while the increase in flexural strength of the L1.5-d12-t12 beam is 4.94 times compared to the control specimen.

The effect of changes in the thickness and diameter of the jacket of the reinforcement bars used in the jacket on the flexural strength of RC beams with 1.5, 3, and 4.5 meters length is investigated in Figure 19. The reinforcement bars area used in concrete jacket containing ANPs has a significant effect on increasing the beams flexural strength. Thus, in beams with lengths of 1.5, 3, and 4.5 meters, increasing the steel reinforcement bars diameter to 1.5 times increased the flexural strength of the beams by 76, 117 and 98%, respectively. According to Figures 19-b and 19-c, increasing the thickness of the concrete jacket has little effect on increasing the beams flexural strength, and only in a few beams, the flexural strength increased. Therefore, in terms of flexural strength and economic issues, the use of RC jackets containing ANPs with less thickness is a better option; because increasing the

TABLE 7. Comparing the results of laboratory and finite element study

Beam name	Crack load P_{cr} (kN)			Yield load P_y (kN)			Maximum Load P_{max} (kN)			Ultimate Load P_u (kN)			Flexural toughness (J)		
	EXP	FEM	Error (%)	EXP	FEM	Error (%)	EXP	FEM	Error (%)	EXP	FEM	Error (%)	EXP	FEM	Error (%)
CB	39	38	2.6	99	98	1	114	112	1.8	49	48	2	616	591	1.4
R75	76	74	2.6	205	180	12.2	229	228	0.4	119	123	3.4	1310	1271	3
R100	81	80	1.2	212	227	1.4	244	249	2	120	125	4.2	1331	1355	1.8
R75N	84	75	10.7	261	250	4.2	277	278	0.4	131	148	13	1294	1385	7
R100N	96	98	2.1	273	275	0.7	314	320	1.9	163	175	7.4	1587	1549	2.4

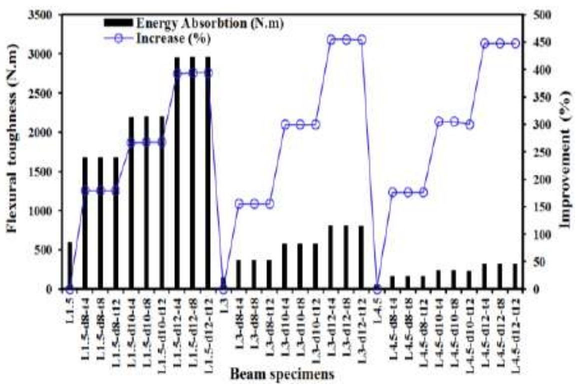

Figure 18. Comparison of flexural strength (energy absorption capacity) of the finite element model of the beams

thickness has little effect on improving the flexural strength result.

The bearing capacity of retrofitted beams with RC jackets containing ANPs did not change significantly due to the change in jacket thickness. Increasing the jacket thickness had little effect on increasing the beams bearing capacity. Increasing the diameter of jackets reinforcement bars from 8 mm to 12 mm for all three beam types with different lengths had a significant effect on increasing the beams bearing capacity. The flexural strength of retrofitted beams with 1.5 m length, which reinforcement bars with 10 and 12 mm diameter were used in jackets, were increased 29 and 85%, respectively, compared to the retrofitted beams with 8 mm rebar in jackets. The energy absorption capacity of the beams with a length of 4.5 meters, in which RC jackets with 10 and 12 mm rebar were used increased by 90 and 34%, respectively, compared to jackets with 8 mm bars.

7. 2. The Maximum Bearing Load The bearing capacity (section resistance moment) and the increase ratio compared to the control beams are presented in Figure 20. The proposed retrofitting method increased the bearing capacity of the beams with a length of 1.5, 3, and 4.5 m about 2.87 to 5.05 times, 2.31 to 4.55, and 2.38 to 4.57 times, respectively.

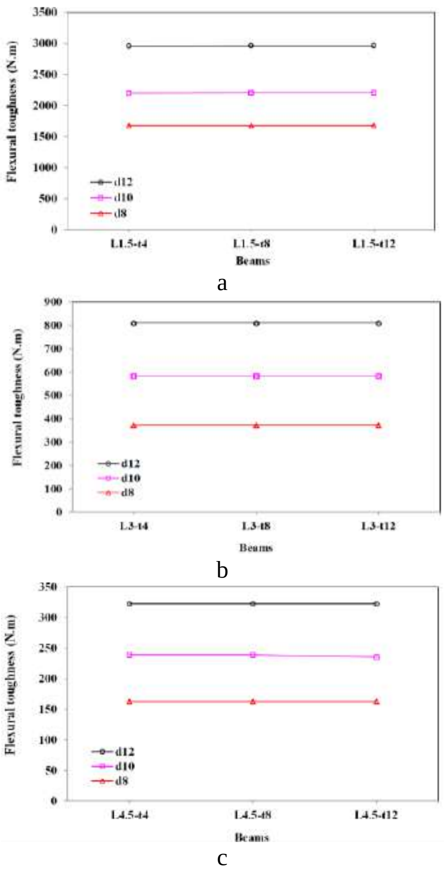

Figure 19. Investigation of the effect of changing the jackets thickness and the diameter of the rebars used in the jackets on the flexural toughness of the beams a: 1.5 meters beam b: 3 meters beam c: 4.5 meters beam

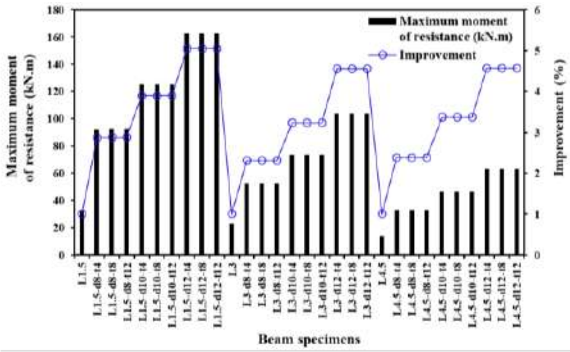

Figure 20. Comparison of the bearing capacity (section resistance moment)

7. 3. Yield Load The yield loads of the thirty beams and their increased values relative to the reference beams are shown in Figure 21. The use of RC jacket containing ANPs has increased the yield load of 1.5, 3, and 4.5 meters beams depending on the diameter of the jacket reinforcement bars and the thickness of the jacket about 2.96 to 5.43, 2.29 to 4.4, and 2.09 to 3.93 times, respectively. According to Figure 21, the percentage of yield load has increased in beams with smaller spans. With increasing the span length, the effect of the proposed method on the increase percentage of yield load has decreased. As changes in the energy absorption capacity and bearing capacity obtained, the yield load of the reinforced beams under study does not change significantly due to changes in the jacket thickness. The percentage of steel used in concrete jackets has an effect on improving the yield load. For example, in 1.5, 3 and 4.5 meters beams that have been retrofitted by concrete jackets containing 12 mm diameter rebars, the yield load is approximately 84, 92 and 83% more than the 1.5, 3 and 4.5 m beams which reinforced with 8 mm diameter rebars.

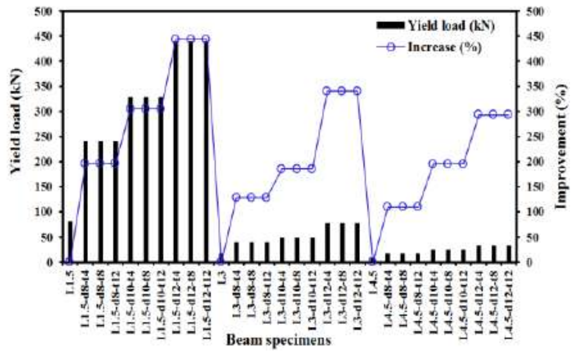

Figure 21. Comparison of the yield load of the examined beams

7. 4. Crack Load The crack loads of the FEM beams is presented in Figure 22. In all cases, the crack load of the retrofitted beams is increased. The proposed concrete jacket has been able to increase the crack load of 1.5, 3 and 4.5 meters beams by 2.03 to 5 times, 3.5 to 7.25 times, and 1.38 to 3.45 times, respectively.

Figures 23 to 25 investigate the effect of changes in the thickness of the jackets and the diameter of the jackets rebars on the percentage of increase in the crack load of beams with a length of 1.5, 3, and 4.5 meters. As can be seen, increasing the thickness of concrete jackets in beams with a span of 1.5 meters has been effective and has been able to increase the resistance of the beam to cracking. For example, the crack load of the L1.5-d12-t12 beam has increased 4 times (400%) compared to the reference beam; This is while the L1.5-d12-t4 beam is 130% more than the reference beam. As the length of the beam increases, the thickness does not play a significant role in improving the crack load (Figures 24 and 25).

Increasing the thickness of concrete jackets in beams with a span of 1.5 meters is effective and has been able to increase the crack load. For example, the crack load of the L1.5-d12-t12 beam has increased 4 times (400%) compared to the reference beam; However, the L1.5-d12-t4 beam is 130% larger than the reference beam. As the length of the beam increases, the thickness does not play a significant role in improving the crack load (Figures 27 and 28).

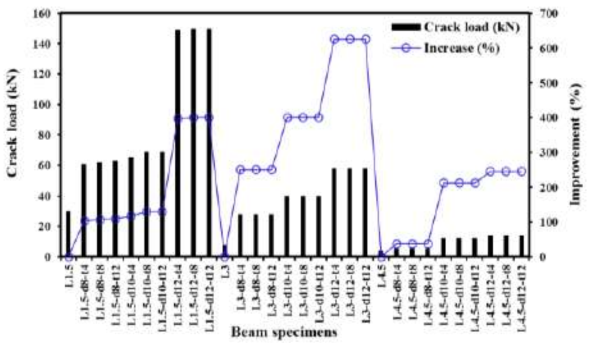

Figure 22. Comparison of the crack load of beams understudy

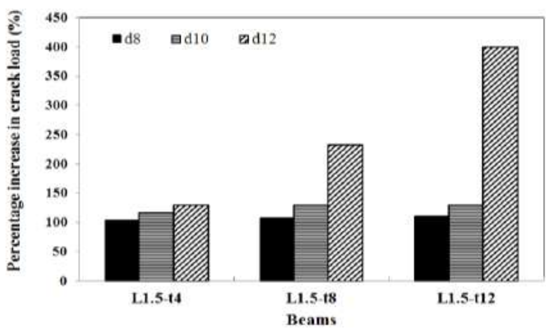

Figure 23. Investigation of the effect of change in the jacket thickness and the diameter of the rebars used in the jacket on the percentage of increase in crack load (1.5-meter beam**)**

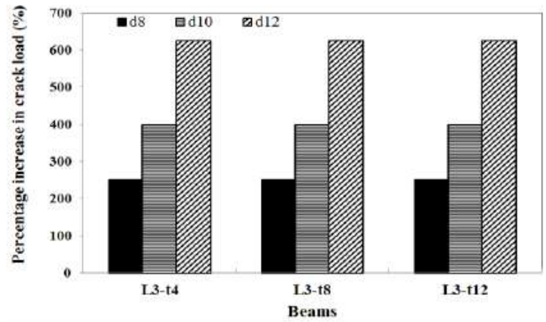

Figure 24. Investigation of the effect of change in the jacket thickness and the diameter of the rebars used in the jacket on the percentage of increase in crack load (3-meter beam**)**

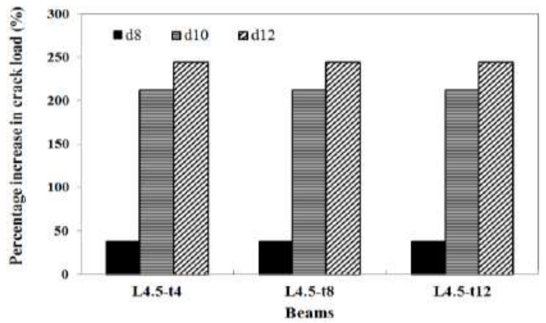

Figure 25. Investigation of the effect of change in the jacket thickness and the diameter of the rebars used in the jacket on the percentage of increase in crack load (4.5-meter beam**)**

7. 5. Comparison of Crack, Yield, and Ultimate Deflections The values of crack, yield, and ultimate deflections of the beams are presented in Figures 26-28.

The use of concrete jackets containing ANPs has a little role in the ultimate deformation of the beams and no significant difference is observed between the ultimate deflection of the beams. Concrete jackets reduced crack and yield deformations. The crack deflection of retrofitted beams with lengths of 1.5, 3, and 4.5 meters was reduced approximately between 55 to 65, 65 to 75, and 256 to 520%, respectively.

The yield deflection of the beams with concrete jackets containing ANPs is reduced in all cases compared

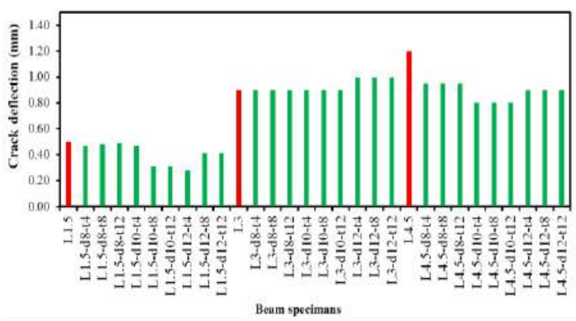

Figure 26. Comparison of crack deflections

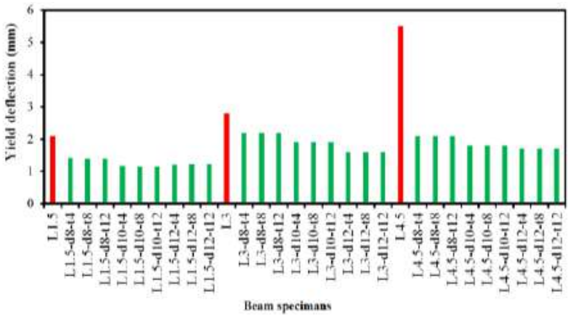

Figure 27. Comparison of yield deflections

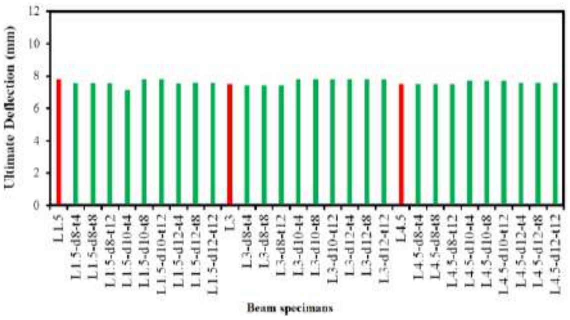

Figure 28. Comparison of ultimate deflections

to control beams. This percentage reduction is much higher in longer beams. The yield deflection of the retrofitted beams with concrete jackets containing ANPs is reduced in all cases compared to control beams.

7. 6. Ductility Capacity The ductility factor of the beams is presented in Figure 29. Concrete jackets containing ANPs have increased the ductility of 1.5 meters of concrete beams by 1.44 to 1.81 times, depending on the thickness and diameter of the rebars. Also, the ductility coefficient of retrofitted beams with a span length of 3 meters has increased approximately 1.26 to 1.82 times. The ductility coefficient of retrofitted beams with a span length of 4.5 meters has increased approximately 2.63 to 3.29 times compared to the reference beam.

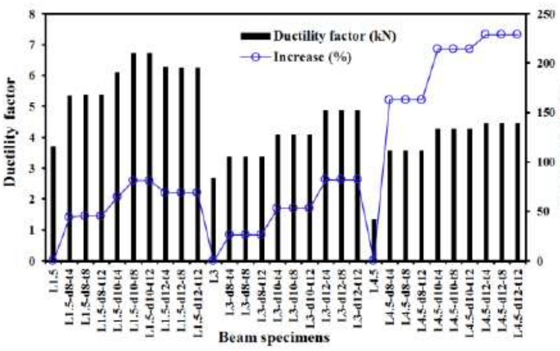

Figure 29. Comparison of ductility factor

8. SUMMARY AND CONCLUSIONS

In this paper, laboratory and numerical investigation of RC beams were performed using RC jackets with SCC containing ANPs and SF. The laboratory study was performed in two stages. In the first stage, the properties of hardened concrete (compressive, tensile, and flexural strengths, water absorption) and the properties of fresh concrete (slump flow, T50, funnel V, box L) of SCC containing ANPs were investigated. In the next step, several beams were made and were retrofitted using the proposed concrete jackets. ANPs were used in 13 different mixing schemes (0 to 3% by weight of cement). Also, the amount of SF in all specimens was considered constant. After examining the characteristics of fresh and hardened concretes containing ANPs and determining the most optimal design (according to the experiments), the retrofitting of RC beams using RC jackets with SCC jackets containing ANPs was investigated. For this purpose, 1.4 metes RC beams with the same dimensions and specifications of steel reinforcement were made and subjected to four-point loading in the conditions with and without retrofitting. Ordinary concrete was used in the concrete jacket once and ANPs (the most optimal design) were used again.

Concrete jackets once covered all of the perimeter and bottom surfaces of the beams and again 75% of the perimeter and bottom surfaces. After completing the laboratory steps, RC beams were simulated according to laboratory conditions using FEM and ABAQUS software. A parametric study was performed and parameters such as beam length (1.5, 3, 4.5 m), concrete jacket thickness (4, 8, and 12 cm), and the diameter of rebars used in the jacket (8, 10, and 12 mm) was examined. The most important results are presented following:

- The addition of ANPs reduced the pore size of the concrete specimens and makes them denser. This can be due to the effects of nanoparticle filling, pozzolanic properties as well as swelling of ANPs.
- Crushing of concrete is one of the common problems in the elements of concrete structures. In this study, it has been observed that the concrete crushing without nanoparticles is more than the concrete contain nanoparticles. Because nanoparticles affect the concrete matrix and reduce its crushing. Reducing the brittleness of concrete by using ANPs and silica fume in RC beams can reduce the cost of reinforcement and maintenance after low to medium magnitude earthquakes.
- The use of RC jackets containing ANPs has increased the yield load by about 164 to 176%, depending on the arrangement of the jacket. Also, the yield load of beams that are not coated with nanoparticles has increased by about 107 to 114%.
- The results show that the use of concrete jackets without and containing nanoparticles, depending on the

arrangement they have, can increase the bearing capacity of reinforced concrete beams by about 107 to 175 percent. Concrete jackets increase the flexural stiffness of the beams by enclosing them around the beam and increasing the moment of inertia of the beam, making the beams able to withstand more loads.

- The flexural strength of all reinforced beams is increased compared to the reference beam. So that the energy absorption capacity of each of the beams R75, R100, R75N, and R100N compared to the reference beam has increased by 112, 116, 110, and 157 %, respectively. The use of nanoparticles in concrete jackets has been effective and has caused the RC beam to have a higher energy absorption capacity.
- In retrofitted beams with a concrete jacket containing ANPs, the more surfaces of the beam are involved with the jacket, the more energy absorption capacity will be. However, in retrofitted beams with concrete jackets without nanoparticles, the change in the type of jacket arrangement has little effect on increasing the energy absorption capacity.
- The use of concrete jackets has caused the behavior of the beams to be more ductile compared to the control beam. The ductility of the beams has increased by about 56 to 85%.
- The area of rebars used in concrete jackets containing ANPs has a significant effect on increasing the flexural strength of beams; Thus, in beams with lengths of 1.5, 3, and 4.5 meters, increasing the diameter of the steel rebar to 1.5 times increased the flexural strength of the beams by 76, 117 and 98%, respectively.
- In terms of flexural strength and economic issues, the use of RC jackets containing nanoparticles with a smaller thickness is a desire option. Because increasing the thickness has little effect on improving the resulting flexural strength.
- The area of rebars used in concrete jackets containing ANPs has a significant effect on increasing the flexural strength of beams. Thus, in beams with lengths of 1.5, 3, and 4.5 meters, increasing the diameter of the steel rebar to 1.5 times, increased the flexural strength of the beams by 76, 117 and 98%, respectively.

According to the results of the present study, the use of ANPs in RC jackets to retrofit RC beams is considered as a suitable solution to increase the bearing capacity. However, retrofitting of beams with this method can depend on several factors. Therefore, to develop the present study, the following suggestions are presented:

- Investigating the effect of dynamic loads on the beams retrofitted with RC jackets containing ANPs.
- Investigating the movement (slip) of the jackets containing nanoparticles on the surface of the old concrete beam.
- Investigating the use of other nanoparticles such as silica oxide nanoparticles and clay nanoparticles in RC jackets for retrofitting of concrete beams.

9. REFERENCES

1. Osman, B. H., Wu, E., Ji, B., and S Abdelgader, A. M., "A state of the art review on reinforced concrete beams with openings retrofitted with FRP", ***International Journal of Advanced Structural Engineering***, Vol. 8, No. 3, (2016), 253–267. doi:10.1007/s40091-016-0128-7

2. Negro, P., and Mola, E., "A performance based approach for the seismic assessment and rehabilitation of existing RC buildings", ***Bulletin of Earthquake Engineering***, Vol. 15, No. 8, (2017), 3349–3364. doi:10.1007/s10518-015-9845-8

3. Seifi, A., Hosseini, A., Marefat, M. S., and Zareian, M. S., "Improving seismic performance of old-type RC frames using NSM technique and FRP jackets", ***Engineering Structures***, Vol. 147, (2017), 705–723. doi:10.1016/j.engstruct.2017.06.034

4. Durgadevi, S., Karthikeyan, S., Lavanya, N., and Kavitha, C., "A review on retrofitting of reinforced concrete elements using FRP", ***Materials Today: Proceedings***, (In Press), (2020). doi:10.1016/j.matpr.2020.03.148

5. Jose, J., Nagarajan, P., and Remanan, M., "Utilisation of Ultra-High Performance Fiber Reinforced Concrete(UHPFRC) for Retroffiting – a Review", ***IOP Conference Series: Materials Science and Engineering***, Vol. 936, No. 1, (2020), 012033. doi:10.1088/1757-899X/936/1/012033

6. Kafi, M. A., Kheyroddin, A., and Omrani, R., "New Steel Divergent Braced Frame Systems for Strengthening of Reinforced Concrete Frames", ***International Journal of Engineering, Transaction A: Basics***, Vol. 33, No. 10, (2020), 1886–1896. doi:10.5829/ije.2020.33.10a.07

7. Jahangir, H., and Bagheri, M., "Evaluation of Seismic Response of Concrete Structures Reinforced by Shape Memory Alloys (Technical Note)", ***International Journal of Engineering, Transaction C: Aspects***, Vol. 33, No. 3, (2020), 410–418. doi:10.5829/ije.2020.33.03c.05

8. Zhu, Y., Zhang, Y., Hussein, H. H., and Chen, G., "Flexural strengthening of reinforced concrete beams or slabs using ultra-high performance concrete (UHPC): A state of the art review", ***Engineering Structures***, Vol. 205, (2020), 110035. doi:10.1016/j.engstruct.2019.110035

9. Tawfik, T. A., Aly Metwally, K., EL-Beshlawy, S. A., Al Saffar, D. M., Tayeh, B. A., and Soltan Hassan, H., "Exploitation of the nanowaste ceramic incorporated with nano silica to improve concrete properties", ***Journal of King Saud University - Engineering Sciences***, (In Press), (2020). doi:10.1016/j.jksues.2020.06.007

10. Sangi, M., Vasegh Amiri, J., Abdollahzadeh, G., and Dehestani, M., "Experimental study on fracture behavior of notched self-consolidating concrete beam strengthened with off-axis CFRP sheet", ***Structural Concrete***, Vol. 20, No. 6, (2019), 2122–2137. doi:10.1002/suco.201800204

11. Shadmand, M., Hedayatnasab, A., and Kohnehpooshi, O., "Retrofitting of Reinforced Concrete Beams with Steel Fiber Reinforced Composite Jackets", ***International Journal of Engineering, Transaction B: Applications***, Vol. 33, No. 5, (2020), 770–783. doi:10.5829/ije.2020.33.05b.08

12. Rahmani, I., Maleki, A., and Lotfollahi-Yaghin, M. A., "A Laboratory Study on the Flexural and Shear Behavior of RC Beams Retrofitted with Steel Fiber-Reinforced Self-compacting Concrete Jacket", ***Iranian Journal of Science and Technology, Transactions of Civil Engineering***, (2020), 1–17. doi:10.1007/s40996-020-00547-x

13. Trang, G. T. T., Linh, N. H., Linh, N. T. T., and Kien, P. H., "The Study of Dynamics Heterogeneity in SiO2 Liquid", ***HighTech and Innovation Journal***, Vol. 1, No. 1, (2020), 1–7. doi:10.28991/HIJ-2020-01-01-01

14. Pinheiro, A. P., "Architectural Rehabilitation and Sustainability of Green Buildings in Historic Preservation", ***HighTech and Innovation Journal***, Vol. 1, No. 4, (2020), 172–178. doi:10.28991/HIJ-2020-01-04-04

15. Das, K., Sen, S., and Biswas, P., "A Review Paper – on the Use of Nanotechnology in Construction Industry", Proceedings of Industry Interactive Innovations in Science, Engineering & Technology (I3SET2K19), (2020), 1–3. doi:10.2139/ssrn.3526716

16. Qasim, O. A., and Al-Ani, S. A., "Effect of nano-silica silica fume and steel fiber on the mechanical properties of concrete at different ages", AIP Conference Proceedings, Vol. 2213, No. 1, (2020), 020198. doi:10.1063/5.0000209

17. Shaiksha Vali, K., Murugan, B. S., Reddy, S. K., and Noroozinejad Farsangi, E., "Eco-friendly Hybrid Concrete Using Pozzolanic Binder and Glass Fibers", ***International Journal of Engineering, Transactions A: Basics***, Vol. 33, No. 7, (2020), 1183–1191. doi:10.5829/ije.2020.33.07a.03

18. Ghanbari, M., Kohnehpooshi, O., and Tohidi, M., "Experimental Study of the Combined Use of Fiber and Nano Silica Particles on the Properties of Lightweight Self Compacting Concrete", ***International Journal of Engineering, Transaction B: Applications***, Vol. 33, No. 8, (2020), 1499–1511. doi:10.5829/ije.2020.33.08b.08

19. Potapov, V., Efimenko, Y., Fediuk, R., and Gorev, D., "Effect of hydrothermal nanosilica on the performances of cement concrete", ***Construction and Building Materials***, Vol. 269, (2021), 121307. doi:10.1016/j.conbuildmat.2020.121307

20. Nazari, A., and Riahi, S., "Microstructural, thermal, physical and mechanical behavior of the self compacting concrete containing SiO2 nanoparticles", ***Materials Science and Engineering: A***, Vol. 527, Nos. 29–30, (2010), 7663–7672. doi:10.1016/j.msea.2010.08.095

21. Nazari, A., and Riahi, S., "RETRACTED: Al2O3 nanoparticles in concrete and different curing media", ***Energy and Buildings***, Vol. 43, No. 6, (2011), 1480–1488. doi:10.1016/j.enbuild.2011.02.018

22. Mosalman, S., Rashahmadi, S., and Hasanzadeh, R., "The Effect of TiO_2 Nanoparticles on Mechanical Properties of Poly Methyl Methacrylate Nanocomposites", ***International Journal of Engineering, Transactions B: Applications***, Vol. 30, No. 5, (2017), 807–813. doi:10.5829/idosi.ije.2017.30.05b.22

23. Nazari, A., Riahi, S., Riahi, S., Shamekhi, S. F., and Khademno, A., "Influence of Al_2O_3 nanoparticles on the compressive strength and workability of blended concrete Enhancing the adhesion of diamond-like carbon films to steel substrates using silicon-containing interlayers View project Influence of Al_2O_3 nanoparticles ", ***Journal of American Science***, Vol. 6, No. 5, (2010), 6–9.

24. Sobolev, K., Flores, I., Hermosillo, R., and Torres-Martínez, L. M., "Nanomaterials and Nanotechnology for High-Performance Cement Composites", Proceedings of ACI Session on Nanotechnology of Concrete: Recent Developments and Future Perspectives, (2006), 91–118.

25. Joshaghani, A., Balapour, M., Mashhadian, M., and Ozbakkaloglu, T., "Effects of nano-TiO_2, nano-Al_2O_3, and nano-Fe_2O_3 on rheology, mechanical and durability properties of self-consolidating concrete (SCC): An experimental study", ***Construction and Building Materials***, Vol. 245, (2020), 118444. doi:10.1016/j.conbuildmat.2020.118444

26. Meddah, M. S., Praveenkumar, T. R., Vijayalakshmi, M. M., Manigandan, S., and Arunachalam, R., "Mechanical and microstructural characterization of rice husk ash and Al_2O_3 nanoparticles modified cement concrete", ***Construction and Building Materials***, Vol. 255, (2020), 119358. doi:10.1016/j.conbuildmat.2020.119358

27. Li, Z., Wang, H., He, S., Lu, Y., and Wang, M., "Investigations on the preparation and mechanical properties of the nano-alumina reinforced cement composite", ***Materials Letters***, Vol. 60, No. 3, (2006), 356–359. doi:10.1016/j.matlet.2005.08.061

28. Oltulu, M., and Şahin, R., "Effect of nano-SiO_2, nano-Al_2O_3 and nano-Fe2O3 powders on compressive strengths and capillary water absorption of cement mortar containing fly ash: A comparative study", ***Energy and Buildings***, Vol. 58, (2013), 292–301. doi:10.1016/j.enbuild.2012.12.014

29. Behfarnia, K., and Salemi, N., "The effects of nano-silica and nano-alumina on frost resistance of normal concrete", ***Construction and Building Materials***, Vol. 48, (2013), 580–584. doi:10.1016/j.conbuildmat.2013.07.088

30. Ismael, R., Silva, J. V., Carmo, R. N. F., Soldado, E., Lourenço, C., Costa, H., and Júlio, E., "Influence of nano-SiO_2 and nano-Al2O3 additions on steel-to-concrete bonding", ***Construction and Building Materials***, Vol. 125, (2016), 1080–1092. doi:10.1016/j.conbuildmat.2016.08.152

31. Niewiadomski, P., Stefaniuk, D., and Hoła, J., "Microstructural Analysis of Self-compacting Concrete Modified with the Addition of Nanoparticles", ***Procedia Engineering***, Vol. 172, (2017), 776–783. doi:10.1016/j.proeng.2017.02.122

32. Ghazanlou, S. I., Jalaly, M., Sadeghzadeh, S., and Korayem, A. H., "A comparative study on the mechanical, physical and morphological properties of cement-micro/nanoFe_3O_4 composite", ***Scientific Reports***, Vol. 10, No. 1, (2020), 1–14. doi:10.1038/s41598-020-59846-y

33. Heidarzad Moghaddam, H., Maleki, A., and Lotfollahi-Yaghin, M. A., "Durability and Mechanical Properties of Self-compacting Concretes with Combined Use of Aluminium Oxide Nanoparticles and Glass Fiber", ***International Journal of Engineering, Transaction A: Basics***, Vol. 34, No. 1, (2021), 26–38. doi:10.5829/ije.2021.34.01a.04

34. Zeinolabedini, A., Tanzadeh, J., and Mamodan, M. T., "Laboratory Investigation of Ultra-High–Performance Fiber-Reinforced Concrete Modified with Nanomaterials", ***Journal of Testing and Evaluation***, Vol. 49, No. 1, (2021), 20180806. doi:10.1520/JTE20180806

35. Muzenski, S., Flores-Vivian, I., and Sobolev, K., "Hydrophobic modification of ultra-high-performance fiber-reinforced composites with matrices enhanced by aluminum oxide nano-fibers", ***Construction and Building Materials***, Vol. 244, (2020), 118354. doi:10.1016/j.conbuildmat.2020.118354

36. Faez, A., Sayari, A., and Manie, S., "Mechanical and Rheological Properties of Self-Compacting Concrete Containing Al2O3 Nanoparticles and Silica Fume", ***Iranian Journal of Science and Technology, Transactions of Civil Engineering***, Vol. 44, No. S1, (2020), 217–227. doi:10.1007/s40996-019-00339-y

37. Self-Compacting Concrete European Project Group, The European guidelines for self-compacting concrete: Specification, production and use. International Bureau for Precast Concrete (BIBM), (2005).

38. ASTM Standard C39/C39M-18, Standard test method for compressive strength of cylindrical concrete specimens, ASTM International, West Conshohocken PA, (2018).

39. ASTM Standard C496/C496M-17 Standard test method for splitting tensile strength of cylindrical concrete specimens, ASTM International, West Conshohocken PA, (2017).

40. ASTM C642-13, Standard Test Method for Density, Absorption, and Voids in Hardened Concrete, ASTM International, West Conshohocken, PA, (2013).

41. Hibbitt, H., Karlsson, B., and Sorensen, E., ‘ABAQUS user’s manual.’ Providence, RI: Dassaulat Systems Simulia Corp, (2016).

42. ASTM Standard C33/C33M-18, Standard specification for concrete aggregates. ASTM International, West Conshohocken

PA, (2018).

43. Hosen, M. A., Jumaat, M. Z., Alengaram, U. J., and Ramli Sulong, N. H., "CFRP strips for enhancing flexural performance of RC beams by SNSM strengthening technique", ***Construction and Building Materials***, Vol. 165, (2018), 28–44. doi:10.1016/j.conbuildmat.2017.12.052

Persian Abstract

چکیده

در مطالعه حاضر به بررسی آزمایشگاهی و عددی مقاوم‌سازی تیرهای بتن مسلح، با استفاده از روکش‌های بتنی مسلح با بتن خودتراکم حاوی نانو ذرات اکسید آلومینیوم و میکروسیلیس پرداخته شد. مطالعه آزمایشگاهی در دو مرحله انجام شد. در مرحله اول، به بررسی خواص بتن تازه (جریان اسلامپ، T50، قیف V، جعبه L) و خواص بتن سخت شده (مقاومت‌های فشاری، کششی و خمشی، جذب آب) حاوی نانوذرات آلومینیوم (۰ تا ۳ درصد وزنی سیمان) و میکروسیلیس (۱۰ درصد وزنی سیمان) پرداخته شد. پس از بررسی مشخصات بتن تازه و سخت شده حاوی نانو ذرات آلومینیوم و تعیین بهینه‌ترین طرح (با توجه به آزمایش‌های انجام شده) به بررسی مقاوم‌سازی تیرهای بتن مسلح با استفاده از روکش‌های بتنی مسلح با بتن خودتراکم حاوی نانو ذرات آلومینیوم و میکروسیلیس پرداخته شد. برای این منظور پنج تیر بتن مسلح ۱/۴ متری با ابعاد و مشخصات فولادگذاری یکسان ساخته شدند و در حالت‌های با و بدون مقاوم‌سازی تحت بارگذاری چهار نقطه‌ای قرار گرفتند. در روکش بتنی یکبار از بتن معمولی و بار دیگر از بتن حاوی نانو ذرات اکسید آلومینیوم (بهینه ترین طرح) استفاده شد. روکش‌های بتنی یکبار در تمام سطوح پیرامونی و پایین تیرها و بار دیگر ۷۵ درصد سطوح پیرامونی و پایین آنها را پوشش دادند. پس از اتمام مراحل آزمایشگاهی، تیرهای بتن مسلح مطابق با شرایط آزمایشگاه با استفاده از روش اجزاء محدود و نرم افزار ABAQUS شبیه‌سازی شدند. پس از حصولِ اطمینان از دقت روش در شبیه‌سازی بکار برده شده، تحلیل پارامتریک انجام شد و پارامترهایی نظیر طول دهانه تیر (۱/۵، ۳، ۴/۵ متر)، ضخامت روکش بتنی (۴، ۸ و ۱۲ سانتی‌متر) و قطر میلگردهای استفاده شده در روکش (۸، ۱۰ و ۱۲ میلی‌متر) مورد بررسی قرار گرفت. نتایج حاصل از تحلیل اجزاء محدود تیرها نشان داد که استفاده از روکش‌های بتنی مسلح حاوی نانوذرات آلومینیوم بسته به ضخامت روکش، تعداد میلگردهای مورد استفاده در روکش و طول دهانه تیر، طاقت خمشی تیرها را حدوداً به مقدار ۱۵۵ تا ۴۴۷ درصد افزایش داده است. خرد شدن پوشش بتنی یکی از مسائل متداول در عناصر سازه‌ای بتنی می‌باشد. در این مطالعه مشاهده شده است که خرد شدگی بتن بدون نانوذرات در مقایسه با بتن حاوی نانوذرات شدید است، زیرا نانوذرات ماتریس بتن را تحت تاثیر قرار می‌دهد و خرد شدگی آن را کاهش می‌دهند.

IJE TRANSACTIONS B: Applications Vol. 34, No. 05, (May 2021) 1213-1224

International Journal of Engineering

Journal Homepage: www.ije.ir

Analytical Evaluation of Core Losses, Thermal Modelling and Insulation Lifespan Prediction for Induction Motor in Presence of Harmonic and Voltage Unbalance

M. Ghods[a], J. Faiz*[a], A. A. Pourmoosa[a], S. Khosrogorji[b]

[a] *Centre of Excellence on Applied Electromagnetic Systems, School of Electrical and Computer Engineering, College of Engineering, University of Tehran, Tehran, Iran*
[b] *Faculty of Electrical Engineering, University of Shahid Beheshti, Tehran, Iran*

PAPER INFO

Paper history:
Received 03 August 2020
Received in revised form 31 March 2021
Accepted 01 April 2021

Keywords:
Induction Motor
Thermal Modeling
Insulation Lifespan
Harmonic
Voltage Unbalance

ABSTRACT

Electrical motors are the ubiquitous workhorses of the industry, working over wide range of conditions and applications. Modern motors, designed to exact ratings using new materials and improved manufacturing techniques, are now much smaller but have higher loadings. They are being operated much close to the overload point than ever before. To ensure a satisfactory life span for the motor, temperature rise must be limited to the safe values. This paper proposes an analytical approach to estimate core losses of induction motor supplied by either harmonic content or voltage unbalance source. A thermal model based on the thermal lumped parameters is introduced and used to predict the insulation lifespan of the motors. Lumped parameters network of the motor is developed based on dimensions of the motor, thermal resistances, thermal capacitances, and loss sources. Then, the model is used to estimate the temperatures in different parts of the machine and the insulation lifespan of the motor. Finally, the predicted results using the model are verified by experiments.

doi*: 10.5829/ije.2021.34.05b.14*

NOMENCLATURE

P_c	Core losses (W)	*VUF*	Voltage unbalance factor
k_h	Steinmetz coefficient	T	Maximum temprature (C)
f	Fundamental frequence (Hz)	F	Loading coefficient
P_e	Eddy current loss (W)	L_x	Percent lifespan at x%
B	Flux density (T)	*HIC*	Halving interval
k_e	Eddy current coefficient	T_c	Total permissible temperature of the insulation,
θ_h	Phase angle of the h^{th} harmonic	T_x	Hotspot temperature of the insulation

1. INTRODUCTION

Nowadays, inverter-fed drives are widely used in industries. The inverter output voltage contains some harmonics, and when variable speed drive (VSD) is supplied by this voltage the core losses of the machine increase. This affects both the efficiency and insulation lifespan of the motor. Besides, estimation of the core losses of the inverter-fed motor is more complicated than that of direct-supply motor [1-2].

Generally, core losses depend on the magnetic flux density and the supply frequency. The distorted input voltage of the motor leads to a non-sinusoidal flux density which increases the core losses. Therefore, accurate estimation of core losses at various conditions is essential in the optimal design of the motor. Owing to the non-uniform flux density in the machines, core loss analysis is a challenging problem. The core losses mainly consist of static and dynamic components. The static component is the hysteresis loss occurring even at zero frequency. The dynamic component is divided into eddy current losses and excess losses which is the result of magnetic domain walls variations. Since the components of the losses have different origins, they

*Corresponding Author Institutional Email: jfaiz@ut.ac.ir (J. Faiz)

Please cite this article as: M. Ghods, J. Faiz, A. A. Pourmoosa, S. Khosrogorji, Analytical Evaluation of Core Losses, Thermal Modelling and Insulation Lifespan Prediction for Induction Motor in Presence of Harmonic and Voltage Unbalance, International Journal of Engineering, Transactions B: Applications Vol. 34, No. 05, (2021) 1213-1224

must be decomposed into hysteresis losses, eddy current losses, and excess losses. The required parameters for core losses modelling are generally obtained from the experiments on the motors [3-6].

If the core losses in the inverter-fed motor are evaluated considering only the fundamental harmonic of the flux density, the estimated losses are certainly underestimated [7-8]. The flux density differs in various parts of the motor, and the core losses are not identical in different parts of the machine [9]. The most precise method for estimating the core losses is the finite element method (FEM) [10-17]. However, precise prediction of the flux density in the actual motor is a difficult task. The method demonstrated by Bradley et al. [10] can estimate the core losses generated by the distorted voltage. The stator core losses have been calculated for a no-load motor by Gyselinck et al. [11], while the rotor core losses have been ignored due to the low-frequency current in the rotor. Also, a method introduced by Boglietti et al. [14] can evaluate the core losses in the different parts of the stator of an inverter-fed induction motor. The impact of the core losses on induction motor parameters has been discussed by [16]. The classical model of calculating the core losses has been presented in literature [18-19]. When the frequency or the flux density is relatively low, the accuracy of the classical model is reasonable. A fast core loss on induction motor has been estimated based on the piecewise variable parameter model by Zhao et al. [20] which considers the voltage harmonic components of the inverter. The rotational losses have been reported by Alatawneh N., and Pillay, [21] in which the effect of minor loops on the core losses have been taken into account. Moreover, an improved generalized Steinmetz equation has been proposed by Venkatachalam et al. [22].

The core losses might cause an overheating in different parts of an electrical machine and decline its performance. Therefore, thermal analysis of the machine plays an important role in the design stage of electrical machines. This analysis can help the designers to design a minimum size and weight machine for certain torque or power. Moreover, in applications where a high-performance motor is required, accurate thermal modelling is crucial [23]. Thermal modelling for stator winding in short-term transient has been proposed in literature [24-25]. Thermal analysis of induction motors has been addressed in literature [26-31]. The thermal behaviour of induction motors in a wash-down environment has been discussed by Jankowski et al. [26], in which thermal properties of the motors have been considered. Different classes of induction motors, in terms of protection requirements, have been discussed by Fernando et al. [28]. The end-winding thermal effect of induction motor has been analyzed by Ahmed and Kar [29] in which the predicted stator winding temperature using a 1st-order and higher-order thermal model has been compared. The thermal model lumped parameters of wound-rotor induction motor and their analytical equations have been given by Boglietti et al. [30].

The first contribution of the present paper is to introduce a core losses estimation method that can calculate losses in the presence of harmonics and voltage unbalance. Compared to the available models, the proposed model has two important features. Firstly, eddy current and hysteresis coefficients are directly expressed as a function of the flux density and then these flux density-dependent coefficients are estimated using the curve fitting technique, while in the existing methods two steps are required to calculate the coefficients. Secondly, unlike available methods, excess losses in the proposed method is not initially considered in the losses equation, but after applying curve fitting and finding coefficients for eddy current and hysteresis losses, the remaining coefficient is the coefficient of excess losses. The second contribution of this paper is to propose a thermal analysis for induction motor when it is supplied by a distorted voltage or exposed to a voltage unbalance. The proposed modelling is a combination of FEA and analytical techniques. The rest of the paper is organized as follows: Section 2 proposes an analytical method based on the curve fitting technique through which the core losses in electrical machines are estimated, and its accuracy is discussed in section 3, then the estimated results are compared to those obtained experimentally. Section 4 presents the thermal model of induction motor in the presence of harmonics and voltage unbalance. The accuracy of the proposed thermal modelling is validated by the test results in section 5. In section 6, the insulation lifespan of the motor is discussed and the lifespan of the motor in the presence of harmonics and voltage unbalance is predicted. Section 7 concludes the paper.

2. CORE LOSSES ESTIMATION METHOD

The core losses influence the performance and shorten the lifespan of the inverter-fed induction motors. Therefore, it is crucial to precisely estimate the core losses caused by the various harmonic components of the magnetic fluxes. At this end, the waveforms of flux densities in different parts of the machine structure must be known. The non-sinusoidal waveforms of flux densities, depending on the amplitude and harmonic order, may generate some minor loops in the magnetization characteristic. For the magnetic flux density less than 1 T with fundamental frequency, the core losses are divided into hysteresis losses (P_h) and eddy current losses (P_e) as follows:

$$P_c=P_h+P_e=k_h f B_m^n+k_e f^2 B_m^2 \tag{1}$$

A curve fitting technique is applied in which the core losses are divided into eddy current losses and hysteresis losses. However, compared to the existing models for core losses estimation, the proposed model has two

important features. Firstly, eddy current and hysteresis coefficients in the model are directly expressed as a function of the flux density and then these coefficients are estimated using the curve fitting technique, while in the existing methods, two steps are required to estimate the hysteresis coefficient k_h. The Steinmetz coefficient and k_h are separately estimated using the curve fitting technique. Secondly, to include the excess losses in the existing method, a new coefficient is proposed and determined using the curve fitting technique; however, it was not initially considered in the losses formula previously, but it is taken into account after curve fitting and finding coefficients for eddy current and hysteresis losses. Based on the above-discussed items, the steps for estimating the core losses are given as follows:
Step I: defining the total core losses as follows:

$$P_c = k_h(\mathrm{f,B})\, f + k_e(\mathrm{f,B})\, f^2 \tag{2}$$

Step II: dividing the total core losses by square root of frequency as follows:

$$\frac{P_c}{\sqrt{f}} = k_h(\mathrm{f,B})\sqrt{f} + k_e(\mathrm{f,B})\, f\sqrt{f} \tag{3}$$

Step III: for different values of flux density, $P_c/\sqrt{f}$ versus square root of frequency is plotted and then a cubic spline fitting technique is applied to each value of the flux density as follows [36]:

$$\frac{P_c}{\sqrt{f}} = a_3\sqrt{f}^3 + a_2\sqrt{f}^2 + a_1\sqrt{f} + a_0 \tag{4}$$

Step IV: by comparing Equation (3) with Equation (4), a_1 is k_h(f,B) and a_3 is k_e(f,B). Also, this comparison shows that the right-hand side of Equation (2) must include an additional term. This additional term is called excess losses. Therefore, the total core losses are rewritten as follows [36]:

$$P_c = k_h(\mathrm{f,B})\, f + k_e(\mathrm{f,B})\, f^2 + k_{ex1}(\mathrm{f,B})\, f^{1.5} + k_{ex2}(\mathrm{f,B})\, f^{0.5} \tag{5}$$

where k_{ex1}(f, B) and k_{ex2}(f, B) are the excess losses coefficients.

The cubic spline fitting of the specific core losses and finding the coefficients in terms of the flux density enables us to estimate these coefficients at any flux density. Using the proposed model, one can easily estimate the total core losses for any flux density which in turn prevents underestimation of the core losses at high-frequency harmonics and its overestimation at low-frequency harmonics.

2. 1. Core Losses in Presence of Harmonics

Core losses under alternating pulse voltage excitation have been predicted in literature [34-36]. In the method, three components of core losses, as well as the form factor of the harmonic voltage, have been used to estimate the losses. Suppose distorted input voltage of the motor is as follows:

$$V(\mathrm{t}) = \sum_{h=1,2,...} V_h \cos(\mathrm{h}\, 2\pi\, ft + \theta_h) \tag{6}$$

where h is the harmonic order, V_h is the amplitude of the hth harmonic of the phase voltage, and θ_h is the phase angle of the hth harmonic. The magnetic flux density in the core generated by the applied voltage is as follows:

$$B(\mathrm{t}) = \sum_{h=1,2,...} B_h \sin(\mathrm{h}\, 2\pi\, ft + \theta_h) \tag{7}$$

where B_h is the amplitude of the h^{th} harmonic of the flux density. Therefore, in the presence of harmonics,
the peak flux density is as follows:

$$B = \sqrt{\sum_{h=1,2,...} h^2 B_h^2} \tag{8}$$

When a distorted voltage is applied to the motor, the hysteresis, eddy current and excess losses coefficients corresponding to the flux density shown in Equation (1) should be determined for estimation of the core losses.

2. 2. Core Losses in Presence of Voltage Unbalance

Unbalanced voltage may apply to the induction motor. The IEEE standard gives the following definition for VUF:

$$VUF = \frac{V^-}{V^+} \times 100\% \tag{9}$$

where V^+ and V^- are the positive and negative sequence voltage components, respectively. Since V^+ and V^- are phasors, the *VUF* has magnitude and angle. These components can be calculated using the fast Fourier transform or Fortescue transform. Similar to the method used to estimate the core losses in the presence of distorted voltage, the hysteresis, eddy current and excess losses coefficients, corresponding to the flux density generated by the voltage unbalance, can be derived from Equation (5) and used for the core losses estimation.

2. 3. Different Methods of Core Losses Estimation

2. 3. 1. Epstein Frame Epstein frame is the most popular method for experimental core losses estimation. The IEC 404-2 describes the structure of the Epstein frame in detail. The standard structure for the Epstein frame is a 28 cm×28 cm frame with four coils of 700 turns on the primary and the secondary. The primary winding or magnetizing winding is wound onto the secondary winding or voltage winding. The samples are located on the frame, so that a double-lapped joint is created. By multiplying the primary winding current and the secondary winding voltage, the instantaneous power loss is obtained. Then, the total core losses are determined by averaging the instantaneous power. To find the specific total losses, the total losses are divided by the weight of the sample. The main disadvantage of the Epstein frame is the generated leakage flux around the joint leading to the non-uniform flux density distribution. Besides, the impact of the harmonic components on the total core losses cannot be evaluated using the standard frame.

2. 3. 2. Toroid Tester The structure of the toroid tester is very similar to that of the Epstein frame. The only difference is that the specimen in the toroid tester is a wound toroid. For small electrical motors, the total losses obtained from the toroid tester is more accurate than those achieved by the Epstein frame. Like the Epstein frame, non-uniform flux density distribution is one of the problems with the toroid tester. Moreover, the toroid tester method is more time-consuming than the Epstein frame method. The reason is that the toroidal winding must be appropriately wound onto the core. It is noted that the toroid tester configuration is much more similar to the structure of a stator in conventional electric motors, making it preferable for calculating the core losses over the Epstein frame method.

2. 3. 3. Single Sheet Tester Compared to the existing methods, the single sheet tester is a simple and economic way for measuring the core losses. In this method, an excitation coil with a low number of turns is wound around a double-yoke sheet. The flux generated by the coil in the yoke produces a current which in turn generates power losses in the sheet. The single sheet tester has two disadvantages. First, the double yoke is large and costly. Second, the tester needs to be calibrated with either the toroid tester or the Epstein frame.

3. TEST SETUP FOR CORE LOSSES MEASUREMENT

To validate the proposed method for core losses estimation, the obtained results by applying the method are compared with the measured core losses. To produce a desired magnetic flux density in the core, a toroid tester, as well as a signal generator, are used. The signal is generated by a single-phase inverter, supplying the toroid transformer. The magnetic flux is produced by the applied signal and induced voltage in the secondary winding. Therefore, the measured current in the primary and measured voltage in the secondary winding corresponds to the magnetic flux intensity and the flux density, respectively. Flux density is obtained by integrating the secondary voltage. Besides, a filter is employed in the output of the inverter to reduce the voltage pulsation. Figure 1 demonstrates the test setup.

Figure 2 compares the predicted core losses using the proposed method and the experimental results. A good agreement between the predicted and test results is achieved. Figure 3 demonstrates the minor loop on the magnetization characteristic for the distorted magnetic flux density. The minor loop in Figure 3 has been created by 10% of 5th harmonic.

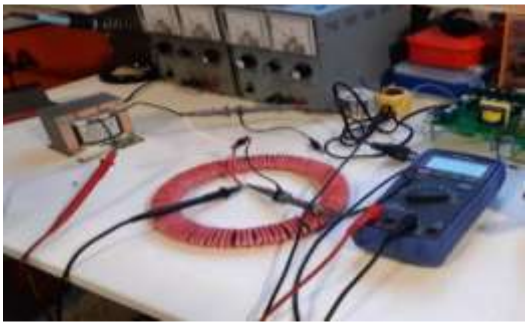

Figure 1. Toroid tester setup

4. THERMAL MODELLING OF INDUCTION MOTOR IN PRENSENCE OF HARMONIC AND VOLTAGE UNBALANCE

The main heat-generating sources in electrical machines are electrical, magnetic, and mechanical losses. In a variable speed drive, the produced harmonics by the inverter lead to more losses compared with the motor directly supplied by mains. It is noted that the impact of harmonics on the core loses is more prominent. As a result, in the presence of harmonics, temperature rise in different parts of the motor are more pronounced. A similar problem is true when the motor is supplied by voltage unbalance. Therefore, thermal modeling of electrical machines in the presence of the harmonics and voltage unbalance are necessary in its design stage. In this section, the main objective is to provide a thermal analysis for an induction motor supplied by a distorted voltage or voltage unbalance. The proposed modeling is a combination of FEA and analytical techniques.

Taking into account all the above-mentioned items, the thermal modeming steps of the induction motor are as follows:

1st Step: To determine the flux density at different parts of the motor, harmonic voltage is applied to the stator winding which is simulated by the Ansoft.

2nd *Step*: Using Equation (1) and the magnetic flux density obtained from the 1st step, the core losses in different parts of the motor such as stator yoke, rotor yoke, and stator teeth, are estimated. The core losses for each part are then divided by its weight through which specific core losses are estimated. Besides, the copper losses.

3rd Step: Using the motor data such as dimensions and number of stator slots, lumped thermal network of the motor is implemented in the Motor-CAD software, which is a tool for the thermal analysis of electrical

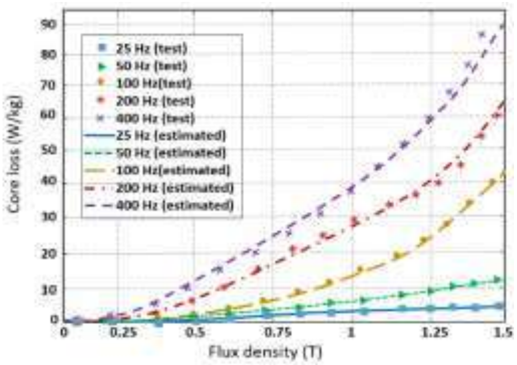

Figure 2. Core losses curve cluster of various frequencies at 50 °C

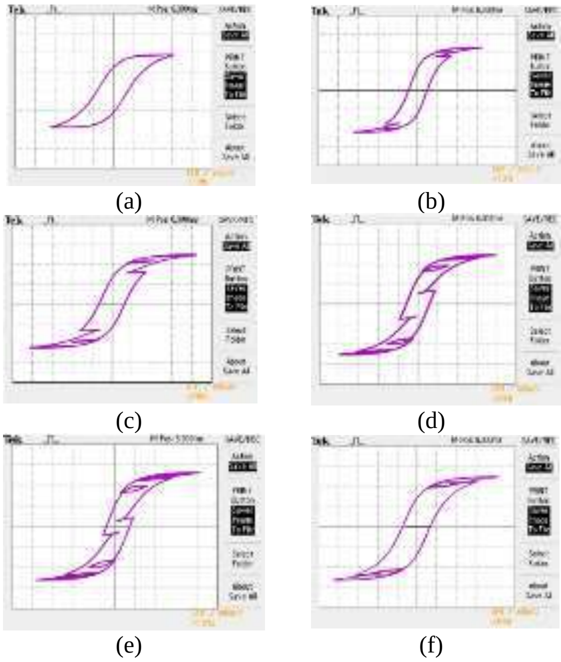

Figure 3. Magnetization characteristics. (a) 1st component, (b) 1st and 10% - 5th harmonic, (c) 1st and 10% - 7th harmonic ,(d) 1st and 10% - 11th harmonic (e) 1st and 10% - 13th harmonic, (f) 1st and 5th , 7th, 11th, 13th harmonics are obtained by simulation.

machines. By solving the lumped thermal circuit, the temperature in various parts of the motor are determined.
4th Step: Using the results obtained from in the 3rd step, the insulation lifespan of the motor is estimated. Figure 4 depicts the flowchart of the thermal analysis of the induction motor.

4. 1. FEM Analysis of Proposed Motor Table 1 summarizes the specifications of the proposed induction motor. Figure 5 shows the 3D view of the motor. Figure 6 illustrates the magnetic flux density distribution in different parts of the motor when a distorted voltage is applied to the stator winding. In each case, the voltage is the sum of the fundamental component of the voltage and the percentage of a certain high-order harmonic. For example, in Figure 6a, the fundamental component with 10% of the 5th harmonic is applied to the stator winding. It is observed that the impact of the unbalanced voltage on the magnetic flux density is more than that of the distorted voltage. Figure 7 shows the core and copper losses variations for different harmonic. As seen, voltage unbalance causes the increase of both copper and core losses compared to the balanced voltage. Also, the lower the harmonic order, the higher the losses.

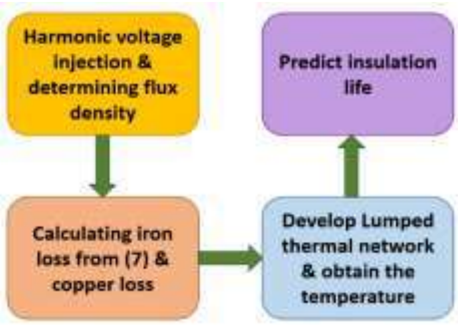

Figure 4. Flowchart for thermal analysis of induction motor

TABLE 1. Motor Specifications

Parameter	Value
Line voltage (V)	380
Frequency (Hz)	50
Number of poles	4
Rated current (A)	2
Rated torque (Nm)	5
Output power (W)	750
Efficiency (%)	79
Power factor	0.707

Figure 5. 3D view of proposed motor

4. 2. Thermal Modelling In this section, the impact of the distorted voltage as well as voltage unbalances on the temperature rise of various parts of the induction motor are predicted using the proposed thermal modeming. Motor-CAD software is used to model the thermal behaviour of the motor as shown in Figure 8. To implement the model, general data such as dimensions, number of stator and rotor slots (39/20), and number of rotor bars are needed. The data then is used to develop the thermal model of the motor. The model consists of a set of thermal resistors, thermal capacitors, and thermal sources. Figure 9a depicts the lumped parameter network (LPN) of the motor. Since the objective is to analyse the motor at steady-state, the thermal capacitors are not considered in the model. The values of the thermal sources are obtained from the losses calculated in the 3rd step. It is noted that the nodes in the LPN demonstrate the temperature at different parts of the motor. Figure 9b presents the thermal resistors and thermal sources corresponding to the LPN (Figure 9a).

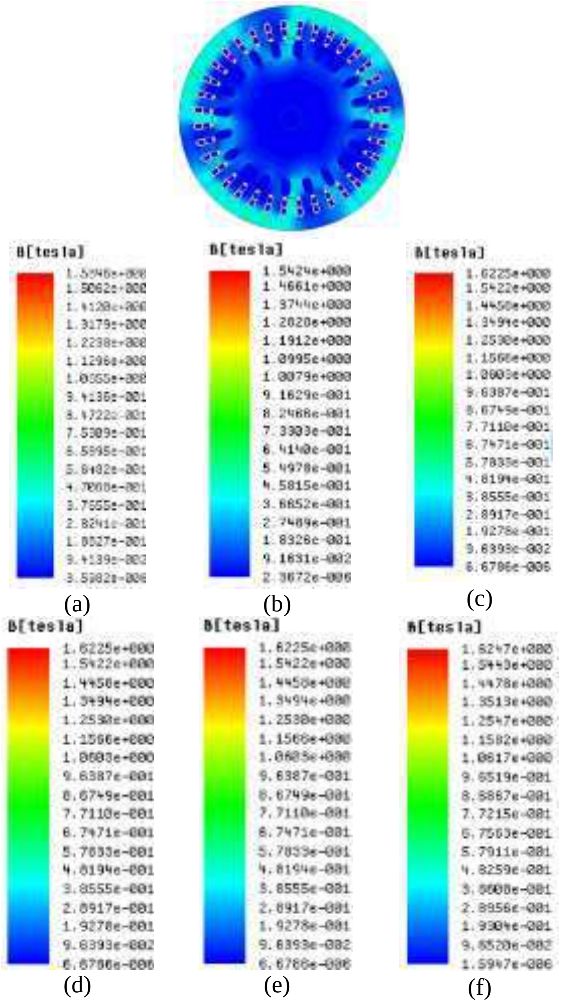

Figure 6. Flux density distribution. (a) 1st component, (b) 1st and 10% of 5th harmonic, (c) 1st and 10% of 7th harmonic,(d) 1st and 10% of 11th harmonic (e) 1st and 10% of 13th harmonic, (f) 1st and 5th , 7th, 11th, 13th harmonics

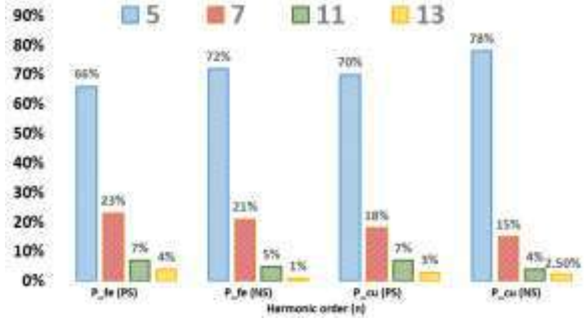

Figure 7. Iron and copper loss variations for different harmonic (PS: Positive seq. and NS: Negative seq.)

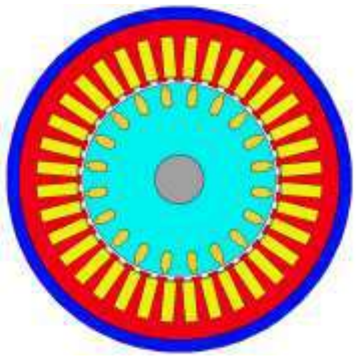

Figure 8. proposed motor in Motor-CAD

The thermal equivalent circuit (TEC) shown in Figure 9b consists of 49 thermal resistors and 15 thermal sources. The definition of each resistor as well as the definition and value of each thermal source have been summarized in Tables 2 and 3, respectively. According to Table 3, the thermal source for each part of the motor corresponds to the estimated losses of that part. The estimated losses for each part are expressed in percentage of the total losses calculated in the presence of the harmonic or voltage unbalance. To obtain the temperature at each node, the network shown in Figure 9b is implemented in Power-sim software as shown in Figure 10. In this case, the TEC is treated as an equivalent electrical circuit and as a result, the temperature at each part of the motor is estimated. The stator and rotor copper losses for the proposed motor at different harmonic and unbalanced conditions are tabulated in Table 4.

5. EXPRIMENTAL SETUP

To validate the accuracy of the proposed thermal model, the induction motor was tested and the experimental results were compared to those obtained by the proposed method. Figures 11a and 11b show the stator and rotor of the motor. Figure 11c presents the experimental test setup. To generate harmonic-polluted voltage, ARM microcontroller was used to build the input voltage with different harmonic contents as well as voltage unbalance. The digital oscilloscope stored this voltage and the current sensor (LTS25) measured the current. Also, to measure the winding temperature a sensor (PT100) was located in the stator winding. Moreover, a thermo-couple measured the temperature in different parts of the motor.

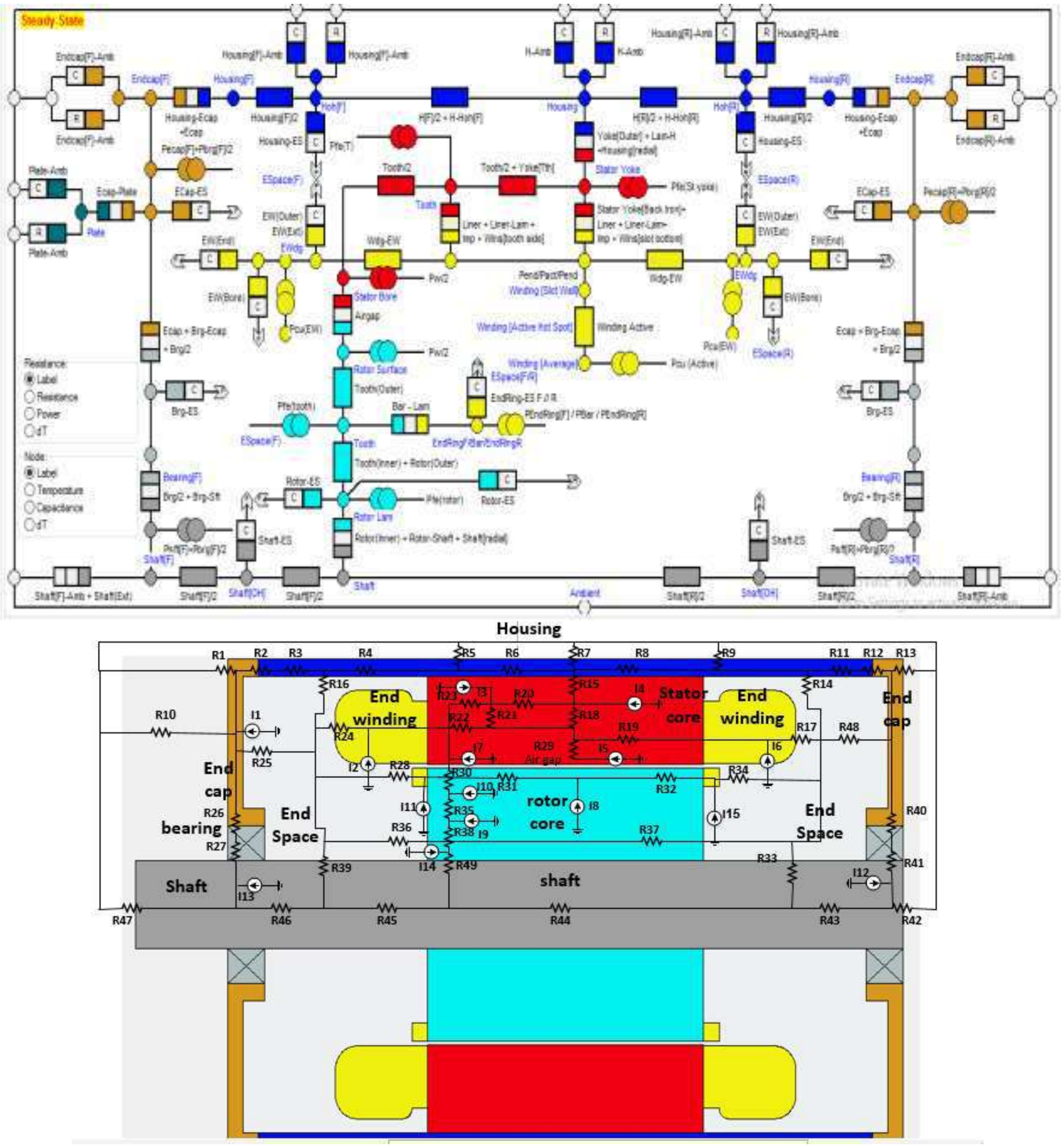

Figure 9. Lumped parameters model: (upper) lumped network, (lower) thermal equivalent circuit

TABLE 2. Thermal model resistances

Convective resistance of cap to environment (R_1 , R_{13})
Conductive resistance of the body (R_3,R_4,R_6,R_8,R_{11})
Resistance between cap and plate to environment (R_{10})
Conductive resistance between body and stator yoke (R_{15})
Convective resistance between stator end-winding and indoor air (R_{24} , R_{17})
Yoke and stator teeth convective resistance (R_{20})
Convective resistance between indoor air and cap (R_{25} , R_{48})
Conductive resistance between bearing and shaft (R_{27} , R_{41})
Winding and rotor conductive resistance (R_{29}), (R_{31}, R_{32})
Shaft conductive resistance (R_{43},R_{44},R_{45},R_{46})
Conductive resistance between body and cap (R12 ,R2)

Convective resistance of body to air (R_5,R_7,R_9)
Convective resistance between a body with indoor air (R_{14},R_{16})
Convective resistance between yoke and stator winding (R_{18},R_{21})
Conductive resistance between stator end-winding and winding (R_{19},R_{22})
Conductive resistance teeth stator (R_{23})
Conductive resistance between cap and bearing (R_{26}, R_{40})
Conductive resistance between rotor load and indoor air (R_{28}, R_{34})
Convective resistance between rotor and stator core (R_{30})
Convective resistance between shaft and indoor air (R_{33},R_{39},R_{47},R_{42})
Convective resistance between rotor core and shaft (R_{49})

TABLE 3. Heat sources values

Heat source	Value (% Total loss)
Cap loss (I_1)	1
Stator end-winding loss (I_2,I_6)	11
Stator tooth loss (I_3)	20
Stator yoke loss (I_4)	15
Stator winding loss (I_5)	17
Stator bore loss (I_7)	1
Rotor bar loss (I_8)	12
Rotor core loss (I_9,$I_{10}I_{14}$)	16
Rotor shaft loss (I_{13},I_{12})	6
Rotor end-ring loss (I_{11},I_{15})	1

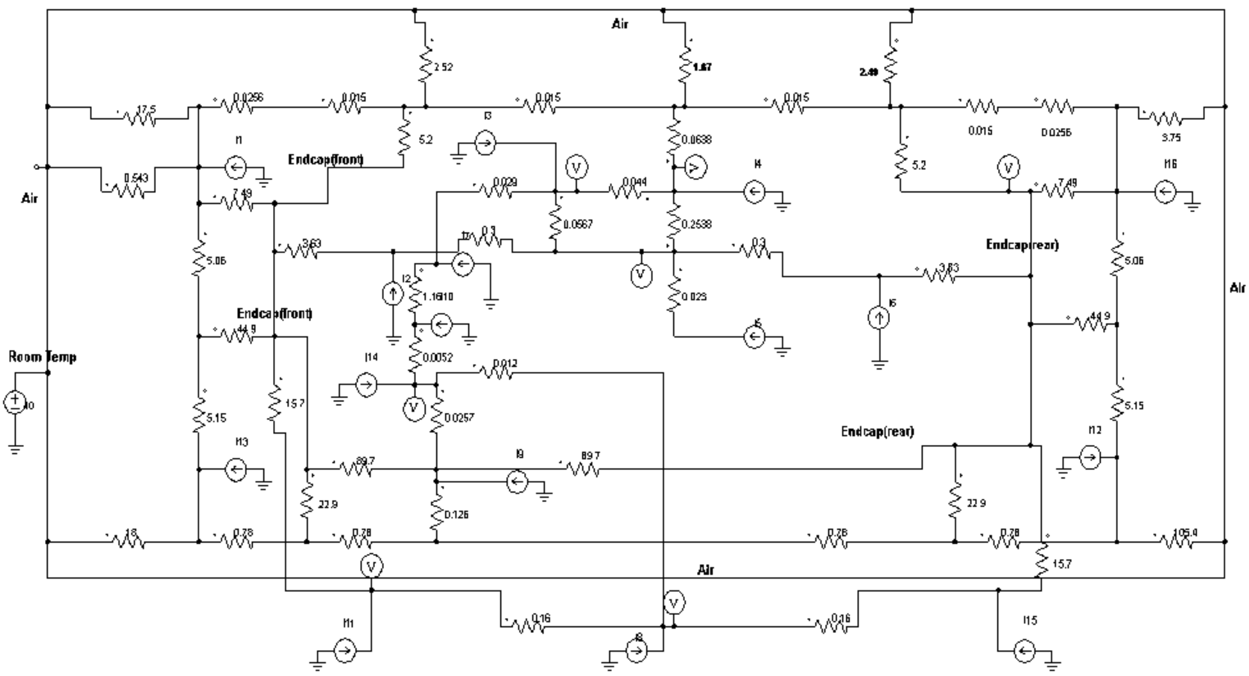

Figure 10. Lumped parameter model of proposed induction motor in Power-sim software

TABLE 4. Stator and rotor copper losses in harmonic and unbalanced voltage conditions

Harmonic Unbalance	Stator end winding loss (W)	Stator winding loss (W)	Rotor end-ring loss (W)	Rotor bar loss (W)
1st	22.4	33.7	12.5	24.9
5th	0.93	1.41	0.52	1.04
7th	1.11	0.74	0.68	1.36
11th	0.62	0.93	0.34	0.69
13th	0.5	0.75	0.29	0.58
5% unb	1.22	1.83	0.71	1.43
10% unb	1.70	2.55	0.99	1.98

6. RESULTS AND DISCUSSION

Table 5 summarizes the comparison between the measured temperature and the temperature obtained from the proposed thermal model at various parts of the motor for different harmonic contents and voltage unbalance. It is assumed that the ambient temperature is 40°C. The obtained results indicate that the high flux density leading to the high core losses generates the hotspot of the motor somewhere between the rotor conductors close to the stator. Besides, by rising the harmonic order, the temperature at different parts of the motor also increases. Moreover, Table 6 shows that the impact of the voltage unbalance on the temperature rise of the motor is more than that of harmonic voltage. For example, the temperature rise of the rotor core is about 16% for 10% voltage unbalance. Also, when the voltage unbalance increases, the losses and as a result the temperature rise of the motor increase. Table 6 compares the measured core and copper losses and the losses obtained by the analytical method.

Figure 12 illustrates the input current waveform for different harmonic voltages applied to the stator winding. According to Figure 12, harmonic and unbalanced currents are generated by the drive and the output voltage of the drive (with harmonic and unbalanced) is applied to the stator winding. Then, with the help of P100 temperature sensors located in the accessible points inside of the motor, the temperature is measured and presented in Table 5.

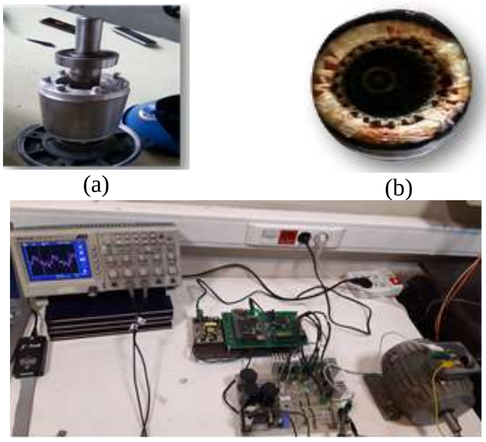

(a) (b) (c)

Figure 11. Experiment (a) stator, (b) rotor, and (c) test-bed

TABLE 5. Comparison of measured and simulated temperature at various parts of motor for different harmonic contents and voltage unbalance (Simulation - **Experimental**)

Unbalanced Harmonic	Stator yoke (°C)		Stator tooth (°C)		Stator end winding (°C)		Stator winding (°C)		Rotor Core (°C)		Rotor bar (°C)		Rotor end-ring (°C)	
1st	80.40	**83**	84.01	**86**	83.34	**86**	85.45	**87**	107.61	**112**	107.47	**112**	84.40	**88**
5th	82.65	**85**	89.25	**94**	89.61	**91**	89.76	**93**	111.01	**115**	111.15	**114**	92.70	**96**
7th	82.57	**86**	87.21	**90**	87.57	**88**	88.12	**91**	107.86	**114**	107.87	**109**	91.56	**94**
11th	81.51	**90**	87.11	**90**	86.48	**88**	87.78	**91**	107.77	**114**	107.62	**109**	91.47	**94**
13th	81.44	**92**	87.05	**91**	86.37	**89**	87.56	**90**	107.64	**117**	107.53	**109**	90.42	**94**
5% unb	94.84	**97**	95.44	**100**	95.81	**100**	96.14	**101**	108.41	**115**	108.26	**110**	98.89	**100**
10% unb	97.98	**101**	99.65	**103**	97.04	**104**	101.65	**107**	110.18	**117**	110.03	**114**	101.13	**106**

TABLE 6. Total losses in harmonic and voltage unbalance conditions

Harmonic Unbalance	Core losses (W) (sim.)	Core losses (W) (exp.)	Copper loss (W) (sim.)	Copper loss (W) (exp.)
1st	64.60	67.00	93.50	98.00
5th	4.4	4.6	3.9	4.12
7th	3.8	4.0	3.1	3.30
11th	3.1	3.3	2.6	2.70
13th	2.9	3.0	2.1	2.30
5% unb	5.0	5.1	5.1	5.70
10% unb	6.2	6.7	7.1	7.80

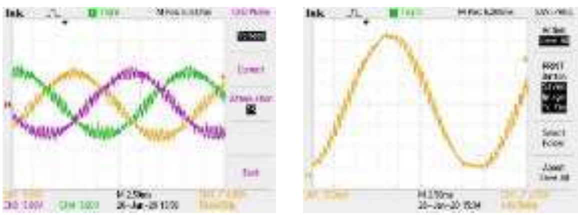

(a) (b)

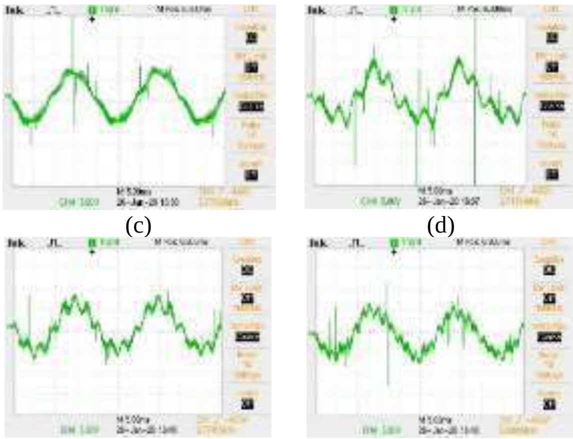

(c) (d) (e) (f)

Figure 12. Input current waveform. (a) three phase , (b) 1st component (c) 1st and 10% - 5th harmonic, (d) 1st and 10% - 7th harmonic ,(e) 1st and 10% - 11th harmonic (f) 1st and 10% - 13th harmonic

7. LIFESPAN ANALYSIS OF INDUCTION MOTOR INSULATION

After determining the temperature at different parts of the motor, the analysis shows that the maximum temperature occurs in the rotor end ring because the magnetic flux density at the end ring is high compared to other parts of the motor. Since the insulation material is not used in the rotor of the squirrel-cage induction motor, the temperature rise of the end ring does not affect the insulation lifespan. Inspecting the temperature at different parts of the motor insulation, it is found that the stator winding experiences the maximum temperature. Therefore, the stator winding insulation reduces the lifespan of the motor. Assuming that the motor operates at 90% of the rated load, the maximum temperature of the motor insulation is as follows [35]:

$$T=F\times\Delta T+40 \tag{10}$$

where F is the loading coefficient of the motor (Table 7), and ΔT is the maximum temperature rise withstood by the motor in the desired insulation class. Since the proposed motor is a class A motor, from Equation (10), the maximum temperature of the motor insulation (T) is found to be 97.2°C. To obtain the insulation lifespan of the motor, the following equation can be used [35]:

$$L_x=L_{100\%}\times 2^{[\frac{T_c-T_x}{HIC}]} \tag{11}$$

where L_x is the percent lifespan at $x\%$ of rated load, L_{100} is the percent lifespan at rated load, T_c is the total permissible temperature of the insulation, T_x is the hotspot temperature of the insulation, and HIC is the halving interval. Using Equation (11), the insulation lifespan of the motor in the presence of harmonics and voltage unbalance are calculated and listed in Table 7.

The reason for the longer insulation lifespan at 90% of the rated load compared to the rated loading is the lower operating temperature compared to the maximum insulation temperature. Table 8 indicates that the effect of harmonic on the insulation temperature rise is low because of the low amplitude of the harmonic component compared to the fundamental one. This in turn leads to a small insulation temperature rise. However, even this small value dramatically affects the insulation lifespan of the motor. For example, 10% 5th harmonic results in the insulation temperature rise by 4.31°C, but it decreases the insulation lifespan of the motor by 376 days. The results also show that the impact of voltage unbalance on the decrease of insulation lifespan is more than that of harmonic voltage.

TABLE 7. F coefficients

Load (%)	F	Load (%)	F
50	52	110	119
75	73	115	130
90	88	125	146
100	100	150	212

TABLE 8. Lifespan prediction of the motor understudy at different harmonic and voltage unbalances (for 3000 days)

Harmonic Unbalanced	Maximum Temperature of insulation (C°)	Temperature variations at 90% of rated load (C°)	Lifespan variations at 90% of rated load (days)
1st	85.45	0	0
5th	89.76	4.31	-376
7th	88.12	2.67	-296
11th	87.78	2.33	-254
13th	87.56	2.11	-212
5% unb	96.14	13.69	-996
10% unb	101.65	16.20	-1114

8. CONCLUSION

This paper demonstrated an analytical method based on the curve fitting technique for calculating the core losses for induction motors. In this method, unlike the existing methods, the excess losses were not initially considered in the losses equation but after curve fitting and finding coefficients for eddy current and hysteresis losses, the excess losses coefficient was automatically extracted. Also, thermal modeling for insulation lifespan prediction in the motor was proposed. The model is a combination of FEM and the proposed losses calculation method. To verify the accuracy of the proposed thermal modeling, a test was conducted on the induction motor. The test results and the proposed method results indicated that the temperature rises of the motor increase with the increase of voltage unbalance. The model showed that the impact of the unbalanced voltage on the temperature rise of the motor is more than that of harmonic voltage. As an example, 10% voltage unbalance leads to the temperature rise, and the rotor losses go up about 4%. Moreover, the hotspot of the motor is somewhere between the rotor conductor and close to the stator. This is due to the high flux density and as a result high core losses at that point. Also, compared to other harmonic components the 5th harmonic generates the maximum temperature at different sections of the motor.

9. REFERENCES

1. Agamloh, E. B., ″Induction motor efficiency″, ***IEEE Industry Applications Magazine***, Vol. 17, No. 6 (2011), 20-28, doi:10.1109/MIAS.2011.942298
2. Al-Badri, M., Pillay, P., and Angers, P., ″A novel algorithm for estimating refurbished three-phase induction motors efficiency using only no-load tests″, ***IEEE Transactions on Energy Conversion***, Vol. 30, No. 2, (2015), 615-625. doi: 10.1109/TEC.2014.2361258
3. Pfingsten, G.V, Steentjes, S. , and Hameyer K., ″Operating point resolved loss calculation approach in saturated induction

machines", ***IEEE Transactions on Industrial Electronics,*** Vol. 31, No. 4, (2016), 1200-1208. doi: 10.1109/TIE.2016.2597761

4. Cabezas Rebolledo, A. A, and Valenzuela M. A., "Expected savings using loss-minimizing flux on induction machine drives—Part I: Optimum flux and power savings for minimum losses", ***IEEE Transactions Industrial Applications,*** Vol. 51, No 2, (2015), 1408-1416. doi: 10.1109/TIA.2014. 2356643
5. Lim, S., and Nam, K., "Loss-minimising control scheme for induction motors", ***IEE Proceedings-Electric Power Applications,*** Vol. 151, No. 4, (2014), 385-397, doi: 10.1049/ ip-epa:20040384
6. Odhano, S. A., Bojoi, R., and Boglietti, A., Rosou, S. G., and Griva, G., "Maximum efficiency per torque direct flux vector control of induction motor drives", ***IEEE Transactions on Industrial Applications,*** Vol. 51, No. 6, (2015), 4415-4424. doi: 10.1109/TIA.2015.2448682
7. Gmyrek, Z., Boglietti, A., and Cavagnino, A., "Estimation of iron losses in induction motors: Calculation method, results, and analysis", ***IEEE Transactions on Industrial Electronics,*** Vol. 57, No. 1, 161-171, (2010) doi: 10.1109/TIE.2009.2024095
8. Kowal, D., Sergeant, P., Dupre, L., and Karmaker, H., "Comparison of frequency and time-domain iron and magnet loss modelling including PWM harmonics in a PMSG for a wind energy applications", ***IEEE Transactions on Energy Conversion***, Vol. 30, No. 2, (2015) 4,76-486. doi: 10.1109/TEC.2014.2373312
9. Reinert, J., Brockmeyer, A., and De Doncker, R. W. A. A., "Calculation of losses in ferro- and ferri-magnetic materials based on the modified Steinmetz equation", ***IEEE Transactions on Industrial Applications*.** Vol. 3, No. 4, (2001), 1055-1061. doi: 10.1109/TEC.2014. 2373312
10. Bradley, K., Cao, W., Clare, J. and Wheeler, P., "Predicting inverter-induced harmonic loss by improved harmonic injection", ***IEEE Transactions on Power Electron***ics, Vol. 23, No. 5, (2008), 2619-2624. doi: 10.1109/TPEL.2008. 2002329
11. Gyselinck, J.J., Dupre, L.R., Vandevelde, L. and Melkebeek, J.A. "Calculation of no-load induction motor core losses using the rate-dependent Preisach model", ***IEEE Transactions on Magnetics*,** Vol. 34, No. 6, (1998), 3876-3881. doi: 10.1109/20.728297
12. Fasil, M., Mijatovic, N., Jensen B. B., and Holboll, J., "Nonlinear dynamic model of PMBLDC motor considering core losses", ***IEEE Transactions on Industrial Electroni***s, Vol. 64 No. 12, ,(2017), 9282-9290. doi: 10. 1109/TIE.2017. 2711536
13. Ruuskanen, V., Nerg, J., Rilla, M., and Pyrhönen, J., "Iron loss analysis of the permanent-magnet synchronous machine based on finite-element analysis over the electrical vehicle drive cycle", ***IEEE Transactions* on *Industrial Electron***ics, 2016, Vol. 63, No. 7, (2016), 4129-4136.doi: 10.1109/TIE. 2016. 2549005
14. Boglietti, A., Cavagnino, A., Ionel, D.M., Popescu, M., Staton, D.A. and Vaschetto, S., "A general model to predict the iron losses in PWM inverter-fed induction motors", ***IEEE Transactions on Industrial Applications*.,** Vol. 46, No. 5, (2010), 1882-1890. doi: 10. 1109/TIA. 2010. 2057393
15. Ionel, D.M., Popescu, M., McGilp, M.I., Miller, T.J.E., Dellinger, S.J. and Heideman, R.J.,"Computation of core losses in electrical machines using improved models for laminated steel", ***IEEE Transactions on Industry Appl*ications**, Vol. 43, No. **7,** (2007), 54-64.doi:
16. Chatterjee, D., "Impact of core losses on parameter identification of three phase induction machines", **IET *Power Electronics,*** Vol. **7**, No 12, (2014), 3126-3136.doi: 10.1049/iet-pel.2014.0121
17. Dlala, E.: "Comparison of models for estimating magnetic core losses in electrical machines using the finite-element method", ***IEEE Transactions on Magnetics*,** Vol. 45, No. 2, (2014), 716-725.doi: 10.1109/TMAG.2008.2009878
18. A Krings, and J Soulard, "Overview and comparison of core loses models for electrical machines", ***Electrical Energy Conversion***, Vol. 10**,** No 3**,** (2010), 162-169.
19. Dongdong, Z., Ruichi A. and Wu, Z., "Effect of voltage unbalance and distortion on the loss characteristics of three-phase cage induction motor", ***IET Electric Power Applications***, Vol. 12, No. 2, (2018) 264-270. doi: 10.1049/iet-epa.2017.0464
20. Zhao, H., Wang, Y., Dongdong, Z., Zhan, and Luo, Y., "Piecewise variable parameter model for precise analysis of core losses in induction motors", ***IET Electric Power Applications***, Vol. 11, (2017), 361-368, doi: 10.1049/iet-epa.2016.0009
21. Alatawneh N., and Pillay, P., "The minor hysteresis loop under rotating magnetic fields in machine laminations", ***IEEE Transactions on Industrial Applications***, Vol. 50**,** No. 4, (2014), 2544-2553, doi: 10.1109/TIA.2014. 2300155
22. Venkatachalam, K., Sullivan, C.R., Abdallah, T. and Tacca, H., "Accurate prediction of ferrite core loss with non-sinusoidal waveforms using only Steinmetz parameters", 8th IEEE Workshop on Computers in Power Electronics (COMPEL), (2002).
23. Jankowski, T.A., Prenger, F.C., Hill, D.D., O'bryan, S.R., Sheth, K.K., Brookbank, E.B., Hunt, D.F. and Orrego, Y.A.,"Development and validation of a thermal model for electric induction motors", ***IEEE Transactions on Industrial Electronics***, Vol. 56, No. 12, (2010), 4043-4054. doi: 10.1109/TIE. 2010. 2043044
24. Boglietti, A., Cossale M., Vaschetto,S., and Dutra, T., "Winding thermal model for short-time transient: Experimental validation in operative condition"s, ***IEEE Transactions on Industrial Applications***, Vol. 54**,** No**.** 2, (2012), 1312-1319. doi: 10.1109/TIA.2017.2777920
25. Boglietti, A., Carpaneto, E., Cossale, M., and Vaschetto S., "Stator winding thermal models for short-time thermal transients: Definition and validation", ***IEEE on Transactions Industrial Electronic***s, Vol. 63, No. 2**,** (2016), 2713-2721.doi: 10. 1109/TIE.2015.2511170
26. Jankowski, T.A., Prenger, F.C., Hill, D.D., O'bryan, S.R., Sheth, K.K., Brookbank, E.B., Hunt, D.F. and Orrego, Y.A.,"Development and validation of a thermal model for electric induction motors", ***IEEE Transactions on Industrial Electronic***s, Vol. 57, No. 12, (2010), 4043-4054. doi: 10.1109/TIE.2010. 2043044
27. Armando, E. G., Boglietti, A., Castagnini, E. C. A., and Seita, M., "Thermal Performances of Induction Motors for Applications in Washdown Environment", ***IEEE Transactions on Industrial Applications,*** Vol. 55, No. 3, (2019),4578-4585. doi: 10. 1109/ICEL, MACH.2018.8507019
28. Fernando J. T. E. Ferreira, Benoit L., and Aníbal T. De., "Comparison of protection requirements in IE2-, IE3- and IE4-Class motors", ***IEEE Transactions on Industrial Applications***, Vol. 52, No.4, (2016), 3603-3610.doi: 10. 1109/TIA.2016.2545647
29. Ahmed, F. and Kar, N. C., "Analysis of end-winding thermal effects in a totally enclosed fan cooled induction motor with die cast copper rotor", ***IEEE Transactions on Industrial Applications***, Vol. 53, No. 2**,** (2017), 3098-3109. doi: 10.1109/TIA.2017.2648780
30. Boglietti, A., Cavagnino, A., and Popescu, M., and Staton, D., "Thermal model and analysis of wound-rotor induction machine", ***IEEE Transactions on Industrial Application***s, Vol. 49. No. 5, (2013). doi: 10.1109/TIA. 2013.2261444
31. Zhang, H., "Online thermal monitoring models for induction machines", ***IEEE Transactions on Energy Conversion,*** Vol. 30 No. 4, (2015), 1279-1287. doi: 10. 1109/TEC. 2015.2431444

32. Reinert, J., Brockmeyer, A., and De Doncker R. W. A. A., ″Calculation of losses in ferro- and ferri-magnetic materials based on the modified Steinmetz equation″, ***IEEE Transactions on Industrial. Applications***, Vol. 37, No. 4, (2001), 1055-1061. di: 10.1109/28.936396
33. Pry R. H., and Bean, C. P., ″Calculation of the energy loss in magnetic sheet materials using a domain model″, ***Journal of Applied Physics***, Vol. 29, No. 3, (1938), 532-533. https://doi.org/10. 1063/1.1723212
34. Amar A., and Protat, F., ″A simple method for the estimation of power losses in silicon iron sheets under alternating pulse voltage excitation″, ***IEEE Transactions Magnetics***, Vol. 32, No. 2, (1994), 942-944. doi: 10.1109/ 20.312453
35. Emanuel L. B., "Estimation of lifespan expectancies of motors", ***IEEE Electrical Insulation Magazine***, Vol. 8, No. 3, (1992), 5-13. doi: 10. 1109/TDEI. 2002.1024441
36. Pillay, P., and Mthombeni, L. T., "Core losses in motor laminations exposed to high frequency or non-sinusoidal excitation", ***IEEE Transactions Industrial Applications***, Vol. 40, No. 2, (2014), 1325-1332. doi: 10. 1109/TIA.2004.834099
37. Ghorbanian, V., Faiz, J., Sabouri, M., and Ojaghi, M., ″Exact modeling and simulation of saturated induction motors with broken rotor bars fault using winding function approach", ***International Journal of Engineering, Transactions A: Basics***, Vol. 27, No. 1, 69-78. doi: 10.5829/idosi.ije.2014.27.01a.10
38. Yektaniroum, T., Niaz Azari, M., and Gholami, M., "Optimal rotor fault detection in induction motor using particle-swarm optimization optimized neural network." ***International Journal of Engineering, Transactions B: Applications***, 2018, Vol. 31, No. 11, 1876-1882. doi: 10.5829/ije.2018.31.11b.11

Persian Abstract

چکیده

موتورهای الکتریکی القایی در طیف گسترده ای از شرایط و موارد صنعتی مورد بهره برداری قرار می گیرند. امروزه موتورهای جدیدبا استفاده از مواد جدید و روش های بهبود یافته و برای محدوده های مختلف توان طراحی شده اند، وگرچه اغلب بسیار کوچکترندولی بارگذاری بیشتری دارند. برای حصول اطمینان از طول عمر رضایت بخش موتورها ، افزایش دما باید به مقادیر ایمن محدود شود. در این مقاله با لحاظ کردن هارمونیک های منبع تغذیه یا عدم تعادل ولتاژ آن, یک رویکرد تحلیلی برای تخمین تلفات اصلی موتورهای القایی ارائه شده است. با معرفی یک مدل حرارتی مبتنی بر پارامترهای فشرده حرارتی, طول عمر عایق موتورهای القایی پیش بینی شده است. شبکه پارامترها بر اساس ابعاد موتورها، مقاومت های حرارتی، خازن های حرارتی و منابع اتلاف بنا شده است. سپس، این مدل برای تخمین دمای قسمت های مختلف موتور ونیز تعیین طول عمر عایق آن به کاررفته است. سرانجام ، نتایج پیش بینی شده از مدل توسط آزمایش های لازم مورد تأیید قرارگرفته است.

IJE TRANSACTIONS B: Applications Vol. 34, No. 05, (May 2021) 1225-1232

International Journal of Engineering

Journal Homepage: www.ije.ir

Fast Color Straight Line Pattern Recognition in an Object using High Speed Self Learning Devices

Rasiq S. M.*, S. Krishnakumar

School of Technology and Applied Sciences, Mahatma Gandhi University Regional Centre, Edappally, Kochi, India

PAPER INFO

Paper history:
Received 23 November 2020
Received in revised form 08 Februery 2021
Accepted 03 March 2021

Keywords:
Rasiq Krishnakumar Algorithm
Rasiq Krishnakumar Device
Fast Object Recognition
Color Straight Line Pattern

ABSTRACT

Most of the man-made objects are having some straight lines with colors. A very high-speed object recognition method using color straight line patterns is carried out using a novel self-learning device: Rasiq Krishnakumar Device(RKD). Instead of that Artificial Neural Networks (ANN), RKD based networks are used for different steps in this pattern classification. The color and straight-line features are extracted by using high-speed color segmentation and fast efficient straight-line segment extraction methods using the RKD based systems. The training and the testing algorithms of the pattern classification are using RKD-based processing. The fast color features extraction method uses an array of RKD-based devices and the fast efficient straight-line segment extraction method employs an array of processing elements and a main control unit. Some fusion devices are used for a straight line with colors features. The area of interest and the area of line segments of a particular object are other features for improving the accuracy of object classification.

doi: *10.5829/ije.2021.34.05b.15*

NOMENCLATURE

c	Common colors	*C*	Common color ratios
lc	Colors related to staight lines	*LC*	Color count ratios
O	Set of objects	*k and k′*	Known values
a_1	Area of region of interest	a_2	Area of line segments

1. INTRODUCTION

An RKD is a self-learning device. RKD networks are used for multi-class pattern recognition problems, fast efficient straight line detection, and color based image segmentation [1-3]. The applications of high-speed object recognition methods are mainly included in robotics, driverless vehicles, and artificial intelligence. The difficulties in object recognition under various circumstances are lightning conditions, the position of the object in the image, image rotation, occlusion, and change in the size of the object [4]. The other main difficulties in a high-speed object recognition system are the hardware complexity and the processing time [5]. The methods carried out are optimized for these difficulties.

The main reason for the hardware complexity and the high processing time is the complications in ANN for training and testing. Convolutional Neural Networks (CNN) are used for object recognition applications that need sophisticated hardware for high-speed applications. The performance of CNN increases when the number of convolutional layers, pooling layers, and fully connected layers increases [6]. The increase in layers causes complications in training and requires large training data [7]. Sometimes these approaches are not suitable for high-speed object recognition applications. The sophisticated processes in CNN methods for training, reduce the scope for further processing of erroneous predictions. Unobservable processes in the hidden layers of ANN are another challenge for further processing and the weight values in the hidden layers cannot be edited [8].

*Corresponding Author Institutional Email: rasiqsm2@gmail.com (Rasiq S. M.)

Please cite this article as: Rasiq S. M., S. Krishnakumar, Fast Color Straight Line Pattern Recognition in an Object using High Speed Self Learning Devices, International Journal of Engineering, Transactions B: Applications Vol. 34, No. 05, (2021) 1225-1232

If a single weight in the trained ANN is edited, the stability of the entire network is affected [9]. In the case of RKD networks, the knowledge acquired by the network can be edited for further applications.

This work uses a novel method for training and testing based on RKD. The RKD is simple, fast, required fewer hardware components and training samples, and having easily accessible processing variables [10]. Three RKDs are formed to a basic color matching device (BCMD) used for learning as well as for detecting a particular color. There is n number of BCMDs used for learning n number of colors of a multiple colored object. An array of BCMDs is needed for segmenting these n number of colors. The BCMD array segments a single color at a time. All colors in the object are recognized after n number of segmentation [3].

The straight-line segment extraction method requires a smaller number of processing elements (PE) compared to a parallel Hough transform (HT) method. The speed and accuracy of straight-line extraction are very high compared to the parallel HT method [2]. Straight lines with colors (SLC) are formed by combining the color recognition method and parallel straight-line segment extraction method. The main methods used here are recognition of multiple colors, straight-line extraction, straight lines with colors recognition, the object area, and the line segments area.

For fast processing, six two-dimensional arrays and a straight line color fusion device are proposed. A few straight line color fusion devices process the six arrays results in fast processing. A significant property of the RKD network is that comparatively higher classification accuracy of 92.3% is obtained with a few training images. Moreover, the processing time and memory requirements are less compared to the ANN methods.

Section 2 discusses the theory and methodology which includes recognition of multiple colors, high-speed straight-line extraction, six arrays for SLC data extraction, straight-line color fusion device, SLC calculations, and multi-class pattern recognition using RKD array. Session 3 deals with results and discussion, and finally session 4 includes the conclusion.

2. THEORY AND METHODOLOGY

A multi-class pattern recognition method is carried out by using an RKD array, which requires color features, SLC features, and the object area. BCMDs are used for learning and detecting color features. Fast efficient straight line extraction method is combined with the color recognition method using six arrays of SLC data extraction. SLC features are obtained by straight line color fusion devices. The object is recognized by multi-class pattern recognition using an RKD array.

2. 1. Recognition of Multiple Colors The BCMD is capable of learning one color in an image at a time. The system can identify multiple colors present in the object by training a number of BCMDs [3]. A single color is learned by a BCMD by selecting some sample points in the colored region of the image. The number of BCMDs needed for learning is n, for n number of colors in the object. The learned colors are represented as color 1 (c_1), color 2 (c_2), color 3 (c_3) ,… , color n(c_n) by the system. Segmentation of a single color from an N x N image needs N^2 number of BCMDs. These BCMDs are arranged like an N x N array and each BCMD has stored the color attributes from the database. BCMDs check every pixel in the image and detect the colored region in the image. The system can recognize n number of colored regions of an object by checking in the image n times using the BCMD array.

2. 2. High-speed Straight-line Extraction The straight-line segment extraction method used here is very fast and efficient and it can extract straight lines within a few nanoseconds [2]. It is calculated that for an N x N image $6N^2$-16N +14 line alignments are possible. Each of these line alignments is connected to a PE. By using this method, hardware complexity is comparatively very much less than the parallel HT method. The least number of PEs required for the parallel HT method is MN^2, the value of M is the angular variations and N depends on the resolution of the image [11]. Those PEs perform arithmetic operations, cosine and sine value calculations, and reconfiguration of the PE mesh. In this method each PE performs pixel scanning in the line alignment, comparing line lengths with nearby PEs and eliminating errors. Parallel HT methods use less resolution line extraction. The method discussed in literature [2] is fast and accurate than parallel HT.

2. 3. Six Arrays for SLC Data Extraction The most processing time required step is SLC data extraction. In order to reduce the time of processing a parallel processing method is employed. For extracting SLC information six arrays are needed as shown in Figure 1. These arrays are having a size N x N. First array stores a binary image in which each element is having one-bit memory and it is split into several line alignments as described in literature [2]. Each element in the second and third array are having word length Log_2 (N), these arrays are x and y coordinates respectively, and are accessible by a PE used for fast line detection. The remaining three arrays are used for storing primary color information and these arrays are split into different line alignments like the first array, for the line extraction. These line alignments can be enabled. By simultaneous and synchronous scanning through these line alignments, the system can evaluate the color data of a line. An actual line has six- imaginary lines as shown in Figure 2. Two-

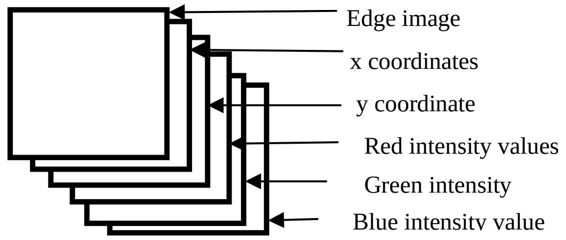

Figure 1. Six arrays for lc data extraction

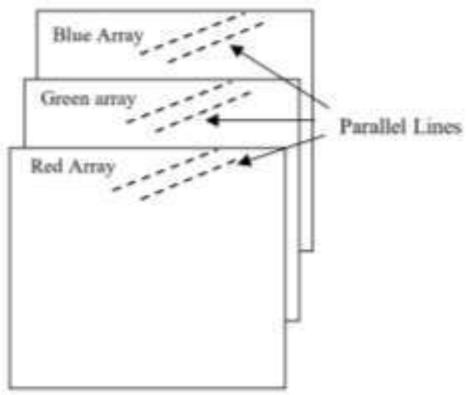

Figure 2. Parallel imaginary straight lines

lines in the red intensity array, two lines in the green intensity array, and two lines in the blue intensity array. Each element in these arrays has a one-byte word length. If these three arrays are combined, the original image is obtained. Simultaneous and synchronous scanning is needed for acquiring actual SLC data of a line.

2. 4. Straight Line Color Fusion Device

Different functions of a line color fusion device are as follows. At first, it acquires the line data from MCU [2] which includes the starting and ending points of a line and its identity in the first layer. Using the line data, the line color fusion device identifies and enables six parallel imaginary lines in the line alignments of fourth, fifth and sixth arrays, the starting and ending point data are used for segmenting the line alignments. Then the fusion device scans through the parallel imaginary lines in the above three layers. This scanning is simultaneous and synchronous inside the three layers. For n number of colors, there are 2 × n number of digital counters inside the line color fusion device and a digital counter count the number of pixels represents a color. There is a 2 × n number of BCMDs for learning/matching colors in the imaginary line segments. For matching, color data are stored from the database. A BCMD has three inputs, the number of imaginary line segments is six for a particular line segment and the number of colors is n. So, the number of BCMD required for a line color fusion device is 2×n. Each input of a BCMD match one primary color of an array mentioned above and each line segment has two imaginary lines in the array.

The number of line color fusion devices are used for scanning the imaginary parallel line segments is m, they scan through the line alignments of the above arrays. The line alignments are enabled by the line color fusion devices corresponding to the data from the MCU.

The line color fusion device enables corresponding starting and ending points in the line alignments in the above arrays. Then a fusion device scans through corresponding arrays' imaginary line segments and it finds the color information lc. A maximum number of fusion devices are equal to the maximum number of line segments receive from the MCU.

The scanning through imaginary parallel line segments is one of the most processing time requiring steps by the system, that is performed by the fusion device. The MCU collects all SLC data for evaluating the color count ratios.

2. 5. SLC Calculations

To identify the straight lines with color patterns, initially, the straight-line segments present in the image are extracted. The edge image is extracted by using parallel differentiators. Then all the line segments are extracted as described in literature [2]. The MCU provides the data of line segments present in a color image. Since these line segments are extracted from edges they do not give accurate colors. Edges are sharp changing pixels intensity values. So, the system draws two parallel imaginary straight line segments with each line segment. An actual straight-line segment should be in the middle of these parallel imaginary straight lines. The parallel imaginary straight lines are h pixels away from the actual straight-line segment; let the value of h be 10. These parallel imaginary straight lines contain color information related to that particular straight-line segment. The system scans through these parallel imaginary straight lines for finding the colors related to those particular straight-line segments. Thus, m number of the straight lines are having n number of color information represented as lc.

$$lc = \{ l_1c_1, l_1c_2, \dots, l_1c_n;\ \dots; l_2c_1, l_2c_2, \dots, l_2c_n;\ ..; l_mc_1, l_mc_2, \dots, l_mc_n \} \quad (1)$$

where m is the number of line segments and n is the number of colors.

The system learns to classify objects using a training algorithm. After learning is completed the system is tested using a testing algorithm. In the training as well as the testing stage, the system has to learn multiple colors present in the objects. For a class of objects, initially, the system learns the common colors present in that class represented as c, where c = $\{c_1, c_2, c_3, \dots, c_n\}$, (n is the maximum number of common colors present in the object class).

$$C = c / \sum_{i=1}^{n} c_i \quad (2)$$

Then the system extracts straight lines and evaluates color count ratios LC.

The ratio of the number of pixels for a particular color of a straight-line segment is divided by the number of all the color pixels detected by different straight-line segments is called a color count ratio LC.

$$LC = lc / \sum_{i=1}^{m} \sum_{j=1}^{n} l_i c_j \quad (3)$$

where i = 1,2,3,.,.m and j = 1,2,3,..,n

The main intention of finding the color count ratio and C is due to the different sizes of objects in the image of the same class. If the object size is large, c and lc values are also large similarly if the object size in the image is small, c and lc values are also small. When C and the color count ratios are calculated they are almost the same for different sizes of objects in the image for a particular class.

Now each class of the objects represented as O_k is having the following attributes.

$O_k = \{C, LC\}$, such that $O_k \in O$, where k=1,2, 3,…,p (p is the number of objects), and O is the set of entire objects.

$C = \{C_1, C_2, C_3, \ldots, C_n\}$, where n is the number of colors

$LC = \{L_1C_1, L_1C_2, \ldots, L_1C_n; \ldots; L_2C_1, L_2C_2, \ldots, L_2C_n; \ldots; L_mC_1, L_mC_2, \ldots, L_mC_n\}$

where m is the number of lines and n is the number of colors RK algorithm converts each attribute as a low value and a high value.

2. 6. Multi-class Pattern Recognition Using RKD Array

Features X_1, X_2, X_3, …., X_d be in d dimensional feature space and which are to be classified into K classes. An RKD array having d number of RKDs and the outputs of these RKDs are ANDed using an AND gate can be used for classifying a particular class as shown in Figure 3.

RKD1 learns attribute values of X_1 which are k_1 and k_1', RKD2 learns attribute values of X_2 which are k_2 and k_2' similarly all RKDs produce their attribute values from corresponding feature variable after training. Thus, for a class O_k a set of attribute values are learned by the RKD array.

For recognizing or classifying a particular object, its attribute values are stored in the RKD array, then the feature vector is given as input to the RKD array, and the RKD array matches the feature vector with attribute values, if it is matched the object is recognized.

The RKD array is used in multi-class pattern recognition problems for high-speed object recognition applications. At a time, a d dimensional array learns to classify a single class of objects. After learning is completed the attribute values produced by the RKD array are stored in the database. Then the same RKD array can be used for learning another class of the object and the attribute values are stored again in the database.

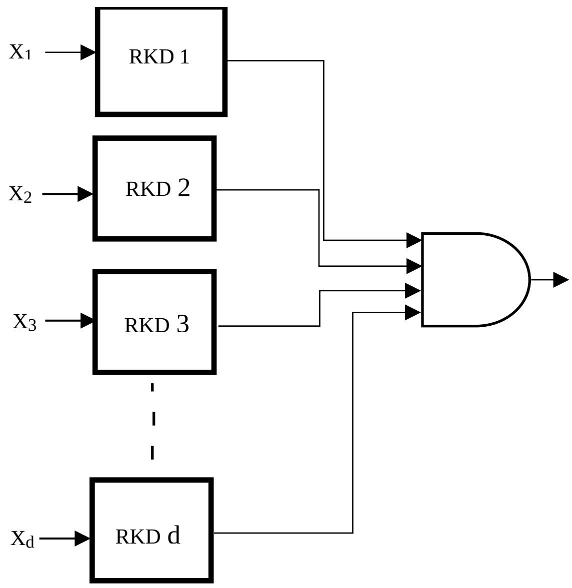

Figure 3. RKD array ANDed for classification

These processes are repeated p number of times for learning to classify p classes of objects.

While testing the input feature vector is given to the RKD array and the attribute values of each class are stored into the RKD array one by one. Let us suppose for a particular class all RKD outputs become high and the AND gate output becomes high then that class is said to be recognized.

This method is very fast and it requires comparatively a few hardware components. It doesn't need the statistical approach of recognition or neural network approach. So, it is simple and requires less complicated processing. For straight-line extraction of an N x N image, each PE has to perform in three arrays of N x N size, because the size of the image is N x N. First array contains the edge image, the second array contains the coordinate x values, and the third array contains the y values. For pattern recognition, three additional arrays are needed.

3. RESULTS AND DISCUSSION

Table 1 shows the accuracies of various methods of object recognition from RGB images. The data sets used are the Washington RGB-D object dataset shown in Figure 4. The accuracy is calculated by averaging over classes and the presented method got an accuracy of 92.3%.

In this work speed of object recognition is in the nanosecond range. The system can process raw images directly, with no need for noise removal. The color segmentation is optimized by using BCMDs based on RKD, it is very fast and accurate. The color segmentation part needs lesser time compared to the straight-line segment extraction method. By using the HT method some lines may not be detected. The accuracy of the HT depends on accumulator cells and the bin size [2]. The proposed line segment extraction method extracts every line present in the image with higher accuracy and lesser hardware than parallel HT. The training and testing algorithms are also simple compared to other methods. Most of the works in this area require a large number of images for training. It is due to the fast learning property of RKDs, only a few images are needed for training the presented system.

Training Algorithm

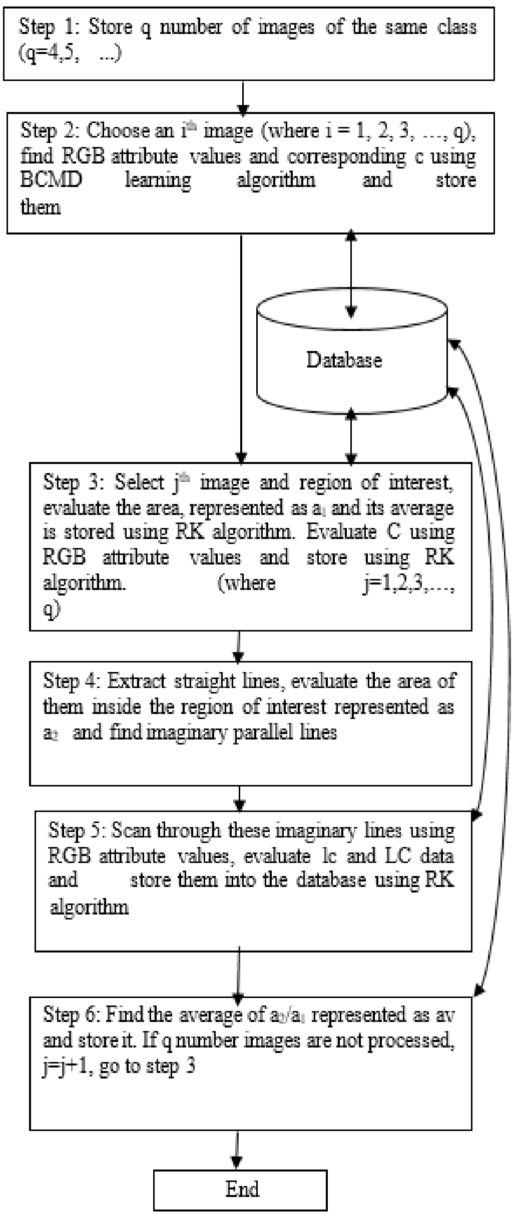

Testing Algorithm

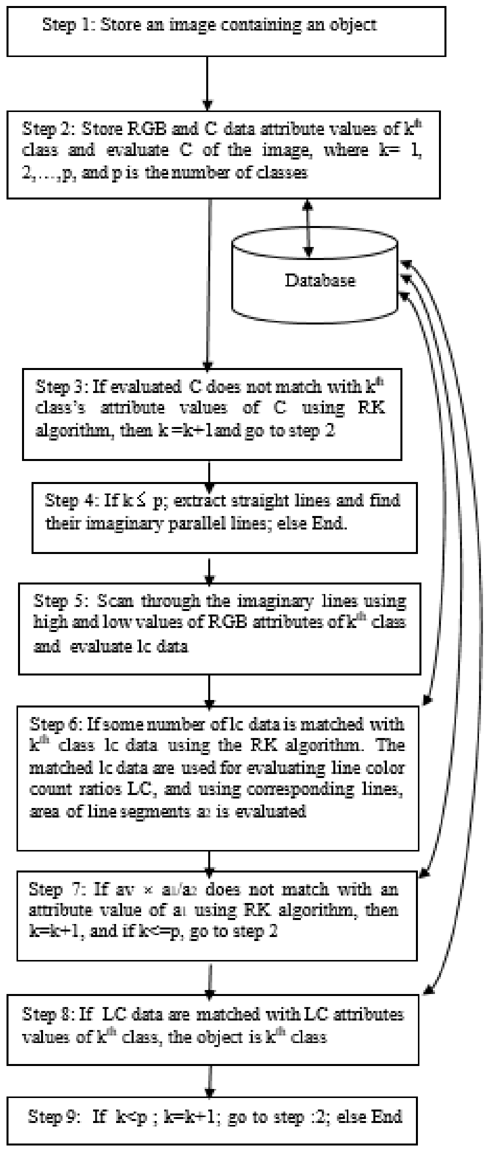

The color noise can be reduced by using the smoothening technique in the learning step. While teaching a color, it is selected a number of points having the same color, then the device learns the color of that area. By adding a smoothening technique, a sharp variation in colors at some points must be avoided because they are considered as noise pixels. The smoothening does not affect the testing algorithm. In the teaching step, smoothening uses additional computation time. The smoothening technique is not required at the recognition algorithm. It is because the recognition algorithm recognizes only the color in a particular range learned by a BCMD.

TABLE 1. Comparison with state-of-the-art methods on the Washington RGB-D object dataset

Method	**Accuracy in %**
Linear SVM [13]	74.3 ± 3.3
kSVM [13]	74.5 ± 3.1
HKDES [14]	76.1 ± 2.2
Kernel Descripto [15]	77.7 ± 1.9
CNN-RNN [16]	80.8 ± 4.2
RGB-D HMP [17]	82.4 ± 3.1
MMSS [18]	74.6 ± 2.9
Fus-CNN (HHA) [19]	84.1 ± 2.7
Fus-CNN (Jet) [19]	84.1 ± 2.7
CFK [20]	86.8 ± 2.2
MDCNN [21]	87.9 ± 2.0
VGGnet + 3D CNN + VGG3D [22]	88.9 ± 2.1
RGB CNN+SVM[23]	87.5 ± 2.1
Presented Method	**92.3 ± 2.5**

CNN-RNN method requires the processing of a large number of image frames [12] for better accuracy. It is identified that the accuracy percentage increases almost proportional to the logarithm of the number of image frames processed. The batch size, as well as the number of epochs, are large. CNN methods require hundreds of epochs for better accuracy.

Figure 5 shows the accuracy percentage change in the RKD network method. Only a few numbers of image frames are processed. Accuracy percentage change increases almost proportional to the exponential of the number of training images and requires only a few numbers of training images for better results. Fast learning property is due to RK algorithm-based learning.

The lower values of LC data are known as k values, and higher values of LC data are known as k′ values. Most of the k and k′ ranges of each variable are not overlapping. If k─k′ values of a single variable in a class is different, the class is fully separated. Here, the classes are almost fully separated or mutually exclusive, and accurate classification results are obtained.

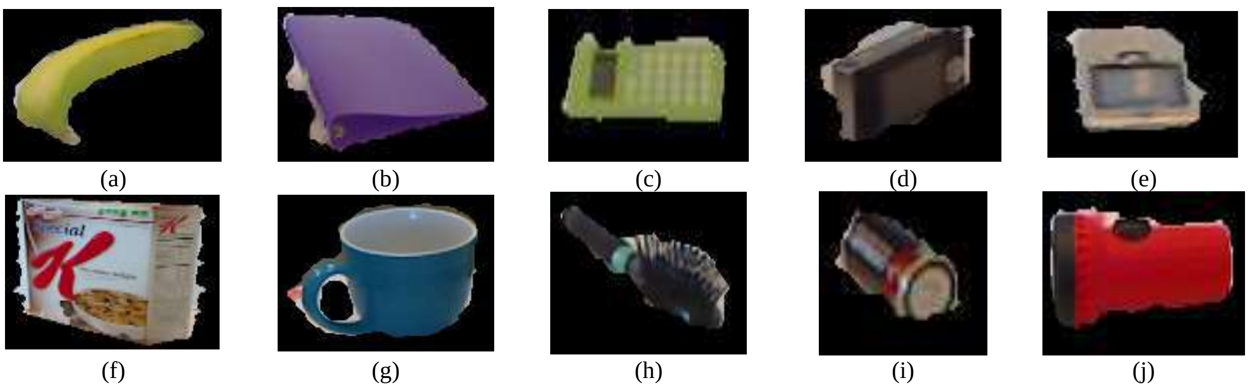

Figure 4. Different classes of Washington RGB D objects dataset (a) banana, (b) binder, (c) calculator,(d) camera, (e) cell phone, (f) cereal_box, (g) coffee mug, (h) comb, (i) dry battery and (j) flashlight

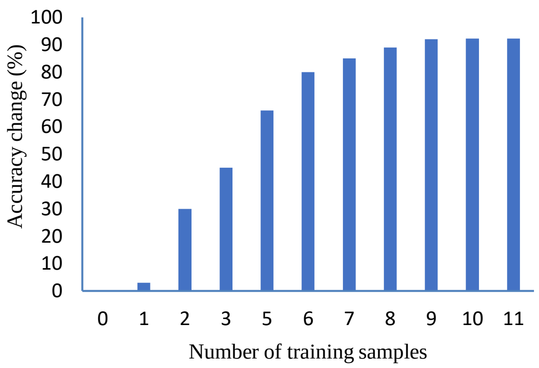

Figure 5. Change in classification accuracy with the number of training samples of the presented method

The accuracy of object recognition is estimated as 92.3% with a standard deviation of 2.5 when 10 classes of objects having different straight lines and color patterns are used. The number of training images used for each class is only 11 and tested with 200 images having 20 images with each class and obtained an accurate result for 185 testing images. The accuracy is averaged over classes. Figure 5 shows the accuracy change with respect to the number of training images. The accuracy change remains almost constant when the number of images is around 10. It is due to the limitations of the dataset. The color and SLC patterns of these classes have variations among them; in other words, the patterns of these classes are mutually exclusive. More accurate results compared to other works are obtained.

TABLE 2. Comparison of the number of computations and memory requirements for the different methods

Model	FLOPs	Bytes
AlexNet	7.29e+8	2.44e+8
CaffeNet	7.27e+8	2.44e+8
CNN-S	2.94e+9	4.12e+8
VGG-16	1.55e+10	5.53e+8
Presented	**7.07e+7**	**3.14e+6**

The computation time relies on the number of computations per frame. Table 2 shows the number of computations and memory requirements for the presented method. Which are significantly less than different neural network methods for a 224 x 224 image [24]. The number of computations and memory requirements are calculated by adding entire counts of different functioning devices and it is verified by simulations. A FLOP is the number of floating-point operations required to classify one image with the convolutional network. In the presented method, most of the calculations are using one-byte integers.

4. CONCLUSION

The present method is used for color and straight-line pattern recognition. The object recognition became very accurate by using features of line segments and colors. The color and SLC are recognized by separate parts, so it recognizes an object at a very high speed. The hardware complexity is very less compared to other methods. The RK algorithm reduces the hardware complexity, processing time, and memory requirements. The RK algorithm-based learning and recognition are faster than other methods. It is a logical device and the parameters are editable and it requires a few images for training. The method used for straight-line segment extraction is highly accurate compared to the parallel HT method. The line extraction algorithm uses comparatively little hardware complexity. The color pattern recognition unit also requires comparatively lesser hardware complexity. So, hardware implementation of this system will give better results.

5. REFERENCES

1. Rasiq S.M and S. Krishnakumar, “A Fast-Efficient Multi Class Pattern Recognition Method***”, International Journal of Innovative Technology and Exploring Engineering*** ,Vol. 8, (2019), 1935-1938, doi: 10.35940/ijitee.L2893.1081219 9.
2. Rasiq S M, Jeevan K M and S Krishnakumar, “A Fast-Efficient parallel processing algorithm for straight line detection***”, Indonesian Journal of Electrical Engineering and Computer Science***, Vol. 16, No. 3, (2019), 1320-1326, doi: 10.11591/ijeecs.v16.i3.pp1320-1326.
3. Rasiq S.M and S. Krishnakumar, “Parallel Processing Technique for Multiple Color Object Recognition”, ***International Journal of Pure and Applied Mathematics***, Vol. 118, No.7, (2018), 125-130.
4. Sukanya C.M., Roopa Gokul, Vince paul, “A survey on object recognition method”, ***International Journal of Computer Science & Engineering Technology***, Vol. 6, (2016), 48-52.
5. D. Maturana and S. Scherer, "VoxNet: A 3D Convolutional Neural Network for real-time object recognition", IEEE/RSJ International Conference on Intelligent Robots and Systems (IROS), Hamburg, Germany, (2015), 922-928, doi: 10.1109/IROS.2015.7353481
6. N. Passalis and A. Tefas, "Training Lightweight Deep Convolutional Neural Networks Using Bag-of-Features Pooling", ***IEEE Transactions on Neural Networks and Learning Systems***, Vol. 30, No. 6, (2019), 1705-1715, doi: 10.1109/TNNLS.2018.2872995.
7. M. Kim, J. H. Jung, J. U. Ko, H. B. Kong, J. Lee and B. D. Youn, "Direct Connection-Based Convolutional Neural Network (DC-CNN) for Fault Diagnosis of Rotor Systems", ***IEEE Access***, Vol. 8, (2020), 172043-172056, doi: 10.1109/ACCESS.2020.3024544.
8. Li J, Chen BM, Lee GH, “So-net: Self-organizing network for point cloud analysis”, Proceedings of the IEEE conference on computer vision and pattern recognition, (2018), 9397-9406, doi: 10.1109/CVPR.2018.00979.
9. X. Guo, J. Wang, F. Liao and R. S. H. Teo, "CNN-Based Distributed Adaptive Control for Vehicle-Following Platoon With Input Saturation", ***IEEE Transactions on Intelligent Transportation Systems,*** Vol. 19, No. 10, (2018), 3121-3132, doi: 10.1109/TITS.2017.2772306.
10. Rasiq S.M., S.Krishnakumar, “Parallel Processing Technique for High Speed Object Recognition”, ***International Journal of Computer Applications***, Vol. 99, No. 4, (2014), 23-27, doi: 10.5120/17361-7874 .
11. Ling Chen and Hongjia Chen, “A fast efficient parallel Hough transform algorithm on LARPBS”, ***The Journal of Supercomputing***, Vol. 29, (2004), 185-195, doi 10.1023/B:SUPE.0000026850.06646.3c.
12. C. Wang, M. Cheng, F. Sohel, M. Bennamoun, J. Li, “NormalNet: a voxel-based CNN for 3D object classification and retrieval”, ***Neurocomputing,*** Vol. 323, (2019), 139-147 doi: 10.1016/j.neucom.2018.09.075.
13. Lai K., Bo L., Ren X., Fox D., “ A large-scale hierarchical multi-view RGB-D object dataset”; Proceedings of the IEEE International Conference on Robotics and Automation; Shanghai, China, (2011), 1817–1824,doi: 10.1109/ICRA.2011.5980382.
14. Girshick R., Donahue J., Darrell T., Malik J., “Rich Feature Hierarchies for Accurate Object Detection and Semantic Segmentation”, Proceedings of the IEEE Conference on Computer Vision and Pattern Recognition; Columbus, OH, USA. (2014), 580-587, doi: 10.1109/CVPR.2014.81.
15. Bo L., Ren X., Fox D., “Depth kernel descriptors for object recognition”, Proceedings of the IEEE/RSJ International Conference on Intelligent Robots and Systems; San Francisco, CA, USA. (2011), 821-826, doi:10.1109/IROS.2011.6095119.
16. Socher R., Huval B., Bhat B., Manning C.D., Ng A.Y., “Convolutional-Recursive Deep Learning for 3D Object Classification***”,*** Proceedings of the International Conference on Neural Information Processing Systems; Lake Tahoe, NV, USA, (2012), 656-664.
17. Bo L., Ren X., Fox D., “Unsupervised Feature Learning for RGB-D Based Object Recognition”, Proceedings of the International

Symposium on Experimental Robotics; Québec City, QC, Canada, (2012), 387–402.

18. Wang A., Cai J., Lu J., Cham T.J., "MMSS: Multi-modal Sharable and Specific Feature Learning for RGB-D Object Recognition", Proceedings of the IEEE International Conference on Computer Vision; Santiago, Chile, (2015); 1125-1133, doi: 10.1109/ICCV.2015.134.
19. Eitel A., Springenberg J.T., Spinello L., Riedmiller M., Burgard W., "Multimodal Deep Learning for Robust RGB-D Object Recognition", Proceedings of the IEEE/RSJ International Conference on Intelligence Robots and Systems; Hamburg, Germany, (2015), 681-687, doi: 10.1109/IROS.2015.7353446.
20. Cheng Y., Cai R., Zhao X., Huang K., "Convolutional Fisher Kernels for RGB-D Object Recognition", Proceedings of the International Conference on 3D Vision; Lyon, France, (2015), 135-143, doi: 10.1109/3DV.2015.23.
21. Rahman M.M., Tan Y., Xue J., Lu K., " RGB-D object recognition with multimodal deep convolutional neural networks", Proceedings of the IEEE International Conference on Multimedia and Expo; Hong Kong, China, (2017), 991-996, doi: 10.1109/ICME.2017.8019538.
22. Zia S., Yüksel B., Yüret D., Yemez Y., "RGB-D Object Recognition Using Deep Convolutional Neural Networks", Proceedings of the IEEE International Conference on Computer Vision Workshops; Venice, Italy, (2017), 887-894, doi: 10.1109/ICCVW.2017.109.
23. Zeng H, Yang B, Wang X, Liu J, Fu D., "RGB-D Object Recognition Using Multi-Modal Deep Neural Network and DS Evidence Theory", ***Sensors (Basel),*** Vol. 19, (2019), 1-19, doi: 10.3390/s19030529 .
24. J. Wu, C. Leng, Y. Wang, Q. Hu and J. Cheng, "Quantized Convolutional Neural Networks for Mobile Devices", IEEE Conference on Computer Vision and Pattern Recognition (CVPR), Las Vegas, NV, (2016), 4820-4828, doi: 10.1109/CVPR.2016.521.

Persian Abstract

چکیده

بیشتر اشیا-ساخته شده توسط انسان دارای برخی از خطوط مستقیم با رنگ هستند. یک روش شناسایی سریع شی با استفاده از الگوهای خط مستقیم رنگ با استفاده از یک دستگاه خودآموز جدید انجام می شود: دستگاه Rasiq Krishnakumar (RKD). به جای شبکه های عصبی مصنوعی (ANN)، شبکه های مبتنی بر RKD برای مراحل مختلف در این طبقه بندی الگو استفاده می شوند. ویژگی های رنگ و خط مستقیم با استفاده از تقسیم بندی رنگی با سرعت بالا و روش های استخراج سریع و مستقیم خط مستقیم با استفاده از سیستم های مبتنی بر RKD استخراج می شود. آموزش و الگوریتم های تست طبقه بندی الگو با استفاده از پردازش مبتنی بر RKD است. روش استخراج سریع ویژگی های رنگی از آرایه ای از دستگاه های مبتنی بر RKD استفاده می کند و روش استخراج قطعه قطعه مستقیم و کارآمد با استفاده از آرایه ای از عناصر پردازشی و یک واحد کنترل اصلی است. برخی از دستگاه های همجوشی برای یک خط مستقیم با ویژگی های رنگ استفاده می شوند. منطقه مورد نظر و منطقه بخشهای خط یک شی خاص از دیگر ویژگیهای بهبود دقت طبقه بندی اشیا است.

International Journal of Engineering

Journal Homepage: www.ije.ir

Gain Boosted Folded Cascode Op-Amp with Capacitor Coupled Auxiliary Amplifiers

M. Rashtian*[a], M. Vafapour[b]

[a] Aviation Electronics Department, Civil Aviation Technology College, Tehran, Iran
[b] Aviation Electronics Laboratory, Civil Aviation Technology College, Tehran, Iran

PAPER INFO

Paper history:
Received 18 August 2020
Received in revised form 13 March 2021
Accepted 23 March 2021

Keywords:
Gain Boosting
Gain Band-width
Power Supply Dissipation
Operational Transconductance Amplifier

ABSTRACT

A novel gain boosted folded cascode Op-Amp using simple single stage auxiliary amplifiers is presented. The proposed auxiliary amplifiers are designed in a way that has proper input and output DC common mode voltage without using common mode feedback network. The inputs of the auxiliary amplifiers are insulated by the coupling capacitors and floating-gate MOS transistors. Thus, the DC input voltage level limit has been removed. Diode connected transistors are also used in the output of the auxiliary amplifiers, which keep the output voltage level at the desired. A simple single stage auxiliary amplifier imposes fewer poles and zeroes on the main amplifier compared to more complicated amplifiers where consumes also less power consumption. Simulation results in a 0.18μm CMOS technology show a DC gain enhancement of about 20 dB while output swing, slew rate, settling time, phase margin, and gain-bandwidth retain almost as the same as previous folded cascode design.

***doi**: 10.5829/ije.2021.34.05b.16*

1. INTRODUCTION

One of the most popular approaches in designing high speed operational transconductance amplifiers (OTA) is the folded cascode (FC) architecture. Its popularity comes from high unity gain frequency, good output, and input swing. However, it has limitations to provide high DC gain which is required for some mixed-mode circuits like data converters. Active gain boosted folded cascode (GBFC) is presented first by Hosticka [1]. Through this technique, the output resistance and total gain can be increased by the gain of an auxiliary amplifier. This method increases the voltage gain without degrading its high-frequency performance. However, the GBFC introduces a pole-zero pair (doublet), which potentially leads to slow-settling behaviour of such op- amps [2,3,4].

The well-known active gain-boosting technique consists of the main amplifier and two auxiliary amplifiers is shown in Figure 1 [5]. By removing the auxiliary amplifiers and connecting the gate transistors of M_{5-6} and M_{7-8} to the appropriate bias voltages; a traditional folded cascode amplifier is shown in Figure 1. The auxiliary amplifiers should be operated at the specific input and output common mode voltages and therefore they usually utilize two individual common mode feedback networks [6].

There are also other methods presented in literatures that focus mostly on increasing the slew rate while their gain enhancement is not impressive [7-11]. Also, many applications like switched capacitor circuits demand a high gain one stage Op-Amp [12,13].

In this paper, a simple differential amplifier with positive feedback load has been utilized as an auxiliary amplifier. For this reason, the auxiliary amplifiers do not need their own common mode feedback circuit. As described later, coupling capacitors are used at the input of the auxiliary amplifiers so that there is no limit to the DC voltage range of the auxiliary amplifier input. Also, two different types of the auxiliary amplifiers with two different DC output voltage levels have been utilized for the purpose of providing proper output bias voltage.

2. PROPOSED AMPLIFIER

Figure 2 illustrates the equivalent half-circuit of the GBFC shown in previous figure. The body effect is ignored.

*Corresponding Author Institutional Email: rashtian@catc.ac.ir (M. Rashtian)

Please cite this article as: M. Rashtian, M. Vafapour, Gain Boosted Folded Cascode Op-Amp with Capacitor Coupled Auxiliary Amplifiers, International Journal of Engineering, Transactions B: Applications Vol. 34, No. 05, (2021) 1233-1238

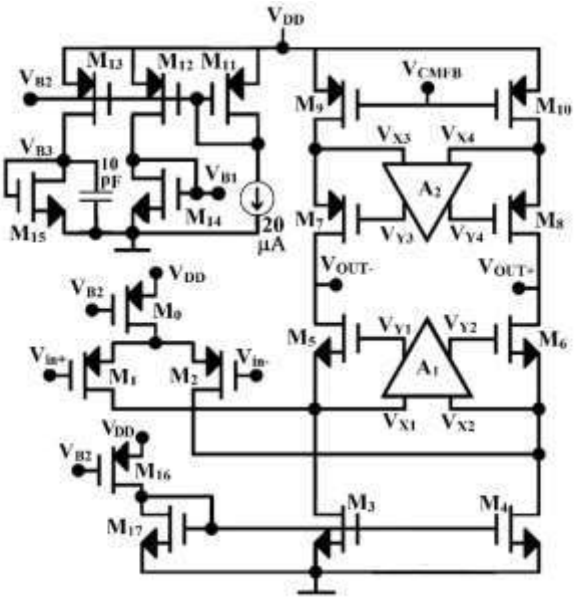

Figure 1. Conventional boosted-gain folded cascode

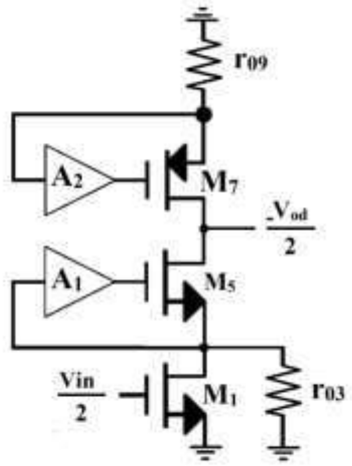

Figure 2. Equivalent half-circuit of the GBFC

Using KVL and KCL, the DC gain of the circuit can be written as:

$$\frac{v_{od}}{v_{in}} = -g_{m1} r_{o5} \frac{A_X^2 g_{m5} r_{o5}(r_{o1} \| r_{o3}) - 2A_X g_{m5} r_{o5}(r_{o1} \| r_{o3}) - 3A_X(r_{o1} \| r_{o3}) + g_{m5} r_{o5}(r_{o1} \| r_{o3}) + 3\,(r_{o1} \| r_{o3}) + 2(r_{o1} \| r_{o3})/g_{m5} r_{o5}}{\frac{3}{g_{m5}} + \frac{r_{o1} \| r_{o3}}{g_{m5} r_{o5}} + r_{o5} + r_{o1} \| r_{o3} - A_X r_{o5} - A_X(r_{o1} \| r_{o3})}$$

$$\cong g_{m1} r_{o5} \frac{A_X^2 g_{m5} r_{o5}(r_{o1} \| r_{o3})}{A_X r_{o5} + A_X(r_{o1} \| r_{o3})} \cong A_X g_{m1} r_{o5} g_{m5} \frac{r_{o5}(r_{o1} \| r_{o3})}{r_{o5} + (r_{o1} \| r_{o3})} \cong A_X g_{m1}(g_{m5} r_{o5}(r_{o1} \| r_{o3}) \| g_{m5} r_{o5} r_{05}) = A_X g_{m1}(g_{m5} r_{o5}(r_{o1} \| r_{o3}) \| g_{m7} r_{o7} r_{09}) = A_X A_{FC} \quad (1)$$

where the voltage gain of both auxiliary amplifiers, A_X, is almost assumed the same and relatively large. Also, $r_{o5} = r_{o7} = r_{o9}$ is considered. As can be seen, the voltage gain of the GBFC is approximately A_X times of FC.

The input DC voltage level of the first auxiliary amplifier A_1 (V_{X1} and V_{X2}) is about one overdrive voltage of M_4 & M_5 (V_{OV4}) and the output common mode voltage of A_1 should be around at $V_{GS5}+V_{OV4}$ for the output swing considerations. The proposed circuit of A_1 is illustrated in Figure 3a. As shown in this figure, gates of M_{1b} & M_{2b} isolated by coupling capacitors C_{1a} and C_{2a} from the main amplifiers, and the gate DC voltage level of M_{1b}-M_{2b} is supplied through quasi-floating gate transistors M_{7a} &M_{7b} which act as large resistors to V_{B3} [14].

The output common mode voltage of A_1 is stabilised by diode connected transistors M_{5a} & M_{6a} without using individual common mode feedback network at the DC voltage V_{G3a} which is proper for a driving gate of M_5 and M_6 transistors. The DC gain of A_1 can be obtained by:

$$A_X = gm_{1a} R_X \quad (2)$$

$$R_X = \left(gm_{5a} - gm_{3a} + gds_{5a} + gds_{3a} + gds_{1a}\right)^{-1} \quad (3)$$

while the value of gm_{3a} and gm_{3b} is approximately selected to 90 and 80 percent of gm_{5a} and gm_{5b}, respectively, to control the probable destructive effect of positive feedback [15]. In the same way, auxiliary amplifier A_2 has the same DC gain as A_1 and input coupling capacitors C_{1b} & C_{2b} as shown in Figure 3b. The output common mode voltage of A_2 is adjusted by diode connected M_{5b} & M_{6b} at dc level of V_{DD}-V_{SG5b} which is proper for biasing the gates of M_7 & M_8.

Boosting technique added a pole-zero doublet into the transfer function of GBFC. It can be shown that the zero location ω_Z is approximately equal to $(1+A_X)\omega_X$ where ω_X is the 3 dB cut-off frequency of auxiliary amplifiers and the zero is right close to its doublet pole [5, p.372]. The zero location ω_Z can be written as:

$$\omega_Z \approx A_X \omega_X \approx gm_{1a} R_X \frac{1}{R_X C_X} \approx \frac{gm_{1a}}{C_X} \quad (4)$$

where C_X donates the total load capacitance in the output of the auxiliary amplifier [16].

Hence, increasing the bias current of A_1 & A_2 has resulted in to greater gm_{1a}; therefore, higher value of zero location of ω_Z. The larger ratio of ω_Z to the unity frequency ω_U, the smaller the doublet effect [3]. Hence, with adjusting the tail current sources of A_1 & A_2 (Id9a & Id9b) slow settling caused by the doublet effect can be suppressed. The second pole location of the proposed auxiliary amplifier is far from its unity gain frequency and can be ignored. However, most of the reported GBFC amplifiers utilizing extra FC with a considerable

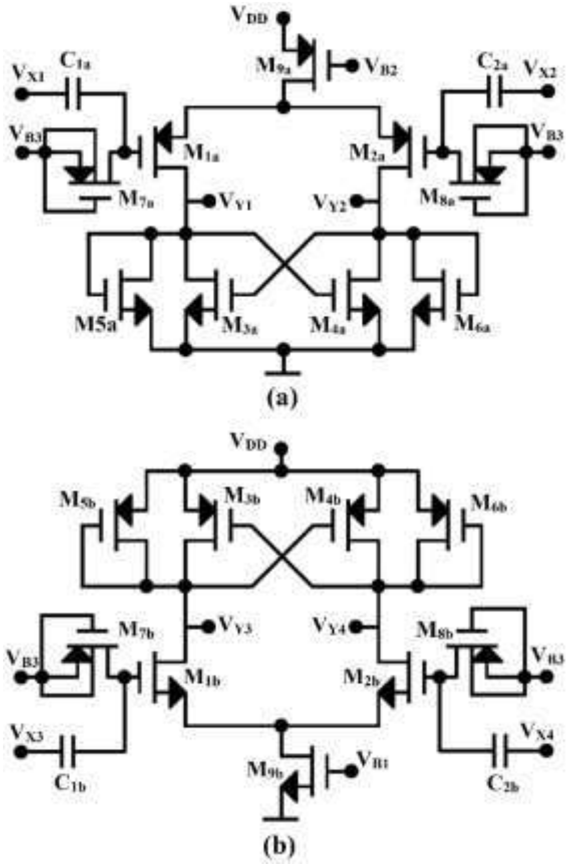

Figure 3. Proposed auxiliary amplifiers, A_1: (Figure 2a) and A_2: (Figure 2b)

TABLE 1. Transistor sizes(μm/μm) and component values

Transistor Number	W/L	Transistor Number	W/L
M_0	$\frac{55}{0.22}$	M_{1a}-M_{2a}	$\frac{8}{0.5}$
M_1-M_2	$\frac{128}{0.36}$	M_{3a}-M_{4a}	$\frac{0.33}{0.75}$
M_3-M_4	$\frac{32}{0.5}$	M_{5a}-M_{6a}	$\frac{0.36}{0.75}$
M_5-M_6	$\frac{16}{0.22}$	M_{7a}-M_{8a}	$\frac{0.5}{0.5}$
M_7-M_8	$\frac{64}{0.22}$	M_{9a}	$\frac{6}{0.22}$
M_9-M_{10}	$\frac{32}{0.22}$	M_{1b}-M_{2b}	$\frac{4}{0.5}$
M_{11}	$\frac{5}{0.22}$	M_{3b}-M_{4b}	$\frac{0.8}{0.5}$
M_{12}	$\frac{0.5}{0.22}$	M_{5b}-M_{6b}	$\frac{1}{0.5}$
M_{13}	$\frac{1.25}{0.18}$	M_{7b}-M_{8b}	$\frac{0.5}{0.5}$
M_{14}	$\frac{0.5}{0.22}$	M_{9b}	$\frac{6}{0.22}$
M_{15}	$\frac{0.36}{0.36}$	C_{1a}-C_{2a}	0.5pf
M_{16}	$\frac{10}{0.18}$	C_{1b}-C_{2b}	0.5pf
M_{17}	$\frac{6.25}{0.18}$		

secondary pole as an auxiliary amplifier which imposes a new pole to the main amplifier transfer function. Table 1 summarized the transistor sizes of the presented GBFC amplifier.

It should be noted that the amount of the C_{1a}, C_{2a}, C_{1b}, and C_{2b} should be large enough to ignore the parasitic capacitors located in the gate of transistors $M_{1a\text{-}2a}$ and $M_{1b\text{-}2b}$. For example, in Figure 3a, the effect of the parasitic capacitors located at the gates of M_{1a} and M_{2a} in differential mode small signal analysis can be written as:

$$v_{g1a} = \xi\, v_{X1};\ \xi = \frac{C_{1a}}{C_{1a} + C_{Par}}\ , C_{Par} \cong C_{GS1a}. \tag{5}$$

In this paper, the value of C_{1a} is considered to 0.5 pF which be much larger than the C_{PAR}, so the ζ value is very close to one (about 0.98).

3. SIMULATION RESULTS

The two amplifiers were simulated in 0.18μm BSIM3v3 level 49 CMOS technology with 1.8 V of supply voltage by Hspice. The value of load capacitors C_{L1} & C_{L2} is 5 pF for both of the amplifiers. The frequency response of the amplifiers is shown in Figure 4 which shows DC gain enhancement of about 20 dB. A simple inverting amplifier with unity gain shown in Figure 5 is proposed for transient time simulation where C_1 = 1.5 pF and R_1 =

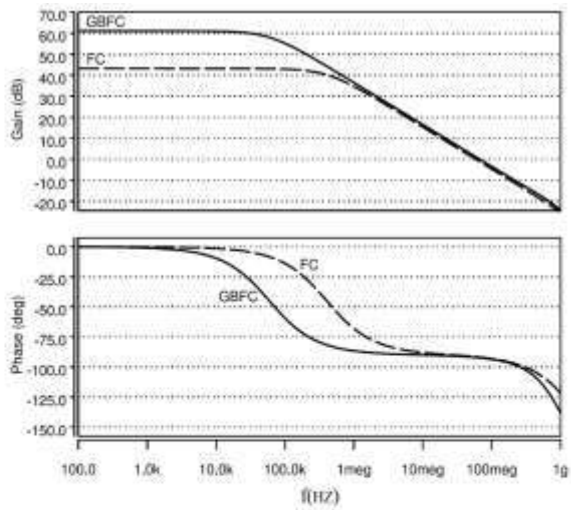

Figure 4. Open-loop frequency response of conventional FC and proposed GBFC amplifiers

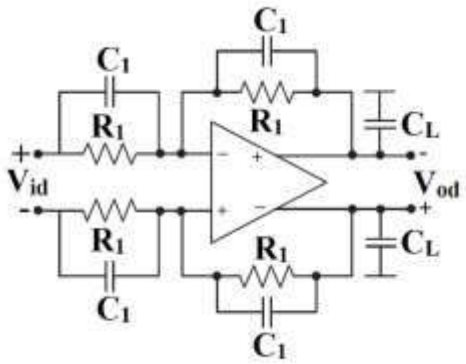

Figure 5. Inverting amplifier with unity gain

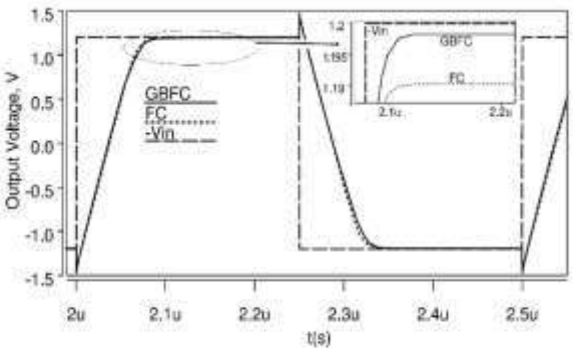

Figure 6. Step response of the amplifiers with 2.4 V_{P-P} of input

TABLE 2. Simulation results summary

Parameter	FC	GBFC
Power Supply	1.8	1.8
Power Dissipation	873	1018
DC Gain(dB)	42.2	61.9
1% Settling Time (nS)	76.8	83.4
Unity Gain Frequency(MHz)	58.5	54.1
Phase Margin(deg)	88.5	88.1
Diff. Output Swing(V)	2.4	2.4

5 MΩ. A square wave voltage with a range of ±1.2 V and a frequency of 2 MHz is applied to its differential input. The simulated differential outputs of the two circuits are shown in Figure 6. The simulation results summary is given in Table 2.

As can be seen, despite the increase in a voltage gain of the proposed amplifier, the maximum output swing of both amplifiers is the same. This is because the addition of auxiliary amplifiers has not caused any change in the DC operating point of the main transistors (M_0-M_{15}) in Figure 1.

To evaluate the effect of auxiliary amplifiers and validity of Equation (1), the frequency response of the auxiliary amplifiers is shown in Figure 7. As can be seen voltage gain of these amplifiers is about 22 dB which close to the enhancement gain of the GBFC over the FC.

Also, Table 3 presents the frequency characteristics of the proposed Op-Amp at different process corners. As can be seen, the GBFC has at least about 61.2 dB gain and 88.1° of phase margin at different process corners. Also, the value of the phase margin is considered under a capacitive load of 1pF and 10 pF which resulted in 76.7° and 88.9°, respectively.

The locations of the poles and zeros of the two amplifiers are shown in Table 4. It can be seen that the pole-zero doublets (-175 & -246 MHz) are large enough in comparison to the unity-gain frequency (ω_U) of the GBFC where ω_U is around 54 MHz. As illustrated by Ju and Lee [17], if the pole-zero doublet natural frequency is approximately four times the ω_U, their destructive effect on the step response can be ignored, which is almost the case here as well. It should be noted that the low-frequency pole and zeros below 1 Hz are omitted in Table 4.

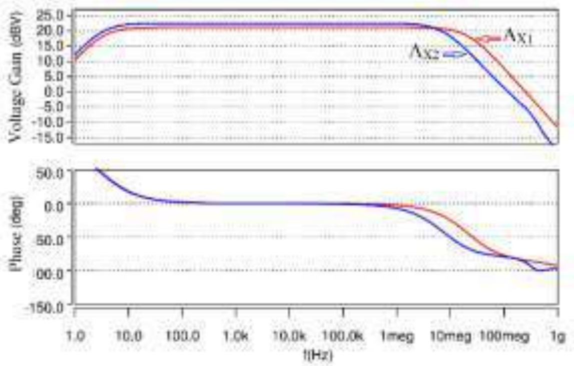

Figure 7. Frequency response of the Auxiliary amplifiers

TABLE 3. Proposed GBFC performance at different process corners with C_L=2×5pF

	TT	SS	SF	FS	FF
DC Gain(dB)	61.9	61.2	61.8	61.8	62.3
Unity Gain Frequency (MHz)	54.1	52	55.3	51.9	58.3
Phase Margin(deg)	88.1	88.1	88.2	88.3	88.3
Average 1% Sett. Time (nS)	83.4	118.5	108.3	98.2	81.9

TABLE 4. The location of poles and zeroes

	Poles (MHz)	Zeroes (MHz)
FC	-0.355	-6771
	-2280	
GBFC	-175.8324	-175.8270
	-246.7793	-246.6072
	-634.5±423.6i	-620.09
	-0.0402	

Figures 8 and 9 show Monte Carlo simulation results of 50 runs for the voltage gain and phase margin with a capacitive load of 5 pF, respectively. As shown in Figure 7, the mean (μ) and standard deviation (σ) of the DC voltage gain are 61.95 dB and 0.85 dB, respectively. Also, as can be seen in Figure 8, the mean and standard deviation of the phase margin are 87.74º and 0.26º, respectively. Monte Carlo simulation results show the GBFC is robust against process variations.

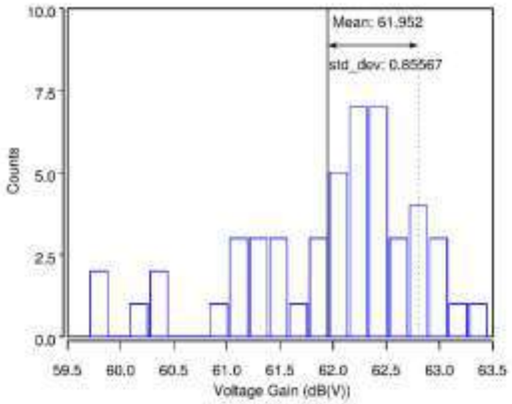

Figure 8. Monte Carlo simulation results for the voltage gain of the GBFC

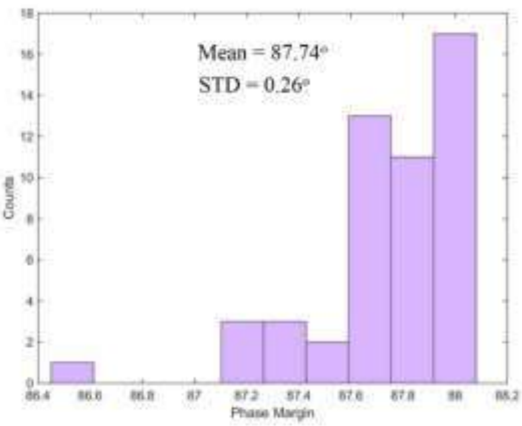

Figure 9. Monte Carlo simulation results for the phase margin of the GBFC

Note that both of the amplifiers have almost the same slew rate, unity gain frequency, phase margin, output swing range, and settling time while the proposed amplifier shows DC gain enhancement of about 20 dB. The power consumption of the GBFC is 1.02 mW while the FC amplifier consumes 0.87 mW, meaning the additional auxiliary amplifiers only consumed 0.145 mW or 14 percent of total power consumption.

4.CONCLUSION

Using two simple single stage amplifiers, the GBFC is presented. To achieve a proper swing at the output of the main amplifier, the input and output DC voltage levels of the auxiliary amplifiers must be set to certain values. The inputs of the auxiliary amplifiers are insulated by the coupling capacitors and therefore they can operate at any input DC voltage level. Diode connected transistors are also used in the output of the auxiliary amplifiers, which keep the output voltage level at the desired level without using an additional common mode feedback circuit. Simulation results show a DC gain enhancement of about 20dB without degrading the output swing and phase margin. The slow settling behaviour arising from the pole-zero doublet is also suppressed since the zero from the single stage auxiliary amplifier is shifted far from unity- gain frequency.

5. REFERENCES

1. Hosticka, B. J. "Improvement of the Gain of CMOS Amplifiers", ***IEEE Journal of Solid-State Circuits***, Vol. 14, No. 6, (1979), 1111-1114. DOI: 10.1109/JSSC.1979.1051324
2. Bult K. & Geelen G. "A Fast-Settling CMOS Operational Amplifier for SC Circuits with 90-dB DC Gain", ***IEEE J. of Solid-State Circuits***, Vol. 25, No 6, (1990), 1379-1384. DOI: 10.1109/4.62165.
3. Chiu, Y. "On the Operation of CMOS Active-Cascode Gain Stage", ***Journal of Computer and Communications***, Vol. 1, No. 6, (2013), 18-24. DOI: 10.4236/jcc.2013.16004.
4. Das, M. "Improved design criteria of gain-boosted CMOS OTA with high-speed optimizations" ***IEEE Transactions on Circuits and Systems II: Analog and Digital Signal Processing***, Vol. 49, No. 3, (2002), 204-207. DOI: 10.1109/TCSII.2002.1013867.
5. Razavi, B., Design of Analog CMOS Integrated Circuits. Second Edition. New York, NY:McGraw-Hill, 2016.
6. Zhang, S., Zhu, Z., Zhang, H., Xiong, Z. and Li, Q. "A 90-dB DC gain high-speed nested gain-boosted folded-cascode opamp", 11th Conference on Ph.D. Research in Microelectronics and Electronics (PRIME), Glasgow, UK, 2015, 357-360, doi: 10.1109/PRIME.2015.7251409.
7. Assaad R. S. &. Martinez S. "The Recycling Folded Cascode: A General Enhancement of the Folded Cascode Amplifier***", IEEE Journal of Solid-State Circuits***, Vol. 44, No. 9, (2009), 2535-2542. DOI: 10.1109/JSSC.2009.2024819.
8. Akbari M. & Hashemipour O. "A super class-AB adaptive biasing amplifier in 65-nm CMOS technology", ***International Journal of***

Electronics Letters, Vol. 6, No. 3, (2018), 302-314. DOI: 10.1080/21681724.2017.1376710.

9. Garde M. P., Lopez-Martin, Carvajal A. & Ramírez-Angulo J. “Super Class-AB Recycling Folded Cascode OTA”, ***IEEE Journal of Solid-State Circuits***, Vol. 53, No. 9, (2018), 2614-2623. DOI: 10.1109/JSSC.2018.2844371.
10. Lopez-Martin, A., Grade, M. P., Algueta, J. M., Cruz Blus, C. A., Carvajal, R. G. & Ramirez-Angulo, J. “Enhanced Single-Stage Folded Cascode OTA Suitable for Large Capacitive Loads”, ***IEEE J. of Trans. on Circuits and Syst._II, Express Brief***, Vol. 65, No. 4, (2018), 441-445. DOI: 10.1109/TCSII.2017.2700060.
11. MiarNaimi, H. and Fallah, M. “A Novel Low Voltage, Low Power and High Gain Operational Amplifier Using Negative Resistance and Self Cascode Transistors”, ***International Journal of Engineering***, ***Transactions C: Aspects***, Vol. 26, No.3, (2013), 303-308.
12. Hashemipour, O. and Ghorvanchi, P. “A Very Low Voltage 9TH Order Linear Phase Baseband Switched Capacitor Filter” ***International Journal of Engineering, Transactions A: Basics,*** Vol. 17, No. 1, (2004), 19-24.
13. Rashtian, M., Hashemipour, O., Navi, K., Jalali, A. “A Novel Structure for Realization of a Pseudo Two Path Band-Pass Filter”. ***International Journal of Engineering, Transactions B: Applications***, Vol. 23, No. 3, (2010), 201-208.
14. Garcia-Alberdi, C., Lopez-Martin, A. J., Acosta, L., Carvajal, R. G. & Ramirez-Angulo, J. “Tunable Class AB CMOS Gm-C Filter Based on Quasi-Floating Gate Techniques”, ***IEEE Transactions on Circuits and Systems I: Regular Papers***, Vol. 60, No. 5, (2013), 1300-1309. DOI: 10.1109/TCSI.2012.2220504.
15. Mesri, A., Pirbazari, M. M, Hadidi, K. and Khoei, A. “High gain two-stage amplifier with positive capacitive feedback compensation”, ***IET Journal of Circuits, Devices and Systems***, Vol. 9, No. 3, (2015), 181-190. DOI: 10.1049/iet-cds.2014.0139.
16. Joshi, A., Shrimali, H., Sharma and S. K. “Systematic design approach for a gain boosted telescopic OTA with cross-coupled capacitor”, ***IET Journal of Circuits, Devices and Systems***, Vol. 11, No. 3, (2017), 225-231. DOI: 10.1049/iet-cds.2016.0448.
17. Ju, H. and Lee, M. “A Hybrid Miller-Cascode Compensation for Fast Settling in Two-Stage Operational Amplifiers”, ***IEEE Transactions on Very Large Scale Integration Systems***, Vol. 28, No. 8, (2020), 1770-1781. DOI: 10.1109/TVLSI.2020.2986508.

Persian Abstract

چکیده

یک آپ امپ فولدد کسکود جدید با بهره افزوده شده و با استفاده از تقویت کننده های ساده کمکی ارائه شده است. تقویت کنندههای کمکی پیشنهادی به گونه ای طراحی شده اند که دارای ولتاژ حالت مشترک ورودی و خروجی مناسب باشند. یک تقویت کننده کمکی یک طبقه ساده ، قطب ها و صفر های کمتری را به تقویت کننده اصلی تحمیل می کند، به علاوه در مقایسه با تقویت کننده های پیچیده تر مصرف توان کمتری نیز دارد. نتایج شبیه سازی با استفاده از فناوری 0.18µm CMOS نشان از افزایش بهره DC تقویت کننده در حدود ۲۰ دسی بل دارد. این در حالی است که سوئینگ مجاز در خروجی ، نرخ چرخش، زمان نشست، حاشیه فاز و پهنای باند تقویت کننده پیشنهادی تقریباً مشابه طراحی فولدد کاسکود مبنا است.

IJE TRANSACTIONS B: Applications Vol. 34, No. 05, (May 2021) 1239-1249

International Journal of Engineering

Journal Homepage: www.ije.ir

A Novel Model Predictive Voltage Control of Brushless Cascade Doubly-fed Induction Generator in Stand-Alone Power Generation System

H. Abdolrahimi*, D. ArabKhaburi

Department of Electrical Engineering, Iran University of Science and Technology, Tehran, Iran

PAPER INFO

Paper history:
Received 12 November 2020
Received in revised form 05 Fabruary 2021
Accepted 13 March 2021

Keywords:
Brushless Cascade Doubly-Fed Induction Generator
Model Predictive Voltage Control
Performance Method
Proportional Integrated

ABSTRACT

The aim of this paper is to present a model predictive voltage control (MPVC) strategy for stabilizing the amplitude and frequency of the output voltages in a Brushless Cascade Doubly-Fed Induction Generator (BCDFIG) under load changing and variable speed of generator shaft in stand-alone mode. BCDFIGs are a particular model of BDFIGs that consist of two induction machines called the control machine and the power machine, so that their rotors are electrically and mechanically coupled together. In this paper, unlike previous studies, which the BCDFIG rotor was integrated, the generator rotor is analyzed as a complex of two rotors of two separate induction machines. Also, the output voltages of generator are predicted and regulated in different operating conditions by using model predictive voltage control. In order to stabilize the amplitude and frequency of BCDFIG output voltages, the appropriate voltage vector is determined to apply to the stator of control machine. This generation system is simulated and simulation results prove the accuracy of proposed method. Experimental results on prototype BCDFIG are provided to validate the proposed methods. Finally, the effectiveness of the proposed controller brings better power capture optimization under variable speed wind turbine.

***doi**: 10.5829/ije.2021.34.05b.17*

NOMENCLATURE

PM, CM	Power machine and control machine	k	Sample number
$\omega_p,\ \omega_{rp}$	PM and its rotor angular frequency	sp, sc, r	PM stator, CM stator and rotor
$\omega_c,\ \omega_{rc}$	CM and its rotor angular frequency	rp, rc	PM rotor, CM rotor
T_s	Sampling time	l, mp, mc	Leakage, PM and CM mutual Inductance
$V,\ i,\ \lambda$	Voltage, current and flux	d, q	d-q rotating frame
R, L	Resistance and Inductance		

1. INTRODUCTION

Nowadays, the wind energy plays an important role in generating renewable energy. Many generators have been used in wind turbines which among them DFIG due to its advantages has the largest share of the market [1]. The controllability of active and reactive power of DFIG is one of the important advantages of this generator. Despite many advantages of DFIG, this generator must be frequently repaired and maintained due to its slip-rings, brushes, and it has a poor performance against network voltage drops [2–5].

In order to take advantages of DFIG and solve its related problems, many studies have been conducted on brushless doubly-fed induction generators (BDFIGs) as future generators of wind turbines [6–13]. Here, BCDFIG is a particular model of DFIG that, instead of putting power and control coils in a structure, are created from the cascade connection of two induction motors and that they are easily implemented. The high controllability and reliability of these generators are their important advantages due to eliminating of slip-rings, brushes and the ease of cascading two separate induction machines [14, 15]. Although there are many studies about the control methods of connected-network BDFIG in different operating conditions, there are few studies on this generator in stand-alone generation systems [16, 17].

*Corresponding Author Email: *hatam.abdolrahimi@gmail.com* (H. Abdolrahimi)

Please cite this article as: H. Abdolrahimi, D. ArabKhaburi, A Novel Model Predictive Voltage Control of Brushless Cascade Doubly-Fed Induction Generator in Stand-Alone Power Generation System, International Journal of Engineering, B: Applications Vol. 34, No. 05, (2021) 1239-1249

To control the grid-connected generator system, the control of active and reactive power generators is remarkable. Whereas for stand-alone generation systems, the stabilization of the amplitude and frequency of the output voltages of generator during load changing and variable speed of generator shaft are very important. Thus, the control methods of grid-connected generator system cannot be used directly in the case of stand-alone generation systems. Among the advanced control techniques, model predictive control is one that has been successfully used in industrial application [18]. This method is a high-performance technique that has advantages such as flexibility in controlling different variables and good dynamic response. To date, this method has been utilized in different drives applications for the aforementioned reasons [8, 15, 19, 20].

In literature, to analyze the dynamic model of BDFIGs, two types of models including coupled-circuit and Unified reference frame model are used. Although the coupled-circuit model of BDFIG, discussed by Kashkooli et al. [21] showed a high accuracy, the physical analysis for the dynamic behavior of the machine using this model due to its complexity, large number of parameters and also their dependence on the position of the rotor is very crucial [21, 22]. The Unified reference frame model of BDFIG by Posa was presented and it for applying new control methods on the generator such as predictive control is very troublous [21].

Extensive researches have been attributed to controller method of DFIG. These control schemes are based on method such as current control, direct torque control (DTC) and direct power control (DPC) [23, 24]. The conventional proportional–integral (PI) method was widely proposed [25]. To design the vector controller based on PI, the resistance of stator or rotor is neglected as well controlling parameter during power generation [26]. The other design is based on controlling the stator current which is neglected the resistance voltage loss [27]. These methods suffer from transformations in structure control during reference frames conversion. Furthermore, the voltage-source converters (VSCs) and DTC were developed for controlling of the machine's torque or power [28]. Nevertheless, during variations of speed and load machine, switching frequency changes for controlling the active and reactive powers [29]. Also, the model predictive control (MPC) has been developed for DFIG with uncertain parameters. The DPC and predictive torque control (PTC) based on MPC has been proposed more recently DFIG [30]. But, this suffers from complex algorithms due to stator flux orientation.

In most studies in the field of BDFIG analysis and even BCDFIG, the rotor of this generator is integrated which causes the voltage and current of different parts of this generator are not detectable, separable and controllable. If a problem occurred, to identify the location of the problem and disturbed machine is not easy. Thus, using the different control methods on this generator with an integrated rotor is more difficult.

In this paper, to stabilize the amplitude and frequency of BCDFIG output voltages in stand-alone mode and their quick dynamic response against the load changing and variable speed of generator shaft, a model predictive voltage control (MPVC) strategy has been presented. In this method, the future output voltages of the generator according to the other parameters of the machine in the presence of electrical and mechanical changes applied to the system are predicted. In addition, the desirable voltages of control machine for stabilizing the output voltages of the generator are determined. Unlike previous studies, the equivalent circuit of BCDFIG with using the electrical connection and mechanical coupling of two induction machines as Power Machine (PM) and Control Machine (CM) are presented and the expansion of their equations are exhibited in the d-q frame. To stabilize the stator voltage of the power machine, the enough current must be injected into rotor of PM. Therefore, one of the main problems of control methods for BCDFIG is the control of rotor current.

By applying voltage to the stator of control machine with a external converter, the current is inductted in the rotor coils of the control machine. Due to the electrically connection between rotor of CM and PM, the generated current in CM is injected to rotor coil of PM. Finally, the injected current and the rotational motion of the rotor stimulate the stator winding field and amplify the generated the energy.

The contribution of this paper is summarized as follows:

- Evaluation of operation BCDFIG
- Comprehensive design and digital implementation of the predictive voltage control method
- Comparison PI controller to MPVC
- Considering of dynamic response in variable load and wind speed

In this study, the mathematic model of BCDFIG and predictive voltage control method are presented and modeled in MATLAB/Simulink/M-File. The consideration simulation results are presented in order to evaluate performance of proposed method under load change and wind speed variation. Then the experimental results will be shown that with using the proposed control method, the voltage and frequency stability of BCDFIG in the above-mentioned changes are maintained and is more effectiveness comparing than the other controller methods. Finally, concluding remarksare summarized in the last section.

2. BCDFIG MODEL

2. 1. Power Machine At first, the structure and performanc e of the BCDFIG are described and then the mathematical equations of this generator are presented. The schematic structure of BCDFIG is shown in Figure 1.

As shown in Figure 1, this generator consists of two induction machines called the control machine and the power machine so that their rotors are electrically and mechanically coupled together. Figures 2 and 3 show the steady state equivalent circuit of BCDFIG consisting of two induction machines on d-q axes.

$$\begin{cases} L_{sp} = L_{lsp} + L_{mp} \\ L_{sc} = L_{lsc} + L_{mc} \end{cases} \qquad \begin{cases} L_{rp} = L_{lrp} + L_{mp} \\ L_{rc} = L_{lrc} + L_{mc} \end{cases} \tag{1}$$

The equations of the rotors flux and the stator flux of power and control machines, in the d-q system stated as follows:

$$\begin{cases} \lambda_{sp}^{dq} = L_{sp} i_{sp}^{dq} + L_{mp} i_{rp}^{dq} \\ \lambda_{rc}^{dq} = L_{rc} i_{rc}^{dq} + L_{mc} i_{sc}^{dq} \end{cases} \qquad \begin{cases} \lambda_{rp}^{dq} = L_{rp} i_{rp}^{dq} + L_{mp} i_{sp}^{dq} \\ \lambda_{sc}^{dq} = L_{sc} i_{sc}^{dq} + L_{mc} i_{rc}^{dq} \end{cases} \tag{2}$$

Also, the equations for the voltage of stators and the rotors of power and control machines can be written as follows:

$$v_{sp}^{dq} = R_{sp} i_{sp}^{dq} + \frac{d\lambda_{sp}^{dq}}{dt} \pm \omega_p \lambda_{sp}^{dq} \tag{3}$$

$$v_{rp}^{dq} = R_{rp} i_{rp}^{dq} + \frac{d\lambda_{rp}^{dq}}{dt} \pm \omega_{rp} \lambda_{rp}^{dq} \tag{4}$$

$$v_{rc}^{dq} = R_{rc} i_{rc}^{dq} + \frac{d\lambda_{rc}^{dq}}{dt} \pm \omega_{rc} \lambda_{rc}^{dq} \tag{5}$$

$$v_{sc}^{dq} = R_{sc} i_{sc}^{dq} + \frac{d\lambda_{sc}^{dq}}{dt} \pm \omega_c \lambda_{sc}^{dq} \tag{6}$$

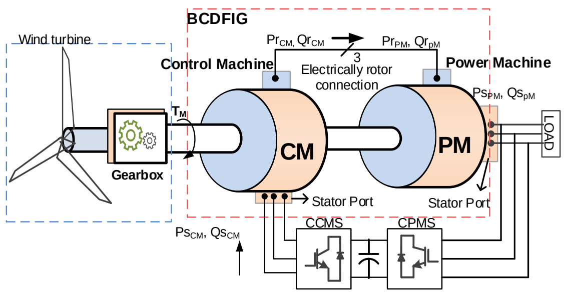

Figure 1. The schematic structure of BCDFIG

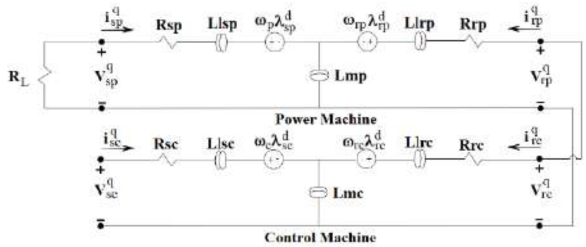

Figure 2. The equivalent circuit of BCDFIG on q axis

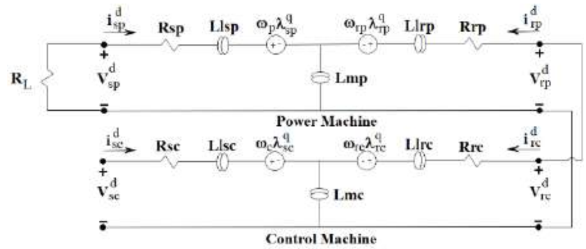

Figure 3. The equivalent circuit of BCDFIG on d axis

In previous studies, which considered the rotor to be integrated, to simplify, the BCDFIG rotor voltage was considered to be zero, which $v_{rp}^{dq} = v_{rc}^{dq}$ is considered in this paper. Recently, predictive control method applied to power and renewable energy systems [15, 16]. However, the modeling of MPVC is based on the voltage derivative relationship of PM stator in dq frame.

According to electrically coupling of BCDFIG rotors, the rotor voltages and current are equal.

$$\begin{aligned} vr_{pm} &= vr_{cm} \\ ir_{pm} &= ir_{cm} \end{aligned} \tag{7}$$

Hence, Equations (4) and (5) can be concluded equal, assuming $j_1 = 1 + \frac{R_{sp}}{R_L}$.

The stator voltage of PM equations in the *dq* reference frame can be expressed as follows:

$$\frac{dv_{sp}^q}{dt} = \frac{R_L}{L_{mp}} \left[R_r i_{rp}^q + L_r \frac{di_{rp}^q}{dt} - L_{mc} \frac{di_{sc}^q}{dt} - \omega_{rp} (\lambda_{rc}^d - \lambda_{rp}^d) \right] \tag{8}$$

It is worth to be mentioned that the rotor winding is shorted in both PM and CM, practically. It causes the rotor voltage equal to zero. Substituting Equations (7) and (3), the current rotor of PM can be found in Equation (9). where, $j_2 = -L_{mp} + \frac{L_r L_{sp}}{L_{mp}}$; so,

$$\begin{aligned} \frac{di_{rp}^q}{dt} = \frac{1}{j_2} \Bigg[& -j_1 v_{sp}^q - \frac{L_{sp}}{L_{mp}} R_r i_{rp}^q + \frac{L_{sp} L_{mc}}{L_{mp}} \frac{di_{sc}^q}{dt} \\ & + \frac{L_{sp}}{L_{mp}} \omega_{rp} (\lambda_{rc}^d - \lambda_{rp}^d) + \omega_p \lambda_{sp}^d \Bigg] \end{aligned} \tag{9}$$

Substituting Equation (9) into Equation (6) results obtained in Equation (10), assuming $j_3 = L_{sc} - \frac{L_{mc}^2 L_{sp}}{j\,2L_{mp}}$

$$\frac{di_{sc}^q}{dt} = \frac{1}{j_3}\Bigg[v_{sc}^q - R_{sc} i_{sc}^q - \frac{j_1}{j_2} L_{mc} v_{sp}^q - \frac{L_{mc}}{j_2}\frac{L_{sp}}{L_{mp}} R_r i_{rp}^q + \frac{L_{mc}}{j_2}\frac{L_{sp}}{L_{mp}}\omega_{rp}(\lambda_{rc}^d - \lambda_{rp}^d) + \frac{L_{mc}}{j_2}\omega_p \lambda_{sp}^d - \omega_c \lambda_{sc}^d\Bigg] \tag{10}$$

Based on Equation (6), as the above procedure continues for the d axis, the rotor and stator equations of PM and CM can be obtained as follows, respectively.

$$\frac{dv_{sp}^d}{dt} = \frac{R_L}{L_{mp}}\left[R_r i_{rp}^d + L_r \frac{di_{rp}^d}{dt} - L_{mc}\frac{di_{sc}^d}{dt} + \omega_{rp}(\lambda_{rc}^q - \lambda_{rp}^q)\right] \tag{11}$$

$$\frac{di_{rp}^d}{dt} = \frac{1}{j_2}\Bigg[-j_1 v_{sp}^d - \frac{L_{sp}}{L_{mp}} R_r i_{rp}^d + \frac{L_{sp}L_{mc}}{L_{mp}}\frac{di_{sc}^d}{dt} - \frac{L_{sp}}{L_{mp}}\omega_{rp}(\lambda_{rc}^q - \lambda_{rp}^q) - \omega_p \lambda_{sp}^q\Bigg] \tag{12}$$

$$\frac{di_{sc}^d}{dt} = \frac{1}{j_3}\Bigg[v_{sc}^d - R_{sc} i_{sc}^d - \frac{j_1}{j_2} L_{mc} v_{sp}^d - \frac{L_{mc}}{j_2}\frac{L_{sp}}{L_{mp}} R_r i_{rp}^d - \frac{L_{mc}}{j_2}\frac{L_{sp}}{L_{mp}}\omega_{rp}(\lambda_{rc}^q - \lambda_{rp}^q) - \frac{L_{mc}}{j_2}\omega_p \lambda_{sp}^q + \omega_c \lambda_{sc}^q\Bigg] \tag{13}$$

2. 2. Control Machine The main contribution of the machine side converter is to control the power rotor of cascaded power machine, which is magnetically transferred to secondary stator terminals. The supplied energy of PM can be further through CM and its converter. Moreover, according to constant speed electrical field, the stator winding relative to rotor winding gives an extra degree of freedom. Consequently, the CM helps to achieve close to unity power factor of PM in variable or asymmetry load. The other advantage is controlling the reactive power by current component of CM's-axis stator and the active power is generated through the stator of PM.

3. MODEL PREDICTIVE CONTROL VOLTAGE

Recently, the Model Predictive Control (MPC) is more attracted for power controlling system which can optimally predicted the main parameters and system variables to provide fast dynamic response while improved overall performance. To achieve this target, the sampling time based on predictive time is fixed to the sampling time. A cost function is defined to identify the optimum controller parameters so that optimizes switching state value is applied to the next sample step. The control system of BCDFIG involved of the rectifier which is provided the controllable DC source voltage for second voltage source inverter that acting as main controller of CM. In this paper the proposed predictive voltage control (MPVC) approach is presented in Figure 4. The proposed MPVC generates an optimize cost function along with the stator voltage to predict the future trajectories. It is worth to be mentioned that this function affects to improve the performance of the system against disturbance, variable speed turbine and load.

The MPVC approach evaluates the PM stator voltage error during sampling time and then identifies the best voltage vector that has the least voltage error value though the over predictive time. The typical sampling sequence of the system shows Figure 5.

3. 1. MPVC Modelling According to continuous-time equations, for simplifying the model system, the discrete-time model is defined by the forward Euler derivative approximation [29]. The equation of Euler derivative approximation is given below:

$$\frac{di}{dt} = \frac{i(k) - i(k-1)}{T_s} \tag{14}$$

where k is the sampling number and Ts is the time scale of these samples. Accordingly, substituting Equation (9) and (12) rotor current into Equations (7) and (11), stator voltage prediction in the synchronous reference frame at the sampling point (k+ 1) are calculated as follows:

$$v_{sp}^q(k+1) = \frac{T_S R_L}{L_{mp}}\Big[R_r i_{rp}^q(k) + L_r i_{rp}^q(k+1) - L_{mc} i_{sc}^q(k+1) - \omega_{rp}(k)[\lambda_{rc}^d(k) - \lambda_{rp}^d(k)]\Big] + v_{sp}^q(k) \tag{15}$$

$$v_{sp}^d(k+1) = \frac{T_S R_L}{L_{mp}}\Big[R_r i_{rp}^d(k) + L_r i_{rp}^d(k+1) - L_{mc} i_{sc}^d(k+1) + \omega_{rp}(k)[\lambda_{rc}^q(k) - \lambda_{rp}^q(k)]\Big] + v_{sp}^d(k) \tag{16}$$

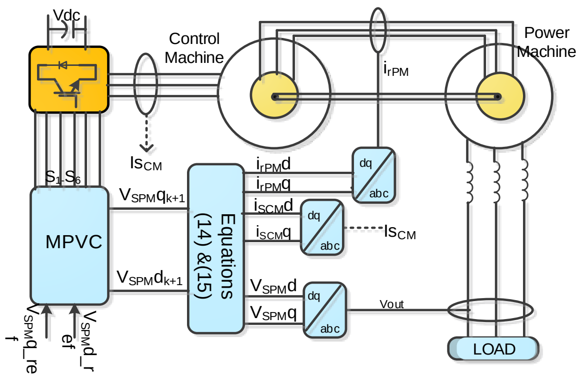

Figure 4. MPVC sachem of BCDFIG

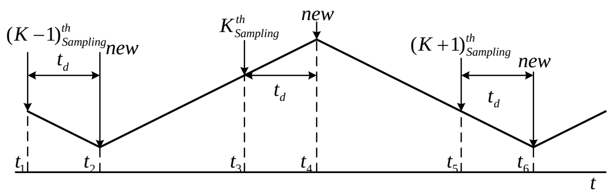

Figure 5. Typical sampling sequence

3. 2. MPVC Voltage Vector

In Equations (15) and (16) the values $i_{rp}^{q}, i_{sc}^{q}, i_{rp}^{d}, i_{sc}^{d}$ in the instantaneous (k+1) can be easily extracted using Euler's approximation and Equations (9), (10), (12) and (13). The function of this method is based on applying the above voltage vectors to Equations (7) to (13). Finally, the 8 different values according to voltage vector will be obtained on both the d- q axes of the synchronous reference frame for generating the output voltages. The function is involved of the absolute error between the reference and the predicted voltage stator in frame reference q and the absolute error among voltage reference and the predicted voltage stator in frame reference d. The cost function always is calculated for each of the 7 feasible switching statuses follows:

$$g = \left| v_{sp\_ref}^{q} - v_{sp}^{q}(sw) \right| + \left| v_{sp\_ref}^{d} - v_{sp}^{d}(sw) \right| \qquad (16)$$

where SW is related to switching mode, which varies from 0 to 7.

The weight factor of the model predictive control cost function straightly affects performance of the controller and robustness under uncommon operating conditions such as model parameter inconformity. It is worth mentioning that the proposed MPVC is capable to control various major parameters with a single control law. For this target, due to the same nature of the two variables parameters voltages V_{SP}^{d} and V_{SP}^{q} of cost function, the unity weighing factor is selected that cases the normalizing the cost function. Consequently, due to the unnecessary for weight coefficients there is no required to use complex methods to tuning these coefficients.

In the MPVC method, a decision will be made according to the status of the switches in the inverter, which gives 8 switching modes, U_1, U_2, $U_{0and(7)}$ as illustrated in Figure 6. In which, cases (000) and (111) are in fact the same state and represent the zero voltage. According to the inverter switches, the value 1 is generated by the cost function to turn ON the upper switches of the inverter and also the value 0 is indicating the connection of the inverter for the lower. In this method, at each step, the generator output voltages are sampled and all the vectors shown in Figure 6 are applied to the stator of the control machine. First, the control machine stator current, then the BCDFIG rotor current, and finally the BCDFIG output voltages at the moment

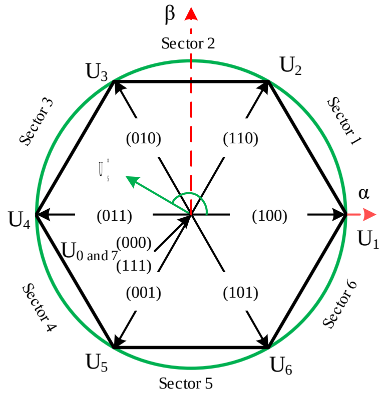

Figure 6. Voltage vectors used in the MPVC

(K+1) are predicted and compared with the generator output voltage references. Each voltage vector applied to the control machine stator that minimizes the objective function is selected in that step and applied to the control machine stator in next step. Since the generator output voltages are predicted at any given moment, in sudden electrical and mechanical changes of the system, the predictive control voltage method has a very high operating speed in maintaining the amplitude and frequency of the generator output voltages.

4. SIMULATION AND PRACTICAL IMPLEMENTATION

In order to demonstrate the effectiveness and performance of proposed method, the obtained equations, in pervious section, are performed in MATLAB/Simulink/M-File. The specifications of prototype BCDFIG used in this simulation are summarized in Table 1. The sampling time has been consideredin this simulation is 1μs. A 2.2 kW inductionmotor driven by a 2.5 kW inverter is used instead of a wind turbine to generate speed. A two–level inverter is provided the controllable energy for stator of CM, produced by the DSP TMS320F28335.

TABLE 1. Parametersused in simulation

Specifications	**Power Machine**	**Control Machine**
Stator resistance (Ω)	0.3332	1.8372
Rotor resistance (Ω)	0.337	2.4261
Stator leakage inductance (H)	0.6995	1.9268
Rotor leakage inductance (H)	0.6995	1.9268
Magnetic inductance (H)	20.81	58.43
Rated power (kW)	9.2	3
Number of poles	4	4

As shown in Figure 7, it is assumed that the mechanical speed of the generator shaft increases from 30 rpm to 300 rpm with increasing wind speed, and that the load step applied to the generator suddenly. These changes are shown in Figure 7.

According to specification of generator, the requirement speed of shaft of turbine should be over 300 rpm/min for achieving sustainable output voltage of generator. The test results are shown in Figure 7 with the rotorspeed maintained constant at 300 rpm/min. In this paper, the proposed MPVC strategy with the sampling time 1μs is applied for BCDFIG. The converter side of PM is provided 220vdc for inverter.

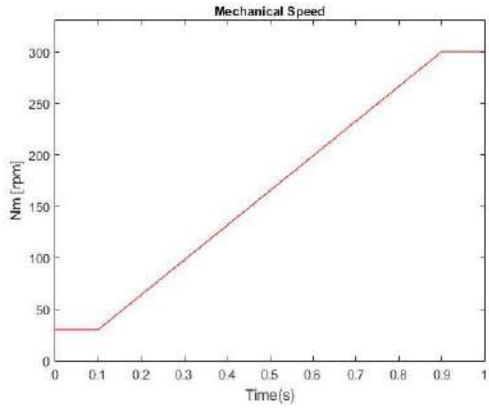

Figure 7. Changes in the mechanical speed of the BCDFIG shaft

4. 1. Controller Dynamic Performances The performance of the proposed MPVC for BCDFIG is compared with PI controller that has been proposed by Wu et al. [22]. The dynamic responses of BCDFIG for both methods under the same condition, against change load are illustrated in Figure 8. The nominal RMS voltage of stator PM is 110vac. However, the performance of the proposed control method is confirmed with precise regulation, minimum current distortions, very low ripples of voltage and current and fast dynamic response under variation load. In order to prove the ability of the proposed controller to stabilize the output voltage in case of over load and change the speed of the wind turbine, it seems that it is necessary to compare the performance of this controller with a conventional controller. The basis of this controller is based on sampling the output voltage and converting it to a d-q reference. The measured voltages are compared with their reference value and then PI controller adjusts the two voltage variables. The control coefficients for this PI controller are as follows: kpd=0.002, kid=0.00007, kpq=0.002, kiq=0.00007. Figure 8 shows the power stator voltage under PI controller. By applying the predictive control voltage method to the generator, the amplitude and frequency of the generator output voltages remain constant as the current changes at 0.4s the consumption load and increases the speed of the generator shaft. This proves the correctness and robustness of the control proposed method, as shown Figure 8a. It is visible that the overshoot

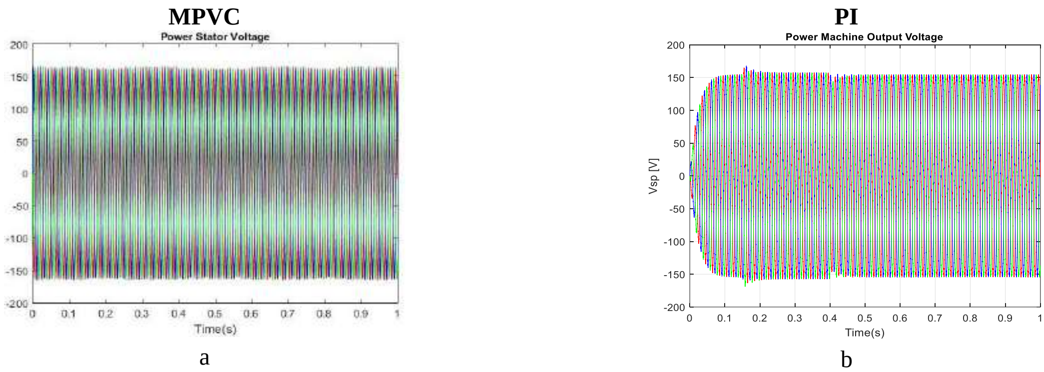

a b

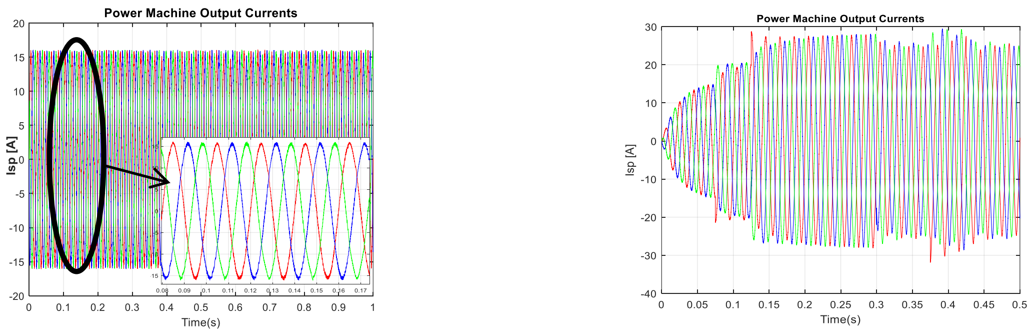

c d

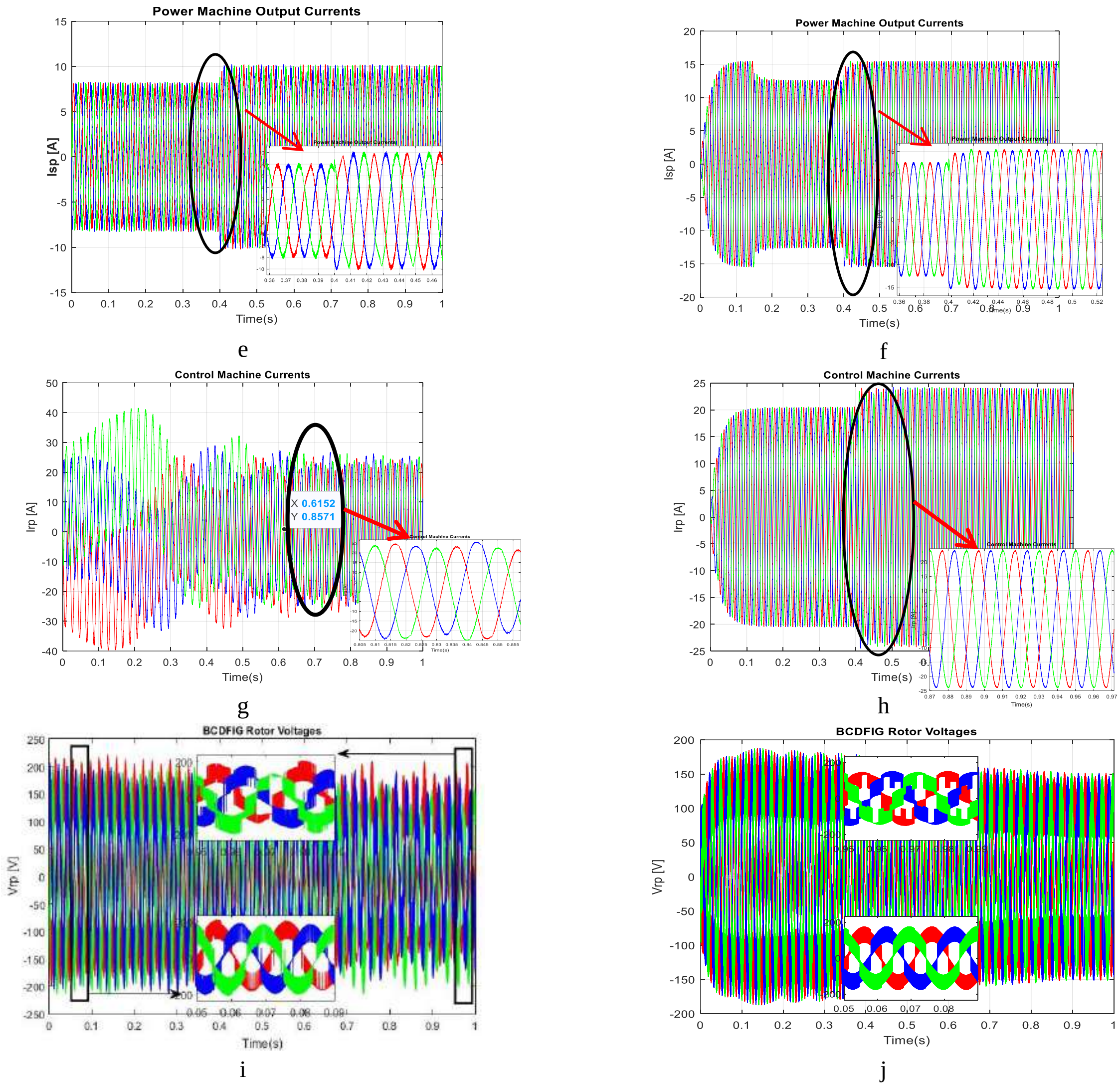

Figure 8. Comparison**;** steady-state performance of with proposed MPVCand PI strategies at rotor speed

or undershoot has not appeared against the PI method that has 3v undershoot voltage during changing load. For Figures 8c and 8d, the distortions of output current with PI method is high comparing with MPVC method due to its insufficient control bandwidth. As seen, the output currents of PM were become balanced (at 15 A) for MPVC at the step load from zero. As seen from Figures 8e and 8f, the BCDFIG with PI method is very slow at the zero step load. But the MPVC has fast reponse at the step load from zero to 8 A and then rised to 10 A. It takes to account that the PI controller does not have the ability to stabilize the output voltage in case of over load and change the speed of the wind turbine. Consequently, the MPVC strategy verifies a very fast dynamic performance during varing rotor slip and and step load compared to PI controller applied for BCDFIG.

The two-wire winding voltage of the power machine and control machine rotors, which was not available in previous studies due to the integration of the generator rotor, as shown in Figure 8i, with increasing mechanical speed of the generator shaft, the distortion created in the generator rotor increases.

4. 2. Experimental Results

Test bench of BCDFIG prototype as presented in Figure 9. I is provided to validate the simulation results of theoretical proposed approach with the control method. The power set-up is consisted of two 4 poles DFIG machines that are connected in cascade configurations. Also, an induction machine with controllable speed shaft is coupled to the BCDFIG to provide initial speed. The back-to-back two-level converter is supplied the stator of CM and the local load is directly fed by stator of PM(110vac, 50 Hz) that the shaft speed of PM was rotated by induction machine at 300 rpm. Regarding to the advantages of digital signal processors (DSPs) such as very fast clock frequency, high frequency analog converters to digital converters (ADC) and the possibility high computational which allows using the intelligent control methods. Accordingly, the control system for both CCMS and CPMS is implemented with TMS320F28335 DSPs development board. The sampling frequency is selected 20 kHz and the predictive time for MPVC is chosen 10µs. The low pass filter with the cutting frequency at 20 kHz is applied to ADC for accuracy sampling in the output analog sampling. For evaluating the steady state performance of the proposed control strategy, the BCDFIG was carried out with different verification tests.

In the first study, the voltagestator of PM under full load operation is shown in Figure 10, that the zoomed voltage without any distortionis validated the quality of generated energy of PM. In order to evaluate the dynamic response of the proposed system, a step output load from 0.0 to 100% of load was conducted as shown in Figure 11. It is worth to be mentioned that fast transient response is fundamental requirement for standalone user such as drive, household consumption and industrial utilization applications to prevent damage to the devices. Therefore, the other study was investigated the dynamic response of BCDFIG in step load from 45 to 100% load (Figure 12) whereas at 5ms rising load is compensated, which validate the superior performance of the proposed method. At the same time it was subjected to the voltage change the CM, forcing the CM to generate the requirement voltage rotor of PM. As evidently appears from Figure 13. The MPVC algorithm is analyzed the

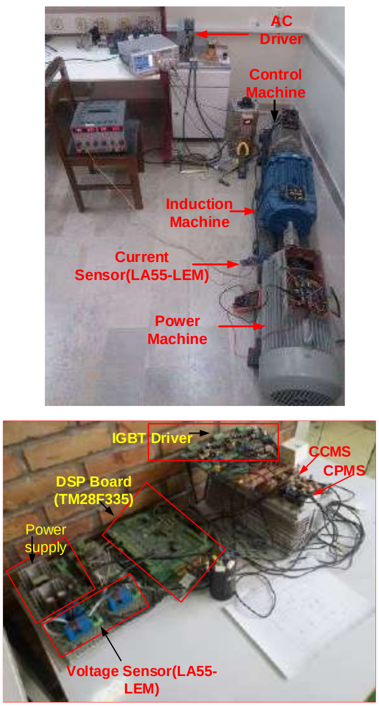

Figure 9. The set-up of the BCDFIG

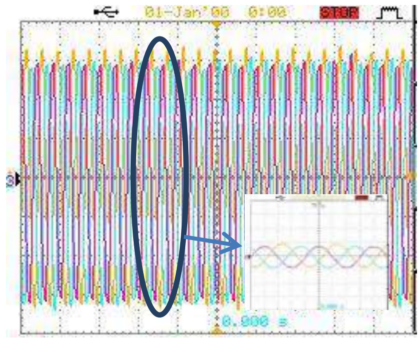

Figure 10. Experimental results under voltage stator of PM(50v/div)

sampled rotor current of CM which were estimated among the sampling period, and compares it with the reference current to introduce the Ir_{CM} error to near zero. The CCMS provided the voltage for the stator of CM very quickly at less than 15 ms.

In the next study, the validation of the performance during the accelerated the shaft speed is demonstrated. The shaft speed is raised from 300 to 900 rpm. It is worth mentioned that the ratio of the generated VArs of stator and rotor winding of PM depended on speed shaft which is directly effects the output power [23]. Under this condition, while the synchronous speed was increased speed from 300 to 900 rpm, the rotor current frequency

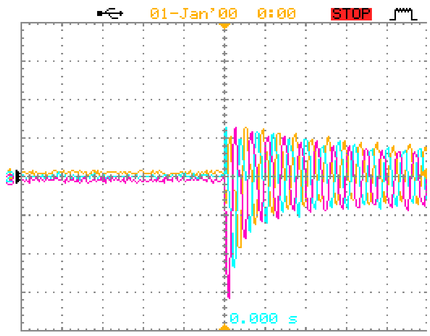

Figure 11. The stator current of PM for 100% step change of the output load(5 A/div)

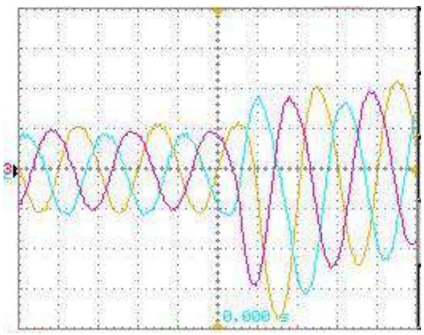

Figure 12. The stator current of PM under step output load from 45 to 100%(5 A/div)

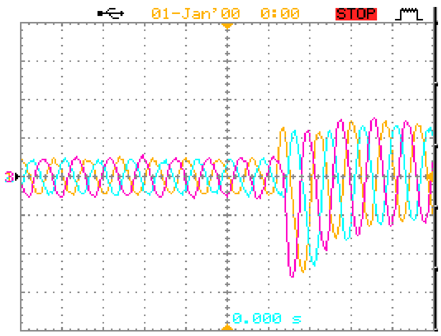

Figure 13. The stator voltage of CM under step output load from 45 to 100% (100V/div)

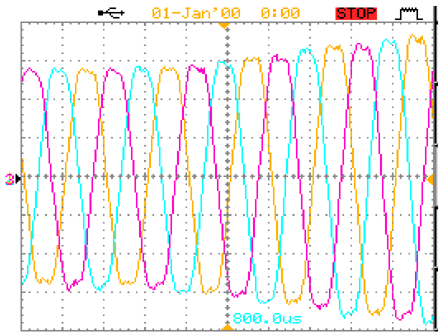

Figure 14. The stator voltage of CM under variable rotor speed (50 A/div)

of PM was decreased. Regarding to prediction of control parameters, the rotor and stator current of CM were predicted to compensate the stator voltage of CM. Due to exact compensation the reaching mininum of PM rotor current was prevented and keeping the constant output power. For $Vstator_{CM}$ shown in Figure 14, The CCMS is applied the $Vstator_{CM}$ compensation 180 vac due to varying the rotor slip. is depicted in Figure 14. Consequenty, The MPVC with high bandwidth exactly follows even small current errors with very high accuracy. But, other common control methods such as PI lead to considerable control errors due to bandwidth limitations. It can be observed from experimental results that the performance of MPVC is very fast and robust against speed and load variations. As shown in Table 2, the BCDFIG with MPVC efficiency is compared with other controller method that is about 93%.

The one factors of wind turbine is large inertia and speed variation at the moment. However, prediction of the very large variation of parameters in wind turbine is inevitable to maintain sustainable dynamic system. The predictive control method is well adapted to anticipate momentary change of parameters. The prediction method is best solution for following out the parameters to achieve optimum controller in order to smoother response of controller and improve dynamic performance of generator.

TABLE 2. Comparison of efficiency of Method controller

Controller	Efficiency (%)
LQG [27]	92
MPC with PTC [29]	90
PID [27]	87
SMC With DPC [30]	90
MPVC (Proposed)	93

5. CONCLUSION

In this paper, the predictive control voltage method is applied to a BCDFIG This study shows that this method has a fast and desirable performance in keeping the amplitude and frequency of the BCDFIG output voltages constant in stand-alone generation systems in sudden current changes in consumption load and mechanical changes in generator shaft speed. This proves the robustness and performance of the control method provided.

Contrary to popular control methods such as vector control, the proposed predictive control voltage method has the following advantages:

a. PI blocks and the trouble of selecting its coefficients were eliminated. In fact, in the vector method, with 8 PI coefficients, 8 appropriate and consistent choices had to be made to achieve the desired result. In this method, these troublesome blocks were removed.
b. No need for PWM in MPVC method. In this method, switching commands based on the cost function are performed. There is no need to generate a carrier wave and compare it to the reference value.
c. More balanced fluctuations in stable mode. In voltage predictive control methods, more accurate reference values are obtained due to predictor variables, resulting in more stable fluctuations in the steady state around the reference value.
d. An assessment of the efficiency between some other method controller and proposed MPVC scheme is presented in Table 2. This verified that BCDFIG with MPVC is efficient in terms of power capture and performance optimization.

6. ACKNOWLEDGMENTS

The authors would like to acknowledge the support received from department of electrical engineering, Iran University of Science and Technology that made possible for the elaboration of this work and also helped in different stages of this work.

7. REFERENCES

1. Jabbour, N., Tsioumas, E., Mademlis, C., and Solomin, E., "A Highly Effective Fault-Ride-Through Strategy for a Wind Energy Conversion System With a Doubly Fed Induction Generator", ***IEEE Transactions on Power Electronics***, Vol. 35, No. 8, (2020), 8154–8164. doi:10.1109/TPEL.2020.2967971
2. Gontijo, G. F., Tricarico, T. C., Franca, B. W., da Silva, L. F., van Emmerik, E. L., and Aredes, M., "Robust Model Predictive Rotor Current Control of a DFIG Connected to a Distorted and Unbalanced Grid Driven by a Direct Matrix Converter", ***IEEE Transactions on Sustainable Energy***, Vol. 10, No. 3, (2019), 1380–1392. doi:10.1109/TSTE.2018.2868406
3. Esfandiari, G., Ebrahimi, M., and Tabesh, A., "Instantaneous Torque Control Method With Rated Torque-Sharing Ratio for Cascaded DFIMs", ***IEEE Transactions on Power Electronics***, Vol. 32, No. 11, (2017), 8671–8680. doi:10.1109/TPEL.2017.2650211
4. Norouzia, S., Ghoreishy, H., Ale Ahmad, A., and Tahami, F., "A New Variable Frequency Zero Voltage Switching Control Method for Boost Converter Operating in Boundary Conduction Mode", ***International Journal of Engineering, Transaction B: Applications***, Vol. 33, No. 11, (2020), 2222–2232. doi:10.5829/ije.2020.33.11b.14
5. Sun, D., Wang, X., Nian, H., and Zhu, Z. Q., "A Sliding-Mode Direct Power Control Strategy for DFIG Under Both Balanced and Unbalanced Grid Conditions Using Extended Active Power", ***IEEE Transactions on Power Electronics***, Vol. 33, No. 2, (2018), 1313–1322. doi:10.1109/TPEL.2017.2686980
6. Liu, Y., Xu, W., Zhi, G., and Zhang, J., "Performance Analysis of a Stand-alone Brushless Doubly-fed Induction Generator Using a New T-type Steady-state Model", ***Journal of Power Electronics***, Vol. 17, No. 4, (2017), 1027–1036. doi:https://doi.org/10.6113/JPE.2017.17.4.1027
7. Sadeghi, R., Madani, S. M., and Ataei, M., "A New Smooth Synchronization of Brushless Doubly-Fed Induction Generator by Applying a Proposed Machine Model", ***IEEE Transactions on Sustainable Energy***, Vol. 9, No. 1, (2018), 371–380. doi:10.1109/TSTE.2017.2734964
8. Kou, P., Liang, D., Li, J., Gao, L., and Ze, Q., "Finite-Control-Set Model Predictive Control for DFIG Wind Turbines", ***IEEE Transactions on Automation Science and Engineering***, Vol. 15, No. 3, (2018), 1004–1013. doi:10.1109/TASE.2017.2682559
9. Chen, J., Zhang, W., Chen, B., and Ma, Y., "Improved Vector Control of Brushless Doubly Fed Induction Generator under Unbalanced Grid Conditions for Offshore Wind Power Generation", ***IEEE Transactions on Energy Conversion***, Vol. 31, No. 1, (2016), 293–302. doi:10.1109/TEC.2015.2479859
10. Khateri-abri, S., Tohidi, S., and Rostami, N., "Improved Direct Power Control of DFIG Wind Turbine by using a Fuzzy Logic Controller", 2019 10th International Power Electronics, Drive Systems and Technologies Conference (PEDSTC), (2019), 458–463. doi:10.1109/PEDSTC.2019.8697581
11. Douadi, T., Harbouchea, Y., Abdessemed, R., and Bakhti, I., "Improvement Performances of Active and Reactive Power Control Applied to DFIG for Variable Speed Wind Turbine Using Sliding Mode Control and FOC", ***International Journal of Engineering, Transactions A: Basics***, Vol. 31, No. 10, (2018), 1689–1697. doi:10.5829/ije.2018.31.10a.11
12. Hussien, M. G., Liu, Y., and Xu, W., "Robust position observer for sensorless direct voltage control of stand-alone ship shaft brushless doubly-fed induction generators", ***CES Transactions on Electrical Machines and Systems***, Vol. 3, No. 4, (2019), 363–376. doi:10.30941/CESTEMS.2019.00048
13. Pichan, M., Rastegar, H., and Monfared, M., "Fuzzy-based direct power control of doubly fed induction generator-based wind energy conversion systems", 2012 2nd International EConference on Computer and Knowledge Engineering (ICCKE), (2012), 66–70. doi:10.1109/ICCKE.2012.6395354
14. Rodrigues, L. L., Vilcanqui, O. A. C., Murari, A. L. L. F., and Filho, A. J. S., "Predictive Power Control for DFIG: A FARE-Based Weighting Matrices Approach", ***IEEE Journal of Emerging and Selected Topics in Power Electronics***, Vol. 7, No. 2, (2019), 967–975. doi:10.1109/JESTPE.2019.2898924
15. Xu, W., Gao, J., Liu, Y., and Yu, K., "Model predictive current control of brushless doubly-fed machine for stand-alone power generation system", IECON 2017 - 43rd Annual Conference of the IEEE Industrial Electronics Society, (2017), 322–327. doi:10.1109/IECON.2017.8216058
16. Xu, W., Hussien, M. G., Liu, Y., and Allam, S. M., "Sensorless Control of Ship Shaft Stand-Alone BDFIGs Based on Reactive-Power MRAS Observer", ***IEEE Journal of Emerging and Selected Topics in Power Electronics***, Vol. 9, No. 2, (2021), 1518–1531. doi:10.1109/JESTPE.2019.2963264
17. Salehi, M., and Davarani, R. Z., "Effect of Different Turbine-generator Shaft Models on the Sub-synchronous Resonance Phenomenon in the Double Cage Induction Generator Based Wind Farm", ***International Journal of Engineering, Transaction B: Applications***, Vol. 29, No. 8, (2016), 1103–1111. doi:10.5829/idosi.ije.2016.29.08b.10
18. Cheng, C., and Nian, H., "Low-Complexity Model Predictive Stator Current Control of DFIG Under Harmonic Grid Voltages", ***IEEE Transactions on Energy Conversion***, Vol. 32, No. 3, (2017), 1072–1080. doi:10.1109/TEC.2017.2694849
19. Mossa, M. A., Saad Al-Sumaiti, A., Duc Do, T., and Zaki Diab, A. A., "Cost-Effective Predictive Flux Control for a Sensorless Doubly Fed Induction Generator", ***IEEE Access***, Vol. 7, (2019), 172606–172627. doi:10.1109/ACCESS.2019.2951361
20. Zhang, Y., Jiang, T., and Jiao, J., "Model-Free Predictive Current Control of a DFIG Using an Ultra-Local Model for Grid Synchronization and Power Regulation", ***IEEE Transactions on Energy Conversion***, Vol. 35, No. 4, (2020), 2269–2280. doi:10.1109/TEC.2020.3004567
21. Agha Kashkooli, M. R., Madani, S. M., and Lipo, T. A., "Improved Direct Torque Control for a DFIG under Symmetrical Voltage Dip With Transient Flux Damping", ***IEEE Transactions on Industrial Electronics***, Vol. 67, No. 1, (2020), 28–37. doi:10.1109/TIE.2019.2893856
22. Wu, C., Zhou, D., and Blaabjerg, F., "Direct Power Magnitude Control of DFIG-DC System Without Orientation Control", ***IEEE Transactions on Industrial Electronics***, Vol. 68, No. 2, (2021), 1365–1373. doi:10.1109/TIE.2020.2970666
23. Pichan, M., Rastegar, H., and Monfared, M., "Two fuzzy-based direct power control strategies for doubly-fed induction generators in wind energy conversion systems", ***Energy***, Vol. 51, (2013), 154–162. doi:10.1016/j.energy.2012.12.047
24. Han, P., Cheng, M., Wei, X., and Li, N., "Modeling and Performance Analysis of A Dual-Stator Brushless Doubly-Fed Induction Machine Based on Spiral Vector Theory", ***IEEE Transactions on Industry Applications***, Vol. 52, No. 2, (2015), 1380–1389. doi:10.1109/TIA.2015.2491893
25. Ma, J., Zhao, D., Yao, L., Qian, M., Yamashita, K., and Zhu, L., "Analysis on application of a current-source based DFIG wind generator model", ***CSEE Journal of Power and Energy Systems***, Vol. 4, No. 3, (2018), 352–361. doi:10.17775/CSEEJPES.2018.00060
26. Gowaid, I. A., Abdel-Khalik, A. S., Massoud, A. M., and Ahmed, S., "Ride-Through Capability of Grid-Connected Brushless Cascade DFIG Wind Turbines in Faulty Grid Conditions—A Comparative Study", ***IEEE Transactions on Sustainable Energy***, Vol. 4, No. 4, (2013), 1002–1015.

doi:10.1109/TSTE.2013.2261830

27. Bektache, A., and Boukhezzar, B., "Nonlinear predictive control of a DFIG-based wind turbine for power capture optimization", ***International Journal of Electrical Power & Energy Systems***, Vol. 101, (2018), 92–102. doi:10.1016/j.ijepes.2018.03.012

28. Errouissi, R., Al-Durra, A., Muyeen, S. M., Leng, S., and Blaabjerg, F., "Offset-Free Direct Power Control of DFIG Under Continuous-Time Model Predictive Control", ***IEEE Transactions on Power Electronics***, Vol. 32, No. 3, (2017), 2265–2277. doi:10.1109/TPEL.2016.2557964

29. Vargas, R., Rodriguez, J., Rojas, C. A., and Rivera, M., "Predictive Control of an Induction Machine Fed by a Matrix Converter With Increased Efficiency and Reduced Common-Mode Voltage", ***IEEE Transactions on Energy Conversion***, Vol. 29, No. 2, (2014), 473–485. doi:10.1109/TEC.2014.2299594

30. Yan, X., Cheng, M., Xu, L., and Zeng, Y., "Dual-Objective Control Using an SMC-Based CW Current Controller for Cascaded Brushless Doubly Fed Induction Generator", ***IEEE Transactions on Industry Applications***, Vol. 56, No. 6, (2020), 7109–7120. doi:10.1109/TIA.2020.3021624

Persian Abstract

چکیده

هدف این مقاله ارائه یک مدل استراتژی کنترل ولتاژ پیش‌بینی کننده (MPVC) برای تثبیت دامنه و فرکانس ولتاژهای خروجی در یک ژنراتور القایی (BCDFIG) تحت تغییر بار و سرعت متغیر شافت ژنراتور در جایگاه است. حالت تنها BCDFIGs یک مدل خاص از BDFIG است که از دو ماشین القایی به نام ماشین کنترل و ماشین قدرت تشکیل شده است، به طوری که روتورهای آنها از نظر الکتریکی و مکانیکی بهم متصل می‌شوند. در این مقاله، برخلاف مطالعات قبلی، که روتور BCDFIG یکپارچه در نظرگرفته شده بود، روتور ژنراتور به عنوان مجموعه‌ای از دو روتور دو ماشین القایی جداگانه مورد تجزیه و تحلیل قرار می‌گیرد. همچنین، ولتاژهای خروجی ژنراتور با استفاده از مدل کنترل ولتاژ پیش‌بینی شده، در شرایط عملیاتی مختلف پیش‌بینی و تنظیم می‌شوند. به منظور تثبیت دامنه و فرکانس ولتاژهای خروجیBCDFIG، بردار ولتاژ مناسب تعیین می‌شود تا به استاتور ماشین کنترل اعمال شود. این سیستم تولیدی شبیه‌سازی شده و نتایج شبیه‌سازی صحت روش پیشنهادی را ثابت می‌کند. برای تأیید روش‌های پیشنهادی، نتایج تجربی در نمونه اولیه BCDFIG ارائه شده است. سرانجام، کنترل‌کننده پیشنهادی اثربخشی بهینه‌سازی بهتر جذب نیرو را تحت توربین بادی با سرعت متغیر به ارمغان می‌آورد.

IJE TRANSACTIONS B: Applications Vol. 34, No. 05, (May 2021) 1250-1256

International Journal of Engineering

Journal Homepage: www.ije.ir

Intrusion Detection in Cyber-physical Layer of Smart Grid using Intelligent Loop Based Artificial Neural Network Technique

P. K. Gupta, N. K. Singh, V. Mahajan*

Electrical Engineering Department, Sardar Vallabhbhai National Institute of Technology, Surat, Gujarat-India

PAPER INFO

Paper history:
Received 26 July 2020
Received 28 Februray 2021
Accepted 03 March 2021

Keywords:
Intelligent Loop Based
Artificial Neural Network
False Data Injection Attack
Smart Grid
Cyber-physical

A B S T R A C T

This paper, proposes an Intelligent Loop Based Artificial Neural Network (ILANN) based detection technique for the detection of cyber intrusion in a smart grid against False Data Injection Attack (FDIA). This method compares the deviation of a system with the equipment load profile present on the system node(s) and any deviation from predefined values generates an alarm. Every 2 milliseconds (ms) the data obtained by the measurement is passed through the attack detection system, in case if the deviation is continuously for 5 measurement cycles i.e. for 10 ms and it does not match with the load combination the operator will get the first alert alarm. In case the deviation is not fixed after 8 measurement cycles then the system alerts the control centre. FDI attack is used by attackers to affect the healthy operation of the smart grid. Using FDI the hackers can permanently damage many power system equipment's which may lead to higher fixing costs. The result and analysis of the proposed cyber detection approach help operator and control centre to identify cyber intrusion in the smart grid scenario. The method is used to detect a cyberattack on IEEE-9 Bus test system using MATLAB software.

***doi**: 10.5829/ije.2021.34.05b.18*

1. INTRODUCTION

The smart grid is an intelligent and complex system designed to work more efficiently, reliable, and economical with the help of computational technologies, advanced communication infrastructure, and state-of-the-art monitoring stations [1, 2]. This goal is achieved by continuous monitoring of power consumption, which leads to large data exchange of information giving opportunity for various cyber intrusion [3]. The main target of ICT is to gather equipment's data, process and transfer to control/monitoring station for proper operation. Integrating with ICT, power grid performance gets enhanced in the following terms (but not limited to):

- Real time monitoring
- Peak load estimation
- Forecasting
- Fast response
- Power factor improvement
- Fault detection and analysis

With a large number of communication sensors deployed in the smart grid has made cybersecurity a critical challenge for engineers [4]. Thus, ensuring security is imperative for smart grid infrastructure [5]. Although enormous research has been published, such as intrusion detection using the weight trust method, using advance cryptographic, and Intrusion Detection Techniques (IDT), despite different countermeasures smart grid still remain vulnerable to different intrusions [6-9].

To prevent intrusion, the smart grid confides on classical security strategy which includes firewall and password protection. Intrusion detection Mechanism (IDM) is capable to generate alarms for viable intrusions via constantly monitoring operations [10, 11]. Although there are several research on well-known IDS in system safety, limited effort has been made especially to the smart grid [12, 13]. Generally, two types of IDM system is used named as: data sourced based and detection based

*Corresponding Author Institutional Email: *vmahajan@eed.svnit.ac.in* (V. Mahajan)

Please cite this article as: P. K. Gupta, N. K. Singh, V. Mahajan, Intrusion Detection in Cyber-physical Layer of Smart Grid using Intelligent Loop Based Artificial Neural Network Technique, International Journal of Engineering, Transactions B: Applications Vol. 34, No. 05, (2021) 1250-1259

method. The majority of industries preferred the detection-based type because of its accuracy and simplicity [14, 15]. This simplicity attracts intruders to perform stealth attacks. The attackers may induce false data which may confuse the operator in their decision making which leads to economic loss [16]. Manandhar et al. [11] have done an extensive investigation of different false data injection attacks. Recently, the method of FDIA has been attracting the attention of engineers and researchers. The FDIA impacts the state estimation by manipulating data [17-19]. In some cases the true digital value of instruments at substation and control centre due to which false operation may occur like the false operation of breakers. In general FDIA targets analog measurement from the power system mainly bus voltage, bus power injection and digital data of switches and breakers [20, 21].

In this paper, a neural network is modelled which continuously monitors the grid energy consumption. Energy consumption totally depends on the load attached to the system, so the proposed technique identifies the equipment connected in the system through intelligent loop feedback. Each equipment has its own power rating, accordingly the system estimate the combination of equipment contributing as load. In case if the load variation matches with the equipment on/off status means no intrusion and the system is working properly, otherwise the system is under fault condition or under the cyber-attack scenario. The main contributions of this paper are three-fold:

1. The proposed model is so effective that it can identify the stealth FDIA, which may easily pass through other Intrusion Detection Techniques (IDT).
2. In the case of a non-stealth attack if the power deviation is for more than 8 cycles then the operator gets an unhealthy alarm.
3. The load combination results can be used for energy management/load shedding during unhealthy operations.

2. SYSTEM MODELLING AND DESCRIPTION

2. 1. Attack Strategy In the power system, bus voltage and its corresponding phase angle are used to represent the state with magnitude $V \in R^n$ and angle $\delta \epsilon [-\pi . \pi]^n$, where *n* is the number of buses. Let *x* is the state vector represented by the equation:

$$x = [V^a \ \delta^a \ V^b \ \delta^b \ V^c \ \delta^c]^T \tag{1}$$

where *a, b, c* represents three-phase. For a given power system the measurement vectors are stated as:

$$V^P = [V_1^P \ V_2^P \ ....V_n^P \ ]^T \tag{2}$$

$$\delta^P = [\delta_1^P \ \delta_2^P \ ....\delta_n^P \ ]^T \tag{3}$$

Using state estimation for the *n*-bus system, there will be 3*n* states for voltage magnitude and 3(*n*-1) states for angle magnitude. The total states for any given system are determined by 3(2*n*-1). To monitor the buses three types of measurements are considered: injected power, voltage magnitude and reactive power injection. The measurement vector *M* is given by the equation:

$$M = [P \ V \ Q]^T \tag{4}$$

where, *P, V, Q* are

$$P = [\, p_i^a \ \ p_i^b \ \ p_i^c \ ]^T \ \forall_i \ \in \{\varphi\} \tag{5}$$

$$V = [v_i^a \ \ v_i^b \ \ v_i^c \ ]^T \ \forall_i \ \in \{\psi\} \tag{6}$$

$$Q = [q_i^a \ \ q_i^b \ \ q_i^c \ ]^T \ \forall_i \ \in \{\varphi\} \tag{7}$$

In Equation (5) φ denotes a set of nodes with power measurement and ψ is the set of nodes with voltage measurement. A simple relation between different elements in the measurements can be written as:

$$M = h(x) + \varpi \tag{8}$$

where *h ()*, represent functions relating measurements with states and ϖ indicates noise present in the system. The relation for the active and reactive power measurement at the bus may be given in terms of states as follow:

$$p_i^p = \sum_{\substack{j=1 \\ j \neq i}}^{n} \sum_{t=abc} \begin{pmatrix} v_i^p Y_{ij}^{pt} v_i^t \cos(\, \delta_i^p - \delta_i^t - \phi_{ij}^{pt}) \\ - v_i^p Y_{ij}^{pt} v_i^t \cos(\, \delta_i^p - \delta_i^t - \phi_{ij}^{pt}) \end{pmatrix} \tag{9}$$

$$q_i^p = \sum_{\substack{j=1 \\ j \neq i}}^{n} \sum_{t=abc} \begin{pmatrix} v_i^p Y_{ij}^{pt} v_i^t \sin(\, \delta_i^p - \delta_i^t - \phi_{ij}^{pt}) \\ - v_i^p Y_{ij}^{pt} v_i^t \sin(\, \delta_i^p - \delta_i^t - \phi_{ij}^{pt}) \end{pmatrix} \tag{10}$$

For each bus, power injection is present in polar form, where *Y* represents admittance and ϕ represents the corresponding admittance angle. The error deviation in the states can be calculate using the weight means square:

$$r = z - h(.) \tag{11}$$

$$E = r^T W r \tag{12}$$

In Equations (11) and (12) *r* represent a residual vector, *E* is the objective function, and *W* is the measurement weight matrix. The error and the noise can be modelled as:

$$x_k = x_{k-1} + \Delta x_{k-1} \tag{13}$$

$$\Delta x_{k-1} = (G)^{-1} H^T W r_{k-1} \tag{14}$$

$$G=H^{T}WH \tag{15}$$

where H is the Jacobian Matrix of $h(.)$. The residual vector is used to update the state's directions. The outliner of the residual vector a scalar function whose value should be below the threshold, otherwise the system contains false data. Many machine learning approaches can sense non-possible states solutions using physical relationships such as Kirchhoff's Current Law (KCL) and Kirchhoff's Voltage Law (KVL). Thus to make the FDIA more stealthy, the injected false data in this paper follows KCL and KCL in the region of attack. For constructing a stealth attack vector the initial states variable is considered as:

$$\begin{bmatrix} V \\ \delta \end{bmatrix} = \begin{bmatrix} V_o \\ \delta_o \end{bmatrix} \tag{16}$$

Now determine if the constraints are satisfied. In case there is some mismatch the go to the next step by checking the limits of the constraints:

$$P_{\min} \le P \le P_{\max} \tag{17}$$

$$Q_{\min} \le Q \le Q_{\max} \tag{18}$$

The attacker must control and inject the power flow to minimize the detection of power mismatch. The load pattern is maintained by updating the state variables.

$$\begin{bmatrix} V \\ \delta \end{bmatrix} = \begin{bmatrix} V_o \\ \delta_o \end{bmatrix} + \begin{bmatrix} \Delta v \\ \Delta \delta \end{bmatrix} \tag{19}$$

Using the above equations attackers can easily able to inject stealth FDIA into the power system. In the next section, the Intelligent Loop Based Artificial Neural Network (ILANN) for false data detection is presented.

2. 2. ILANN System Modelling In this section, an overview of the proposed technique for detecting false data injection is shown in Figure 1. The proposed technique mainly consists of two Artificial Neural Network Stage (ANNS) and a loop that compares the tested results with the real-time scenario data. The ANNS consists of two neural networks such that the output of ANNS1 is acting as input for ANNS2. For the ANNS-1, voltages (Input-I1) and current (Input-I2) measurements are used to estimate the bus output (Output-O1) i.e power delivery through the corresponding bus. The output of ANNS-1 acts as the first input of ANNS-2. The other input (Input-I3) for ANNS-2 consists of different load details connected to particular buses.

According to the power consumption the load pattern is estimated which is compared with the actual reading of the system using the loop associate with the ANN system. As stealth FDIA has no fixed pattern and can be injected at any time to make the system unhealthy. For training neurons, estimation is performed for different conditions with and without FDIA. In the first stage of ANN, the residual vector is saved. Using this vector the power deviation is monitored, and error (e) is estimated is performed for different conditions with and without FDIA. In the first stage of ANN the residual vector is saved. Using this vector the power deviation is monitored, and error (e) is estimated.

$$e \to r \to \Delta P \tag{20}$$

Two different approach for intrusion detection process are a mismatch in overall power and mismatch in power consumed by induvial equipment (Load). The second approach is more appropriate for stealth FDIA. This is because during normal fault the overall power mismatch occurs which may lead to wrong interpretation. So the main characteristic of the ILANN model is, it uses individual load consumption data to predict the cyber intrusion due to FDIA. The change in load combination is given by:

$$\Delta P \to Change\ in\ load\ combination \tag{21}$$

$$\Delta P \to \sum_{b=1\ldots n}^{m=1..z} L_{bm} \tag{22}$$

where b denotes bus number and m denotes load number. The exchange of power to different loads must be satisfied and the load must respond accordingly.

$$P_b = \sum_{b=1\ldots n}^{m=1..z} L_{bm} \in \{Actual\ equipment\ connected\} \tag{23}$$

Through the feedback loop, the bus load combination is compared with the control centre load status.

$$P \to \sum_{b=1\ldots n}^{m=1..z} L_{bm} = Status\ of\ individual\ loads \tag{24}$$

Figure 2 shows the flow chart of the proposed technique. In the first step, the ANNS-1 gets input details which include voltage and current associated with each bus. Also, the second input consists of historical past data accomplice with each bus. In the next stage, the power deviation for each bus is calculated. With the help of ANNS-2, the ILANN predict the possible combination of active load connected to each load bus.

This load combination is rechecked with the control centre through the feedback loop. Through control centre status of the individual load is acquired and compare with the predicted equipment status. If both are the same with high accuracy means the system is healthy otherwise the presence of the wrong status data. The wrong status is due to malicious information put by the attackers after getting the system access. The % power error (P_a) of the system is measured using the formula:

$$P_a = \frac{A_{lc} - P_{lc}}{P_{lc}} \times 100 \tag{25}$$

where A_{lc} is the actual power consumed by the load combination and P_{lc} is predicted power computation by load combination during the cyber intrusion. The

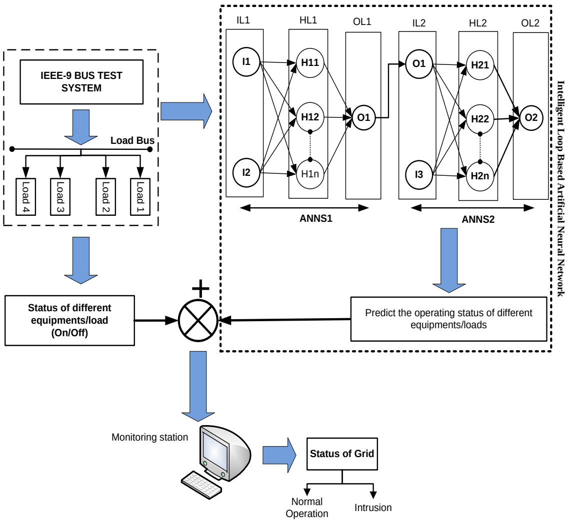

Figure 1. Basic diagram of proposed technique

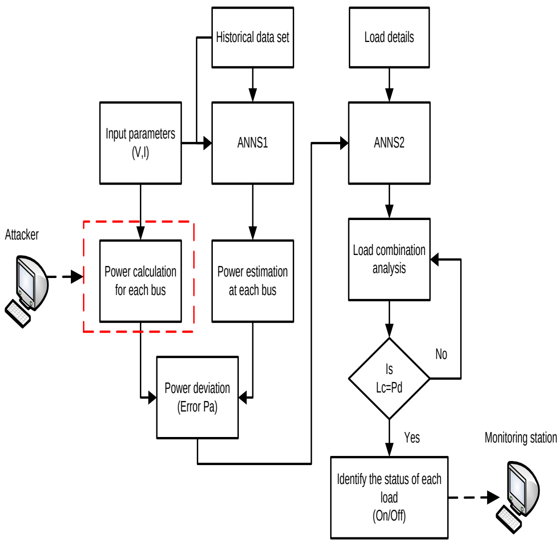

Figure 2. Flow chart for load identification

equipment identification accuracy *(A_S)* is measured using the formula:

$$A_s = \frac{T_{on} + T_{off}}{T_{on} + T_{off} + F_{on} + F_{off}} \times 100 \quad (26)$$

where T_{on} means the number of time load is correctly classified as on; T_{off} means the number of time load is correctly classified as off; F_{on} indicates the number of time load is incorrectly classified as on; F_{off} inverse of T_{off}. In similar manner sensitivity (S) and precision (P_{rec}) can be evaluated as:

$$S = \frac{T_{on}}{T_{on} + F_{off}} \times 100 \quad (27)$$

$$P_{rec} = \frac{T_{on}}{T_{on} + F_{on}} \times 100 \quad (28)$$

In case of a non-stealth attack, the power deviation will be monitored and if it crosses the threshold value of the time limit the operator will get an alarm. To evaluate the proposed model ability to recognize attack, recall/detection rate *(R)* is calculated using the equation given below:

$$R = \frac{T_{on}}{T_{on} + F_{off}} \times 100 \quad (29)$$

Using Equations (27) and (28) F-measure (F) is defined as:

$$F = \frac{2 \times R \times P_{rec}}{R + P_{rec}} \times 100 \quad (30)$$

F-measure highlights the performance of the system during the cyber intrusion.

3. SIMULATION RESULTS AND DISCUSSION

3. 1. Evaluation of Proposed Technqiue Stealth false data attack is one of the most severe attacks om the power system. The IEEE-9 bus test system is used to examine the proposed method. To investigate the method, some details are discussed. Each load bus is connected with more than 2 loads. The details of the load on different buses are given in Table 1. To check the accuracy of the proposed method four cases are considered as follow:

1. **Case 1:** No FDIA
2. **Case 2:** Stealth FDIA on bus no. 6 and 8
3. **Case 3:** Stealth FDIA on all the load bus
4. **Case 4:** Non-stealth FDIA on all the buses

To train and test the proposed technique, a dataset of historical data is provided. As, mentioned residual error,

TABLE 1. Load details

Bus No.	Actual Load Attached (MW)	Load Details (MW)
		L_{51} = 0.5
5	1.2	L_{52} = 0.3
		L_{53} = 0.4
		L_{61} = 1.5
6	5	L_{62} =2.5
		L_{63} =2
		L_{81} =2
		L_{82} =3
8	10	L_{83} =4
		L_{84} =1

state variables and state estimation are computed by using load profile and generation units. Figures 3-6 depict the performance of the proposed method with 30 Neurons each for ANNS1 and ANNS2. The mean square error shown in the figure indicates the value predicted by the model is very close to the actual observed values.

During the training phase, the active and reactive power consumption of the individual load is recorded and saved. Figure 3, as indicated by the training best epoch, shows the best results at 1000. The training, testing and validation of data are very accurate as shown in Figure 4. Figure 5 shows the error histogram with 70% data used for training, 15% is used to validate and the reaming 15% used for a completely independent test. Table 2 highlights the detection time for stealth/non-stealth FDIA. The prediction of load combination by ILANN is given in Table 3. It can be observed that for cases 2, 3 and 4 the on/off status of ILANN is not matching with control centre status. So it can be concluded that in the above-said cases the system is under FDIA. The sensitivity, precision and accuracy of the proposed ILANN technique are shown in Figure 6 for each load.

In case 1 detection time is not applicable although the change in system parameter was detected at a period of 5.32 s. A very little deviation in ILANN prediction is due to small loads. Its accuracy may increase with a loads with a large difference in its's capacity.

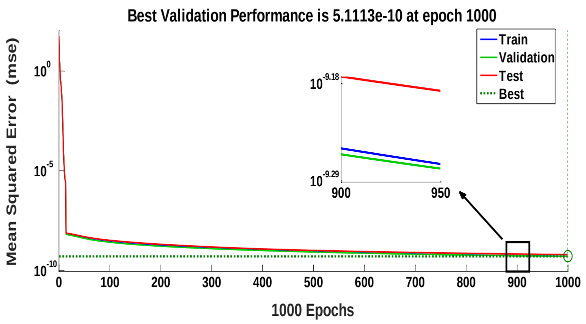

Figure 3. Mean square error of the proposed modelled

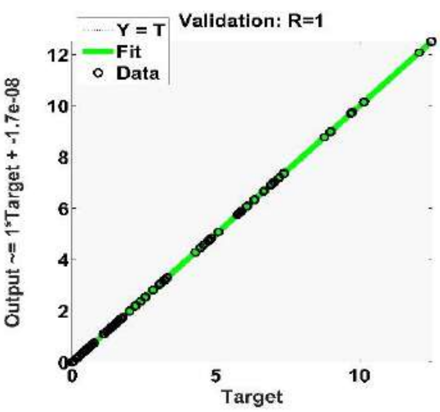

Figure 4. Validation of historical data

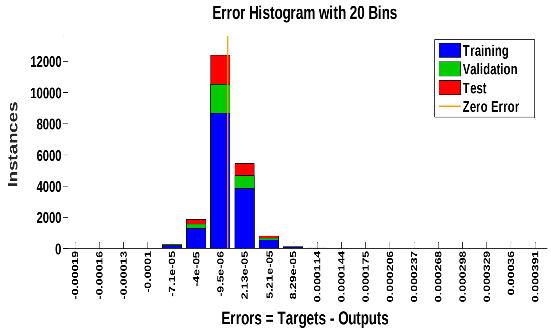

Figure 5. Error histogram

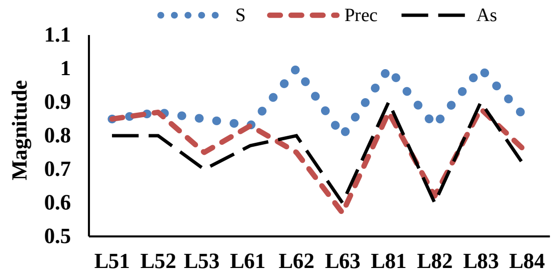

Figure 6. Sensitivity, precision and accuracy of proposed ILANN technique for individual loads

TABLE 1. Simulation result for different cases

Case No.	A_{lc} (MW)	P_{lc} (MW)	P_a (%)	Detection time of FDIA (Sec)
1	16.2	15.2	6.17	NA
2	13.2	12.5	5.30	3.64
3	13.4	12.9	3.73	3.87
4	12.5	11.4	8.8	9.12

TABLE 2. ILANN prediction

Case No.	A_{lc} (MW)	P_{lc} (MW)	Status of Load at control centre	ILANN Load prediction
1	16.2	15.2	L_{84} is off	L_{84} is off
2	13.2	12.5	L_{63}, L_{81} is off	L_{52}, L_{53}, L_{63}, L_{81} is off
3	13.4	12.9	L_{51}, L_{52}, L_{63}, L_{84} is off	L_{52}, L_{63}, L_{81} is off
4	12.5	11.4	L_{52}, L_{53}, L_{61}, L_{62} is off	L_{51}, L_{52}, L_{61}, L_{62}, L_{84} is off

From Table 2 it is clear that nodes having more load connection required a little more time to detect FDIA. The performance metrics *R* and *F* of ILANN are shown in Figure 7. It can be observed that the range is between 80-95%, indicating desired performance.

3. 2. Comparison With Existing Technique This section compares the ILANN technique with a few existing techniques stated in Table 4. All the comparison is based on the data/sample used by the system during the detection process. Overall, the accuracy of system is around 97% (for multiple load combination its 76%) making it efficient and accurate. Comparing with detection rate and false alarm rate, the ILANN prove to be the most trusted method as shown in Figure 8.

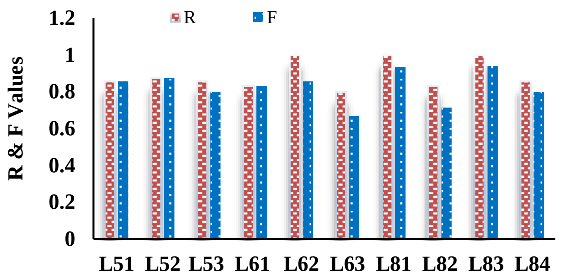

Figure 7. Recall and F-measure for different load using ILANN

TABLE 3. Comparison of ILANN with existing techniques

Method	Parameter	Accuracy (%)
Single Sensor Score (SSS) [22]	Sensor data streams	3.2
Deep Neural Network (DNN)[23]	Data samples	70
Support Vector Machine (SVM) [22, 24]	Data samples	45-60
Back Propagation Neural Network (BPNN) [25]	Sensor data streams	82
Stacking-Bagging Ensemble (SBE) [26]	System data	60
k-RNN and OCSVM [27]	Sample data from sensors	60.61
Fuzzy C-Means Clustering (FCC) [28] [29]	Sample data	75
Proposed ILANN	Node and load data sample	97

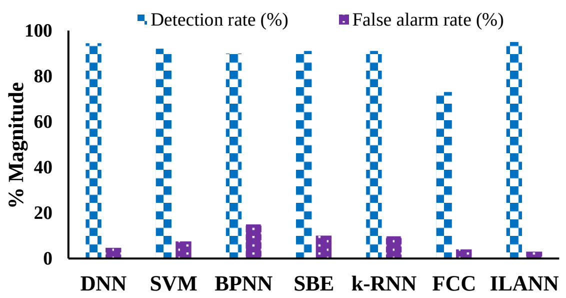

Figure 8. Comparison for detection rate and false alarm rate

4. CONCLUSION

The artificial neural network provides several advantages in the detection of FDIA. In this paper, ILANN is introduced using the concept of ANN to detect stealth/non-stealth false injection attacks. The proposed method is implemented in the IEEE-9 bus system with the help of MATLAB software. After having prepared enough historical information for the power system an ILANN is developed to train, test, and update the system for intrusion detection. The feedback comparison gives better results with a low chance of failure. The ability of ILANN is tested to predict the status of load which can be compared with the actual status and deviation can be noted. This deviation can be due to load change or due to cyber intrusion. From the results, the overall performance of the system is high with 97% of accuracy.

The simulation result shows the sensitivity, precision, and accuracy of the proposed method for load detection is high. It can be implemented on large-scale power systems to train individual subsections for monitoring against FDIA.

5. REFERENCES

1. Mansouri, H.R., Mozafari, B., Soleymani, S. and Mohammadnezhad, H., "A new optimal distributed strategy to mitigate the phase imbalance in smart grids", ***International Journal of Engineering***, Vol. 33, No. 12, (2020), 2489-2495. DOI: 10.5829/ije.2020.33.12c.08.
2. Singh, N.K. and Mahajan, V., "Analysis and evaluation of cyber-attack impact on critical power system infrastructure", ***Smart Science***, (2021), 1-13. DOI: 10.1080/23080477.2020.1861502
3. Sunitha, R. and Chandrikab, J., "Evolutionary computing assisted wireless sensor network mining for qos-centric and energy-efficient routing protocol", ***International Journal of Engineering***, Vol. 33, No. 5, (2020), 791-797. DOI: 10.5829/ije.2020.33.05b.10.
4. Wang, W. and Lu, Z., "Cyber security in the smart grid: Survey and challenges", ***Computer Networks***, Vol. 57, No. 5, (2013), 1344-1371. DOI: 10.1016/j.comnet.2012.12.017
5. Sou, K.C., Sandberg, H. and Johansson, K.H., "On the exact solution to a smart grid cyber-security analysis problem", ***IEEE Transactions on Smart Grid***, Vol. 4, No. 2, (2013), 856-865. DOI: 10.1109/TSG.2012.2230199
6. Alfantookh, A.A., "Dos attacks intelligent detection using neural networks", ***Journal of King Saud University-Computer and Information Sciences***, Vol. 18, (2006), 31-51. DOI: 10.1016/S1319-1578(06)80002-9
7. Kwon, Y., Kim, H.K., Lim, Y.H. and Lim, J.I., "A behavior-based intrusion detection technique for smart grid infrastructure", in 2015 IEEE Eindhoven PowerTech, IEEE. 1-6. DOI: 10.1109/PTC.2015.7232339
8. Zhang, J., Ai, Z., Guo, L. and Cui, X., "Reliability evaluation of a disaster airflow emergency control system based on bayesian networks", ***International Journal of Engineering***, Vol. 33, No. 11, (2020), 2416-2424. DOI: 10.5829/ije.2020.33.11b.32.
9. Singh, N.K., Gupta, P.K. and Mahajan, V., "Intrusion detection in wireless network of smart grid using intelligent trust-weight method", ***Smart Science***, Vol. 8, No. 3, (2020), 152-162. DOI: 10.1080/23080477.2020.1805679

10. Lo, C.-H. and Ansari, N., "Consumer: A novel hybrid intrusion detection system for distribution networks in smart grid", ***IEEE Transactions on Emerging Topics in Computing***, Vol. 1, No. 1, (2013), 33-44. DOI: 10.1109/TETC.2013.2274043
11. Manandhar, K., Cao, X., Hu, F. and Liu, Y., "Detection of faults and attacks including false data injection attack in smart grid using kalman filter", ***IEEE Transactions on Control of Network Systems***, Vol. 1, No. 4, (2014), 370-379. DOI: 10.1109/TETC.2013.2274043
12. Jow, J., Xiao, Y. and Han, W., "A survey of intrusion detection systems in smart grid", ***International Journal of Sensor Networks***, Vol. 23, No. 3, (2017), 170-186. DOI: 10.1504/IJSNET.2017.083410
13. Wang, Q., Tai, W., Tang, Y. and Ni, M., "Review of the false data injection attack against the cyber-physical power system", ***IET Cyber-Physical Systems: Theory & Applications***, Vol. 4, No. 2, (2019), 101-107. DOI: 10.1049/iet-cps.2018.5022
14. Singh, N.K. and Mahajan, V., "End-user privacy protection scheme from cyber intrusion in smart grid advanced metering infrastructure", ***International Journal of Critical Infrastructure Protection***, (2021), 100410. DOI: 10.1016/j.ijcip.2021.100410
15. Singh, N.K. and Mahajan, V., "Detection of cyber cascade failure in smart grid substation using advance grey wolf optimization", ***Journal of Interdisciplinary Mathematics***, Vol. 23, No. 1, (2020), 69-79. DOI: 10.1080/09720502.2020.1721664
16. Wang, G., Giannakis, G.B. and Chen, J., "Robust and scalable power system state estimation via composite optimization", ***IEEE Transactions on Smart Grid***, Vol. 10, No. 6, (2019), 6137-6147. DOI: 10.1109/TSG.2019.2897100
17. Esmalifalak, M., Nguyen, H., Zheng, R. and Han, Z., "Stealth false data injection using independent component analysis in smart grid", in 2011 IEEE International Conference on Smart Grid Communications (SmartGridComm), IEEE. 244-248. DOI: 10.1109/SmartGridComm.2011.6102326
18. Kosut, O., Jia, L., Thomas, R.J. and Tong, L., "Limiting false data attacks on power system state estimation", in 2010 44th Annual Conference on Information Sciences and Systems (CISS), IEEE. 1-6. DOI: 10.1109/SmartGridComm.2011.6102326
19. Ashok, A., Govindarasu, M. and Ajjarapu, V., "Online detection of stealthy false data injection attacks in power system state estimation", ***IEEE Transactions on Smart Grid***, Vol. 9, No. 3, (2016), 1636-1646. DOI: 10.1109/TSG.2016.2596298
20. Pan, S., Morris, T. and Adhikari, U., "Developing a hybrid intrusion detection system using data mining for power systems", ***IEEE Transactions on Smart Grid***, Vol. 6, No. 6, (2015), 3104-3113. DOI: 10.1109/TSG.2015.2409775
21. Vuković, O. and Dán, G., "Security of fully distributed power system state estimation: Detection and mitigation of data integrity attacks", ***IEEE Journal on Selected Areas in Communications***, Vol. 32, No. 7, (2014), 1500-1508. DOI: 10.1109/JSAC.2014.2332106
22. Ferragut, E.M., Laska, J., Olama, M.M. and Ozmen, O., "Real-time cyber-physical false data attack detection in smart grids using neural networks", in 2017 International Conference on Computational Science and Computational Intelligence (CSCI), IEEE. 1-6. DOI: 10.1109/CSCI.2017.1
23. Zhou, L., Ouyang, X., Ying, H., Han, L., Cheng, Y. and Zhang, T., "Cyber-attack classification in smart grid via deep neural network", in Proceedings of the 2nd International Conference on Computer Science and Application Engineering. 1-5. DOI: 10.1145/3207677.3278054
24. Ernst, J., Hamed, T. and Kremer, S., A survey and comparison of performance evaluation in intrusion detection systems, in Computer and network security essentials. 2018, Springer.555-568. DOI: 10.1007/978-3-319-58424-9_32
25. Niu, X., Li, J., Sun, J. and Tomsovic, K., "Dynamic detection of false data injection attack in smart grid using deep learning", in 2019 IEEE Power & Energy Society Innovative Smart Grid Technologies Conference (ISGT), IEEE. 1-6. DOI: 10.1109/ISGT.2019.8791598
26. Phua, C., Alahakoon, D. and Lee, V., "Minority report in fraud detection: Classification of skewed data", ***Acm Sigkdd Explorations Newsletter***, Vol. 6, No. 1, (2004), 50-59. DOI: 10.1145/1007730.1007738
27. Sundarkumar, G.G. and Ravi, V., "A novel hybrid undersampling method for mining unbalanced datasets in banking and insurance", ***Engineering Applications of Artificial Intelligence***, Vol. 37, (2015), 368-377. DOI: 10.1016/j.engappai.2014.09.019
28. Kulhare, R. and Singh, D., "Intrusion detection system based on fuzzy c means clusteringand probabilistic neural network", ***International Journal of Computer Applications***, Vol. 74, No. 2, (2013). DOI: 10.1145/3207677.3278054
29. Ren, W., Cao, J. and Wu, X., "Application of network intrusion detection based on fuzzy c-means clustering algorithm", in 2009 Third International Symposium on Intelligent Information Technology Application, IEEE. Vol. 3, 19-22. DOI: 10.1109/IITA.2009.269

Persian Abstract

چکیده

در این مقاله ، یک روش تشخیص مبتنی بر شبکه عصبی مصنوعی مبتنی بر حلقه (ILANN) برای تشخیص نفوذ سایبری در یک شبکه هوشمند در برابر حمله تزریق داده های کاذب (FDIA) پیشنهاد شده است. این روش انحراف یک سیستم را با مشخصات بار تجهیزات موجود در گره (های) سیستم مقایسه می کند و هرگونه انحراف از مقادیر از پیش تعریف شده زنگ خطر ایجاد می کند. هر ۲ میلی ثانیه (میلی ثانیه) داده های بدست آمده توسط اندازه گیری از طریق سیستم تشخیص حمله منتقل می شود ، در صورتی که انحراف به طور مداوم برای ۵ چرخه اندازه گیری یعنی برای ۱۰ میلی ثانیه باشد و با ترکیب بار مطابقت نداشته باشد، اپراتور اولین بار را دریافت می کند هشدار هشدار در صورت عدم انحراف پس از ۸ چرخه اندازه گیری ، سیستم به مرکز کنترل هشدار می دهد. حمله FDI توسط مهاجمین استفاده می شود تا عملکرد سالم شبکه هوشمند را تحت تأثیر قرار دهد. با استفاده از FDI، هکرها می توانند به طور دائمی به بسیاری از تجهیزات سیستم برق آسیب برسانند که ممکن است منجر به افزایش هزینه های رفع مشکل شود. نتیجه و تجزیه و تحلیل روش پیشنهادی تشخیص سایبری به اپراتور و مرکز کنترل کمک می کند تا نفوذ سایبری را در سناریوی شبکه هوشمند شناسایی کنند. این روش برای شناسایی حمله سایبری به سیستم تست IEEE-9 Bus با استفاده از نرم افزار MATLAB استفاده می شود.

International Journal of Engineering

Journal Homepage: www.ije.ir

Developing a Bi-objective Mathematical Model to Design the Fish Closed-loop Supply Chain

M. Fasihi[a], R. Tavakkoli-Moghaddam*[b], S. E. Najafi[a], M. Hahiaghaei-Keshteli[c]

[a] *Department of Industrial Engineering, Science and Research Branch, Islamic Azad University, Tehran, Iran*
[b] *School of Industrial Engineering, College of Engineering, University of Tehran, Tehran, Iran*
[c] *Tecnologico de Monterrey, Escuela de Ingeniería y Ciencias, Puebla, Mexico*

PAPER INFO

Paper history:
Received 09 July 2020
Received in revised form 25 December 2020
Accepted 14 January 2021

Keywords:
Bi-objective Mathematical Model
Closed-loop Supply Chain
Fish Reverse Logistics

ABSTRACT

In recent years, many industries in developed countries have integrated the important process of reverse logistics into their supply chain for different reasons, including growing environmental concerns. Given fish as perishable food, re-employing unused products and waste in each step of the chain constitute a major concern for the decision-makers. The present study is conducted to maximize responsiveness to customer demand and minimize the cost of the fish closed-loop supply chain (CLSC) by proposing a novel mathematical model. To solve this model, the epsilon-constraint method and Lp-metric were employed. Then, the solution methods were compared with each other based on the performance metrics and a statistical hypothesis. The superior method is ultimately determined using the TOPSIS method. The model application is tested on a case study of the trout CLSC in the north of Iran by performing a sensitivity analysis of demand. This analysis showed the promising results of using the proposed solution method and model.

doi: *10.5829/ije.2021.34.05b.19*

1. INTRODUCTION

In its classical forward form, a supply chain refers to a combination of processes that aims at meeting customer requirements. These processes include all the possible entities, such as warehouses, retailers, transporters, manufacturers, suppliers, and customers [1]. Although this type of supply chain is not in charge of end-of-life products, a reverse supply chain or reverse logistics seeks to account for end-of-life products [2]. A closed-loop supply chain (CLSC) is a network that comprises both forward and reverse supply chains to add value throughout the life cycle of products [3]. Organizations focused on reverse logistics processes consider it as effective processes since the concept of reverse logistics enhances the economic value of consumption while considering environmental aspects [4, 5].

The scarcity of the earth's resources is well known today, and catastrophic consequences would bring about in case humans continue to be as wasteful as before. The growing population of the world has also exacerbated nutritional problems in communities. Previous food supply chains should be therefore modified in a way that they satisfy today's growing demand [6]. Nowadays, seafood and the associated products account for a major portion of the household consumption basket in different countries. In 2018, the Food and Agriculture Organization (FAO) highlighted the effects of optimization on fish farming [7]. The Iranian Fisheries Organization and the FAO have reported the growing rate of cold-water fish production in Iran. Trout is considered the most well-known fish species among all the numerous species [8].

A global decrease in aquaculture resources and increasing production costs require more attention to the processes and wastes in the aquaculture industry. Implementing reverse logistics in the fish supply chain is therefore crucial. To the best of the authors' knowledge, the present research pioneers the investigation of implementing reverse logistics in fish supply chains. A

*Corresponding Author Institutional Email: *tavakoli@ut.ac.ir* (R. Tavakkoli-Moghaddam)

Please cite this article as: M. Fasihi, R. Tavakkoli-Moghaddam, S. E. Najafi, M. Hahiaghaei-Keshteli, Developing a Bi-objective Mathematical Model to Design the Fish Closed-loop Supply Chain, International Journal of Engineering, Transactions B:Applications Vol. 34, No. 05, (2021) 1257-1268

network is first developed for the fish CLSC. As a common recycling method of fish waste, fish powder production is performed to produce huge amounts of organic fish food, maintain human health, and preserve the environment. Therefore, this study uses fish waste recycling facilities to perform reverse logistics. A novel mathematical model has also been developed to minimize the cost of the fish CLSC and maximize the responsiveness of customer demand in forward and reverse supply chains. The model is validated by examining an actual application of the method in a case study. Moreover, the epsilon-constraint and Lp-metrics are employed to solve the present multi-objective decision making problem of six different sizes in Lingo. The two methods are compared in terms of their average outcome and based on three prespecified criteria and ranked using the TOPSIS method.

The following sections of this paper are organized as follows. Sections 2 and 3 present a review of the literature and details the mathematical model, respectively. Section 4 presents the solution techniques and section 5 describes their performance metrics and compares the model results between the two methods. Section 6 presents a case study and numerical examples of the trout supply chain in Mazandaran province, Iran. Section 7 presents the computational results. Section 8 ranks the solution methods in terms of the metric measures by employing a multi-criteria decision-making technique. A sensitivity analysis is conducted in section 9, and conclusions and propositions are ultimately made for further studies in section 10.

2. LITERATURE REVIEW

Manufacturing costs can be effectively minimized in competitive markets by managing supply chains. The public, academia, and industrial practitioners have recently paid much attention to reverse logistics and CLSCs [9–13]. The present study focused on fish supply chains by first reviewing cold supply chains and perishable foods. The management and design of food supply chains are significantly affected by perishability [14]. In 1963, Ghare [15] pioneered the investigation of perishability and found the inventory decay to significantly influence the total inventory cost if it is included in the inventory analysis. Perishability has also attracted the attention of researchers and practitioners in the field of supply chains [16]. The management of the supply chains of perishable products has been investigated in review articles [17, 18].

Numerous studies have addressed the efficiency maximization of food supply chains by proposing diverse methods [16]. Exact and metaheuristic algorithms were employed by Mirmajlesi and Shafaei [19] to manage a multi-echelon, multi-product, multi-period, and capacitated supply chain of short-lifetime products. Abedi and Zhu [20] optimized fish farming, the purchase of spawn, and the distribution of harvested fish in a fish supply chain by developing a mixed-integer linear programming model for the maximization of the total profit. An inventory routing problem with environmental constraints on food was solved by Soysal et al. [21]. Cheraghalipour et al. [22] developed a multi-period, single-product, and multi-objective programming model and designed a CLSC for citrus. Metaheuristic algorithms were also employed to decrease the burden of computation in actual problems. Tabrizi et al. [14] investigated equilibrium models in perishable food supply chains by proposing a novel optimization model and performing a case study of the supply chain of warm-water farmed fish.

Masruroh et al. [23] proposed an integrated multi-product distribution allocation and production planning for a dairy supply chain. Onggo et al. [24] solved a perishable inventory routing problem with probabilistic demand using a mixed-integer programming model and a simheuristic algorithm comprising an iterated local search and Monte Carlo simulation. Naderi et al. [25] studied the wheat supply chain network design (SCND) as a case study considering capacity and fleet management. Also, Motevalli-Taher et al. [26] optimized the wheat SCND considering the sustainability criteria and uncertainty. Leng et al. [27] minimized the total logistics cost and vehicle and client waiting times by proposing a comprehensive low-carbon cold-chain based location-routing model. Chan et al. [28] used multi-objective mixed-integer linear programming for smart food logistics systems. Several review studies have been also performed on perishable food supply chains [29–31].

3. MATHEMATICAL MODELING

3. 1. Problem Statement The present research design a CLSC for fish logistic networks. The designed logistics network is single-period, including producers (Pool-Farm, Rice-Farm, and Sea-Farm) as can be seen in Figure 1, distribution centers, reprocessing centers (fish powder centers), processing centers (processed fish centers), and customers (markets: fresh fish markets, processed fish markets, and fish powder markets).

Figure 2 shows the forward flow, in which goods are transported from producers to distribution centers and customers, and from distribution centers to customers to satisfy their unsupplied demand by producers. Fixed

Figure 1. Fish farms

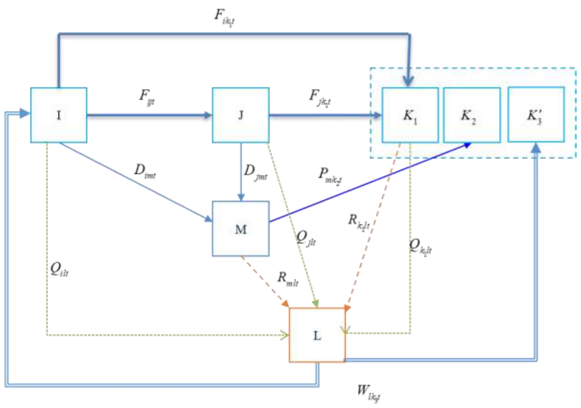

Figure 2. Flowchart for the fish CLSC

locations are also assumed for processing centers and customers. Producer locations and distribution and reprocessing centers can include fixed or potential points of the locations. The products returned in the reverse flow are shipped to reprocessing centers to be converted to byproducts and again are shipped to the customers of the fish powder market. Given farms (producers) as the potential customers of fish feed, the network can be considered a CLSC where producers play the role of fish powder customers. Significant reductions in product life, natural resources, and landfills have turned waste management into an important problem. A dedicated recovery plan should be assigned to individual end-of-life products given their dissimilarity [32].

The present research designed a CLSC for farmed fish in forward and reverse flow modes by developing a bi-objective mathematical model. The chain cost was minimized and responsiveness to customer demand maximized by collecting the fish waste and losses in the fish supply chain using a network.

3. 2. Notations

Indices

$i_1 = 1,2,...,I_1$	Production locations (Pool-Farm)- Fixed points
$i_2 = 1,2,...,I_2$	Production locations (Rice-Farm)- Potential points
$i_3 = 1,2,...,I_3$	Production locations (Sea-Farm)- Potential points
$i = i_1 + i_2 + i_3$	Production locations (fish farms)- All points
$j_1 = 1,2,...,J_1$	Distribution locations- Fixed points
$j_2 = 1,2,...,J_2$	Distribution locations- Potential points
$j = j_1 + j_2$	Distribution locations- All points
$k_1 = 1,2,...,K_1$	Customer locations (fresh fish markets)
$k_2 = 1,2,...,K_2$	Customer locations (processed fish markets)
$k'_3 = 1,2,...,K'_3$	Customer locations (fish powder markets)
$k''_3 = 1,2,...,K''_3$	Some of the producers (fish farms) as fish powder's customers
$k_3 = k'_3 + k''_3$	Fish powder customer locations
$l_1 = 1,2,\ldots,L_1$	The fish waste recycling center locations- Fixed points
$l_2 = 1,2,\ldots,L_2$	Fish waste recycling center locations- Potential points
$l = l_1 + l_2$	Fish waste recycling center locations- All points
$m = 1,2,\ldots,M$	Fish processing center locations

Parameters

f_i	Fixed cost required for opening production center *i*
f_j	Fixed cost required for opening distribution center *j*
f_l	Fixed cost required for opening fish waste recycling center *l*
Cf_{ij}	Shipping cost per unit of live products from producer *i* to distribution center *j*
Cf_{ik_1}	Shipping cost per unit of fresh products from producer *i* to customer k_1
Cf_{jk_1}	Shipping cost per unit of fresh products from distribution center *j* to customer k_1
Cd_{im}	Shipping cost per unit of fresh products from producer *i* to fish processing center *m*
Cd_{jm}	Shipping cost per unit of fresh products from distribution center *j* fish processing center *m*
Cp_{mk_2}	Shipping cost per unit of processed products from fish processing center *m* to customer k_2
Cr_{k_1l}	Shipping cost per unit of waste products from customer k_1 to fish waste recycling center *l*
Cr_{ml}	Shipping cost per unit of waste products fish processing center *m* to fish waste recycling center *l*
Cw_{lk_3}	Shipping cost per unit of reprocessed products from fish waste recycling center *l* to fish powder markets k_3
Cq_{il}	Shipping cost per unit of low-quality products from producer *i* to fish waste recycling center *l*
Cq_{jl}	Shipping cost per unit of low-quality products from distribution center *j* fish waste recycling center *l*
Cq_{k_1l}	Shipping cost per unit of low-quality products from customer k_1 fish waste recycling center *l*
Cp	Processing cost per unit of products from fish processing centers
Cr	Fish powder manufacturing cost per unit of products from fish waste recycling centers
Cp'	Production cost per unit of products from producers
d_{k_1}	Demand of fresh product by the customer k_1
d_{k_2}	Demand of processed product by the customer k_2
d_{k_3}	Demand of reprocessed product (fish powder) by fish powder markets k_3
λc_i	Maximum production capacity of producer *i*
λh_j	Holding capacity of distribution center *j*
λr_l	Fish powder manufacturing capacity of fish waste recycling center *l*
λr_m	Processing capacity of fish processing center *m*
α_i	Deteriorating percentage of the product by producers
α_j	Deteriorating percentage of the product by distribution centers

α_{k_1}	Deteriorating percentage of the product by the customer k_1
β_{k_1}	Waste percentage of the product by the customer k_1
β_m	Waste percentage of the product by fish processing centers
θ	Minimum rate of using the capacity of each distribution center
δ	Maximum rate of supplying customer demand for fresh fish directly from the producer
ρ	Weighted importance coefficient to make a response the forward flows
$1-\rho$	Weighted importance coefficient to make a response the reverse flows
φ	Conversion rate of the waste product to a reprocessed product (fish powder)
φ'	Conversion rate of a product to a processed product
MM	A big positive number

Decision Variables

F_{ij}	Quantity of live products shipped from producer *i* to distribution center *j*
F_{ik_1}	Quantity of fresh products shipped from producer *i* to customer k_1
F_{jk_1}	Quantity of fresh products shipped from distribution center *j* to customer k_1
$R_{k_1 l}$	Quantity of waste products shipped from the customer k_1 to fish waste recycling center *l*
R_{ml}	Quantity of waste products shipped from fish processing center *m* to fish waste recycling center *l*
D_{im}	Quantity of fresh products shipped from producer *i* to fish processing center *m*
D_{jm}	Quantity of fresh products shipped from distribution center *j* to fish processing center *m*
P_{mk_2}	Quantity of processed products shipped from fish processing center *m* to customer k_2
W_{lk_3}	Quantity of reprocessed products (fish powder) shipped from fish waste recycling centers *l* to fish powder markets k_3
Q_{il}	Quantity of low-quality products shipped from producer *i* to fish waste recycling centers *l*
Q_{jl}	Quantity of low-quality products shipped from distribution center *j* to fish waste recycling centers *l*
$Q_{k_1 l}$	Quantity of low-quality products shipped from the customer k_1 to fish waste recycling centers *l*
λ_i	Quantity of production by producer *i*
X_i	1 If production center *i* is opened at the location, 0 otherwise
W_j	1 If distribution center *j* is opened at the location, 0 otherwise
Y_l	1 If fish waste recycling center *l* is opened at the location, 0 otherwise

3. 3. Mathematical Model The bi-objective design of the fish CLSC is formulated as folloddws:

$$Min\ Z = z_1 + z_2 + z_3 \tag{1}$$

$$z_1 = \sum_{i=1}^{I} f_i \times X_i + \sum_{j=1}^{J} f_j \times W_j + \sum_{l=1}^{L} f_l \times Y_l \tag{2}$$

$$\begin{aligned} z_2 = & \sum_{i=1}^{I}\sum_{j=1}^{J} Cf_{ij} \times F_{ij} + \sum_{j=1}^{J}\sum_{k_1=1}^{K_1} Cf_{jk_1} \times F_{jk_1} + \sum_{i=1}^{I}\sum_{k_1=1}^{K_1} Cf_{ik_1} \times F_{ik_1} \\ & + \sum_{i=1}^{I}\sum_{m=1}^{M} Cd_{im} \times D_{im} + \sum_{j=1}^{J}\sum_{m=1}^{M} Cd_{jm} \times D_{jm} + \sum_{m=1}^{M}\sum_{k_2=1}^{K_2} Cp_{mk_2} \times P_{mk_2} \\ & + \sum_{m=1}^{M}\sum_{l=1}^{L} Cr_{ml} \times R_{ml} + \sum_{k_1=1}^{K_1}\sum_{l=1}^{L} Cr_{k_1 l} \times R_{k_1 l} \\ & + \sum_{l=1}^{L}\sum_{k_3=1}^{K_3} Cw_{lk_3} \times W_{lk_3} \\ & + \sum_{i=1}^{I}\sum_{l=1}^{L} Cq_{il} \times Q_{il} + \sum_{j=1}^{J}\sum_{l=1}^{L} Cq_{jl} \times Q_{jl} + \sum_{k_1=1}^{K_1}\sum_{l=1}^{L} Cq_{k_1 l} \times Q_{k_1 l} \end{aligned} \tag{3}$$

$$z_3 = \sum_{m=1}^{M}\sum_{k_2=1}^{K} P_{mk_2} \times Cp + \sum_{l=1}^{L}\sum_{k_3=1}^{K_3} W_{lk_3} \times Cr + \sum_{i=1}^{I} \lambda_i \times Cp' \tag{4}$$

$$\begin{aligned} Max\ Z' = & (\rho/2) \times \left(\sum_{k_1=1}^{K_1}\sum_{i=1}^{I} F_{ik_1} + \sum_{k=1}^{K_1}\sum_{j=1}^{J} F_{jk_1}) / \sum_{k_1=1}^{K_1} d_{k_1} \right) \\ & + (\rho/2) \times \left(\sum_{k_2=1}^{K_2}\sum_{m=1}^{M} P_{mk_2} / \sum_{k_2=1}^{K_2} d_{k_2} \right) \\ & + (1-\rho) \times \left(\sum_{l=1}^{L}\sum_{k_3=1}^{K_3} W_{lk_3} \right) / \left(\sum_{k_3=1}^{K_3} d_{k_3} \right) \end{aligned} \tag{5}$$

The first objective function (Z) is the total cost comprising fixed opening costs, transportation and production costs, and costs of the fish processing centers and waste recycling (reprocessing) centers (2)-(4). The second objective function (Z') with a maximum value of 1 comprises the forward and reverse responsiveness of the closed-loop network. The fraction's numerator and denominator respectively showed the products shipped to customers and customer demand. A zero inventory is initially assumed for all the centers.

Subject to:

$$\lambda_i \times (1-\alpha_i) - \sum_{m=1}^{M} D_{im} = \sum_{j=1}^{J} F_{ij} + \sum_{k_1=1}^{K_1} F_{ik_1} \qquad \forall\ i \in I \tag{6}$$

$$\sum_{i=1}^{I} F_{ij} \le MM \times W_j \qquad \forall j \in J \tag{7}$$

$$\lambda_i \le \lambda c_i \qquad \forall\ i \in I \tag{8}$$

$$\sum_{i=1}^{I} F_{ij} \le \lambda h_j \qquad \forall\ j \in J \tag{9-a}$$

$$\sum_{i=1}^{I} F_{ij} \ge \theta \times \lambda h_j \qquad \forall\ j \in J_1 \tag{9-b}$$

$$\sum_{i=1}^{I} F_{ij} = \sum_{k_1=1}^{K_1} F_{jk_1} + \sum_{m=1}^{M} D_{jm} + \sum_{l=1}^{L} Q_{jl} \qquad \forall\ j \in J \tag{10}$$

$$\sum_{j=1}^{J} F_{jk_1} + \sum_{i=1}^{I} F_{ik_1} \le d_{k_1} \qquad \forall\ k_1 \in K_1 \tag{11}$$

$$\sum_{i=1}^{I} F_{ik_1} \le \delta \times d_{k_1} \qquad \forall k_1 \in K_1 \tag{12}$$

$$(\sum_{i=1}^{I} D_{im} + \sum_{j=1}^{J} D_{jm} - \sum_{l=1}^{L} R_{ml}) \times \varphi' = \sum_{k_2=1}^{K_2} P_{mk_2} \qquad \forall m \in M \tag{13}$$

$$\sum_{k_2=1}^{K_2} P_{mk_2} \le \lambda r_m \qquad \forall \text{ m} \in M \tag{14}$$

$$\sum_{m=1}^{M} P_{mk_2} \le d_{k_2} \qquad \forall \ k_2 \in K_2 \tag{15}$$

$$\sum_{l=1}^{L} Q_{il} \le \alpha_i \times \lambda_i \qquad \forall i \in I \tag{16}$$

$$\sum_{i=1}^{I} Q_{il} \le MM \times Y_l \qquad \forall l \in L \tag{17}$$

$$\sum_{l=1}^{L} Q_{jl} \le \alpha_j \times \sum_{i=1}^{I} F_{ij} \qquad \forall j \in J \tag{18}$$

$$\sum_{j=1}^{J} Q_{jl} \le MM \times Y_l \qquad \forall l \in L \tag{19}$$

$$\sum_{l=1}^{L} Q_{k_1 l} \le \alpha_{k_1} \times (\sum_{i=1}^{I} F_{ik_1} + \sum_{j=1}^{J} F_{jk_1}) \qquad \forall k_1 \in K_1 \tag{20}$$

$$\sum_{k_1=1}^{K_1} Q_{K_1 l} \le MM \times Y_l \qquad \forall l \in L \tag{21}$$

$$\sum_{l=1}^{L} R_{k_1 lt} \le \beta_{k_1 t} \times (\sum_{i=1}^{I} F_{ik_1} + \sum_{j=1}^{J} F_{jk_1}) \times (1\text{-}\alpha_{k_1}) \qquad \forall k_1 \in K_1 \tag{22}$$

$$\sum_{k_1=1}^{K_1} R_{k_1 l} \le MM \times Y_l \qquad \forall l \in L \tag{23}$$

$$\sum_{l=1}^{L} R_{ml} \le \beta_m \times (\sum_{i=1}^{I} D_{im} + \sum_{j=1}^{J} D_{jm}) \qquad \forall m \in M \tag{24}$$

$$\sum_{m=1}^{M} R_{ml} \le MM \times Y_l \qquad \forall l \in L \tag{25}$$

$$(\sum_{m=1}^{M} R_{mlt} + \sum_{k_1=1}^{K_1} R_{k_1 l} + \sum_{i=1}^{I} Q_{il} + \sum_{j=1}^{J} Q_{jl} + \sum_{k_1=1}^{K_1} Q_{k_1 l}) \times \varphi = \sum_{k_3=1}^{K_3} W_{lk_3} \qquad \forall \ l \in L \tag{26}$$

$$\sum_{k_3=1}^{K_3} W_{lk_3} \le \lambda r_l \qquad \forall \ l \in L \tag{27}$$

$$\sum_{l=1}^{L} W_{lk_3} \le d_{k_3} \qquad \forall k_3 \in K_3 \tag{28}$$

$$\sum_{j=1}^{J} F_{ij} \le MM \times X_i \qquad \forall i \in I \tag{29}$$

$$\sum_{k_1=1}^{K_1} F_{ik_1} \le MM \times X_i \qquad \forall i \in I \tag{30}$$

$$\sum_{m=1}^{M} D_{im} \le MM \times X_i \qquad \forall i \in I \tag{31}$$

$$\sum_{l=1}^{L} Q_{il} \le MM \times X_i \qquad \forall i \in I \tag{32}$$

$$X_i, \ Y_l, W_j \in \{0,1\} \qquad \forall i \in I, \forall l \in L, \forall \ j \in J \tag{33}$$

$$\begin{gathered} F_{ij}, F_{ik_1}, F_{jk_1}, D_{im}, D_{jm}, D_{jm}, R_{k_1 l}, R_{ml}, W_{lk_3}, Q_{il}, Q_{jl}, Q_{k_1 l} \ge 0 \\ \forall i \in I, j \in J, k_1 \in K_1, k_2 \in K_2, k_3 \in K_3, m \in M, l \in L \end{gathered} \tag{34}$$

$$\lambda_i \ge 0 \qquad \forall i \in I \tag{35}$$

According to constraint (6), the production level minus the amounts of deteriorated product and that transported to the processing centers equals the number of products transported from the producers to the customers and distribution centers. According to constraint (7), a product is transported to a potential location only if a distribution center is open there. According to constraint (8), the maximum amount of products of a producer, i.e. its production capacity, equals an expected maximum production rate. Constraints (9-a) and (9-b) respectively ensure that the amount of products received from the producers in a distribution center is at most equal to its holding capacity and that a minimum amount of the capacity of a distribution center is used.

According to constraint (10), the amount of products received from the producers in a distribution center equals the sum of the number of products transported to the customers and processing centers and that of deteriorated products transported to the reprocessing centers. Constraint (11) ensures that the demand for a fresh product at least equals the number of products received from the producers and distribution centers. According to constraint (12), the producers directly supply the maximum customer demand for fresh fish. According to constraint (13), all the products received from the distribution centers and producers minus the wasted products transported to the reprocessing centers multiplied by the conversion rate equals the total processed product transported to the processed product market. Constraints (14) and (15) respectively ensure that the amount of products transported to the processed product market is at most equal to the expected maximum processing rate and the customer demand for the processed products.

According to constraint (16), the waste production rate at least equals the amount of returned products transported from the producers to the reprocessing centers. Constraint (17) ensures that the returned products are transported from a production center to a reprocessing center only if a reprocessing center is open in the potential place for this facility. As in the case of constraints (16)-(17), constraints (18)-(19), (20)-(21), (22)-(23) and (24)-(25) put the maximum capacity of the facilities as a limit on the transported products and determine the opening of the facility as a precondition for shipping the goods. According to constraint (26), the total fish powder transported as the reprocessed product to the fish powder market equals all the products returned from the processing centers, producers, customers, and distribution centers multiplied by the conversion rate.

Constraints (27)-(28) respectively ensure that the manufacturing capacity and demand of a fish powder market at least equal the amount of fish powder transported to the fish powder market. According to constraints (29)-(32), the products can be transported to places where there is an open production center. Constraints (33)-(35) also show binary and non-negativity limitations on the associated decision variables.

4. SOLUTION TECHNIQUES

The Lp-metrics and epsilon-constraint detail as follows and are used to solve the multi-objective problem. They are evaluated in terms of their CPU time and solution quality as performance indicators.

4. 1. LP-Metric Method The metric distance is utilized in *Lp*-metrics to measure the distance between an existing and the optimal solution [33]. Xu [34] proposed Equation (36) for "the more the better" problems based on an anti-ideal concept.

$$Lp=\left\{\sum_{j=1}^{k}w_j\left[\frac{f_j(x^{*j})-f_j(x)}{f_j(x^{*j})-f_j(\bar{x}^{j})}\right]^p\right\}^{1/p} \tag{36}$$

The compatible *Lp* function is minimized to minimize deviation from the optimal solution. Equation (36) is utilized as a normalized form to obtain the efficiency of the compatible *Lp* function for various objectives with diverse scales. The decision-maker determines p as the level of emphasis on the available values of deviation. This study assumed p to equal 2. The optimal solution ($f_j(x^{*j})$) is first obtained by individually solving all the objective functions based on the relevant constraints. Anti-ideal values are then obtained by solving the reverse objective functions, i.e. minimization was converted to maximization and vice versa. These values are inserted into the *Lp* model, which was then minimized based on its constraints. The optimal values and *Lp* deviation are ultimately obtained through solving the model. With w_j representing the degree of importance of the j-th objective ($\sum_{j=1}^{k}w_j=1$), the gradual-priority weighting [35] is employed to search the entire solution space, as well as obtaining Pareto-optimal solutions. Equations (37) are used to determine the weights of a generation.

$$\theta_t=\frac{90}{N_s-1}\times(t-1),\ p_{1t}=\cos(\theta_t),\ p_{2t}=\sin(\theta_t),$$
$$w_{1t}=\frac{p_{1t}}{p_{1t}+p_{2t}},w_{2t}=\frac{p_{2t}}{p_{1t}+p_{2t}}\qquad \forall t=1,2,...,N_s \tag{37}$$

where t is the t^{th} Pareto solution (t = 1, … ,10).

4. 2. Epsilon-Constraint Method A maximization multi-objective integer programming problem is considered as follows:

$$\begin{aligned}&\max\ \left\{f_1(x),f_2(x),...,f_p(x)\right\}\\&\text{s.t.}\quad x\in S\end{aligned} \tag{38}$$

where p represents the number of objective functions, f_i (x) the i-th objective function, , x the decision vector, S the solution space, n the number of decision variables and $x_j \in Z$ for $j\in 1,2,$ …, p. The conventional epsilon-constraint technique is performed by optimizing an objective function while adding the other objectives into the constraint space to ensure that the basic requirements are met. The method of AUGMECON is employed to convert inequality constraints of the objective functions to equality constraints and obtain efficient solutions through introducing non-negative slack or surplus variables and augmenting the objective function using a weighted sum of the surplus or slack variables [36]. The problem is re-written as follows:

$$\begin{aligned}&\max\ \mathrm{f_p(x)}+\delta(s_1/r_1+s_2/r_2+...+s_{p-1}/r_{p-1})\\&\text{s.t.}\quad \mathrm{f_1(x)\text{-}s_1=e_1}\\&\qquad ...\\&\qquad \mathrm{f_{p\text{-}1}(x)\text{-}s}_{p-1}=\mathrm{e_{p\text{-}1}}\\&\qquad \mathrm{x\in S}\ \text{ and } \mathrm{s}_i\in Z^+, i\in[1,p-1]\end{aligned} \tag{39}$$

where r_i, $i\in[1,p-1]$ represents the range of the i-th objective function, δ an adequately-small value between 10^{-3} and 10^{-6} and e_1, … , e_{p-1} the satisfaction level vector showing minimum requirements for the constrained objective functions.

5. PERFORMANCE METRICS

The solution methods were compared with each other in terms of their performance using the following three indicators, each of which appraising a different dimension.

a) Mean ideal distance (MID): This distance defined as Equation (40) is utilized to calculate the distance between the ideal point and Pareto solutions [37]. The method performance was higher at lower values of this index.

$$MID=\frac{\sum_{i=1}^{n}\sqrt{\left(\frac{f1_i-f1_{best}}{f1_{total}^{max}-f1_{total}^{min}}\right)^2+\left(\frac{f2_i-f2_{best}}{f2_{total}^{max}-f2_{total}^{min}}\right)^2}}{n} \tag{40}$$

where $f1_i$ and $f2_i$ represent the value of the i-th non-dominated solution to the two objective functions, respectively, n is the number of non-dominated solutions, ($f1_{best}$, $f2_{best}$) are the ideal point (i.e., (0, 1) in this study), and $fj_{total}^{\max}$ and $fj_{total}^{\min}$ are the highest and lowest values of a fitness function among all the non-dominated solutions, respectively.

b) Rate of achievement to two objectives Simultaneously (RAS): This method introduces a set of solutions to strike a more effective balance between the values of the objective functions as superior Equation (41) shows the extent to which this balance is achieved between different goals [38].

$$RAS = \frac{\sum_{i=1}^{n}\left(\frac{f_{1i}-F_i}{F_i}\right)+\left(\frac{f_{2i}-F_i}{F_i}\right)}{n} \tag{41}$$

where n represents the number of non-defeated solutions and $F_i = \min\{f_{1i}, f_{2i}\}$.

According to the equilibrium method, this criterion increases if a solution along an axis suits one goal and contradicts the other (unbalanced solutions). This study normalized the objective functions to use this criterion.

c) Computational time (CPU time): This index is used for evaluating the running speed of a method.

6. NUMERICAL EXAMPLES AND CASE STUDY

Six problems are generated and tested to examine the performance of the solution techniques. They are categorized by their numbers of producers (I), reprocessing centers (L), customers (K_1), distribution centers (J), processing centers (M), and customers of processed products (K_2) and the fish powder (K_3). Table 1 shows the values of these parameters. The first problem is the case study and each problem is simulated ten times to obtain Pareto solutions.

A case study is conducted in Northern Iran to demonstrate the application of the solution method and study model. Different parameters and conditions are considered in using solution methods to examine the proposed model. The data are collected in Mazandaran, Iran. Figure 3 shows the main towns in this province.

The transportation cost is defined between the towns in Iran by their distances in km, fare rates ($ per km), and transport mode (live fish: 1.36, fresh or processed fish: 0.18, and fish powder: $0.09 /ton.km). Table 2 presents the values of the other parameters of the model. Tables 3 and 4, respectively show the selected towns for the individual places in the case study and their distances. Table 5 presents the model parameters of the case study.

7. COMPUTATIONAL RESULTS

To validate and evaluate the efficiency of the model and compare the two proposed solution methods, the model in six different sizes with Lp-metrics methods and epsilon-constraint was run on a computer with Intel® Core ™ i7-8750H CPU @ 2.20GHz specifications using Lingo software (LINGO 18.0 x64).

The proposed methods were statistically compared with each other by testing the hypothesis of equality of means, comparing the values of the first and second objective functions, and examining the execution time and average results of sixty times of implementing the model for all the three criteria. Testing the hypothesis of equality of means is appropriate for comparing the results of two samples [39]. The null hypothesis suggested the equality of the means of Lp-metrics and epsilon-constraint methods and hypothesis one suggested that their opposite means.

Table 6 presents the results of testing the hypotheses in Minitab 18 at a 95% confidence interval. The null hypothesis is rejected in terms of the computation time of the model and the criterion of the first and second objective functions, which suggested significant differences in the mean values of these criteria between the two methods.

The solution methods are compared with each other by conducting a pairwise comparison based on the metrics proposed in Section 6 (Table 7). The lower values of the metrics suggest an increased performance.

ANOVA is applied to compare the obtained metrics and statistically-significant differences between the methods are shown in terms of their performance. Figure 4 shows the plots of the intervals for each metric used in these methods at a 95% confidence interval. The interval plots are individually obtained for each solution method and metric using six points in Table 7, suggesting that epsilon-constraint outperforms the other method in terms of MID, RAS, and CPU time metrics.

TABLE 1. General data of the test problems

Test #	I_1	I_2	I_3	I	J_1	J_2	J	K_1	K_2	M	L_1	L_2	L	K'_3	K''_3	K_3
1	3	1	1	5	5	1	6	9	2	1	0	2	2	1	2	3
2	4	2	2	8	7	2	9	13	5	2	1	3	4	2	3	5
3	5	3	3	11	9	3	12	17	8	3	2	4	6	3	4	7
4	6	4	4	14	11	4	15	21	11	4	3	5	8	4	5	9
5	7	5	5	17	13	5	18	25	14	5	4	6	10	5	6	11
6	8	6	6	20	15	6	21	29	17	6	5	7	12	6	7	13

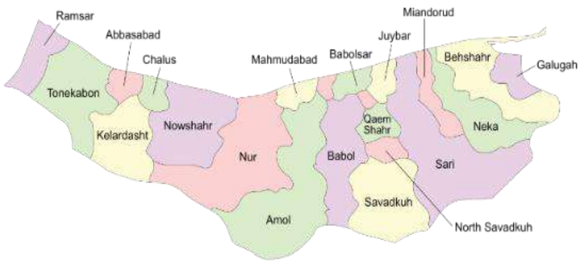

Figure 3. Main towns in Mazandaran

TABLE 2. Other model parameters setting

Parameter	Values	Unit
f_i	Uniform ~ [2.73, 144]	Dollar ($)
f_j	Uniform ~ [48.61, 347]	Dollar ($)
f_l	Uniform ~ [69.44, 190]	Dollar ($)
d_{k_1}	Uniform ~ [0.99, 11]	Ton
d_{k_2}	Uniform ~ [0.66, 2]	Ton
d_{k_3}	Uniform ~ [0.17, 0.4]	Ton
λc_i	Uniform ~ [1.25, 19]	Ton
λh_j	Uniform ~ [0.7, 11]	Ton
λr_m	Uniform ~ [2.78, 6]	Ton
λr_l	Uniform ~ [1.1, 3]	Ton
α_i =0.01, α_j =0.02, α_{k_1} =0.03, β_{k_1} =0.15, β_m = 0.4, θ =0.5, δ =0.2, ρ=0.6, φ=0.25, φ'=1.2		Percentage
Cp =2273, Cr =454, Cp' =909		Dollar per Ton

TABLE 3. Selected cities for each index

i	***j***	***K1***	***K2***
Tonekabon	Tonekabon	Ramsar	Chalus
Chalus	Abbasabad	Tonekabon	Ramsar
Amol	Noshahr	Kelardasht	
Amol (Rice-farm)	Mahmoodabad	Abbasabad	***K3***
Noshahr (Sea-farm)	Amol	Chalus	Noor
	Chalus	Noshahr	Tonekabon
l		Noor	Amol
Tonekabon	***m***	Mahmoodabad	
Noshahr	Amol	Amol	

TABLE 4. Distance between the mentioned towns (Km)

	(1)	**(2)**	**(3)**	**(4)**	**(5)**	**(6)**	**(7)**	**(8)**	**(9)**
(1)	1	22	46	94	101	133	149	156	181
(2)	22	1	25	73	80	11	128	135	159
(3)	46	25	1	49	55	87	103	110	135
(4)	94	73	49	1	8.1	41	57	64	89
(5)	101	80	55	8.1	1	33	50	56	81
(6)	133	111	87	41	33	1	38	25	49
(7)	149	128	103	57	50	38	g1	61	86
(8)	156	35	110	64	56	25	61	1	25
(9)	181	159	135	89	81	49	86	25	1

(1) Amol, (2) Mahmoodabad, (3) Noor, (4) Noshahr, (5) Chalus, (6) Abbasabad, (7) Kelardasht, (8) Tonekabon, (9) Ramsar.

TABLE 5. Model parameters setting for the case study

Parameter	Values	Unit
f_i	[0, 0, 0, 11.32, 2.73]	Dollar ($)
f_j	[0, 0, 0, 0, 0, 48.61]	Dollar ($)
f_l	[82.07, 69.44]	Dollar ($)
d_{k_1}	[0.99, 2.22, 0.7, 1.85, 1.55, 0.32, 1.62, 1.31, 5.36]	Ton
d_{k_2}	[1.03, 0.66]	Ton
d_{k_3}	[0.17, 0.18, 0.19]	Ton
λc_i	[9.13, 1.25, 9.51, 5.60, 0.36]	Ton
λh_j	[2.2 0.7 1.84 1.30 5.32 1.54]	Ton
λr_m	[2.78]	Ton
λr_l	[1.3, 1.1]	Ton

TABLE 6. Result of the hypothesis test

Method	Obj. 1	Obj. 2	CPU Time
ε-constraint	98,601.1380	0.8762	1.9794
Lp-metrics	74,622.3557	0.7940	25.2738
	Reject H_0	Reject H_0	Reject H_0

8. RANKING THE SOLUTION METHODS

TOPSIS is employed to determine the performance of the solution methods in terms of all the metrics. The metrics and solution methods are respectively considered criteria and alternatives. The average values of the metrics are

TABLE 7. Evaluation of mentioned methods in each metric measure

Problem	MID		RAS		CPU Time	
	ε-constraint	**LP-Metric**	**ε-constraint**	**LP-Metric**	**ε-constraint**	**LP-Metric**
1	3.8467	3.4671	1.4076	1.9390	0.3229	0.2450
2	3.6648	3.4642	2.9087	4.9836	0.4029	1.5400
3	3.7217	3.4739	2.1986	3.7789	0.7600	9.3420
4	3.7527	3.5942	1.9349	3.5410	1.5114	37.7370
5	3.7562	3.6826	1.9077	3.3465	2.4443	57.7340
6	3.7456	3.7193	1.9839	3.7368	6.4350	45.0450
Average	3.7480	3.5669	2.0569	3.5543	1.9794	25.2738

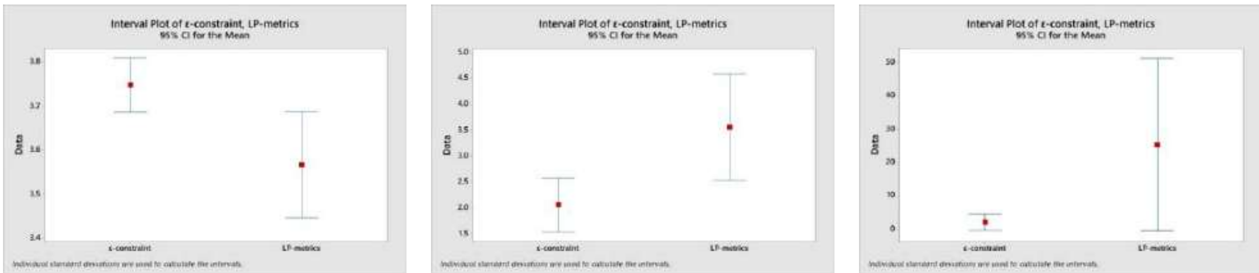

(a) (b) (c)

Figure 4. Intervals plots (at the 95% confidence level): (a) MID, (b) RAS, (c) CPU Time

utilized as the input to the proposed method in all the problems. TOPSIS developed as a compromise model by Hwang and Yoon [40], is commonly used in multi-criteria decision makings. The following steps explain the procedure of this method.

According to the results of TOPSIS shown in Table 8, the epsilon-constraint is determined as the superior method given its higher coefficient.

Procedure of the TOPSIS method

Step 1	$F_{ij} = \frac{f_{ij}}{\sqrt{\sum_{i=1}^{m} f_{ij}^2}}$, i=1,...,m, j=1,...,n. Normalized decision matrix with m rows (alternatives) and n columns (criteria)
Step 2	$v_{ij} = F_{ij} \times w_j$ Weighted normalized decision matrix *Wj:* criteria weight, $\sum_{j=1}^{n} w_j = 1,\ w_j \geq 0,$
Step 3	$v_j^+ = \max_i v_{ij}$; $v_j^- = \min_i v_{ij}$, j=1,...,n. Assumption: "more is better" criteria.
Step 4	$d_i^+ = \sqrt{\sum_{j=1}^{n} \left(v_{ij} - v_j^+\right)^2}$, $d_i^- = \sqrt{\sum_{j=1}^{n} \left(v_{ij} - v_j^-\right)^2}$ i=1,...,m Euclidean distance between each solution and the ideal and negative-ideal solution
Step 5	$C_i = \frac{d_i^-}{d_i^- + d_i^+}$ The optimal solution having the largest C_i is the recommended solution.

TABLE 8. Results of TOPSIS

Method	C_i	Rank
ε-constraint	0.943696	1
Lp-metrics	0.056304	2

9. DISCUSSION

In this section, a sensitivity analysis is performed to determine the accuracy and performance of the model in the case study. The performance of the proposed model was evaluated for the individual scenarios defined based on variations in the demand for fresh, processed, and reprocessed products. Table 9 presents these scenarios and the values of the objective functions obtained for the individual scenarios and determined using the epsilon-constraint method. Figure 6 shows variations in the values of the two objective functions for the individual scenarios.

According to Table 9 and Figure 5, an increase or decline in the demand does not improve or decline the values of the two objective functions, respectively, which validates the model results. These results can help with making decisions in cases of disruptive reductions or rises in demand. For instance, for fresh products, an up to 20% increase in demand would decrease the customer satisfaction, while it remains steady for an increasing demand for processed and reprocessed products.

TABLE 9. Sensitivity analysis of the demand parameters

Scenario	Change intervals of demands	d_{k_1}		d_{k_2}		d_{k_3}	
		Obj. 1	**Obj. 2**	**Obj. 1**	**Obj. 2**	**Obj. 1**	**Obj. 2**
1	-30%	0.88	12726.55	0.88	13524.85	0.88	14345.64
2	-20%	0.88	13405.47	0.88	13977.82	0.88	14465.85
3	-10%	0.88	14136.73	0.88	14431.05	0.88	14656.79
4	0%	0.88	14889.52	0.88	14889.52	0.88	14889.52
5	10%	0.86	14984.09	0.88	15364.07	0.88	15171.19
6	20%	0.85	14944.35	0.88	15838.71	0.88	15482.35
7	30%	0.85	15586.49	0.88	16319.26	0.88	15825.21

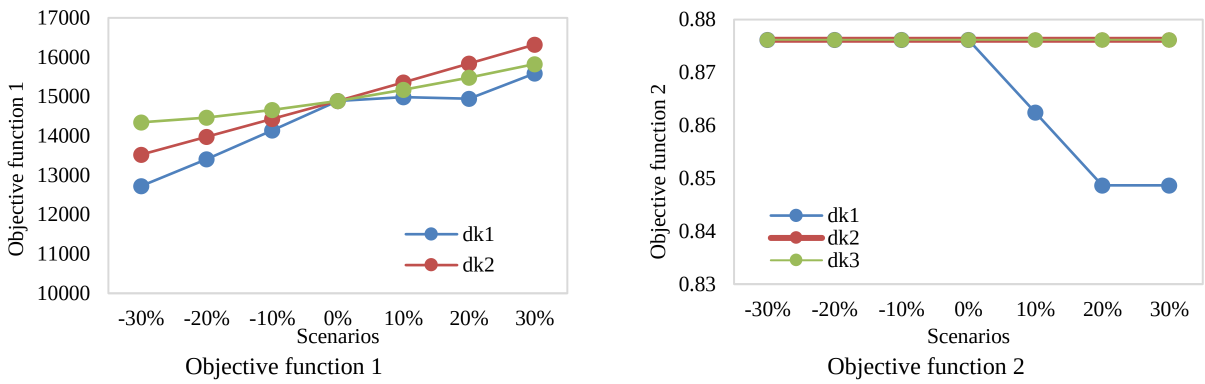

Figure 5. Sensitivity analysis of the demand parameters

10. CONCLUSION

This study proposed a novel bi-objective seven-echelon CLSC problem for the fish. The objectives comprised minimizing the total cost of the network and maximizing the responsiveness to customer demand in forward and reverse cases.

Lp-metrics and epsilon-constraint were employed to solve the proposed model. The present findings were validated by examining a real-world case in Iran. This model was applied to six test problems and the metrics were calculated by employing the solution methods. Using TOPSIS as a multi-criteria decision-making approach to determine the method with the higher performance in terms of all the metrics showed the satisfactory efficiency of epsilon-constraint.

It is recommended that further studies be conducted to include uncertainty of parameters and sustainability criteria in multi-period and multi-product problems. Other multi-objective optimization methods can also be used to solve the model. Given the significant increase in the burden of computation with an increase in the dimensions of the problem, heuristic and metaheuristic algorithms can be used in future research. Also, discussing the model complexity and some mathematical aspects of the model can be proposed for future research.

11. REFERENCES

1. Akbari-Kasgari, M., Khademi-Zare, H., Fakhrzad, M. B., Hajiaghaei-Keshteli, M., and Honarvar, M., "A Closed-loop Supply Chain Network Design Problem in Copper Industry", ***International Journal of Engineering - Transaction B: Applications***, Vol. 33, No. 10, (2020), 2008–2015. doi:10.5829/ije.2020.33.10a.19
2. Govindan, K., and Soleimani, H., "A review of reverse logistics and closed-loop supply chains: a Journal of Cleaner Production focus", ***Journal of Cleaner Production***, Vol. 142, (2017), 371–384. doi:10.1016/j.jclepro.2016.03.126
3. Tavakkoli-Moghaddam, R., Yadegari, M., and Ahmadi, G., "Closed-loop Supply Chain Inventory-location Problem with Spare Parts in a Multi-Modal Repair Condition", ***International Journal of Engineering - Transaction B: Applications***, Vol. 31, No. 2, (2018), 346–356. doi:10.5829/ije.2018.31.02b.20
4. Cheraghalipour, A., Paydar, M. M., and Hajiaghaei-Keshteli, M., "An Integrated Approach for Collection Center Selection in Reverse Logistic", ***International Journal of Engineering - Transaction A: Basics***, Vol. 30, No. 7, (2017), 1005–1016. doi:10.5829/ije.2017.30.07a.10
5. Hajiaghaei-Keshteli, M., Abdallah, K. S., and Fathollahi-Fard, A. M., "A Collaborative Stochastic Closed-loop Supply Chain Network Design for Tire Industry", ***International Journal of Engineering - Transaction A: Basics***, Vol. 31, No. 10, (2018), 1715–1722. doi:10.5829/ije.2018.31.10a.14
6. Govindan, K., "Sustainable consumption and production in the food supply chain: A conceptual framework", ***International***

Journal of Production Economics, Vol. 195, (2018), 419–431. doi:10.1016/j.ijpe.2017.03.003

7. Food and Agriculture Organization of the United Nations. "The State of World Fisheries and Aquaculture 2018–Meeting the sustainable development goals." FAO (2018). http://www.fao.org/3/i9540en/I9540EN.pdf

8. Cinemre, H. A., Ceyhan, V., Bozoğlu, M., Demiryürek, K., and Kılıç, O., "The cost efficiency of trout farms in the Black Sea Region, Turkey", ***Aquaculture***, Vol. 251, Nos. 2–4, (2006), 324–332. doi:10.1016/j.aquaculture.2005.06.016

9. Shekarian, E., "A review of factors affecting closed-loop supply chain models", ***Journal of Cleaner Production***, Vol. 253, (2020), 119823. doi:10.1016/j.jclepro.2019.119823

10. Raza, S. A., "A systematic literature review of closed-loop supply chains", ***Benchmarking: An International Journal***, Vol. 27, No. 6, (2020), 1765–1798. doi:10.1108/BIJ-10-2019-0464

11. Peng, H., Shen, N., Liao, H., Xue, H., and Wang, Q., "Uncertainty factors, methods, and solutions of closed-loop supply chain — A review for current situation and future prospects", ***Journal of Cleaner Production***, Vol. 254, (2020), 120032. doi:10.1016/j.jclepro.2020.120032

12. Fathollahi-Fard, A. M., Hajiaghaei-Keshteli, M., Tian, G., and Li, Z., "An adaptive Lagrangian relaxation-based algorithm for a coordinated water supply and wastewater collection network design problem", ***Information Sciences***, Vol. 512, (2020), 1335–1359. doi:10.1016/j.ins.2019.10.062

13. Fathollahi-Fard, A. M., Ahmadi, A., and Al-e-Hashem, S. M. J. M., "Sustainable closed-loop supply chain network for an integrated water supply and wastewater collection system under uncertainty", ***Journal of Environmental Management***, Vol. 275, (2020), 111277. doi:10.1016/j.jenvman.2020.111277

14. Tabrizi, S., Ghodsypour, S. H., and Ahmadi, A., "Modelling three-echelon warm-water fish supply chain: A bi-level optimization approach under Nash–Cournot equilibrium", ***Applied Soft Computing***, Vol. 71, (2018), 1035–1053. doi:10.1016/j.asoc.2017.10.009

15. Ghare, P. M., "A model for exponential decaying inventory." Journal of Industrial Engineering, Vol. 14, (1963), 238–243. https://ci.nii.ac.jp/naid/10004591187/

16. Govindan, K., Jafarian, A., Khodaverdi, R., and Devika, K., "Two-echelon multiple-vehicle location–routing problem with time windows for optimization of sustainable supply chain network of perishable food", ***International Journal of Production Economics***, Vol. 152, (2014), 9–28. doi:10.1016/j.ijpe.2013.12.028

17. Chaudhuri, A., Dukovska-Popovska, I., Subramanian, N., Chan, H. K., and Bai, R., "Decision-making in cold chain logistics using data analytics: a literature review", ***The International Journal of Logistics Management***, Vol. 29, No. 3, (2018), 839–861. doi:10.1108/IJLM-03-2017-0059

18. Lusiantoro, L., Yates, N., Mena, C., and Varga, L., "A refined framework of information sharing in perishable product supply chains", ***International Journal of Physical Distribution and Logistics Management***, Vol. 48, No. 3, (2018), 254–283. doi:10.1108/IJPDLM-08-2017-0250

19. Mirmajlesi, S. R., and Shafaei, R., "An integrated approach to solve a robust forward/reverse supply chain for short lifetime products", ***Computers & Industrial Engineering***, Vol. 97, (2016), 222–239. doi:10.1016/j.cie.2016.05.015

20. Abedi, A., and Zhu, W., "An optimisation model for purchase, production and distribution in fish supply chain – a case study", ***International Journal of Production Research***, Vol. 55, No. 12, (2017), 3451–3464. doi:10.1080/00207543.2016.1242800

21. Soysal, M., Bloemhof-Ruwaard, J. M., Haijema, R., and van der Vorst, J. G. A. J., "Modeling a green inventory routing problem for perishable products with horizontal collaboration", ***Computers & Operations Research***, Vol. 89, (2018), 168–182. doi:10.1016/j.cor.2016.02.003

22. Cheraghalipour, A., Paydar, M. M., and Hajiaghaei-Keshteli, M., "A bi-objective optimization for citrus closed-loop supply chain using Pareto-based algorithms", ***Applied Soft Computing***, Vol. 69, (2018), 33–59. doi:10.1016/j.asoc.2018.04.022

23. Masruroh, N. A., Fauziah, H. A., and Sulistyo, S. R., "Integrated production scheduling and distribution allocation for multi-products considering sequence-dependent setups: a practical application", ***Production Engineering***, Vol. 14, No. 2, (2020), 191–206. doi:10.1007/s11740-020-00954-z

24. Onggo, B. S., Panadero, J., Corlu, C. G., and Juan, A. A., "Agri-food supply chains with stochastic demands: A multi-period inventory routing problem with perishable products", ***Simulation Modelling Practice and Theory***, Vol. 97, (2019), 101970. doi:10.1016/j.simpat.2019.101970

25. Naderi, B., Govindan, K., and Soleimani, H., "A Benders decomposition approach for a real case supply chain network design with capacity acquisition and transporter planning: wheat distribution network", ***Annals of Operations Research***, Vol. 291, Nos. 1–2, (2020), 685–705. doi:10.1007/s10479-019-03137-x

26. Motevalli-Taher, F., Paydar, M. M., and Emami, S., "Wheat sustainable supply chain network design with forecasted demand by simulation", ***Computers and Electronics in Agriculture***, Vol. 178, (2020), 105763. doi:10.1016/j.compag.2020.105763

27. Leng, L., Zhang, C., Zhao, Y., Wang, W., Zhang, J., and Li, G., "Biobjective low-carbon location-routing problem for cold chain logistics: Formulation and heuristic approaches", ***Journal of Cleaner Production***, Vol. 273, (2020), 122801. doi:10.1016/j.jclepro.2020.122801

28. Chan, F. T. S., Wang, Z. X., Goswami, A., Singhania, A., and Tiwari, M. K., "Multi-objective particle swarm optimisation based integrated production inventory routing planning for efficient perishable food logistics operations", ***International Journal of Production Research***, Vol. 58, No. 17, (2020), 5155–5174. doi:10.1080/00207543.2019.1701209

29. Siddh, M. M., Soni, G., Jain, R., and Sharma, M. K., "Structural model of perishable food supply chain quality (PFSCQ) to improve sustainable organizational performance", ***Benchmarking: An International Journal***, Vol. 25, No. 7, (2018), 2272–2317. doi:10.1108/BIJ-01-2017-0003

30. Utomo, D. S., Onggo, B. S., and Eldridge, S., "Applications of agent-based modelling and simulation in the agri-food supply chains", ***European Journal of Operational Research***, Vol. 269, No. 3, (2018), 794–805. doi:10.1016/j.ejor.2017.10.041

31. Dania, W. A. P., Xing, K., and Amer, Y., "Collaboration behavioural factors for sustainable agri-food supply chains: A systematic review", ***Journal of Cleaner Production***, Vol. 186, (2018), 851–864. doi:10.1016/j.jclepro.2018.03.148

32. Joshi, A. D., and Gupta, S. M., "Evaluation of design alternatives of End-Of-Life products using internet of things", ***International Journal of Production Economics***, Vol. 208, (2019), 281–293. doi:10.1016/j.ijpe.2018.12.010

33. Isaloo, F., and Paydar, M. M., "Optimizing a robust bi-objective supply chain network considering environmental aspects: a case study in plastic injection industry", ***International Journal of Management Science and Engineering Management***, Vol. 15, No. 1, (2020), 26–38. doi:10.1080/17509653.2019.1592720

34. Xu, X., "A note on the subjective and objective integrated approach to determine attribute weights", ***European Journal of Operational Research***, Vol. 156, No. 2, (2004), 530–532. doi:10.1016/S0377-2217(03)00146-2

35. Chang, P.-C., Hsieh, J.-C., and Lin, S.-G., "The development of gradual-priority weighting approach for the multi-objective flowshop scheduling problem", ***International Journal of Production Economics***, Vol. 79, No. 3, (2002), 171–183. doi:10.1016/S0925-5273(02)00141-X

36. Mavrotas, G., "Effective implementation of the ε-constraint

method in Multi-Objective Mathematical Programming problems", ***Applied Mathematics and Computation***, Vol. 213, No. 2, (2009), 455–465. doi:10.1016/j.amc.2009.03.037

37. Karimi, N., Zandieh, M., and Karamooz, H. R., "Bi-objective group scheduling in hybrid flexible flowshop: A multi-phase approach", ***Expert Systems with Applications***, Vol. 37, No. 6, (2010), 4024–4032. doi:10.1016/j.eswa.2009.09.005

38. Behnamian, J., Fatemi Ghomi, S. M. T., and Zandieh, M., "A multi-phase covering Pareto-optimal front method to multi-objective scheduling in a realistic hybrid flowshop using a hybrid metaheuristic", ***Expert Systems with Applications***, Vol. 36, No. 8, (2009), 11057–11069. doi:10.1016/j.eswa.2009.02.080

39. Wellek, S., "Testing Statistical Hypotheses of Equivalence and Noninferiority", CRC press, (2010).

40. Hwang, C.-L., and Yoon, K., "Methods for Multiple Attribute Decision Making", In Multiple Attribute Decision Making, Pp. 58-191. Springer, Berlin, Heidelberg, (1981), 58–191. doi:10.1007/978-3-642-48318-9_3

Persian Abstract

چکیده

در سال‌های اخیر، بسیاری از صنایع در کشورهای پیشرفته به دلایل مختلف از جمله افزایش نگرانی‌های زیست محیطی، لجستیک معکوس را فرآیندی مهم در زنجیره تأمین خود دانسته‌اند. از آنجا که ماهی یک ماده غذایی فسادپذیر است، استفاده مجدد از محصولات بلااستفاده و ضایعات در هر سطح از زنجیره تامین یکی از دغدغه‌های اصلی تصمیم‌گیرندگان است. در این مقاله، یک مدل ریاضی جدید با هدف به حداقل رساندن هزینه‌های زنجیره تامین حلقه‌بسته ماهی و به حداکثر رساندن پاسخگویی به تقاضای مشتری ارائه شده است. به منظور حل مدل، از دو روش معیار جامع و اپسیلون محدودیت استفاده می‌شود. سپس براساس معیارهای عملکرد و با بکارگیری آزمون فرض آماری، روش‌های حل با یکدیگر مقایسه می‌شوند. سرانجام، از الگوریتم تاپسیس برای انتخاب روش برتر استفاده می‌گردد. به منظور اثبات کاربرد مدل، یک مطالعه موردی از یک زنجیره تامین حلقه بسته ماهی قزل آلا در شمال ایران با انجام تحلیل حساسیت تقاضا ارائه شده است. نتایج تجزیه و تحلیل نشان می‌دهد که مدل پیشنهادی و روش حل مورد تاییدند.

IJE TRANSACTIONS B: Applications Vol. 34, No. 05, (May 2021) 1269-1273

International Journal of Engineering

Journal Homepage: www.ije.ir

An Improved Modeling of Parkinson's Tremor and Investigation of Some Approaches to Remove this Symptom

F. Ghoreishian, M. Pooyan*

Biomedical Engineering Dept., Engineering faculty, Shahed University, Tehran, Iran

PAPER INFO

Paper history:
Received 14 January 2020
Received in revised form 27 January 2021
Accepted 20 March 2021

Keywords:
Parkinson's Disease
Modeling
Tremor Removing

ABSTRACT

In this research, an improved model of Parkinsonian tremor is presented by using a mathematical and computational approach. In Parkinson's disease (PD), an abnormal signal is produced by basal ganglia (BG). This signal goes to the thalamus, then enters cortex and after interaction with peripheral system goes to muscle and finally appears as tremor. In the presented model, all of the mentioned process are simulated. Also, the skeletal muscle model as well as the central nervous system (basal ganglia, thalamus, cortex and supplementary motor area) and peripheral nervous system (spinal reflex) mechanisms are considered. In addition, two methods for tremor suppression are applied in this paper, 1) deep brain stimulation (DBS) which affects dopamine level in BG and 2) a mechanical method which is based on a negative feedback. The accuracy and efficiency of the presented simulation are demonstrated by comparison of the obtained results with those obtained by clinical tests.

***doi**: 10.5829/ije.2021.34.05b.20*

1. INTRODUCTION

The Parkinson's disease was first described in 1817 by James Parkinson [1]. This disease is related to central nervous system and is caused by death of dopamine-generating cells in the substantia nigra pars compacta (SNc) which is a region of basal ganglia [2, 3]. PD develops gradually and can be recognized by four symptoms which are rest tremor, rigidity, bradykinesia and postural instability [1, 3]. Tremor is the most common and well-known symptom of disease which is usually a rest tremor. The frequency of rest tremor in PD is between 4 and 6 HZ [2, 3]. PD changes electrophysiological activities in basal ganglia-thalamocortical system (BGTCS) [4]. There are two primary treatments for PD which are Medical treatment and deep brain stimulation (DBS).

Researchers use mathematical models to analyze various objects [5-7]. A lot of mathematical and computational studies for PD are presented. MashhadiMalek et al. [3] investigated the relationship between rigidity and tremor in PD. They considered central and peripheral nervous parts and muscle model. The result of their research demonstrates that rigidity and tremor are interdependent and simultaneous treatment of these two symptoms is more beneficial.

Haeri et al. [2] modeled the physiological and pathological behavior of BG; BG components were modeled as first-order systems. Hand tremor is the output of their model. Ghoreishian et al. [8] presented a mathematical model for tremor in Parkinson disease. The structures involved in tremor genesis are analyzed in their model. They used the largest lyapunov exponent, the correlation dimension and kolmogorov entropy to compare the model output with clinical results. A mechanical method for tremor suppression was designed by Pledgie et al. [9]. This method is through impedance control of patient muscle. A resistive force applied on patient's limb in order to decrease tremor movements.

Nahvi et al. [1] examined the effect of DBS on PD. In their model, the DBS targets were subthalamic nucleus (STN), internal and external globus pallidus (GPi and

*Corresponding Author Institutional Email: pooyan@shahed.ac.ir (M. pooyan)

Please cite this article as: F. Ghoreishian, M. Pooyan, An Improved Modeling of Parkinson's Tremor and Investigation of Some Approaches to Remove this Symptom, International Journal of Engineering, Transactions B: Applications Vol. 34, No. 05, (2021) 1269-1273

GPe). They used a mean field model for this purpose. The result of their research indicates that DBS of STN and GPe can reform the activity of thalamus relay neurons but GPi DBS will inhibit it. A model of BG which determines the inter-relation of BG's components was introduced by Parent et al [10]. In this model neurotransmitters and their excitatory and inhibitory characteristics are specified.
In this paper, a mathematical and computational model of BGTCS is presented. This model is based on clinical and physiological information. In this study, the effect of DBS and medical treatment is investigated and also a mechanical method for tremor suppression is applied.

2. PHISIOLOGICAL BACKGROUND

In BGTCS, the nuclei may exert an excitatory or an inhibitory influence upon each other. The inhibitory connections contain gamma amino butyric acid (GABA) and excitatory connections hold glutamate (GLU). Haeri et al. have used a first-order system for modeling the components of BG, the behavior of neurotransmitters were modeled by a gain between BG components. In this research, we applied these approaches for BG and thalamus.

Each neuron has three features: longitudinal resistance at axons and dendrites, membrane resistance and membrane capacitance. An exponential output will occur, when the input of membrane is step. It shows that the resistance and capacitance of neuron are joined in parallel and longitudinal resistance at axons and dendrites is in series with them, because the signal would pass along axons without any changes. So each neuron would be presented by a first-order system. It is notable that there are nonlinear characteristics in neurons. As mentioned above, SNc is the main component which generates tremor, so all nonlinearities are assumed to be in this block. There are a lot of parallel neurons in each component of thalamus and BG. So the whole behavior of each component can be presented by a first-order system [2].

For modeling the behavior of BGTCS the parameters of each block are needed. It is obvious from physiological literature that the quantity of components firing rate in Parkinson's disease is related to the components activity. Indeed, if component activity is more than normal state in PD, its firing rate is also more than normal and vice versa. So we used the relationship between component's firing rates to estimate the parameters of each first-order system of BGTCS blocks, in PD state. These firing rates are in physiologically realistic ranges detected from monkeys. Figure 1 shows the inter-relation of BGTCS in PD state. The hyperactivity and hypoactivity of blocks are indicated by thick and dashed lines respectively. In this figure the inhibitory and excitatory connections are presented too.

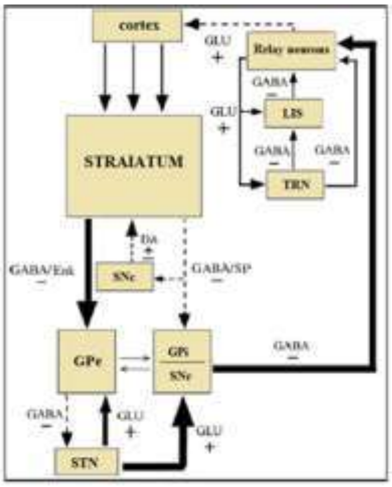

Figure 1. The inter-relation of BGTCS in PD state

3. MATHEMATICAL MODEL

3. 1. BG and Thalamus Model As mentioned above, each block of BG and thalamus is considered as a first-order system. In this section the transfer function of the blocks are presented. The transfer functions are represented by $P_i(s)$. $P_1(s)$ represents the dynamics of striatum. This block has two outputs (So_1 and So_2). Its input has an excitatory effect on outputs.

$$P_1 : So_1(s) = g \times \frac{300}{s+30} SNco(s),$$
$$So_2(s) = \frac{1}{g} \times \frac{5500}{s+30} SNco(s) \qquad (1)$$

$P_2(s)$ is the transfer function of SNc. So_2 is the input of this block which has an inhibitory effect on SNc. A nonlinear function (sign function) is in continuation of this block [2].

$$P_2(s) : SNco(t) = \text{sgn}(A(t)),$$
$$A(s) = \frac{1}{g} \times \frac{1}{s} \times \frac{-100}{s+40} So_2(s) \qquad (2)$$

$P_3(s)$ represents the behavior of GPe. This component has an excitatory input and an inhibitory input.

$$P_3(s) : GPeo(s) = \frac{1}{g} \times (\frac{-1425}{s+10} So_1(s) + \frac{200}{s+10} STNo(s)) \qquad (3)$$

$P_4(s)$ represents the transfer function of STN. This component has an inhibitory input.

$$P_4(s) : STNo(s) = g \times \frac{-4.7}{s+50} GPeo(s) \qquad (4)$$

Transfer function of $P_5(s)$ represents the dynamics of GPi (and SNr) with one excitatory and one inhibitory input.

$$P_5(s): GPio(s) = g \times (\frac{-40}{s+10} So_2(s) + \frac{11.5}{s+10} STNo(s)) \quad (5)$$

$P_6(s)$ models relay neurons (REN) of thalamus which has three inhibitory inputs.

$$P_6(s): RENo(s) = \frac{1}{g} \times (\frac{-40}{s+30} GPio(s) + \frac{-35}{s+30} LISo(s) + \frac{-80}{s+30} TRNo(s)) \quad (6)$$

$P_7(s)$ models the thalamic reticular nucleus (TRN). This component has one excitatory input.

$$P_7(s): TRNo(s) = \frac{96}{s+10} RENo(s) \quad (7)$$

Finally, $P_8(s)$ models local interneuron (LIS) with an inhibitory and an excitatory input.

$$P_8(s): LISo(s) = \frac{20}{s+20} RENo(s) + \frac{-20}{s+20} TRNo(s) \quad (8)$$

The behavior of neurotransmitters is modeled as connection strength (gain). A direct relation is assumed for the amount of the gain and the quantity of neurotransmitters. So increment of neurotransmitter is modeled as gain of ‘g’ and the decrease is supposed as ‘1/g’. It should be mentioned that the signal from cortex is not considered, because the malfunction of BG is assumed to be the origin of PD.

3. 2. Cortex Model The input of cortex is from thalamus and supplementary motor area (SMA) and its output goes to alpha motor neuron and muscle. SMA has an inhibitory effect on cortex in normal state. However, in PD state this inhibitory effect decreases and has an excitatory effect on cortex [3].

3. 3. SMA Model The model of SMA contains a saturation function and a gain. The quantity of saturation function is assumed to be 1-2 in PD and 0.5-1 in normal state [3].

3. 4. Muscle and Peripheral System Model In this study, the formulas of hand muscles which are presented by mains and Soechting [11] are used. The input of muscle is stimulation rate from cortex to muscle (α) and the output is Angular displacement (θ). The transformation function of θ(s) is as follows:

$$\frac{\theta(s)}{\alpha(s)} = \frac{m}{Is^3 + DIs^2 + (K+B)S + DB} \quad (9)$$

The complete model of this study is represented in Figure 2. The peripheral system is modeled by a long loop which begins from muscle, goes to peripheral part (spinal cord) and after passing SMA and cortex returns to the muscle [3].

4. TREMOR SUPPRESSION

Two tremor suppression methods are used in this study:

1. DBS.
2. A mechanical method.

4. 1. DBS The exact mechanism in which tremor suppresses by DBS is still unknown [12]. However, it is mentioned in literature [13-15] that dopamine level in BG changes by DBS. It changes the system parameters which cause change in PD symptoms [2]. In this model, neurotransmitters variation is modeled by gains (g and 1/g). Before DBS g equals 10 and after that it will be 1. The model output without any treatment is represented in Figure 3, which is fairly like the clinical data presented in (www.physionet.org). The output of model with DBS treatment is shown in Figure 4.

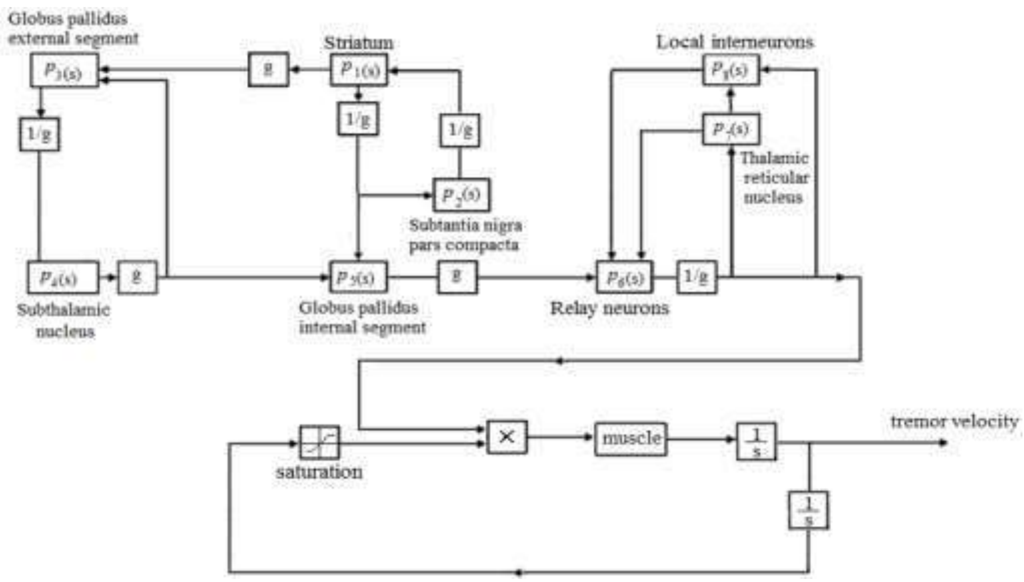

Figure 2. The complete model, used in this study

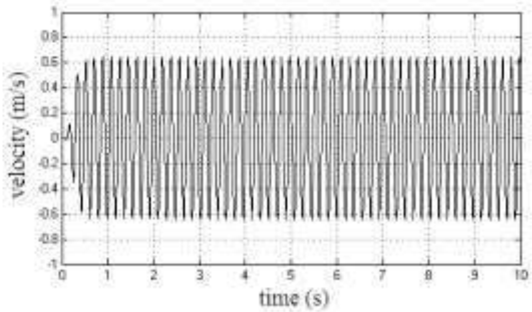

Figure 3. Model output with no DBS

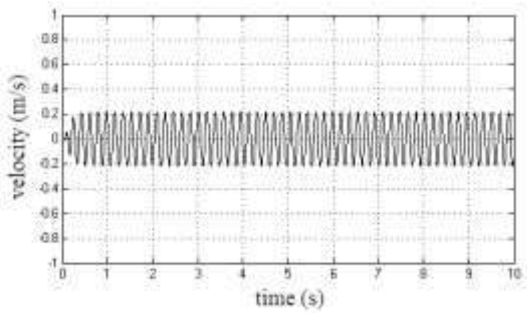

Figure 4. Model output after applying DBS

5. MECHANICAL METHOD

In this study, the experimental work of Pledgie et al. [9] is simulated as the second technique for tremor suppression to examine the efficiency and accuracy of presented model. In order to suppress the tremor, they have used an impedance control method that applies a resistive force to patient's limb. To achieve this purpose, the patient should grasp the end-effector of a small robotic arm (PHANTOM). The manipulator of phantom applies force to muscle by a second order negative feedback. The feedback input is hand movement (X(s)) and the output is force (F(s)). The transfer function of the closed-loop is as follows:

$$T(s)=\frac{1}{(M+a_1)s^2+(C+a_2)s+(K+a_3)} \tag{10}$$

The mass (M), damping (C), and stiffness (K) are the combined properties of human limb and the robotic arm. The nominal parameter values used for M, C and K are 1.3 kg, 5 Ns/m and 200 N/m, respectively. The negative feedback is a second order system which creates a closed-loop system.

As a matter of fact, the feedback coefficients (a_1, a_2, a_3) impact the closed-loop system coefficients in an additive fashion. The closed-loop system magnitude response can be estimated as follows:

$$R_{\omega}=\frac{1}{\sqrt{[K+a_3-(M+a_1)\omega^2]^2+(C+a_2)^2\omega^2}} \tag{11}$$

The purpose of this method is decreasing the magnitude response of the closed-loop system in order to decrease the system output (hand movement). So the feedback coefficients are selected in a manner to increase the attenuation of magnitude response at tremor frequency. It is notable that by setting ω to zero (there is no tremor), feedback system shouldn't have any effect on muscle (because there is no input). So a_3 is set to zero; otherwise it will cause undesirable attenuation in closed-loop system whereas there is no tremor. A method is presented to estimate a_1 and a_2 (acceleration and rate coefficients) which permits selecting one of them. At first step a desired level of closed-loop attenuation (R_{ω_t}) should be selected, and then by using the following expressions, feedback coefficients will be determinated.

$$a_1=\frac{1}{{\omega_t}^2}\left[K+\sqrt{\left(\frac{1}{R_{\omega_t}}\right)^2-C^2{\omega_t}^2}\right]-M \tag{12}$$

$$a_2=\frac{1}{\omega_t}\sqrt{\left(\frac{1}{R_{\omega_t}}\right)^2-(K-M{\omega_t}^2)^2}-C \tag{13}$$

Figures 5 and 6 represent the model output after applying negative feedback with acceleration and rate coefficients, respectively. The model outputs are in accordance with clinical results obtained by Pledgie et al. [9]. It is visible that negative feedback will suppress tremor in an acceptable manner.

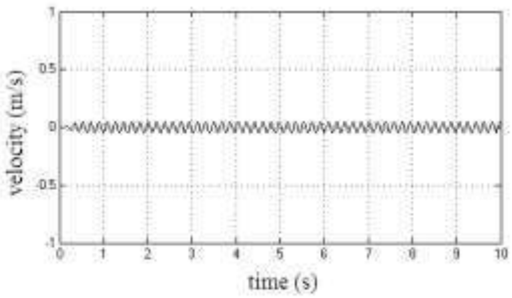

Figure 5. The model output after acceleration feedback (without DBS)

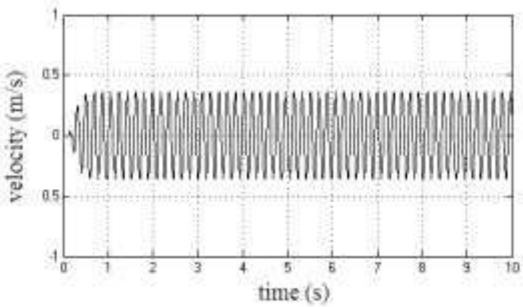

Figure 6. The model output after rate feedback (without DBS)

6. COCLUSION

Understanding the functions of the human brain is one of the most important goals of contemporary science. Mathematical medicine is a truly interdisciplinary area that brings together medical researches and engineering science. In this study a mathemtical and computational model of PD tremor is presented to analyze the brain behaviour on tremor genesis. Two methods for tremor suppression is applied in this paper. These methods are deep brain stimulation (DBS) and a mechanical technique. Similar to real condition, the strength of block connections (gains) will change by variation in dopamine level. According to litrature DBS affects dopamine level in BG; therefore, DBS effect is exerted by chanhing the connections' gain. The second method for tremor suppression is a mechanical method. This method is based on a negative feedback. The model results are in good agreement with the clinical results.

The presented model helps to have a better understanding of PD tremor. This model includes physiological information about tremor and some methods to control this disease.

7. REFERENCES

1. Nahvi, A. R., Bahrami, F., Hemmati, S. "Investigating different targets in deep brain stimulation on parkinson's disease using a mean-field model of the basal ganglia-thalamocortical system." ***Mechanics in Medicine and Biology***, Vol. 12, No. 2, (2011), 1-13. doi: 10.1109/MECBME.2011.5752089.
2. Haeri, M., Sarbaz, Y., Gharibzadeh, Sh. "Modeling the Parkinson's tremor and its treatments," ***Theoretical Biology***, Vol. 236, (2005), 311-322. doi: 10.1016/j.jtbi.2005.03.014.
3. MashhadiMalek, M., Towhidkhah, F., Gharibzadeh, Sh., Daeichin, V., Ahmadi-Pajouh, M. A. "Are rigidity and tremor two sides of the same coin in Parkinson's disease?", ***Computers in Biology and Medicine***, Vol. 38, (2008), 1133-1139. doi: 10.1016/j.compbiomed.2008.08.007.
4. vanAlbada, S. J., Robinson, P. A. "Mean-field modeling of the basal ganglia-thalamocortical system. I Firing rates in healthy and parkinsonian states", ***Theoretical Biology***, Vol. 257, (2009), 642-663. doi:10.1016/j.jtbi.2008.12.018.
5. Dvoynikov, M., Kunshin, A., Blinov, P., Morozov, V. "Development of Mathematical Model for Controlling Drilling Parameters with Screw Downhole Motor", ***International Journal of Engineering, Transactions A: Basics***, Vol. 33, No. 7 (2020), 1423-1430. doi: 10.5829/ije.2020.33.07a.30.
6. Tehrani, F. T. "A Model of the Respiratory System in the Newborn Infant", ***International Journal of Engineering,*** Vol. 4, No. 3 (1991), 101-106.
7. Zolfaghari, M., ghoreshi, M., tahmasbi, v. "Temperature in bone drilling process: Mathematical modeling and Optimization of effective parameters", ***International Journal of Engineering, Transactions A: Basics,*** Vol. 29, No. 7, (2016), 946-953. doi: 10.5829/idosi.ije.2016.29.07a.09.
8. Ghoreishian, F., Pooyan, M. "A mathematical model for tremor genesis in Parkinson disease from a chaotic view", in 21st Iranian Confrence on Biomedical Engineering, (2014), 353-357. doi: 10.1109/ICBME.2014.7043950.
9. Pledgie, S., Barner, K., Agrawal, S. "Tremor Suppression Through Impedance Control", ***IEEE Transactions on Rehabilitation Engineering***, Vol. 8, No. 1, (2000), 53–59. doi: 10.1109/86.830949.
10. Parent, A., LeÂvesque, M., Parent, M. "A re-evaluation of the current model of the basal ganglia", ***Parkinsonism and Related Disorders***, Vol. 7, (2001), 193-198. doi: 10.1016/s1353-8020(00)00058-4.
11. Mains, R. E., Soechting, J. F. "A model for the neuromuscular response to sudden disturbances", ***Journal of Dynamic Systems, Measurement, and Control***, Vol. 93, No. 4, (1971), 247-251. doi: 10.1115/1.3426508
12. Montgomery, J. r., Baker, K. B. "Mechanisms of deep brain stimulation and future technical developments", ***Neurological Research***, Vol. 22, No. 3, (2000), 259–266. doi: 10.1080/01616412.2000.11740668.
13. Figee, M., Koning, P., Klaassen, S., Vulink, N., Mantione, M., Munckhof, P., Schuurman, R., Wingen, G., Amelsvoort, Th., Booij, J., Denys, D. "Deep Brain Stimulation Induces Striatal Dopamine Release in Obsessive-Compulsive Disorder", ***Biological Psychiatry***, Vol. 75, (2014), 647-652. doi: 10.1016/j.biopsych.2013.06.021.
14. Klanker, M., Feenstra, M., Willuhn, L., Denys, D. "Deep brain stimulation of the medial forebrain bundle elevates striatal dopamine concentration without affecting spontaneous or reward-induced phasic release", ***Neuroscience***, Vol. 364, (2017), 82-92. doi: 10.1016/j.neuroscience.2017.09.012.
15. Smith, G. S., Mills, K. A., Pontone, G. M., Anderson, W. S., Perepezko, K. M., Brasic, J., Zhou, Y., Brandt, J., Butson, Ch. R., Holt, D. P., Mathews, W. B., Dannals, R. F., Wong, D. F., Mari, Z. "Effect of STN DBS on vesicular monoamine transporter 2 and glucose metabolism in Parkinson's disease", ***Parkinsonism & Related Disorders***, Vol. 64, (2019), 235-241. doi: 10.1016/j.parkreldis.2019.04.006.

Persian Abstract

چکیده

در این تحقیق، لرزش پارکینسونی با استفاده از روش‌های ریاضیاتی و محاسباتی مدل‌سازی شده است. در بیماری پارکینسون، سیگنالی غیرطبیعی توسط عقده‌های قاعده‌ای تولید می‌شود. این سیگنال وارد تالاموس شده و پس از تعامل با قشر مغز و سیستم عصبی محیطی نهایتا در عضله به شکل لرزش ظاهر می‌گردد. در مدل ارائه شده در این مقاله، کلیه مراحل ذکر شده در بالا به کمک مدلسازی عضله و سیستم عصبی مرکزی (عقده‌های قاعده‌ای، تالاموس، قشر مغز و منطقه حرکتی مکمل) و سیستم عصبی محیطی (رفلکس نخاعی) شبیه سازی شده است. در نهایت دو روش برای کاهش لرزش مورد استفاده قرار گرفته است ۱) تحریک عمیق مغز که بر سطح دوپامین در عقده‌های قاعده‌ای تأثیر می‌گذارد و ۲) یک روش مکانیکی که بر اساس بازخورد منفی است. مقایسه نتایج مدل و نتایج آزمایشات بالینی نشان می‌دهد که مدل ارائه شده در این مقاله دقت و کارایی قابل قبولی دارد.

IJE TRANSACTIONS B: Applications Vol. 34, No. 05, (May 2021) 1274-1283

International Journal of Engineering

Journal Homepage: www.ije.ir

A Novel Control Strategy of an Islanded Microgrid Based on Virtual Flux Droop Control and Direct Flux Fuzzy Control

S. Khanabdal[a], M. Banejad[a], F. Blaabjerg[b], N. Hosseinzadeh[c]

[a] *Department of Electrical Engineering, Shahrood University of Technology, Shahrood, Iran*
[b] *Department of Energy Technology, Aalborg University, Aalborg, Denmark*
[c] *School of Engineering, Deakin University, Geelong, Australia*

PAPER INFO

Paper history:
Received 21 December 2020
Received in revised form 12 March 2021
Accepted 13 March 2021

Keywords:
Islanded Microgrid
Virtual Flux Droop Control
Fuzzy Logic Control
Optimal Duty Cycle

ABSTRACT

This paper proposes a novel control strategy of an islanded microgrid based on virtual flux droop (VFD) control. In the conventional VFD method, the direct flux control (DFC) technique is used to generate the switching signals using the hysteresis regulators and a switching look-up table. Therefore, the voltage and the current ripples are inevitable. Moreover, as a single switching vector is applied in each control period and none of the switching vectors can produce the desired voltage, the desired dynamic performance is not achieved. Here, a novel direct flux fuzzy control (DFFC) technique is proposed to choose the best switching vector based on fuzzy logic. Furthermore, only a fraction of the control period is allocated to an appropriate active switching vector which is selected by the DFFC technique whereas the rest of the time is allocated to a null vector. The duty cycle of the selected active switching vector is optimized using a simple and robust mechanism. In order to evaluate the performance of the proposed method, an islanded microgrid and the proposed control strategy is simulated in Matlab/Simulink software. The results prove that the dynamic performance response is improved and the demanded load power is proportionately shared between the sources, while the voltage and current ripples are significantly reduced.

***doi**: 10.5829/ije.2021.34.05b.21*

1. INTRODUCTION

In recent decades, distributed generation (DG) has attracted growing attention of researchers as an efficient solution for worldwide demand to reduce the reliance on fossil fuels and increase the use of renewable energy. In this regard, the concept of microgrid plays an important role in moving towards the realization of the future smart grids by integrating multiple DG units using renewable energy resources, energy storage systems and local loads with a coordinated control strategy. Inverters are usually employed to interface DG units to the microgrid. As a result, they should be connected in parallel through the point of common coupling (PCC) which increases the reliability of the system by providing redundancy [1-6].

Microgrid is able to operate in grid connected or islanded mode. However, the control of an islanded microgrid is a more challenging issue because of no access to the main grid. In this case, maintaining the stable regulation of the voltage and frequency is important as well as proportional sharing the load among multiple parallel inverters in order to achieve better power management and to avoid overloading of some inverters [7-11]. Therefore, an appropriate control strategy should be applied to meet the requirement.

Droop control strategy is widely used in the islanded microgrid which emulates the behavior of synchronous generators without the dependency on communication. Therefore, the "plug and play" feature is achieved, with the result that the expansion of such a system becomes easier which allows to replace or add one unit with no need to stop the whole system. Based on this strategy, the frequency is adjusted as a function of active power and the voltage amplitude of the inverter is regulated as a

*Corresponding Author Institutional Email: m.banejad@shahroodut.ac.ir (M. Banejad)

Please cite this article as: S. Khanabdal, M. Banejad, F. Blaabjerg, N. Hosseinzadeh, A Novel Control Strategy of an Islanded Microgrid Based on Virtual Flux Droop Control and Direct Flux Fuzzy Control, International Journal of Engineering, Transactions B: Applications Vol. 34, No. 05, (2021) 1274-1283

function of reactive power. Despite the advantages of the droop control strategy, it suffers from drawbacks that the unavoidable deviations of frequency and voltage amplitude in the steady state condition, poor dynamic stability of active power sharing controller and poor reactive power sharing [12-14].

Several improved control methods were proposed in the literature to solve the above problems. One group of them try to revise the overall control strategy through optimization and implementation of modern control theory. A novel secondary control scheme was proposed by Lou et al. [15] for voltage and frequency restoration. It uses the distributed model predictive control for voltage regulation. Moreover, a distributed finite time observer is employed to realize the frequency adjustment and proper active power sharing and frequency restoration. The effectiveness of the droop control strategy in accurate power sharing was improved by Lai et al. [16] which is based on the distributed cooperative control scheme. It introduces a pinning-based frequency/voltage controller using a distributed voltage observer and employed a consensus power controller to generate nominal values for droop control of DGs. A distributed secondary control based on droop control strategy was proposed by Wu and Shen [17] for stability enhancement of microgrid which uses supplementary control variables. Small signal modeling of the system is employed to define an optimization problem and consequently tune the control parameters robustly. An optimized droop control based on a dynamic model of the microgrid is proposed by Yu et al. [18]. Firstly, a precise small signal model of the whole microgrid and the droop controller is derived. Consequently, the dynamic stability of the system is investigated by the eigenvalue analysis method. Then, a genetic algorithm is employed to find the optimal values of key parameters. In the case of optimization, the optimum values should be found after each change of the parameters of the system. However, the mentioned control strategies are usually complicated and complex coordinated transformations are also needed. Moreover, they required mostly high speed communication to achieve precise power sharing.

Another group of methods in the literature proposes to add compensatory terms to the droop equations to enhance the performance of the conventional droop control. In order to enhance the power loop dynamics, a mode-adaptive droop control method was proposed by Kim et al. [19], where the derivative controller is added in the relationship of the frequency-active power and the integral controller is added in the relationship of the voltage amplitude-reactive power. An improved proportional power sharing strategy was proposed by Zhang et al. [20] which can deal with the problem of the coupling between the active and reactive power in the droop control strategy. In this regard, integral controllers are employed to generate the compensatory terms in the proposed droop equations. An improved droop controller is proposed by Zhong [21] which added the load voltage drop with an amplifier to the droop characteristics. As a result, the proposed control strategy is robust to computational errors, disturbances, noises and parameter drifts. However, in this group of methods, complex transformations are needed and communication with the central control unit of the microgrid is needed to send measured parameters and receive reference values which are required to generate compensatory terms. Therefore, the reliability of the control strategy is degraded.

The proper power sharing in an islanded microgrid can be achieved by changing the parameters and equations of the droop method. The output voltage phase is employed instead of frequency reported in literature [22] to improve the power sharing accuracy and to effectively reduce the circulating current. Chen et al. [23] proposed $P-\dot{V}$ droop control; where $\dot{V}$ represents the time rate of change of the output voltage reference. As a result, the effect of mismatched line impedance is mitigated and the accuracy of the active power sharing is improved. In order to improve the reactive power sharing accuracy, a $Q-\dot{V}$ droop control method was proposed by Lee et al. [24]. But the effectiveness of this method is degraded by the output voltage variation and a restoration technique is required to avoid it. To deal with this problem, a modified $Q-\dot{V}$ was proposed by Zhou and Cheng [25], where a novel $\dot{V}$ restoration mechanism is employed to pull the $\dot{V}$ back to zero. However, these strategies use one of the equations of conventional droop control which leads to a decrease in the power sharing accuracy. In this regard, a new control strategy called virtual flux droop was proposed by Hu et al. [26], where the phase angle difference and the virtual flux amplitude are respectively being used instead of the frequency and the voltage amplitude of the inverter. Therefore, a simple control strategy is achieved while there is no need to complex coordinate transformation as well as PI controllers are avoided. In the structure of the VFD control method, direct flux control is employed to generate the switching signals, which works similarly to direct torque control and direct power control. Therefore, simple structure, fast dynamic response and robustness against parameter variation are the advantages. However, DFC suffers from some disadvantages which are mainly due to using the hysteresis regulators. As a result, the ripples appear in the virtual flux amplitude and the phase angle difference which can be reflected on the voltage and the current waveforms and affect power quality.

This paper proposes a novel microgrid control strategy by using fuzzy logic control to overcome the disadvantages of the conventional virtual flux droop control. Fuzzy logic control is considered as an effective approach in case of complicated processes, where the mathematical model does not exist or it is nonlinear.

Regarding that the VFD control is a nonlinear method, it is combined with direct flux fuzzy control as proposed in this paper. In the structure of DFFC, a fuzzy switching table is employed to replace the conventional switching look-up table and hysteresis regulators. Moreover, instead of applying a single switching vector throughout each control period, only a fraction of the control period is allocated to the active switching vector which is selected by DFFC whereas a null vector is applied for the rest of the time. Furthermore, a simple and robust method is proposed to compute the optimal duty ratio of the active switching vector. As a result, the performance of the microgrid control strategy in power sharing is improved by reducing the voltage and the current ripples. Therefore, the main contributions of this paper are:

1. Developing the virtual flux droop control based on direct flux fuzzy control
2. Applying duty cycle control to the microgrid control strategy by the proposed duty ratio optimization method.

The rest of this paper is organized as follows: Section 2 describes mathematically the VFD control. The microgrid control strategy is discussed in section 3, so that, firstly the conventional method is briefly described. Then, the proposed control strategy is explained in detail. In order to validate the effectiveness of the proposed strategy for controlling the islanded microgrid, the simulation is carried out in the environment of Matlab/Simulink and the results are reported and also compared with the conventional method in section 4. Finally, this paper is summarized in section 5.

2. PRINCIPLE OF VIRTUAL FLUX DROOP METHOD

In an islanded microgrid with parallel configuration, the inverters are connected to the point of common coupling (PCC) through the line impedances as shown in Figure 1. The mathematical equation of this equivalent circuit can be written using Kirchhoff's voltage law stated as follows:

$$V_i = R_i I_i + L_i \frac{dI_i}{dt} + E \tag{1}$$

where E and V_i are the voltages of the PCC and the inverter, respectively. Moreover, I_i is the line current.

In addition, R_i and L_i are the line resistance and inductance, respectively. Furthermore, the number of the inverter is denoted by the subscript "*i*".

The supplied power by the inverter to the PCC is calculated as follows:

$$S_i = P_i + jQ_i = E \times I_i^* \tag{2}$$

where S_i is complex power, P_i is active power and Q_i is reactive power. The superscript "*" denotes the complex conjugate.

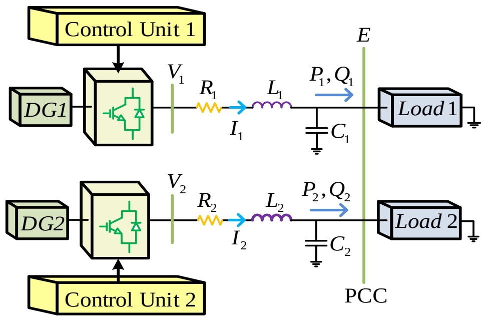

Figure 1. An islanded microgrid with parallel inverters

Similar to electrical machines, in which the flux is defined as time integral of voltage, the virtual flux vectors are defined [26]:

$$\psi_i = \int V_i \, dt = \frac{|V_i|}{\omega} e^{j\varphi_i} \tag{3}$$

$$\psi_E = \int E dt = \frac{|E|}{\omega} e^{j\varphi_E} \tag{4}$$

In these equations, ψ_i and ψ_E are the virtual flux vectors of the inverter and the PCC, respectively, φ_i and φ_E are their angles, and ω is the angular frequency.

It is assumed for simplicity that the line is highly inductive and the line resistance is negligible. As a result, the line current can be written in terms of virtual fluxes as:

$$I_i = \frac{1}{L_i}(\psi_i - \psi_E) \tag{5}$$

Substituting the line current from Equation (5) and the voltage of the PCC in terms of virtual flux from Equation (4) in Equation (2) and then separating its real and imaginary parts, the active power and the reactive power are obtained as follows:

$$P_i = \frac{\omega}{L_i} |\psi_i| |\psi_E| \sin(\delta_i) \tag{6}$$

$$Q_i = \frac{\omega}{L_i} \left(|\psi_i| |\psi_E| \cos(\delta) - |\psi_E|^2 \right) \tag{7}$$

where $\delta_i = \varphi_i - \varphi_E$. Since δ_i is also equal to the phase angle difference between the voltages of the PCC and the inverter, which is typically small, it can be considered that, $\sin\delta \cong \delta$ and $\cos\delta \cong 1$ [24, 26-28] which result in:

$$P_i = \frac{\omega}{L_i} |\psi_i| |\psi_E| \delta_i \tag{8}$$

$$Q_i = \frac{\omega |\psi_E|}{L_i} \left(|\psi_i| - |\psi_E| \right) \tag{9}$$

The above equations imply that the active power and the reactive power are respectively coupled with the phase angle difference and amplitude difference between the virtual fluxes of the inverter and the PCC. Thus, the mathematical equations of virtual flux droop control for the inverter are achieved [26]:

$$\delta_i^{com} = \delta_i^n - k_{\delta i}\left(P_i^n - P_i\right) \quad (10)$$

$$\left|\psi_i^{com}\right| = \left|\psi_i^n\right| - k_{\psi i}\left(Q_i^n - Q_i\right) \quad (11)$$

where P_i^n and Q_i^n are nominal active power and nominal reactive power, respectively, δ_i^n is nominal phase angle difference, $\left|\psi_i^n\right|$ is the nominal virtual flux amplitude of the inverter, $k_{\delta i}$ and $k_{\psi i}$ are the slopes of the droop characteristics. Moreover, δ_i^{com} and $\left|\psi_i^{com}\right|$ are respectively the command values of the phase angle difference and the virtual flux amplitude of the inverter.

3. MICROGRID CONTROL STRATEGY

3. 1. The Conventional Method Based on DFC

The conventional control strategy of the islanded microgrid based on the virtual flux droop control and direct flux control is shown in Figure 2. Firstly, the command values of the phase angle difference between the virtual fluxes of the inverter and the PCC and the virtual flux amplitude of the inverter are specified by the VFD control method. Then, DFC is employed to apply them to the inverters. In this regard, the output voltage of the inverter is calculated using the current state of the inverter switches. Subsequently, the virtual flux vector of the inverter is estimated using Equation (3). The amplitude of the estimated virtual flux of the inverter is subtracted from its command value which is obtained from VFD and therefore the error of the virtual flux amplitude is generated in this way. On the other side, the angle of the virtual flux vector of the PCC is obtained using a virtual set of three-phase AC voltage with the nominal frequency of the grid. Then, the phase angle difference between the virtual fluxes of the inverter and the PCC can be estimated by subtracting the angle of the estimated virtual flux vector of the inverter from the angle of the virtual flux vector of the PCC. Subsequently, the estimated phase angle difference is subtracted from its command value obtained from VFD, and consequently, the error of the phase angle difference is computed. On the other hand, the $\alpha-\beta$ plane is divided into six sections and the section, where the virtual flux vector of the inverter is located, is determined.

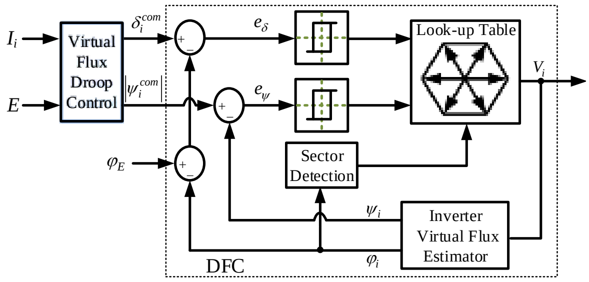

Figure 2. The conventional microgrid control strategy based on VFD control and DFC

In the DFC scheme, the errors of the virtual flux amplitude and the phase angle difference are entered into the hysteresis regulators. Eventually, the appropriate switching vector to apply to the inverter is selected from a look-up table, which has three inputs, including the number of the section, where the virtual flux vector of the inverter is located, along with the outputs of the hysteresis regulators. In this method, regardless of where the virtual flux vector of the inverter is located, the choice of the best switching vector is independent of the amplitude of the flux and angle errors and depends only on the sign of the phase angle difference and the virtual flux amplitude errors specified by the hysteresis regulators. As the hysteresis band increases, the switching frequency decreases; nevertheless, the accuracy of voltage and frequency control is reduced. As the hysteresis band decreases, although the accuracy of voltage and frequency control increases, the switching frequency increases. The use of the hysteresis regulators in the structure of the DFC leads to ripples of the virtual flux vector of the inverter and the phase angle difference; therefore, may be reflected on current and voltage THD indices.

3. 2. The Proposed Method Based on Dffc

This paper aims to deal with the disadvantages of the conventional microgrid control strategy caused by the direct flux control. Figure 3 shows the proposed microgrid control strategy which consists of VFD control, DFFC and duty ratio optimization. The following describes each part.

1) Virtual Flux Droop Control: As described in section 2, the proportional power sharing between the DGs is achieved by the VFD control method. For this reason, the values of the active power and the reactive power injected into the PCC are calculated and the command values for the phase angle difference and the virtual flux amplitude of the inverter are obtained by Equations (10) and (11).

2) Direct Flux Fuzzy Control: Fuzzy logic makes it possible to control systems without knowing the mathematical model of the process [29-31]. As a result, a

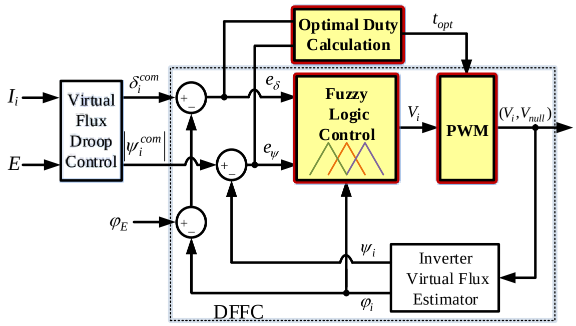

Figure 3. The proposed microgrid control strategy based on VFD control, DFFC and duty ratio optimization

novel control scheme to select the appropriate switching vector is proposed in this paper. First, the switching vector and subsequently, the three-phase inverter output voltages are calculated using the current state of the inverter switches as reported in literature [32]:

$$\begin{bmatrix} v_a \\ v_b \\ v_c \end{bmatrix} = V_{dc} \cdot \begin{bmatrix} \frac{2}{3} & \frac{-1}{3} & \frac{-1}{3} \\ \frac{-1}{3} & \frac{2}{3} & \frac{-1}{3} \\ \frac{-1}{3} & \frac{-1}{3} & \frac{2}{3} \end{bmatrix} \times \begin{bmatrix} s_a \\ s_b \\ s_c \end{bmatrix} \tag{12}$$

$$\begin{bmatrix} V_\alpha \\ V_\beta \end{bmatrix} = \begin{bmatrix} \frac{2}{3} & \frac{-1}{3} & \frac{-1}{3} \\ 0 & \frac{\sqrt{3}}{3} & \frac{-\sqrt{3}}{3} \end{bmatrix} \times \begin{bmatrix} v_a \\ v_b \\ v_c \end{bmatrix} \tag{13}$$

$$V_i = V_\alpha + jV_\beta \tag{14}$$

where V_{dc} is the input voltage of the inverter, v_a, v_b and v_c are the three-phase inverter output voltages, s_a, s_b and s_c are the current state of the inverter switches. $s_i = 0\ (i = a,b,c)$, while the related switch is open and $s_i = 1\ (i = a,b,c)$, while the related switch is closed. In addition, V_α and V_β are the component of the inverter voltage in the $\alpha-\beta$ plane.

The phase angle and the virtual flux amplitude of the inverter are estimated using Equation (3). On the other hand, the phase angle of the virtual flux vector of the PCC is calculated using a set of three-phase AC voltage with the nominal frequency. As a result, the estimated phase angle difference between the virtual fluxes of the inverter and the PCC can be obtained. Finally, the estimated values of the phase angle difference and the virtual flux amplitude of the inverter are compared with their commands.

In DFFC, the fuzzy logic controller (FLC) is replaced with the hysteresis regulators and the switching look-up table which are used in DFC. The inputs of FLC are the phase angle difference and the virtual flux amplitude of the inverter errors as well as the phase angle of the current virtual flux of the inverter. Consequently, the output of FLC is the best switching vector that should be applied to the inverter. As shown in Figure 4, an FLC is generally composed of four principal parts, namely Fuzzification, Fuzzy rule base, Inference system and Defuzzification. In the process of Fuzzification, the numerical input variables are converted to fuzzy values using membership functions (MFs) shown in Figures 5 to 7, where the triangular MFs are utilized. The error of the phase angle difference, i.e. e_δ, can be negative large (NL), negative small (NS), zero (Z), positive small (PS) and positive large (PL). Moreover, the error of the virtual flux amplitude i.e. e_ψ can be negative (N), zero (Z), and positive (P).In addition, the phase angle of the virtual flux of the inverter in the $\alpha-\beta$ plane, i.e. θ, can change in the range of $[0-2\pi]$ which is divided into six sections and the corresponding MFs are denoted as θ_1 to θ_6. The number of switching vectors equals 2^3=8 including six active vectors and two zero vectors as shown in Figure 8. As a result, seven singleton subsets including one null vector and six active vectors are assigned to the MFs of the output variable, which are denoted by V_0 to V_6, as shown in Figure 9. The FLC specifies the relationship between the inputs and the output using fuzzy rule base, as shown in Table 1. Then, the appropriate control rules at each time are evaluated by the fuzzy inference mechanism which is Mamdani's procedure based on a min-max decision in this paper. If the MF values of the input variables, i.e. e_δ, e_ψ and θ are respectively μ_φ, μ_ψ, μ_θ and the MF value of the output variable is μ_V, the corresponding weighting factor a_i for i^{th} rule is achieved as follows:

$$a_i = \min(\mu_{\varphi i}, \mu_{\psi i}, \mu_{\theta i}) \tag{15}$$

$$\mu'_{V i} = \max(a_i, \mu_{V i}) \tag{16}$$

Finally, the fuzzy values are converted back into crisp values which is the best switching vector between V_0 to V_6 in Defuzzification process using the SOP method:

$$\mu'_{V\,out} = \max_{i=1}^{90}(\mu'_{V i}) \tag{17}$$

3) Duty Ratio Optimization: As the desired voltage which is needed to provide the appropriate changes in the

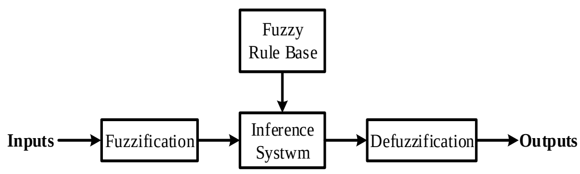

Figure 4. Block diagram of FLC

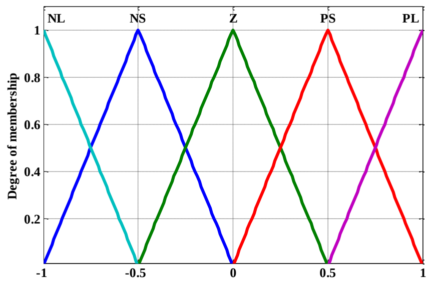

Figure 5. Membership functions of e_δ

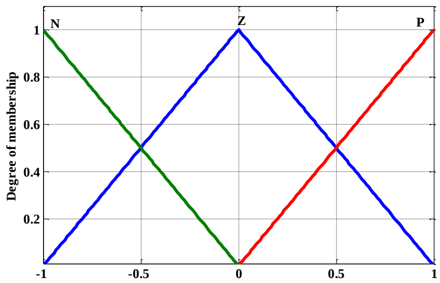

Figure. 6. Membership functions of e_ψ

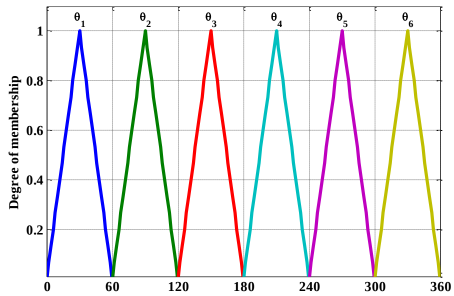

Figure 7. Membership functions of θ

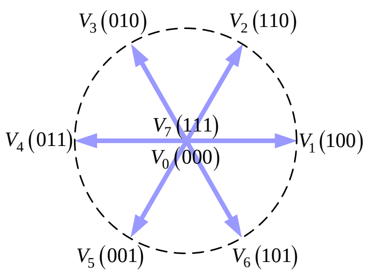

Figure 8. Switching vectors in the $\alpha-\beta$ plane

TABLE 1. Switching Vector Table based on FLC

e_ψ	e_δ	θ_1	θ_2	θ_3	θ_4	θ_5	
	NL	V_5	V_6	V_1	V_2	V_3	V_4
	NS	V_5	V_6	V_1	V_2	V_3	V_4
N	Z	V_0	V_0	V_0	V_0	V_0	V_0
	PS	V_3	V_4	V_5	V_6	V_1	V_2
	PL	V_3	V_4	V_5	V_6	V_1	V_2
	NL	V_6	V_1	V_2	V_3	V_4	V_5
	NS	V_6	V_1	V_2	V_3	V_4	V_5
Z	Z	V_0	V_0	V_0	V_0	V_0	V_0
	PS	V_2	V_3	V_4	V_5	V_6	V_1
	PL	V_2	V_3	V_4	V_5	V_6	V_1
	NL	V_6	V_1	V_2	V_3	V_4	V_5
	NS	V_6	V_1	V_2	V_3	V_4	V_5
P	Z	V_0	V_0	V_0	V_0	V_0	V_0
	PS	V_2	V_3	V_4	V_5	V_6	V_1
	PL	V_2	V_3	V_4	V_5	V_6	V_1

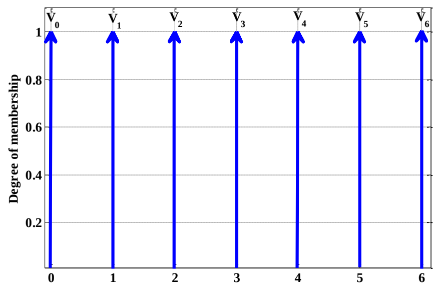

Figure 9. Membership functions of the output

phase angle and amplitude of the inverter virtual flux cannot be generated by any of the switching vectors, the virtual flux ripples is unavoidable. A solution to solve this issue, as proposed in this paper, is to apply two switching vectors during each control period instead of a single switching vector which fails to reduce the voltage and current ripples to the minimum values. This idea has already been used in the induction motor drives based on DTC and MPTC and now generalized in the application of power sharing in the islanding microgrid in this paper. As a result, only a fraction of the control period is allocated for the active vector which is selected from DFFC and a null vector is applied to the inverter during the rest of the time. The optimal duty ratio d for the active vector is obtained by:

$$d=\left|\frac{e_\delta}{C_\delta}\right|+\left|\frac{e_\psi}{C_\psi}\right|=\left|\frac{\delta^{com}-\delta^{est}(k)}{C_\delta}\right|+\left|\frac{|\psi|^{com}-|\psi|^{est}(k)}{C_\psi}\right| \tag{18}$$

where $\delta^{est}(k)$ and $|\psi|^{est}(k)$ are respectively the estimated values for the phase angle difference and the virtual flux amplitude of the inverter at the k^{th} instant; C_δ and C_ψ are two positive coefficients. As can be seen, the duty ratio is obtained in a simple, fast and robust method without dependency on the grid parameters.

4. SIMULATION RESULTS

In order to study the performance of the proposed method, the islanded microgrid shown in Figure 1 is simulated in the MATLAB/Simulink software environment. The results obtained from applying the proposed control scheme are compared with the conventional method. The simulation parameters of the islanded microgrid are listed in Table 2. A step decrease of the load power occurs at t=1s. Then, the load power is increased to its initial value at t=2s.

Based on the conventional method and the proposed control strategy, Figures 10 and 11 show the PCC voltage and its THD spectra respectively. As can be seen, in spite of the load change, the voltage is maintained within the allowable limit ($\pm 5\%$) using the proposed method, while

TABLE 2. Microgrid and Control Parameters

Item	Value
Line Resistance	0.04 Ω
Line Inductance	6 mH
Tie- line Resistance	1.5 Ω
Tie-line Inductance	12 mH
Filter Capacitance	120 µF
Nominal Voltage	3600 V
Nominal Frequency	60 Hz
DGs Output Voltage	10 kV
Nominal Flux Amplitude	7.797 Wb
Nominal Active Power 1	1650 kW
Nominal Reactive Power 1	800 kVar
Nominal Active Power 2	1300 kW
Nominal Reactive Power 2	600 kVar
Slope of P – δ Droop 1	-1.67×10^{-8} rad/W
Slope of $Q - \lvert\psi\rvert$ Droop 1	-2.65×10^{-6} Wb/Var
Slope of P – δ Droop 2	-1.54×10^{-7} rad/W
Slope of $Q - \lvert\psi\rvert$ Droop 2	-2.55×10^{-6} Wb/Var

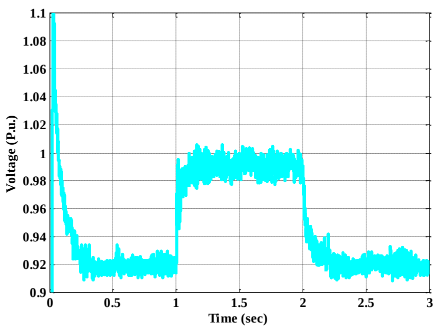

(a)

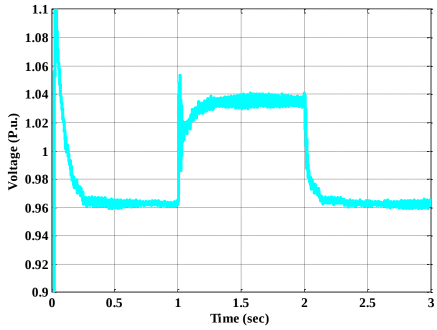

(b)

Figure 10. PCC voltage: (a) Conventional method (b) Proposed method

the voltage changes are greater than the allowable value based on the conventional method. Moreover, the voltage ripple using the proposed method is lower than the conventional method, which improves the THD index.

The three-phase injected current of DG1 into the PCC and its THD spectra are respectively shown in Figures 12 and 13. It can be seen that the THD index based on the proposed method is less than the conventional method which leads to less current ripples.

The injected power of DGs to the PCC is shown in Figure 14. The load is modeled as a constant impedance. Therefore, the power which is absorbed by the load, is proportional to the square of the PCC voltage. In both methods, good dynamic performance is observed in response to the load changes. However, due to the better, performance of the proposed method in voltage control the voltage amplitude in the conventional method is

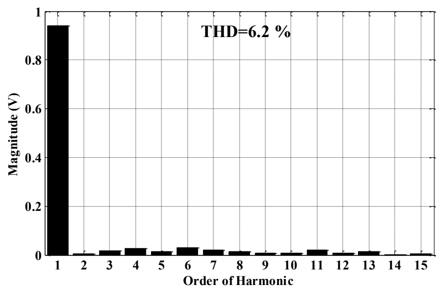

(a)

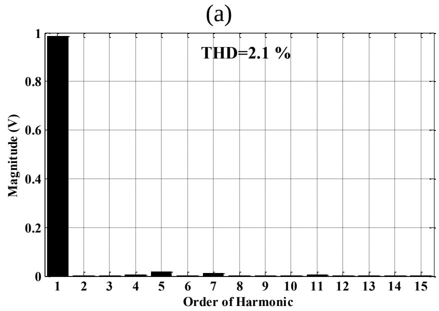

(b)

Figure 11. THD spectra of the PCC voltage: (a) Conventional method (b) Proposed method

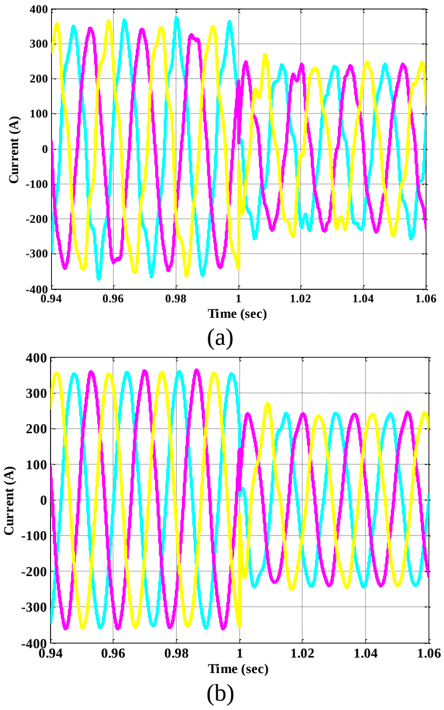

Figure 12. Injected current of DG1 to the PCC: (a) Conventional method (b) Proposed method

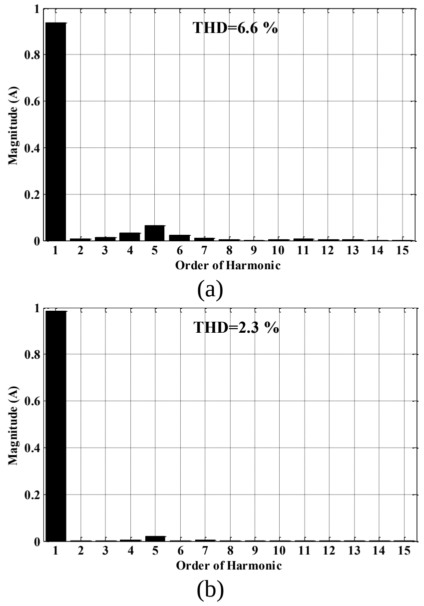

Figure 13. THD spectra of injected current of DG1: (a) Conventional method (b) Proposed method

lower than the proposed method, which reduces the power injection in the conventional method.

Figure 15 shows the virtual flux vector trajectory of inverter 1 in the $\alpha-\beta$ plane. The aim of the virtual flux control of the inverters is to enable them to have the specified amplitude and specific relative distance to the virtual flux vector of the PCC. The tip of the virtual flux trajectory is closer to the circle using the proposed method, which proves better dynamic performance compared to the conventional method.

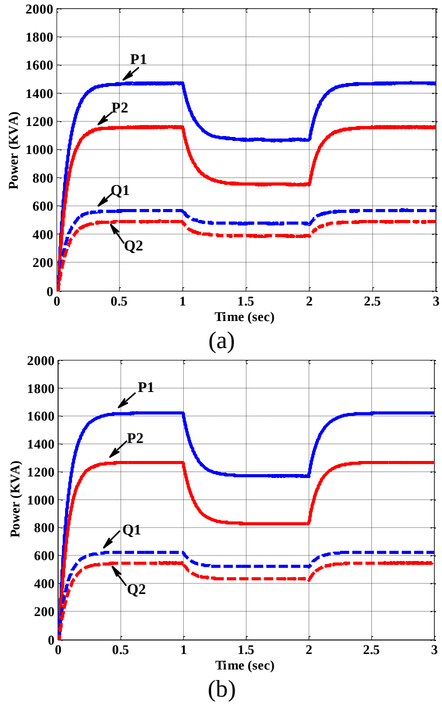

Figure. 14. Injected powers of DGs to the PCC: (a) Conventional method (b) Proposed method

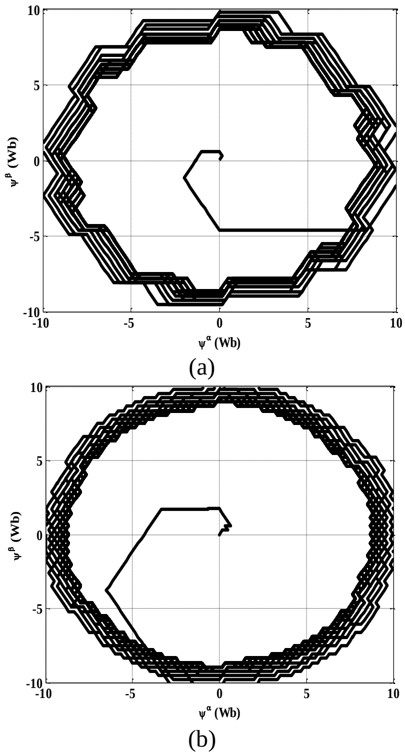

Figure 15. Virtual flux trajectory of Inverter 1: (a) Conventional method (b) Proposed method

5. CONCLUSION

The use of hysteresis regulators in the DFC method results in the current and voltage ripples. In addition, since none of the switching vectors can generate the desired voltage, the accuracy of the microgrid control strategy decreases and the desired dynamic performance cannot be achieved. In this paper, a novel control strategy of an islanded microgrid was proposed. First, using the virtual flux droop control, the command values i.e. the phase angle difference and the virtual flux amplitude of the inverter, were obtained. Then, the proposed fuzzy based control was employed to select the best switching vector to apply to the inverter. As a result, an effective control method was obtained, while there was no need to use PI controllers or hysteresis regulators Moreover, the duty cycle of the selected active switching vector was optimally calculated using a simple and robust method whereas the rest of the time of the control period was allocated to the null vector. Therefore, voltage and current ripples were significantly reduced. The proposed method was evaluated using simulation in MATLAB/Simulink software environment and was compared with the conventional method based on the VFD and the DFC. The results showed that the proposed method can proportionally share the power between DGs while the voltage and current ripples were also reduced significantly.

6. REFERENCES

1. Chen. Y., Guerrero. J. M., Shuai. Z., Chen. Z, Zhou. L., and Luo. A., "Fast reactive power sharing, circulating current and resonance suppression for parallel inverters using resistive-capacitive output impedance," ***IEEE Transactions on Power Electronics***, Vol. 31, (2016), 5524-5537. DOI: 10.1109/TPEL.2015.2493103.
2. Zhong. Q. –C., and Hornik. T., "Parallel operation of inverters," in Control of Power Inverters in Renewable Energy and Smart Grid Integration, ***John Wiley and Sons***, London, (2013), 297-333, (Chapter 19). DOI: 10.1002/9781118481806.ch19.
3. Hosseinzadeh. N., Khanabdal. S., Al-Jabri. Y., Al-Abri. R., Hinai. A., and Banejad. M, "Voltage stabiliry of microgrids," in Variability, Scalability and Stability of Microgrids, ***IET***, London, (2019), 327-376, (Chapter 10). DOI: 10.1049/PBPO139E_ch10.
4. Sagar. G. V. R., and Debela. T., "Implementation of optimal load balancing strategy for hybrid energy management system in DC/AC microgrid with PV and battery storage," ***International Journal of Engineering, Transactions A: Basics***, Vol. 32, (2019), 1437-1445. DOI: 10.5829/IJE.2019.32.10A.13.
5. Gholami. M., "Islanding detection method of distributed generation based on wavenet," ***International Journal of Engineering, Transactions B: Applications***, Vol. 32, (2019), 242-248. DOI: 10.5829/IJE.2019.32.02b.09.
6. Heidari. M., and Tarafdar Hagh. M., "Optimal reconfiguration of solar photovoltaic arrays using a fast parallelized particle swarm optimization in confront of partial shading," ***International Journal of Engineering, Transactions B: Applications***, Vol. 32, (2019), 1177-1185. DOI: 10.5829/IJE.2019.32.08B.14.
7. Han. H., Hou. X., Yang. J., Wu. J., Su. M., and Guerrero. J. M., "Review of power sharing control strategies for islanding operation of AC microgrids," ***IEEE Transactions on Smart Grid***, Vol. 7, (2016), 200-215. DOI: 10.1109/TSG.2015.2434849.
8. He. J., Pan. Y., Liang. B., and Wang. C., "A simple decentralized islanding microgrid power sharing method without using droop control," ***IEEE Transactions on Smart Grid***, Vol. 9, (2018), 6128-6139. DOI: 10.1109/TSG.2017.2703978.
9. Chauhan. R. K., and Chauhan. K., "Distributed energy resources in Microgrid: integration, challenges and optimization," ***Elsevier***, (2019), 33-56, (Chapter 2). DOI: 10.1016/B978-0-12-817774-7.00002-8.
10. Mondal. A., Illindala. M. S., Khalsa. A. S., Klapp. D. A., and Eto. J. H., "Design and operation of smart loads to prevent stalling in a microgrid," ***IEEE Transactions on Industry Applications***, Vol. 52, (2016), 1184-1192. DOI: 10.1109/TIA.2015.2483579.
11. Lashkar Ara, A., Bagheri Tolabi, H., and Hosseini, R., "Dynamic modeling and controller design of distribution static compensator in a microgrid based on combination of fuzzy set and galaxy-based search algorithm," ***International Journal of Engineering-Transactions A: Basics***, Vol. 29, (2016), 1392-1400. DOI: 10.5829/idosi.ije.2016.29.10a.10.
12. Lu. X., Yu. X., Lai. J., Wang. Y., and Guerrero. J. M., "A novel distributed secondary coordination control approach for islanded microgrids," ***IEEE Transactions on Smart Grid***, Vol. 9, (2018). 2726-2740. DOI: 10.1109/TSG.2016.2618120.
13. Nutkani. I. U., Loh. P. C., Wang. P., and Blaabjerg. F, "Linear decentralized power sharing schemes for economic operation of AC microgrids," ***IEEE Transactions on Industrial Electronics***, Vol. 63, (2016), 225-234. DOI: 10.1109/TIE.2015.2472361.
14. Mahmood. H., Michaelson. D., and Jiang. J., "Accurate reactive power sharing in an islanded microgrid using adaptive virtual impedances," ***IEEE Transactions on Power Electronics***, Vol. 30, (2015), 1605-1617. DOI: 10.1109/TPEL.2014.2314721.
15. Lou. G., Gu. W., Xu. Y., Cheng. M., and Liu. W., "Distributed MPC-based secondary voltage control scheme for autonomous droop-controlled microgrids," ***IEEE Transactions on Sustainable Energy***, Vol. 8, (2017), 792-804. DOI: 10.1109/TSTE.2016.2620283.
16. Lai. J., Zhou. H., Lu. X., Yu. X., and Hu. W., "Droop-based distributed cooperative control for microgrids with time-varying delays," ***IEEE Transactions on Smart Grid***, Vol. 7, (2016), 1775-1789. DOI: 10.1109/TSG.2016.2557813.
17. Wu. X., and Shen. C., "Distributed optimal control for stability enhancement of microgrids with multiple distributed generators," ***IEEE Transaction on Power Systems***, Vol. 32, (2017), 4045-4059. DOI: 10.1109/TPWRS.2017.2651412.
18. Yu. K., Ai. Q., Wang. S., Ni. J., and Lv. T., "Analysis and optimization of droop controller for microgrid system based on small-signal dynamic model," ***IEEE Transactions on Smart Grid***, Vol. 7, (2016), 695-705. DOI: 10.1109/TSG.2015.2501316.
19. Kim. J., Guerrero. J. M., Rodriguez. P., Teodorescu. R., and Nam. K., "Mode adaptive droop control with virtual output impedances for an inverter-based flexible AC microgrid," ***IEEE Transactions Power Electronics***, Vol. 26, (2011), 689-701. DOI: 10.1109/TPEL.2010.2091685.
20. Zhang. J., Shu. J., Ning. J., Huang. L., and Wang. H., "Enhanced proportional power sharing strategy based on adaptive virtual impedance in low-voltage networked microgrid," ***IET Generation, Transmission & Distribution***, Vol. 12, (2018), 2566-2576. DOI: 10.1049/iet-gtd.2018.0051.
21. Zhong. Q. –C, "Robust droop controller for accurate proportional load sharing among inverters operated in parallel," ***IEEE Transactions on Industrial Electronics***, Vol. 60, (2013), 1281-1290. DOI: 10.1109/TIE.2011.2146221.

22. Zhang. M., Song. B., and Wang. J., "Circulating current control strategy based on equivalent feeder for parallel inverters in islanded microgrid," ***IEEE Transactions on Power Systems***, Vol. 34, (2019), 595-605. DOI: 10.1109/TPWRS.2018.2867588.
23. Chen. J., Yue. D., Dou. C., Chen. L., Weng. S., and Li. Y., "A virtual complex impedance based $P-\dot{V}$ droop method for parallel-connected inverters in low-voltage AC microgrids," ***IEEE Transactions on. Industrial Informatics***, Vol. 17, (2021), 1763-1773. DOI: 10.1109/TII.2020.2997054.
24. Lee. C. –T, C. Chu. –C, and Cheng. P. –T., "A new droop control method for the autonomous operation of distributed energy resource interface converters," ***IEEE Transactions on Power Electronics***, Vol. 28, (2013), 1980-1993. DOI: 10.1109/TPEL.2012.2205944.
25. Zhou, J., and Cheng, P. "A modified $Q-\dot{V}$ droop control for accurate reactive power sharing in distributed generation microgrid," ***IEEE Transactions on Industry Applications***, Vol. 55, (2019), 4100-4109. DOI: 10.1109/TIA.2019.2903093.
26. Hu. J., Zhu. J., Dorrell. D. G., and Guerrero. J. M., "Virtual flux droop method—A new control strategy of inverters in microgrids," ***IEEE Transactions on Power Electronics***, Vol. 29, (2014), 4704-4711. DOI: 10.1109/TPEL.2013.2286159.
27. Ashabani. M., Mohamed. Y. A. -R. I., Mirsalim. M., and Aghashabani. M., "Multivariable droop control of synchronous current converters in weak grids/microgrids with decoupled dq-axes currents," ***IEEE Transactions on Smart Grid***, Vol. 6, (2015), 1610-1620. DOI: 10.1109/TSG.2015.2392373.
28. Heydari. R., Dragicevic. T., and Blaabjerg. F., "High-bandwidth secondary voltage and frequency control of VSC-based AC microgrid," ***IEEE Transactions on Power Electronics***, Vol. 34, (2019), 11320-11331. DOI: 10.1109/TPEL.2019.2896955.
29. Gdaim. S., Mtibaa. A., and Mimouni. M. F., "Design and experimental implementation of DTC of an induction machine based on fuzzy logic control on FPGA," ***IEEE Transactions Fuzzy Systems***, Vol. 3, (2015), 644-655. DOI: 10.1109/TFUZZ.2014.2321612.
30. Uddin. M. N., and Hafeez. M., "FLC-based DTC scheme to improve the dynamic performance of an IM drive," ***IEEE Transactions on Industry Applications***, Vol. 48, (2012), 823-831. DOI: 10.1109/TIA.2011.2181287.
31. Solat. A. R., Ranjbari. A. M., and Mozafari. B., "Coordinated control of doubly fed induction generator virtual inertia and power system oscillation damping using fuzzy logic," ***International Journal of Engineering, Transactions A: Basics***, Vol. 32, (2019), 536-547. DOI: 10.5829/IJE.2019.32.04A.11.
32. El Ouanjli. N., Motahhir. S., Derouich. A., El Ghzizal. A., Chebabhi. A., and Taoussi. M., "Improved DTC strategy of doubly fed induction motor using fuzzy logic controller," ***Energy Reports***, Vol. 5, (2019), 271-279. DOI: 10.1016/j.egyr.2019.02.001.

Persian Abstract

چکیده

در این مقاله یک استراتژی کنترل جدید برای ریزشبکه جزیره‌ای مبتنی بر کنترل مشخصه افتی شار مجازی (VFD) پیشنهاد شده است. در روش مرسوم مشخصه افتی شار مجازی از تکنیک کنترل مستقیم شار (DFC) برای تولید سیگنال‌های کلیدزنی استفاده می‌شود که مبتنی بر تنظیم‌کننده‌های هیسترزیس و جدول کلیدزنی است. بنابراین، ایجاد موجک ولتاژ و جریان اجتناب‌ناپذیر است. علاوه بر این، در هر دوره تناوب کنترلی، تنها یک بردار کلیدزنی اعمال می‌شود و از آنجایی که هیچ یک از بردارهای کلیدزنی نمی‌توانند ولتاژ مورد نظر را تولید کنند، عملکرد دینامیکی مطلوب حاصل نمی‌شود. در اینجا، روش جدیدِ کنترل فازی شار مستقیم (DFFC) برای انتخاب بهترین بردار کلیدزنی بر اساس منطق فازی پیشنهاد شده است. همچنین، فقط کسری از دوره تناوبِ کنترل به یک بردار کلیدزنی فعال مناسب اختصاص داده می شود که با روش کنترل فازی شار مستقیم انتخاب می‌شود؛ در حالی که زمان باقی‌مانده از دوره تناوبِ کنترل به یک بردار کلیدزنی صفر اختصاص می‌یابد. زمان وظیفه بردار کلیدزنی فعالی که انتخاب شده است با استفاده از مکانیسمی ساده و مقاوم به طور بهینه تعیین می‌شود. به منظور ارزیابی عملکرد روش پیشنهادی، یک ریز شبکه جزیره‌ای و استراتژی کنترل پیشنهادی در نرم افزار Matlab/Simulink شبیه‌سازی شده است. نتایج ثابت می‌کند که پاسخ عملکرد دینامیکی بهبود می‌یابد و توان مورد نیاز بار به طور متناسب بین منابعِ تولید توان، تقسیم می‌شود، در حالی که موجک ولتاژ و جریان به طور چشمگیری کاهش می‌یابد.

IJE TRANSACTIONS B: Applications Vol. 34, No. 05, (May 2021) 1284-1289

International Journal of Engineering

Journal Homepage: www.ije.ir

Reducing Quantum Cost for Reversible Realization of Densely-packed-decimal Converters

S. Diamond Thabah, P. Saha*

Department of Electronics and Communication Engineering, National Institute of Technology Meghalaya, Shillong, India

PAPER INFO

Paper history:
Received 06 February 2020
Received in revised form 17 March 2021
Accepted 30 March 2021

Keywords:
Binary-coded-decimal
Densely-packed-decimal
Quantum Cost
Primitive-quantum-gates
Delay

ABSTRACT

At present, the reduction of circuit design power is a prime research topic. The reversible computation satisfies the criteria of the power consumption reduction compared to the traditional logic design. Thereby, reversible computation is gaining much attention in recent decades. Two reversible design approaches of binary-coded-decimal (BCD) to densely-packed-decimal (DPD) converter (encoder) and two design approaches of DPD to BCD converter (decoder) are proposed in this paper. The designs are carried out through the appropriate selection of the gates and further proper organization of such gates with parallel implementation. The proposed design approaches offer a low quantum cost implementation compared to state-of-the-art design. The cost results analysis of reversible DPD encoder shows appreciable reduction by at least ~23%, and that of decoder by at least ~62% compared to the state-of-art design found in the literature. Furthermore, the structures are decomposed into the primitive-quantum-gates and compressed in compact form for delay calculation.

***doi**: 10.5829/ije.2021.34.05b.22*

NOMENCLATURE

K	Boltzmann's constant	**Symbols**	
T	Absolute temperature	Δ	A unit delay

1. INTRODUCTION

The inaccuracy errors and exactness problem using the binary representation of decimal numbers for decimal calculations are not acceptable in commercial and financial systems. Thus, decimal representation is necessary for decimal calculations of such data sets. In 2019, the IEEE standard for floating-point arithmetic [1] was revised (from the IEEE 754-2008), where the significand part of the decimal number format is represented by the densely-packed-decimal (DPD) encoding [2]. The DPD encoding is an approach where three decimal digits can be represented by 10 bits than 12 bits in pure binary-coded-decimal (BCD). The hardware encoding/decoding approach of such coding can be achieved with only 2-3 gate delays. However, circuit design for low power consumption of such an encoder/decoder is challenging for researchers.

In 1961, Landauer [3]stated that the circuits' hardware computation through the classical gates results in information loss; that is, each bit loss contributed at least $KTln2$ Joules of energy, where K is the Boltzmann's constant and T is the absolute temperature. However, in 1973, Bennett [4] showed that such energy loss was removed using reversible methodology, which can be achieved through reversible gates. These reversible gates/circuits sustained their reversibility with the equivalent number of input and output lines. Also, the mapping between inputs and outputs must be unique such that the information can be processed from the outcomes uniquely. Some restrictions in reversible computing are the fan-out as well as feedback.

Reversible implementation of arithmetics circuits such as reversible adder and reversible multiplier [5-6] has gained interest over the last decades, where low power designs are achievable. In 2006, an approach for

*Corresponding Author Institutional Email: *prabir.saha@nitm.ac.in* (P. Saha)

Please cite this article as: S. Diamond Thabah, P. Saha, Reducing Quantum Cost for Reversible Realization of Densely-packed-decimal Converters, International Journal of Engineering, Transactions B: Applications Vol. 34, No. 05, (2021) 1284-1289

the reversible implementation of DPD encoder and decoder from and to BCD was proposed [7], where they use two reversible gates, namely, Feynman gate (FG) [8] and Toffoli gate (TG) [9]. However, both the design approaches (for encoder and decoder) possess a higher quantum cost (QC) of 199 and 612, respectively. Thus, in this paper, two reversible design approaches for encoder and decoder respectively are proposed to minimize the QC where it utilizes reversible gates such as FG, TG, Peres gate (PG) [10], and BJN gate [11]. The cost results analysis of reversible DPD encoder shows appreciable reduction by at least ~23%, and that of decoder shows a significant reduction of at least ~62% compared to the state-of-art design found in the literature.

2. REVERSIBLE LOGIC CONCEPTS

Reversible logic involves designing hardware circuits using the same count of input lines and output lines. Reversible gates used in this paper are listed and shown in Table 1.

3. DENSELY-PACKED-DECIMAL CONVERTERS

3. 1. Encoder Design The encoder converts the three decimal digits from BCD (letters a through k, and m) format into DPD (p through y) format, where it constitutes twelve inputs and ten outputs. The encoder implementation is according to the following simplified expression shown in Equation (1) [2]:

$$\begin{aligned}
p &= b + (a\, j) + (a\, f\, i)\\
q &= c + (a\, k) + (a\, g\, i)\\
r &= d\\
s &= (f\,(\bar{a} + \bar{\imath})) + (\bar{a}\, e\, j) + (e\, i)\\
t &= g + (\bar{a}\, e\, k) + (a\, i)\\
u &= h\\
v &= a + e + i\\
w &= a + (e\, i) + (\bar{e}\, j)\\
x &= e + (a\, i) + (\bar{a}\, k)\\
y &= m
\end{aligned} \tag{1}$$

3. 2. Decoder Design The decoder performs the conversion of the DPD data into original BCD data. The decoder with ten inputs (letters, p through y) and twelve outputs (letters a through k, and m) has the following simplified Boolean expression shown in Equation (2) [2]:

TABLE 1. Reversible gates with logic equations and QC

GATES	EQUATIONS	QC
FG [8]	P=A, Q=A⊕B	1
TG [9]	P=A, Q=B, R=AB ⊕C	5
PG [10]	P=A, Q=A⊕B, R=AB⊕C	4
BJN [11]	P=A, Q=B, R=(A+B)⊕C	5

$$\begin{aligned}
a &= (v\, w)\,(\bar{s} + t + \bar{x})\\
b &= p\,(\bar{v} + \bar{w} + (x\, s\, \bar{t}\,))\\
c &= q\,(\bar{v} + \bar{w} + (x\, s\, \bar{t}\,))\\
d &= r\\
e &= v\,((\bar{w}\, x) + (\bar{t}\, x) + (s\, x\,))\\
f &= \left(s\,(\bar{v} + \bar{x}\,)\right) + (p\, v\, w\, x\, \bar{s}\, t)\\
g &= \left(t\,(\bar{v} + \bar{x}\,)\right) + (q\, w\, \bar{s}\, t)\\
h &= u\\
i &= v\,((\bar{w}\, \bar{x}\,) + \left(w\, x\,(s + t)\right))\\
j &= (w\, \bar{v}\,) + (s\, v\, \bar{w}\, x\,) + \left(p\, w\left(\bar{x} + (\bar{s}\, \bar{t}\,)\right)\right)\\
k &= (x\, \bar{v}\,) + (t\, \bar{w}\, x\,) + \left(q\, v\, w\left(\bar{x} + (\bar{s}\, \bar{t}\,)\right)\right)\\
m &= y
\end{aligned} \tag{2}$$

4. PROPOSED DESIGN APPROACHES FOR REVERSIBLE DENSELY-PACKED-DECIMAL CONVERTERS

4. 1. Reversible Encoder From BCD to DPD Two design approaches are proposed for the reversible realization of the BCD-to-DPD encoder (B2DE). The realization of the first proposal (design 1) of reversible B2DE is through twenty-seven gates (that is, with the combination of the three gates, namely, FG, TG, and PG) as shown in Figure 1. The encoder's inputs are letters, a through c, e through g, and i through k, whereas the outputs are letters p, q, s, t, v, w, and x as shown in Figure 1. However, the inputs d, h, and m and the outputs r, u, and y are not engaged in the circuit (Figure 1) since the inputs directly contributed to the outputs. To obtained the required B2DE circuit (using Equation (1)), twenty-seven constant inputs (CIs) were integrated into the inputs of the reversible gates, which results in a total of twenty-nine garbage outputs (GOs) in the circuit.

The second proposal (design 2) implemented with twenty-nine reversible gates where an additional gate, namely, BJN gate, is combined with FG, TG, and PG, as shown in Figure 2. Similarly, the encoder's inputs are letters, a through c, e through g, and i through k, whereas the outputs are letters p, q, s, t, v, w, and x as shown in Figure 2. The inputs d, h, and m are directly conferred to the outputs r, u, and y, respectively. As shown in Figure 2, the design involved twenty-nine CIs to achieve the circuit's necessary function, directing thirty-one GOs in the outputs.

4. 2. Reversible Decoder From DPD to BCD For the reversible realization of DPD-to-BCD decoder (D2BD), two design approaches are proposed: design 1 and design 2, respectively. Design 1 of reversible D2BD is implemented with the help of FG, TG, and PG, as shown in Figure 3, where it employed a total of fourty eight reversible gates to perfect the circuit (using Equation (2)). The decoder's inputs are p, q, s, t, v, w, and x and the outputs are a through c, e through g, and i

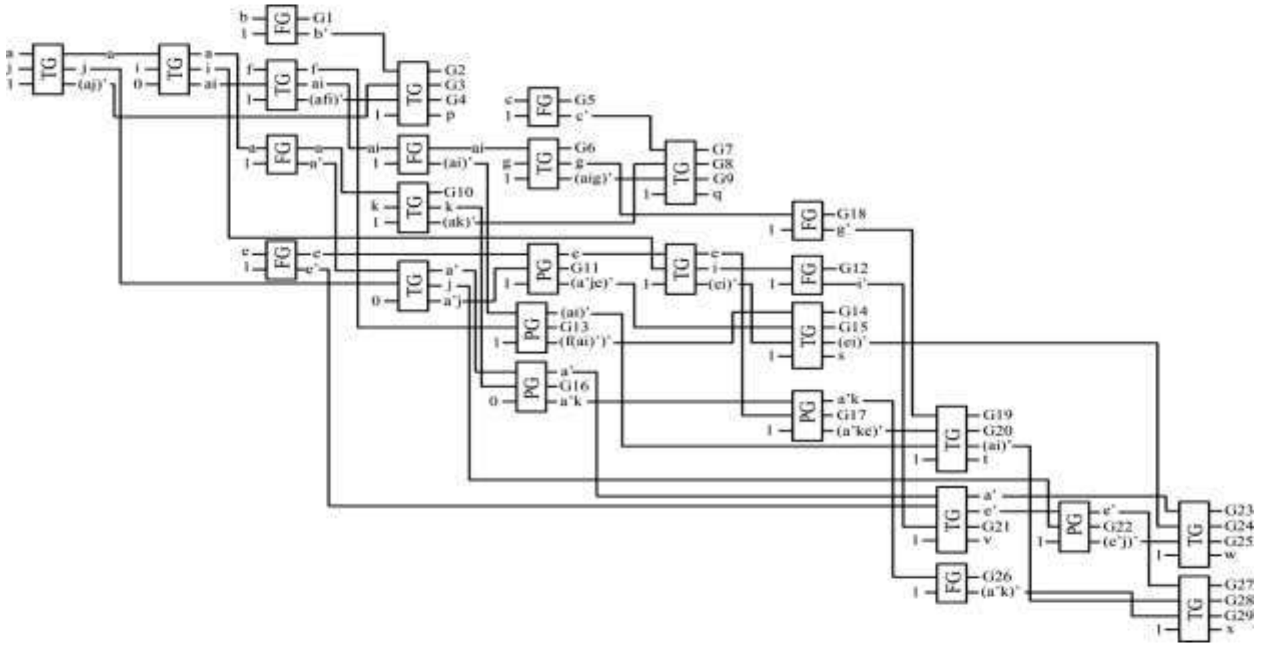

Figure 1. Proposed reversible implementation of B2DE (design 1)

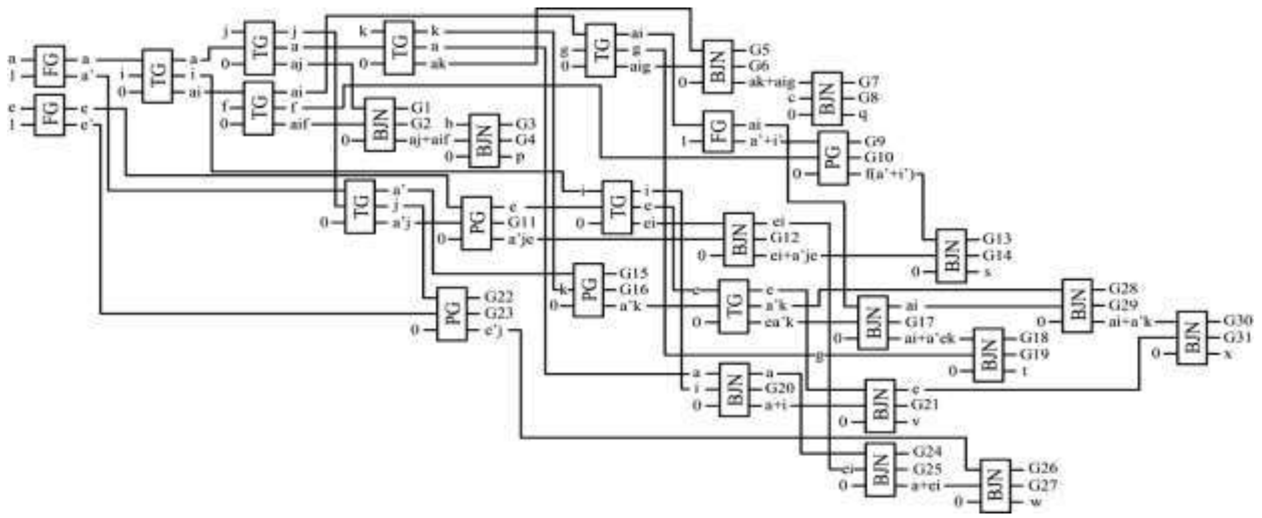

Figure 2. Proposed reversible implementation of B2DE (design 2)

through k, respectively, as shown in Figure 3. The inputs r, u, and y and the outputs d, h, and m not communicated in the circuit (Figure 3) since the inputs contributed directly to the circuit's outputs. The decoder circuit of design 1 integrated fourty-eight CIs to acquired the essential decoder functions, which results in fourty-six of GOs in the circuit's outputs. Design 2 of reversible D2BD realizes with the combinations of FG, TG, PG, and BJN gates. It necessitates a total of fifty reversible gates to achieve the essential function, as shown in Figure 4. The circuit makes use of fifty CIs and produced fourty-eight GOs in the circuit.

5. RESULTS, ANALYSIS AND, DISCUSSIONS

Table 2 shows the analysis results of the proposed designs of the DPD converters. The performance parameters, such as the gate count (GC), CI, GO, and QC, is summarized for each of the two proposed designs and are verified using the RCViewer+ tool [12]. The proposed designs compared with the existing design [7] found in the technical literature are shown in Table 2. The gate counts (GCs), CIs, and GOs of the proposed design 1 of B2DE are 27, 27, and 29, respectively, and

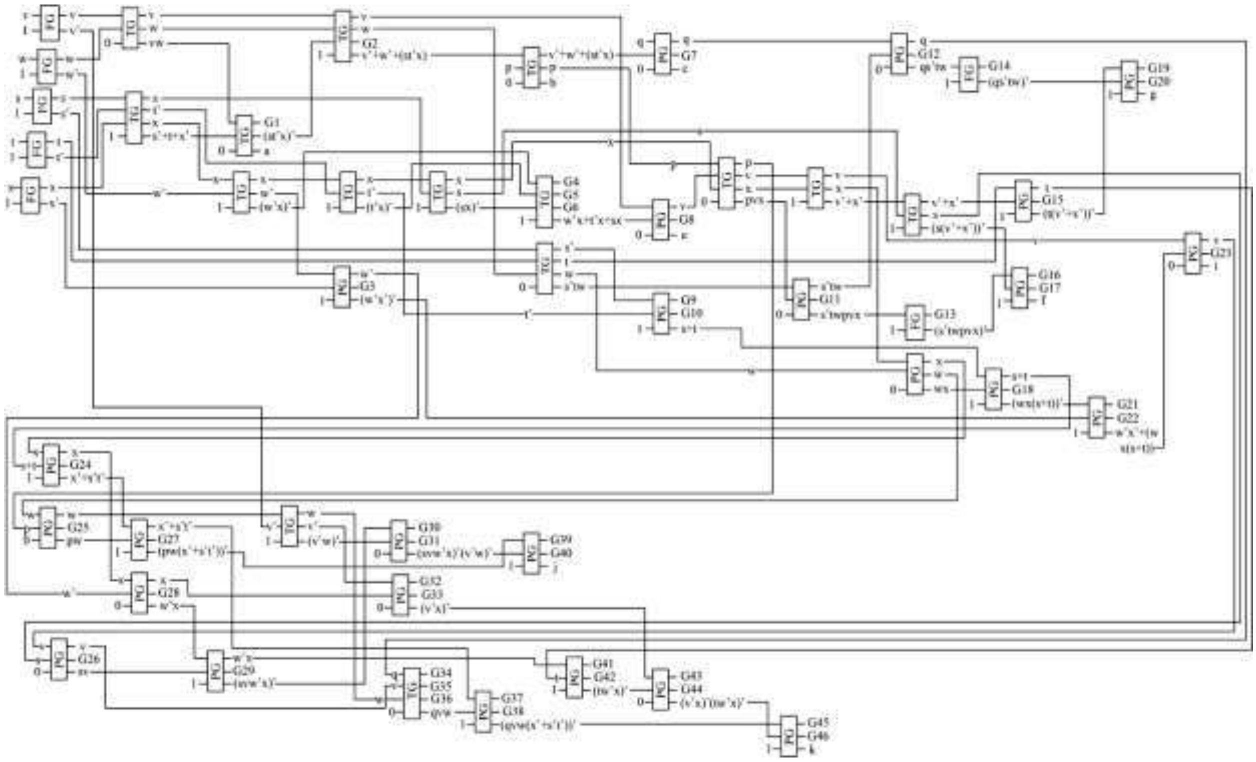

Figure 3. Proposed reversible implementation of D2BD (design 1)

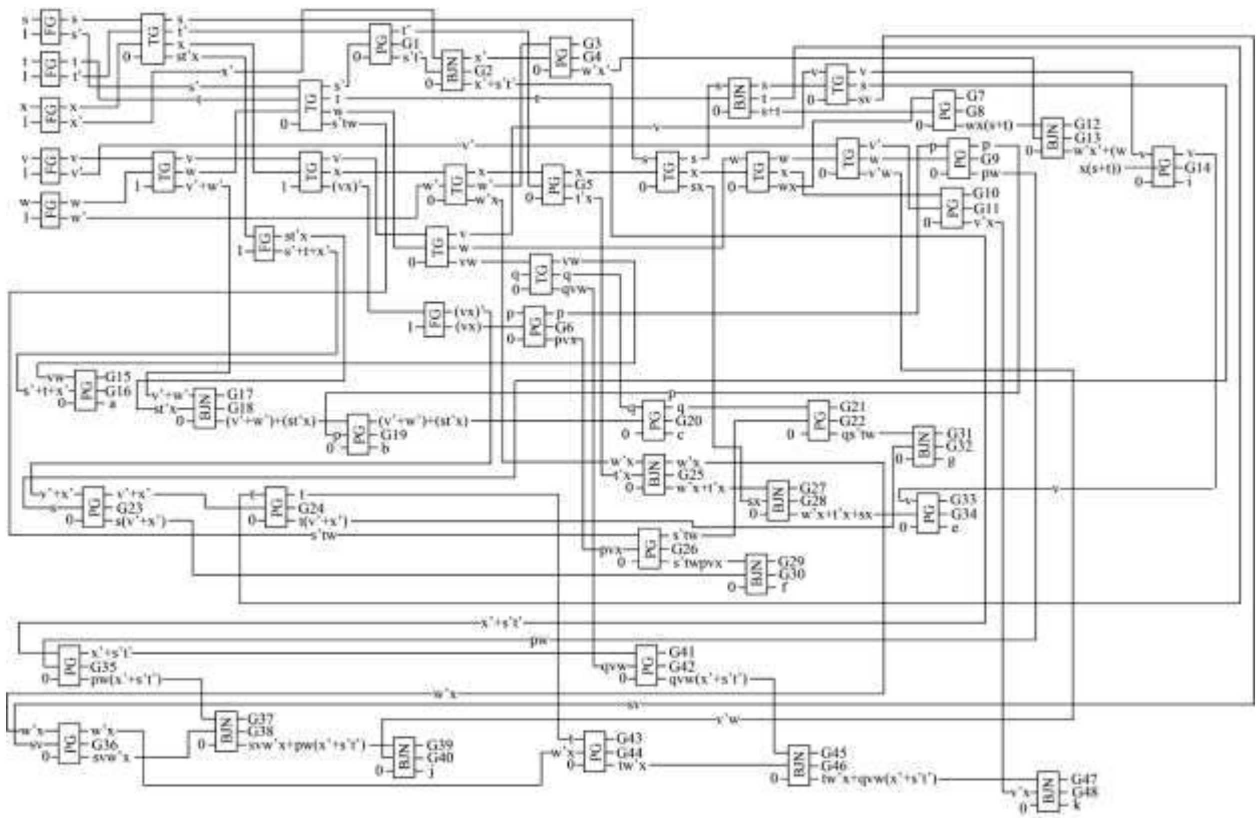

Figure 4. Proposed reversible implementation of D2BD (design 2)

that of the proposed design 2 of B2DE is 29, 29, and 31, respectively. The encoder's existing design by Kaivani et al. [7] engaged 22, 22, and 24 of GCs, CIs, and GOs, respectively. There is an increase of 5 units and 7 units in the proposed design 1 and design 2 of encoder compared with the encoder design of Kaivani et al. [7] in the three (GC, CI, and GO) parameters, as shown in Table 2. However, the proposed design 1 and design 2 of B2DE significantly reduce the QC by 23.11% and 35.17%, respectively.

The proposed design 1 of the D2BD has GCs, CIs, and GOs of 48, 48, and 46, respectively, and that of proposed design 2 of D2BD has 50, 50, and 48, respectively, as shown in Table 2. The existing approach by Kaivani et al. [7] possessed 43 GCs, 43 CIs, and 41 GOs. Similarly, as the encoder, the proposed design 1 and design 2 of D2BD utilize 5 units and 7 units more of GCs, CIs, and GOs, respectively, compared with the existing design [7]. The existing design [7] has a QC of 612, whereas the proposed design 1 of the decoder reduces the QC to 234 and further reduces to 218 by proposed design 2 of D2BD. The proposed design 1 and design 2 of D2BD impressively show improvements of 61.76% and 64.54%, respectively, when compared with the existing design [7] found in the literature.

Furthermore, the delay is calculated with the help of the RCViewer+ tool and noted, as shown in Table 2. All (four designs) the proposed designs and existing designs [7] are decomposed into primitive-quantum-gates (PQGs) and arranged into a compact form (parallel form), where the number of levels is evaluated. Each level comprises a primitive gate or several primitive gates in parallel, and each of them is realized to have a unit delay, denoted as Δ. The total number of levels represents the total delay of the circuit. As shown in Table 2, the delay (or the total number of levels) of the proposed B2DE of design 1 and design 2 is 99Δ and 25Δ, respectively, and the proposed D2BD of design 1 and design 2 is 93Δ and 48Δ, respectively. However, the delay of the existing encoder and decoder of Kaivani et al. [7] were 163Δ and 561Δ, respectively. Therefore, it is noted that the proposed designs show significant improvements in terms of delay compared to the existing design [7] found in the literature.

TABLE 2. Results of the proposed designs and comparison analysis with previous works

DESIGNS	GC	CI	GO	QC	DELAY
Encoder [7]	22	22	24	199	163Δ
Proposed B2DE: a) Design 1	27	27	29	154	99Δ
b) Design 2	29	29	31	129	25Δ
Decoder [7]	43	43	41	612	561Δ
Proposed D2BD: a) Design 1	48	48	46	234	93Δ
b) Design 2	50	50	48	218	48Δ

6. CONCLUSIONS

In this paper, two design approaches of reversible BCD to DPD converter and two reversible DPD to BCD converter are proposed. The proposed designs' analysis results show a significant reduction of QC than the existing design found in the literature with a considerable promotion of 5 units to 7 units in the other performance parameters. Also, since reversible computation has its one application in quantum computation, the designs which offer a low QC and high-speed circuit are the encouraging steps towards the complex reversible system computation.

7. REFERENCES

1. ANSI/IEEE: 'ANSI/IEEE 754-2019, "IEEE Standard for Floating-Point Arithmetic", in IEEE Std 754-2019 (Revision of IEEE 754-2008), 1-84, (2019). doi: 10.1109/IEEESTD.2019.8766229
2. Cowlishaw, M., "Densely packed decimal encoding", ***IEE Proceedings - Computers and Digital Techniques***, Vol. 149, No. 3, (2002), 102-104, doi: 10.1049/ip-cdt:20020407.
3. Landauer, R., "Irreversibility and heat generation in the computing process", ***IBM Journal of Research and Development***, Vol. 5, (1961), 183-191, doi: 10.1147/rd.53.0183.
4. Bennett, C. H., "Logical reversibility of computation", ***IBM Journal of Research and Development,*** Vol. 17, (1973), 525-532, doi: 10.1147/rd.176.0525.
5. Moallem, P. and Ehsanpour, M., "A Novel Design of Reversible Multiplier Circuit", ***International Journal of Engineering, Transactions C: Aspects,*** Vol. 26, No. 6, (2013), 577-586, doi: 10.5829/idosi.ije.2013.26.06c.03.
6. Eslami-Chalandar, F., Valinataj, M. and Jazayeri, H., "Reversible Logic Multipliers: Novel Low-Cost Parity Preserving Designs", ***International Journal of Engineering, Transactions C: Aspects,*** Vol. 32, No. 3, (2019), 381-392.
7. Kaivani, A., Alhosseini, A. Z., Gorgin, S. and Fazlali, M., "Reversible implementation of densely-packed-decimal converter to and from binary-coded-decimal format using in IEEE-754R", in 9th International Conference on Information Technology, Bhubaneswar, India, 273-276, (2006), doi: 10.1109/ICIT.2006.78.
8. Feynman, R., "Quantum Mechanical Computers", ***Optics News***, Vol. 11, (1985), 11-20, doi: 10.1364/ON.11.11.000020.
9. Toffoli, T., "Reversible Computing", in Lab. for Computer Science, Mass. Inst. of Technol., Cambridge, MA, Tech. Memo. MIT/LCS/TM-151, (1980), doi: 10.21236/ADA082021.
10. Peres, A.,"Reversible logic and quantum computers", ***Physical Review A,*** Vol. 32, No. 6, (1985), 3266-3276, doi: 10.1103/PhysRevA.32.3266.
11. Nagamani, A. N., Jayashree, H. V. and Bhagyalakshmi, H. R., "Novel Low Power Comparator Design Using Reversible Logic Gates", ***Indian Journal of Computer Science and Engineering***, Vol. 2, (2011), 566-574, (2011), http://ceit.aut.ac.ir/QDA/RCV.htm.

Persian Abstract

چکیده

در حال حاضر ، کاهش قدرت طراحی مدار یک موضوع اصلی تحقیق است. محاسبه برگشت پذیر معیارهای کاهش مصرف برق را در مقایسه با طراحی منطق سنتی برآورده می کند. بدین ترتیب ، محاسبات برگشت پذیر در دهه های اخیر بسیار مورد توجه قرار گرفته است. در این مقاله دو رویکرد طراحی برگشت پذیر مبدل دودویی کد گذاری شده ((BCDبه دهانه متراکم بسته بندی شده (DPD) (رمزگذار) و دو رویکرد طراحی مبدل DPD به) BCDرسیور) ارائه شده است. طراحی ها از طریق انتخاب مناسب دروازه ها و سازماندهی مناسب بیشتر چنین دروازه هایی با اجرای موازی انجام می شود. رویکردهای طراحی پیشنهادی ، اجرای کم هزینه کوانتومی را در مقایسه با طراحی پیشرفته ارائه می دهند. تجزیه و تحلیل نتایج هزینه رمزگذار برگشت پذیر DPD نشان می دهد کاهش قابل توجهی حداقل ۲۳% ~ و رمزگشای حداقل ۶۲% ~ نسبت به طراحی پیشرفته موجود در ادبیات. علاوه بر این ، ساختارها به دروازه های کوانتومی بدوی تجزیه می شوند و برای محاسبه تأخیر به صورت فشرده فشرده می شوند.

IJE TRANSACTIONS B: Applications Vol. 34, No. 05, (May 2021) 1290-1296

International Journal of Engineering

Journal Homepage: www.ije.ir

Robust Three Stage Central Difference Kalman Filter for Helicopter Unmanned Aerial Vehicle Actuators Fault Estimation

Z. Nejati[a], A. Faraji*[a], M. Abedi[b]

[a] *Department of Electrical and Computer Engineering, University of Kashan, Kashan, Iran*
[b] *Department of Electrical Engineering, University of Shahid Beheshti, Tehran, Iran*

PAPER INFO

Paper history:
Received 08 January 2020
Received in revised form 16 March 2021
Accepted 25 March 2021

Keywords:
Nonlinear Model
Floating actuator Fault
Stuck Actuator Faults

ABSTRACT

This paper proposes state and fault estimations for uncertain time-varying nonlinear stochastic systems with unknown inputs. we suppose, the information about the fault and unknown inputs is not perfectly known. For this purpose, in this manuscript, we developed a robust three-stage central difference Kalman filter (RThSCDKF). We used RThSCDKF for model-based fault detection and identification (FDI) in nonlinear hover mode of helicopter unmanned aerial vehicle (HUAV) in the presence of external disturbance. In this system, actuator faults are affected by each other. The proposed method estimates and decouples actuator faults in the presence of external disturbances. This model can detect stuck and floating faults that are important to detect. At the end, this method is compared with the three-stage extended Kalman filter (ThSEKF). Simulation results show the effectiveness of the proposed robust method for detection and isolation of various actuator faults and also this shows more accuracy with respect to ThSEKF.

doi: *10.5829/ije.2021.34.05b.23*

NOMENCLATURE

$V^B=[u \quad v \quad w]^T$	Linear speed vector	h_{mr}	Height of main rotor hub above center of mass
$\theta=[\varphi \quad \theta \quad \psi]^T$	Euler angles	g	Gravity acceleration
a_{1f}, b_{1f}	Longitudinal and lateral stabilizer flapping angles	k_β	Main rotor blade restoring spring constant
$W^B=[p \quad q \quad r]^T$	Roll, pitch, and yaw rates in body frame	h_{tr}	Height of tail rotor axis above center of mass
$T_{mr}^h, T_{tr}^h,$	Main and tail rotor thrust	Q_{mr}^h, Q_{tr}^h	Main and tail rotor counter-torque

1. INTRODUCTION[1]

Over recent decades, unmanned aerial vehicles (UAVs) have become an important research topic in the academic and military communities worldwide [1]. Among various UAVs, the ability of helicopter UAV (HUAV) to take off and landing vertically, hover flight, and various flight maneuvers, make them the ideal vehicles for a range of applications in a variety of environments [2]. HUAVs are categorized in different weights and sizes and used for various military and civilian purposes, such as taking photos, identifying in different areas, finding dead, or injured people by analyzing images in Hazardous environments, inspecting oil and gas pipelines, and so on [3]. In order to provide a safe flight on a helicopter, it is necessary to detect its faults and make emergency landings at the appropriate time [4]. Three main kinds of faults should be identified in aircraft or other flying vehicles that are sensor fault, actuator fault, and process fault [5]. Sensor loss makes an error or a prohibition on carrying out a mission, but in many cases, it can be compensated by control. But if the control is lost, it will lead to the crash of the HUAV [6]. Also, the possibility of an actuator's fault is more than sensors for mechanical reasons and loss of control is the most important factor in air events [7]. In this regard, dealing with the actuator's faults is a very important issue. This paper addresses the bias fault and stuck and floating actuators faults in the

*Corresponding Author Institutional Email: *ar.faraji@kashanu.ac.ir* (A. Faraji)

Please cite this article as: Z. Nejati, A. Faraji, M. Abedi, Robust Three Stage Central Difference Kalman Filter for Helicopter Unmanned Aerial Vehicle Actuators Fault Estimation, International Journal of Engineering, Transactions B: Applications Vol. 34, No. 05, (2021) 1290-1296

presence of external disturbance. In case of a bias fault, the control level always has a constant difference between the actual and expected deviation. In the stuck fault, the actuator is locked in a place and when a floating fault occurs, the control surface floats on its joint and may not be able to receive the control commands [8,9].In the last decade, some FDI methods have been proposed to deal with actuator faults and enhance the safety of various UAVs [6,10,11].

In general, the major problem in this paper is joint state and fault estimation in HUAV when it is under the influence of external disturbances such as wind. In this regard, some research has been done. A two-stage Kalman filter method was developed for fault and state simultaneous estimation [12]. Zhong et al. [13] presents the augmented three-stage extended Kalman filter (AThSKF) FDD scheme for a QUAV in the presence of external disturbances.

Xiao et al. [14] proposed an augmented robust three-stage extended Kalman filter (ARThSEKF) for the state estimation of Mars entry navigation under uncertain atmosphere density and unknown measurement errors. Hmida et al. [15] proposed an optimal three-stage Kalman filter (OThSKF). Based on the TKF, for the state and fault estimation of linear systems with unknown inputs, which decouple the ASKF covariance matrices. In this article, we cover various actuator faults in the presence of wind gust disturbance for a nonlinear model of HUAV in hover mode with develop ThSKF and based on central difference Kalman filter (CDKF). CDKF uses sterling polynomial interpolation to approximate the nonlinear function instead of analytical derivatives in the Taylor series. This makes the task very convenient and does not require the Jacobin and Hessian matrix, like the EKF. In this method, like the unscented Kalman filter, after considering the initial values, the Sigma points are calculated, and then time update and measurement update are considered.

In general, the main contributions of this paper include:
1) Use of nonlinear FDI for a nonlinear model of HUAV. 2) Because fault and disturbance affect the system, in the same manner, separating faults and disturbances is more difficult. So we develop actuator FDI when HUAV is under influence of external disturbance. 3) develop RThSCDKF when exact stochastic information of actuator faults and external disturbances is not available for FDI that is able to decouple the effect of actuator faults on each other because, in HUAV, roll, pitch, and yaw actuators faults are coupled and affect each other. For example, if a fault occurs in the yaw channel, it affects all channels. 4) considered stuck and floating actuator fault Which are a great danger for the HUAV and a few of the studies consider these faults.

The rest of this paper is organized as follows: Section 2 describes the model. In section 3, ThSCDKF is designed. Section 4 presents a simulation of the designed observers. Finally, the results are given in section 5.

2. HUAV MODEL DESCRIPTION

HUAVs are categorized in terms of weight and size and have four input references to perform various flight maneuvers. 1) The collective input (d_{col}) can change the reference value of the main rotor thrust. In fact, this input changes the thrust vector and HUAV flight height. 2) The longitudinal input (d_{lon}) causes the device to move forward and backward. 3) The lateral input (d_{lat}) causes the device to deflect right and left. 4) The pedal input (d_{ped}) changes value of the tail rotor thrust as a result of which, the HUAV rotates around it [16,17]. This inputs are applied to HUAV with four servo actuators. that are collective pitch servo, elevator servo, aileron servo and rudder servo.

2. 1. Mathematical Model

Equations of the helicopter are explained in literature [17,18], that cross-coupling terms are neglected as small in hover mode and summarized in a single $\dot{x} = f(x.u)$ expression as Equation (1).

$$
\begin{aligned}
\dot{u} &= -g\sin\theta + \frac{1}{m}(-T_{mr}^{h}(K_B d_{lon} + K_F a_{1f}))\\
\dot{v} &= -g\sin\varphi\cos\theta + \frac{1}{m}(T_{mr}^{h}(K_B d_{lat} + K_F b_{1f}) - T_{tr}^{h})\\
\dot{w} &= g\cos\varphi\cos\theta + \frac{1}{m}T_{mr}^{h}\\
\dot{p} &= \frac{1}{J_{xx}}((T_{mr}^{h}h_{mr} + k_{\beta})(K_B d_{lat} + K_F b_{1f}) - T_{tr}^{h}h_{tr})\\
\dot{q} &= \frac{1}{J_{yy}}((T_{mr}^{h}h_{mr} + k_{\beta})(K_B d_{lon} + K_F a_{1f}) - Q_{tr}^{h})\\
\dot{r} &= \frac{1}{J_{zz}}(T_{tr}^{h}d_{tr} - Q_{mr}^{h})\\
\dot{\varphi} &= p + (q\sin\varphi\tan\theta + r\cos\varphi)\tan\theta\\
\dot{\theta} &= q\cos\varphi - r\sin\varphi\\
\dot{a}_{1f} &= -\frac{a_{1f}}{\tau_f} - q + \frac{K_H}{\tau_f}d_{lon}\\
\dot{b}_{1f} &= -\frac{b_{1f}}{\tau_f} - p + \frac{K_H}{\tau_f}d_{lat}
\end{aligned}
\tag{1}
$$

The main rotor thrust (T_{mr}^{h}) and counter-torque (Q_{mr}^{h}) is in following form Equation (2).

$$
\begin{aligned}
T_{mr}^{h} &= C_{mr}^{h}(C_c d_{col} + D_c) + \frac{(D_{mr}^{T})^2}{2} - \dots\\
& D_{mr}^{T}\sqrt{C_{mr}^{T}(C_c d_{col} + D_c) + \frac{(D_{mr}^{T})^2}{4}}
\end{aligned}
\tag{2}
$$

$$Q_{mr}^{h} = C_{mr}^{Q}(T_{mr}^{h})^{3/2} + D_{mr}^{Q} \tag{3}$$

where C_{mr}^{T}, D_{mr}^{T}, C_{mr}^{Q} and D_{mr}^{Q} are constant, and depend on the density of air and some characteristic of HUAV main rotor including the radius of disc, angular rotation rate, lift curve slope and blade chord length. The tail rotor thrust and counter-torque is in following form:

$$\begin{aligned} T_{tr}^{h} &= C_{tr}^{h}(C_t d_{ped} + D_t) + \frac{(D_{tr}^{T})^2}{2} - ... \\ D_{tr}^{T} &\sqrt{C_{tr}^{T}(C_t d_{ped} + D_t) + \frac{(D_{tr}^{T})^2}{4}} \end{aligned} \tag{4}$$

$$Q_{tr}^{h} = C_{tr}^{Q}(T_{tr}^{h})^{3/2} + D_{tr}^{Q} \tag{5}$$

C_{tr}^{T}, D_{tr}^{T}, C_{tr}^{Q} and D_{tr}^{Q} are constant, and depend on density of air and some characteristic of HUAV tail rotor such as the radius of disc, angular rotation rate, Lift curve slope and blade chord length.

3. THREE STAGE CENTRAL DIFFERENCE KALMAN FILTER

We assume to have a discrete-time nonlinear system with fault and unknown inputs.

$$x_{k+1} = f(x_k, u_k, b_k, d_k) + w_k^x \tag{6}$$

$$b_{k+1} = b_k + w_k^b \tag{7}$$

$$d_{k+1} = d_k + w_k^d \tag{8}$$

$$y_k = h(x_k, u_k, b_k, d_k) + v_k \tag{9}$$

where

$$E\left[\begin{bmatrix} w_k^x \\ w_k^b \\ w_k^d \\ v_k \end{bmatrix} \begin{bmatrix} w_j^x \\ w_j^b \\ w_j^d \\ v_j \end{bmatrix}^T\right] = \begin{bmatrix} Q_k^x & Q_k^{xb} & Q_k^{xd} & 0 \\ Q_k^{bx} & Q_k^b & Q_k^{bd} & 0 \\ Q_k^{dx} & Q_k^{db} & Q_k^d & 0 \\ 0 & 0 & 0 & R_k \end{bmatrix} \delta_{kj}, \tag{10}$$

where

$$\delta_{kj} \begin{cases} 1; k = j \\ 0; k \neq j \end{cases}, Q_k^x \succ 0, Q_k^b \succ 0, Q_k^d \succ 0, R_k \succ 0$$

Initial state, fault, disturbance estimation and estimation of covariance are in following form:

$$\begin{aligned} &\hat{x}_0 = E(x_0), \hat{b}_0 = E(b_0), \hat{d}_0 = E(d_0). \\ &\hat{P}_0^x = E\left[(x_0 - \hat{x}_0)(x_0 - \hat{x}_0)^T\right], \hat{P}_0^b = E\left[(b_0 - \hat{b}_0)(b_0 - \hat{b}_0)^T\right], \\ &\hat{P}_0^d = E\left[(d_0 - \hat{d}_0)(d_0 - \hat{d}_0)^T\right], \hat{P}_0^{xd} = E\left[(x_0 - \hat{x}_0)(d_0 - \hat{d}_0)^T\right], \\ &\hat{P}_0^{xb} = E\left[(x_0 - \hat{x}_0)(b_0 - \hat{b}_0)^T\right], \hat{P}_0^{bd} = E\left[(b_0 - \hat{b}_0)(d_0 - \hat{d}_0)^T\right]. \end{aligned} \tag{11}$$

We try that linearize the system respect to fault and unknown input.

$$B_k^x = \frac{\partial f(x_k, u_k, b_k, d_k)}{\partial b_k}\Big|_{x_k = \hat{x}_{k/k}, b_k = \hat{b}_{k/k}, d_k = \bar{d}_{k/k}} \tag{12}$$

$$E_k^x = \frac{\partial f(x_k, u_k, b_k, d_k)}{\partial d_k}\Big|_{x_k = \hat{x}_{k/k}, b_k = \hat{b}_{k/k}, d_k = \bar{d}_{k/k}} \tag{13}$$

$$B_k^y = \frac{\partial h(x_k, u_k, b_k, d_k)}{\partial b_k}\Big|_{x_k = \hat{x}_{k/k-1}, b_k = \hat{b}_{k/k-1}, d_k = \bar{d}_{k/k-1}} \tag{14}$$

$$E_k^y = \frac{\partial h(x_k, u_k, b_k, d_k)}{\partial b_k}\Big|_{x_k = \hat{x}_{k/k-1}, b_k = \hat{b}_{k/k-1}, d_k = \bar{d}_{k/k-1}} \tag{15}$$

Then, the nonlinear discrete-time varying system that was described in Equations (6) and (10) can approximate by:

$$x_{k+1} \approx f^*(x_k, u_k, \hat{b}_{k/k}, \bar{d}_{k/k}) + B_k^x b_k + E_k^x d_k + w_k^x \tag{16}$$

$$y_k \approx h^*(x_k, u_k, \hat{b}_{k/k-1}, \bar{d}_{k/k-1}) + B_k^y b_k + E_k^y d_k + v_k \tag{17}$$

where:

$$\begin{aligned} f^*(x_k, u_k, \hat{b}_{k/k}, \bar{d}_{k/k}) &= f(x_k, u_k, \hat{b}_{k/k}, \bar{d}_{k/k}) \\ &- B_k^x \hat{b}_{k/k} - E_k^x \bar{d}_{k/k} \end{aligned} \tag{18}$$

$$\begin{aligned} h^*(x_k, u_k, \hat{b}_{k/k-1}, \bar{d}_{k/k-1}) &= h(x_k, u_k, \hat{b}_{k/k-1}, \bar{d}_{k/k-1}) \\ &- B_k^y \hat{b}_{k/k-1} - E_k^y \bar{d}_{k/k-1} \end{aligned} \tag{19}$$

3. 1. Augmented State CDKF (ASCDKF)

By adding faults and unknown input, we could obtain a vector with new dimension. The state equations in the developed state are as follows:

$$x_k^a = \begin{bmatrix} x_k^T & b_k^T & d_k^T \end{bmatrix}, n^a = n + p + q \tag{20}$$

$$f^a(x_{k-1}^a) = \begin{bmatrix} f^*(x_{k-1}, u_{k-1}, \hat{b}_{k-1/k-1}) \\ + B_{k-1}^x b_{k-1} + E_{k-1}^x d_{k-1} \\ b_{k-1} \\ d_{k-1} \end{bmatrix} \tag{21}$$

$$\begin{aligned} h^a(x_k^a) &= h^*(x_k, u_k, \hat{b}_{k/k-1}, \bar{d}_{k/k-1}) \\ &+ B_k^y b_k + E_k^y d_k + v_k \end{aligned} \tag{22}$$

So we can write

$$x_{k+1}^a = f^a(x_k^a) + w_k^a \tag{23}$$

$$y_k = h^a(x_k^a) + v_k \tag{24}$$

where:

$$w_{k-1}^a = \begin{bmatrix} w_{k-1}^x \\ w_{k-1}^b \\ w_{k-1}^d \end{bmatrix}, Q_{k-1}^a = E\left[w_{k-1}^a (w_{k-1}^a)^T \right] \tag{25}$$

ASCDKF can be written in four steps.

TABLE 1. ASCDKF Algorithm

Step 1: Initialization

$$x_{0/0}^a = \left[\hat{x}_0^T \quad \hat{b}_0^T \quad \hat{d}_0^T \right], \hat{P}_{0/0}^a = \begin{bmatrix} \hat{P}_0^x & \hat{P}_0^{xb} & \hat{P}_0^{xd} \\ (\hat{P}_0^{xb})^T & \hat{P}_0^b & \hat{P}_0^{bd} \\ (\hat{P}_0^{xd})^T & (\hat{P}_0^{bd})^T & \hat{P}_0^d \end{bmatrix}$$

Step 2: Sigma point calculation

$$\chi_{k-1,i}^a = \begin{bmatrix} x_{k-1/k-1}^a \\ x_{k-1/k-1}^a - h(\sqrt{\hat{P}_{k-1/k-1}^a})_i \\ x_{k-1/k-1}^a + h(\sqrt{\hat{P}_{k-1/k-1}^a})_{i-n^a} \end{bmatrix}$$

Step 3: Time update

$$\chi_{k-1,i}^{*a} = f_{k-1}^a(\chi_{k-1,i}^a), i = 0...2L$$

$$x_{k/k-1}^a = \sum_{i=0}^{2n^a} w_i^{(m)} \chi_{k/k-1,i}^{*a}$$

$$\hat{P}_{k/k-1}^a = \sum_{i=0}^{2n^a} \begin{Bmatrix} w_i^{(c_1)} (\chi_{k/k-1,i}^a - x_{k/k-1}^a)^2 \\ + w_i^{(c_2)} (\chi_{k/k-1,i}^a + x_{k/k-1}^a - 2x_0)^2 \end{Bmatrix} + Q_{k-1}^a$$

$$\chi_{k/k-1,i}^a =$$

$$\left[x_{k/k-1}^a \quad x_{k/k-1}^a - h(\sqrt{\hat{P}_{k/k-1}^a})_i \quad x_{k/k-1}^a + h(\sqrt{\hat{P}_{k/k-1}^a})_{i-n^a} \right]$$

$$y_{k/k-1,i}^a = h_k^a(\chi_{k/k-1,i}^a)$$

$$y_{k/k-1}^a = \sum_{i=0}^{2n^a} w_i^{(m)} y_{k/k-1,i}^a$$

Step 4: Measurment update

$$\hat{P}_{xy}^a = \sum_{i=0}^{2n^a} \left\{ w_i^{(c)} [\chi_{k/k-1,i}^a - x_{k/k-1}^a][y_{k/k-1,i}^a - y_{k/k-1}^a]^T \right\}$$

$$\hat{P}_{yy}^a = \sum_{i=0}^{2n^a} \begin{Bmatrix} w_i^{(c)} [y_{k/k-1,i}^a - y_{k/k-1}^a] \\ [y_{k/k-1,i}^a - y_{k/k-1}^a]^T \end{Bmatrix} + R_k$$

$$K_k^a = \hat{P}_{xy}^a (\hat{P}_{yy}^a)^{-1}$$

$$x_{k/k}^a = x_{k/k-1}^a + K_k^a (y_k^a - y_{k/k-1}^a)$$

$$P_{k/k}^a = P_{k/k-1}^a - K_k^a P_{yy}^a (K_k^a)^T$$

3. 2. Robust Three Stage CDKF (RThCDKF) Design

The three stage U-V transformation is given by:

$$\hat{P}_{k/k-1}^a = U_k \bar{P}_{k/k-1}^a (U_k)^T \tag{26}$$

$$\hat{P}_{k/k}^a = V_k \bar{P}_{k/k}^a (V_k)^T \tag{27}$$

$$x_{k/k-1}^a = U_k \bar{x}_{k/k-1}^a \tag{28}$$

$$x_{k/k}^a = V_k \bar{x}_{k/k}^a \tag{29}$$

$$K_k^a = V_k \bar{K}_k^a \tag{30}$$

U and V are in the following form and determin later:

$$U_k = \begin{bmatrix} I & U_k^{12} & U_k^{13} \\ 0 & I & U_k^{23} \\ 0 & 0 & I \end{bmatrix}, V_k = \begin{bmatrix} I & V_k^{12} & V_k^{13} \\ 0 & I & V_k^{23} \\ 0 & 0 & I \end{bmatrix} \tag{31}$$

According to the inverse transformation of Equation (31), we have:

$$\bar{P}_{k/k-1}^a = (U_k)^{-1} \hat{P}_{k/k-1}^a [(U_k)^{-1}]^T \tag{32}$$

$$\bar{x}_{k/k-1}^a = (U_k)^{-1} x_{k/k-1}^a \tag{33}$$

$$\bar{x}_{k/k}^a = (V_k)^{-1} x_{k/k}^a \tag{34}$$

$$\bar{K}_k^a = (V_k)^{-1} K_k^a \tag{35}$$

$$\bar{P}_{k/k}^a = (V_k)^{-1} \hat{P}_{k/k}^a [(V_k)^{-1}]^T \tag{36}$$

According to above equation, ASCDKF equation can be transformed into:

$$\bar{\chi}_{k-1,i}^a = \begin{bmatrix} \bar{x}_{k-1/k-1}^a \\ \bar{x}_{k-1/k-1}^a - h(\sqrt{\bar{P}_{k-1/k-1}^a})_i \\ \bar{x}_{k-1/k-1}^a + h(\sqrt{\bar{P}_{k-1/k-1}^a})_{i-n^a} \end{bmatrix} \tag{37}$$

$$\chi_{K/k-1,i}^{*a} = (U_k)^{-1} f_k^a (V_{K-1} \bar{\chi}_{k-1,i}^a) \tag{38}$$

$$\bar{x}_{k/k-1}^a = \sum_{i=0}^{2n^a} w_i^{(m)} \bar{\chi}_{k/k-1,i}^{*a} \tag{39}$$

$$\bar{P}^a_{k/k-1}=\sum_{i=0}^{2n^a}\left\{w_i^{(c)}(\bar{\chi}^a_{k/k-1,i}-\bar{x}^a_{k/k-1})(\bar{\chi}^{*a}_{k/k-1,i}-\bar{x}^a_{k/k-1})^T\right\} + (U_k)^{-1}Q^a_{k-1}[(U_k)^{-1}]^T \quad (40)$$

$$\bar{\chi}^a_{k/k-1,i}=\begin{bmatrix}\bar{x}^a_{k/k-1}\\ \bar{x}^a_{k/k-1}-h(\sqrt{\bar{P}^a_{k-1/k-1}})_i\\ \bar{x}^a_{k/k-1}+h(\sqrt{\bar{P}^a_{k-1/k-1}})_{i-n^a}\end{bmatrix} \quad (41)$$

$$y^a_{k/k-1,i}=h^a_k(U_k\bar{\chi}^a_{k/k-1,i}) \quad (42)$$

$$y^a_{k/k-1}=\sum_{i=0}^{2n^a}w_i^{(m)}y^a_{k/k-1,i} \quad (43)$$

$$\hat{P}^a_{xy}=\sum_{i=0}^{2n^a}\left\{w_i^{(c)}[\bar{\chi}^a_{k/k-1,i}-\bar{x}^a_{k/k-1}][y^a_{k/k-1,i}-y^a_{k/k-1}]^T\right\} \quad (44)$$

$$\hat{P}^a_{yy}=\sum_{i=0}^{2n^a}\left\{w_i^{(c)}[y^a_{k/k-1,i}-y^a_{k/k-1}][y^a_{k/k-1,i}-y^a_{k/k-1}]^T\right\} + R_k \quad (45)$$

$$\bar{K}^a_k=(V_k)^{-1}\hat{P}^a_{xy}(\hat{P}^a_{yy})^{-1} \quad (46)$$

$$\bar{x}^a_{k/k}=(V_k)^{-1}U_k\bar{x}^a_{k/k-1}+\bar{K}^a_k(y^a_k-y^a_{k/k-1}) \quad (47)$$

$$\bar{P}^a_{k/k}=(V_k)^{-1}U_k\bar{P}^a_{k/k-1}(U_k)^T[(V_k)^{-1}]^T-\bar{K}^a_kP^a_{yy}(\bar{K}^a_k)^T \quad (48)$$

Substituting Equation (37) into Equation (38) and then Equations (38) and (39) in Equation (37), we have augmented covariance matrix. according to covariance matrix is diagonal, and with equal two matrix, we can obtain $\bar{P}^d_{k/k-1}$, $\bar{P}^b_{k/k-1}, \bar{P}^x_{k/k-1}$ and also U matrix. Subsequently, we replace Equation (41) in Equation (42) and use the first-order approximation of the Taylor series. We apply the result to Equations (44) and (45). With replacing the result in Equation (47) and by considered to relation of x doesn't have fault and unknown input and relation of fault doesn't have state and unknown input terms and relation of unknown input does not have state and fault, we can obtain equation of state, fault and unknown input and V matrix. The three-stage central difference Kalman filter is optimal when the statistical properties of models are perfectly known and when they are unknown we can use robust ThSCDKF. Accourding to equation for eliminate initial condition have to eliminate the terms of contain of fault and unknown input from equations and we can write RThSCDKF in six step in the following form:

TABLE 2. RThSCDKF Algorithm

Step 1: Initialization

$$k=0,\hat{x}_{0/0}=\hat{x}_0,\hat{P}^x_{0/0}=P^x_0\ ,V^{23}_0$$

Step 2: State sub-filter

$$\chi_{k-1,i}=\begin{bmatrix}\hat{x}_{k-1/k-1}\\ \hat{x}_{k-1/k-1}-h\left(\sqrt{P_{k-1}}\right)_i\\ \hat{x}_{k-1/k-1}+h\left(\sqrt{P_{k-1}}\right)_{i-L}\end{bmatrix}$$

$$\bar{\chi}^*_{k/k-1,i}=f^*_{k-1}\left(\chi_{k-1,i},u_{k-1},\hat{b}_{k-1/k-1},\bar{d}_{k-1/k-1}\right),$$

$$\bar{x}_{k/k-1}=\sum_{i=0}^{2n}w_i^{(m)}\bar{\chi}^*_{k/k-1,i}$$

$$\bar{P}^x_{k/k-1}=\sum_{i=0}^{2n}\begin{bmatrix}w_i^{(c_1)}\left(x_{i,k|k-1}-x_{L+i,k|k-1}\right)^2\\ ...+w_i^{(c_2)}\left(x_{i,k|k-1}+x_{L+i,k|k-1}-2x_{0,k|k-1}\right)^2\end{bmatrix}+Q^x_k$$

$$\bar{\chi}_{k/k-1,i}=\begin{bmatrix}\bar{x}_{k/k-1}\\ \bar{x}_{k/k-1}-h\left(\sqrt{P_{k-1}}\right)_i\\ \bar{x}_{k/k-1}+h\left(\sqrt{P_{k-1}}\right)_{i-L}\end{bmatrix}$$

$$\bar{y}_{k/k-1,i}=h^*_k\left(\bar{\chi}_{k/k-1,i},u_{k-1},\hat{b}_{k-1/k-1},\bar{d}_{k-1/k-1}\right)$$

$$\bar{y}_{k/k-1}=\sum_{i=0}^{2n}w_i^{(m)}\bar{y}_{k/k-1,i}$$

$$\bar{P}_{xy}=\sqrt{w_1^{(c_1)}P_k^-}\left(y_{1:L,k|k-1}-y_{L+1:2L,k|k-1}\right)$$

$$\bar{P}_{yy}=\sum_{i=1}^{2n}\begin{bmatrix}w_i^{(c_1)}\left(y_{i,k|k-1}-y_{L+i,k|k-1}\right)^2\\ ...+w_i^{(c_2)}\left(y_{i,k|k-1}+y_{L+i,k|k-1}-2y_{0,k|k-1}\right)^2\end{bmatrix} ...+Q_v$$

$$\bar{K}^x_k=\bar{P}_{xy}\left(\bar{P}_{yy}\right)^{-1},\bar{x}_{k/k}=\bar{x}_{k/k-1}+\bar{K}^x_k\left(y_k-\bar{y}_{k/k-1}\right)$$

$$\bar{P}^x_{k/k}=\bar{P}^x_{k/k-1}-\bar{K}^x_k\bar{P}_{yy}\left(\bar{K}^x_k\right)^T$$

Step 3: Fault sub-filter

$$U^{12}_k=B^x_{k-1},\ S^2_k=H_kU^{12}_k+B^y_k$$

$$\bar{P}^b_{k/k}=\left(S^{2T}_k\bar{P}^{-1}_{yy}S^2_k\right)^+$$

$$\bar{K}^b_k=\bar{P}^b_{k/k}S^{2T}_k\bar{P}^{-1}_{yy},\ \bar{b}_{k/k}=\bar{K}^b_k\left(y_k-\bar{y}_{k/k-1}\right)$$

Step 4: Unknown input sub-filter

$$U^{23}_k=V^{23}_{k-1}\ ,\ U^{13}_k=E^x_{k-1}+U^{12}_kU^{23}_k$$

$$S^3_k=H_kU^{13}_k+B^y_kU^{23}_k+E^y_k$$

$$\bar{P}^d_{k/k}=\left(S^{3T}_k\bar{P}^{-1}_{yy}S^3_k\right)^+$$

$$\bar{K}^d_k=\bar{P}^d_{k/k}S^{3T}_k\bar{P}^{-1}_{yy}\alpha_k(I-S^2_k\left(S^2_k\right))^+$$

$$\bar{d}_{k/k}=\bar{K}^d_k\left(y_k-\bar{y}_{k/k-1}\right)$$

Step 5: the correction of the state and the fault estimations

$$V_k^{12} = U_k^{12} - \bar{K}_k^x S_k^2 \,,\; V_k^{23} = U_k^{23} - \bar{K}_k^b S_k^3$$

$$V_k^{13} = U_k^{13} - V_k^{12}\bar{K}_k^b S_k^3 - \bar{K}_k^x S_k^3$$

$$\hat{x}_{k/k} = \bar{x}_{k/k} + V_k^{12}\bar{b}_{k/k} + V_k^{13}\bar{d}_{k/k}$$

$$\hat{b}_{k/k} = \bar{b}_{k/k} + V_k^{23}\bar{d}_{k/k}$$

$$P_{k/k}^x = \bar{P}_{k/k}^x + V_k^{12}\bar{P}_{k/k}^b (V_k^{12})^T + V_k^{13}\bar{P}_{k/k}^d (V_k^{13})^T$$

$$P_{k/k}^b = \bar{P}_{k/k}^b + V_k^{23}\bar{P}_{k/k}^d (V_k^{23})^T$$

Step 6: k=k+1 and return to step 1.

4. SIMULATION RESULT

In order to validate the RThSCDKF approach, four scenarios are simulated on an unmanned helicopter. In this paper, model parameters are adopted from literature [18]. Process noise and measurement noise are selected based on typical specification of low-cost sensor considering real simulation results of the system. The discrete wind gust model block implements a wind gust of standard “1-cosine” shape. fault and disturbance covariance matrix are not required. In this section, performance of RThSCDKF in the presence of some actuator bias faults is examined and are compared with RThSEKF.

Scenario 4.1: Bias Fault

Small bias faults are simulated for three actuator inputs in the presence of disturbances. So, a sequence of consecutive faults is generated. From t=4-8s, lateral servo has a bias fault between two positions of value -0.01 and 0.01 in a square-wave fashion. For t=8-10s, longitudinal servo has a bias fault near to equilibrium position in no fault mode. For t=10-14s, ruder servo has a bias fault which its value equals -0.01 that is near to control input in no fault mode. Figure 1 shows True faults, RThSEKF estimation and RThSCDKF estimation for lateral, longitudinal and yaw channels.

4. 2. Scenario 2: Floating and Stuck Fault

Floating and stuck faults are simulated for two actuator inputs in the presence of disturbances. So, a sequence of consecutive faults is generated. From t=4-8s, lateral servo has a floating fault between two positions of value 0.01 and -0.01 in a square-wave fashion. For t=14-18s, longitudinal servo has a stuck fault near to equilibrium position in no fault mode. Figure 2 shows True faults and their estimation in the presence of disturbance for lateral, longitudinal and yaw channels. As shown, ThSCDKF can accurately diagnose the faults and decouple them from each other respect to RThSEKF.

4. 3. Scenario 3: Simultaneous Faults

In this section, simultaneous faults of the model are checked.

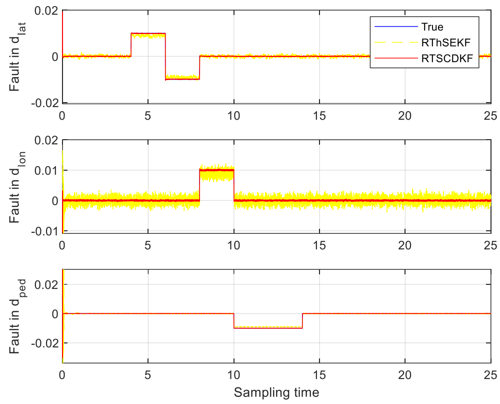

Figure. 1. Bias estimation in scenario 1

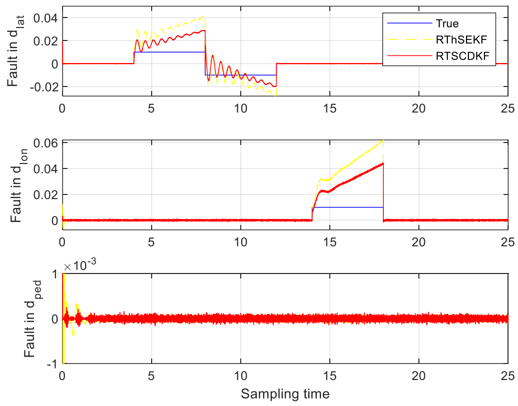

Figure 2. floating and stuck Fault Estimation of ThSCDKF in Scenario 2

Simulation results are given in Figure 3. Fault occurs in lateral and ruder servo actuators at the same time. As shown in this figure, d_{lat} has a floatting fault, and d_{ped} has a bias fault at 8-14s and RThSCDKF is able to estimate the faults better than RThSEKF.

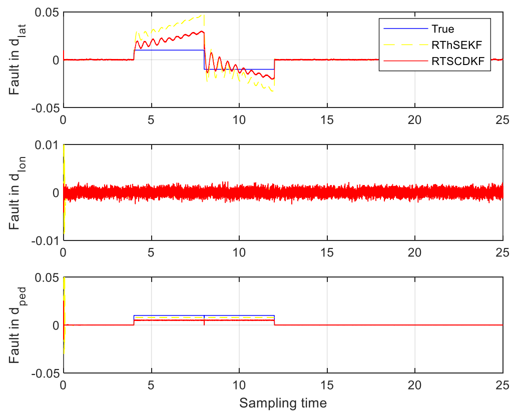

Figure 3. Simultaneous Fault Estimation in Scenario 3

5.CONCLUSION

describes FDI for HUAV actuators for detecting and isolating additive faults such as bias, floating, stuck in the presence of external disturbances in hover mode. It is important that, actuator fault detection can be decoupled and separated from disturbance. For this purpose, ThSCDKF is proposed. ThSCDKF scheme is simulated and compared with ASCDKF under different fault scenarios. Simulations deal with bias faults (scenario 1), floating and stuck faults (scenario 2), simultaneous faults (scenario 3), comparison between ASCDKF and ThSCDKF (scenario 4). Results show effectiveness of the proposed method for various additive faults in HUAV actuators and simultaneous faults in the presence of external disturbance respect to RTSEKF. The proposed method can be used for other plants with proposed faults.

6. REFERENCES

1. Cai, G., Chen, B. M., Dong, X., Lee, T. H., "Design and implementation of a robust and nonlinear flight control system for an unmanned helicopter," ***Mechatronics,*** Vol. 21, No. 5, (2011), 803-820, DOI: 10.1016/j.mechatronics.2011.02.002.
2. Mettler, B., Tischler, M. B., Kanade, T, "System identification modeling of a small-scale unmanned rotorcraft for flight control design," ***Journal of the American Helicopter Society***, Vol. 47, No. 1, (2002), 50-63, DOI: 10.4050/JAHS.47.50.
3. Cai, G., Chen, B. M., Lee, T. H, "Unmanned rotorcraft systems", ***Springer Science & Business Media***, (2011), DOI: 10.1007/978-0-85729-635-1.
4. Zhang, Y., Jiang, J, "Bibliographical review on reconfigurable fault-tolerant control systems." ***Annual Reviews in Control***, Vol. 32, No. 2, (2008), 229-252, DOI: 10.1016/j.arcontrol.2008.03.008.
5. Marzat, J., Piet-Lahanier, H., Damongeot, F., Walter, E., "Model-based fault diagnosis for aerospace systems: a survey." ***Proceedings of the Institution of Mechanical Engineers, Part G: Journal of Aerospace Engineering***, Vol. 226, No. 10, (2012), 1329-1360. DOI: 10.1177/0954410011421717
6. Liu, C., Jiang, B., Zhang, K, "Incipient fault detection using an associated adaptive and sliding-mode observer for quadrotor helicopter attitude control systems." ***Circuits, Systems, and Signal Processing***, Vol. 35, No. 10, (2016), 3555-3574. DOI: 10.1007/s00034-015-0229-8.
7. Avram, R. C., Zhang, X., Muse, J, "Quadrotor actuator fault diagnosis and accommodation using nonlinear adaptive estimators." ***IEEE Transactions on Control Systems Technology***, Vol. 25, No. 6, (2017), 2219-2226. DOI: 10.1109/TCST.2016.2640941
8. Freeman, P., Balas, G. J, Balas. "Actuation failure modes and effects analysis for a small UAV." American control conference. IEEE, 2014, DOI: 10.1109/ACC.2014.6859482.
9. Padeld, G. D. "Helicopter Flight Dynamics: The Theory and Application of Flying Qualities and Simulation Modelling." AIAA Education Series, *AIAA Inc*, (1996), DOI: 10.1017/S0001924000067075
10. Lan, J., Patton, R. J., Zhu, X, "Integrated fault-tolerant control for a 3-DOF helicopter with actuator faults and saturation." ***IET Control Theory & Applications***, Vol. 11, No. 14, (2017), 2232-2241. DOI: 10.1049/iet-cta.2016.1602.
11. Ma, H.J., Liu, Y., Li, T. and Yang, G.H., "Nonlinear high-gain observer-based diagnosis and compensation for actuators and sensors faults in a quadrotor unmanned aerial vehicle." ***IEEE Transactions on Industrial Informatics,*** Vol. 15, No. 1 (2018): 550-562. DOI: 10.1109/TII.2018.2865522.
12. Amoozgar, M. H., Chamseddine, A., Zhang, Y, "Experimental test of a two-stage Kalman filter for actuator fault detection and diagnosis of an unmanned quadrotor helicopter." ***Journal of Intelligent & Robotic Systems***, Vol. 70, No. 1, (2013), 107-117. DOI: 10.1007/s10846-012-9757-7.
13. Zhong, Y., Zhang, Y., Zhang, W., Zuo, J., Zhan, H, "Robust actuator fault detection and diagnosis for a quadrotor UAV with external disturbances." ***IEEE Access,*** Vol. 6 (2018), 48169-48180. DOI: 10.1109/ACCESS.2018.2867574.
14. Xiao, M., Zhang, Y., Wang, Z., Fu, H, "Augmented robust three-stage extended Kalman filter for Mars entry-phase autonomous navigation." ***International Journal of Systems Science***, Vol. 49, No. 1, (2018), 27-42, DOI: 10.1080/00207721.2017.1397807.
15. Hmida, F. B., Khémiri, K., Ragot, J., Gossa, M, "Three-stage Kalman filter for state and fault estimation of linear stochastic systems with unknown inputs." ***Journal of the Franklin Institute***, Vol. 349, No. 7, (2012), 2369-2388 DOI: 10.1016/j.jfranklin.2012.05.004.
16. McLean, D. "Aircraft flight control systems." ***The Aeronautical Journal***, Vol. 103, (1999), 159-166. DOI: 10.1017/S0001924000064976
17. Barczyk, M. "Nonlinear state estimation and modeling of a helicopter UAV." PhD Thesis, University of Alberta, Canada (2012), DOI: 10.7939/R3732T.
18. Alvarenga, J., Vitzilaios, N. I., Valavanis, K. P., Rutherford, M. J, "Survey of unmanned helicopter model-based navigation and control techniques." ***Journal of Intelligent & Robotic Systems***, Vol. 80, No. 1 (2015), 87-138. DOI: 10.1007/s10846-014-0143-5.

Persian Abstract

چکیده

این مقاله به تخمین حالت و عیب برای سیستمهای تصادفی غیر خطی متغیر با زمان وقتی اطلاعات مربوط به عیب و ورودیهای ناشناخته کاملاً مشخص نیست و در حضور ورودیهای ناشناخته می پردازد. برای این منظور ، فیلتر سه مرحله ای تفاضل مرکزی کالمان فیلتر (RThSCDKF) برای تشخیص و شناسایی خطای مبتنی بر مدل (FDI) در یک هلکوپتر بدون سرنشین در حضور نامعینی توسعه داده شده است. در این سیستم خطاهای عملگر تحت تأثیر یکدیگر قرار می گیرند. روش پیشنهادی در صورت وجود اغتشاشات خارجی ، عیبهای عملگر را تخمین می زند. این مدل می تواند عیب های قفل عملگر و شناور را که بسیار مهم هستند تشخیص می دهد.. در پایان این روش با فیلتر کالمن توسعه یافته سه مرحله ای (ThSEKF) مقایسه می شود. نتایج شبیه سازی نشان می دهد روش پیشنهادی نتایج خوبی داشته و دارای دقت بیشتری نسبت به ThSEKF است.

IJE TRANSACTIONS B: Applications Vol. 34, No. 05, (May 2021) 1297-1304

International Journal of Engineering

Journal Homepage: www.ije.ir

Influence of Process Parameters on the Microstructural Characteristics and Mechanical Properties of Recast Layer Thickness Coating on Die Steel Machined Surface after Electrical Discharge Machining

N. H. Phan*[a], P. V. Dong[a], V. S. Jatti[b], N. C. Tam[a], N. D. Minh[a], N. T. Ly[a], B. T. Tai[a], D. V. Truong[a]

[a] *Hanoi University of Industry, No. 298, Cau Dien Street, Bac Tu Liem District, Hanoi, Vietnam*
[b] *Symbiosis Institute of Technology (SIT), Symbiosis International University (SIU), Pune, Maharashtra, India*

PAPER INFO

Paper history:
Received 11 December 2020
Received in revised form 14 January 2021
Accepted 03 February 2020

Keywords:
EDM
Recast Layer Thickness Coating
Machined Surface

ABSTRACT

The surface layer machined after electrical discharge machining (EDM) is different from it after traditional methods, and studying the surface layer structure machined by this method will contribute significantly to the selection of finishing methods. In this study, the surface layer of SKD61 steel after EDM using copper (Cu) electrode was analyzed. Technological parameters, including discharge current (Ie), pulse on time (Ton), pulse off time (Tof), and voltage (Ue) were used in the study. The minimum recast layer thickness (RLT) was determined using the Taguchi method. The results showed that Ie, Ton, and Tof were significant influences on RLT, and Ue was insignificant. Minimum value of RLT = 3.72 µm at process parameters Ie = 1 A, Ton = 50 µs, Tof = 12 µs, and Ue = 30 V. The machined surface layer after EDM is inconsistent with the workability of the product, and it should be removed from the machined surface.

doi: *10.5829/ije.2021.34.05b.24*

1. INTRODUCTION

Electrical discharge machining (EDM) is widely used to shape the surface of moulds and tools. In this method, the material of the workpiece with any mechanical properties can be processed by the electrode with much lower mechanical properties [1]. This will facilitate overcoming difficulties with the mechanical requirements of tools in traditional machining. However, the EDM machining principle is practiced by the high thermal energy of the sparks to cause the melting and evaporation of the surface material layer of the workpiece and electrode. Therefore, the quality of the machined surface in EDM is also different from it in traditional machining. The white layer on the machined surface should be removed by grinding or polishing [2]. Therefore, the research results to clarify the quality of the surface layer after EDM, and it will make an important contribution to reduce the cost of machining of the surfaces and helping to lower the manufacturing costs of the product.

Surface quality after EDM affects the durability of the mould surface. The mechanical and chemical properties of the white layer on the EDM surface not only affect the surface strength of the product, but it also directly affect the machining productivity and electrode wear in EDM [3]. White layer that form continuously on the workpiece surface during machining tend to lead to increased machining productivity and reduced electrode wear. The type of workpiece material and the different machining methods in EDM (Die sinking EDM or Wire EDM) have little effect on recast layer thickness (RLT) (or white layer thickness) [4]. The energy of the spark is a strong influence on the RLT. Also, besides the energy level of the spark and the type of work (finished or roughed) will strongly influence the hardness of the white layer. The increased spark energy leads to increased hardness of the RLT, and the hardness of the machined surface after

*Corresponding Author Institutional Email: nguyenhuuphan@haui.edu.vn (N. H. Phan)

Please cite this article as: N. H. Phan, P. V. Dong, V. S. Jatti, N. C. Tam, N. D. Minh, N. T. Ly, B. T. Tai, D. V. Truong, Influence of Process Parameters on the Microstructural characteristics and Mechanical Properties of Recast Layer Thickness Coating on Die Steel Machined Surface after Electrical Discharge Machining, International Journal of Engineering, Transactions B: Applications Vol. 34, No. 05, (2021) 1297-1304

roughing is higher than that in finishing. The residual stress that appears in the white layer is the residual tensile stress, and this will adversely affect the workability of the product surface. The white layer of AISI 316SS surface after EDM is the material layer with many phases, of which austenite is the most common, and the residual tensile stress in RLT is quite large [5]. Although the hardness of the surface layer is higher than that of the substrate, its wear resistance is very low. The workpiece surface layer affected by the heat energy of the spark after the EDM consists of 3 layers of RLT, heat affected zone (HAZ), and tempered layer [6]. RLT increased with discharge energy (Ee) increase. The organization of the main phase on the white layer includes martensite and austenite [7]. HAZ is a material layer formed by the phase transition from the substrate, the phase transition temperature is the temperature of the electric spark that has been reduced by transmission through the white layer. The exact size of the RLT and HAZ depends mainly on the technical parameters, and the larger the pulse energy, the larger the size of these layers. Increased spark energy (Ee) will result in an increased RLT, and this effect on the RLT is quite apparent [8]. HAZ is significantly affected by the pulse time (Ton). Increased discharge current (Ie) will cause Ee to be increased, and the phenomena of short circuit and arc discharge are responsible for the increase of surface roughness (SR) and the uniformity of the white layer on the machining surface is reduced [9]. An increase in Ee led to an increase in the size and number of adhesion particles, microscopic cracks, micro-voids, and porosity of the machined surface layer. Micro-cell cracking caused by residual thermal stress, and its size and quantity depend on the machining condition [10-12]. The influence of Ton and Ie on the surface layer of the workpiece and electrode is quite strong [13]. The increase in Ton resulted in a significant increase in the RLT of both the workpiece and the electrode surface. However, the increase in Ie caused a negligible change in their RLT. The radius of the plasma channel will increase with the increase of the discharge time, however, the pulsed thermal energy is impacted on the workpiece surface and the discharge density on the machining surface is reduced [14]. The influence of Ton, Ie on RLT and HAZ of the machining surface after EDM was shown by numerical simulation method combined with research experiment [15]. Results showed that the increase of Ton = 8-25 µs resulted in a large increase in RLT, and Ie = 8- 24 A resulted in a slight decrease in RLT. This is because the change of Ton and Ie leds to the change of the spark energy and the plasma flushing efficiency. The increase in the spark energy leads to the size of the globule and the radius of the craters on the machining surface is larger, and the porosity of the white layer is greater than [16]. The RLT in EDM for Ti-6Al-4V was accurately determined using the RSM method [17]. The Ie, Ton, and Tof all strongly influence the value of RLT. The best technological parameter set for RLT and HAZ is the smallest as determined by the Taguchi method [18]. Taguchi combined with ANFIS was also able to accurately determine the dimensions of the RLT [19]. The results showed that Ie, Ton and Tof strongly influenced RLT and that RLT was smallest at Ie and Ton at the lowest, and Tof was at the highest. The white layer on the machined surface after EDM was precisely determined by modeling by the FEA method [20]. The results showed that the random distribution of the sparks that led to the solid structure of the RLT and HAZ is uneven. Using the same algorithm, FEA showed that layers of materials with different organizations were formed on the workpiece surface by the influence of sparks [21]. This has led to the physical and chemical properties of the RLT layer being different from that of the substrate. Many methods combining simulation with experiment have been introduced to determine the most suitable value of RLT including RSM, Taguchi, ANN, etc [22-24]. However, due to the complexity of the machining mechanism and the level of the technological parameters that vary over a wide range, the results are often influenced by large noise. Therefore, the Taguchi method is still the most commonly used today.

The survey results have shown that the influence of technical parameters on the white surface layer in EDM machining types is different. The value of the RLT of each surveyed case is different, so it is essential to accurately determine the change of RLT and its exact value. In this study, the effects of Ie, Ton, Tof, and Ue on the RLT of the machined surface layer after EDM with Cu electrode were studied. The workpiece is used with SKD61 die steel. Minimum RLT is determined with the respective technology parameter set, and the surface quality has been analyzed and evaluated.

2. THEORY OF THE TEMPERATURE EFFECTS OF DISCHARGES

To this day, precise control of spark formation and maintenance in EDM is not possible. The reason is that the values of these technological parameters are constantly changed during the machining process (see Figure 1) [8]. In practice, determining the exact values of t_d and t_e is impossible because it depends on many factors including surface roughness of the electrode and workpiece, physical and chemical properties of the material, and type of dielectric fluid, conditions in the gap between the electrode and workpiece, etc. In the present calculation, the value of Ton will be chosen to approximate to t_e. This causes the EDM machining mechanism to be unclear, and it also causes difficulty in controlling productivity, machining quality, and machining accuracy in EDM.

The RLT of the surface layer in the EDM depends on the energy of the sparks and the propagation of the thermal energy of the sparks into the machining surface layer. The thermal energy of discharge sparks depends on technological parameters including Ue, Ie, Ton, and Tof [9]. Ue, Ie, and Ton are the parameters that strongly affect the energy of the discharge sparks [19]. The energy of the discharge sparks is determined by Equation (1).

$$E_e = \int_0^{te} u_e(t).i_e(t).dt \approx u_e.i_e.t_{on} \quad (1)$$

The thermal energy of each spark (qe) is determined by Equation (2) [8].

$$E_e = \int_0^{te} u_e(t).i_e(t).dt \approx u_e.i_e.t_{on} \quad (2)$$

where, r_e is the radius of the spark.

The amount of heat transferred to the surface layer of the workpiece is assessed by the coefficient of heat distribution to the surface of the workpiece ωq= qw/qe, Figure 2a. Where qw is the amount of heat transferred to the surface of the workpiece and it is shown in Figure 2b.

Heat propagation into the machining surface layer in EDM is influenced by the thermal and physical properties of the electrode material, the dielectric fluid, and the workpiece material. The greater the thermal conductivity of the electrode and the solvent, the lower the thermal energy in the machining area, and this leads to a decrease in heat transfer to the workpiece surface. Conversely, a good workpiece thermal conductivity will lead to an increase in the heat-affected workpiece surface layer thickness. This has resulted in the machined surface layer after EDM shown in Figure 3 [20]. This change will directly affect the melted and evaporated workpiece quantity, the change of the mechanical and physical characteristics and the surface material layer structure, the topography formation of the machined surface, and machining accuracy. The RLT formed by the electrode material and melted and evaporated workpiece was not pushed out by the dielectric solution to initiate the discharge gap. They combine with the compound of the dielectric solution separated by the spark to form another compound, and they adhere firmly to the machining surface. AHZ layer appears on the surface by the impact of the heat of sparks that leads to phase change of the substrate layer. The RLT after EDM is low, and it must be removed from the surface of the product. The WLT modification study, therefore, contributes to the exact determination of the layer to be removed and reduces the time and cost of the next finishing work.

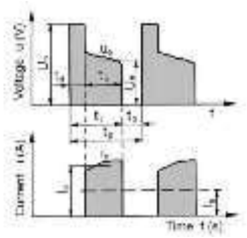

Figure 1. The variation of U and I in EDM. U_o - Open gap voltage, Ue - Discharge voltage, t_d - Ignition delay time, t_e - Discharge duration, t_i (Ton) - Pulse on time, t_o (Tof) - Pulse off time, t_p - pulse cycle time, Ie - Discharge current, I_a - Average current

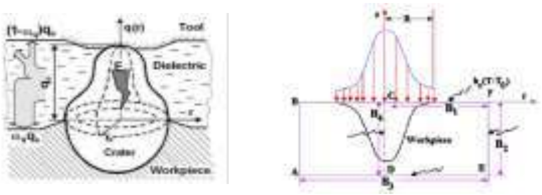

(a) Thermal model in EDM (b) Thermal model imparts to workpiece in EDM

Figure 2. Thermal in EDM

3. EXPERIMENTAL DESIGN

Experimental studies are performed on the CHEMER - EDM machine (CM323C- Taiwan). SKD61 die steel is used as a workpiece and its dimensions are 15 x 15 x 10 mm, and the electrode material is copper (Cu) and its diameter is Ø10 mm. The levels of the technical parameters are selected in EDM finishing, and they are shown in Table 1. The Taguchi method was used to design the matrix of the experiment (L25). The surface layer of the workpiece after EDM was investigated and analyzed for the surface layer structure. Research studies published by Habib et al. [5] have shown that the AHZ is the layer formed has significantly improved the working ability of the templates, and RLT is the layer at the top of the machined surface but it negatively affects the workability of the product (see Figure 4). Therefore, this study to accurately determine the value of RLT, because this will significantly contribute to reducing the cost of material consumption. and finish machining next.

The surface roughness (SR) was measured using a contact probe (SJ-210) type profilometer (MITUTOYO, JAPAN) with an evaluation length of 5 mm. Two measurements were acquired for each test sample and the average value of each measurement was considered. The

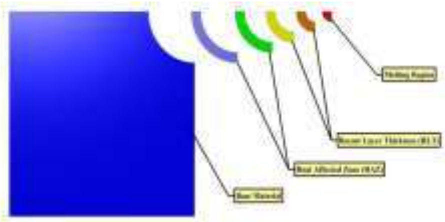

Figure 3. Layers of the machined material on the machined surface after EDM [20]

TABLE 1. Experimental results for the conducted machining trials.

Trial	Ie	Ue	Ton	Tof	RLT(μm)
1	1	30	18	9	4.023
2	1	40	25	12	3.629
3	1	50	37	18	3.277
4	1	60	50	25	4.284
5	1	70	75	37	6.755
6	2	30	25	18	6.199
7	2	40	37	25	6.805
8	2	50	50	37	6.856
9	2	60	75	9	6.552
10	2	70	18	12	5.799
11	3	30	37	37	7.965
12	3	40	50	9	5.243
13	3	50	75	12	4.933
14	3	60	18	18	7.911
15	3	70	25	25	7.430
16	4	30	50	12	4.738

Figure 4. Layer formation on the machined specimen

surface morphology was acquired using a scanning electron microscope (Jeol-6490 JED-2300, JEOL JAPAN) and optical microscope(OPM).

4. RESULT AND DISCUSSION

4. 1. Effect of Process Parameters on WLT Coating

Analysis of variance (ANOVA) of RLT is shown the influence of parameters on RLT (see Tables 2 and 3). Based on the value of the coefficient Fisher (F) showed that process parameters including Ie (F = 13.83), Ton (F = 8.08), and Tof (F = 7.52) are a significant influence on RLT, and Ue (F = 2.44) is insignificant influence on RLT. Where Ie is the most significant influence, Tof is the 2nd most significant influence, and the smallest influence is Ue.

The change of the technological parameters has led to the RLT being altered (see Figures 5-8). The increase in current (Ie) leads to the increase in the energy of the sparks (Ee), and this causes the increase of the RLT, Figure 5. e = 1-3 A, it resulted in the RLT being slightly changed, the cause was that the spark energy was not significantly affected. Therefore, the thermal energy of the sparks causes the amount of electrode material and the workpiece to be melted and evaporated with a small change. RLT has been drastically changed with I = 4-5 A. Compared with the RLT at I = 1A, the RLT at I = 5 A was increased by 179.2%. Ue increase is shown in Figure 6. Ue = 30 - 50 V led to RLT being increased, but when U> 50 V led to a decrease in RLT. The reason this happens is that a change of U leads to altered machining productivity, and this will affect the amount of electrode material and workpiece adhering to the machining surface. RLT is maximum at U = 50 V and it is minimum at U = 30 V. Figures 7 and 8 show the effects of Ton and Tof on RLT, and the influence of these process parameters is contradictory. In theory, an increase in Ton and a decrease in Tof will lead to increase machining productivity, and this leads to an increase in RLT. This could be due to the change of Ton and Tof leading to the increase in the plasma flushing efficiency, and this has

TABLE 2. Analysis of variance for RLT

Factor	DF	SS	V	F	P	Ranking
Ie	4	213.11	53.276	**13.83**	0.001	1
Ue	4	37.53	9.382	2.44	0.132	4
Ton	4	115.79	28.948	**7.52**	0.008	3
Tof	4	124.50	31.126	**8.08**	0.007	2
Error	8	30.81	3.851	-	-	-
Total	24	521.74	-	-	-	-

TABLE 3. ANOVA for S/N ratio of RLT

Factor	DF	SS	V	F	P
Ie	4	215.31	53.827	28.64	0.000
Ue	4	16.40	4.099	2.18	0.162
Ton	4	63.23	15.809	8.41	0.006
Tof	4	104.14	26.036	13.85	0.001
Error	8	15.04	1.879	-	-
Total	24	414.12	-	-	-

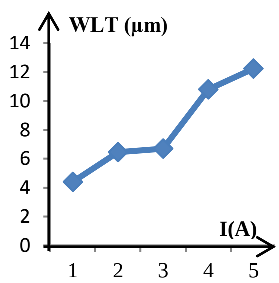

Figure 5. Effect of Ie on RLT

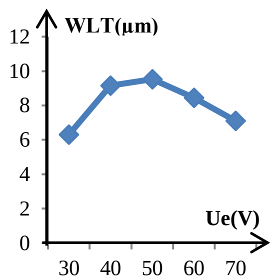

Figure 6. Effect of Ue on RLT

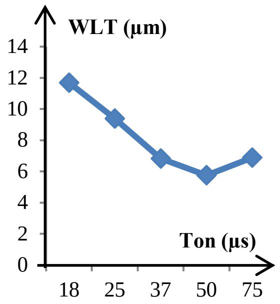

Figure 7. Effect of Ton on RLT

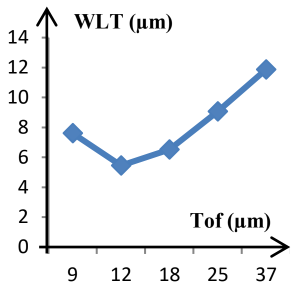

Figure 8. Effect of Tof on RLT

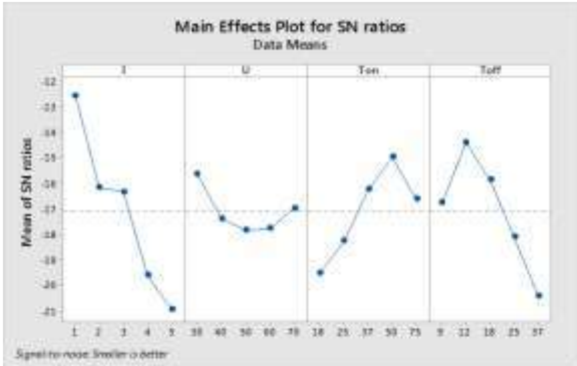

Figure 10. Effect of process parameters on S/N ratio of RLT

resulted in the molten and evaporated mass of the workpiece and the electrode being ejected from the crater easier [15]. Hence the amount of material deposited on the machining surface is reduced, and it leads to a decrease in RLT. The Ton that is too large will lead to the predominant time to pulse during machining, thus the time to eject the dielectric fluid and chip from the discharge gap is also reduced, and the time for the dielectric fluid to recover is very short. This will lead to an unstable machining process and multiple short-circuit pulses, and local arcing so the RLT is small. Hence, the RLT is unevenly distributed on the machining surface, Figure 9. Increased Tof can lead to increased machining productivity, and RLT increased accordingly. RLT is minimum at Ton = 50 µs and at Tof = 12 µs.

4. 2. Determine the Optimal Value of RLT The RLT is formed on the machined surface layer after EDM, which needs to be removed by the next finishing method. Therefore, the S / N coefficient of RLT is "*The lower is better*". The ANOVA result of S / N of the RLT is shown in Table 4, and the confidence interval of the ANOVA result of the S / N is 95%. The results showed that Ie (F = 28.64), Tof (F = 13.85), and Ton (F = 8.41) are parameters that significantly affect the S / N ratio of RLT. It is the basis to build the formula to determine the optimal value of RLT (RLTopt), and significant parameters including Ie, Ton, and Tof were used to determine RLTopt. Figure 10 shows the optimal technology parameters including Ie = 1A; Ton = 50µs, Tof = 12µs; Ue = 30 V. The optimal value of RLT is determined by formula (3), the calculation results of RLToptcal = 3.50 µm. Verifying the experiment with the

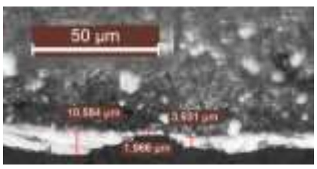

Figure 9. RLT of a machined surface at Ton = 50 µs

optimal parameters has identified RLTopt = 3.72 µm, and the difference between calculation results and experimental results is only 6.21%. This proves that the computational model can accurately predict RLT.

$$RLTopt = I1 + Ton4 + Tof2 - 2.T \quad (3)$$

4. 3. Surface Topography Analysis of Machined Surface The machined surface is composed of many craters and micro-voids, and they are arbitrarily distributed, Figure 11. This is because the energies of the sparks are randomly generated and arbitrarily distributed in the machining area. The material layer of the workpiece surface and electrode is caused by the enormous thermal energy of the electric sparks (8000-12000 ^{0}C) to melt and evaporate, and it is immediately cooled by a dielectric fluid [3]. Consequently, many of the globules and debris are adhered to the machining surface, Figure 12. The external surface tension of the dielectric solution causes the geometry of craters and particles to adhere to the radius of curvature or spherical. Adhesion particles are formed when the material is melted and evaporated. Therefore, he adhesion strength of the particles to the machining surface can be in the form as shown in Figure 13. The machining characteristics of EDM differ from that of traditional machining, and it has resulted in the profile of the machined surface layer after EDM being very complex, Figure 14. This is directly related to the method used and the finishing cost. A lot of microscopic cracks appeared on the workpiece surface after EDM, Figure 15. This is because the electrode and workpiece material on the workpiece surface at very high temperatures cools very quickly, and residual thermal stress occurs at the surface layer appears [3]. Any cracks distributed on the machined surface and depth developed in a direction perpendicular to the machined surface, Figure 16. The depth of microscopic cracking is approximately equal to that of RLT, and micro-voids also exist in RLT. EDS of the post-EDM surface layer showed that % C was greatly increased (≈ 8.84%) and a sizable amount of % Cu appeared on the surface layer, Figure 17. The increase in % C is because the oil dielectric solution is cracking by the thermal energy of the sparks, and the increase of % Cu is due to molten and evaporation of the material on the electrode surface having penetrated the machined surface. The appearance of these elements under high - temperature conditions has led to a change in the composition of the element compounds and phases at the machined surface layer, Figure 18. Since a sizeable amount of element C is diffused into the machining surface layer, it combines with element Fe and some alloying elements in steel SKD61 to form the carbides including Fe2C, Fe3C, Fe7C3, V8C7, and Mo3C7. This led to a change in the physical and chemical properties of the surface layer, and the hardness of RLT was smaller than that of HAZ and base metal, Figure 19. The reason may be that the majority of the white layer formed phases are austenites [15]. This will affect the product's ability to work. The thickness of RLT at the optimum condition is shown in Figure 20. Although the distribution has been significantly improved, the uniformity of this layer on the machined surface is still very low. This makes it more difficult to choose the correct removal thickness for the next finishing.

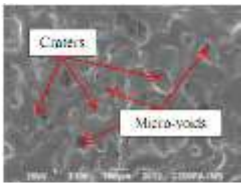

Figure 11. EDM surface morphology

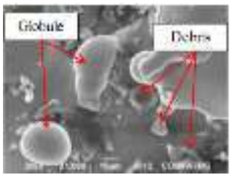

Figure 12. Surface texture after EDM

Figure 13. Globule formation and residue of melted material in recast layer

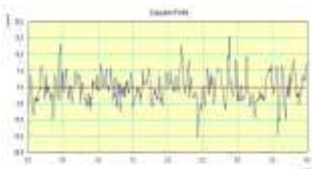

Figure 14. Profile of the machined surface

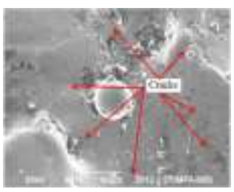

Figure 15. Cracks distribution

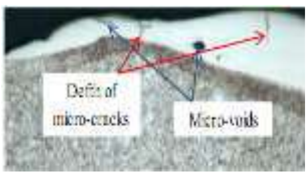

Figure 16. Recast layer and heat-affected zone induced by EDM

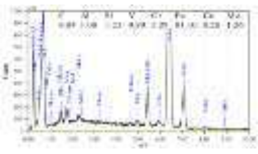

Figure 17. EDS elemental analysis of surface after EDM

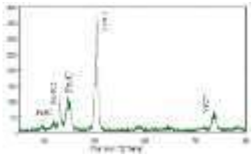

Figure 18. XRD pattern of a machined surface

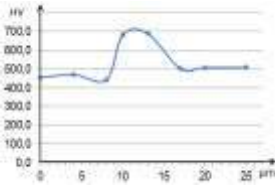

Figure 19. Profile of micro-hardness on the EDMed surface

Figure 20. Recast layer thickness on a machined surface

4. CONCLUSION

In the present study, the surface layer of the SKD61 die steel in EDM using Cu electrode on machining SKD61 was analyzed and evaluated. From the experimental investigation, the following conclusions were made.

➢ Peak Current (Ie) is the most significant influence and Ue is the insignificant influence on surface morphology.

➢ The minimum RLT was found at Ie = 1 A, Ton = 50 µs, Tof = 12 µs and Ue = 30 V with the unevenly distributed thickness of the white layer on the machining surface.

➢ The removed layer thickness of the machining surface in EDM is to be approximately 2-3 times greater than that of the RLTopt.

➢ The main research directions include integrating vibration into the EDM process can lead to the smallest RLT and the size of the RLT to be more uniform.

➢ The utilization of suitable powder mixed in the dielectric fluid in EDM can reduce the size of the RLT considerably.

5. ACKNOWLEDGMENT

This research is funded by the Ministry of industry and trade of the socialist republic of Viet Nam.

6. REFERENCES

1. Sinval, P.S., Alexandre, M.A., Peter, G.W., Ernane, R.S., Marcelo, A.C., "Investigation of nitride layers deposited on annealed AISI H13 steel by die-sinking electrical discharge machining", ***The International Journal of Advanced Manufacturing Technology,*** Vol. 109, (2020), 2325-2336. DOI: 10.1007/s00170-020-05784-y

2. Rodrigo, P. Z., Thiago, V., Fernando, M. Z., Mariana, C., "Metallurgical alterations in the surface of steel cavities machined by EDM", ***Revista Matéria***, Vol. 18, No. 04, (2013), 1541-1548. DOI: http://dx.doi.org/10.1590/S1517-70762013000400014
3. José, D.M., "EDM performance is affected by the white layer", Proceedings of the 36th International MATADOR Conference, (2010), 419-423.
4. Boujelbene, M., Bayraktar, E., Tebni, W., and Salem, S.B., "Influence of machining parameters on the surface integrity in electrical discharge machining", ***Archives of Materials Science and Engineering***, Vol. 37, No. 2, (2009),110-116.
5. Habib, S., Farhat, G., Tidiane, A., Gonzalo, G., Chedly, B., "Effect of electro discharge machining (EDM) on the AISI316L SS white layer microstructure and corrosion resistance", ***The International Journal of Advanced Manufacturing Technology***, Vol. 65, No. 1-4, (2013), 141-153. DOI: https://doi.org/10.1007/s00170-012-4156-6
6. Rafał, Ś., and Radovan, H., "Experimental investigation of influence electrical discharge energy on the surface layer properties after EDM", ***Welding Technology Review***, Vol. 92, No. 5, (2020). DOI: 10.26628/wtr.v92i5.1115.
7. Mohammad, S. M., "Recast layer and heat-affected zone structure of ultra-fined grained low carbon steel machined by electrical discharge machining", ***Journal of Engineering Manufacture***, Vol. 1-12, (2019), 933-944. DOI: https://doi.org/10.1177/0954405419889202
8. Gostimirovic, M., Kovac, P., Sekulic, M. et al. "Influence of discharge energy on machining characteristics in EDM". ***Journal of Mechanical Science and Technology,*** Vol. 26, No. 1 (2012), 173-179. https://doi.org/10.1007/s12206-011-09221-x
9. Feng, Y., and GuoYongfeng, L.Z., "Experimental Investigation of EDM Parameters for TiC/Ni Cermet Machining", **Procedia CIRP**, Vol. 42, (2016), 18-22. DOI: https://doi.org/10.1016/j.procir.2016.02.177
10. Karmiris, O., Zagórski, P., Papazoglou, K. E. L. "Surface texture and integrity of electrical discharged machined titanium alloy." ***The International Journal of Advanced Manufacturing Technology***, (2020) 1-15. DOI: https://doi.org/10.1007/s00170-020-06159-z
11. Qosim. N, Supriadi. S, Puspitasari. P, Kreshanti. P, *Mechanical Surface Treatments of Ti-6Al-4V Miniplate Implant Manufactured by Electrical Discharge Machining*, ***International Journal of Engineering, Transactions A: Basics***, Vol. 31, No. 7, (2018), 1103-1108. DOI: 10.5829/ije.2018.31.07a.14
12. Patel. Ss, and Prajapati, Jm, *Experimental Investigation of Surface Roughness and Kerf Width During Machining of Blanking Die Material on Wire Electric Discharge Machine*, ***International Journal of Engineering, Transactions A: Basics,*** Vol. 31, No. 10, (2018), 1760-1766. DOI: 10.5829/ije.2018.31.10a.19
13. Mohammadreza, S., Reza, A., Mirsadegh, S., Samad, N. B. O., "Mathematical and numerical modelling of the effect of input-parameters on the flushing efficiency of plasma channel in EDM process", ***International Journal of Machine Tools & Manufacture***, Vol. 65, (2013) 79-87. DOI: https://doi.org/10.1016/j.ijmachtools.2012.10.004
14. Saeed, A., and Majid, G., "Electro-thermal-based finite element simulation and experimental validation of material removal in static gap single-spark die-sinking electro-discharge machining process", ***Journal of Engineering Manufacture***, Vol. 231, No. 1, (2017), 28-47. DOI: 10.1177/0954405415572661
15. Shabgard, M., Oliaei, S. N. B., Seyedzavvar, M., "Experimental investigation and 3D finite element prediction of the white layer thickness, heat affected zone, and surface roughness in EDM process", ***Journal of Mechanical Science and Technology***, Vol. 25, (2011), 3173-3183. https://doi.org/10.1007/s12206-011-0905-y
16. Markopoulos, A. P., Papazoglou, E. L., and Karmiris, O. P., "Experimental Study on the Influence of Machining Conditions on the Quality of Electrical Discharge Machined Surfaces of aluminium alloy Al5052", ***Machines,*** Vol. 8, No. 12, **(**2020). DOI: https://doi.org/10.3390/machines8010012
17. Jun, L., Xiaoyu, L., and Shiping, Z., "Prediction model of recast layer thickness in die-sinking EDM process on Ti-6Al-4V machining through response surface methodology coupled with least squares support vector machine", ***Computer Modelling & New Technologies***, Vol. 18, No. 7, (2014), 398-405.
18. Najm, V.N., "Experimental Investigation of Wire EDM Process Parameters on Heat Affected Zone", ***Engineering and Technology Journal***, Vol. 36, No. 1, (2018), 64- 65.
19. Maher, I., Sarhan, A. A. D., Marashi, H., Barzani, M. M. Hamdi, M., "White layer thickness prediction in wire-EDM using CuZn-coated wire electrode - ANFIS modelling", ***Transactions of the IMF***, Vol. 94, No. 4,(2016), 204-210.
20. Liu, J.F., and Guo, Y.B., "Modeling of White Layer Formation in Electric Discharge Machining (EDM) by Incorporating Massive Random Discharge Characteristics", ***Procedia CIRP***, Vol. 42, (2016), 697-702. DOI: https://doi.org/10.1016/j.procir.2016.02.304
21. Mohd, A. B. L., and Ghassan, S. A. R., "A new methodology for predicting quantity of agglomeration between electrodes in pmedm environment", ***International Journal of Mechanical Engineering and Technology***, Vol. 10, No. 2, (2019), 1461-1480
22. Hesam, S., Yazdi, M. R. S., Aminollah, M., Ehsan, I., "Optimization of surface roughness and thickness of white layer in wire electrical discharge machining of DIN 1.4542 stainless steel using micro-genetic algorithm and signal to noise ratio techniques", ***Journal of Engineering Manufacture***, Vol. 226, No. 5, (2012), 803-812. https://doi.org/10.1177/0954405411434234
23. Yousefpour, M., Vali, I., and Saebnoori, E., "Surface Activation of NiTi Alloy By Using Electrochemical Process For Biomimetic Deposition Of Hydroxyapatite Coating", ***International Journal of Engineering, Transactions A: Basics***, Vol. 27, No. 10, (2014), 1627-1634. DOI: 10.5829/idosi.ije.2014.27.10a.17
24. Farrahi, G. H., Kashyzadeh, K. R., Minaei, M., Sharifpour, A., Riazi, S., "Analysis of resistance spot welding processnparameters effect on the weld quality of three-steel sheets used in automotive industry: Experimental and Finite element simulation", ***International Journal of Engineering, Transactions A: Basics,*** Vol. 33, No. 1, (2020), 148-157.

Persian Abstract

چکیده

لایه سطحی ماشین کاری شده پس از ماشینکاری تخلیه الکتریکی (EDM) عد از روش های سنتی با آن متفاوت است و مطالعه ساختار لایه سطحی ماشین کاری شده با این روش به طور قابل توجهی در انتخاب روش های اتمام کمک می کند. در این مطالعه ، لایه سطحی فولاد SKD61 پس از EDM با استفاده از الکترود مس (Cu) مورد تجزیه و تحلیل قرار گرفت. پارامترهای فن آوری ، از جمله جریان تخلیه (IE)، پالس در زمان (تن) ، زمان پالس (Tof)، و ولتاژ (Ue) در مطالعه استفاده شد. حداقل ضخامت لایه بازسازی ((RLT) با استفاده از روش تاگوچی تعیین شد. نتایج نشان داد که Ie، Ton و Tof تأثیر قابل توجهی بر RLT دارند و Ue ناچیز است. حداقل مقدار RLT = 3.72 میکرومتر در پارامترهای فرآیند Ie = 1 A، Ton = 50 میکرو ثانیه ، Tof = 12 میکرو ثانیه و Ue = 30 ولت از سطح ماشینکاری شده برداشته شود.

IJE TRANSACTIONS B: Applications Vol. 34, No. 05, (May 2021) 1305-1312

International Journal of Engineering

Journal Homepage: www.ije.ir

Multi-objective Optimization of HMGF Process Parameters for Manufacturing AA6063 Stepped Tubes using FEM-RSM

M. Rajaee[a], S. J. Hosseinipour*[b], H. Jamshidi Aval[b]

[a] *Department of Mechanics, Faculty of Neyshabour, Khorasan Razavi Branch, Technical and Vocational University, Neyshabour, Iran*
[b] *Research Center for Advanced Processes of Materials Forming, Babol Noshirvani University of Technology, Babol, Iran*

PAPER INFO

Paper history:
Received 11 December 2020
Received in revised form 16 March 2021
Accepted 26 March 2021

Keywords:
AA6063 Alloy Tube
Hot Metal Gas Forming
Response Surface Methodology
Finite Elements Analysis
Optimization

ABSTRACT

In this paper, the loading path was optimized in hot metal gas forming (HMGF) process for making AA6063 cylindrical stepped tubes. For this purpose, the response surface method (RSM) and finite element method (FEM) were applied using Design-Expert and ABAQUS softwares, respectively. The parameters of internal pressure, pressure rate, axial feeding, and punch speed were examined based on the central-composite design in the three levels. The maximum die filling and the minimum tube thinning percentages were selected as the objective functions. The analysis of variance showed that the axial feeding, internal pressure, and their interaction were the most significant parameter in the die filling and tube thinning. The optimum loading path at the temperature of 550 °C was obtained at pressure of about 7 bars, pressure rate of 0.01 bar/s, axial feeding of 7 mm from each side and punch speed of 0.02 mm/s. Experimental tests were performed for the specified process parameters. The numerical results were validated by experimental testing.

doi: *10.5829/ije.2021.34.05b.25*

1. INTRODUCTION

Although the deformation of high-strength and lightweight alloys are difficult, their applications are widely expanded in various industries, including the aerospace and automotive industries [1-5]. Hot metal gas forming (HMGF) is a high temperature forming processes, which serves for forming metal sheets and tubes using gas with low pressure. This technique is used for the deformation of alloys that have limited formability at ambient temperature [6, 7]. Paul et al. [8] developed a one-step HMGF process to produce an exhaust component made of titanium grade 2. Mosel et al. [9] described a process chain for the HMGF process to produce exhaust components made of ferritic stainless steel 1.4509. Talebi-Anaraki et al. [10] used a flame heating technique for forming aluminum alloy tubes by HMGF process. Rajaee et al. [11] showed that the effect of HMGF parameters on the deformation behavior is complicated, and it is necessary to obtain their optimal range. Response surface methodology (RSM) is one of the modeling methods, which uses mathematical and statistical techniques, leading to the reduction of costly experimental tests and the prediction of the optimized trend of the process. Many research works were carried out using this method to optimize parameters in various processes [12, 13]. Here are a few of them on the subject of forming metal tubes. Alaswad et al. [14] investigated the effect of geometric parameters on tube thickness and protrusion height in the hydroforming process of a T-shaped two-layer tube. The finite element model and RSM were used in this research. Chebbah et al. [15] optimized the loading path in the tube hydroforming process using a reverse finite element simulation method and RSM based on scattering approximation. The optimization purpose was to minimize the probability of some defects like necking and wrinkling. To search the global optimum of the objective function, they used the sequential quadratic programming (SQP) algorithm. Kadkhodayan et al. [16] determined the mathematical

*Corresponding Author Institutional Email: *j.hosseini@nit.ac.ir* (S. J. Hosseinipour)

Please cite this article as: M. Rajaee, S. J. Hosseinipour, H. Jamshidi Aval, Multi-objective Optimization of HMGF Process Parameters for Manufacturing AA6063 Stepped Tubes using FEM-RSM, International Journal of Engineering, Transactions B: Applications Vol. 34, No. 05, (2021) 1305-1312

model between force variables and ductility using statistical analysis and the simulation of the tube hydroforming process. They acquired optimal loading curves for the production of T-shaped parts by applying the mathematical models initiated from an evolution algorithm. Safari et al. [17] maximized the convolution height and thickness of bellows congress parts by applying the mathematical models initiated from RSM. They reported that an increase in the convolution height and decrease in the thickness of the top point of bellows congress will occur by increasing the internal pressure and die stroke. Ahmadi Brooghani et al. [18] used a statistical manner established upon finite element simulation to find the optimal loading path. The exact finite element model of the forming process was prepared, and the created model verified in comparison with the experimental specimen. Huang et al. [19] optimized the loading path in the hydroforming of a T-shaped tube based on the response surface and non-probabilistic methods. The purpose of this research was to achieve the maximum protrusion and minimum thinning ratio with optimization of pressure path. Ge et al. [20] recommended a multi-objective optimization method for determining the parameters related to the hydroforming process of the tube using a differential evolution algorithm. They used several finite element simulations to set up a least-squares support vector machine-based on response surface model.

Studies show that little research carried out to find the optimal loading path of the HMGF process, and also most of the research was done on the tubes with specific geometrical properties. In this paper, optimization was performed using RSM and FEM to obtain the highest die filling and lowest tube thinning percentages for fabricating AA6063 cylindrical stepped tubes by the HMGF process.

2. MATERIALS AND METHODS

2. 1. Process Description and Simulation

AA6063 tube with a diameter of 25 mm and a thickness of 1.3 mm was employed. Figure 1 shows the die geometry, which the die diameter was 32 mm, and the length of the deformation zone was 60 mm. The axial feeding was carried out from the both sides of the die by two step-motors, and an air compressor was used to applying internal pressure. Uniform heating was created by applying resistance heaters inside the die and tube.

As shown in Figure 2, a one-fourth model was considered to simulate the process with ABAQUS finite element software. The tube was modeled deformable by C3D8R element with a mesh size of 1×1×0.43 mm^3, and the die was modeled as discrete rigid by R3D4 element. A distributed load was used to apply the effect of gas pressure, and the process was considered as an isotherm process. A friction coefficient of 0.5 was used for contact surfaces [21, 22]. More details about the experiments and simulations are found in literature [10].

2. 2. Response Surface Methodology (RSM)

RSM was used to optimize the process parameters. The level of variables was specified, and then a matrix of the experiments was obtained based on the standard models. Afterward, the quadratic regression model and the mutual effect of the parameters were estimated using the analysis of variance (ANOVA). Finally, the optimal model was identified.

The process parameters, including internal pressure, pressure rate, axial feeding, and punch speed, were selected as independent variables. The forming temperature was constant at 550 °C during the process. The first objective function was the highest die filling percentage, which was defined as follows:

$$\mathrm{Obj_{filling}}\ (\%) = \frac{V_s}{V_d} \times 100 \quad (1)$$

where V_d and V_s denoted the volume of the die and the specimen, respectively. The second objective function was the lowest tube thinning percentage, which was defined as follows:

$$\mathrm{Obj_{thining}}\ (\%) = \frac{t_0 - t_{min}}{t_0} \times 100 \quad (2)$$

where t_0 and t_{min} were the initial and minimum thickness of the tube, respectively.

Design-Expert software was used for the test design. Table 1 presents the independent variables, which

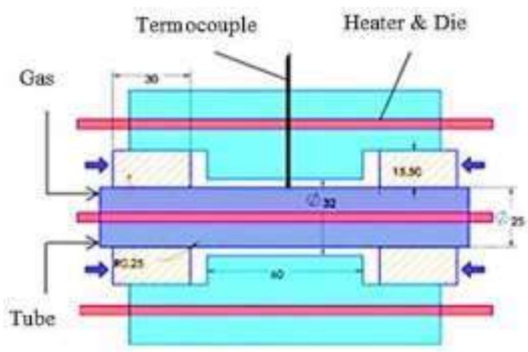

Figure 1. The die geometry, heaters, and tube (dimension in mm)

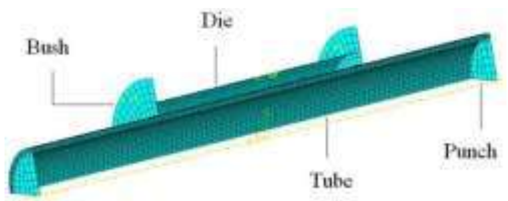

Figure 2. Finite element simulation model

evaluated at three levels based on the central composite design (CCD), and the matrix related to the test design is presented in Table 2.

3. RESULTS AND DISCUSSION

3. 1. Statistical analysis Twenty five tests were obtained considering four continuous variables, including pressure, pressure rate, axial feed on each side, and punch speed, where the results are reported in Table 2. The diagrams related to the main effect of the four variables mentioned above on the die filling percentage and the thinning percentage can be observed in Figure 3. For the die filling percentage, the effect of the axial feed on each side was positive, meaning that by increasing this variable, the filling percentage is increased. The material flow to the die is facilitated by increasing the axial feed, causing the filling percentage to be increased. When the punch speed and pressure rate increased, the material flow does not have sufficient time to enter the die; therefore, the filling percentage is reduced. Increasing the pressure up to 7 bars leads to the enhancement of the die filling. However, increasing the pressure more than 7 bars leads to the collision of the tube with the die wall, and as a result of the generated friction, the filling percentage will decrease. About the effects of the pressure and axial feed on the thinning percentage, it can be seen that the effects of these two parameters on the thinning percentage are similar, meaning that the thinning percentage will increase first, and then, it will decrease by increasing these two parameters. Increasing

TABLE 1. The studied variables and their levels

Forming Parameters	Symbol	-1	0	1
Pressure (bar)	P	5	7	9
Pressure Rate (bar/s)	Ṗ	0.01	0.03	0.05
Axial feed (mm)	X	0	3.5	7
Punch speed (mm/s)	V	0.01	0.03	0.05

TABLE 2. The design matrix of experiments

No.	P (bar)	Ṗ (bar/s)	X (mm)	V (mm/s)	Filling (%)	(%)	Condition
1	5	0.01	0	0.01	-	-	Not filled
2	9	0.01	0	0.01	27.4	10.8	Ruptured
3	5	0.05	0	0.01	-	-	Not filled
4	9	0.05	0	0.01	11.58	4.97	Ruptured
5	5	0.01	7	0.01	82.72	8.98	Accepted
6	9	0.01	7	0.01	84.39	9.12	Accepted
7	5	0.05	7	0.01	89.22	14.62	Accepted
8	9	0.05	7	0.01	18.74	2.39	Ruptured
9	5	0.01	0	0.05	-	-	Not filled
10	9	0.01	0	0.05	27.77	11.2	Ruptured
11	5	0.05	0	0.05	-	-	Not filled
12	9	0.05	0	0.05	9.42	3.67	Ruptured
13	5	0.01	7	0.05	42.41	-0.02	Wrinkled
14	9	0.01	7	0.05	68.95	7.16	Wrinkled
15	5	0.05	7	0.05	72.67	4.3	Accepted
16	9	0.05	7	0.05	71.23	6.38	Ruptured
17	5	0.03	3.5	0.03	32.98	4.32	Accepted
18	9	0.03	3.5	0.03	79.28	8.46	Accepted
19	7	0.01	3.5	0.03	73.58	14.21	Accepted
20	7	0.05	3.5	0.03	69.27	12.26	Accepted
21	7	0.03	0	0.03	15.81	7.82	Accepted
22	7	0.03	7	0.03	81.98	6.44	Accepted
23	7	0.03	3.5	0.01	82.84	14.57	Accepted
24	7	0.03	3.5	0.05	73.04	13.04	Accepted
25	7	0.03	3.5	0.03	71.32	10.6	Accepted

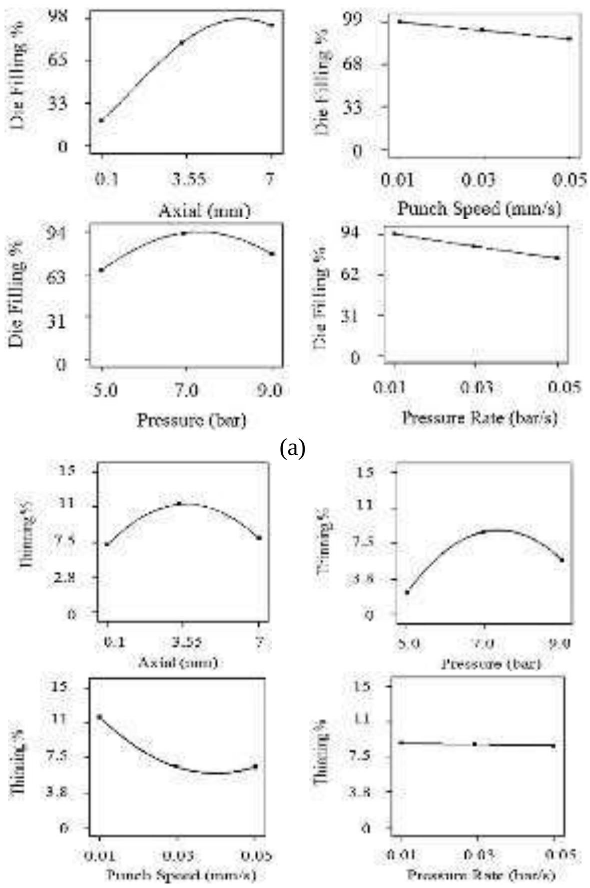

Figure 3. The effect of HMGF parameters on; a) die filling percent, and b) thinning percent

the pressure leads to the deformation of the tube inside the die cavity. Therefore, the thinning percentage of the die in the die cavity area will increase. However, due to the collision of the tube to the die surface, with a further increase in the pressure, the material flow becomes more difficult, and the thinning percentage will be reduced. Due to the formation of wrinkles in the tube, the excessive increase in the axial feed prevents the material to flow easily during the forming process, and the thinning percentage decrease. As can be seen, while the impact of the pressure applying speed on the thinning percentage is insignificant, the thinning percentage decreased by increasing the punch speed due to the generation of non-uniform flows inside the tube.

The results of the statistical investigation on the filling percentage based on different models are presented in Table 3. P-value is used to make sure of the accuracy of the model. The smaller the P-value (the significance value), the better the result fitting of the proposed model. Models and parameters that have P values less than 0.05 can statistically predict the data with errors of less than 5%. Due to the P-value, the quadratic equation was chosen as the most convenient model for the data fitting. Also, some of the statistical data related to the mentioned model, such as the coefficient of determination and the standard deviation, are briefly shown. If two parameters have equal significance value, the parameter that has a higher F-value (the test statistic) is more important. In Table 4, the results of the statistical investigation on the thinning percentage based on different models are presented. Here, the quadratic equation was also chosen as the most convenient model for the data fitting due to the P-value.

After choosing the quadratic equation as the proper model for the die filling, the ANOVA variance analysis was carried out, where the results are shown in Table 5.

TABLE 3. Statistical data of filling percentage based on different models

Source	SS	DF	MS	F value	P value	
Mean vs Total	1297.08	1	1297.08			
Linear vs Mean	142.41	4	35.6	8.33	0.0002	
2FI vs Linear	30.47	6	5.08	1.26	0.3204	
Quadratic vs 2FI	66.32	4	16.58	24.57	< 0.0001	Suggested
Cubic vs Quadratic	9.22	8	1.15	8.92	0.0046	Aliased
Residual	0.9	7	0.13			
Total	1546.4	30	51.55			

TABLE 4. Statistical data of thinning percentage based on different models

Source	SS	DF	MS	F value	p value	
Mean vs Total	1755.49	1	1755.49			
Linear vs Mean	105.66	4	2.64E+1	1.28	0.3046	
2FI vs Linear	184.2	6	3.07E+1	1.76	0.1622	
Quadratic vs 2FI	279.39	4	69.85	19.92	< 0.0001	Suggested
Cubic vs Quadratic	4.4E+1	8	5.53E+0	4.61	0.0294	Aliased
Residual	8.4E+0	7	1.20E+0			
Total	2377.3	30	79.24			

It can be observed that the two linear effects of pressure (P), and axial feeding (X) as well as their quadratic effects, and the two mutual effects of PX and $P\dot{P}$ are meaningful to the die filling. According to the ANOVA results, the parameters of axial feeding (X) and the mutual effect of PX have the most significant impact on the die filling. The obtained results indicated that the fitted quadratic model corresponds to the experimental data with a reliability coefficient of more than 93% (R^2>93). After statistical analysis of the simulated data, the mathematical model (Eq. 3) presented using the four parameters, including pressure, pressure rate, axial feed on each side, and punch speed, to predict the value of the filling percentage.

$$(\%\ \text{Die Filling})^{0.5} = -17.69 + 5.40\,P + 73.52\,\dot{P} + 3.05\,X - 103.28\,V - 17.33\,P\dot{P} - 0.15\,PX + 10.10\,PV + 975.91\,\dot{P}V - 0.31\,P^2 - 0.17\,X^2 \quad (3)$$

Also, after selecting the quadratic model as the proper model for the thinning percentage, the ANOVA variance analysis was carried out, where the results are given in Table 6. It is seen that the three linear effects of pressure (P), axial feeding (X), and punch speed (V) as well as their quadratic effects, and the three mutual effects of $P\dot{P}$, PX, and PV are meaningful to the tube thinning. According to the ANOVA results, the parameters of pressure (P) and the mutual effect of PX have the most significant impact on the tube thinning. Moreover, after the statistical analysis of the simulated data, the following mathematical model is presented to predict the thinning percentage.

$$\%\ \text{Thinning} = -59.48 + 18.80\,P + 250.91\,\dot{P} + 4.74617\,X - 634.55\,V - 48.25\,P\dot{P} - 0.29\,PX + 31.88\,PV + 14.35\,\dot{P}X - 14.78\,XV - 1.17\,P^2 - 0.33\,X^2 + 6814.91\,V^2 \quad (4)$$

TABLE 5. The ANOVA results for the die filling percentage

	SS	DF	MS	F Value	P Value
Model	238.86	10	23.89	43.37	< 0.0001
P	9.79	1	9.79	17.78	0.0005
Ṗ	2.48	1	2.48	4.50	0.0474
X	130.07	1	130.07	236.17	< 0.0001
V	0.076	1	0.076	0.14	0.7140
PṖ	7.69	1	7.69	13.97	0.0014
PX	17.54	1	17.54	31.85	< 0.0001
PV	2.61	1	2.61	4.75	0.0421
ṖV	2.44	1	2.44	4.43	0.0489
P^2	5.14	1	5.14	9.33	0.0065
X^2	14.18	1	14.18	25.75	< 0.0001
Residual	10.46	19	0.55		
Lack of Fit	10.46	14	0.75		
Pure Error	0.000	5	0.000		
Cor Total	249.32	29			
				R^2 =95.8 %	
				R^2(adj) = 93.59 %	

Confirmation charts were utilized to determine the suitability of the filling percentage and thinning percentage regression models. Figure 4 shows the images of the actual values and the predicted values for each response. The straight line with a 45-degree angle represents the model, and the square dots represent the results obtained from the tests. The closer the dots to the line, the higher the accuracy of the model. This diagram confirms that the selected model describes the experimental values relatively well because the dots are around a line with a constant slope.

TABLE 6. The ANOVA results for the tube thinning percentage

	SS	DF	MS	F Value	P Value
Model	561.52	12	46.79	13.19	< 0.0001
P	52.93	1	52.93	14.92	0.0013
Ṗ	9.29	1	9.29	2.62	0.1241
X	21.71	1	21.71	6.12	0.0242
V	21.73	1	21.73	6.12	0.0242
PṖ	59.60	1	59.60	16.80	0.0007
PX	65.71	1	65.71	18.52	0.0005
PV	26.02	1	26.02	7.33	0.0149
ṖV	15.68	1	15.68	4.42	0.0508
XV	16.64	1	16.64	4.69	0.0449
P^2	62.42	1	62.42	17.59	0.0006
X^2	44.39	1	44.39	12.51	0.0025
V^2	21.09	1	21.09	5.94	0.0260
Residual	60.33	17	3.55		
Lack of Fit	60.33	12	5.03		
Pure Error	0.000	5	0.000		
Cor Total	621.84	29			
					R^2 =90.94 %
					R^2(adj)= 86.47 %

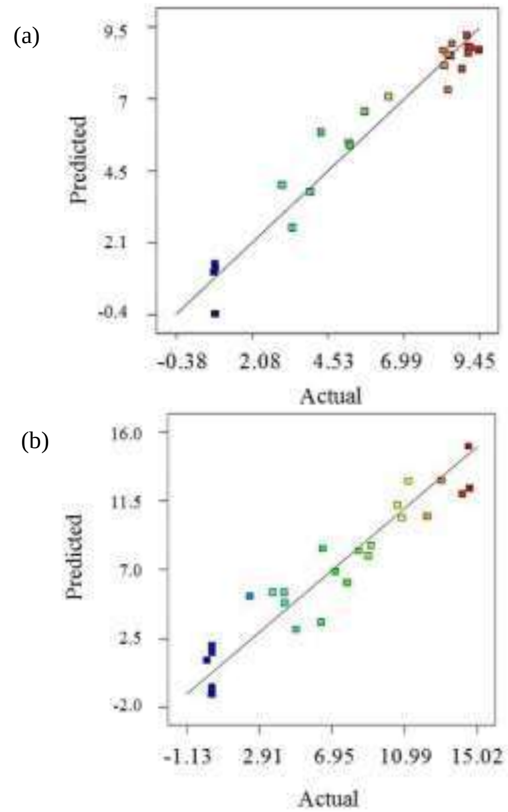

Figure 4. The predicted values of the regression model based on the actual values for; a) the filling percentage of the die, and b) the thinning percentage of the tube

3. 2. Mutual effect of parameters Fig. 5 shows the mutual effect of PX and PṖ on the die filling and tube thinning. Figure 5a indicates the effect of axial feeding on the die filling percentage is enhanced by increasing the pressure. The reason is that the probability of wrinkling due to increasing the axial feeding is reduced by increasing the pressure. The response surface is dome-shaped shown in Figure 5b, which means that the highest tube thinning is obtained at the center of the surface. Increasing the internal pressure increases the tube thinning, while increasing the axial feeding decreases the tube thinning [10]. Figures 5c and 5d indicate that at low pressure, increasing the pressure rate has no significant effect on the die filling, while it increases the tube thinning sharply. However, at high pressure, increasing the pressure rate decreases both the die filling and tube thinning. It can be due to increasing the probability of bursting at the initial of the deformation.

3. 3. Optimization Optimization was performed to obtain the maximum die filling and the minimum tube

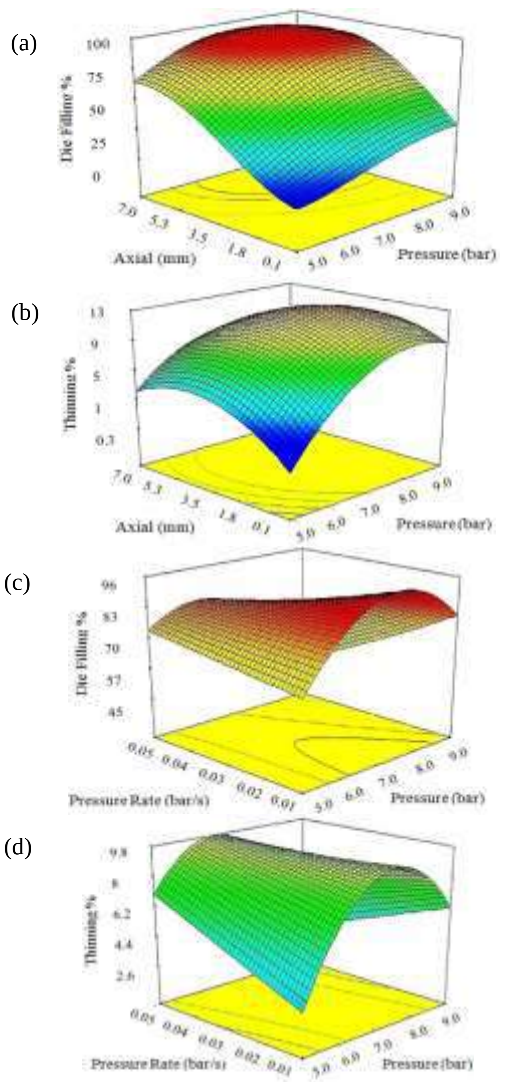

Figure 5. Response surfaces of die filling and tube thinning in terms of input parameters

thinning percentages. The result showed that the optimal loading path was obtained at pressure of 7 bars, pressure rate of 0.01 bar/s, axial feeding of about 7 mm on each side, and a punch speed of 0.02 mm/s. At this condition, the amounts of die filling and tube thinning of 95% and 9.5% were achieved, respectively. Figure 6 shows the loading path obtained from the optimization. It can be seen that the axial feeding reached its maximum value after 350 s and then remained constant by increasing the pressure for 700 s.

Figure 7 shows a cylindrical stepped tube, which formed experimentally using the optimal loading path. The deformation behavior of the tube at different times in the optimal loading path condition is shown in Figure 8. As can be seen, up to 350 s wrinkles were created in the tube due to high axial feeding and low internal pressure, which resulted in a significant amount of the material flowing from the tube edges to the die cavity. Then, by increasing the internal pressure for duration of 700 s, the wrinkles were gradually eliminated, and the die cavity was filled. The internal pressure and axial feeding for different t/d and D/d ratios in the thin-walled tubes range were changed using simulations based on the optimal loading path. Figure 9 shows the perfect specimens, which obtained from experiments for tubes with different t/d and D/d ratios according to the simulations.

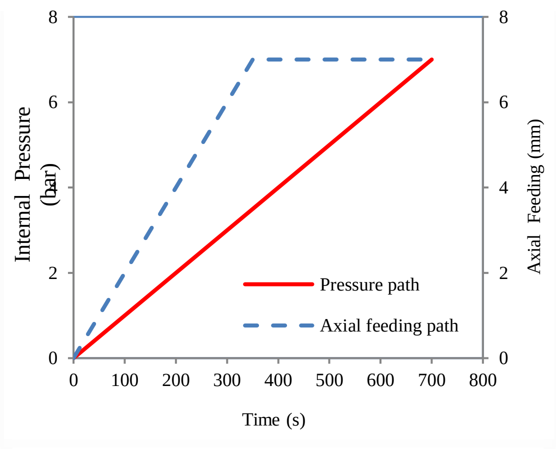

Figure 6. The loading path obtained from the optimization

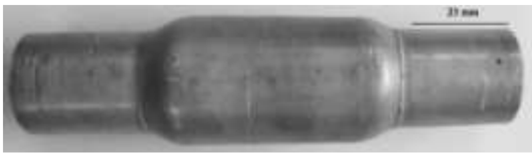

Figure 7. A stepped tube formed with the optimal loading path

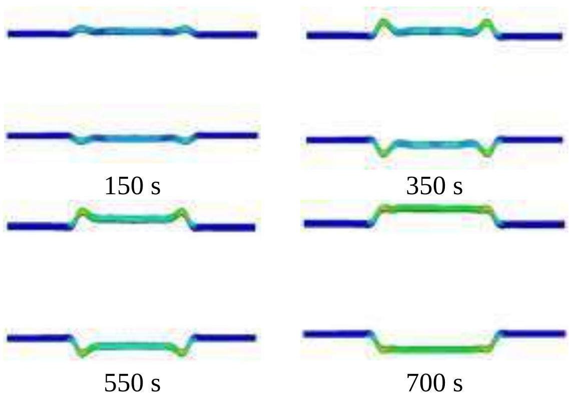

Figure 8. The deformation behavior in the optimal loading path condition

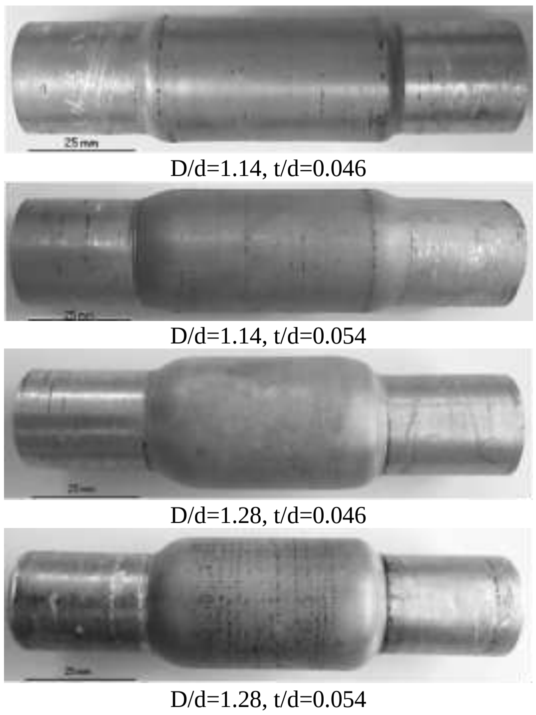

Figure 9. Stepped tubes formed at various D/d and t/d ratios

4. CONCLUSION

A combination of the response surface method and finite element method were used to optimize the loading path of the HMGF process for producing a cylindrical stepped tube from AA6063 alloy at 550 ºC. The process variables, including pressure, pressure rate, axial feeding, and punch speed, were investigated to obtain the maximum die filling and minimum tube thinning. The ANOVA results showed that the axial feeding, internal pressure, and their interaction had the most significant effect on the die filling and tube thinning. At low pressure, increasing the pressure rate had no significant effect on the die filling, while it increases the tube thinning sharply. The optimal parameters were obtained based on the highest die filling rate and the lowest tube thinning at the pressure of 7 bars, pressure rate of 0.01 bar/s, axial feeding of 7 mm from each side, and a punch speed of 0.02 mm/s. At this condition, the amounts of die filling and tube thinning of 95% and 9.5% were achieved, respectively. At optimal loading path, first wrinkles were created in the tube due to high axial feeding and low internal pressure, which resulted in a significant amount of the material flowing from the tube edges to the die cavity. Then, by increasing the internal pressure, the wrinkles were gradually eliminated, and the die cavity was filled.

5. ACKNOWLEDGMENTS

The authors acknowledge Babol Noshirvani University of Technology for the funding and financial support through Grant number BNUT/370203/96.

6. REFERENCES

1. Oraon, M., Sharma, V., "Predicting Force in Single Point Incremental Forming by Using Artificial Neural Network", ***International Journal of Engineering, Transactions A: Basics***, Vol. 31, No. 1, (2018) 88-95. DOI: 10.5829/ije.2018.31.01a.13
2. Tabatabaeia, S. M. R., Alasvand Zarasvand, K., "Investigating the Effects of Cold Bulge Forming Speed on Thickness Variation and Mechanical Properties of Aluminium Alloys: Experimental and Numerical", ***International Journal of Engineering, Transactions C: Aspects,*** Vol. 31, No. 9, (2018) 1602-1608. DOI: 10.5829/ije.2018.31.09c.17
3. Rahmania, F., Seyedkashi, S. M. H., Hashemi, S. J., "Experimental Study on Warm Incremental Tube Forming of AA6063 Aluminum Tubes", ***International Journal of Engineering, Transactions C: Aspects***, Vol. 33, No. 9, (2020) 1773-1779. DOI: 10.5829/ije.2020.33.09c.11
4. Alijani Renani, H., Haji Aboutalebi, F., "Evaluation of Ductile Damage Criteria in Warm and Hot Forming Processes", ***International Journal of Engineering, Transactions A: Basics,*** Vol. 29, No. 10, (2016) 1441-1449. DOI: 10.5829/ije.2016.29.10a.15
5. Chausov, M., Pylypenko, A., Berezin, V., Volyanska, K., Maruschak, P., Hutsaylyuk, V., Markashova, L., Nedoseka, S., Menou, A., "Influence of dynamic non-equilibrium processes on strength and plasticity of materials of transportation systems", ***Transport***, Vol. 33, No.1, (2018) 231-241, DOI: 10.3846/16484142.2017.1301549
6. Li, Z., Qu, H., Chen, F., Wang, Y., Tan, Z., Kopec, M., Wang, K., Zheng, K., "Deformation Behavior and Microstructural Evolution during Hot Stamping of TA15 Sheets: Experimentation and Modelling", ***Materials*** Vol. 12, (2019), 223-236. DOI: 10.3390/ma12020223
7. Roohi, A.H., Hashemi, S.J., Allahyari, M., "Hot metal gas forming of closed-cell aluminium foam sandwich panels", ***Transactions of the Indian Institute of Metals,*** Vol. 73, (2020) 2231-2238. DOI: 10.1007/s12666-020-02027-2
8. Paul, A., Werner, M., Trân, R., Landgrebe, D., "Hot metal gas forming of titanium grade 2 bent tubes", AIP Conference Proceedings, Vol. 1896, (2017), 050009. DOI: 10.1063/1.5008054

9. Mosel, A., Lambarri, J., Degenkol, L., Reuther, F., Hinojo, J., Robiger, L., Eurich, J., Albert, E., Landgrebe, A., Wenzel, D., "Novel process chain for hot metal gas forming of ferritic stainless steel 1.4509", AIP Conference Proceedings, Vol. 1960, (2018), 160019. DOI: 10.1063/1.5035045.
10. Talebi-Anaraki, A., Chougan, M., Loh-Mousavi, M., Maeno, T., "Hot gas forming of aluminium alloy tubes using flame heating", ***Journal of Manufacturing and Materials Processing,*** Vol. 4, (2020), 56-64. DOI: 10.3390/jmmp4020056
11. Rajaee, M., Hosseinipour, S.J., Jamshidi Aval, H., "Tearing criterion and process window of hot metal gas forming for AA6063 cylindrical stepped tubes", ***International Journal of Advanced Manufacturing Technology,*** Vol. 101, (2019), 2609-2620. DOI:10.1007/s00170-018-3052-0
12. Modanloo, V., Alimirzaloo, V., "Minimization of the sheet thinning in hydraulic deep drawing process using response surface methodology and finite element method", ***International Journal of Engineering, Transactions B: Applications,*** Vol. 29, No. 2, (2016) 264-273. DOI: 10.5829/ije.2016.29.02b.16
13. Mahmood Ali, S., "Optimization of Centrifugal Casting Parameters of AlSi Alloy by using the Response Surface Methodology", ***International Journal of Engineering, Transactions B: Applications,*** Vol. 32, No. 11, (2019) 1516-1526. DOI: 10.5829/ije.2019.32.11b.02
14. Alaswad, A., Benyounis, K., Olabi, A., "Employment of finite element analysis and Response Surface Methodology to investigate the geometrical factors in T-type bi-layered tube hydroforming. ***Advances in Engineering Software,*** Vol. 42, (2011), 917-926. DOI: 10.1016/j.advengsoft.2011.07.002
15. Chebbah, M. S., Azaouzi, M., "Geometrical parameters optimization for tube hydroforming using response surface method", AIP Conference Proceedings, Vol. 1618 (2014), 998. DOI: 10.1063/1.4897902.
16. Kadkhodayan, M., Erfani-Moghadam, A., "An investigation of the optimal load paths for the hydroforming of T-shaped tubes", ***International Journal of Advanced Manufacturing Technology,*** Vol. 61, (2012), 73-85. DOI: 10.1007/s00170-011-3700-0
17. Safari, M., Joudaki, J., Ghadiri, Y., "A Comprehensive Study of the Hydroforming Process of Metallic Bellows: Investigation and Multi-objective Optimization of the Process Parameters", ***International Journal of Engineering, Transactions B: Applications,*** Vol. 32, (2019), 1681-1688. DOI: 10.5829/IJE.2019.32.11B.19
18. Ahmadi Brooghani, S., Khalili, K., Shahri, S. E., Kang, B., "Loading path optimization of a hydroformed part using multilevel response surface method", ***International Journal of Advanced Manufacturing Technology,*** Vol. 70, (2014), 1523-1531. DOI: 10.1007/s00170-013-5359-1
19. Huang, T., Song, X., Liu, M., "The multi-objective non-probabilistic interval optimization of the loading paths for T-shape tube hydroforming", ***International Journal of Advanced Manufacturing Technology,*** Vol. 94, (2018), 677-686. DOI: 10.1007/s00170-017-0927-4
20. Ge, Y., Li, X., Lang, L., Ruan, S., "Optimized design of tube hydroforming loading path using multi-objective differential evolution", ***International Journal of Advanced Manufacturing Technology,*** Vol. 88, (2017), 837-846. DOI: 10.1007/s00170-016-8790-2
21. Shamsi-Sarband, A., Hosseinipour, S. J., Bakhshi-Jooybari, M., Shakeri, M., "The effect of geometric parameters of conical cups on the preform shape in two-stage superplastic forming process', ***Journal of Materials Engineering and Performance,*** Vol. 22, (2013), 3601-3611. DOI: 10.1007/s11665-013-0636-6
22. Hojjati, M., Zoorabadi, M., Hosseinipour, S. J., "Optimization of superplastic hydroforming process of Aluminium alloy 5083", ***Journal of Materials Processing Technology,*** Vol. 205, (2008), 482-488. DOI: 10.1016/j.jmatprotec.2007.11.208

Persian Abstract

چکیده

در این مقاله مسیر بارگذاری در فرایند شکل‌دهی فلز داغ با گاز (HMGF) برای ساخت لوله‌های استوانه‌ای پله‌ای از آلیاژ آلومینیوم ۶۰۶۳ بهینه‌سازی شد. برای این منظور، از روش‌های سطح پاسخ (RSM) و اجزای محدود (FEM)، به ترتیب به کمک نرم افزارهای دیزاین اکسپرت و آباکوس، استفاده شد. پارامترهای مقدار فشار داخلی، نرخ اعمال فشار، تغذیه محوری و سرعت سنبه بر اساس طراحی آزمایش ترکیبی-مرکزی در سه سطح مورد بررسی قرار گرفت. حداکثر پرشدگی قالب و حداقل درصد نازک شدگی لوله به عنوان توابع هدف انتخاب شدند. تجزیه و تحلیل واریانس نشان داد که تغذیه محوری، فشار داخلی و برهم کنش آنها مهمترین پارامترهای تاثیرگذار در پرشدگی قالب و نازک شدگی لوله می‌باشند. مسیر بارگذاری مطلوب در دمای ۵۵۰ درجه سانتیگراد تحت فشار حدود ۷ بار، نرخ اعمال فشار ۰.۰۱ بار در ثانیه، تغذیه محوری ۷ میلی متر از هر طرف و سرعت سنبه ۰/۰۲۲ میلی متر بر ثانیه بدست آمد. آزمون‌های تجربی آزمایشی برای پارامترهای مشخص شده انجام شد که نتایج بهینه‌سازی را تأیید می‌کند.

IJE TRANSACTIONS B: Applications Vol. 34, No. 05, (May 2021) 1313-1320

International Journal of Engineering

Journal Homepage: www.ije.ir

Numerical Investigation of the Heat-fluid Characteristic inside High-speed Angular Contact Ball Bearing Lubricated with Grease

B. Wang*, Z. Wang, C. Sun, Y. Wu

School of Mechanical & Electrical Engineering, Lanzhou University of Technology, Lanzhou 730050, China

PAPER INFO

Paper history:
Received 5 June 2020
Received in revised form 22 March 2021
Accepted 24 March 2021

Keywords:
Angular Contact Ball Bearing
Grease Lubrication
Thermal-fluid Characteristic
Heat-fluid-solid Coupling Method

ABSTRACT

The development of special grease makes it possible for angular contact ball bearings to operate at high speed and temperature; so, it become necessary to investigate thermal-fluid characterisics inside high-speed angular contact ball bearing lubricated with grease. In this paper, a simulation model for angular contact ball bearing was established with CFD software Fluent, the heat-fluid-solid coupling method was used to analyze the distribution and flow of grease, heat transfer, and temperature field inside the bearing chamber. The results showed that, grease distribution inside bearing chamber was very inhomogeneous, most of grease was distributed on the both sides of the rolling elements along outer raceway and its flow velocity was very low, only a little grease was adhered on the surface of rolling elements, cage, and inner ring, its flow velocity was high; grease distribution inside bearing chamber becomes more inhomogeneous with the increase of bearing speed; in bearing heat transfer conduction was dominant and grease plays a key role, convection of air and grease was insignificant; affected by heat transfer condition the temperature rise of bearing components was obviously different, rolling elements have the highest temperature, the temperature of inner ring was slightly lower than that of rolling elements, and temperature of outer ring was the lowest. Bearing temperature experiment was conducted on self-made test rig and verified the validity and accuracy of numerical simulation. The results of this study will provide some reference for lubrication design and thermal analysis of high speed angular contact ball bearing lubricated with grease.

***doi**: 10.5829/ije.2021.34.05b.26*

NOMENCLATURE

H	friction heat generation of tested bearing	f_0	a factor depending upon bearing type and lubrication method
n	bearing rotation speed	v_0	the kinematic viscosity of lubricant
M	bearing frictional torque	N_u	the Nusselt number
M_l	bearing frictional torque due to load	R_e	the Reynolds number
M_v	bearing frictional torque due to lubricant	P_r	the Prandlt number
f_l	a factor depending upon bearing type and load	ω	inner ring speed
p_l	bearing load	v	kinematic viscosity of air
d_m	bearing mean diameter	d	diameter of main shaft

1. INTRODUCTION

Rolling bearing is a critical component of many modern engines and machinery, it can reduce the friction and ensure rotary accuracy [1, 2]. Lubrication, as an effective way to reduce friction, is one of the important issues in rolling bearing. With an increase in bearing speed and load, lubrication performance has become more and more demanding. According to available findings, grease lubrication has been widely used in high-speed rolling bearing because of its good sealing performance, wide application and convenient operation [3-5]. However, it is difficult for a grease-lubricated rolling bearing to dissipate heat by friction because of the

*Corresponding Author Institutional Email: wbm2007@163.com (B. Wang)

Please cite this article as: B. Wang, Z. Wang, C. Sun, Y. Wu, Numerical Investigation of the Heat-fluid Characteristic inside High-speed Angular Contact Ball Bearing Lubricated with Grease, International Journal of Engineering, Transactions B: Applications Vol. 34, No. 05, (2021) 1313-1320

limited flow ability of grease, high temperature rise often results in premature failure of rolling bearing [6]. Hence, it is very important to investigate the thermal behavior and fluid characteristics of greases in operating rolling bearings.

Considerable efforts have been devoted to investigate the work mechanism [7-9] and rheological behavior [10-12] of grease lubrication in high-speed rolling bearing. Thermal characteristics of rolling bearing has also attracted much attention due to the industrial demands for high speed and long working life. Ma Fangbo et al. [13] provided a calculation model for heat generation rate in a grease-lubricated spherical roller bearing (SRB) by adopting the local heat source analysis approach, the heat generation rates of roller-raceway contact, cage and inner ring land contact, roller and cage pocket contact, and power loss of roller churning were calculated. Wurzbach et al. [14] investigated the thermal behavior, flow characteristics of the non-Newtonian greases, and changes in grease properties in operating rolling-element bearings. Neurouth et al. [15] analyzed the heat transfer inside a grease lubricated thrust ball bearing, two models were developed using the thermal network method. Based on generalized Ohm′s law, Siyuan et al. [16] developed a thermal network model for double-row tapered roller bearing lubricated with grease, bearing temperature at different speeds, grease filling ratios, and roller large end radius was investigated. Fangbo et al. [17] developed a transient thermal model for a grease-lubricated spherical roller bearings-shaft-bearing housing system using a thermal network method, the effect of rotating speed, radial load and grease filling ratio on bearing temperature rise was analyzed. Xue et al. [18] conducted the temperature performance tests of high-speed sealed angular-contact ball bearings using different grease filling rate, the temperature performance of bearing with different grease filling rate was compared and analyzed under different working conditions.

The studies mentioned above investigated the bearing thermal characteristics and fluid properties of grease. However, fluid flow and heat transfer are not two independent processes [19, 20], the flow of fluid contributes to heat transfer, the temperature change of fluid will affect its viscosity, and then affects its flow in turn; so, the flow and heat transfer of fluid interact with each other [21, 22]. But few studies have been done on the coupling relationship between them and didn't consider the heat transfer between grease and bearing components, the exact behavior of greases in operating rolling bearing needs to be well understood. Therefore, in this paper a simulation model for angular contact ball bearing was established with CFD software Fluent, based on this model, the distribution and flow of grease, heat transfer, and temperature field inside the bearing chamber were analyzed using the heat-fluid-solid coupling method. A bearing test rig was designed and manufactured, bearing temperature measurement was conducted to verify the validity and accuracy of numerical simulation.

2. TEST RIG

In order to investigate the thermal behavior of high-speed angular contact ball bearing, some measurement of bearing temperature was conducted on self-made test rig. As shown in Figure1, the test rig is mainly composed of a test section and a motorized spindle unit. The test section is driven by the motorized spindle through a flexible coupling. The highest speed and rated power of the motorized spindle are 36000rpm and 5 kW, respectively. More detail of the tested bearings assembly is shown in Figure 2. The two tested bearings are B71909 angular contact ball bearings lubricated with grease; their major specifications are listed in Table 1. The tested bearings were press fitted onto the rotation shaft with back-to-back configuration, and the rotation shaft was supported by two pairs of ball bearings. Bearing loads were applied on tested bearing housing which installed between two tested bearings.

In experiments, motorized spindle rotates the inner ring of test bearings through the main shaft. The main shaft is connected with motorized spindle by a coupling. Special attention should be given to the coupling; design of flexible coupling was aimed to isolate test bearings

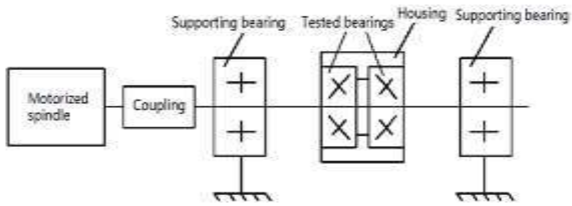

Figure 1. The structure diagram of test rig

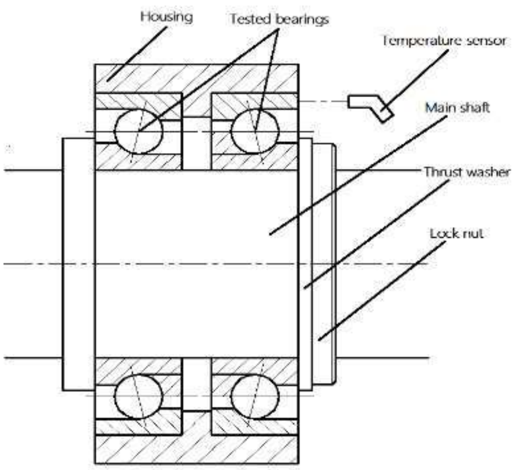

Figure 2. Drawing of tested bearings assembly

TABLE 1. The parameters of tested bearing B71909

Parameter	Value
Bore diameter	45 mm
Outer diameter	68 mm
Width	12 mm
Initial contact angular	15 deg.
Number of rolling elements	20
Ring material	Steel
Density of rings[g/cm^3]	7.8
Heat capacity of rings [J/kg·K]	460
Thermal conductivity of rings [W/m^2·K]	30
Ball material	Si_3N_4
Density of ball[g/cm^3]	3.2
Heat capacity of ball [J/kg·K]	800
Thermal conductivity of ball [W/m^2·K]	20

from the vibration of motorized spindle as much as possible. The two parts of coupling are not directly contacted each other and connected through Nealon rope, so the torsional impact of motorized spindle cannot be transmitted to test bearings, this structure ensures the stability of test bearings.

In order to get the temperature data of test bearings, an infrared temperature sensor was fixed on a self-made bracket to monitor the temperature of the bearing inner ring, the bracket is easy to adjust sensor position according to the experimental requirements, as shown in Figure 3.

Figure 3. The physical picture of test rig

3. NUMERICAL SIMULATION

3. 1. Thermal Analysis Model

Due to the symmetrical structure of the tested bearings assembly, its half structure was modeled in order to save computing cost. Inside the chamber of tested bearings lubricated with grease, the heat transfers between the fluid and the solid is involved, however, it is difficult to be determined. So, the heat-fluid-solid coupling method is used in this numerical simulation, this method is often used to solve the complex heat transfer problem, it can convert the complex outer boundary conditions between the fluid and the solid into a relatively simple inner boundary condition, and make the simulation more approach to practical condition. As shown in Figure 4, the simulation model of tested bearings assembly includes solid domain and fluid domain.

The structure of bearing chamber is very complicated. Therefore, in order to make finite element meshing easy, the bearing cavity is divided into multiple fluid domains. The domain among the balls is very irregular and meshed using tetrahedral elements. The domain along both sides of the balls is relatively regular and meshed using hexagonal elements. These fluid domains are connected with each other through an interface. The 3D grid model of fluid domain in bearing chamber is shown in detail in Figure 5. The final number of elements is 3215677, and the mesh quality is above 0.6.

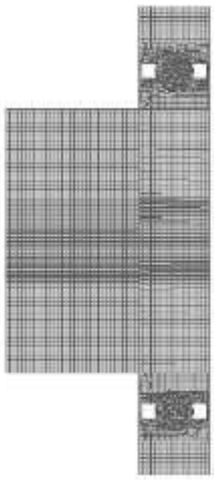

Figure 4. The heat-fluid-solid coupling model of tested bearings assembly

Figure 5. The 3D grid model of fluid domain inside bearing chamber

3. 2. Boundary Conditions

3. 2. 1. Heat Generation

During bearing operation, bearing friction represents an energy loss and results in temperature rise. The friction heat generation of the tested bearing can be obtained by the following equation [23]:

$$H = 1.047 \times 10^{-4} Mn \tag{1}$$

where H is the friction heat generation of tested bearing (w), n is bearing rotation speed (rpm), M is bearing frictional torque (N·mm). The frictional torque M consists of two components stated as follows:

$$M = M_1 + M_V \tag{2}$$

where M_l is bearing frictional torque due to load, and M_v is bearing frictional torque due to lubricant.

M_l can be approximated by the following equation:

$$M_1 = f_1 p_1 d_m \tag{3}$$

where f_1 is a factor depending upon bearing type and load, p_1 is bearing load (N), d_m is bearing mean diameter (mm).

M_v can be calculated by the following equation:

$$M_V = 10^{-7} f_0 (v_0 n)^{2/3} d_m^3 \quad \text{if} \quad n \geq 2000 \tag{4}$$

$$M_V = 160 \times 10^{-7} f_0 d_m \quad \text{if} \quad n \geq 2000 \tag{5}$$

where f_0 is a factor depending upon bearing type and lubrication method, v0 is the kinematic viscosity of lubricant (mm^2/s).

In numerical calculation it's assumed that the bearing friction heat generation is divided into two equal parts, one half was applied to bearing rings and the other was applied to rolling elements in the form of heat generating rate [24].

3. 2. 2. Heat Transfer According to the working conditions of the tested bearings assembly, convective heat transfer occurs on the outer surface of bearing housing and main shaft. The convection form of bearing housing is natural convection and the convection heat transfer coefficients is assumed to be 9.7 W/(m^{2}K) according to the practical experiences [25]. The convective heat transfer coefficients h_s of the main shaft can be obtained by the following equations.

$$N_u = 0.133 R_e^{2/3} P_r^{1/3} \tag{6}$$

$$R_e = \omega d^2 / v \tag{7}$$

$$h_s = \frac{N_u \cdot \lambda}{d} \tag{8}$$

where N_u is the Nusselt number, R_e and P_r are the Reynolds number and the Prandlt number, respectively, w is inner ring speed, v is the kinematic viscosity of air, d is the diameter of main shaft.

Inside bearing chamber heat transfer among grease, air and bearing components is a heat-fluid-solid coupling process and cannot be specified in advance. So, under the FLUENT platform, in numerical calculation the contacting surfaces between fluids and solid were set as default coupling-surface, and the heat transfer was calculated automatically. Finally, the second-order upside-style discrete momentum equation and turbulence equation are used. The pressure term is discretized in the PRESTO! (pressure staggering option) format, and the phase volume fraction is discretized in the geometric reconstruction format, and then the Semi-Implicit Method for Pressure Linked Equations (SIMPLE) algorithm is used. Solve the discrete algebraic equation and converge when the residual value drops below 10^{-3}.

3. 3. Solution and Parameters Set Heat-fluid-solid coupling is an interaction process among fluid domain, solid domain and temperature field. So, in order to obtain the flow field and temperature field of bearing, it is necessary to connect them. In the heat-fluid-solid coupling model of tested bearing, heat transfers among temperature field, fluid domain and solid domain through the fluid-solid interface, the interface method was used to connect the solid domain with the fluid domain, and the standard wall function is used to deal with the flow boundary layer and the heat transfer boundary layer at the fluid-solid coupling interface, which ensures the continuity of temperature and heat flux. In order to obtain the grease distribution inside bearing chamber, the interface of grease air two-phase flow was captured by the VOF method which is specifically used to solve the flow interface position of two immiscible fluids. The VOF method is from Europe Derived from Euler method, it is based on observation points, rather than following a fluid particle for research. In the flow field of bearing grease lubrication, the boundary of the two-phase flow is judged by solving the volume fraction of the two phases at the observation point. The turbulence inside bearing chamber was simulated by the RNG k-ε model which is suitable for analyzing turbulent motion in complex regions.

Moreover, the reference pressure was set as atmospheric pressure, and the air was selected incompressible gas model, non-equilibrium wall function was selected and solved by pressure velocity coupling equation. In the numerical simulation, the control variable method was used to simulate the flow field of the bearing chamber. The specific parameters of grease are shown in Table 2 [9].

4. RESULTS AND DISCUSSION

4. 1. Grease Distribution inside Bearing Chamber In the process of bearing operation, the bearing speed has a very important influence on the distribution of grease. When grease filling ratio is 0.3, under different rotation speed the grease distribution inside bearing chamber is

TABLE 2. The specific parameters of the grease

Grease	Lithium base grease
The consistency of grease	NLGI 3
The rheological model of grease	Herschel-Bulkley flow model
Viscosity coefficient k	20.5
Rheological index n	0.71
Yield stress τ_0	1076
Density [kg/m^3]	872
grease filling ratio	0.3
Heat capacity [J/kg·K]	2000
Thermal conductivity[W/m^2·K]	0.14

shown in Figure 6. It can be seen that the grease distribution was very inhomogeneous inside bearing chamber, grease was mainly distributed over the both sides of the rolling element along outer raceway, a small amount of grease was adhered on the inner side of the cage, grease adhered on the surface of rolling elements and inner raceway was very little due to centrifugal effect. It's also noted that the grease distribution inside bearing chamber become more inhomogeneous with the increase of bearing rotation speed, more grease is adhered on the outer raceway, the volume fraction of the grease between inner raceway and cage was accordingly decreased. It is perhaps a further finding that at high rotation speed bearing outer raceway is in full lubrication, meanwhile, bearing inner raceway is in starved lubrication.

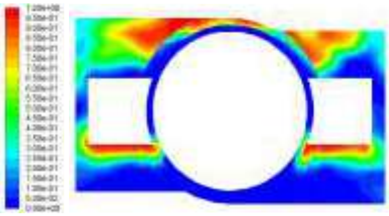

(a) n=6000r/min

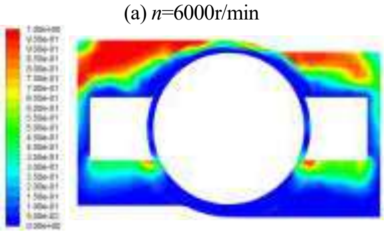

(b) n=12000r/min

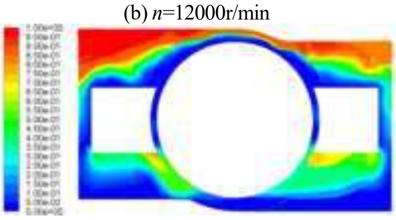

(c) n=20000r/min

Figure 6. Grease distribution inside bearing chamber at different rotation speed

4. 2. Flow Velocity of Grease inside Bearing Chamber

The flow velocity of grease inside the bearing chamber is shown in Figure 7. It is shown that grease adhered on the outer raceway was in viscous state, its flow velocity was very low; however, the flow velocity of grease adhered on inner ring and cage was relatively high, grease between cage and rolling elements has the highest flow speed. It's also found that, with the increase of bearing speed, the flow velocity of grease between inner raceway and cage increases obviously; however, an increase in bearing speed has very little effect on flow velocity of grease adhered on outer raceway.

4. 3. Heat transfer Coefficient on inner Surface of Bearing Chamber

In the working process of the bearing, heat is an important factor affecting the performance of the bearing. Heat will dilute the grease and reduce the lubrication efficiency of the bearing. Figure 8 shows heat transfer coefficient on the interface between the fluid domain and the solid domain inside bearing chamber at different speeds. It's shown that, heat transfer coefficient was high on the area of outer raceway surface where more grease was adhered on; heat transfer coefficient was also high on rolling elements surface which frequently contact with raceway, cage and grease; heat transfer coefficient was the lowest on inner raceway where little grease was adhered while its velocity was high, which was due to the fact that air convective heat transfer inside bearing chamber was

(a) n=6000r/min

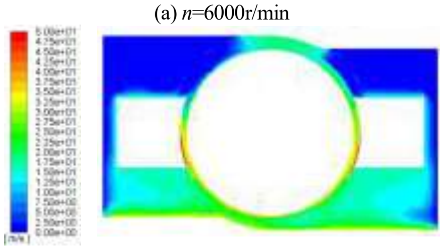

(b) n=12000r/min

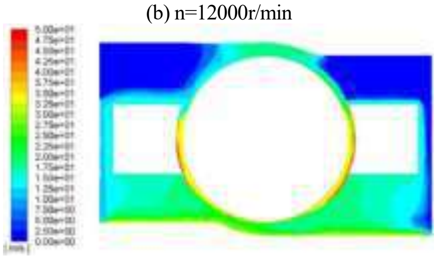

(c) n=20000r/min

Figure 7. The flow velocity distribution of grease inside bearing chamber at different speeds

very small; heat transfer coefficient was high on the area of inner and outer raceway surface where rolling elements pass. It also can be seen that with the increase of bearing speed heat transfer coefficient was accordingly increased on surface of outer raceway and rolling elements, which was due to the temperature rise of bearing components.

It can be concluded that inside bearing chamber conduction heat transfer is dominant in which grease plays a key role, the convective heat transfer of air and grease is insignificant.

4. 4. Temperature Rise of Bearing The temperature distribution of tested bearing is shown in Figure 9. It can be seen that bearing temperature field was nonuniform. The temperature of rolling elements was the highest, its heat mainly transfers to outer raceway through grease between rolling elements and outer raceway; the heat transfer condition of inner ring was poor, the temperature of inner ring was also high and slightly lower than that of rolling elements; outer ring has an effective heat transfer way, its heat can conduct to bearing housing and then transfer to ambient air, so the temperature of outer ring

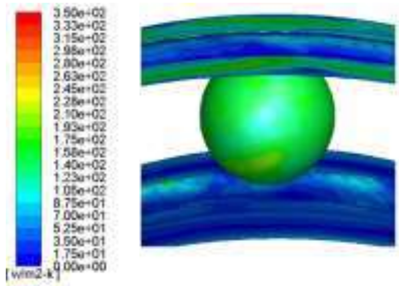

(a) n=6000r/min

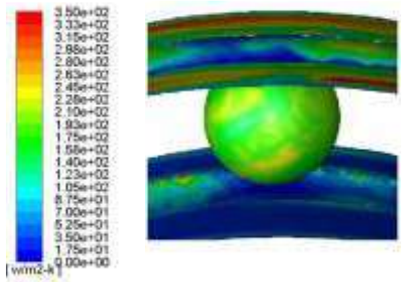

(b) n=12000r/min

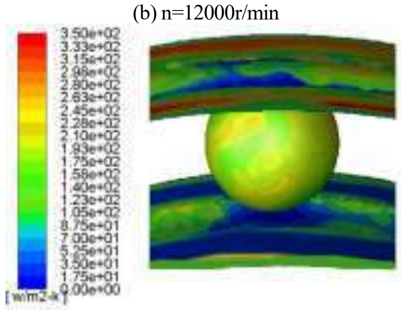

(c) n=20000r/min

Figure 8. The heat transfer coefficient inside bearing chamber at different rotation speed

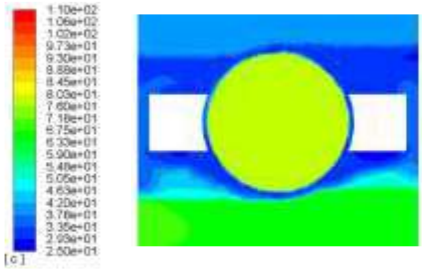

(a) n=6000 r/min

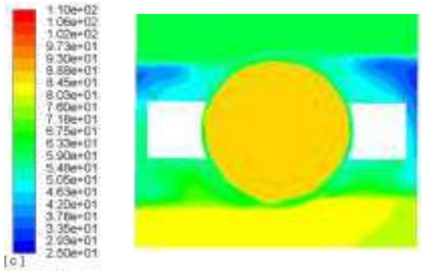

(b) n=12000 r/min

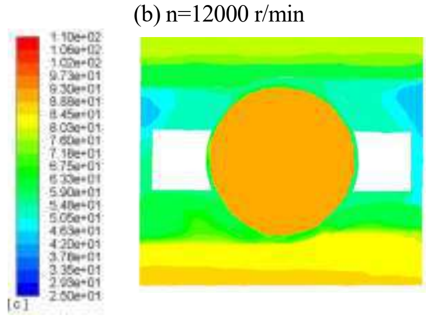

(c) n=20000 r/min

Figure 9. Temperature field of tested bearing at different rotation speed

was the lowest. With an increase in rotational speed bearing temperature was increased, the temperature of grease adhered on outer raceway was also increased, which indicated that more grease involves in conduction heat transfer.

4. 5. Verification In order to verify the validity and accuracy of numerical simulation, bearing temperature rise was measured on a self-made test rig. In the experiment, bearing axial load is 200N, and radial load is 100N, the tested bearing was started to run from zero speed to 9000 rpm, after running for 300 seconds at 9000 rpm, it was turned off. The measured data and simulation data of bearing temperature are shown in Figure 10. It's indicated that the simulation results were in good agreement with the experimental results, the residual error was below 8%, and the maximum residual error happened after bearing stop rotating. When bearing stops rotating, the natural convection of bearing housing plays a dominant role in bearing temperature, and the natural convection heat transfer coefficients come from experiences, this value 9.7 W/(m^2·K) is not very accurate. This is one reason of residual error. The other reason is nonlinear effects of

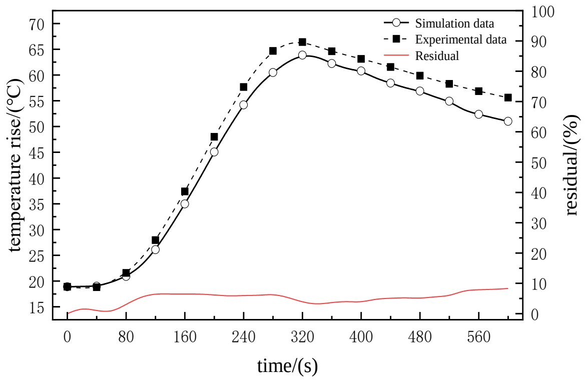

Figure 10. Bearing temperature measurements for the validation of numerical simulation

bearing temperature rise. Regardless of all these effects, numerical simulation showed good validity and accuracy.

5. CONCLUSION

The thermal-fluid characteristics of angular contact ball bearing lubricated grease was analyzed using thermal-fluid-solid coupling method. It was concluded that, grease distribution inside bearing chamber is very inhomogeneous, most of grease was distributed over the both sides of the rolling element along outer raceway, grease adhered on the surface of rolling elements, cage, and inner ring is very little, which becomes more inhomogeneous with the increase of bearing speed; grease adhered on the outer ring was in viscous state; however, it plays a dominant role in bearing heat transfer, convective heat transfer of air and grease was insignificant; affected by heat transfer condition the temperature rise of bearing components was obviously different, the temperature rise of rolling elements was the highest, the temperature of inner ring was slightly lower than that of rolling elements; outer ring has the lowest temperature.

The results provide some reference for lubrication design and thermal analysis of high-speed angular contact ball bearing. The method in the paper is also applicable to the analysis of heat-fluid behaviors of oil-air or oil lubricated rolling bearings. In this study bearing temperature experiment was conducted on self-made test rig and verified the validity and accuracy of numerical simulation, grease flow experiment can be considered in the future work.

6. ACKNOWLEDGEMENTS

This work was support by the National Science Foundation of China (Grant No. 51965038).

7. REFERENCES

1. Koulocheris, D., Stathis, A., Costopoulos, T. and Tsantiotis, D., "Experimental study of the impact of grease particle contaminants on wear and fatigue life of ball bearings", ***Engineering Failure Analysis***, Vol. 39, (2014), 164-180. doi: 10.1016/j. engfailanal. 2014.01.016.
2. Patil, S. and Phalle, V., "Fault detection of anti-friction bearing using ensemble machine learning methods", ***International Journal of Engineering***, ***Transactions B: Applications,*** Vol. 31, No. 11, (2018), 1972-1981. doi: 10.5829/ije.2018.31. 11b.22.
3. Lugt, P.M., "A review on grease lubrication in rolling bearings", ***Tribology Transactions***, Vol. 52, No. 4, (2009), 470-480. doi: 10.1080/10402000802687940.
4. Jang, J. and Khonsari, M., "Performance analysis of grease-lubricated journal bearings including thermal effects", (1997). doi: 10.1115/1.2833897.
5. Wu, Z., Xu, Y., Liu, K. and Chen, Z., "Numerical analysis of grease film characteristics in tapered roller bearing subject to shaft deflection", ***International Journal of Engineering***, ***Transactions A: Basics***, Vol. 33, No. 7, (2020), 1403-1412. doi: 10.5829/ije.2020.33.07a.28.
6. Kim, K.-S., Lee, D.-W., Lee, S.-M., Lee, S.-J. and Hwang, J.-H., "A numerical approach to determine the frictional torque and temperature of an angular contact ball bearing in a spindle system", ***International Journal of Precision Engineering and Manufacturing***, Vol. 16, No. 1, (2015), 135-142. doi: 10.1007/s12541-015-0017-1.
7. Cann, P. and Lubrecht, A., "An analysis of the mechanisms of grease lubrication in rolling element bearings", ***Lubrication Science***, Vol. 11, No. 3, (1999), 227-245. doi: 10.1002/ls. 3010110303.
8. Pan, J., Cheng, Y., Zhu, Z. and Yang, J., "Flow characteristics of grease in circular pipeline at varied temperatures", ***CIESC Journal***, Vol. 65, No. 6, (2014), 2063-2069. doi: 10.3969/j.issn.0438-1157.2014.06.016.
9. WU, Z.h., XU, Y.q., LIU, K.a. and ZHAO, X., "Thermal film-forming ability of grease lubrication at roller-raceway pair in tapered roller bearings", ***Journal of ZheJiang University (Engineering Science)***, Vol. 54, No. 3, (2020), 459-466. doi.
10. Singh, J., Kumar, D. and Tandon, N., "Development of nanocomposite grease: Microstructure, flow, and tribological studies", ***Journal of Tribology***, Vol. 139, No. 5, (2017). doi: 10.1115/1.4035775.
11. Su, B. and Lu, X.-t., "Study on the traction characteristics and model of a special grease for middle-low speed bearings", in 6th International Conference on Mechatronics, Materials, Biotechnology and Environment (ICMMBE 2016), Atlantis Press.
12. Xu, N., Wang, X., Ma, R., Li, W. and Zhang, M., "Insights into the rheological behaviors and tribological performances of lubricating grease: Entangled structure of a fiber thickener and functional groups of a base oil", ***New Journal of Chemistry***, Vol. 42, No. 2, (2018), 1484-1491. doi: 10.1039/C7NJ04833E.
13. Ma, F., Li, Z., Wu, B. and An, Q., "An accurate calculation method for heat generation rate in grease-lubricated spherical roller bearings", ***Proceedings of the Institution of Mechanical Engineers, Part J: Journal of Engineering Tribology***, Vol. 230, No. 4, (2016), 472-480. doi: 10.1177/1350650115604873.
14. Wurzbach, R.N., Bupp, E.W. and Williams, L.A., "Monitoring and thermal effects of relubrication of greased bearings", in Thermosense: Thermal Infrared Applications XXXIV, International Society for Optics and Photonics. Vol. 8354, 83540L.
15. Neurouth, A., Changenet, C., Ville, F. and Arnaudon, A., "Thermal modeling of a grease lubricated thrust ball bearing", ***Proceedings of the Institution of Mechanical Engineers, Part J: Journal of Engineering Tribology***, Vol. 228, No. 11, (2014), 1266-1275. doi: 10.1177/1350650114526387.
16. Ai, S., Wang, W., Wang, Y. and Zhao, Z., "Temperature rise of double-row tapered roller bearings analyzed with the thermal network method", ***Tribology International***, Vol. 87, (2015), 11-22. doi: 10.1016/j.triboint.2015.02.011.

17. Ma, F., Li, Z., Qiu, S., Wu, B. and An, Q., "Transient thermal analysis of grease-lubricated spherical roller bearings", ***Tribology International***, Vol. 93, (2016), 115-123. doi: 10.1016/j.triboint.2015.09.004.
18. Xue, J., Zhang, Y. and Wang, L., "The effects of grease filling amount on temperature performance of high-speed sealed angular-contact ball bearings", in 6th International Conference on Mechatronics, Materials, Biotechnology and Environment (ICMMBE 2016), Atlantis Press., 317-321.
19. Sengupta, A.R., Gupta, R. and Biswas, A., "Computational fluid dynamics analysis of stove systems for cooking and drying of muga silk", ***Emerging Science Journal***, Vol. 3, No. 5, (2019), 285-292. doi: 10.28991/esj-2019-01191.
20. Jung, S., Peetz, S. and Koch, M., "Poeam–a method for the part orientation evaluation for additive manufacturing", in Sim-AM 2019: II International Conference on Simulation for Additive Manufacturing, CIMNE. 440-443.
21. Dirbude, S.B. and Maurya, V.K., "Effect of uniform magnetic field on melting at various rayleigh numbers", ***Emerging Science Journal***, Vol. 3, No. 4, (2019), 263-273. doi: 10.28991/esj-2019-01189.
22. Touaibi, R., Koten, H. and Boydak, O., "Parametric study of an organic rankine cycle using different fluids", ***Emerging Science Journal***, Vol. 4, No. 2, (2020), 122-128. doi: 10.28991/esj-2020-01216.
23. Harris, T.A., "Rolling bearing analysis, John Wiley and sons, (2001).
24. Burton, R.A. and Staph, H., "Thermally activated seizure of angular contact bearings", ***ASLE Transactions***, Vol. 10, No. 4, (1967), 408-417. doi: 10.1080/05698196708972200.
25. Tong, B., Wang, G. and Sun, X., "Investigation of the fluid-solid thermal coupling for rolling bearing under oil-air lubrication", ***Advances in Mechanical Engineering***, Vol. 7, No. 2, (2015), 835036. doi: 10.1155/2014/835036.

Persian Abstract

چکیده

تولید گریس ویژه این امکان را برای بلبرینگ های ساچمه ای با تماس با زاویه در سرعت و دما بالا فراهم می کند. بنابراین لازم است که خصوصیات گرمایی درون یاتاقانهای توپی زاویه دار با سرعت بالا و روغن کاری شده با گریس را بررسی کنیم. در این مقاله ، یک مدل شبیه سازی برای یاتاقان ساچمه ای زاویه ای با نرم افزار ***CFD Fluent*** ایجاد شد ، از روش اتصال کوپلینگ مایع و گرما برای تجزیه و تحلیل توزیع و جریان چربی ، انتقال گرما و میدان حرارت در داخل استفاده شد. تحمل چمبر. نتایج نشان داد که ، توزیع گریس در داخل محفظه تحمل بسیار ناهمگن است ، بیشتر چربی در دو طرف عناصر نورد در امتداد مسیر بیرونی توزیع شده و سرعت جریان آن بسیار کم است ، فقط کمی چربی روی سطح چسبیده شده است عناصر نورد ، قفس و حلقه داخلی ، سرعت جریان آن زیاد بود. توزیع چربی در داخل محفظه تحمل با افزایش سرعت تحمل ناهمگن تر می شود. در انتقال انتقال حرارت تحمل غالب بود و گریس نقش اساسی دارد ، همرفت هوا و گریس ناچیز بود. تحت تأثیر شرایط انتقال حرارت ، افزایش دما اجزای تحمل آشکارا متفاوت بود ، نوردهای نورد بالاترین دما را دارند ، دمای حلقه داخلی کمی پایین تر از عناصر نورد است و دمای حلقه خارجی پایین ترین است. آزمایش دمای تحمل بر روی دکل آزمایشی خود ساخته انجام شد و اعتبار و صحت شبیه سازی عددی را تأیید کرد. نتایج این مطالعه مرجعی برای طراحی روغنکاری و آنالیز حرارتی یاتاقان های توپ با زاویه تماس با روغن روانکاری شده با گریس فراهم می کند.

International Journal of Engineering

Journal Homepage: www.ije.ir

Finite Element Simulation and Experimental Test of Ovine Corneal Tissue Cutting Process in Cataract Surgery Operation

H. Band Band[a], M. Arbabtafti*[a], A. Nahvi[b], M. Zarei-Ghanavati[c]

[a] *Department of Mechanical Engineering, Shahid Rajaee Teacher Training University, Tehran, Iran*
[b] *Department of Mechanical Engineering, K.N. Toosi University of Technology, Tehran, Iran*
[c] *Department of Ophthalmology, Tehran University of Medical Sciences, Tehran, Iran*

P A P E R I N F O

Paper history:
Received 09 December 2020
Received in revised form 13 March 2021
Accepted 09 April 2021

Keywords:
Finite Element Model
Corneal Cutting Force
Soft Tissue Damage Model
Corneal Surgery Modeling
Needle Insertion

A B S T R A C T

The modeling of corneal tissue cutting is essential in developing haptic training simulators and robot-assisted surgeries. A finite element model was developed in this study for the ovine corneal cutting process and validated with an experimental setup for the first time. The experimental setup forces are measured in pre-cutting, cutting, and relaxation phases. The mechanical behavior of corneal incision was modeled by the finite element method. A test setup was built to conduct experiments on 32 fresh and well-preserved ovine cornea. Force was recorded with the sampling rate of 200 Hz. The tests were performed for intraocular pressures from 15 mm-Hg to 18 mm-Hg, and keratome velocities of 1 mm/s and 2 mm/s. The finite element model characterized the nonlinear behavior of the ovine corneal tissue. In the pre-cutting phase, the force is increased until the instrument tip penetrates. A 12.3% (2 mm/s) and 19.1% (1 mm/s) reduction in force indicated the onset of the cutting phase after which force remained constant. At the relaxation phase, force returned to zero. The cutting force values varied by pressure between 0.183N and 0.287 N for 1 mm/s and between 0.211 N and 0.281 N for 2 mm/s of keratome velocity, respectively. The finite element simulations show that the maximum force errors predicted by the model is 0.042 N for 2 mm/s of keratome velocity. The root mean square of force error between the finite element simulations and the experiments is 0.025 N.

doi: *10.5829/ije.2021.34.05b.27*

1. INTRODUCTION

Cataract surgery simulations are useful for training surgeons and to administer surgery via teleoperation. Finite element method (FEM) can be used to model corneal mechanical behavior when subjected to internal and external forces [1]. There are a few valuable research works in the literature investigating the finite element (FE) models of the cornea under various types of loading, but the FEM of the corneal cutting procedure during cataract surgery is not adequately studied yet. Experiments on the corneal tissue can greatly help researchers understand the mechanics of deformation and rupture during cataract surgery and develop valid FE models. In previous studies, a few types of FE models of cornea have been presented. Also, there are some research works on FE models of needle insertion. These FE models can be broken down into three main categories including corneal surgery, corneal impact, trauma, and needle insertion into soft and artificial tissues. FE models of corneal surgeries, impacts and trauma are somehow comparable to the FE simulation of cataract surgeries. However, none of these FE models has addressed cutting of the corneal tissue. The most relevant simulations of cataract surgery operation are needle insertion experiments and FE simulations.

FE model of refractive surgery and corneal deformation has been developed to plan surgical procedures and predict corneal mechanical properties. The curvature of the corneal surfaces affects its refractive power significantly. Refractive surgery is used to improve the visual acuity of patients with common

*Corresponding Author Institutional Email: *arbabtafti@sru.ac.ir* (M. Arbabtafti)

Please cite this article as: H. Band Band, M. Arbabtafti, A. Nahvi, M. Zarei-Ghanavati, Finite Element Simulation and Experimental Test of Ovine Corneal Tissue Cutting Process in Cataract Surgery Operation, International Journal of Engineering, Transactions B: Applications Vol. 34, No. 05, (2021) 1321-1328

refractive illnesses. FEM has been used to analyze mechanical properties and corneal curvature before and after the refractive surgery [2-9]. Moreover, an FE model has been developed for simulating corneal tissue cutting by using boundary condition [10]. The FE model has been employed to compare and revise nomogram tables or graphics used by surgeons to plan surgical procedures [11, 12]. In other studies, a 3-D FE model has been used to compare the results of small-incision and LASIK operations [13]. Additionally, FE simulation has been used to correct astigmatism [14]. Moreover, a 3-D FE model has been used to study the accommodation behavior of crystalline lens after Femtosecond (FS) laser treatment [15]. Additionally, a 3-D FE simulation has been used to investigate the deformation of cornea during tonometry [16]. However, none of these FE models concerns the cutting process of the corneal tissue.

FEM has been employed as a useful and inexpensive tool for simulating ocular injuries and bringing solutions to reduce eye injuries. In these types of studies, factors such as velocity, mass, material, and size of the projectile have been taken into account [17-19]. Additionally, FE simulation of rupture of corneal tissue due to airbag injuries has been developed [20-21].

The FE model of needle insertion has been developed to determine needle forces during soft tissue cutting. Two-dimensional FE model of needle insertion has been developed to predict needle deflection, and also for steering the needle towards soft tissue in robotic systems [22]. FEM can be used for needle–tissue interactions by simulating material properties, material rupture, large deformation, and boundary conditions [23]. A FE simulation with cohesive zone model can be used to investigate tip rupture [24-25]. However, a cohesive zone algorithm requires a priori needle route. FE model has also been used to simulate needle-tissue interaction forces with an element deletion-based method [26-27]. In these studies, a micro-needle was inserted into a 2D and 3D multilayer skin model.

This paper presents an experimental setup for simulating the first step of cataract surgery operation by recording cutting force of the ovine corneal tissue for the first time. The effect of intra-ocular pressure and surgeon’s hand velocity on the incision force was investigated. Moreover, a FE simulation of the ovine corneal tissue cutting process was developed based on the nonlinear behavior of the corneal tissue and it was validated experimentally.

The remaining of the paper is organized as follows. In section 2, we describe the experimental setup and the FE model. In the results section, we compare the corneal experimental results with those of the FE simulations. Finally, the paper is concluded by discussing the effect of the cutting force and repeatability of the tests.

2. MATERIALS AND METHODS

2. 1. Experiments The experimental setup was designed to penetrate the keratome inside the corneal tissue and record position, velocity, and force (see Figure 1). This setup simulates the cataract surgery operation with any desired penetration velocity. The setup allows adjustment of intraocular pressure, and keratome motion velocity during the incision process. The aim was to use a keratome to penetrate the soft tissue with a constant velocity while monitoring the force of cutting the tissue exerted on the keratome during the incision process.

Other experimental apparatus studies include needle insertion of prostate brachytherapy procedures [25, 28], needle insertion into an artificial material [29-30], needle insertion into agar gel by using three types of copper needle with bevel tips [31-32], and needle insertion into porcine cardiac tissue [33]. This paper models operation of the keratome tool on corneal tissue during cataract surgery .

The equipment consists of a keratome incision instrument, a data-acquisition card, a high-speed 120 frames per second camera, a linear potentiometer, a load cell, and a personal computer. The entire incision mechanism stands on a base and fixed with vertical

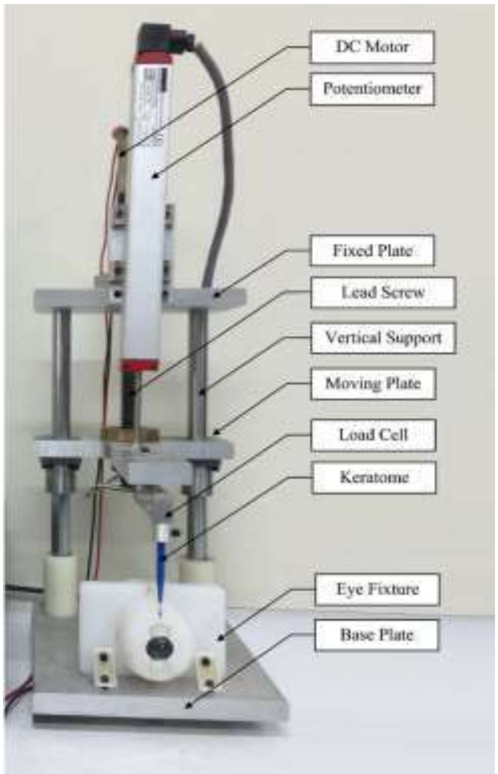

Figure 1. The test devices and equipment of cataract surgery mechanism

supports. A lead screw rotate by using a geared DC motor and the change of moving plate position measured by potentiometer (Opkon LPT 225 D 5K); also, a one axis force sensor (Scaime AR0.2 serial number 001503) fixed on moving plate and the keratome was screwed to the force sensor. The force sensor was fixed on an aluminum plate with one side attached to the anti-backlash nut traveling along the lead screw and the other side to a guiding shaft with a linear bearing to reduce friction of travel. The design and fabrication of the cutting assembly ensured that the system was sufficiently rigid. Accordingly, the forces recorded by the force sensor were those obtained by cutting the tissue alone like real forces, acting on the surgeon's hand during the cataract surgery operation.

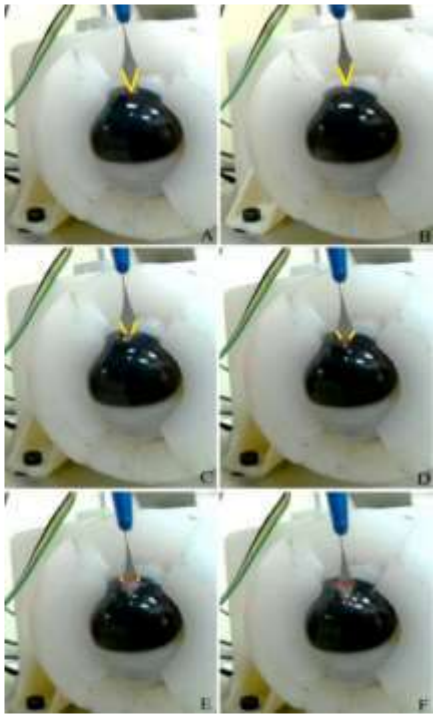

Figure 2. Keratome penetration into the cornea. A: Initial contact. B: deformation. C: initial cutting, D: cutting process. E: cutting process. F: complete pass of Keratome

To match the recorded values from the test and incision procedure, find the meaning of each variation in numerical values of the recorded force and tissue deformation, a high speed camera system was employed during the surgery simulation. The camera was placed close to the experimental setup to record scenes of the incision and tissue deformations step by step for later analysis. This consideration was made for recognition and accommodation of the force-time values with the steps of corneal tissue incision.

An experimental test was performed to record reaction forces to the surgeon's hand during the cataract surgery and use these forces for evaluating the finite element simulation. These forces play a substantial role in specifying the pattern of incision and defining the failure criteria of the cornea soft tissue. In light of this, 32 ovine eyes, because of their similarity to human eyes [34], and as it is the most practical choice of cataract surgery for trainers in wet labs in the Middle East and Central Asia [35], were used and prepared for the test within 4 hours of post-mortem. Since the experiments were implemented on the ex-vivo corneal tissue, the preparation procedure of the corneal tissue before the experiment helped maintain the properties of the tissue as close as to the in-vivo corneal tissue properties. The eyes were placed in an eye fixture during the implantation of the test, the design of which was inspired from previous studies [36], with some changes based on test situation. Finally, the test was repeated four times for each scenario. The effect of keratome motion velocity and intraocular pressure was considered.

The preceding pictures in Figure 2 present the penetration of keratome into the corneal tissue step by step. As it is obvious in this figure, the yellow lines show the edge of instrument while the red line shows the width of cutting.

2. 2. Finite Element Analysis A validated computational model can describe the incision process and predict the mechanical behavior of the cornea during incision. An FE model provides a quantitative estimation of the corneal tissue deformation resistance both before and during the incision process. This model iteratively solves for the characterizing parameters of the corneal soft tissue failure criterion.

The FE model determines the keratome-tissue interaction and the resulting forces applied by the surgeon's hand during operation. A three-dimensional FE model of the eye using 81771 linear hexahedral elements of type 8-node linear brick, including 2193 elements with average size of 1mm in region A, 54000 elements with average size of 0.52mm in region B associated with the location of incision, and 390 elements with average size of 0.54mm in region C, and also keratome with 186 linear hexahedral elements with average size of 0.36mm, was developed to simulate the first step of cataract surgery operation as shown in Figure 3.

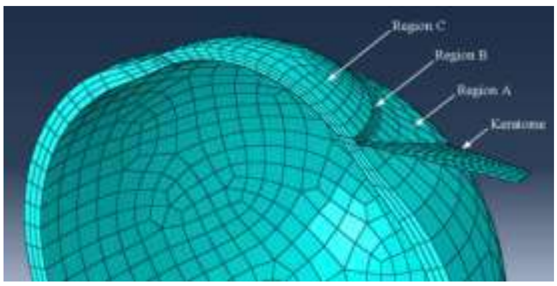

Figure 3. FE model of the eye and the keratome

The FE analysis was conducted with the ABAQUS finite element software using the VUMAT subroutine. The corneal tissue has non-linear behavior and its Young's modulus increases during deformation [34]. A constitutive model was used to demonstrate the exponential effect of the strain on the material's stress–strain behavior as obtained experimentally. In this consideration, a non-linear constitutive model was adopted from earlier studies [34]:

$$\sigma = a(e^{b\varepsilon} - 1) \tag{1}$$

where a is equal to 0.22 MPa and b is dimensionless and equal to 32.88. The Young's modulus is extracted from the first derivative of σ with respect to ε:

$$E = \frac{d\sigma}{d\varepsilon} = abe^{b\varepsilon} \tag{2}$$

The strain ε is replaced by the equivalent strain ε_{eq} obtained from the principal strains ε_1, ε_2 and ε_3:

$$\varepsilon_{eq} = \frac{2}{3}\sqrt{(\varepsilon_1 - \varepsilon_2)^2 + (\varepsilon_2 - \varepsilon_3)^2 + (\varepsilon_3 - \varepsilon_1)^2} \tag{3}$$

Defining this type of material behavior as the corneal tissue, as well as simulating the incision step and cutting the cornea is not possible in ABAQUS CAE. We developed a user-defined material model (VUMAT) FORTRAN subroutine to implement the material behavior of the corneal soft tissue and soft tissue cutting. For simulating the damage of the soft tissue by keratome incision, the explicit solver is more efficient and convergence of the solution in the explicit solver is easier compared to the implicit solver. In this analysis, a modified Johnson-Cook model and an element deletion-based method were used [17]. The damage behavior was implemented into ABAQUS via a VUMAT in conjunction with the non-linear elastic model. The modified Johnson-Cook model is simplified to the Von Misses stress as below:

$$\sigma = A \tag{4}$$

Which A is a constant value. At the low strain rates encountered in the cataract surgery simulation, the effect of strain rate, strain hardening, and thermal softening are vanished in the modified Johnson-Cook model. To implement the material formulation by using vumat subroutine of ABAQUS the user must provide, the yield stress of corneal tissue from experimental results.

3. RESULTS

Experimental results for two keratome velocities, i.e., 1mm/s and 2 mm/s, were carried out at four intraocular pressures ranging between 15 mm-Hg and 18 mm-Hg. Figure 4 demenstrates the results of the test when the keratome moved at the speed of 1 mm/s. As the intraocular pressure increases from 15 mm-Hg to 18 mm-Hg, force trajectory increases as well. Force increases until it reaches a peak at P as shown in Figure 4. This corresponds to the deformation of the corneal tissue before the incision of the tissue. Quickly after the peak, force declines from P to Q as a consequence of penetration. At Q, the edges of the keratome are in contact with the punched corneal tissue. The keratome continues to cut the tissue and push forward from Q to R. Consequently, force remains almost constant as time passes until the indentation reaches 1.6 mm at R, which coincides with the maximum width of keratome (3.2 mm) at this point. The soft tissue has been cut open by the full width of the keratome at R. From R to S, the keratome penetrates more into the cornea rather effortlessly through the cornea thickness, while force diminishes steadily and ultimately vanishes at T. The general behavior of experimental results in our research are similar to results of needle insertion into the soft gel in previous study [30].

Similarly, Figure 5 persents the test results for the keratome speed of 2 mm/s. The general behavior of Figures 4 and 5 are similar. We observe an 7.7% average increase in force when the speed doubled from 1 mm/s to 2 mm/s.

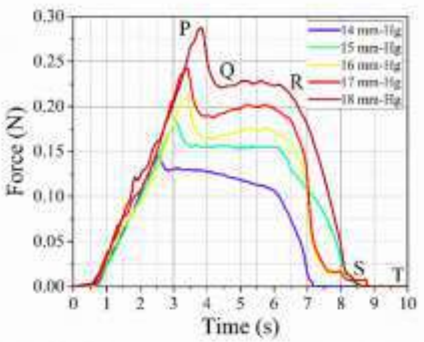

Figure 4. Experimental results for the 1-mm/s velocity with different pressure values

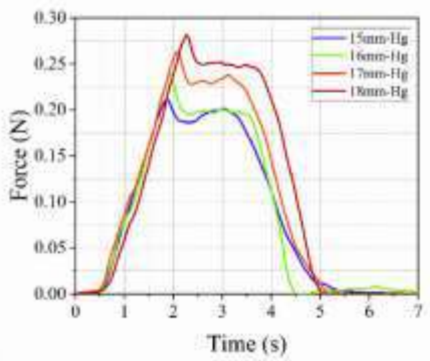

Figure 5. Experimental test results for the 2-mm/s velocity with different pressure values

Figure 6 compares incision force at four intraocular pressures for both velocities. The experimental results show that the keratome velocity does not affect force considerably. Also, the amount of force increase due to the faster velocity of 2 mm/s is diminished at higher intraocular pressures.

The FE model of the corneal tissue cutting process during cataract surgery operation was developed for four intraocular pressures between 15 mm-Hg and 18 mm-Hg.

The keratome velocity was set to 2 mm/s as the most common velocity during cornea cutting. Figure 7 shows four stages of keratome penetration into the corneal tissue for the intraocular pressure of 15 mm-Hg. Force exertion on the corneal tissue increases before incision as shown in Figure 7(a). Quickly thereafter the keratome tip penetrates into the corneal tissue and the edges of keratome remains in contact with the corneal tissue as shown in Figure 7(b). The keratome continues to cut open the corneal tissue by the full width of the keratome as shown in Figure 7(c). The keratome continues to penetrate into the cornea without further cutting as shown in Figure 7(d). The Von Misses stress of the corneal tissue resulting from the keratome penetration is expressed in MPa in a legend next to each figure.

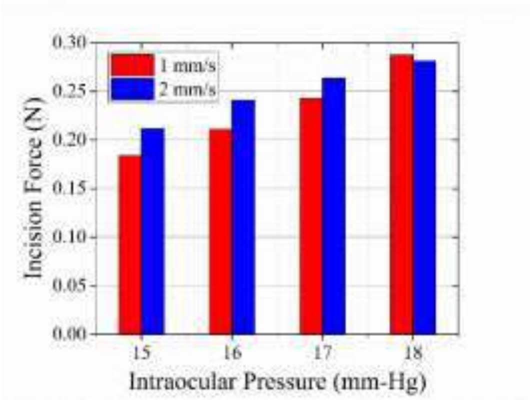

Figure 6. Comparison of the incision force at two keratome velocities of 1 mm/s and 2 mm/s

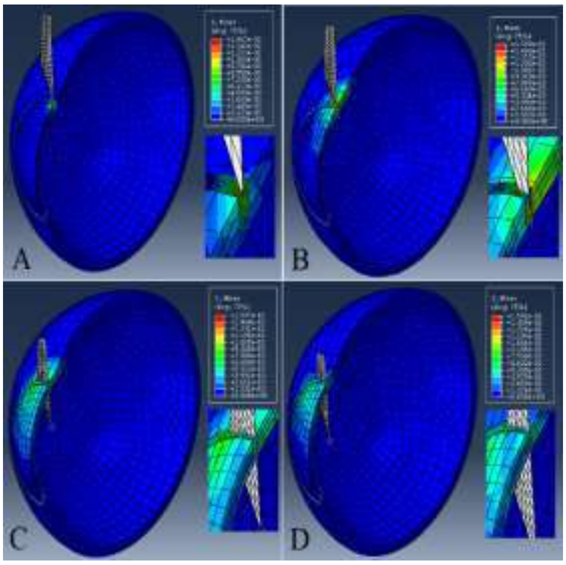

Figure 7. Von Misses stress during penetration; only half of the eye and keratome are drawn because of the eye symmertry about the prime meridian plane. A: Force exertion on the corneal tissue before incision; B: Keratome tip penetration into the corneal tissue; C: Corneal tissue cut open by the full width of the keratome; D: Continuation of keratome penetration into the cornea without further cutting

The resultant force on the keratome was calculated by ABAQUS and compared with the experimental results. Figures 8 presents the FEM results for the 2 mm/s velocity of the keratome motion for different intraocular pressures. The pattern of PQRST in experimental results in Figures 4 and 5 are observed in Figure 8.

The results of the experiments and the FEM are compared for the keratome velocity of 2 mm/s with two intraocular pressures of 15 mm-Hg and 18 mm-Hg as shown in Figures 9(a) and 9(b). These pressure values are chosen because they are the minimum and maximum common pressures used during cataract surgery operation by most surgeons. The pattern of experimental results and FE simulations are similar. Both experimental results and FE simulations show that the maximum force in Figure 9(b) is 24% bigger than that of in Figure 9(a) because of difference in intraocular pressures of 15 mm-Hg and 18 mm-Hg. Figures 9(c) and 9(d) show the errors of the FEM from the experimental results. In Figure 9(c), the root mean square and the maximum of the error are 0.009 N and 0.042 N, respectively. Similarly, in Figure 9(d), the root mean square and the maximum of the error are 0.007 N and 0.021 N, respectively.

4. DISCUSSION

A physics-based simulation of cataract surgery operation can improve surgical training by increasing the fidelity of

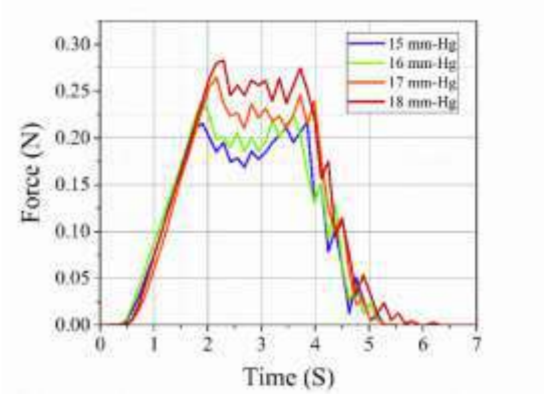

Figure 8. FEM results for the 2-mm/s velocity with different pressure values

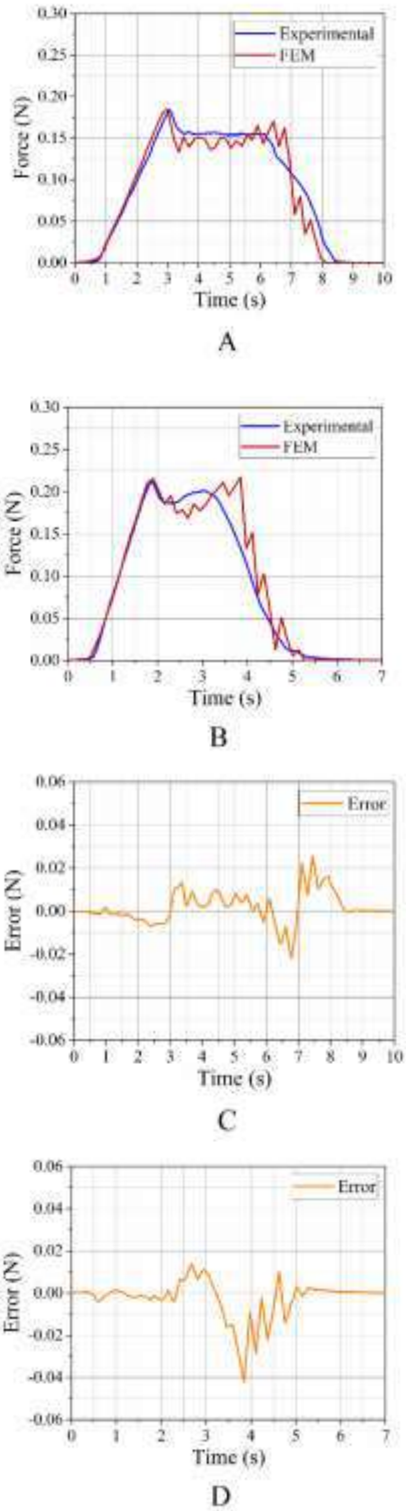

Figure 9. Experimental and FEM results. A: 15-mm-Hg pressure and the 2-mm/s velocity. B: 18-mm-Hg pressure and the 2-mm/s velocity. C: FEM difference from the experimental results for the 15-mm-Hg pressue and the 2-mm/s velocity. D: FEM difference from the experimental results for the 18-mm-Hg pressue and the 2-mm/s velocity

haptic simulators. Simulation of corneal tissue cutting process is an important part of cataract surgery training, but has not been adequately explored in the previous studies. For instance, recent studies in the field of refractive surgery [3, 4], and also previous studies on refractive surgery simulation [2, 37] modeled the geometry of corneal tissue before and after the surgical procedure without considering the cutting process. Similarly, researches in the field of projectile impact and trauma finite element simulation [17, 18] focused on the results of different parameters of the projectile affecting the intensity of injuries. Simulation of airbag injuries [20, 21] is similar to that of projectile impact injuries as both are not focused on the cutting process of the cornea. In fact, the mechanism and pattern of rupture in projectile and airbag studies are not under control. In other words, these studies aimed to predict the effects of different impact types on cornea to improve designs by creating a better protection. Therefore, the cutting procedure was not a key issue in such studies.

Research works in the field of needle insertion into a biological material [25, 33] have shown similar force-time patterns to the findings of this paper. The differences are the experimental setup, the surgical instrument, and the material properties of the soft tissue.

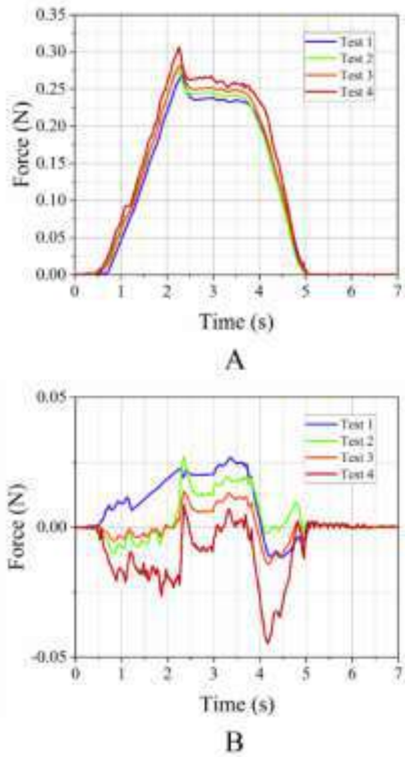

Figure 10. Repeatability of the test results. A: Test results for four ovine eyes (pressure of 18 mm-Hg and velocity of 2 mm/s). B: The difference of each test from the mean of all four tests

The repeatability of the experiments was investigated by four ovine eyes for each test. For example, Figure 10(a) shows the experimental results for the intraocular pressure of 18 mm-Hg and the keratome velocity of 2 mm/s. Figure 10(b) shows the test errors from the mean values. The force-time curves are close to each other with the root mean square of 0.013 N, 0.009 N, 0.006 N, and 0.014N for tests 1 to 4.

5. CONCLUSION

We designed and fabricated an experimental setup to measure force during the process of corneal tissue cutting in cataract surgery operation. We also developed a three-dimensional FE model for simulating keratome insertion into the corneal tissue. We validated this FE model by the experimental data at four intraocular pressures with the keratome velocity of 2 mm/s. The FE model included non-linear properties of the corneal tissue and a modified Johnson-Cook model for the cutting behavior during cataract surgery operation. The material behavior of this corneal tissue model is computationally inexpensive and can be used in real-time haptic simulators in order to better train surgeons and prepare them for handling potential complications of surgery. These simulations could also be useful to design better cataract surgery instruments. Real-time simulation of corneal cutting process by using haptic device is left for future work.

6. REFERENCES

1. Dhatt, G., Touzot, G. and Lefrançois, E., "Finite element method, Numerical methods series, London Hoboken, N.J., ISTE; Wiley, (2012), 600 p.
2. Pandolfi, A., Fotia, G. and Manganiello, F., "Finite element simulations of laser refractive corneal surgery", ***Engineering with Computers***, Vol. 25, No. 1, (2008), 15-24. DOI: 10.1007/s00366-008-0102-5.
3. Lehtikangas, O., Tarvainen, T., Kim, A.D. and Arridge, S.R., "Finite element approximation of the radiative transport equation in a medium with piece-wise constant refractive index", ***Journal of Computational Physics***, Vol. 282, No., (2015), 345-359. DOI: 10.1016/j.jcp.2014.11.025.
4. Sanchez, P., Moutsouris, K. and Pandolfi, A., "Biomechanical and optical behavior of human corneas before and after photorefractive keratectomy", ***Journal of Cataract & Refract Surgery***, Vol. 40, No. 6, (2014), 905-917. DOI: 10.1016/j.jcrs.2014.03.020.
5. Alastrue, V., Calvo, B., Pena, E. and Doblare, M., "Biomechanical modeling of refractive corneal surgery", ***Journal of Biomechanical Engineering***, Vol. 128, No. 1, (2006), 150-160. DOI: 10.1115/1.2132368.
6. Jessica R. Crouch, J.C.M., Earl R. Crouch III, "Finite element model of cornea deformation", in Medical Image Computing and Computer-Assisted Intervention - MICCAI. Vol., No. Issue, (2005 of Conference), 591-598.
7. Sinha Roy, A. and Dupps, W.J., Jr., "Effects of altered corneal stiffness on native and postoperative lasik corneal biomechanical behavior: A whole-eye finite element analysis", ***Journal of Refractive Surgery***, Vol. 25, No. 10, (2009), 875-887. DOI: 10.3928/1081597X-20090917-09.
8. Genest, R., "Finite element model of the chick eye to study myopia", ***Journal of Medical and Biological Engineering***, Vol. 33, No. 2, (2013). DOI: 10.5405/jmbe.1057.
9. Seven, I., Lloyd, J.S. and Dupps, W.J., "Differences in simulated refractive outcomes of photorefractive keratectomy (prk) and laser in-situ keratomileusis (lasik) for myopia in same-eye virtual trials", ***International Journal of Environmental Research and Public Health***, Vol. 17, No. 1, (2019). DOI: 10.3390/ijerph17010287.
10. Studer, H.P., Riedwyl, H., Amstutz, C.A., Hanson, J.V. and Buchler, P., "Patient-specific finite-element simulation of the human cornea: A clinical validation study on cataract surgery", ***Journal of Biomechanics***, Vol. 46, No. 4, (2013), 751-758. DOI: 10.1016/j.jbiomech.2012.11.018.
11. Cristobal, J.A., del Buey, M.A., Ascaso, F.J., Lanchares, E., Calvo, B. and Doblare, M., "Effect of limbal relaxing incisions during phacoemulsification surgery based on nomogram review and numerical simulation", ***Cornea***, Vol. 28, No. 9, (2009), 1042-1049. DOI: 10.1097/ICO.0b013e3181a27387.
12. Lapid-Gortzak, R., van der Linden, J.W., van der Meulen, I.J. and Nieuwendaal, C.P., "Advanced personalized nomogram for myopic laser surgery: First 100 eyes", ***Journal of Cataract & Refractive Surgery***, Vol. 34, No. 11, (2008), 1881-1885. DOI: 10.1016/j.jcrs.2008.06.041.
13. Sinha Roy, A., Dupps, W.J., Jr. and Roberts, C.J., "Comparison of biomechanical effects of small-incision lenticule extraction and laser in situ keratomileusis: Finite-element analysis", ***Journal of Cataract & Refract Surgery***, Vol. 40, No. 6, (2014), 971-980. DOI: 10.1016/j.jcrs.2013.08.065.
14. Lanchares, E., Calvo, B., Cristobal, J.A. and Doblare, M., "Finite element simulation of arcuates for astigmatism correction", ***Journal of Biomechanics***, Vol. 41, No. 4, (2008), 797-805. DOI: 10.1016/j.jbiomech.2007.11.010.
15. Besdo, S., Wiegand, J., Hahn, J., Ripken, T., Krüger, A., Fromm, M. and Lubatschowski, H., "Finite element study of the accommodation behaviour of the crystalline lens after fs-laser treatment", ***Biomedical Engineering / Biomedizinische Technik***, Vol., No., (2013). DOI: 10.1515/bmt-2013-4337.
16. R. B, B., Prabhu, G., S. Ve, R., Poojary, R. and Sundaram, S.M., "Investigation of deformation of the cornea during tonometry using fem", ***International Journal of Electrical and Computer Engineering***, Vol. 10, No. 6, (2020). DOI: 10.11591/ijece.v10i6.pp5631-5641.
17. Weaver, A.A., Kennedy, E.A., Duma, S.M. and Stitzel, J.D., "Evaluation of different projectiles in matched experimental eye impact simulations", ***Journal of Biomechanical Engineering***, Vol. 133, No. 3, (2011), 031002. DOI: 10.1115/1.4003328.
18. Gray, W., Sponsel, W.E., Scribbick, F.W., Stern, A.R., Weiss, C.E., Groth, S.L. and Walker, J.D., "Numerical modeling of paintball impact ocular trauma: Identification of progressive injury mechanisms", ***Investigative Ophthalmology & Visual Science***, Vol. 52, No. 10, (2011), 7506-7513. DOI: 10.1167/iovs.11-7942.
19. Koberda, M., Skorek, A., Kłosowski, P., Żmuda-Trzebiatowski, M., Żerdzicki, K., Lemski, P. and Stodolska-Koberda, U., "Extended numerical analysis of an eyeball injury under direct impact", Vol., No., (2021). DOI: 10.1101/2021.02.26.433021.
20. Uchio, E., Ohno, S., Kudoh, K., Kadonosono, K., Andoh, K. and Kisielewicz, L.T., "Simulation of air-bag impact on post-radial keratotomy eye using finite element analysis", ***Journal of Cataract & Refractive Surgery***, Vol. 27, No. 11, (2001), 1847-1853. DOI: 10.1016/s0886-3350(01)00966-x.

21. Uchio, E., Kadonosono, K., Matsuoka, Y. and Goto, S., "Simulation of air-bag impact on an eye with transsclerally fixated posterior chamber intraocular lens using finite element analysis", ***Journal of Cataract & Refractive Surgery***, Vol. 30, No. 2, (2004), 483-490. DOI: 10.1016/S0886-3350(03)00520-0.
22. S.P. DiMaio, S.E.S., "Needle insertion modeling and simulation", ***IEEE Transactions on Robotics and Automation***, Vol. 19, No. 5, (2003), 864 - 875. DOI: 10.1109/Tra.2003.817044.
23. Moustris, G.P., Hiridis, S.C., Deliparaschos, K.M. and Konstantinidis, K.M., "Evolution of autonomous and semi-autonomous robotic surgical systems: A review of the literature", ***The International Journal of Medical Robotics***, Vol. 7, No. 4, (2011), 375-392. DOI: 10.1002/rcs.408.
24. Misra, S., Reed, K.B., Douglas, A.S., Ramesh, K.T. and Okamura, A.M., "Needle-tissue interaction forces for bevel-tip steerable needles", ***Proc IEEE RAS EMBS Int Conf Biomed Robot Biomechatron***, (2008), 224-231. DOI: 10.1109/BIOROB.2008.4762872.
25. Oldfield, M., Dini, D., Giordano, G. and Rodriguez, Y.B.F., "Detailed finite element modelling of deep needle insertions into a soft tissue phantom using a cohesive approach", ***Comput Methods Biomech Biomed Engin***, Vol. 16, No. 5, (2013), 530-543. DOI: 10.1080/10255842.2011.628448.
26. Kong, X.Q., Zhou, P. and Wu, C.W., "Numerical simulation of microneedles' insertion into skin", ***Computer Methods in Biomechanics and Biomedical Engineering***, Vol. 14, No. 9, (2011), 827-835. DOI: 10.1080/10255842.2010.497144.
27. Assaad, W., Jahya, A., Moreira, P. and Misra, S., "Finite-element modeling of a bevel-tipped needle interacting with gel", ***Journal of Mechanics in Medicine and Biology***, Vol. 15, No. 05, (2015). DOI: 10.1142/s0219519415500797.
28. Podder, T.K., Sherman, J., Messing, E.M., Rubens, D.J., Fuller, D., Strang, J.G., Brasacchio, R.A. and Yu, Y., "Needle insertion force estimation model using procedure-specific and patient-specific criteria", Conference proceedings - IEEE engineering in medicine and biology society, Vol. 2006, No., (2006), 555-558. DOI: 10.1109/IEMBS.2006.259921.
29. Asadian, A., Kermani, M.R. and Patel, R.V., "A novel force modeling scheme for needle insertion using multiple kalman filters", ***IEEE Transactions on Instrumentation and Measurement***, Vol. 61, No. 2, (2012), 429-438. DOI: 10.1109/tim.2011.2169178.
30. van Veen, Y.R., Jahya, A. and Misra, S., "Macroscopic and microscopic observations of needle insertion into gels", ***Proceedings of the Institution of Mechanical Engineers, Part H***, Vol. 226, No. 6, (2012), 441-449. DOI: 10.1177/0954411912443207.
31. Jushiddi, M.G., Cahalane, R.M., Byrne, M., Mani, A., Silien, C., Tofail, S.A.M., Mulvihill, J.J.E. and Tiernan, P., "Bevel angle study of flexible hollow needle insertion into biological mimetic soft-gel: Simulation and experimental validation", ***Journal of the Mechanical Behavior of Biomedical Materials***, Vol. 111, No., (2020), 103896. DOI: 10.1016/j.jmbbm.2020.103896.
32. Yamaguchi, S., Tsutsui, K., Satake, K., Morikawa, S., Shirai, Y. and Tanaka, H.T., "Dynamic analysis of a needle insertion for soft materials: Arbitrary lagrangian-eulerian-based three-dimensional finite element analysis", ***Computers in Biology and Medicine***, Vol. 53, (2014), 42-47. DOI: 10.1016/j.compbiomed.2014.07.012.
33. Mahvash, M. and Dupont, P.E., "Mechanics of dynamic needle insertion into a biological material", ***IEEE Transactions on Biomedical Engineering***, Vol. 57, No. 4, (2010), 934-943. DOI: 10.1109/TBME.2009.2036856.
34. Elsheikh, A., Kassem, W. and Jones, S.W., "Strain-rate sensitivity of porcine and ovine corneas", ***Acta of Bioengineering And Biomechanics***, Vol. 13, No. 2, (2011), 25-36.
35. Mohammadi, S.F., Mazouri, A., Jabbarvand, M., Rahman, A.N. and Mohammadi, A., "Sheep practice eye for ophthalmic surgery training in skills laboratory", ***Journal of Cataract & Refractive Surgery***, Vol. 37, No. 6, (2011), 987-991. DOI: 10.1016/j.jcrs.2011.03.030.
36. Mohammadi, S.F., Mazouri, A., Rahman, A.N., Jabbarvand, M. and Peyman, G.A., "Globe-fixation system for animal eye practice", ***Journal of Cataract & Refractive Surgery***, Vol. 37, No. 1, (2011), 4-7. DOI: 10.1016/j.jcrs.2010.10.026.
37. Sinha Roy, A. and Dupps, W.J., Jr., "Patient-specific modeling of corneal refractive surgery outcomes and inverse estimation of elastic property changes", ***Journal of Biomechanical Engineering***, Vol. 133, No. 1, (2011), 011002. DOI: 10.1115/1.4002934.

Persian Abstract

چکیده

مدلسازی برش sقرنیه یکی از اساسی‌ترین مسائل در توسعه شبیه سازهای آموزشی هپتیکی و ربات‌های جراحی می‌باشد. یک مدل المان محدود برای شبیه سازی مرحله برش قرنیه چشم گوسفند ایجاده شده و اعتبار بخشی آن توسط یک دستگاه تست که برای اولین بار ساخته شده است، صورت پذیرفته است. دستگاه تست، نیروها را در مرحله های مختلف برش قرنیه اندازه گیری می‌نماید. رفتار مکانیکی بافت قرنیه در هنگام برش به روش المان محدود مدلسازی شده است. تست های برش بر روی ۳۲ عدد چشم گوسفند در شرایط کاملا مشابه در بدن موجود زنده مورد تست قرار گرفته اند. نیرو با سرعت داده برداری ۲۰۰ هرتز ثبت شده است. تست در فشارهای داخلی مختلف قرنیه یعنی ۱۵ تا ۱۸ میلی متر جیوه و سرعت حرکت ۱ میلی متر بر ثانیه و ۲ میلی متر بر ثانیه انجام شده است. توسط مدل المان محدود رفتار غیر خطی بافت قرنیه چشم گوسفند مدلسازی شده است. قبل از اولین برش بافت قرنیه و ورود نوک ابزار برش داخل بافت نیرو افزایش می‌یابد. در لحظه ورود نوک ابزار به داخل بافت قرنیه به میزان ۱۲.۳ درصد در سرعت ۲ میلی متر بر ثانیه و به میزان ۱۹.۱ درصد در سرعت ۱ میلی متر بر ثانیه نیرو کاهش می یابد و بعد از آن نیرو تقریبا ثابت باقی می ماند. بعد از برش کامل که معادل با بیشترین عرض ابزار می‌باشد، نیرو از روی ابزار برداشته می‌شود و به سمت ناپدید شدن پیش می‌رود. نیروی برش قرنیه با تغییرات فشار در سرعت ۱ میلی متر بر ثانیه در بازه ۰.۱۸۳ نیوتن تا ۰.۲۸۷ نیوتن و در سرعت ۲ میلی متر بر ثانیه در بازه ۰.۲۱۱ نیوتن تا ۰.۲۸۱ نیوتن متغییر می‌باشد. مدل المان محدود نشان می‌دهد که بیشینه خطای پیش بینی شده توسط این مدلسازی برای سرعت ۲ میلی متر بر ثانیه برابر با ۰.۰۴۲ می باشد. خطای جذر میانگین مربعات بین مدلسازی المان محدود صورت گرفته و آزمایش های تجربی انجام شده برابر با ۰.۰۲۵ می باشد.

International Journal of Engineering

Journal Homepage: www.ije.ir

Study of Friction Stir Spot Welding of Aluminum/Copper Dissimilar Sheets using Taguchi Approach

H. Khatami, T. Azdast*, M. Mojaver, R. Hasanzadeh, A. Rafiei

Mechanical Engineering Department, Faculty of Engineering, Urmia University, Urmia, Iran

PAPER INFO

Paper history:
Received 5 June 2020
Received in revised form 22 March 2021
Accepted 24 March 2021

Keywords:
Friction Stir Spot Welding
Dissimilar Sheets
Tensile Properties
Taguchi Approach

ABSTRACT

Friction stir spot welding of dissimilar aluminum and copper sheets was investigated in details using Taguchi approach in this study. Analysis of variance was conducted to identify the effective parameters and their contributions on the mechanical performance. The findings revealed that the outputs followed normal distribution. The results indicated that the rotational speed with the contribution of 87.7% was the most effective parameter on the maximum tensile force tolerated by the welded samples. Dwell time and penetration depth were in second and third ranks from effectiveness viewpoint with the contributions of 8.8 and 2.9%, respectively. The results revealed that the maximum tensile force was significantly improved with the rotational speed. The maximum tensile force was enhanced by almost 228% by increasing the rotational speed from 550 rpm to 1500 rpm. Increasing the dwell time from 10 to 20 s led to improve the maximum tensile force by 31%.The sequence of the parameters was as rotational speed, dwell time and penetration depth from standpoint of influence on the maximum force according to the results of signal to noise ratio analysis. The signal to noise ratio analysis showed that the rotational speed of 1500 rpm, the penetration depth of 2.85 mm, and the dwell time of 20 s were the optimum conditions.

***doi**: 10.5829/ije.2021.34.05b.28*

1. INTRODUCTION

Friction welding is a type of solid-state welding. Heat is generated using mechanical friction between two workpieces in this process. Rotary friction welding, linear friction welding, friction surfacing, and friction stir welding (FSW) are the most improtant classes of friction welding. FSW is a solid-state bonding process invented in 1991 by the British Welding Association used to bond metallic and polymeric materials [1]. In this method, the base parts are heated by friction with a non-consumable rotational tool and then, are pressed to each other. This causes two parts to be joined to each other. The main advantage of this method is the non-melting of the work pieces and the solid phase bonding. Friction stir spot welding (FSSW) is a subset of the FSW with this difference that there is no linear motion in this process and it is used to make point bonding in thin sheets. Several studies have been done on the FSSW process, including the study of the influence of various parameters on the mechanical properties of the bonded area.

Azdast et al. [2] investigated the influence of nanoparticle addition and processing parameters on the behavior of welds of polycarbonate nanocomposites parts using the FSW process. The results showed that the amount of nano-alumina powder, rotational speed, and transverse speed had the greatest effects on the impact strength, respectively. Sun et al. [3] used the FSSW process to bond aluminum AA6061 sheet and mild steel with a thickness of 2 mm. Bisadi et al. [4] used the FSW process to bond aluminum AA5083 and pure copper at different rotational and transverse speeds. Ozdemir et al. [5] investigated the effect of the penetration depth of the tool pin in the FSSW of aluminum 1050 and pure copper. Lin et al. [6] investigated the effects of different parameters on the FSW of aluminum alloys. Sun et al. [7] investigated the mechanical properties of the FSSW process of aluminum 1050 and 6061-T6 sheets.

*Corresponding Author Institutional Email: t.azdast@urmia.ac.ir (T Azdast)

Please cite this article as: H. Khatami, T. Azdast, M. Mojaver, R. Hasanzadeh, A. Rafiei, Study of Friction Stir Spot Welding of Aluminum/Copper Dissimilar Sheets using Taguchi Approach, International Journal of Engineering, Transactions B: Applications Vol. 34, No. 05, (2021) 1329-1335

Pure copper is a soft, malleable, and ductile metal with very high electrical conductivity with applications in building construction, power generation and transmission and aerospace industry. Aluminum alloys with good heat transfer, high strength, ductility and good weldability are used in aerospace, railway cars and shipbuilding.

Previous researches have shown that different process parameters affect the mechanical properties of the FSSW welds. However, a comprehensive study of the effects of these parameters on dissimilar metal welding is still challenging and needs further study. Therefore, in this research work, it is attempted to comprehensively investigate the main and interaction effects of the processing parameters on the mechanical properties of aluminum and copper dissimilar welds using Taguchi method. The contributions of different parameters on the mechanical performance of the welded samples are recognized using the analysis of variance. Furthermore, the optimization of the process conditions to achieve the maximum mechanical properties is investigated using the signal to noise ratio analysis of Taguchi approach.

2. MATERIALS AND METHODS

Industrial grade of aluminum sheets with the thickness of 2 mm and copper sheets with the thickness of 1 mm were purchased. The sheets were cut to 50×100 mm sheets. Alloying elements are shown in Table 1.

The copper sheets were placed as the upper layer and the aluminum sheets were positioned as the lower layer. The schematic of the sheets layout and their dimensions are presented in Figure 1.

TABLE 1. Alloying element of materials [8, 9]

Aluminum				
Al	Cu	Fe	Mg+Mn+Si+Ti	
99.5	0.05	0.4	0.05	
Copper				
Cu	Al	Zn	Ti	Cr+Mg+Pb+Si
99.86	0.001	0.009	0.0002	0.0014

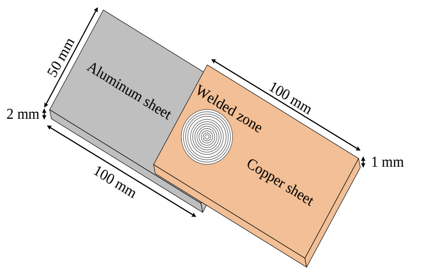

Figure 1. Schematic of sheets layout and their dimensions

Welding was done at ambient temperature using a H13 stainless steel tool with hardness of 52 HRC (hardness Rockwell-C). The pin height and diameter were 2.6 mm 2.2 mm, respectively. The tool height was 90 mm and the shoulder diameter was 18 mm. Figure 2 shows the real picture and schematic of the used tool.

The welding operations were performed on the LUNAN ZX6350 (China) milling machine with the aim of an appropriate designed and manufactured fixture.

The tool was in touch with the copper sheet. The rotating tool penetrates the sheets with a specific depth. In the following, the tool was held there for an adjusted time called dwell time. During welding, a stopwatch was used to calculate the time.

In the present study, the rotational speed, the penetration depth, and the dwell time were selected as the variable parameters. Each parameter was set at three different levels according to the pre-experiments. Table 2 shows the variable parameters and their levels.

The rotational speed was set at 550, 950, and 1500 rpm. The reason for choosing the rotational speed of 1500 rpm as the highest level of the rotational speed is the limitation of the device used for welding. The welds performed at the rotational speeds lower than 550 rpm were inappropriate due to the insufficient heat produced at these rotational speeds. Figure 3 shows a representative inappropriate weld performed at the rotational speeds lower than 550 rpm. Therefore, the rotational speed was set between 550-1500 rpm.

The levels of the dwell time were considered as 10, 15, and 20 s. The dwell time was not chosen lower than 10 seconds because of the incomplete mixing and melting of the materials during the welding operation. Also, the dwell time selection above 20 seconds caused the aluminum side to fracture due to overheating.

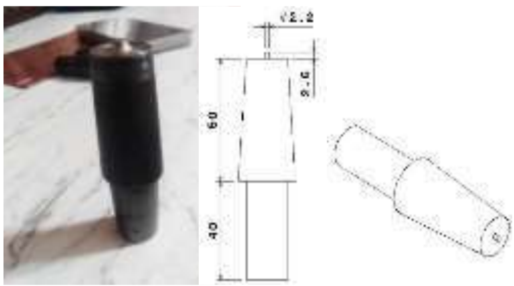

Figure 2. Real picture and schematic of the tool used in the present study (all dimensions are in mm)

TABLE 2. Variable parameters and their levels

Parameters	Low	Middel	High
Rotational speed(rpm)	550	950	1500
Penetration depth(mm)	2.80	2.85	2.90
Dwell time(s)	10	15	20

Figure 3. Representative inappropriate weld performed at rotational speeds lower than 550 rpm

Nowadays, design of experiment (DOE) methods have a broad range in engineering applications [10-14]. Taguchi method is one of the most popular DOE methods [15-18].

Studying the effect of the input parameters on different responses, investigating the contribution of the input parameters on the response variables using analysis of variance (ANOVA), and optimizing the process using the signal to noise ratio (S/N) analysis are different tools of Taguchi approach.

Signal to noise has different formulations with respect to various problems. In the present study, the main aim is to maximize the tensile properties. Therefore, the "larger-is-better" state is used as follows in Equation (1) [17]:

$$S/N = -10\log\left[\frac{1}{n}\sum_{i=1}^{n}\frac{1}{y_i^2}\right] \quad (1)$$

where y is the response variable and n is the number of the experiments.

All the statistical analyzes were performed using Minitab-18 software.

According to the considered parameters and their levels, the L_9 orthogonal array of Taguchi approach was utilized in order to investigate the process as Table 3.

TABLE 3. L_9 orthogonal array of Taguchi approach utilized in the present study

Trial	Rotational speed (rpm)	Penetration depth (mm)	Dwell time (s)
T1	550	2.80	10
T2	550	2.85	15
T3	550	2.90	20
T4	950	2.80	15
T5	950	2.85	20
T6	950	2.90	10
T7	1500	2.80	20
T8	1500	2.85	10
T9	1500	2.95	15

The welds were performed according to Table 3.

The tensile tests were performed using Santam-ST150 tensile testing machine with a tensile speed of 10 mm/min. For each trial, at least three specimens were tested and the results were reported as mean ± standard deviation.

3. RESULTS AND DISCUSSION

Figure 4 shows the representative force-extension diagrams of nine different welded samples.

The maximum tensile force tolerated by the welded samples was considered as the response variable. Table 4 indicates the response variable i.e. the maximum tensile force tolerated by the welded samples. Also, the standard deviations of the measurements are represented in Table 4. According to the results, the standard deviations were desirable and were below 10%.

Normal probability diagram of the maximum tensile force according to the Anderson-Darling method showed that the p-value=0.506 was larger than the statistical error considered by the Minitab software (0.05), and therefore, the distribution of the results was normal. Therefore, the analysis of variance could be performed.

Table 5 shows the analysis of variance of the maximum tensile force. The results indicated that the rotational speed was the most effective parameter on the maximum tensile force. The contribution of the rotational speed was 87.7% on the maximum tensile force. The dwell time and the penetration depth were in the

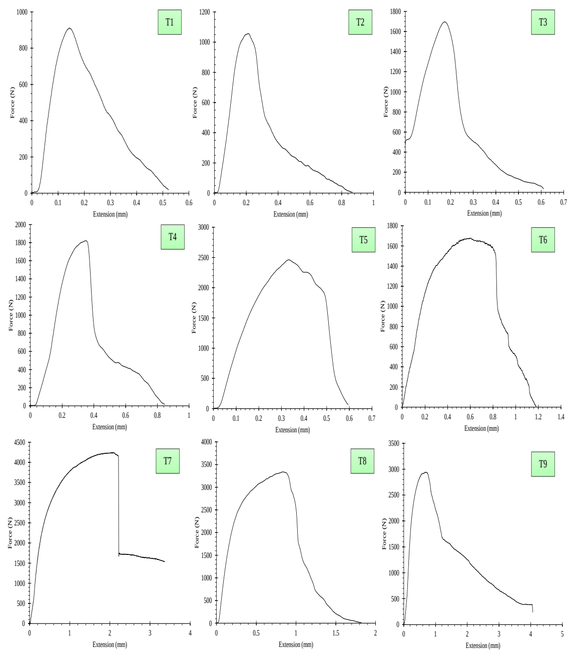

Figure 4. Representative force-extension diagrams of the welded samples

TABLE 4. Experimental results

Trial	Maximum tensile force (N)
T1	924 ± 15
T2	995 ± 85
T3	1163 ± 77
T4	1734 ± 122
T5	2376 ± 119
T6	1599 ± 90
T7	4040 ± 282
T8	3267 ± 98
T9	2789 ± 192

second and the third ranks from effectiveness viewpoint on the maximum tensile force, respectively. The contributions of the dwell time and the penetration depth on the maximum tensile force were 8.8% and 2.9%, respectively. Also, the contribution of the error in this model was 0.6%. In other words, the R^2 value was 99.4%. Therefore, the results had high validity.

The main effects of the considered parameters on the maximum tensile force are depicted in Figure 5.

TABLE 5. Analysis of variance results

Source	DF	SS	MS	Contribution (%)
Rotational speed (rpm)	2	8371455	4185727	87.7
Penetration depth (mm)	2	277864	138932	2.9
Dwell time (s)	2	835803	417901	8.8
Error	2	58172	29086	0.6
Total	8	9543294	4185727	100

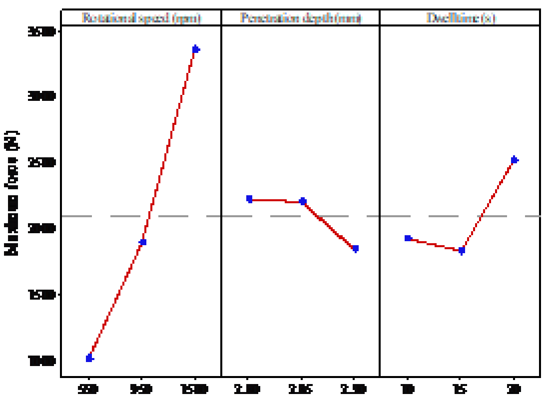

Figure 5. Main effect of processing parameters on maximum tensile force

As the results showed, the maximum tensile force was improved significantly by the rotational speed. The maximum tensile force was increased from 1027 N to 1903 N by increasing the rotational speed from 550 rpm to 950 rpm. In other words, an improvement of 85.3% in the maximum tensile force was observed by increasing the rotational speed from 550 rpm to 950 rpm. This improvement was continued by more increment in the rotational speed and the maximum tensile force was increased to 3365 N at the rotational speeds of 1500 rpm. The maximum tensile force at the rotational speed of 1500 rpm was improved by 76.8 and 227.7% compared to the rotational speeds of 950 rpm and 550 rpm, respectively. More heat is generated in higher rotational speeds because there are more friction and stirring phenomena at higher rotational speeds. Therefore, the welded samples had higher mechanical properties at higher rotational speeds. The results indicated that the maximum tensile force was reduced by increasing the penetration depth. This reduction was more considerable at the highest level of the penetration depth. A reduction of 17.2% (from 2233 N to 1850 N) was observed by increasing the penetration depth from 2.80 mm to 2.90 mm. According to the results, the maximum tensile force was enhanced by increasing the dwell time. The maximum tensile force was improved by 30.9% (from 1930 N to 2526 N) by increasing the dwell time from 10 s to 20 s.

Figure 6 shows the interaction effect of the rotational speed and the penetration depth on the maximum tensile force. According to the results, the maximum tensile force was enhanced by increasing the rotational speed at all penetration depth. However, this enhancement was more significant at low penetration depths. The results revealed that the maximum tensile force was decreased by increasing the penetration depth at the rotational speed of 1500 rpm while it was slightly increased by increasing the penetration depth at the rotational speed of 550 rpm.

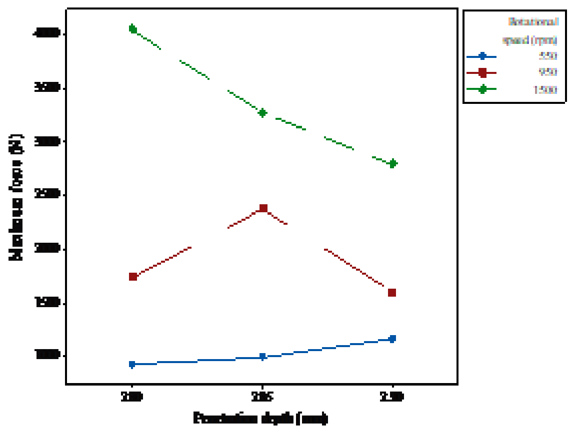

Figure 6. Interaction effect of rotational speed and penetration depth on maximum tensile force

There was an optimum penetration depth to achieve the highest maximum tensile force at the rotational speed of 950 rpm.

The interaction effect of the rotational speed and the dwell time on the maximum tensile force is depicted in Figure 7. The results showed that the maximum tensile force was increased by increasing the rotational speed at all dwell times. Also, the maximum tensile force was improved by increasing the dwell time at all rotational speeds.

Figure 8 indicates the interaction effect of the penetration depth and the dwell time on the maximum tensile force. The results showed that the penetration depth in which the highest maximum tensile force occurred was different at different dwell times. The highest maximum tensile force was occurred at the penetration depth of 2.85 mm in the dwell time of 10 s, at the penetration depth of 2.90 mm in the dwell time of 15 s, and at the penetration depth of 2.80 mm in the dwell time of 20 s. The maximum tensile force is reduced by increasing the penetration depth at high level of the dwell time.

The signal to noise ratio analysis was performed to recognize the optimum conditions to achieve the highest maximum tensile force. Table 6 shows the results of the signal to noise ratio analysis. The level with the highest signal to noise value is the optimum level. Therefore, the optimum conditions were the third level of the rotational speed, the second level of the penetration depth, and the third level of the dwell time. In other word, the rotational speed of 1500 rpm, the penetration depth of 2.85 mm, and the dwell time of 20 s were the optimum conditions. According to Table 3, these conditions were not one of the experiments. Therefore, the prediction tool of Taguchi approach was utilized to estimate the maximum tensile force at the optimum condition. The results showed that the maximum tensile force was 4097 N at the optimum condition.

Another important result of the signal to noise ratio analysis is the ranking of the parameters from the standpoint of the effectiveness. This ranking is according to the delta value. The delta is the difference between the highest and the lowest signal to noise values. The results revealed that the rotational speed was in the first rank followed by the dwell time and the penetration depth. According to the results, the ranking of the parameters obtained from the signal to noise ratio analysis was in agreement with the results of the analysis of variance.

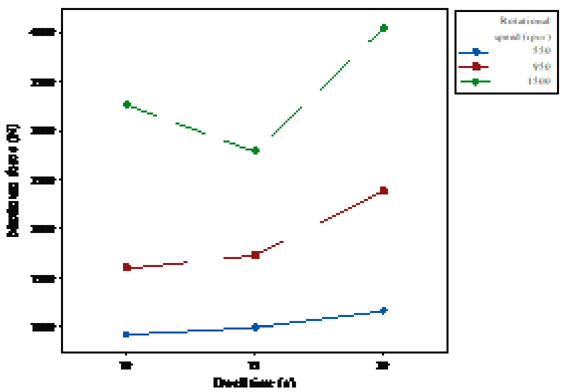

Figure 7. Interaction effect of rotational speed and dwell time on maximum tensile force

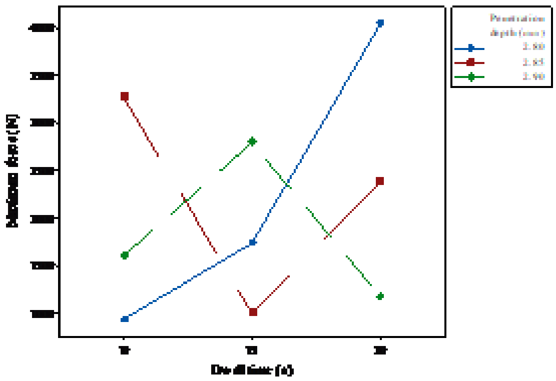

Figure 8. Interaction effect of penetration depth and dwell time on maximum tensile force

TABLE 6. Signal to noise ratio analysis for maximum force

Level	Rotational speed	Penetration depth	Dwell time
1	60.19	65.41	64.56
2	65.46	65.92	64.55
3	70.44	64.77	66.99
Delta	10.25	1.15	2.44
Rank	1	3	2

4. CONCLUSIONS

Friction stir spot welding of dissimilar sheets of aluminum/copper was performed in the present study. Rotational speed, penetration depth, and dwell time were selected as the variable parameters and maximum tensile force was considered as the response parameter. Taguchi approach was utilized as the design of experiment method to study the process in details. Analysis of variance and signal to noise ratio analysis were used to recognize the effective parameters and optimize the process, respectively. The findings can be summarized as follows:

- Rotational speed was the most effective parameter on the maximum tensile force.
- Dwell time and penetration depth were in the second and third ranks from effectiveness viewpoint on the maximum tensile force.
- The maximum tensile force was enhanced with increasing the rotational speed.

- The maximum tensile force was improved by decreasing the penetration depth and increasing the dwell time.
- The optimum condition was the rotational speed of 1500 rpm, the penetration depth of 2.85 mm, and the dwell time of 20 s.
- The maximum tensile force was increased to 4097 N at the optimum conditions based on the prediction tool of Taguchi approach.

5. REFERENCES

1. Mishra, R. S., Ma, Z. Y. "Friction stir welding and processing." ***Materials Science and Engineering R: Reports,*** Vol. *50*, No. 1, (2005), 01-78. DOI: 10.1007/s11661-007-9459-0
2. Azdast, T., Hasanzadeh, R., Moradian, M. "Improving impact strength in FSW of polymeric nanocomposites using stepwise tool design." ***Materials and Manufacturing Processes***, Vol. 33, No. 3, (2018), 343-349. DOI: 10.1080/10426914.2017.1339324
3. Sun, Y. F., Fujii, H., Takaki, N., Okitsu, Y. "Microstructure and mechanical properties of dissimilar Al alloy/steel joints prepared by a flat spot friction stir welding technique." ***Materials & Design***, Vol. 47, (2013), 350-357. DOI: 10.1016/j.matdes.2012.12.007
4. Bisadi, H., Tavakoli, A., Sangsaraki, M. T., Sangsaraki, K. T. "The influences of rotational and welding speeds on microstructures and mechanical properties of friction stir welded Al5083 and commercially pure copper sheets lap joints." ***Materials & Design,*** Vol. 43, (2013), 80-88. DOI: 10.1016/j.matdes.2012.06.029
5. Özdemir, U., Sayer, S., Yeni, Ç. "Effect of pin penetration depth on the mechanical properties of friction stir spot welded Aluminum and copper." ***Materials Testing***, Vol. 54, No. 4, (2012), 233-239. DOI: 10.3139/120.110322
6. Lin, Y. C, Chen, J. N. "Influence of process parameters on friction stir spot welded Aluminum joints by various threaded tools." ***Journal of Materials Processing Technology***, Vol. 225, (2015), 347-356. DOI: 10.1016/j.jmatprotec.2015.06.024
7. Sun, Y. F., Fujii, H., Tsuji, N. "Microstructure and mechanical properties of spot friction stir welded ultrafine grained 1050 Al and conventional grained 6061-T6 Al alloys." ***Materials Science and Engineering A***, Vol. 585, (2013), 17-24. DOI: 10.1016/j.msea.2013.07.030
8. Stern, A., Aizenshtein, M., Moshe, G., Cohen, S. R., Frage, N. "The nature of interfaces in Al-1050/Al-1050 and Al-1050/Mg-AZ31 couples joined by magnetic pulse welding (MPW)." ***Journal of Materials Engineering and Performance***, Vol. 22, No. 7, (2013), 2098-2103. DOI: 10.1007/s11665-013-0481-7
9. Akinlabi, E. T., Andrews, A., Akinlabi, S. A. "Effects of processing parameters on corrosion properties of dissimilar friction stir welds of aluminium and copper." ***Transactions of Nonferrous Metals Society of China***, Vol. 24, No. 5, (2014), 1323-1330. DOI: 10.1016/S1003-6326(14)63195-2
10. Nejad, S. J. H., Hasanzadeh, R., Doniavi, A., Modanloo, V. "Finite element simulation analysis of laminated sheets in deep drawing process using response surface method." ***The International Journal of Advanced Manufacturing Technology***, Vol. 93, No. 9-12, (2017), 3245-3259. DOI: 10.1007/s00170-017-0780-5
11. Hasanzadeh, R., Azdast, T., Doniavi, A., Rostami, M. "A prediction model using response surface methodology based on cell size and foam density to predict thermal conductivity of polystyrene foams." ***Heat and Mass Transfer***, Vol. 55, No. 10, (2019), 2845-2855. DOI: 10.1007/s00231-019-02628-8
12. Safari, M., Tahmasbi, V., Hassanpour, P. "Statistical Modeling, Optimization and Sensitivity Analysis of Tool's Geometrical Parameters on Process Force in Automatic Cortical Bone Drilling Process." ***International Journal of Engineering, Transactions B: Applications***, Vol. 34, No. 2, (2021), 528-535. DOI: 10.5829/IJE.2021.34.02B.26
13. Azdast, T., Lee, R. E., Hasanzadeh, R., Moradian, M., Shishavan, S. M. "Investigation of mechanical and morphological properties of acrylonitrile butadiene styrene nanocomposite foams from analytical hierarchy process point of view." ***Polymer Bulletin***, Vol. 76, No. 5, (2019), 2579-2599. DOI: 10.1007/s00289-018-2517-5
14. Yousefi, M., Safikhani, H., Jabbari, E., Yousefi, M., Tahmsbi, V. "Numerical modeling and Optimization of Respirational Emergency Drug Delivery Device using Computational Fluid Dynamics and Response Surface Method." ***International Journal of Engineering, Transactions B: Applications***, Vol. 34, No. 2, (2021), 547-555. DOI: 10.5829/IJE.2021.34.02B.28
15. Abedini, A., Asiyabi, T., Campbell, H. R., Hasanzadeh, R., Azdast, T. "On fabrication and characteristics of injection molded ABS/Al_2O_3 nanocomposites." ***The International Journal of Advanced Manufacturing Technology***, Vol. 102, No. 5-8, (2019), 1747-1758. DOI: 10.1007/s00170-019-03311-2
16. Molani, S., Azdast, T., Doniavi, A., Hasanzadeh, R., Moradian, M., Mamaghani Shishavan, S. "A Taguchi analysis on structural properties of polypropylene microcellular nanocomposite foams containing Fe_2O_3 nanoparticles in batch process." ***Plastics, Rubber and Composites***, Vol. 47, No. 3, (2018), 106-112. DOI: 10.1080/14658011.2018.1441778
17. Toocharoen, S., Kaewkuekool, S., Peasura, P. "Rejuvenation Heat Treatment of Nickel Base Superalloy Grade GTD111 after Long-term Service via Taguchi Method for Optimization." ***International Journal of Engineering, Transactions A: Basics,*** Vol. 34, No. 4, (2021), 956-965. DOI: 10.5829/IJE.2021.34.04A.22
18. Jithendra, C., Elavenil, S. "Parametric Effects on Slump and Compressive Strength Properties of Geopolymer Concrete using Taguchi Method." ***International Journal of Engineering, Transactions C: Aspects***, Vol. 34, No. 3, (2021), 629-635. DOI: 10.5829/IJE.2021.34.03C.06

Persian Abstract

چکیده

جوشکاری اصطکاکی اغتشاشی نقطه ای ورق های غیر همجنس آلومینیوم و مس، با استفاده از روش تاگوچی مورد بررسی قرار گرفت. آنالیز واریانس برای شناسایی پارامترهای مؤثر و سهم آنها در عملکرد مکانیکی انجام شد. مقادیر خروجی از توزیع نرمال پیروی نمودند. نتایج نشان داد که سرعت چرخشی با سهم ۸۷/۷ درصد، مؤثرترین پارامتر بر روی حداکثر نیروی کششی نمونه های جوش داده شده است. زمان مکث و عمق نفوذ با درصد مشارکت به ترتیب ۸/۸ درصد و ۲/۹ درصد در رتبه‌های دوم و سوم قرار گرفتند. نتایج نشان داد که حداکثر نیروی کششی با افزایش سرعت چرخشی به طور قابل توجهی بهبود یافته است. با افزایش سرعت چرخش از ۵۵۰ دور در دقیقه به ۱۵۰۰ دور در دقیقه حداکثر نیروی کششی تقریباً ۲۲۸٪ افزایش یافته است. افزایش زمان مکث از ۱۰ ثانیه به ۲۰ ثانیه منجر به بهبود حداکثر نیروی کششی به میزان ۳۱ درصد شد. مطابق نتایج آنالیز سیگنال به نویز، ترتیب اثرگذاری پارامترها بر روی حداکثر نیروی کششی بصورت سرعت دورانی، زمان مکث و عمق نفوذ است. تجزیه و تحلیل نسبت سیگنال به نویز نشان داد که سرعت چرخش ۱۵۰۰ دور در دقیقه ، عمق نفوذ ۲/۸۵ میلی متر و زمان ساکن ۲۰ ثانیه شرایط بهینه هستند.

International Journal of Engineering
Journal Homepage: www.ije.ir

Axial Compression Performance of Square Tube Filled with Foam Aluminum

K. Yang*, Y. Sha, T. Yu

College of Mechanical Engineering and Automation, Liaoning University of Technology, Jinzhou, China

PAPER INFO

Paper history:
Received 10 January 2021
Received in revised form 17 March 2021
Accepted 23 March 2021

Keywords:
Foam Aluminum
Filling Structure
Square Tube
Impact Resistance
Axial Compression

ABSTRACT

As a typical buffer energy absorbing structure, thin-walled tube filled with foam aluminum has good mechanical properties and energy absorption characteristics. Therefore, the axial compression performance of square tube and foam aluminum filled square tube was experimentally studied by quasi-static mechanical loading method. On the basis of the existing experimental research and theoretical analysis, the strain rate is introduced into the dynamic compression theory, and the mathematical model of the average crushing force of foam aluminum filled square tube under the axial quasi-static and impact loads is obtained. By comparing the theoretical results with the simulation results, the error of quasi-static and impact state is 2.8 and 8%, respectively. The feasibility of the theoretical analysis is verified. This paper not only proves that foam aluminum filling can significantly improve the bearing capacity and energy absorption performance of square tube structure in the axial compression process, but also provides a more specific theoretical basis for the axial compression energy absorption design of square tube filled with foam aluminum.

doi: *10.5829/ije.2021.34.05b.29*

NOMENCLATURE

ρ	Density ($kg \cdot m^{-3}$)	P_1	Loads borne by the interaction between foam aluminum and metal thin-walled square tubes (MPa)
σ_s	Yield strength (MPa)	P_{mf}	Average crushing load of square tube filled with foam aluminum under quasi-static axial load (MPa)
P_m	Average load of single collapse of thin-walled square tube (MPa)	P_m^d	Average crushing load of square tube under axial impact load (MPa)
σ_f	Platform stress of foam aluminum core bearing alone (MPa)	$\dot{\varepsilon}_f$	The strain rate of foam aluminum under quasi-static axial load
σ_0	Yield stress of thin-walled square tube materials (MPa)	$\dot{\varepsilon}_f^d$	The strain rate of foam aluminum under dynamic impact load
b	The width of the square tube (mm)	P_{mf}^d	Average crushing load of square tube filled with foam aluminum (MPa)
t	The thickness of square tube's wall (mm)	m	Strain rate sensitivity coefficient
C	Interaction coefficient between foam aluminum and tube wall	L	Height of foam aluminum specimen(mm)
Φ	The volume fraction of solids contained in the edges of foam aluminum cells	**Subscript**	
ε_f	The maximum strain value during the deformation of foam aluminum	d	Dynamic

1. INTRODUCTION

Foam aluminum is a new type of structural and functional porous material developed rapidly in recent years. It has low density, high porosity, closed holes or open holes structure characteristics. However, due to the large number of holes in the structure of foam aluminum, foam aluminum is not suitable for use as structural material alone. It is usually used as a composite member with traditional dense metal, so as to achieve the best mechanical properties under certain loads, such as compression and bending properties. At the same time, foam material hided in closed and dense components can play a certain role of corrosion protection. At present, it

*Corresponding Author Institutional Email: yangkunwh@163.com (K. Yang)

Please cite this article as: K. Yang, Y. Sha, T. Yu, Axial Compression Performance of Square Tube Filled with Foam Aluminum, International Journal of Engineering, Transactions B: Applications Vol. 34, No. 05, (2021) 1336-1344

has been widely used in mechanical, construction, aerospace, especially in automobiles [1-3].

The sandwich structure consisting of foam aluminum core and metal panel generally has the advantages of light weight, high specific strength, high specific stiffness and good shock absorption. In recent years, domestic and foreign scholars have carried out a lot of experiments and numerical simulation research on foam aluminum filling structure. To overcome the 3D modelling problem of closed-cell foams structure, Akhavan et al. [4] present the method based on CT-scan and digital optic microscope imaging combination. The quasi-static axial compression performance of foam aluminum sandwich double tube structure was studied by Yu et al. [5] It was found that the energy absorption efficiency of the new structure was much higher than that of the conventional foam aluminum sandwich tube. Zhang [6] carried out the crashworthiness optimization model of aluminum alloy cone tubes filled with functional density gradient foam aluminum under low velocity impact. The research shows that the peak load of the strong bonded foam aluminum filled cone tube in collision is lower, the load change is more stable, and the energy absorption is greater than the energy absorption. The torsion test of the galvanized steel tube filled with foam aluminum under high temperature was carried out by Wang et al. [7], and the test results showed that the torsion bearing capacity of the galvanized steel filled with foam aluminum decreased with the increase of porosity, and increased with the increase of steel content and slenderness ratio. The conducted quasi-static compression energy absorption experiments on foam aluminum filled corrugated plate structures by Yan [8,9] et al, and found that the compression stress of foam aluminum filled corrugated plate was much higher than the sum of the compression stress of foam aluminum filled corrugated plate and hollow corrugated plate alone, showing an obvious coupling enhancement effect. In addition, the compression test and numerical simulation of the composite structure formed in the void and corrugated core of the closed cell foam aluminum filled sandwich plate were carried out under low-speed impact. The results show that the filling of foam aluminum reduces the buckling wavelength, and the plastic energy dissipation of the foam-filled core is much higher than that of the hollow core. The axial-compressive experiment of circular tube filled with foam aluminum core was studied by Gilchrist et al. [10], the results showed that the tube with the smallest inner diameter and the largest foam thickness is more suitable for energy absorbing parts. Duarte et al. [11] had studied the deformation mode of pipe the filled with foam aluminum. During the deformation process, the foam aluminum filler restrained the tube wall to buckle inward and made the energy absorption process more stable. Kader et al. [12] demonstrated the deformation mechanism of foam aluminum by using topology optimization for the first time, and relate the deformation to the mechanical response in the impact process.

At present many literature has the mechanical properties of the foam aluminum is carried on the detailed elaboration, but the study of structure of foam aluminum filler is relatively small, and most only involves numerical simulation research, the foam aluminum filled square tube under quasi-static and impact load is the average crushing load and energy absorption properties of the mathematical model of research are still lacking .This paper aims to studied the axial compression performance of square tube filled with foam aluminum by using experiment and simulation method. Through the experiments, the difference of deformation mode, bearing capacity and energy absorption efficiency between square tube and foam aluminum filled tube are analyzed. And the mathematical model of average crushing load of foam aluminum filled square tube under static and dynamic compression is obtained. In order to verify the theoretical analysis results, the theoretical calculation results and simulation results are compared with the experimental results. The results are to further explain the deformation mechanism of the foam aluminum filled structure, and it also provides a theoretical basis for the design of axial compression energy absorption the of square tube filling structure.

2. EXPERIMENTAL STUDY

2. 1. Sample Preparation The hollow square tube used in this experiment is Q235 low carbon steel cold drawn thin-walled square tube, the size is 30×30×80 mm, and the wall thickness is 1.2 mm. For the uniaxial compression test of square tube specimen, taking into account the processing technology level of the laboratory and the particularity of the foam aluminum filled square tube structure, the cuboid shape of 27×27×80 mm is determined by the wire cutting method as a sandwich body for filling the empty square pipe. The closed cell foam aluminum used for filling thin wall square core is produced by melt foaming method from Shenyang Dongda advanced material development limited company. Its matrix material is ZL102 aluminum alloy, with an average pore size of 3 mm~4 mm and a relative density of 0.22. The data of material parameters and mechanical properties are provided by the manufacturing company, as shown in Table 1. The stress-strain curve of the closed cell foam aluminum under unaxial quasi-static compression is shown in Figure 1.

The tube wall and the foam aluminum core are bonded by epoxy resin. After the epoxy resin has been completely cured, a thin-walled square tube filled with foam aluminum is prepared, as shown in Figure 2.

TABLE 1. Material parameters of closed-cell foam aluminum

Parameter	Value
Density ρ/kg·m^{-3}	540
Elastic modulus E/MPa	254
Poisson's ratio μ	0.33
Yield strength σ_s /MPa	8.1

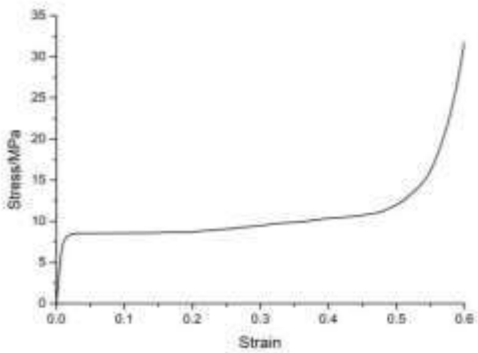

Figure 1. Compression stress-strain of foam aluminum

Figure 2. Specimen of compression experiment

2. 2. Experimental Equipment and Methods SANS-CMT5205 microcomputer controlled electronic universal testing machine is used in the experiment. The whole experiment process is controlled by microcomputer. The load value, displacement value, experimental loading speed and experimental curve are displayed dynamically in real time. The loading displacement curve is recorded automatically.

During the experiment, there is no special fixture (such as clamp), the specimen is placed in the middle of the rigid platform, and the pressure plate of the testing machine directly loads the end face of the square tube specimen. The loading rate is 0.1 mm/s (the strain rate is 10^{-2}). The loading stops, when the displacement of the plate is 55 mm (the total strain is 0.7) or the specimen collapse. In order to compare the experimental results, the quasi-static compression experiments of hollow square tubes and square tubes filled with foam aluminum are carried out, the process of text as shown in Figures 4 and 5. Three repetitions are tested in each case, and the average value is taken as the experimental result.

2. 3. Experimental Results and Analysis The axial compression load displacement curves of foam aluminum, hollow tube, foam aluminum filled tube and foam aluminum + hollow square tube (calculated value) is placed in the same coordinate system, as shown in Figure 7.

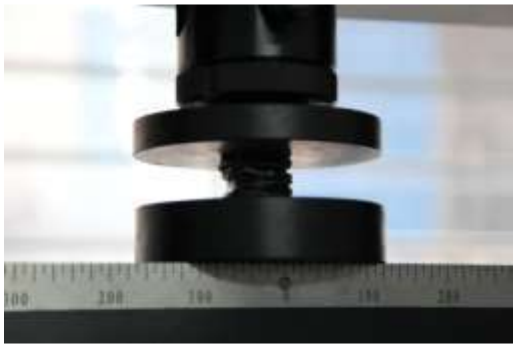

Figure 3. Quasi-static compression result of thin-walled square tube with foam aluminum filler

Figure 4. Quasi-static compression result of hollow square tube

Figure 5. Comparison of compression test results between square and square tubes filled with foam aluminum

Combined with Figures 5 and 7, it can be seen that when the square tube is compressed, the loading force first reaches an initial peak value, then decreases sharply, and then fluctuates periodically into a stable bearing area. Each load fluctuation on the load displacement curve corresponds to the formation and complete flattening of a fold. The formation of each fold includes the inner and outer folds of the pipe wall, corresponding to the two peaks of each fluctuation. After being completely flattened, the folds are regularly distributed on both sides of the undeformed tube wall. Similarly, we can also find out from the analysis of Figures 4 and 7. The fluctuation on the load displacement curve of the square tube filled with foam aluminum is related to the number and location of the fold in the crushing process. Before the upper and lower pipe walls which formed the fold contacted with each other but were not compacted, the load was reduced to the minimum, and it was shown as a trough on the load displacement curve. At the same time, the peak load of the foam aluminum filled square tube is not obvious when it collapsing. When the compressible part of the square tube is fully compacted, the bearing capacity of the structure increases rapidly.

By comparing the load-displacement curves of foam aluminum filled square tubes and empty square tubes, it is known that the equivalent yield strength of square tubes filled with foam aluminum increases, and the crest, trough and corresponding load and average load increase on the compression load displacement curve. In the whole crushing process, the compression load is much higher than that of the corresponding empty square tube under the same compression displacement. From Figure 7, the mean load of the empty square tube is only 17.26KN, while the mean load of the square tube filled with foam aluminum is 33.04KN, which is 1.91 times the mean load of the empty square tube. At the same time, the compression process can also be found that due to the filling of foam aluminum, the compression distance of the structure is reduced, as shown in Figure 6.

Due to the filling of the foam aluminum core, the trend of the bending of the square tube is restrained. It makes

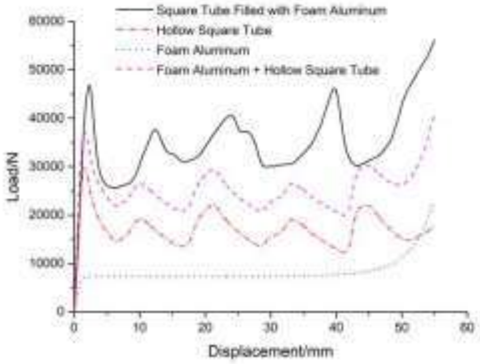

Figure 6. Interaction between foam aluminum and tube wall

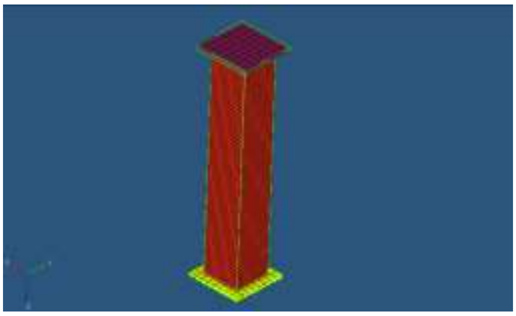

Figure 7. Finite element model of compression

the folds of thin-walled tube shorter and the number increased. At the same time, when the tube wall folds into the foam aluminum core, the multi-directional extrusion of the foam aluminum material increases the plastic deformation of the foam aluminum. As a result, the bearing capacity and energy absorption capacity of the foam aluminum filled tube structure are greatly improved. Because the yield stress of the metal tube wall is much larger than the yield stress of the foam aluminum, the deformation of the aluminum foam core is restricted by the wall of the tube, which results in the same deformation mode of the aluminum foam core as the fold of the tube. This is the contribution of interaction to the crushing load, which makes the average crushing load of aluminum foam-filled structure increase by 30%, which is higher than the sum of the crushing load of thin-walled empty square tube structure and foam aluminum filled structure.

3. QUASI STATIC COMPRESSION PERFORMANCE ANALYSIS OF SQUARE TUBE FILLED WITH FOAM ALUMINUM

The axial compression load of thin-walled square tubes filled with foam aluminum can be divided into three parts: the load bearing capacity of the foam aluminum alone, the load carrying capacity of the thin-walled hollow tube separately, and the load acting on the interaction between the foam aluminum and the thin-walled hollow pipe.

Hanssen et al. [13] through the experimental study of the thin-walled square tube filled with foam aluminum under axial impact condition, the average load formula of the filled structure under quasi-static axial load is obtained.

$$P_{\mathrm{mf}} = P_{\mathrm{m}} + b^2\sigma_{\mathrm{f}} + Cbt\sqrt{\sigma_{\mathrm{f}}\sigma_0} \tag{1}$$

3. 1. Average Crushing Load of Square Tube Under Quasi-Static Load Wierzbicki and Abramowicz [14] have studied the collapse process of thin-walled square tubes by experiments, and have given the typical fold of symmetrical deformation mode. The average load formula of single crushing of thin-walled square tubes stated as follows:

$$P_{\mathrm{m}} = 13.06\sigma_0 t^{\frac{5}{3}} b^{\frac{1}{3}} \tag{2}$$

$$\sigma_0 = \frac{\sigma_{\mathrm{u}} + \sigma_{\mathrm{y}}}{2} \tag{3}$$

For the foam aluminum filled square tubes studied in this paper, the material is Q235 low carbon steel square tube, its yield strength is 235 MPa, tensile yield strength is 380 MPa, and the above values are calculated by substitution formula P_m=16.909KN.

3. 2. Average Crushing Load of Foam Aluminum under Quasi-static Loading

The ratio of plateau stress σ_{f} of closed cell foam aluminum to the yield stress σ_{s} of foam aluminum matrix is:

$$\frac{\sigma_{\mathrm{f}}}{\sigma_{\mathrm{s}}} \approx 0.3\left(\phi\frac{\rho_{\mathrm{f}}}{\rho_{\mathrm{s}}}\right)^{3/2} + 0.4(1-\phi)\left(\frac{\rho_{\mathrm{f}}}{\rho_{\mathrm{s}}}\right) \tag{4}$$

By fitting the stress-strain curve of foam aluminum, the constitutive relation expression of foam aluminum material is obtained:

$$\sigma(\varepsilon) = \begin{cases} \sigma_{\mathrm{f}} & \varepsilon \le \varepsilon_{\mathrm{c}} \\ \left(1 + a_0 e^{\varepsilon/b_0}\right)\sigma_{\mathrm{f}} & \varepsilon_{\mathrm{c}} < \varepsilon \le \varepsilon_{\mathrm{f}} \end{cases} \tag{5}$$

The coefficients of a_0 and b_0 can be obtained by fitting the stress-strain curves. $a_0 = 2.3\times10^5$ and b_0 =0.06411. By integrating Equation (5), the average stress of foam aluminum material in the process of 0~ ε_{f} strain is:

$$\sigma(\varepsilon_{\mathrm{f}}) = \frac{1}{\varepsilon_{\mathrm{f}}}\int_0^{\varepsilon_{\mathrm{f}}} \sigma(\varepsilon)\mathrm{d}\varepsilon = \sigma_{\mathrm{f}} + \frac{1}{\varepsilon_{\mathrm{f}}} a_0 b_0 \sigma_{\mathrm{f}} \left(e^{\varepsilon_{\mathrm{f}}/b_0} - e^{\varepsilon_{\mathrm{c}}/b_0}\right) \tag{6}$$

The base material of foam aluminum used in this paper is ZL102 aluminum alloy, and its yield strength is σ_{s} =240MPa. The substitution stress (4) can obtain the theoretical value of the platform stress of σ_{f} =7.340MPa.

According to the stress-strain curve in Figure 1, ε_{c} and ε_{f} are taken as 0.7 and 0.5, respectively. By substituting the parameters into Equation (6), $\sigma(\varepsilon_{\mathrm{f}})$ =8.393MPa can be obtained. The theoretical results agree well with the platform stress values of 8.1MPa for foam aluminum specimens.

3. 3. Interaction between Foam Aluminum Core and Tube Wall

Due to the filling of foam aluminum, the foam aluminum core provides constraints when the tube wall buckled inward. The effective length of each plastic fold decreases. The proportion of the tube wall bending inward also decreased. This results in a higher average load. The contribution of the interaction between the foam aluminum core and the metal thin-walled square tube to the average load is expressed as follows:

$$P_1 = C \times \sigma_{\mathrm{f}}^{\alpha_1} \times \sigma_0^{\alpha_2} \times r^{\alpha_3} \times t^{\alpha_4} \tag{7}$$

According to the experiment of Hassen and Abramowicz [13, 14], when α1=α2=0.5, α3=α4=1, C is a dimensionless constant, and the value of C is 5. Therefore, Equation (7) can be simplified as: follows:

$$P_1 = 5bt\sqrt{\sigma_{\mathrm{f}}\sigma_0} \tag{8}$$

The interaction between the foam aluminum core and the tube wall can contribute to the average crushing load by introducing the relevant data into the formula (8). The contribution of the interaction between the foam aluminum core and the tube wall is P_1 =7.853KN.

By subbing into Equation (1) the average crushing load of the thin-walled square tube under the quasi-static axial load obtained through theoretical analysis, the platform stress of the foam aluminum material under the single load, and the interaction between the foam aluminum core and the tube wall, the average crushing load of the thin-walled square tube under the quasi-static axial load can be obtained:

$$P_{\mathrm{mf}} = P_{\mathrm{m}} + b^2\sigma_{\mathrm{f}} + Cbt\sqrt{\sigma_{\mathrm{f}}\sigma_0} =$$

$$16.909 + 0.03^2 \times 8.39\times10^6 + 7.853 = 32.3157\ \mathrm{KN}$$

The experimental data are taken into the formula of quasi-static compression average crushing load of foam aluminum filled square tubes deduced by Hanssen et al. [13] The results are compared with the theoretical and experimental results. It can be seen that the error between the theoretical results and the experimental results is smaller and more accurate. The comparison results are shown in Table 2.

4. DYNAMIC COMPRESSION PERFORMANCE ANALYSIS OF SQUARE TUBE FILLED WITH FOAM ALUMINUM

Different from the deformation behavior under quasi-static load, the member is subjected to large impact load in a short time, and the whole deformation process is a complex nonlinear dynamic response process. It has very obvious dynamic characteristics, and the plastic flow usually occurs in the collision area of the component. The plastic flow deformation of many materials will be affected by the strain rate.

4. 1. Collapse Load of Square Tube Under Impact Load

Due to the obvious strain rate effect of low carbon steel, Cowper-Symonds model is used to consider the effect of strain rate on the mechanical properties of

TABLE 2. The theoretical calculation results of the average crushing load of square tubes filled with foam aluminum are compared with the experimental results

Experimental result	Theoretical calculation results		Compare the calculation results	
	P_m /KN	Relative error /%	P_m /KN	Relative error /%
33.04	32.3157	2.2	32.1998	2.6

pipe wall materials. Combined with the dynamic yield stress formula described by the model and the experimental and theoretical analysis results of Abramowicz and Jones [15], the average crushing load of thin-walled square tube under axial impact load is obtained as follows:

$$P_{\mathrm{m}}^{\mathrm{d}} = 13.06\sigma_0 b^{\frac{1}{3}} t^{\frac{5}{3}} \left[1 + \left(0.33 \frac{V_0}{bD} \right)^{\frac{1}{q}} \right] \tag{9}$$

In the above equation D, q are constants, D= 6844s-1, q=3.91. Put relevant parameters into Equation (9) to calculate the load response of empty square pipe impact is 22.068KN.

4. 2. Crushing Load of Foam Aluminum Under Impact Loading

For foam aluminum, the yield stress under dynamic loading is:

$$\sigma_{\mathrm{f}}^{\mathrm{d}} = \sigma_{\mathrm{f}} \left(\frac{\dot{\varepsilon}_{\mathrm{f}}^{\mathrm{d}}}{\dot{\varepsilon}_{\mathrm{f}}} \right)^m \tag{10}$$

In the formula, σ_{f} is the yield stress of foam aluminum under quasi-static axial load; $\dot{\varepsilon}_{\mathrm{f}}$ is the strain rate of foam aluminum under quasi-static axial load; $\dot{\varepsilon}_{\mathrm{f}}^{\mathrm{d}}$ is the strain rate of foam aluminum under dynamic impact load, V_0 is strain rate sensitivity coefficient, and the value is 0.039.

When the impact velocity is V_0 the strain rate of foam aluminum under dynamic impact load is:

$$\dot{\varepsilon}_{\mathrm{f}}^{\mathrm{d}} = \frac{\varepsilon_{\mathrm{f}}}{T} = \frac{\varepsilon_{\mathrm{f}}}{\varepsilon_{\mathrm{f}} L / V_0} = \frac{V_0}{L} \tag{11}$$

Substituting Equation (12) into Equation (11).

$$\sigma_{\mathrm{f}}^{\mathrm{d}} = \sigma_{\mathrm{f}} \left(\frac{V_0}{\dot{\varepsilon}_{\mathrm{f}} L} \right)^m \tag{12}$$

4. 3. Energy Absorption Characteristics of Square Tubes Filled with Foam Aluminum under Impact Loading

Under the dynamic impact axial compression load, the interaction between the foam aluminum core and the tube wall has a smaller impact on the average load than that of the thin-walled hollow tube and the foam aluminum core. Therefore, the effect of strain rate on the average load of foam aluminum core and tube wall is not considered. Substitute Equations (9) and (12) into Equation (1), and the average crushing load of foam aluminum filled square tube under dynamic impact axial compression load is:

$$\begin{aligned} P_{\mathrm{mf}}^{\mathrm{d}} &= P_{\mathrm{m}}^{\mathrm{f}} + b^2 \sigma_{\mathrm{f}}^{\mathrm{d}} + Cbt\sqrt{\sigma_{\mathrm{f}}\sigma_0} \\ &= 13.06\sigma_0 b^{\frac{1}{3}} t^{\frac{5}{3}} \left[1 + \left(0.33 \frac{V_0}{bD} \right)^{\frac{1}{q}} \right] \\ &+ b^2 \sigma_{\mathrm{f}} \left(\frac{V_0}{\dot{\varepsilon}_{\mathrm{f}} l} \right)^m + Cbt\sqrt{\sigma_{\mathrm{f}}\sigma_0} \end{aligned} \tag{13}$$

By putting relevant parameters into Equation (13), the average crushing load of foam aluminum filled square tube under impact can be calculated as 39.1KN.

5. SIMULATION

In order to further study, the accuracy of theoretical analysis, HyperMesh and LS-DYNA finite element analysis software were used to simulate the axial compression deformation of the structure under impact.

5. 1. Modeling and Meshing

Figure 8 shows the finite element model of axial compression. The tube wall and foam aluminum are all divided into 2 mm mesh sizes. The shell of the thin-walled square tube is made of two dimensional Shell163 thin shell element. The thickness of the element is 1.2 mm and the shape of the cell is quadrilateral. The foam aluminum core is divided into three dimensional Solid164 elements, and the cell shape is hexahedron. The compression model is divided into 11760 individual elements, 3360 thin shell elements and 128 rigid elements. The rate of deformation is an important factor in the impact process. It is necessary to consider the strain rate effect in the impact simulation analysis. So, the Cowper-Symonds model is used as the material model for the impact simulation of aluminum foam filled square tube structure [16,17].

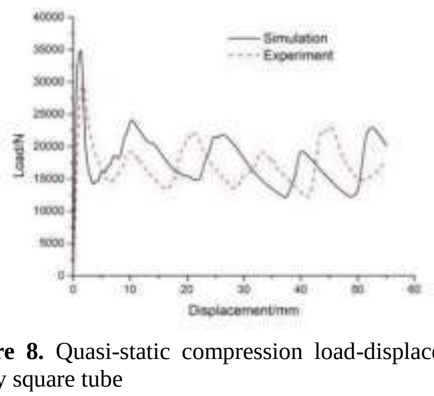

Figure 8. Quasi-static compression load-displacement of empty square tube

5. 2. Analysis of Compression Simulation Results

The compression deformation behaviors of empty square tube and foam aluminum filled square tube samples under quasi-static and impact loads were numerically simulated. The results obtained were compared with the experimental results and analyzed as follows.

(1) Compression simulation results and analysis of square tube

Figures 9 and 10 are the numerical analysis results of load displacement curve and the simulation results of quasi-static compression of hollow square tube.

The relative error of the three methods is shown in Table 3. The results of numerical simulation and theoretical calculation are very close to the experimental results, which shows that the process and conclusion of theoretical analysis of low carbon steel square tube structure are consistent.

(2) Compression simulation results and analysis of square tube filled with foam aluminum

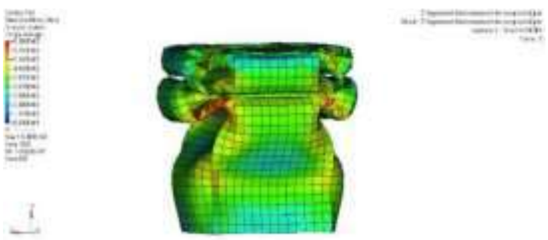

Figure 9. Quasi-static compression simulation results of square empty tube

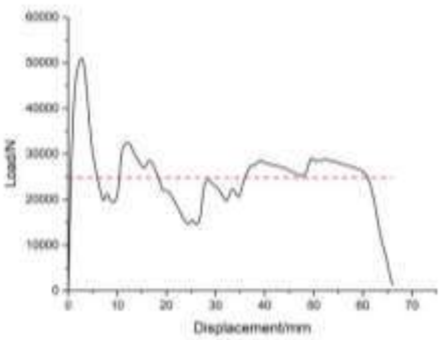

Figure 10. Dynamic compression load-displacement curve of square empty tube

TABLE 3. Average crushing load of square empty tube by theoretical calculation, numerical simulation and experimental

Experimental result	Theoretical calculation results		Numerical simulation results	
	P_m /KN	Relative error /%	P_m /KN	Relative error /%
17.26	16.909	2.1	17.931	3.9

Figures 11 and 12 are the comparison of the load displacement curves obtained from the quasi-static compression simulation analysis of the foam aluminum filled square tube with the experimental data and the quasi-static compression simulation results of the foam aluminum filled square tube.

By comparing the two curves, it can be seen that the initial peak load, average crushing load and the overall trend of load displacement curve obtained by simulation analysis are close to the experimental data. The average crushing load obtained by simulation analysis is 33.27KN, which is slightly larger than the average crushing load obtained by experiment 33.04KN, and the error is only 0.7%. It shows that the process and conclusion of theoretical analysis of the quasi-static compression load of square tube filled with foam aluminum are effective.

The compression load displacement curve of the foam aluminum filled square tube under dynamic load is shown in Figure 13.

It can be seen from Figure 13 that the average crushing load of the square tube filled with foam aluminum under impact loading is 36.22KN, and the error between theoretical analysis value 39.1KN and the average crushing load theoretical value of foam aluminum filled square pipe under impact is 8%. It is proved that the theoretical analysis results of the average crushing load of foam aluminum filled square tubes are

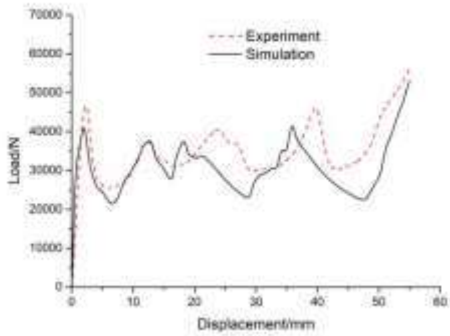

Figure 11. Quasi-static compression load-displacement of square tube with foam aluminum filler

Figure 12. Quasi-static simulation results of square tube with foam aluminum filler

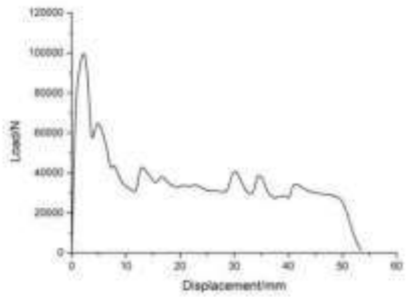

Figure 13. Dynamic compression load-displacement curve of square tube filled with foam aluminum

available when the dynamic impact axial compression load is proved.

6. CONCLUSION

(1) The research results show that the filling of foam aluminum improves the bearing capacity and energy absorption performance of the square tube structure during axial crushing process. Not only is the foam aluminum core bearing some load, but the interaction between the foam aluminum core and the tube wall also contributes to the improvement of the load capacity and energy absorption.

(2) The initial peak load and average crushing load of the specimen obtained from the simulation analysis are close to the experimental data. The simulation results show that the average crushing load is 33.27 KN, and the experimental results show that the average crushing load is 33.04 KN, and the error between them is only 0.7%. The calculated average load of quasi-static collapse failure is 32.32KN, which is very close to the simulation and experimental results. It shows that the process and conclusion of theoretical analysis of the quasi-static compression load of square tube filled with foam aluminum are effective.

(3) The effect of strain rate on the average crushing load of filled square tube is introduced into the theoretical analysis of dynamic compression, and the theoretical analysis value of dynamic compression is 39.1KN. Compared with the average crushing load of 36.22KN, the error is 8%. The error between the two is small. It can be seen that the formula for calculating the average load of axial compression failure of foam aluminum filled square tube structure under impact load is correct and reliable.

7. REFERENCES

1. Wang, S.L., Feng, Y., Xu, Y., Zhang, X.B., Shen, J., "Study on longitudinal and transverse compressive mechanical properties of aluminum foam filled circular tubes", ***Journal of Heat Treatment of Materials***, No. 1, (2007), 9-13+17, DOI: 10.3969/j.issn.1009-6264.2007.01.003.
2. Kou, Y. L., Chen, C. Q., Lu, T. J. "Foam aluminum rate dependent constitutive model and its application to impact energy absorption characteristics of sandwich panels", ***Journal of Solid Mechanics***, Vol. 32, No. 3, (2011), 217-227, DOI: 10.19636/j.cnki.cjsm42-1250/o3.2011.03.001.
3. Li F. "Study on impact characteristics of a new type of filled protective structure based on foam metal materials", Harbin: Master Degree Thesis of Harbin Institute of Technolog*y*, (2009), DOI: kns.cnki.net/KCMS/detail/detail.aspx?dbname=CMFD2011&filename=2010064272.nh
4. Akhavan B., Pourkamali Anaraki A., Malian A., Taraz Jamshidi Y., "Micro-structural Deformation Field Analysis of Aluminum Foam using Finite Element Method and Digital Image Correlation", ***International Journal of Engineering, Transactions A: Basics,*** Vol. 33, No. 10, (2020), 2065-2078, DOI: 10.5829/ije.2020.33.10a.25
5. Guo, L. W., Yu, J. L., Yang, G. D. "Quasi-static axial compression behavior of foam aluminum sandwich tube structure". ***Experimental Mechanics***, Vol. 26, No.2, (2011), 181-189, DOI: CNKI:SUN: Sylx.0.2011-02-012.
6. Zhang, Y. H., Gan, N. F. "Crashworthiness analysis of foam aluminum ed cone tubes by contact strength and induction slot", ***Mechanical Design and Manufacture***, No. 4, (2018), 129-132, DOI: 10.19356/j.cnki.1001-3997.2018.04.037.
7. Wang, Z. G., Wang Y., "Torsional behavior of foam aluminum filled galvanized steel tube after high temperature", ***Journal of Building Structures***, Vol. 39, No. S2, (2018), 155-161. DOI: 10.14006/j.j ZJGXB. 2018. S2.021.
8. Yan L.L., Zhao X., Zhao J.B., Li B.C., Zhang Q.C., Lu T. J. "Study on the coupling and strengthening mechanism of foam aluminum filled corrugated metal plates", ***Rare Metal Materials and Engineering***, Vol. 47, No. 2, (2018), 503-508, DOI: SUN:COSE.0.2018-02-017.
9. Yan, L.L., Yu, B., Han, B., Zhang, Q.C., Lu, T.J., Lu, B.H., "Effects of foam aluminum filling on the low-velocity impact response of sandwich panels with corrugated cores", ***Journal of Sandwich Structures and Materials***, Vol. 22, No. 4, (2020), 929-947, DOI: 10.1177/1099636218776585.
10. A. Baroutaji, M.D. Gilchrist, D. Smyth, A.G. Olabi. "Analysis and optimization of sandwich tubes energy absorbers under lateral loading" ***International Journal of Impact Engineering***, No. 82, (2015), 74-88, DOI: 10.1016/j.ijimpeng.2015.01.005.
11. Isabel Duarte, Matej Vesenjak, Lovre Krstulović-Opara, Zoran Ren, "Static and dynamic axial crush performance of in-situ foam-filled tubes", ***Composite Structures***, No. 124, (2015):128-139, DOI: 10.1016/j.compstruct.2015.01.014.
12. M.A. Kader, A.D. Brown, P.J. Hazell, V. Robins, J.P. Escobedo, M. Saadatfar, "Geometrical and topological evolution of a closed-cell aluminium foam subject to drop-weight impact: An X-ray tomography study", ***International Journal of Impact Engineering***, No. 139, (2020), DOI: 10.1016/j.ijimpeng.2020.103510.
13. A.G. Hanssen, M. Langseth, O.S. Hopperstad, "Static and dynamic crushing of square aluminium extrusions with aluminium foam filler". ***International Journal of Impact Engineering***, Vol. 24, No. 5, (2020), 475-507, DOI: 10.1016/S0734-743X(99)00169-4.
14. Abramowicz W, Wierzbicki T, "Axial crushing of foam filled columns", ***International Journal of Mechanical Sciences***, Vol. 30, No. 3-4, (1988), 263-271, DOI: 10.1016/0020-7403(88)90059-8.
15. Abrmaowiez W, Jones N, "Dynamic progressive buckling of circular and square tubes". ***International Journal of Impact***

Engeering, Vol. 10, No. 4, (1986), 243-270, DOI: 10.1016/0734-743X(86)90017-5.

16. S.V. Panin, D.D. Moiseenko, P.V. Maksimov, A. Vinogradov, "Influence of energy dissipation at the interphase boundaries on impact fracture behaviour of a plain carbon steel", ***Theoretical and Applied Fracture Mechanics***, No. 97, (2017), 478-499, DOI: 10.1016/j.tafmec.2017.09.010.

17. Lytvynenko I., Maruschak P., Prentkovskis O., Sorochak A, "Modelling Kinetics of Dynamic Crack Propagation in a Gas Mains Pipe as Cyclic Random Process", IOP Conference Series: Earth and Environmental Science, Vol. 115, No. 1, (2018), 262-269, DOI: 10.1088/1755-1315/115/1/012047

Persian Abstract

چکیده

به عنوان یک ساختار معمولی جذب کننده انرژی بافر ، لوله دیواره نازک پر از آلومینیوم فوم دارای خواص مکانیکی خوب و ویژگی های جذب انرژی است. بنابراین ، عملکرد فشرده سازی محوری لوله مربع و لوله مربع پر از آلومینیوم فوم به طور آزمایشی با استفاده از روش بارگذاری مکانیکی شبه استاتیک مورد مطالعه قرار گرفت. بر اساس تحقیقات تجربی و تجزیه و تحلیل نظری موجود ، نرخ کرنش به تئوری فشرده سازی دینامیکی وارد می شود و مدل ریاضی متوسط نیروی خردایش لوله مربع پر از آلومینیوم فوم تحت بارهای شبه استاتیکی و ضربه محوری به دست می آید. با مقایسه نتایج نظری با نتایج شبیه سازی ، خطای شبه استاتیک و حالت ضربه به ترتیب ۲.۸ و ۸٪ است. امکان تجزیه و تحلیل نظری تأیید شده است. این مقاله نه تنها اثبات می کند که پر کردن آلومینیوم فوم می تواند به طور قابل توجهی ظرفیت تحمل و عملکرد جذب انرژی ساختار لوله مربع را در فرآیند فشرده سازی محوری بهبود بخشد ، بلکه مبانی نظری خاص تری را برای طراحی جذب انرژی فشرده سازی محوری لوله مربع پر از کف آلومینیوم فراهم می کند

International Journal of Engineering

Journal Homepage: www.ije.ir

Single-phase and Two-phase Smoothed Particle Hydrodynamics for Sloshing in the Low Filling Ratio of the Prismatic Tank

A. Trimulyono*[a,b], D. Chrismianto[a], Samuel[a,b], M. H. Aslami[c]

[a] Department of Naval Architecture, Faculty of Engineering, Diponegoro University, Jl. Prof. Soedarto, S.H, Tembalang, Semarang, Indonesia
[b] Ship Hydrodynamics Laboratory, Departement of Naval Architecture, Diponegoro University
[c] Department of Mechanical, Aerospace and Civil Engineering, University of Machester, UK

PAPER INFO

Paper history:
Received 21 January 2021
Received in revised form 02 April 2021
Accepted 07 April 2021

Keywords:
Smoothed Particle Hydrodynamics
Prismatic Tank
Hydrostatic Pressure
Dynamics Pressure
Free Surface Deformation

ABSTRACT

The present study is to carry out a numerical sloshing using smoothed particle hydrodynamics (SPH) in the prismatic tank. Sloshing is a violent flow caused by the resonance of fluid in the tank by external oscillation. The prismatic tank was used to resemble a membrane LNG type carrier. The sloshing experiment was carried out using three pressure sensors, a camera high resolution, and four degrees of freedom forced oscillation machine. In this study, a filling ratio of 25% was used to reproduce sloshing in a low filling ratio. Only roll motion is used in the numerical simulation. Roll motion is directly imposing from the experiment displacement, and a comparison of hydrostatic and dynamic pressure was made to validate the SPH result. The time duration of the sloshing is the same as the experiment. Single-phase and multiphase SPH are conducted to reproduce sloshing in the prismatic tank. Sloshing was done both for the 2D and 3D domain. It shows that SPH has a good agreement with analytical and experimental results. The dynamic pressure is similar to an experiment through a spurious pressure oscillation exist. The dynamics pressure results show fairly for short time simulation and slightly decrease after that. The free surface deformation tendency is similar to experiment.

***doi**: 10.5829/ije.2021.34.05b.30*

NOMENCLATURE

F	Force	t	Time
P	Pressure	δ_φ	Delta-SPH
r	Position vector	ρ	Density
m	Mass	v	Velocity
h	Smoothing length	w	interpolation kernel
α	Coefficient of artificial viscosity	γ	Adiabatic index

1. INTRODUCTION

The sloshing phenomenon is one of the challenging event in a liquid carrier such as an LNG ship, tanker, and oil truck carrier. Sloshing can define as a resonance of fluid inside a tank caused by an external oscillation. As sloshing dealing with nonlinear behavior, numerical and experiment method is the appropriate approach to tackle this problem. Many studies have been carried out to overcome sloshing using numerical method both of mesh CFD (computational fluid dynamics) and meshless CFD. Using an open-source CFD solver OpenFOAM [1] dynamic pressure was well-validated with the experimental result. Jiang et al. [2] did a numerical simulation of the coupling effect between ship motion and liquid sloshing under wave conditions. The results revealed that sloshing impact loading has no significant coupling effect on global ship response. Sanapala et al. [3] have used OpenFOAM to simulate parametric liquid sloshing with the baffled rectangular container to get optimal baffles. The results showed optimal baffles were obtained with reference to the quiescent free surface. Xu et al. [4] perform sloshing

*Corresponding Author Institutional Email: anditrimulyono@lecturer.undip.ac.id (A. Trimulyono)

Please cite this article as: A. Trimulyono, D. Chrismianto, Samuel, M. H. Aslami, Single-phase and Two-phase Smoothed Particle Hydrodynamics for Sloshing in the Low Filling Ratio of the Prismatic Tank, International Journal of Engineering, Transactions B: Applications Vol. 34, No. 05, (2021) 1345-1351

simulation using OpenFOAM to validate the OWC model. Xue et al. [5] used a different shape of tank to validate impact pressure distribution using OpenFOAM. Hu et al. [6] performed numerical sloshing using the boundary element method with different shapes of tanks. It showed that natural frequency has a relationship with the tank shape and empirical formulas were proposed by Hu et al. [6]. Sengupta et al. [7] have modeled a drying of MUGA silk using Fluent. It was showed mesh-based CFD has been used to overcome sloshing or real-life problems. It shows CFD as one of the prominent methods in numerical simulation. However, to deal with large deformation and violent flow mesh-based CFD needs special treatment to track free surface position; moreover, it will need a very fine mesh to get appropriate accuracy. In contrast, meshless CFD has the advantage to overcome large deformation and free surface deformation because of nature meshless and Lagrangian approach.

Smoothed particle hydrodynamics (SPH) is one of the meshless CFD methods developed for free surface flow by Monaghan [8]. Since then there is a lot of application of SPH for free surface flow for instance sloshing and water waves. Simulation of water waves has been sucessfully carried out in a large wave basin [9]. The result showed SPH had a good agreement with experiment. Using long-duration sloshing Green and Peiró has been successfully reproduced sloshing phenomena in low-fill and high stretching [10]. The hydrodynamics force and water height were well-captured compare to the analytic solution. However, there is no experimental data is used to verify or validate the results. This study was also carried out using a rectangular tank. Experimental validation has been conducted to reproduce violent sloshing using single-phase and two-phase SPH [11]. The results revealed that two-phase SPH had a better result than single-phase SPH in dynamic pressure and pressure evolution. In addition, to reduce pressure oscillation in dynamic pressure a low-pass filter technique is used [12]. A study was carried out using a large number of particles, more than 10 million. Gotoh et al. [13] performed a violent sloshing using an enhancement of Incompressible SPH in the rectangular tank. The result revealed higher order Laplacian SPH has a good agreement for pressure field. However, this study is presented in 2D with a rectangular tank. Two-phase SPH was carried out to simulate violent sloshing flows in a higher density ratio by Yun et al. [14] and it was revealed dynamics pressure has good accuracy with single-SPH and experiment results although the computation domain in 2D with a rectangular tank. Hashimoto et al. [15] performed numerical sloshing for oil storage using explicit moving particle simulation (MPS). This numerical computation was carried out using a large number of particles in a single phase. Dehghani and Shafiei [16] used SPH for cooling on the orthogonal cutting process of Ti-6Al-4V. It showed SPH can be used to simulate other fields that are related to real-life engineering problems. Simulation of water waves was carried out to validate SPH with experimental results done by Trimulyono and Hashimoto [17, 18]. In this study, SPH was used to reproduce of large deformation of water waves using an obstacle box. Besides, long-distance propagation is validated against experimental data. The results as predicted SPH has a good agreement with the experiment. Amanifarda et al. [19] used ISPH to simulate gravity waves in a short domain to reproduce water waves. Ghalandari et al. [20] did a numerical simulation of Squeezed Flow of a Viscoplastic Material. It shows SPH has a promising method to apply in complex and large deformation problems. Because of the merit of the meshless method that particle is carrying their own properties and solved using Lagrangian approach.

In the present study, multiphase sloshing simulation is carried out using open source SPH solver DualSPHysics ver 4.2 [21]. DualSPHysics has implemented general computing on graphics processing units (GPGPU) technology makes computation faster and reliable to simulate a large number of particles. Multiphase DualSPHysics has been developed for liquid and gases by Mokos et al. [22] with benchmarking cases for sloshing flow and dam break. The study itself carried out using the 2D domain. The sloshing simulation was carried out using the same condition with sloshing experiment duration time. The low filling ratio was used i.e. 25% filling ratio with one pressure sensor is used to validate dynamic pressure. The comparison of free surface deformation has made using single- and two-phase SPH. In addition, numerical computation of 3D two-phase SPH is carried out to take into account of air-phase in sloshing. Finally, a comparison is made both single- and two-phase with experiment results. It was found that SPH has acceptable results for both single- and two-phase. Free surface deformation is fairly reproduced by SPH both single- and two-phase SPH.

2. MATERIALS AND METHODS

2. 1. Smoothed Particle Hydrodynamics (SPH)

Sloshing is one of the challenging events in liquid carriers especially for large vehicles such as ships or airplanes. Because sloshing is dealing with large deformations of fluid inside the tank, meshless CFD has merit to apply to this problem. One of the meshless CFD is smoothed particle hydrodynamics that was developed by Monaghan for free surface flows [8]. SPH is a pure Lagrangian method that is based on integral interpolants that describe in detail in references [23]. SPH uses an interpolation approach to estimate fluid physical properties value and derivatives of a continuous field using discrete evaluation point/ particle. If there is a function of *F(r)* in the domain *(Ω)* to evaluate the contribution of the neighbouring particle using a kernel function (*W*) and smoothing length (*h*). Smoothing length is a characteristic length used to define the area of influence of the kernel. The integral approximation shows by Equation (1) and the particle approximation shows in Equation (2) at a particle *a* where is *m* is a mass, ρ is density and *r* is position.

$$F(r) = \int_{\Omega} F(r) W(r - r', h)\, dr \tag{1}$$

$$F(r_a) \approx \sum_b F(r_b) W(r_a - r_b, h) \frac{m_b}{\rho_b} \tag{2}$$

Equation (3) shows a continuity equation with delta-SPH to suppress density fluctuation. where δ_{Φ} is delta-SPH. Equation (4) is a momentum equation in the Lagrangian form in SPH. Π_{ab} is artificial viscosity term based on Monaghan's work and *v* is velocity. *r* is the distance between two particles. Equations (5) and (6) are the equation of state in the SPH form for water, and air, respectively. γ is polytropic constant and c_0 is the speed of sound at reference density. where $a = 1.5g\left(\frac{\rho_w}{\rho_a}\right)L$ with ρ_w, ρ_a, L, and X are initial water density, air density, characteristic length of the domain, and the constant background pressure. The time step is calculated base on the works of Monaghan et al. [24].

The experiment condition was based on the work of Trimulyono et al. [11]. In this study, only a low filling ratio with violent motion was used. The pressure sensor was set in the near-free surface for the detailed information reported in literature [11].

$$\frac{d\rho_a}{dt} = \sum_b m_b v_{ab} \cdot \nabla_a W_{ab} + 2\delta_{\Phi} h c_0 \sum_b (\rho_b - \rho_a) \frac{r_{ab} \cdot \nabla_a W_{ab}}{r_{ab}^2} \frac{m_b}{\rho_b} \tag{3}$$

$$\frac{dv_a}{dt} = -\sum_b m_b \left(\frac{P_{a+P_b}}{\rho_a \cdot \rho_b} + \Pi_{ab}\right) \nabla_a W_{ab} - 2a\rho_a^2 \sum_b \frac{m_b}{\rho_b} \nabla_a W_{ab} \tag{4}$$

$$\text{where } \Pi_{ab} = \begin{cases} \dfrac{-\alpha \overline{c_{ab}} \mu_{ab}}{\overline{\rho_{ab}}} & v_{ab} \cdot r_{ab} < 0 \\ 0 & v_{ab} \cdot r_{ab} > 0 \end{cases}$$

$$P = \frac{c_0^2 \rho_0}{\gamma} \left[\left(\frac{\rho}{\rho_0}\right)^{\gamma} - 1\right] \tag{5}$$

$$P = \frac{c_0^2 \rho_0}{\gamma} \left[\left(\frac{\rho}{\rho_0}\right)^{\gamma} - 1\right] + X - a\rho^2 \tag{6}$$

$$\Delta t_{cv} = \min \frac{h}{c_s + max\left|\frac{h v_{ab} \vec{r}_{ab}}{(r_{ab}^2 + \eta^2)}\right|} \tag{7}$$

Figure 1 depicts the prismatic tank that was used in the experiment. It shows pressure sensor location is at a free surface in rest condition. The filling ratio is 25 %, where this condition is very risky for the filling ratio of the tank, especially for a ship in roll motion.

3. RESULTS AND DISCUSSION

Sloshing simulation in the prismatic tank has conducted in two- and three-dimensional, firstly two-dimension numerical simulation conducted. Two-phase SPH is more reliable executed in the two-dimensional domain because the speed of sound is larger in two-phase SPH as a result of the speed of sound in the air. As a consequence time-step in two-phase SPH more small as defined in Equation (7). This makes computation in two-phase SPH very high compare to using single-phase. However, in the reality almost free surface flow is two-phase SPH or multiphase. In this study, 3D sloshing of two-phase SPH was carried out to reproduce sloshing in a low filling ratio.

Table 1 shows parameters setup for two-phase SPH both for 2D and 3D. Some parameter is changed in 3D domain because to compromise computational cost that increases caused by two-phase SPH in 3D. It can be explained that computation increase drastically by interpolation of neighbouring particle and speed of sound in the air phase. It can be caused by the speed of sound are directly using real numbers but it will increase computation time as expressed in Equation (7). To get appropriate accuracy and reliable computation time, selected speed of sound chosen based on the 2D result. Another reason is interpolation for the neighbour particle in the 3D domain higher to take into account air-phase particle. The total particle for the 2D domain is less than 100.000 and more than 1 million for 3D. Computation time for two-phase SPH in 3D approximately 2 months only for 72 seconds using GPU GTX GeForce 1080 ti. On the contrary for single-phase, computation time only needs 2 days. It showed computation SPH for two-phase flow still high, not preferable for a large domain, but this obstacle will vanish when a multi-GPU code of DualSPHysics is released [25]. Coefh is the coefficient of smoothing

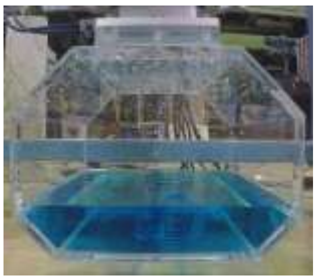

Figure 1. Prismatic tank with 25% filling ratio [11]

length, a different magnitude is used between 2D and 3D because time computation in 2D is less compare in 3D. Other parameters such as CFL was used in different number because the effect of computation time in 3D is very high. Because this reason some parameters are not yet optimized for the 3D domain. For the 3D domain, the initial particle distance change three times from the 2D domain, because the total particle will be more than 10 million using the same particle distance. Furthermore, the effect of speed of sound makes computation time larger than using single-phase SPH.
Hydrostatic pressure illustrated in Figure 2 showed hydrostatic pressure is well predicted by SPH. The accuracy of static pressure depicts from the color gradient which is a red color for high pressure located in the bottom of the tank both for single-phase and two-phase SPH. The pressure at the bottom showed 500 Pa, moreover, the difference from the analytic solution is below 3% compared with the analytical solution. The same results reported by Trimulyono et al. [11].

Figure 3 shows the comparison of dynamic pressure between single-phase SPH with the experiment in the two-dimensional domain. In this study, the movement of the tank is the same as the experiment condition. Simulation time is set for 72 seconds. Three timing time of simulation is used to show beginning, mid and edge of simulation. Figure 3 shows that there is no phase between SPH with experiment. It describes the velocity of water as the same both in SPH and experiment. As a result, the timing of the pressure sensor in SPH and the experiment is the same at time pressure sensor capture dynamic pressure. The red line is SPH and the purple line is the experiment result. The single-phase SPH showed the tendency of dynamic pressure is similar but the accuracy is slightly reduced after duration reaches 55 seconds in the simulation. The toe of dynamics pressure is not reproduced by single-phase SPH, the graph is flat in SPH but in the experiment, it has a toe. It can be explained that air-phase has an effect to dynamic pressure after run up and water is moved to the opposite wall. This result also consistent to the end of the simulation. The pressure fluctuation is very high in time simulation 55 to 65 seconds because of density fluctuation. this is the nature of weakly compressible SPH (WCSPH) because the equation of state is very stiff, although delta-SPH has been applied; however, it's only reduced density fluctuation. Incompressible SPH (ISPH) is one remedy of this problem that solved the equation of state using pressure poission equation (PPE), as result computation time increased. DualSPHysics was implemented ISPH, but not yet released as an open-source package in an online version.

Figure 4 shows the dynamic pressure between two-phase SPH with experiment results for the two-dimensional domain. Two-phase SPH shows a similar result with single-phase SPH; however, the accuracy is

TABEL 1. Parameter setup in numerical simulation

Parameters	2D	3D
Kernel function	Wendland	Wendland
Time step algorithm	Symplectic	Symplectic
Artificial viscosity coeff. α	0.07	0.07
Speed of sound (water & air)	65 & 478	46 & 200
Particle spacing (mm)	0.8	2.4
Coefh	0.95	1.2
CFL number	0.2	0.3
Delta-SPH (δ_φ)	0.1	0.1
Simulation time (s)	72.0	72.0

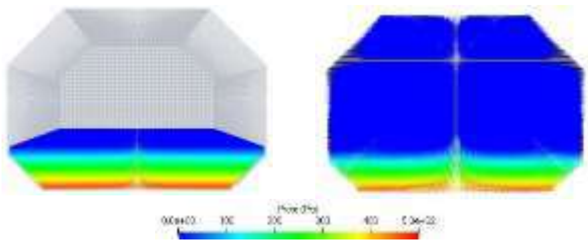

Figure 2. Hydrostatic Pressure in 3D domain

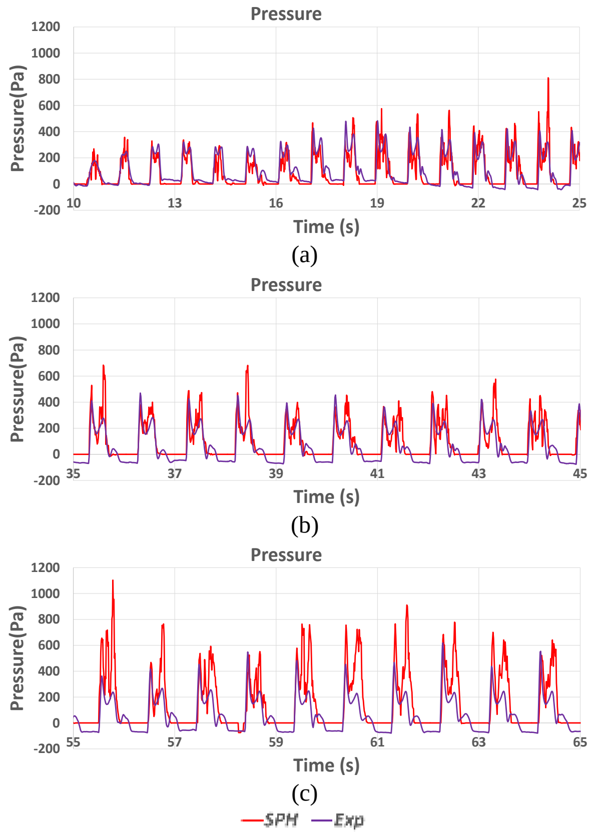

Figure 3. Comparison of dynamics pressure for single-phase SPH in (a) 15-25 s, (b) 35-45 s, (c) 55-65 s

much better to compare with single-phase. The toe of dynamic pressure in the experiment has successfully reproduced using two-phase SPH. It was found that air-phase has influence on dynamic pressure, as result, the toe in dynamic pressure was captured. The accuracy of two-phase SPH in the time simulation 55 to 65 seconds is better compare to single-phase SPH. The pressure noise is less than single-phase SPH. It depicts that air-phase has a significant effect in the sloshing phenomenon, moreover particle resolution is another parameter that needs to pay attention to as in the 3D domain it will be difficult to use high resolution for two-phase SPH.

Figure 5 shows the free surface deformation of water inside the tank. One of the merits of using SPH is mesh-free as a result, large deformation of fluid is easily captured by SPH as the nature of SPH does not need a special algorithm to capture the free surface position. This makes SPH suitable for violent flow such as sloshing. Figure 5 reveals two-phase SPH has good agreement with the experiment as in the single-phase SPH the fluid particle easy to detach from the boundary particle. It shows in run-up condition in single-phase SPH

Figure 6 shows a comparison of dynamic pressure single-phase SPH in the 3D domain. It shows the accuracy slightly decrease in simulation time 55 to 65

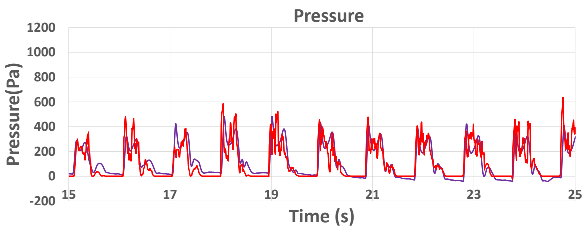

(a)

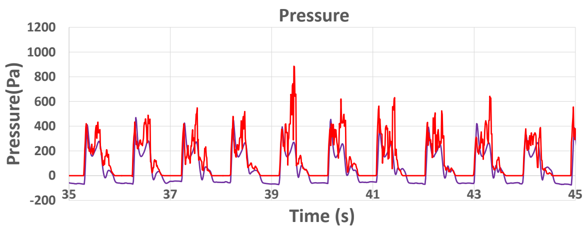

(b)

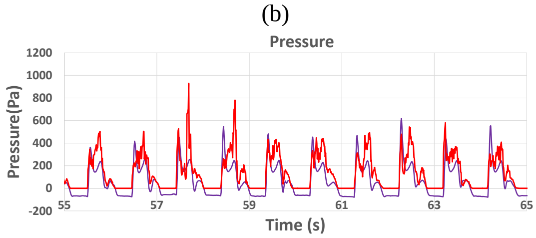

(c)

—SPH —Exp

Figure 4. Comparison of dynamics pressure for two-phase SPH in (a) 15-25 s, (b) 35-45 s, (c) 55-65 s

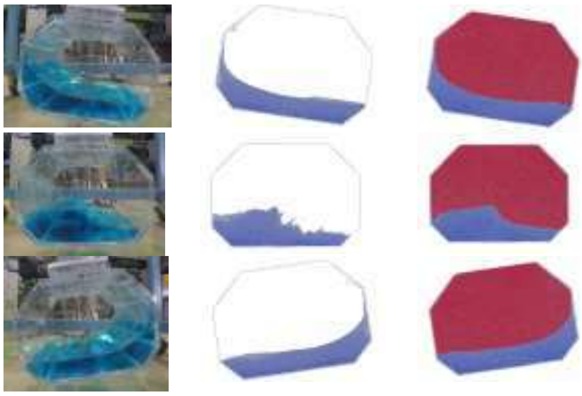

Figure 5. Comparison of free surface evolution in the 2D domain for SPH and experiment.

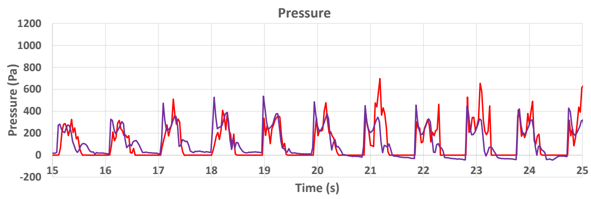

(a)

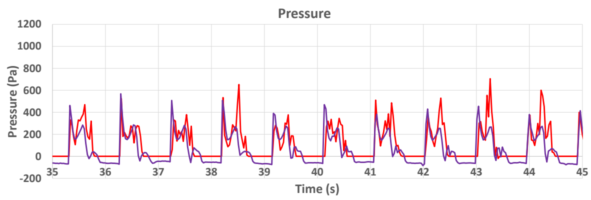

(b)

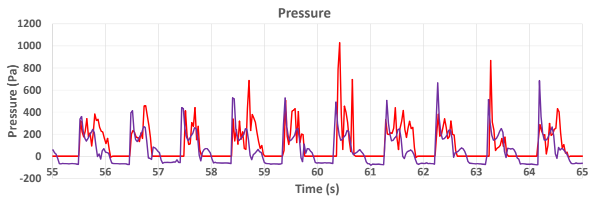

(c)

—SPH —Exp

Figure 6. Comparison of dynamics pressure for single-phase SPH in 3D at (a) 15-25 s, (b) 35-45 s, (c) 55-65 s

second. It can be caused by resolution was changed compare to 2D cases. The same phenomena as seen in the 2D domain. The toe of dynamic pressure could not capture by single-phase SPH, the same results as single-phase SPH in 2D simulation. Figure 8 depicts two-phase SPH in 3D. It showed two-phase SPH in the 3D domain is more complicated to handle as the time-step is larger and higher computation time. As result, dynamic pressure only reliable for short time simulation, after 35 seconds dynamic pressure showed pressure noise more dominant though in this study delta-SPH was used. The same result was achieved that is two-phase SPH could capture pressure toe as shown in Figure 4. Comparison of free surface deformation of water shown in Figure 8. It showed a smooth free surface deformation produced by single-phase SPH which is a bit different in 2D simulation. It can be caused by the 2D domain particle spacing is more dense compare to the 3D domain. Free surface deformation of water in two-phase SPH seen as there is an air-phase inside the tank cover up water particle that is some detail, the run-up in the tank was not clearly shown. However, a similar phenomenon was captured by SPH.

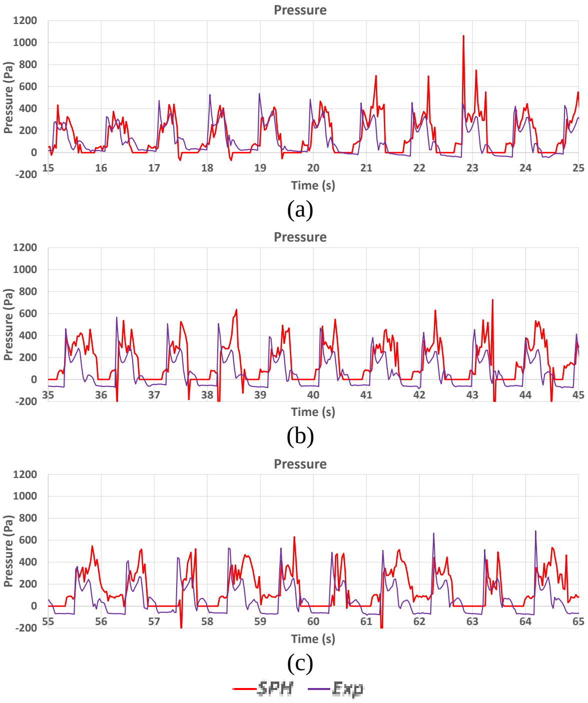

Figure 7. Comparison of dynamics pressure for two-phase SPH in 3D at (a) 15-25 s, (b) 35-45 s, (c) 55-65 s

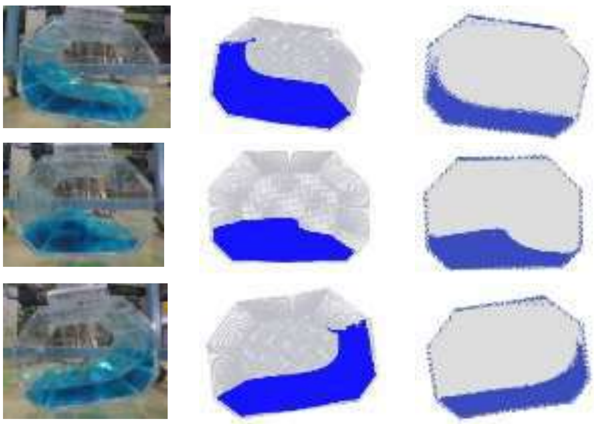

Figure 8. Comparison of free surface evolution between experiment and SPH

4. CONCLUSION

Single-phase and two-phase SPH of sloshing in the prismatic tank was successfully carried out in this study. The hydrostatic pressure has a good agreement with the analytical solution both for the 2D and 3D computation. It was shown that SPH has reasonably reproduced the dynamic pressure in the low filling ratio tank. Although in single-phase SPH, the toe of dynamic pressure cannot capture by SPH; however, multiphase SPH has successfully reproduced this phenomenon. It was revealed that air-phase has a significant effect on the sloshing phenomenon. Furthermore, Three-dimension SPH was carried out to reproduce the sloshing phenomena. It shows two-phase SPH reasonably reproduces dynamics pressure compared to single-phase SPH in short duration time simulation, and pressure fluctuations become dominant for long-duration simulation time. Free surface deformation is well captured by SPH, both single-phase or two-phase SPH. Moreover, two-phase SPH has a good agreement with the experiment result for 2D simulation because of a high-resolution particle spacing. The same results are shown by multiphase SPH, but accuracy slightly decreased for dynamic pressure. It was found to reproduce air entrapment in SPH needs a high-resolution particle spacing. Multiphase SPH in 3D is highly computational cost and accuracy tendency similar in the 2D domain for regular motion, as results for large domain computation multiphase SPH are not feasible. Sensitive parameters for sloshing in multiphase are needed to carry out future works, especially for the 3D domain. Future works such as the effect of baffle in the prismatic tank can be a candidate to reduce impact pressure in this study.

5. ACKNOWLGDMENT

The author wishes to thank to ship hydrodynamics laboratory for the computer facilities. The author sincerely gratitude to Dr. Yuuki Taniguchi and Prof. Hirotada Hashimoto for the experimental data.

6. REFERENCES

1. Chen, Y. and Xue, M. A. "Numerical simulation of liquid sloshing with different filling levels using OpenFOAM and experimental validation." ***Water,*** Vol. 10, (2018). DOI: 10.3390/w10121752.
2. Jiang, S., Teng, B., Bai, W., and Gou, Y. "Numerical simulation of coupling effect between ship motion and liquid sloshing under wave action." ***Ocean Engineering***, Vol. 108, (2015), 140-154. DOI: 10.1016/j.oceaneng.2015.07.044.
3. Sanapala, V. S., Velusamy, R. M, K., and Patnaik, B. S. V. "Numerical simulation of parametric liquid sloshing in a horizontally baffled rectangular container." ***Journal of Fluids***

and Structures, Vol. 76, (2018), 229-250. DOI: 10.1016/j.jfluidstructs.2017.10.001.

4. Xu, C. and Huang, Z. "Three-dimensional CFD simulation of a circular OWC with a nonlinear power-takeoff: Model validation and a discussion on resonant sloshing inside the pneumatic chamber." ***Ocean Engineering,*** Vol. 176, (2019), 184-198. DOI: 10.1016/j.oceaneng.2019.02.010.
5. Xue, M.-A., Chen, Y., Zheng, J., Qian, L., and Yuan, X. "Fluid dynamics analysis of sloshing pressure distribution in storage vessels of different shapes." ***Ocean Engineering,*** Vol. 192, (2019). DOI: 10.1016/j.oceaneng.2019.106582.
6. Hu, Z., Zhang, X., Li, X., and Li, Y. "On natural frequencies of liquid sloshing in 2-D tanks using Boundary Element Method." ***Ocean Engineering***, Vol. 153, (2018), 88-103. DOI: 10.1016/j.oceaneng.2018.01.062.
7. Sengupta, A.R., Gupta, R., and Biswas, A."Computational Fluid Dynamics Analysis of Stove Systems for Cooking and Drying of Muga Silk." ***Emerging Science Journal***, Vol. 3, (2019), 285-292. DOI: 10.28991/esj-2019-01191.
8. Monaghan J.J. "Simulating Free Surface Flows with SPH." ***Journal of Computational Physics***, Vol. 110, (1994), 399-406. DOI: 10.1006/jcph.1994.1034.
9. Trimulyono. A, Hashimoto. H and Kawamura. K. "Experimental Validation of SPH for Wave Generation and Propagation in Large Wave Tank." Proceedings of the International Offshore and Polar Engineering Conference. International Society of Offshore and Polar Engineers, San Francisco, CA, USA, 584-590, (2017).
10. Green, M. D. and Peiró, J."Long duration SPH simulations of sloshing in tanks with a low fill ratio and high stretching." ***Computer and Fluids***, Vol. 174, (2018), 179-199. DOI: 10.1016/j.compfluid.2018.07.006.
11. Trimulyono. A, Hashimoto. H, and Matsuda. A. "Experimental validation of single- and two-phase smoothed particle hydrodynamics on sloshing in a prismatic tank." ***Journal Marine Science and Engineering***, Vol. 7, (2019). DOI: 10.3390/jmse7080247.
12. Trimulyono. A, Samuel, and Iqbal. M. "Sloshing Simulation of Single-Phase and Two-Phase SPH using DualSPHysics." ***Kapal: Jurnal Ilmu Pengetahuan dan Teknologi Kelautan,*** Vol. 17, (2020), 50-57. DOI: https://doi.org/10.14710/kapal.v17i2.27892.
13. Gotoh. H, Khayyer. A, Ikari. H, Arikawa. T, and Shimosako. K. "On enhancement of Incompressible SPH method for simulation of violent sloshing flows." ***Applied Ocean Research***., Vol. 46, (2014), 104-115. DOI: 10.1016/j.apor.2014.02.005.
14. Yun, S. M., Park, J. C., Khayyer, A., and Jeong, S. M. "Two-phase particle simulation of violent sloshing flows with large density ratios."Proceedings of the International Offshore and Polar Engineering Conference. International Society of Offshore and Polar Engineers, Sapporo, Japan, 775-779, (2018).
15. Hashimoto. H, Hata. Y., and Kawamura. K. "Estimation of oil overflow due to sloshing from oil storage tanks subjected to a possible Nankai Trough earthquake in Osaka bay area." ***Journal of Loss Prevention in the Process Industries***., Vol. 50, (2017), 337-346. DOI: 10.1016/j.jlp.2016.10.008.
16. Dehghani, M. and Shafiei, A. R."Influence of Water Cooling on Orthogonal Cutting Process of Ti-6Al-4V Using Smooth-Particle Hydrodynamics Method" ***International Journal of Engineering-Transactions B: Applications***, Vol. 32, (2019), 1210-1217. DOI: 10.5829/IJE.2019.32.08b.18.
17. Trimulyono. A, and Hashimoto. H. "Experimental validation of smoothed particle hydrodynamics on generation and propagation of waterwaves." ***Journal of Marine Scince and Engineering***, Vol. 7, (2019). DOI: 10.3390/jmse7010017.
18. Trimulyono. A, and Wicaksono. A. "Numerical simulation of large-deformation surface waves with smoothed particle hydrodynamics." ***Kapal: Jurnal Ilmu Pengetahuan. dan Teknologi Kelautan***., Vol. 15, (2018), 102-106. DOI: https://doi.org/10.14710/kapal.v15i3.21535.
19. Amanifarda, N., Mahnama, S. M., Neshaei, S. A. L., Mehrdad, M. A., Farahani, M. H."Simulation of Gravity Wave Propagation in Free Surface Flows by an Incompressible SPH Algorithm." ***International Journal of Engineering-Transactions A: Basic,*** Vol. 25, (2012), 239-247.
20. Ghalandari, P., Amanifard, N., Javaherdeh, K., Darvizeh, A. "Numerical Simulation of Squeezed Flow of a Viscoplastic Material by a Three-step Smoothed Particle Hydrodynamics Method." ***International Journal of Engineering-Transactions A: Basics***, Vol. 26, (2013), 341-350.
21. Crespo, A.J.C., Domínguez, J.M., Rogers, B.D., Gómez-Gesteira, M., Longshaw, S., Canelas, R., García-Feal, O. "DualSPHysics: Open-source parallel CFD solver based on Smoothed Particle Hydrodynamics (SPH)." ***Computer Physics Communications***, Vol. 187, (2015), 204-216. DOI: 10.1016/j.cpc.2014.10.004.
22. Mokos, A., Rogers, B. D, Stansby, P. K. and Domínguez, J. M. "Multi-phase SPH modelling of violent hydrodynamics on GPUs." ***Computer Physics Communications,*** Vol. 196, (2015), 304-316. DOI: 10.1016/J.CPC.2015.06.020.
23. Liu, G. R and M. B. Liu. *Smoothed Particle Hydrodynamics: A Meshfree Particle Method*. World Scientific Publishing Company, 2003.

24 Monaghan, J.J. and Kos, A. "Solitary Waves on a Cretan Beach." ***Journal Waterway. Port, Coastal, Ocean Engineering,*** vol. 125, (1995), 145-155. DOI: 10.1061/(ASCE)0733-950X(1999)125:3(145).

25 Domínguez, J.M., Crespo, A.J.C., Valdez-Balderas, D., Rogers, B.D. "New multi-GPU implementation for smoothed particle hydrodynamics on heterogeneous clusters." ***Computer Physics Communications,*** Vol. 184, (2013), 1848-1860. DOI: 10.1016/j.cpc.2013.03.00.

Persian Abstract

چکیده

مقاله حاضر انجام یک برش عددی با استفاده از هیدرودینامیک ذرات صاف (SPH) در مخزن منشوری است. اسلشینگ یک جریان شدید است که در اثر تشدید مایع در مخزن در اثر نوسان خارجی ایجاد می شود. مخزن منشوری برای شبیه سازی یک حامل نوع LNG غشایی استفاده شد. آزمایش برش با استفاده از سه سنسور فشار ، یک دوربین با وضوح بالا و چهار درجه دستگاه آزادی نوسان مجبور انجام شد. در این مطالعه ، از نسبت پر شدن ٪۲۵ برای تولید مثل شلختگی در نسبت پرکردن کم استفاده شد. فقط حرکت رول در شبیه سازی عددی استفاده می شود. حرکت رول مستقیماً از جابجایی آزمایش تحمیل می کند و مقایسه فشار هیدرواستاتیک و دینامیکی برای تأیید نتیجه SPH انجام شده است. مدت زمان شلیک کردن همان آزمایش است. تک فاز و چند فاز SPH برای تولید مثل شل شدن در مخزن منشوری انجام می شود. Sloshing هر دو برای دامنه D۲ و D۳ انجام شد. این نشان می دهد که SPH توافق خوبی با نتایج تحلیلی و تجربی دارد. فشار دینامیکی مشابه آزمایش از طریق نوسان فشار جعلی است. نتایج فشار دینامیکی نسبتاً برای شبیه سازی کوتاه مدت نشان داده می شود و پس از آن اندکی کاهش می یابد. گرایش تغییر شکل سطح آزاد مشابه آزمایش است.

IJE TRANSACTIONS B: Applications Vol. 34, No. 05, (May 2021) 1352-1361

International Journal of Engineering

Journal Homepage: www.ije.ir

Influence of Immersion Corrosion on Mechanical Properties of AISI 430/AISI 316L Dissimilar Welded Joints

A. M. Barrios[a], L. M. Burgos[a], E. E. Niebles-Nuñez[b], L. A. Espitia[a], J. Unfried-Silgado*[a]

[a] *Department of Mechanical Engineering, ICT research group, Universidad de Córdoba, Montería, Colombia*
[b] *Mechanical Engineering Program, IMTEF research group, Universidad Autónoma del Caribe, Barranquilla, Colombia*

PAPER INFO

Paper history:
Received 10 February 2021
Received in revised form 27 March 2021
Accepted 30 March 2021

Keywords:
Dissimilar Welded joints
Stainless Steel
Corrosion
Tensile Test
Heat-affected Zone

ABSTRACT

Dissimilar welded joints of AISI 430 and AISI 316L stainless steel were produced by the GMAW process using two different shielding gas mixtures composed of 97Ar-3N_2 and 80Ar-19He-1O_2. The microstructure of the heat-affected zone was characterized by optical and scanning electron microscopy, and Vickers microhardness measurements were carried out along the cross-section of the specimens. The dissimilar welded joints were submitted to immersion corrosion test in a 10%v/v hydrochloric acid solution for 24 and 72 hours. Afterward, yields strength, tensile strength, and elongation percentage were measured using tensile tests according to ASTM E8 standard. Non-immersed welded joints were used for comparison purposes. An analysis of variance was developed to evaluate the influence of immersion time and shielding gas mixture on yielding strength and tensile strength. The microstructure characterization showed that the heat-affected zone on AISI 430 side was the widest, and it was observed a significant presence of acicular ferrite, martensite, and coarsened ferritic grains. In contrast, on the heat-affected zone on AISI 316L side was not observed coarsening nor refinement of austenite grains. The AISI 430 heat-affected zone showed the maximum hardness values and higher susceptibility to corrosion damage. Tensile tests results evidenced that immersion corrosion tests did not change significantly ultimate strength in comparison to non-immersed specimens while yielding strength and elongation percentage were drastically decreased due to immersion time. According to the p-value, the immersion time is the most influencing factor on yielding strength and tensile strength of the dissimilar welded joints.

***doi**: 10.5829/ije.2021.34.05b.31*

NOMENCLATURE

Sy	Yield Strength	LF-A	Fusion line on the austenitic side
UTS	Ultimate Tensile Strength	HAZ-F	Heat-affected zone on the ferritic side
ε%	Elongation Percentage	HAZ-A	Heat-affected zone on the austenitic side
LF-F	Fusion line on the ferritic side		

1. INTRODUCTION

Dissimilar welded joints have been extensively employed in industrial applications where different combination of mechanical, chemical, and physical properties are required. Several parts of machinery and devices used in pharmaceutical, petrochemical, food processing, and mining industries make use of dissimilar welded joints, where functional combinations of high tensile strength, high corrosion resistance, and cost reductions with maximum performance on service are mandatory [1-3]. Typical metallic dissimilar welded joints in industrial applications are composed of carbon steel/stainless steel, stainless steel/nickel alloys, cooper alloys/carbon steels, aluminum alloys/galvanized steel alloys, among others [4-8]. To achieve a balance among chemical composition, microstructure, and properties, some special welding techniques are used. The most

*Corresponding Author Institutional Email: *jimyunfried@correo.unicordoba.edu.co* (J. Unfried-Silgado)

Please cite this article as: A. M. Barrios, L. M. Burgos, E. E. Niebles-Nuñez, L. A. Espitia, J. Unfried-Silgado, Influence of Immersion Corrosion on Mechanical Properties of AISI 430/AISI 316L Dissimilar Welded Joints, International Journal of Engineering, Transactions B: Applications Vol. 34, No. 05, (2021) 1352-1361

representative techniques for obtaining dissimilar welding joints include buttering, using a third metal or a filler metal different to base metals, prefilling, among others [9-11]. Particularly, dissimilar austenitic/ferritic stainless steels welded joints due to the low susceptibility of stress corrosion cracking of AISI 430 and the high corrosion resistance and weldability of AISI 316L are a remarkable choice when these conditions are required [12-14]. Rajput el al. [15] indicated that one of the major problems ocurring in dissimilar welded joints of austenitic/ferritic stainless steels is the hot corrosion cracking ocurring on the austenitic side in chloride enviroments. Unlike, ferritic stainless steels showed good stress corrosion cracking resistance and pitting corrosion resistance. Nevertheless, it is widely accepted that ferritic stainless steels exhibit less corrosion resistance than austenitic stainless steels. Additionally, phase transformations of these dissimilar welded joints have been extensively investigated. Both ferritic and austenitic stainless plates of steels may undergo coarsening and refinement of grain at different regions, as well as, several phase transformations along the heat-affected zone [16-18]. All these metallurgical changes may modify the corrosion behavior of welded joints and they are functions of several factors, such as the as-received condition of base metals, shielding gas mixtures, thermal cycling, heat input, temperatures, and cooling rates imposed during the welding process. The corrosion behavior of stainless steels has been evaluated using potentiostatic and potentiodynamic tests [18-20], stress corrosion cracking tests (SCC) [21], and in few cases, using immersion corrosion tests [22]. Corrosion behavior on acid environments of dissimilar welded joints of stainless steels [19, 20-22], and tensile and microstructural properties of welded joints of different grades of austenitic stainless steels [23] have been evaluated by several authors. For instance, Maheswara and Srinivasa [24] evaluated the pitting corrosion of AISI 304/AISI 430 dissimilar welded joints exposed to NaOH, NaCl, and HCl solutions. It was reported that the fusion zone showed higher corrosion damage compared to the heat-affected zone due to the higher heat input and the chromium depletion at this area during the welding process. However, the characterization carried out in those works was focused on small regions of the welded joints, which makes it difficult to establish correlations between corrosion behavior and mechanical properties of the entire joint. These relationships are especially important to understand the behavior of dissimilar welded joints exposed to aggressive acid environments during service. These relationships might be achieved using design and analysis of experiments such as the analysis of variance (ANOVA) [25-26]. In this work, the influence of immersion corrosion in hydrochloric acid solution on microstructure, corrosion resistance, and mechanical properties of AISI 430/AISI 316L dissimilar welded joints was assessed, and the effect of process parameters and corrosion immersion time on mechanical properties was determined using the ANOVA model.

2. MATERIALS AND METHODS

2. 1. Materials and welding procedure

Commercial AISI 430 and AISI 316L stainless steel plates were used in this work. Table 1 showed the nominal [27] and the measured chemical composition of the steels determined by optical emission spectrometry.

Dissimilar welded joints were fabricated from workpieces of 400 x 200 x 3 mm using a square butt joint and gas metal arc welding (GMAW) process. Table 2 shows the process parameters, the shielding gas mixtures, and the heat inputs used to obtain two dissimilar welded joints referred to from this point on as GA and GB specimens.

The welding processes were carried out in a single pass at the flat position with a commercial ER309L rod wire as filler metal. Table 3 shows the nominal chemical composition of the AWS ER309L electrode [28].

TABLE 1. Nominal [27] and measured chemical composition of the stainless steels. N: Nominal. M: Measured

Material		Fe	C	Si	Mn	Cr	Ni	Mo	S	P
AISI 430	N	Bal.	0.12 max	1.0 max	1.0 max	16.0 – 18.0	0.75 max	0.60 max	0.030 max	0.040 max
	M	Bal.	0.019	0.245	0.377	16.07	0.225	0.055	0.03	0.01
AISI 316L	N	Bal.	0.030 max	0.75 max	2.00 max	16.0 – 18.0	10.0 – 14.0	2.0 – 3.0	0.030 max	0.045 max
	M	Bal.	0.027	0.275	1.748	17.08	9.758	1.2	0.01	0.03

TABLE 2. Welding process parameters

Dissimilar welded joints	Shielding gases mixture	I (A)	V (V)	Average Heat Input ($kJ.cm^{-1}$)	Welding speed ($mm.s^{-1}$)
GA	97Ar - $3N_2$	130.5	22.5	3.2	5.7
GB	80Ar - 19He - $1O_2$	140.5	22.8	2.8	7.3

TABLE 3. Nominal chemical composition of the ER309L wire rode electrode [28]

Element	C	Cr	Ni	Mo	Mn	Si	P	S	Cu
wt%	0.03 max	23.0 – 25.0	12.0 – 14.0	0.75 max	1.0 – 2.5	0.30 – 0.65	0.03 max	0.03 max	0.75 max

2. 2. Microstructure Characterization and Hardness Measurements Cross-section specimens with 50 mm length were extracted from the steady region of each welded joint and then mounted in epoxy resin for microstructure characterization and microhardness measurements, as shown in Figure 1.

Cross-section specimens were ground with emery papers and polished with 1 μm alumina particles. The microstructure was revealed using aqua regia reagent during 15 s according to ASTM E407 standard [29], and subsequently examined by stereoscopic microscopy, optical microscopy, and scanning electron microscopy. Vickers microhardness measurements before and after the corrosion tests were carried out along the cross-section of specimen length using a 500 g load during 10 s according to ASTM E384 standard [30], as illustrated in Figure 1c. Schaeffler diagram was used to predict microstructure of the fusion zone, and subsequently, to assess its susceptibility to corrosion damage. Chromium and Nickel equivalent was calculated using equations 1 and 2, employing the chemical composition of the electrode, base metals and assuming a 43 % dilution at the fusion zone, as suggested in similar works [33-35].

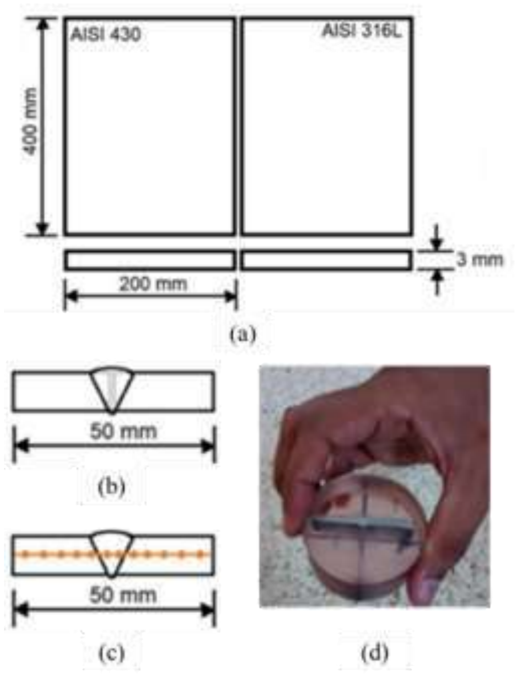

Figure 1. (a) Schematic of dissimilar welded joint (b) Schematic of cross-section specimen. (c) Microhardness measurements profile. (d) Specimen for microhardness measurements

$$Creq = Cr + Mo + 1.5Si + 0.5\,Nb \tag{1}$$

$$Nieq = Ni + 30C + 0.5\,Mn \tag{2}$$

2. 3. Tensile and Corrosion Immersion Tests Flat tensile specimens according to ASTM E8 standard [31] were manufactured from the 3 mm thick dissimilar welded joint using a water jet cutter as shown in Figure 2. The specimens were ground until 600 emery paper and the welded joint was perpendicular to the rolling direction.

Corrosion immersion tests were carried out in a 10%v/v hydrochloric acid solution according to practice C of ASTM A262-02 standard [32]. GA and GB specimens were completely submerged into the HCl solution during 24 and 72 hours at 303 K.The specimens were isolated from environmental contaminants, as shown in Figure 3. Temperature, humidity, and pH of the solution were continuously controlled during the tests. Specimens mass was measured before and after the tests using a scale with 0.01 mg resolution.

Tensile tests were carried out in a 300 kN MTS Criterion C45.305 universal machine using a testing speed of 0.06 mm s^{-1}. Yield Strength (Sy), Ultimate Tensile Strength (UTS), and Elongation Percentage (ε%) were calculated from stress-strain diagrams. Non immersed welded joints, together with AISI 430 and AISI 316L stainless steels in the as-received condition were used for comparison purposes. The results are the average of four random tests performed under the same conditions. Furthermore, an analysis of variance (ANOVA) was carried out to evaluate the effect of immersion time and shielding gas type on Sy and UTS.

The experiment was conducted at three levels of immersion time (0h, 24 h, and 72 h), two levels of shielding gas type (97Ar - $3N_2$ and 80Ar - 19He - $1O_2$), and four replicates for each condition. The effect

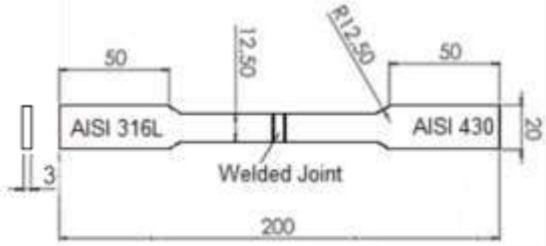

Figure 2. Flat tensile specimens according to ASTM E8 standard. Dimensions in mm [32]

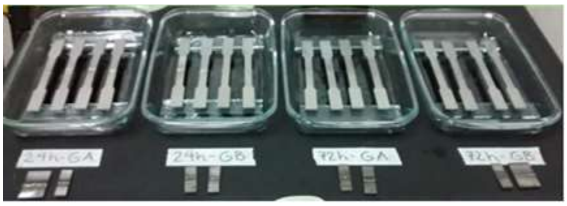

(a) Immersed specimens.

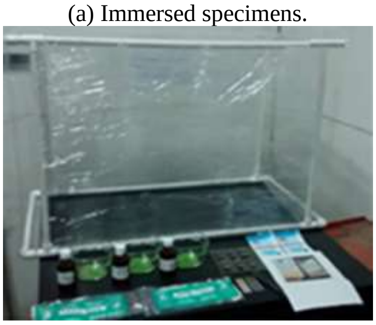

(b) Isolation Chamber

Figure 3. Immersion corrosion tests setup

estimation was carried out using a randomized block design, the classical sum of squares - type II, and a 95 % confidence interval.

3. RESULTS AND DISCUSSION

Figure 4 shows the microstructure of AISI 430 and AISI 316L stainless steels in the as-received condition.

Both materials showed ferrite and austenite grains, the typical microstructure of ferritic and austenitic stainless steels, with an average microhardness of 150 ± 6 HV1kgf and 158 ± 6 HV1kgf, respectively. Considering the hardness, size, and shape of the grains, and the twins in AISI 316L microstructure, it is assumed that the stainless steels were annealed after cold rolling.

Figures 5, 6, and 7 show the appearance and microstructure characteristics of GA and GB specimens in the non-immersed condition and after corrosion immersion tests. The welded joints were free of weld defects such as cracking and porosity.

Length and microstructure on HAZ of GA and GB specimens were strongly influenced by welding

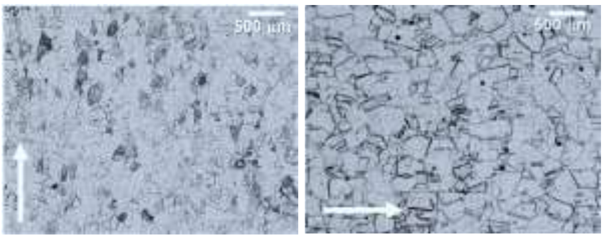

(a) (b)

Figure 4. The microstructure of the stainless steels in the as-received condition, a) AISI 430 and b) AISI 316L. White arrows indicate rolling direction. OM 500x

(a) (b)

Figure 5. The appearance of GA and GB specimens in the (a) non-immersed condition and (b) after corrosion immersion tests. The welded joints were free of weld defects such as cracking and porosity

processes. HAZ-F length on GA specimens was from 3.5 to 4.5 mm, while on GB specimens were from 2.2 to 2.5 mm. Likewise, HAZ-A length was in the range from 3.0 to 3.2 mm, and 2.0 to 2.5 mm on GA and GB specimens, respectively. These length differences on HAZ of GA and GB specimens are the consequence of welding process parameters and thermal conductivity of the stainless steels. Heat input was higher in GA specimens, therefore, a longer HAZ is expected. Moreover, thermal conductivity in ferritic stainless steels is ~ 40 % higher in comparison to austenitic stainless steels [36]. Regarding microstructure, on HAZ- F was observed coarsening of ferrite grains and presence of acicular ferrite and Martensite near to LF-F, as shown in Figure 8a. Towards to base metal, the HAZ-F microstructure showed a gradual grain refinement. On HAZ – A was not observed grain coarsening nor refinement; in fact, elongated grains structure produced by cold rolling remained unchanged. However, near to LF-A, due to the temperature and cooling rates achieved at this region during the welding process, the microstructure showed a slightly homogeneous austenitic grain size and presence of $M_{23}C_6$ carbides [16], as can be seen in Figure 8b.

On the other hand, HAZ of GA and GB specimens suffered higher corrosion damage. It was observed pitting and intergranular corrosion, mainly at HAZ-F, as shown in Figures 6c and 6d, and Figures 7c and 7d (highlighted with yellow arrows). Additionally, corrosion damage increased with immersion time. It has been reported that ferritic stainless steels exhibit lower corrosion resistance than austenitic stainless steels under similar conditions, [12, 16]. Furthermore, dissolution behavior is fastest on AISI 430 than AISI 316 stainless steel in acidic chloride solutions with ions dissolution of Fe and Cr in each stainless steel, respectively [21]. Due to heterogeneity of located corrosion, mass losses after the immersion corrosion tests were disregarded in this work.

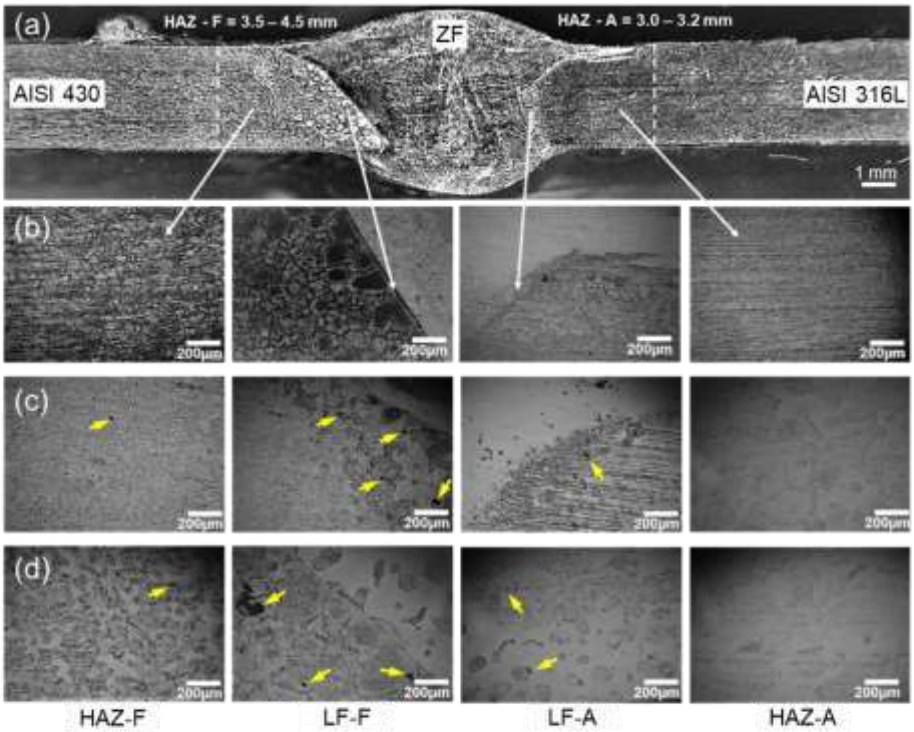

Figure 6. a) Welded joint of GA specimens, b) Non-immersed GA specimen, c) 24 hours immersed GA specimen, and d) 72 hours immersed GA specimen. HAZ-F: heat-affected zone on the ferritic side, LF-F: fusion line on the ferritic side, LF-A: fusion line on the austenitic side, HAZ-A: heat-affected zone on the austenitic side

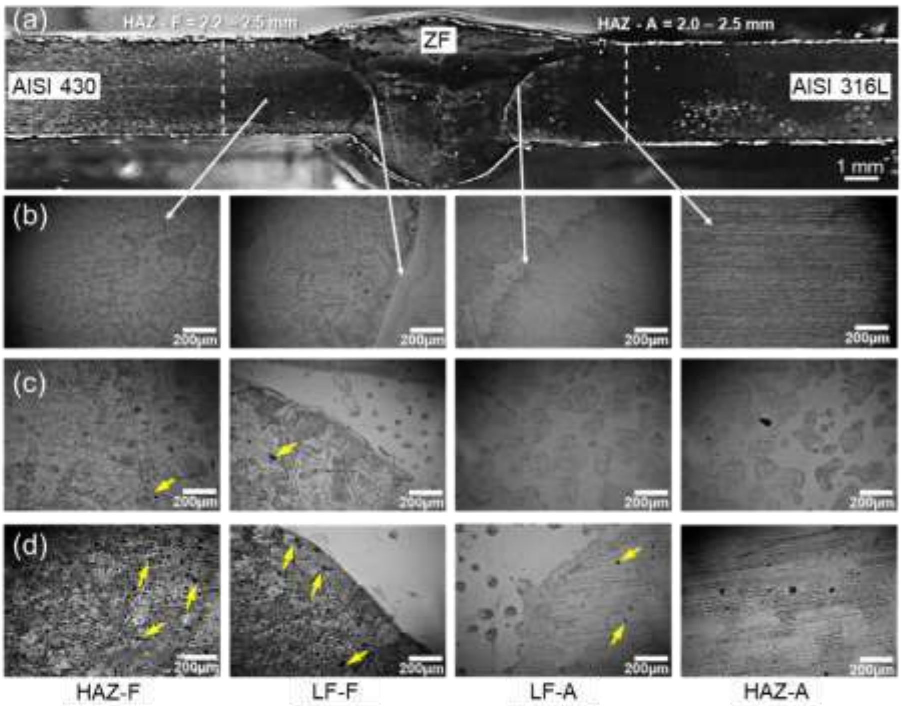

Figure 7. a) Welded joint of GB specimens, b) Non-immersed GB specimen, c) 24 hours immersed GB specimen, and d) 72 hours immersed GB specimen. HAZ-F heat-affected zone on the ferritic side, LF-F: fusion line on the ferritic side, LF-A: fusion line on the austenitic side, HAZ-A: heat-affected zone on the austenitic side

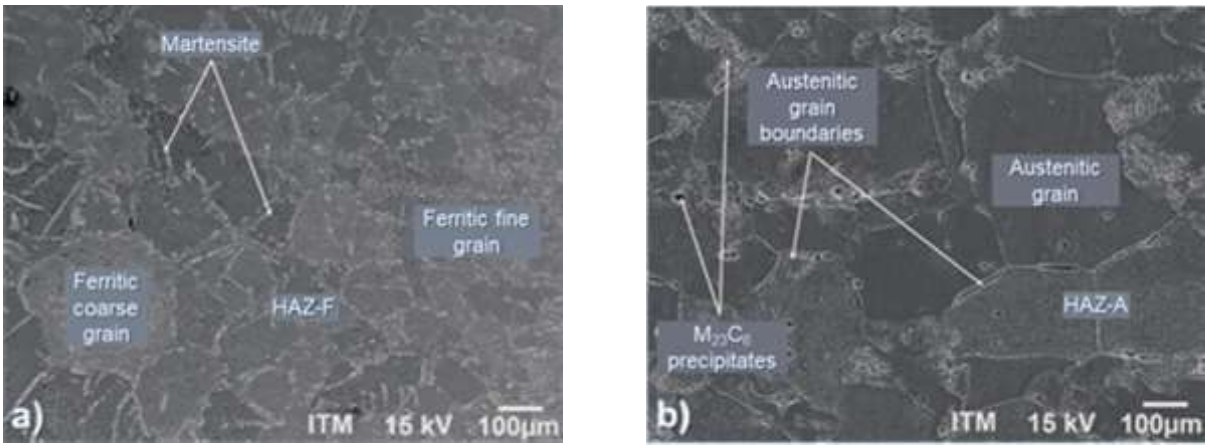

(a) (b)

Figure 8. a) Coarsened ferrite grains and presence of acicular ferrite and Martensite on HAZ- F near to LF-F, b) Homogeneous austenitic grain size and presence of M23C6 carbides on HAZ- A near to LF-A

Figure 9 shows the Vickers microhardness profile along the cross-section of GA and GB specimens before and after immersion tests. Higher microhardness values were registered at the HAZ-F near to LF-F due to Martensite formation and the highest microhardness values were on GA specimen, as a result of the bigger heat input during the welding process. Microhardness profiles of GA and GB specimens are quite similar, regardless of welding process parameters, moreover, after immersion corrosion tests, the microhardness profiles showed a slight variation of ~1 % at HAZ in both specimens, a fact attributed to microstructure damage caused by pitting and intergranular corrosion. Similar results have been reported by other researchers [16, 37].

Figure 10 illustrates the predicted microstructure of the fusion zone corresponding to 43 % of dilution and Chromium and nickel equivalent of 22, 3 and 11,8 respectively. The microstructure of the fusion zone is composed of 84 % of austenite and 16 % of ferrite and its Creq/Nieq ratio is 1.9, a low and common ratio on austenitic stainless steels. Low Creq/Nieq ratios mean low susceptibility to develop welding metallurgical defects. Also, the low content of ferrite decreases hot and cold cracking, embrittlement, grain growth, and sigma phase formation [12,18, 38], consequently, it is expected a high corrosion resistance in the fusion zone. It is worth mentioning that mechanisms and mode of solidification were not considered in this analysis.

Figure 11 shows Sy, UTS, and ε% of AISI 316L, AISI 430, and GA and GB specimens before (non-immersed condition - NI) and after corrosion immersion. Mechanical properties of AISI 316L and AISI 430 correspond to the annealed condition of these steels, as reported in other works [39, 40].

UTS of GA and GB specimens in all conditions exhibited statistically similar results to those of AISI 430 in as-received condition despite corrosion damage, moreover, the failure of all specimens was in AISI 430 side, suggesting that the welding process did not modify significantly UTS of metal bases, and interesting fact to

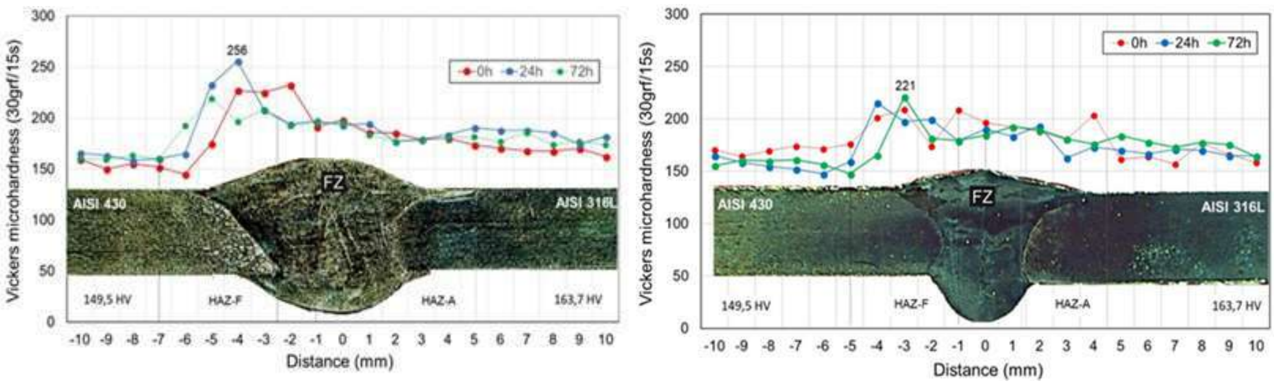

(a) (b)

Figure 9. Vickers microhardness profile along the cross-section of welded joints specimens before and after immersion tests. (a) GA specimen, and (b) GB specimen

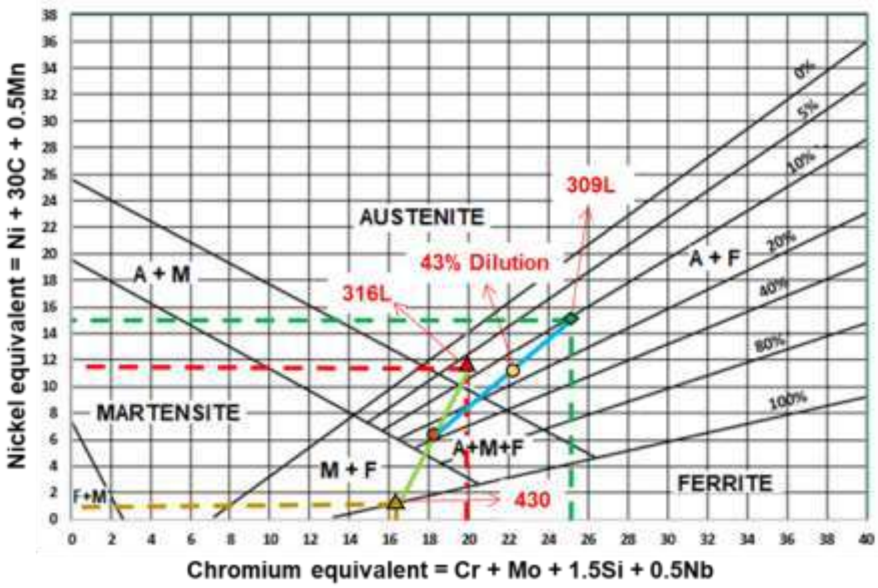

Figure 10. Schaeffler diagram illustrating the predicted microstructure of fusion zone corresponding to 43 % of dilution and Chromium and nickel equivalent of 22.3 and 11.8 respectively. 309L, 316L, and 430 are corresponding to AISI 309L, AISI 316L and AISI 430 stainless steels.

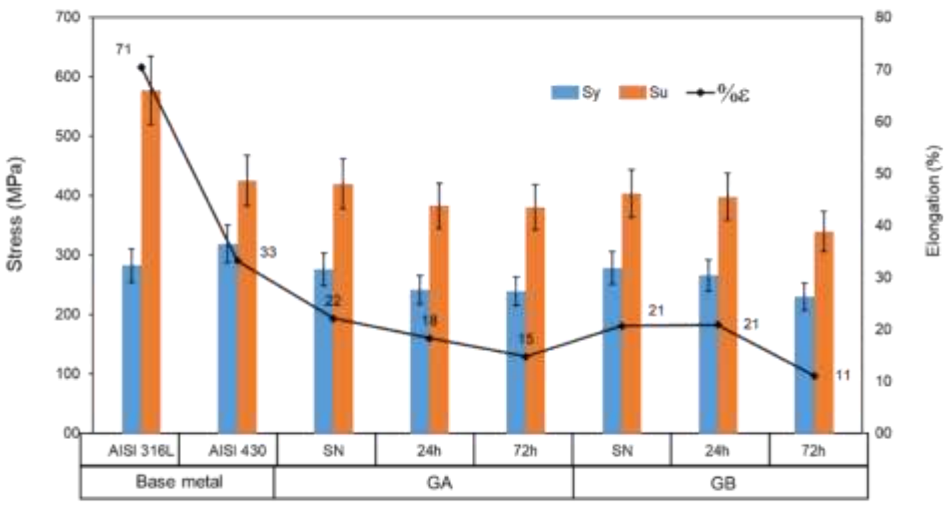

Figure 11. Yield Strength (Sy), Ultimate Tensile Strength (UTS), and Elongation Percentage (ε%) calculated from stress-strain diagrams

consider for mechanical design. In contrast, Sy and ε% decreased with immersion time, particularly the latter at 72 hours of immersion time. ε% reduction is a consequence of Martensite formation and coarsening of ferrite grains at HAZ-F, features that deteriorate ductility of welded joints [41, 42]. Furthermore, Sy and ε% were lower on GB specimens compared to GA specimens, which is attributed to heat input differences. Lower heat input on GB specimen was accomplished by a combination of welding parameters and shielding gas mixtures, including oxygen with lower ionization energy compared to argon and helium. Consequently, on HAZ-F of GB specimen, a narrower region containing coarsened ferrite grains and Martensite was formed. As shown before, HAZ-F suffered higher corrosion damage. Pitting and intergranular corrosion were nucleation sites for tensile failure and decreased the effective area of specimens, therefore, a reduction in mechanical properties is expected.

ANOVA results for Sy and UTS as a function of immersion time and shielding gas type are shown in Tables 4 and 5. Independence of variables and homoscedasticity were satisfactorily fulfilled.

TABLE 4. ANOVA results for Sy - Classical sum of squares – type II

Source	Sum of squares	Degree of freedom	Mean square	F- Values	*p*-value (Prob. > F)
Model	5738.37	5	1147.67	4.18	0.0155
X – immersion time	3440.42	2	1720.21	6.27	0.0114
Y – Shielding gas type	7.20	1	7.20	0.026	0.8736
XY	2290.75	2	1145.38	4.18	0.0378
Pure error	3839.66	14	274.26		
Cor. Total	9578.03	19			

TABLE 5. ANOVA results for UTS - Classical sum of squares – type II

Source	Sum of squares	Degree of freedom	Mean square	F- Values	*p*-value (Prob. > F)
Model	12145.35	5	2429.07	5.12	0.0071
X – immersion time	6448.48	2	3224.24	6.79	0.0087
Y – Shielding gas type	1454.86	1	1454.86	3.07	0.1018
XY	4242.02	2	2121.01	4.47	0.0315
Pure error	6643.94	14	474.57		
Cor. Total	18789.30	19			

According to the ANOVA results, the immersion time (X source) and the combination of immersion time and shielding gas type (XY source) are the most influencing factors on Sy and UTS due to their p-values are lower than the probability of error. These results are coherent with the Sy reduction of the specimens with the augment of immersion time which is shown in Figure 11.

4. CONCLUSIONS

Dissimilar welded joints of AISI 430 and AISI 316L stainless steels free of weld defects were produced by the GMAW process using two different shielding gas mixtures. The comclusions can be summarized as follows:

1. Coarsening of ferrite grains and the presence of acicular ferrite and martensite were observed on the heat-affected zone on AISI 430 stainless steel side. In contrast, neither refinement nor coarsening of grains were evident on the heat-affected zone on AISI 316L stainless steel side.
2. The heat-affected zone on AISI 430 stainless steel side suffered higher corrosion damage. It was observed pitting and intergranular corrosion and the damage increased with immersion time.
3. UTS of dissimilar welded joint specimens in all conditions exhibited statistically similar results to those of AISI 430 in the as-received condition, despite corrosion damage. However, Sy and ε% decreased with immersion time, particularly the latter at 72 h of immersion time, due to coarsened ferrite grains, acicular ferrite, martensite, and corrosion damage on the heat-affected zone on AISI 430 stainless steel side.
4. According to the p-value, the immersion time is the most influencing factor on Sy and UTS of the dissimilar welded joints.

5. ACKNOWLEDGMENTS

The authors acknowledge the financial support of Universidad de Cordoba and Universidad Autónoma del Caribe. Likewise, the authors are grateful to Dr. J. F. Santa for his contributions and the scanning electron microscopy characterization.

6. REFERENCES

1. Tabuchi, M., Hongo, H., Abe, F. "Creep strength of dissimilar welded joints using high B-9Cr steel for advanced USC boiler", ***Metallurgical and Materials Transactions A,*** Vol. 45, No. 11, (2014), 5068-5075. DOI: 10.1007/s11661-014-2471-2
2. Lundin, C. D. "Dissimilar metal welds-transition joints literature review", ***Welding Journal,*** Vol. 61, No. 2, (1982), 58-63. http://files.aws.org/wj/supplement/WJ_1982_02_s58.pdf
3. Verma, J., Taiwade, R. V., Khatirkar, R. K., Kumar, A. "A comparative study on the effect of electrode on microstructure and mechanical properties of dissimilar welds of 2205 austeno-ferritic and 316L austenitic stainless steel". ***Materials Transactions,*** Vol. 57, No. 4, (2016), 494-500. DOI: 10.2320/matertrans.M2015321

4. Marashi, P., Pouranvari, M., Amirabdollahian, S., Abedi, A., Goodarzi, M. "Microstructure and failure behavior of dissimilar resistance spot welds between low carbon galvanized and austenitic stainless steels", ***Materials Science and Engineering: A,*** Vol. 480, No. 1-2, (2008), 175-180. DOI: https://doi.org/10.1016/j.msea.2007.07.007

5. Zarooni, M., "Effect of Welding Heat Input on the Intermetallic Compound Layer and Mechanical Properties in Arc Welding-brazing Dissimilar Joining of Aluminum Alloy to Galvanized Steel", ***International Journal of Engineering, Transactions B: Applications,*** Vol. 29, No. 5, (2016), 669-676. DOI: 10.5829/idosi.ije.2016.29.05b.11

6. Shah, L. H., Ishak, M. "Review of research progress on aluminum–steel dissimilar welding", ***Materials and Manufacturing Processes,*** Vol. 29, No. 8, (2014), 928-933. DOI: 10.1080/10426914.2014.880461

7. Ma, Q. H., Wang, S. G., Zhang, L., Li, Y. "Review of Dissimilar Metal Welding Between Duplex Stainless Steel and Carbon Steel [J]". ***Welded Pipe and Tube,*** Vol. 8. (2009).

8. Naffakh, H., Shamanian, M., Ashrafizadeh, F. "Dissimilar welding of AISI 310 austenitic stainless steel to nickel-based alloy Inconel 657", ***Journal of materials processing technology,*** Vol. 209, No. 7, (2009), 3628-3639. DOI: 0.1016/j.jmatprotec.2008.08.019

9. Rathod, D. W., Singh, P. K., Pandey, S., Aravindan, S. "Effect of buffer-layered buttering on microstructure and mechanical properties of dissimilar metal weld joints for nuclear plant application", ***Materials Science and Engineering: A,*** Vol. 666, (2016), 100-113. DOI: 10.1016/j.msea.2016.04.053

10. Joshi, J. R., Potta, M., Adepu, K., Gankidi, M. R., Katta, R. K. "Influence of welding techniques on heat affected zone softening of dissimilar metal maraging steel and high strength low alloy steel gas tungsten arc weldments", ***Transactions of the Indian Institute of Metals,*** Vol. 70, No. 1, (2017), 69-81. DOI: 10.1007/s12666-016-0861-4

11. Mehta, K. (ed.) "Advanced joining and welding techniques: an overview", ***Advanced Manufacturing Technologies,*** 101-136. Springer International Publishing, (2017). DOI: 10.1007/978-3-319-56099-1_5

12. Samal, M. K., Seidenfuss, M., Roos, E., Balani, K. "Investigation of failure behavior of ferritic–austenitic type of dissimilar steel welded joints", ***Engineering Failure Analysis,*** Vol. 18, No. 3, (2011), 999-1008. DOI: 10.1016/j.engfailanal.2010.12.011

13. Rahmani, M., Eghlimi, A., Shamanian, M. "Evaluation of microstructure and mechanical properties in dissimilar austenitic/super duplex stainless steel joint". ***Journal of Materials Engineering and Performance,*** Vol. 23, No. 10, (2014), 3745-3753. DOI: 10.1007/s11665-014-1136-z

14. Ghasemi, R., Beidokhti, B., Fazel-Najafabadi, M. "Effect of delta ferrite on the mechanical properties of dissimilar ferritic-austenitic stainless steel welds", ***Archives of Metallurgy and Materials,*** Vol. 63, No. 1, (2018), 437-443. DOI: 10.24425/118958

15. Rajput, S. K., Kumar, A., Tripathi, S. S., Sachan, E. "Investigation of microstructural behavior and mechanical properties of dissimilar weld joints of austenitic-ferritic stainless steel", ***Materials Today: Proceedings***, Vol. 25, (2020), 778-784. DOI: 10.1016/j.matpr.2019.09.018

16. Aguilar, S.; Tabares, R.; Serna, C. "Microstructural transformations of dissimilar austenite-ferrite stainless steels welded joints.", ***Journal of Materials and Physical Chemistry,*** Vol. 1, No. 4, (2013), 65-68. DOI: 10.12691/jmpc-1-4-2

17. Paul, V. T., Karthikeyan, T., Dasgupta, A., Sudha, C., Hajra, R. N., Albert, S. K., S. Saroja and Jayakumar, T. "Microstructural variations across a dissimilar 316L austenitic: 9Cr reduced activation ferritic martensitic steel weld joint", ***Metallurgical and Materials Transactions A,*** Vol. 47, No. 3, (2016), 1153-1168. DOI: 10.1007/s11661-015-3281-x

18. DuPont, J. N. "Microstructural evolution and high temperature failure of ferritic to austenitic dissimilar welds", ***International Materials Reviews,*** Vol. 57, No. 4, (2012), 208-234. DOI: 10.1179/1743280412Y.0000000006

19. Hastuty, S., Nishikata, A., Tsuru, T. "Pitting corrosion of Type 430 stainless steel under chloride solution droplet", ***Corrosion Science,*** Vol. 52, No. 6, (2010), 2035-2043. DOI: 10.1016/j.corsci.2010.02.031

20. Wang, C., Yu, Y., Yu, J., Zhang, Y., Zhao, Y., Yuan, Q. (2020). "Microstructure evolution and corrosion behavior of dissimilar 304/430 stainless steel welded joints", ***Journal of Manufacturing Processes***, Vol. 50, (2020), 183-191. DOI: 10.1016/j.jmapro.2019.12.01

21. Nishimura, R., Maeda, Y. "Metal dissolution and maximum stress during SCC process of ferritic (type 430) and austenitic (type 304 and type 316) stainless steels in acidic chloride solutions under constant applied stress", ***Corrosion Science***, Vol. 46, No. 3, (2004), 755-768. DOI: 10.1016/j.corsci.2003.07.002

22. Li, C. X., Bell, T. "Corrosion properties of plasma nitrided AISI 410 martensitic stainless steel in 3.5% NaCl and 1% HCl aqueous solutions", ***Corrosion Science,*** Vol. 48, No. 8, (2006), 2036-2049. DOI: 10.1016/j.corsci.2005.08.011

23. Ethiraj, N., Sivabalan, T., Sivakumar, B., Vignesh Amar, S., Vengadeswaran, N., Vetrivel, K. Effect of Tool Rotational Speed on the Tensile and Microstructural Properties of Friction Stir Welded Different Grades of Stainless Steel Joints. ***International Journal of Engineering, Transactions A: Basics,*** Vol. 33, No. 1, (2020), 141-147. DOI: 10.5829/ije.2020.33.01a.16

24. Maheswara G. U., Srinivasa Ch. "Investigation of Pitting Corrosion Rate on Micro Plasma Arc Welded Dissimilar Weld Joints of AISI 304 and AISI 430 Stainless Steel Sheets", ***ADMT Journal***, Vol. 13, No. 3, (2020), 59-66. DOI: 10.30495/admt.2020.1898623.1195

25. Ranjbari, G., and Doniavi, A. "Prediction and optimization of mechanical properties of st52 in gas metal arc weld using response surface methodology and anova", ***International Journal of Engineering, Transactions C: Aspects,*** Vol. 29, No. 9, (2016), 1307-1313. DOI: 10.5829/idosi.ije.2016.29.09c.17

26. Ghaderi, A, Bani Mostafa Arab, N., Sheikhi, M. M., Nikoi, R., and Arham Nmazi, A. "Experimental Analysis of Effects of Ultrasonic Welding on Weld Strength of Polypropylene Composite Samples", ***International Journal of Engineering, Transactions C: Aspects,*** Vol. 28, No. 3, (2015), 447-53. DOI: 10.5829/idosi.ije.2015.28.03c.15

27. Davis, J. R. (Ed.). (1994). Stainless steels. ASM international.

28. AWS A5.9/A5.9M, 9th Edition, 2017 - Welding Consumables-Wire Electrodes, Strip Electrodes, Wires, and Rods for Arc Welding of Stainless and Heat Resisting Steels- Classification

29. ASTM E407-07(2015)e1, Standard Practice for Microetching Metals and Alloys, ASTM International, West Conshohocken, PA, 2015, www.astm.org DOI: 10.1520/E0407-07R15E01

30. ASTM E384-17, Standard Test Method for Microindentation Hardness of Materials, ASTM International, West Conshohocken, PA, 2017, www.astm.org DOI: 10.1520/E0384-17

31. ASTM E8 / E8M-21, Standard Test Methods for Tension Testing of Metallic Materials, ASTM International, West Conshohocken, PA, 2021, www.astm.org DOI: 10.1520/E0008_E0008M-21

32. ASTM A262-02, Standard Practices for Detecting Susceptibility to Intergranular Attack in Austenitic Stainless Steels, ASTM International, West Conshohocken, PA, 2002, www.astm.org DOI: 10.1520/A0262-02

33. Gupta S. K., Raja A. R., Vashista M. and Yusufzai M. Z. K., "Effect of heat input on microstructure and mechanical properties in gas metal arc welding of ferritic stainless steel", ***Materials Research Express,*** Vol. 6, No. 3, (2018), 036516. DOI: 10.1088/2053-1591/aaf492

34. Saha S., Mukherjee M. and Kumar T., "Microstructure, Texture, and Mechanical Property Analysis of Gas Metal Arc Welded AISI 304 Austenitic Stainless Steel", ***Journal of Materials Engineering and Performance***, Vol. 24, No. 3, (2018), 1125-1139. DOI: 10.1007/s11665-014-1374-0

35. Mukherjee M. and Pal T., "Influence of Heat Input on Martensite Formation and Impact Property of Ferritic-Austenitic Dissimilar Weld Metals", ***Journal of Materials Science & Technology***, Vol. 28, No. 4, (2012), 343-352. DOI: 10.1016/S1005-0302(12)60066-8

36. Bogaard, R. H. "Thermal conductivity of selected stainless steels". ***Thermal Conductivity***, Vol. 18, (1985), 175-185. DOI: 10.1007/978-1-4684-4916-7_20

37. Olmos, M., Martinez, K., and Unfried, J. "Efecto del ciclo térmico sobre la microestructura de la zona afectada térmicamente de juntas soldadas de aceros inoxidables disímiles obtenidas por el proceso SMAW", in XII International Conference–Latin American and Caribbean Consortium of Engineering Institutions-LACCEI. Guayaquil, Ecuador, (2014).

38. Teker T. and Kursun T., "Effect of the manual (GMAW) and pulsed (P-GMAW) welding processes on impact strength and fracture behavior of AISI 304-AISI 1040 dissimilar steel joints fabricated by ASP316L austenitic stainless steel filler metal", ***Kovove materialy - Metallic Materials***, Vol. 55, No. 2, (2017), 141-148. DOI: 10.4149/km_2017_2_141

39. Kheiri, S., Mirzadeh, H., and Naghizadeh, M. "Tailoring the microstructure and mechanical properties of AISI 316L austenitic stainless steel via cold rolling and reversion annealing", ***Materials Science and Engineering: A***, Vol. 759, (2019), 90-96. DOI: 10.1016/j.msea.2019.05.028

40. Tavares, S., Souza, L., Chuvas, C., Machado, C., and Almeida, C. "Influence of heat treatments on the microstructure and degree of sensitization of base metal and weld of AISI 430 stainless steel", ***Matéria*** (Rio de Janeiro), Vol. 22, No. 1, (2017). DOI: 10.1590/s1517-707620170005.0275

41. Ghosh, N., Pal, P. K., and Nandi, G." GMAW dissimilar welding of AISI 409 ferritic stainless steel to AISI 316L austenitic stainless steel by using AISI 308 filler wire", ***Engineering Science and Technology, an International Journal***, Vol. 20, No. 4, (2017), 1334-1341. DOI: 10.1016/j.jestch.2017.08.002

42. Pańcikiewicz, K., Świerczyńska, A., Hućko, P., and Tumidajewicz, M. "Laser dissimilar welding of AISI 430F and AISI 304 stainless steels", ***Materials***, Vol. 13, No. 20, (2020), 4540. DOI: 10.3390/ma13204540

Persian Abstract

چکیده

اتصالات جوش داده شده غیر مشابه فولاد ضد زنگ AISI 430 و AISI 316L توسط فرآیند GMAW با استفاده از دو مخلوط مختلف گاز محافظ متشکل از ۹۷-Ar 3N2 و ۸۰Ar-19He-1O2 تولید شده است. ریزساختار منطقه تحت تأثیر گرما توسط میکروسکوپ الکترونی نوری و روبشی مشخص شد و اندازه گیری های سختی ویکرز در سطح مقطع نمونه ها انجام شد. اتصالات جوش داده شده غیرمشابه به مدت ۲۴ و ۷۲ ساعت به آزمایش خوردگی غوطه وری در محلول اسید کلریدریک ۱۰٪ (v/v) ارسال شد. پس از آن ، استحکام بازده ، مقاومت کششی و درصد کشیدگی با استفاده از آزمون های کششی مطابق با استاندارد ASTM E8 اندازه گیری شد. برای مقایسه از اتصالات جوشکاری نشده غوطه ور استفاده شد. تجزیه و تحلیل واریانس برای ارزیابی تأثیر زمان غوطه وری و مخلوط گاز محافظ بر مقاومت در برابر مقاومت و مقاومت در برابر کشش ایجاد شد. خصوصیات ریزساختار نشان داد که منطقه تحت تأثیر گرما در سمت AISI 430 وسیع ترین بوده و وجود چشمگیر دانه های فریتی ، مارتنزیت و دانه درشت مشاهده شده است. در مقابل ، در منطقه تحت تأثیر گرما در سمت AISI 316L درشت و تصفیه دانه های آستنیت مشاهده نشد. منطقه تحت تأثیر گرما AISI 430 حداکثر مقادیر سختی و حساسیت بیشتر به آسیب خوردگی را نشان داد. نتایج آزمون های کششی نشان داد که آزمون های خوردگی غوطه وری در مقایسه با نمونه های غیر غوطه وری مقاومت نهایی به طور قابل توجهی تغییر نمی کند در حالی که به دلیل زمان غوطه وری مقاومت و بازده عملکرد به شدت کاهش می یابد. با توجه به مقدار p ، زمان غوطه وری بیشترین عامل تأثیر در مقاومت در برابر بازده و مقاومت کششی اتصالات جوش داده شده غیر مشابه دارد.

IJE TRANSACTIONS B: Applications Vol. 34, No. 05, (May 2021) 1362-1370

International Journal of Engineering

Journal Homepage: www.ije.ir

Effect of Critical Variables on Air Dense Medium Fluidized Bed Coal Drying Efficiency and Kinetics

A. Chelongar, E. Azimi*, M. R. Hosseini

Department of Mining Engineering, Isfahan University of Technology, Isfahan 84156-83111, Iran

PAPER INFO

Paper history:
Received 25 January 2021
Received in revised form 24 February 2021
Accepted 25February 2021

Keywords:
Air Dense Medium Fluidized Bed
Fixed Bed
Coal Drying
Kinetics

ABSTRACT

Calorific value, as a key component for fuel quality assessment, directly affects the thermal power plants' efficiency. While high-quality coal is consumed as metallurgical coal, low-rank coals are used by coal-fired power plants. The high moisture content of the thermal coals significantly influences their heating values. In this study, the drying performances of the fixed bed and air dense medium fluidized bed (ADMFB) dryers were investigated under the superficial air velocity of 15-18 cm/s, inlet air temperature of 55-75 ºC, and up to 80 minutes of operation. Low air consumption is an intrinsic characteristic for ADMFB, while a low-temperature range for drying air was selected to address the coal-fired power plants' waste heat. It was found that an increase in air velocity and temperature favored the drying efficiency of both systems (i.e., 18 cm/s and 75 ºC), with the temperature being more effective than the air velocity. The ADMFB dryer removed comparatively more moisture than the fixed bed for the shorter drying durations. For example, for 10% moisture reduction at 75 °C, the ADMFB dryer needed 5 minutes less time than the fixed bed. The fitting quality and goodness of serval well-known thin-layer models for describing fluidized bed and ADMFB coal drying kinetics were assessed by several models and statistical evaluators, respectively. It was found that the Middilli & Kucuk model best describes the fixed bed coal drying (i.e., R^2=0.999, *RSE*=0.001, *RMSE*=0.008), while the Page model much properly simulates the ADMFB coal drying (i.e., R^2=0.998, *RSE*=0.002, *RMSE*=0.009).

***doi**: 10.5829/ije.2021.34.05b.32*

1. INTRODUCTION

According to IEA (International Energy Agency), coal is the second primary energy source of the world after oil and the primary energy source for electricity generation. IEA estimated approximately 60% growth for world energy demand over the next 30 years, which necessitates low-rank coal (LRC) utilization for supporting low-cost energy production [1]. Different coal classification systems are developed and implemented, according to downstream utilization purposes. Four classes of coal could be considered according to the ASTM classification system, which has been developed based on the fixed carbon and gross calorific value on a moist basis, i.e., lignite, sub-bituminous, bituminous, and anthracite. Lignite coal attributes with the lowest calorific heat value (<4600 cal/g) and highest moisture content (up to 70%), while anthracite coal has the highest calorific heat value (>8300 cal/g) and lowest moisture content (<5%) [2, 3].

However, higher ash and moisture contents and comparatively lower heating values are the limiting factors for LRCs, despite their lower mining costs, abundance, and usually lower sulfur content [4]. Therefore, any reduction in moisture and ash content of the LRCs could improve their application as the thermal coal in coal-fired power plants.

The lower heating value of the coal, due to high moisture content, reduces coal-fired power plant thermal efficiency. Such efficiency reduction is a consequence of using high-temperature heat (high quality) in the boiler/furnace for moisture evaporation before ignition. For solid fuels such as thermal coal, it is well proven that high moisture content delays coal ignition, creates

*Corresponding Author Institutional Email: eazimi@iut.ac.ir (E. Azimi)

Please cite this article as: A. Chelongar, E. Azimi, M. R. Hosseini, Effect of Critical Variables on Air Dense Medium Fluidized Bed Coal Drying Efficiency and Kinetics, International Journal of Engineering, Transactions B: Applications Vol. 34, No. 05, (2021) 1362-1370

additional exhaust discharge, causes inappropriate combustion, and delays the start of emission of the combustible volatile matter [5-9]. The 3-5% increase in boiler efficiency due to the elimination of moisture before feeding it to the furnace has been reported by several researchers [10-13]. Bullinger et al. [10] reported even more energy-saving opportunities (up to 50% less energy requirement in milling), once 20% or more moisture reduction has been achieved. Hu et al. [13] did simulate the effect of moisture content on the efficiency of the boiler and overall power plant. They showed that, in a 1000MW conventional coal-fired power plant, a 20% reduction in coal moisture by a fluidized bed dryer would result in a 1.43% increase in overall plant efficiency. In another study, Liu et al. [12] discussed the effect of pre-drying on the performance of a hypothetical lignite-based coal-fired power plant. They showed that a 10% reduction in moisture content due to pre-drying, could increase plant efficiency by 1.78%. It is necessary that the consumed energy for moisture removal imposes minimum costs, therefore, employing waste heat from a coal-fired power plant for excess moisture removal could be a suitable solution.

Several drying systems are prevalent in the industry for LRC drying. Drying arrangements such as, packed/fixed bed dryer, moving bed dryer, fluidized bed dryer, assisted fluidized bed dryer (microwave, vibration, pulsed, immersed heater), flash dryer, rotary tube/drum dryer, microwave dryer …, or the non-evaporative methods such as, mechanical, thermal, hydrothermal, and solvent dewatering are well discussed in details in literature [4, 8, 14-19], with each method merits and issues [4, 20-22], such as energy consumption, efficiency, heat and mass transfer rates, and capital/process expenses. But regardless of the implemented method type, improvements in mass and heat transfer rates play a significant role in the success of the process. It should be addressed that, in evaporative methods, the provided heat can just remove freezable moisture from the surfaces and pores of particles while the carrying phase transfers it out.

Some inherent properties of the fluidized beds, i.e., solid mixing and relatively high heat and mass transfer rates between gas and solid phase, are relevant to the fluid dynamics of the system [23]. These unique properties have made fluidized bed dryers a right choice for LRC drying such as Illinois coals [11], Turkish coals [16, 19, 24], polish coal [25], Indonesian coal [26], Chinese coals [5, 27], Victorian brown coal [28-30]. The high capacity, maximum gas-solid contact surface, low maintenance costs, and rapid moisture transfer between phases (shorter drying time), could be entitled as the advantages of the fluidized bed coal drying. In contrast, the possibility of self-ignition during the drying process, higher superficial air velocity requirements, unsuitability for irregularly shaped particles, agglomeration of wide particle size range feeds in high moisture coals, attrition of particles while drying, and channeling could be addressed as this methods' disadvantages [5, 13, 20, 24, 30]. Jangam et al. [21] have summarized the advantages and limitations of different coal drying methods thoroughly. According to available references [4, 5, 15, 20, 30], the effective parameters in favor of performance improvement of the fluidized bed coal dryers are air temperature, air velocity and residence time, where bed thickness, particle size, and initial moisture content of both phases (coal and hot air), have some adverse effect on the operation output.

The air dense medium fluidized bed (ADMFB) idea was introduced after the development of the fluidization concept. In an ADMFB the upward airflow fluidizes very fine particles (i.e., fluidization medium), and consequently, the generated suspension creates a pseudo fluid with an average density between air and solid particles. Any external particle with higher densities than the pseudo fluid density sinks in the bed while lighter ones remain suspended on the top.

The ADMFB system has several advantages over the conventional packed/fluidized bed coal drying systems and highly benefits the overall economy/efficiency of the coal-fired power plants. The necessary airflow and drying heat could be supplied via the final exhaust flue gas from the furnace (waste heat) with no limitations. The major difference between an ADMFB and a conventional fluidized beds the lower superficial air velocity requirements for floating the coarse coal particles (e.g., on average, 8 times less for the coal particles studied here) due to the much higher average density of the created pseudo fluid than the regular hot air. In an ADMFB, the coal particles float in a pseudo-fluid instead of entirely or partially being lifted by air as it occurs in conventional fluidized beds. Therefore, the subsequent exhaust gas handling or dust collecting system would be even smaller than conventional fluidized beds, which would need less energy for gas de-moisturizing and particulate matter emission control.

The heat and mass transfer are high in a fluidized bed, where feeding a pre-heated fluidization medium would decrease the drying time as the hot medium particles act as high energy packs floating in the hot gas. In fact, the hotter fluidization medium results in faster and more efficient drying with lower residual moisture on the final product .

Not much of a proper beneficiation or efficient pre-drying systems are practiced by the power industry yet, but it is receiving more and more recognition. Elimination of moisture, ash, and harmful components from thermal coals (non-metallurgical) even though imposes some extra costs, but reduces overall electricity generation expenses, energy production carbon footprint, as well as expanding mining opportunities for some low-rank thermal coal deposits (e.g., lignite coals) [31-34].

In this study, the effectiveness of the critical parameters on the fixed bed and ADMFB low-temperature coal drying was studied and compared using a thermal coal sample (could be classified as lignite coal). The hot air temperature was limited to 75 °C to support the idea of the coal-fired power plant waste heat utilization for LRC heat value improvement. The drying air superficial velocity was selected to be suitable for ADMFB operations (enough to fluidize medium particles, but not coal particles), therefore for mono-coal particles, fixed bed status occurred. It was intended to examine if lower air consumption in ADMFB system could benefit the drying process or not. Also, the hotness of air was limited to lower temperatures (in the range of waste heat of power plants), which facilitates faster medium heat up and recovery. The kinetics of drying phenomena is a key component once conducting process performance evaluation, as well as, industrial application considerations. Therefore, both systems drying capabilities and kinetics were studied and evaluated using well-known thin layer kinetics models and were compared respectively.

2. MATERIALS AND METHODS

2. 1. Coal Sample and Fluidization Medium

The prepared coal sample was crushed to finer than 13.2 mm, and after mixing, sub-samples were prepared by Jones riffle. The 2 to 4.6 mm size fraction was sieved and used in the experiments.

The proximate analysis of the coal was performed following the ASTM D3174, D3175, and D3302 procedures using a muffle furnace. Samples were dried in a vacuum oven for 8 h considering ASTM D-7582 method, before the proximate analysis. The amount of the removed moisture in the vacuum oven was also taken into consideration once the total moisture contents for the samples were reported. The average moisture content, volatile matter, and ash content of the 2-4.6 mm samples were determined to be 21.5, 34.5, and 29.6 %, respectively.

Different solids were used as a fluidization medium and are reported in literature [35-37]. In this study, the silica sand with a density of 2.6 g/cm^3 and average particle size of 327 µm (the -354, +300 µm particles were separated by dry sieving) was used as the fluidization medium. The selected fluidization medium (silica sand) is classified as Geldart group B [38] particles and has low acquisition and preparation costs. In this case, the abondance and chemical inertness are the other advantages of the silica sand over the other medium types employed in ADMFB systems.

2. 2. Experimental Setup And Procedure

The inlet airflow rate, and consequently, the superficial air velocity, was adjusted by a mass flow controller (with Accuracy: ±1%) and the air temperature was adjusted to the desired temperature by an inline 2500 Watt electric heater. A 150 µm steel screen was used at the bottom of the bed to support solid materials as well as to distribute airflow uniformly into the bed-chamber. Plexiglas pieces (ID of 8 cm) with a maximum height of 60 cm were used to form the bed body. Layers of glass wool were used to cover pipes, connections, and the bed body to minimize heat loss between the air heater and the ADMFB. The employed setup is presented in Figure 1 (not including the heating system, since it was fully covered in glass wool).

In general, two different types of experiments were conducted: packed bed or ADMFB drying experiments. During the drying procedure, hot air passed through the system to heat up components and apparatus prior to adding coal samples and initiating the test. The determined hot air temperature was achieved and steady-state status inside the bed was insured by minimizing the temperature difference of thermocouples installed at the bottom of the bed, and the second one, 20 cm above it. Once a steady-state was reached, an empty bed weight (or bed filled with the determined fluidization medium) was obtained by a balance (accuracy of ±0.1 g). Following the same procedure, the aggregate weight of the bed, fluidization medium, and added coal sample were measured in the determined time intervals, and then moisture loss was calculated considering the fixed and variable mass components. For ADMFB coal drying, the fluidization medium was also heated up with the bed body until reaching a stable temperature, and its weight was considered as a part of the bed body during the periodic weight measurements as they were dried entirely before introducing to the bed.

Three different drying temperatures, 55, 65, and 75 °C, were used, and weight loss was tracked for up to 80

Figure 1. ADMFB filled with silica sand and connected to the mass flow controller (not covered in the wool glass yet)

minutes, from the moment a coal sample was added to the bed, either fixed or fluidized system. At the end of any drying experiment, coal particles were collected or separated from the fluidization medium, weighted, and sealed to avoid moisture loss/gain. Later ash and moisture content of the dried coal samples were determined. The weight loss during the drying period was calculated considering the initial sample weight, net sample weights in time intervals, and final moisture content of the dried particles.

2. 3. Kinetics Modelling The most commonly used empirical thin-layer models (examined successfully for coal drying) were selected (Table 2) and employed to determine the drying kinetics of the moisture removal.

M_0, M_t, M_R, W_t, and W_c are the samples' initial moisture content, residual moisture content at time *t*, relative moisture content at relevant time *t*, wet coal sample weight at time *t*, and dry coal (just solid material) weight, respectively. The M_t and M_R are obtainable through Equations (1) and (2).

$$M_t = \frac{W_t - W_c}{W_c} \times 100 \quad (1)$$

$$M_R = \frac{M_t}{M_0} \quad (2)$$

The fitting qualities of the selected models were evaluated by the standard statistical evaluators such as coefficient of determination (R^2), residual sum of square (RSE, i.e., Equation (3)), and root mean square error (RMSE, i.e., Equation (4)) once parameters were determined by non-linear regression analysis. The higher values of R^2, lower values of RSE, and RMSE indicate better and consistent model fitting.

TABLE 1. Packed bed and ADMFB drying parameters

Experiment	Superficial air vleocity (cm/s)	Solid height in bed (cm)	Set temp. (°C)	Duration (min)
Fixed bed	15-18	>5	55, 65, 74	Up to 80
ADMFB	15-18	~23	55, 65, 74	Up to 80

TABLE 2. Thin-layer drying models [39-44]

Model name	Mathematical presentation*
Newton	$M_R = \exp(-kt)$
Page	$M_R = \exp(-kt^n)$
Modified Page	$M_R = \exp(-(kt)^n)$
Henderson & Pabis	$M_R = a\exp(-kt)$
Wang & Singh	$M_R = 1 + at + bt^2$
Logarithmic	$M_R = a + b\exp(-kt)$
Middilli & Kucuk	$M_R = a\exp(-kt^n) + bt$

* *a, b, n, and k are constants*

$$RSE = \sum_{i=1}^{n}(MR_{exp,i} - MR_{prd,i})^2 \quad (3)$$

$$RMSE = \sqrt{\sum_{i=1}^{n}(MR_{exp,i} - MR_{prd,i})^2 / n} \quad (4)$$

The $MR_{exp,i}$, $MR_{pre,i}$, and n are the experimental moisture ratio, predicted moisture ratio, and the number of the data points used for modelling, respectively.

3. RESULTS AND DISCUSSIONS

3. 1. The Effect Of Air Velocity And Temperature The effect of an increase in superficial air velocity (at 65 °C as representative) for fixed and ADMFB coal drying is presented in Figures 2a and b, respectively. At first glance and as expected, coal drying improves for both systems by the increase of air velocity from 15 to 18 cm/s, since both heat and moisture transfer (from coal surface to gaseous phase) rates improve with it. A similar increasing trend has been observed for two other temperatures and both systems. Also, the gap between corresponding points for similar drying times increased by increasing air temperature from 55 °C to 75 °C. Once drying continues for over 40 to 50 minutes, an increase in moisture loss becomes almost negligible (<1%) for the fixed bed system, while moisture loss continues to increase for ADMFB rather than staying constant. It

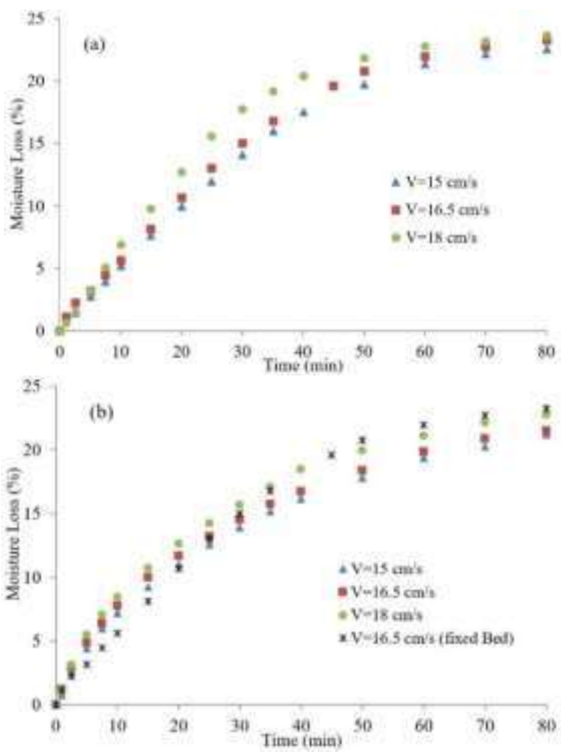

Figure 2. The effect of superficial air velocity on coal drying at 65 °C, (a) fixed bed, (b) ADMFB

should be noted that the superficial air velocity at which sand particles are fluidized is almost 8 times less than the examined coal particles. At the employed air velocities, there was almost no bubbling while fluidization status was maintained satisfactorily.

Comparison between the corresponding fixed bed and ADMFB drying experiment showed that, for drying times lower 20 minutes and at any of the air velocities, the moisture reduction happens with faster rates for ADMFB drying than fixed bed, and then it gets reverse once drying continues for longer times. That was because of the heat energy saved in sand particles, enhancing faster evaporation of the moister. The final moisture reduction after 80 minutes is slightly higher for fixed bed than ADMFB.

As addressed in the literature [5, 20], improvements in fluidized bed coal drying would continue up to 2-2.2 of the coal particles' Umf (i.e., 2.2-3.65 m/s for the tested coal particles [23, 45]). Kim et al. [28] suggested that the optimum drying gas velocity is around the Umf of particles, and higher velocities would only raise energy consumption and elutriation phenomenon. But in this study, the air velocity was limited to 0.18 m/s, which is almost 30% more than the sand particles' Umf and far less than coal particles' Umf.

Figures 3a and 3b show the effect of drying air temperature for fixed and ADMFB coal drying, respectively, at 15 cm/s air velocity. Generally, the drying rate increases in both Figures 3a and 3b, while drier coal is obtainable with an increase in air temperature, as data have been reported in literature [17, 46]. Unlike Figure 2a, drying curves do not reach a steady-state for fixed-bed once drying prolongs, indicating a higher significance of the temperature compared to the air velocity .

The comparison between Figure 1a and 3b indicate that ADMFB reduces moisture faster than the fixed bed for shorter drying durations at any hot air temperature. For 10% moisture reduction at 55 or 75 °C, drying should be continued 25 or 13 minutes within the fixed bed, while it takes 22 or 8 minutes once ADMFB has been used.

Similar to Figure 2b, fixed bed and ADMFB drying curves for the corresponding set temperatures, cross each other, but at higher drying times. As discussed, drying for shorter times yields more moisture removal by the ADMFB system (Figure 3b), and an ADMFB is more preferred. In the fixed bed, the heat exchange capacity of the system is limited and could just be partially used for evaporating the moisture off from the coal particles. Initially, when coal enters the ADMFB, due to higher heat energy saved in the sand particles, heat and consequently moisture transfer rates increase significantly. After almost 20 minutes and once sand particles lost some heat, some of the energy entering the bed by hot air would be consumed by sand particles for maintaining higher temperatures, rather than moisture

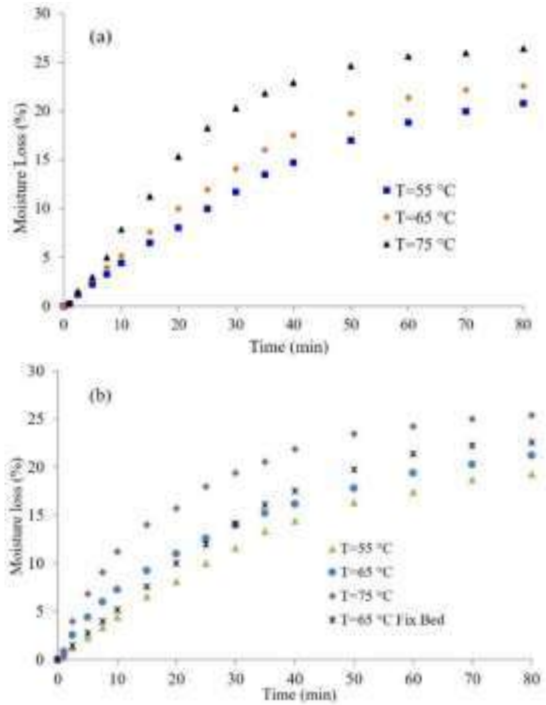

Figure 3. The effect of drying air temperature on coal drying at 15 cm/s, (a) fixed bed, (b) ADMFB

on the coal particles. That is when drying by ADMFB becomes less effective than the fixed bed (almost after 20 minutes). Such an issue could be solved easily, once ADMFB operates continuously, and reheating of the fluidization medium occurs while recirculating it back to the ADMFB (after separation of the dry coal somewhere out of the fluidization chamber).

Based on the obtained results, the performance of the batch ADMFB drying system is superior to the fixed bed system for drying times less than 20-25minutes, but if a significant reduction in product moisture is needed, employment of a continuous ADMFB dryer would be beneficial. In a batch ADMFB system, due to the nature of the operation, continuous support of the hot sand to the system during the operation is not possible. In a continuous operation, it is feasible to inject pre-heated sand with the same or even higher temperatures of the drying air to the system, while drying carries on in the bed-chamber. Fresh hotter sand has higher trapped heat energy in it and can improve drying efficiency in shorter process times. Auxiliary hot sand can get its energy from un-used hot flue gas (waste heat) once a coal-fired plant is in the vicinity or even a small preparation furnace.

3. 3. Coal Drying Kinetics

The collected time versus moisture loss (in terms of MR) data from both ADMFB and the fixed bed was used to study the coal drying kinetics and modelling based on the selected thin layer models in Table 2. However, modelling efforts showed that the coal drying in fixed bed and ADMFB could not be represented by Wang & Singh model [44]. Also, the constant value of the Logarithmic model for the fixed bed was calculated to be zero. Therefore, the Henderson & Pabis model was considered here for coal drying modelling. Similarly, Middilli & Kucuk models' constant was also calculated to be zero for all nine ADMFB drying experiments and consequently was taken out from the comparison list. The average and standard deviations (nine experiments for each system) of R^2, RSE, and RMSE of the models for both fix and ADMFB systems, regardless of operating parameter variations, are presented in Table 3.

Based on the goodness, the statistical evaluators, and their standard deviations are given in Table 3, the Middilli & Kucukand, and then equally, both Page and Modified Page models do best represent fixed bed coal drying phenomena. For all mentioned models, the standard deviations of R^2s' were less than 1% of the corresponding R^2. The results of the model fitting on any individual fixed bed drying data set for the Middilli & Kucukand model, as well as model constants (*a*, *b*, *n*, and *k*), are presented in Table 4.

Figure 4a-b compares the experimental M_R vs. predicted M_R by Middilli & Kucuk model, for different air velocities at 65 and 75 °C. In both graphs, excellent fitness between experimental and simulated moisture ratio is presented. Generally, higher superficial air velocity and temperature increase moisture ratio, which is clearly presented in Figure 4a as moisture ratio (loss) for 18 cm/s is descending more sharply. The experimental and simulated moisture ratio curves are closer to each other at 75 °C dryings (Figure 4b).

TABLE 3. Average (Ave.) and standard deviation (St.D.) of the statistical evaluators for ADMFB and fixed bed systems coal drying

Model name		***Fix bed drying***			***ADMFB drying***		
		R^2	***RSE***	***RMSE***	R^2	***RSE***	***RMSE***
Newton	Ave.	0.994	0.015	0.030	0.994	0.016	0.031
	St.D.	0.002	0.007	0.008	0.004	0.007	0.007
Page	Ave.	0.997	0.005	0.016	0.998	0.002	0.009
	St.D.	0.001	0.002	0.005	0.001	0.002	0.005
Modified Page	Ave.	0.997	0.005	0.016	0.998	0.0025	0.009
	St.D.	0.001	0.003	0.005	0.001	0.002	0.005
Henderson & Pabis	Ave.	0.994	0.01	0.024	0.991	0.009	0.024
	St.D.	0.002	0.004	0.006	0.005	0.005	0.000
Middilli & Kucuk	Ave.	0.999	0.001	0.008	--	--	--
	St.D.	0.001	0.001	0.002	--	--	--
Logarithmic	Ave.	--	--	--	0.997	0.003	0.014
	St.D.	--	--	--	0.001	0.001	0.003

TABLE 4. Results of statistical parameters for Middilli & Kucuk model fitting and model coefficients

V **(cm/s)**	***T*** **(°C)**	R^2	***RSE***	***RMSE***	***a***	***b***	***n***	***k***
15	55	0.998	0.001	0.006	0.993	0.001	1.214	0.008
16.5	55	0.999	0.001	0.006	0.996	0.001	1.246	0.010
18	55	0.999	0.000	0.005	0.995	0.001	1.220	0.011
15	65	0.998	0.002	0.010	0.994	0.001	1.304	0.008
16.5	65	0.999	0.002	0.010	0.974	0.001	1.352	0.007
18	65	0.998	0.001	0.007	0.993	0.001	1.323	0.011
15	75	0.998	0.001	0.008	0.997	0.001	1.351	0.012
16.5	75	0.998	0.002	0.012	0.990	0.001	1.286	0.015
18	75	0.999	0.001	0.010	1.009	0.001	1.337	0.014

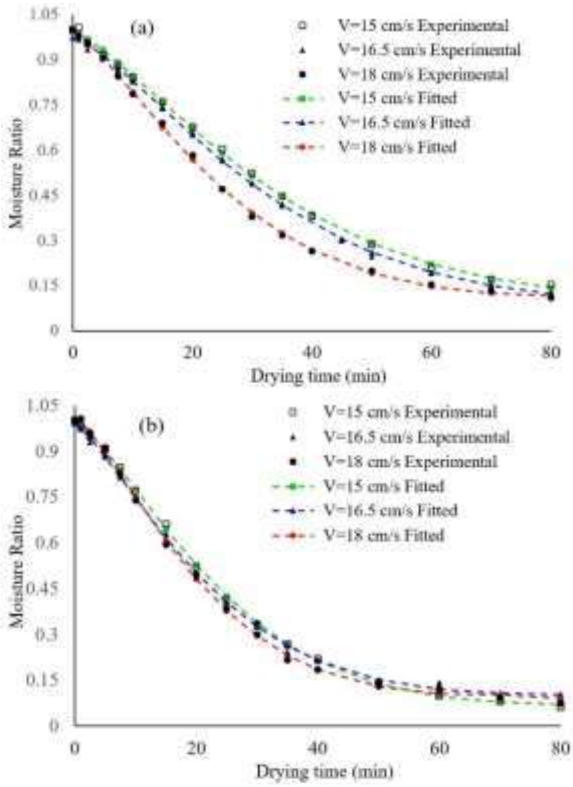

Figure 4. The experimental vs. fitted moisture ratio by Middilli & Kucuk model for fixed bed drying, (a) 65 °C, (b) 75 °C

Reaching almost the highest mass and heat transfer capacity could be an interpretation.

For ADMFB, model, fitting and statistical evaluator's analysis showed that both Page and Modified Page models equally describe coal drying precisely, where, Logarithmic model stands after them. The standard deviations of the modes were calculated and resulted in being less than 1%. The results of the model fitting on any individual ADMFB drying experiment for the Page model and model constants (n and k) are presented in TABLE . For any air temperature setting, k increases by the increase of air velocity, and for any certain air velocity, k increases with the increase of air temperature. In fact, stronger drying condition results in higher k values, indicating a direct relationship between k and drying force intensity.

Figures 5a and 5b show the capability of the Page model in representing ADMFB coal drying at 65 and 75 °C and different air velocities. Same as Figure 4 a-c, the simulated and experimental results are matching acceptably well. At lower drying times, the slopes of the curves are higher than the corresponding fixed bed curves. Drying was intense for 75 °C compared to the 65 °C, where curves are closer at a higher temperature than two other lower ones (55 °C curves are not included here)

3. 4. Benefits of Drying The main goal of this study was to upgrade LRC for thermal applications. Therefore, the higher heating value (HHV) of the head coal sample was determined using available correlations in the literature [5, 86]. Based on the ultimate analysis results, the HHV of the head sample was determined to be 19.32 MJ/kg.

Elimination of moisture (e.g., 10%) due to ADMFB drying (8 minutes of drying 75 °C), could increase HHV up to 21.45 MJ/kg. Several experimental/simulation studies have been conducted on the effect of ash or moisture reduction on the performance of coal-based power generation plants [14-17]. All emphasized the unit/plant efficiency improvements. A 10% reduction in moisture content (using ADMFB dryer) could promise around a 1.5 % increase in plant efficiency, as discussed in literature [16, 17].

In a conventional coal-fired power plant, the substitution of a 19.32 MJ/kg, feed stream with its upgraded product with 21.45 MJ/kg (upgraded using furnace waste heat) could increase the available energy for the furnace, at least 11%. A lower amount of flue gas

TABLE 5. Results of statistical parameters for Page model fitting and model coefficients

***V* (cm/s)**	***T* (°C)**	***R^2***	***RSE***	***RMSE***	***n***	***k***
15	55	0.997	0.001	0.007	0.836	0.032
16.5	55	0.999	0.000	0.005	0.795	0.037
18	55	0.998	0.000	0.005	0.842	0.039
15	65	0.999	0.000	0.005	0.852	0.034
16.5	65	0.999	0.000	0.004	0.835	0.040
18	65	0.999	0.001	0.008	0.855	0.041
15	75	0.999	0.001	0.008	0.863	0.051
16.5	75	0.996	0.005	0.018	0.816	0.055
18	75	0.999	0.002	0.010	0.774	0.068

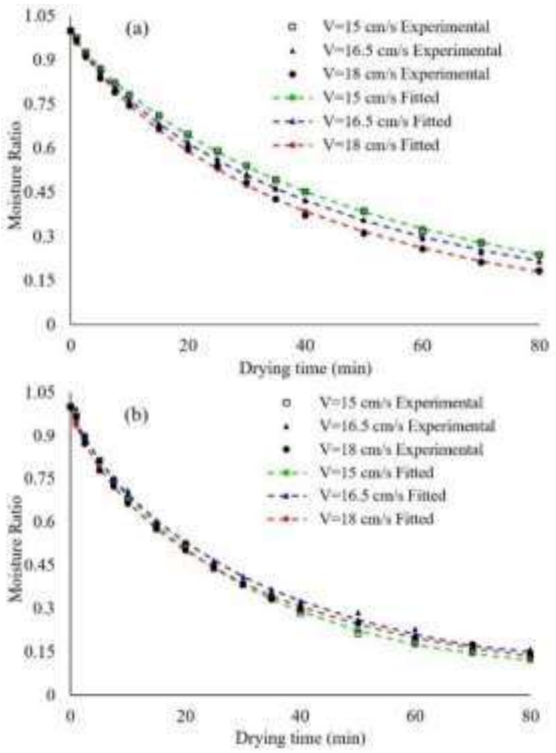

Figure 5. Experimental vs. fitted moisture ratio by Page model for ADMFB drying, (a) 65 °C, (b) 75 °C

to be dealt with would reduce the size of the flue gas treatment operation as well as a possible increase in its efficiency.

4. CONCLUSION

In this study, the effects of drying air temperature and its superficial velocity on a fixed bed and ADMFB coal drying were assessed. As LRCs are usually used as thermal coal in coal-fired power plants, a low-temperature range (<75 °C) was selected for drying air. Also, the superficial air velocity was selected to be suitable for dense medium fluidization (<18 cm/s), thus was not enough to fluidize coal particles (at least 8 times less than the required velocity to fluidize coal particles). After determination of the effects of parameters on both systems, simulation of coal drying for fixed ben and ADMFB systems were conducted using seven thin-layer kinetics models. Valid statistical evaluators were determined for model significance assessment. The following major conclusions were drawn.

For both fixed bed and ADMFB systems, moisture removal improved by increasing superficial air velocity and air temperature. Maximum moister removal was achieved at a superficial air velocity of 18 cm/s and 75 °C (i.e., 25% moisture removal). It should be addressed that the temperature was found to be more influential than the air velocity.

ADMFB drying is preferred if a shorter process time is favorable. For 10 % moisture reduction, increasing air temperature from 55 °C to 75 °C decreases drying time by 50 and 62% for fixed bed and ADMFB systems, respectively.

Kinetics studies using thin-layer models showed that fixed bed and ADMFB coal drying could be best presented by Middilli & Kucuk and Page models, respectively. Different statistical evaluators such as R^2, RSE, and RMSE were employed to determine the models fitting goodness. The model coefficients were determined for any set of conditions.

5. ACKNOWLEDGMENT

The corresponding author would like to acknowledge the Iran National Science Foundation (INSF) for supporting this research under the grant number of 97004223 and the Mining Engineering Department of the Isfahan University of Technology for granting access to the infrastructures.

6. REFERENCES

1. IEA. *World energy balances: Overview (2019 edition)*. https://www.iea.org/reports/world-energy-balances-2019].
2. Riley, J.T., "Routine coal and coke analysis: Collection, interpretation, and use of analytical data, 2nd edition, ASTM International Pennsylvania, (2014). doi: 10.1520/MNL57-2ND-EB
3. Berkowitz, N., "An introduction to coal technology, Elsevier, (2012). doi: 10.1016/C2012-0-01440-8
4. Osman, H., Jangam, S., Lease, J. and Mujumdar, A.S., "Drying of low-rank coal (lrc)—a review of recent patents and innovations", ***Drying Technology***, Vol. 29, No. 15, (2011), 1763-1783. doi: 10.1080/07373937.2011.616443
5. Zhao, P., Zhao, Y., Luo, Z., Chen, Z., Duan, C. and Song, S., "Effect of operating conditions on drying of chinese lignite in a vibration fluidized bed", ***Fuel Processing Technology***, Vol. 128, (2014), 257-264. doi: 10.1016/j.fuproc.2014.07.014
6. Khankari, G. and Karmakar, S., "Improvement of efficiency of coal-fired steam power plant by reducing heat rejection temperature at condenser using kalina cycle", ***International Journal of Engineering, Transactions A: Basics***, Vol. 31, No. 10, (2018), 1789-1795. doi: 10.5829/ije.2018.31.10a.23
7. Shi, Y.C., Li, J., Li, X.Y., Wu, J., Wu, M.G., Li, S., Wang, H.Y., Zhao, G.J. and Yin, F.J., "Experimental study on super-heated steam drying of lignite", in ***Advanced Materials Research,*** Trans Tech Publications Ltd. Vol. 347, No., (2012), 3077-3082. doi: 10.4028/www.scientific.net/AMR.347-353.3077
8. Ross, D., Doguparthy, S., Huynh, D. and McIntosh, M., "Pressurised flash drying of yallourn lignite", ***Fuel***, Vol. 84, No. 1, (2005), 47-52. doi: 10.1016/j.fuel.2004.08.006
9. Tiara, T., Agustina, T. and Faizal, M., "The effect of air fuel ratio and temperature on syngas composition and calorific value produced from downdraft gasifier of rubber wood-coal mixture", ***International Journal of Engineering, TransactionsC:Aspects***, Vol. 31, No. 9, (2018), 1480-1486. doi: 10.5829/ije.2018.31.09c.02
10. Bullinger, C., Ness, M. and Sarunac, N., "Coal creek prototype fluidized bed coal dryer: Performance improvement, emissions reduction, and operating experience", in 31st International Technical Conference on Coal Utilization and Fuel Systems, Clearwater, Florida., (2006).
11. Kakaras, E., Ahladas, P. and Syrmopoulos, S., "Computer simulation studies for the integration of an external dryer into a greek lignite-fired power plant", ***Fuel***, Vol. 81, No. 5, (2002), 583-593. doi: 10.1016/S0016-2361(01)00146-6
12. Liu, M., Yan, J., Bai, B., Chong, D., Guo, X. and Xiao, F., "Theoretical study and case analysis for a predried lignite-fired power system", ***Drying Technology***, Vol. 29, No. 10, (2011), 1219-1229. doi: 10.1080/07373937.2011.582559
13. Hu, S., Man, C., Gao, X., Zhang, J., Xu, X. and Che, D., "Energy analysis of low-rank coal pre-drying power generation systems", ***Drying Technology***, Vol. 31, No. 11, (2013), 1194-1205. doi: 10.1080/07373937.2013.775146
14. Tahmasebi, A., Yu, J., Li, X. and Meesri, C., "Experimental study on microwave drying of chinese and indonesian low-rank coals", ***Fuel Processing Technology***, Vol. 92, No. 10, (2011), 1821-1829. doi: 10.1016/j.fuproc.2011.04.004
15. Kannan, C.S., Thomas, P. and Varma, Y., "Drying of solids in fluidized beds", ***Industrial & engineering chemistry research***, Vol. 34, No. 9, (1995), 3068-3077. doi: 10.1021/ie00048a018
16. Calban, T. and Ersahan, H., "Drying of a turkish lignite in a batch fluidized bed", ***Energy Sources***, Vol. 25, No. 12, (2003), 1129-1135. doi: 10.1080/00908310390233568
17. Jeon, D., Kang, T., Kim, H., Lee, S. and Kim, S., "Investigation of drying characteristics of low rank coal of bubbling fluidization through experiment using lab scale", ***Science China Technological Sciences***, Vol. 54, No. 7, (2011), 1680-1683. doi: 10.1007/s11431-011-4414-0
18. Kanda, H. and Makino, H., "Energy-efficient coal dewatering using liquefied dimethyl ether", ***Fuel***, Vol. 89, No. 8, (2010), 2104-2109. doi: 10.1016/j.fuel.2010.02.019
19. Pusat, S., Akkoyunlu, M.T. and Erdem, H.H., "Fragmentation of a turkish low rank coal during fixed-bed evaporative drying process", ***International Journal of Coal Preparation and Utilization***, (2018), 1-9. doi: 10.1080/19392699.2018.1451847
20. Si, C., Wu, J., Wang, Y., Zhang, Y. and Shang, X., "Drying of low-rank coals: A review of fluidized bed technologies", ***Drying Technology***, Vol. 33, No. 3, (2015), 277-287. doi: 10.1080/07373937.2014.952382
21. Jangam, S.V., Karthikeyan, M. and Mujumdar, A., "A critical assessment of industrial coal drying technologies: Role of energy, emissions, risk and sustainability", ***Drying Technology***, Vol. 29, No. 4, (2011), 395-407. doi: 10.1080/07373937.2010.498070
22. Arima, K., Tsuchiyama, Y., Sawatsubashi, T., Kinoshita, M. and Ishii, H., "Drying of wet brown coal particles by a steam-fluidized bed dryer", ***Drying Technology***, Vol. 36, No. 6, (2018), 664-672. doi: 10.1080/07373937.2017.1323337
23. Rhodes, M.J., "Introduction to particle technology, John Wiley & Sons, (2008). doi: 10.1002/9780470727102
24. Pusat, S., Akkoyunlu, M.T., Erdem, H.H. and Dağdaş, A., "Drying kinetics of coarse lignite particles in a fixed bed", ***Fuel Processing Technology***, Vol. 130, (2015), 208-213. doi: 10.1016/j.fuproc.2014.10.023
25. Pawlak-Kruczek, H., Plutecki, Z. and Michalski, M., "Brown coal drying in a fluidized bed applying a low-temperature gaseous medium", ***Drying Technology***, Vol. 32, No. 11, (2014), 1334-1342. doi: 10.1080/07373937.2014.909845

26. Park, J.H., Lee, C.-H., Park, Y.C., Shun, D., Bae, D.-H. and Park, J., "Drying efficiency of indonesian lignite in a batch-circulating fluidized bed dryer", ***Drying Technology***, Vol. 32, No. 3, (2014), 268-278. doi: 10.1080/07373937.2013.822385

27. Tahmasebi, A., Yu, J., Han, Y. and Li, X., "A study of chemical structure changes of chinese lignite during fluidized-bed drying in nitrogen and air", ***Fuel Processing Technology***, Vol. 101, (2012), 85-93. doi: 10.1016/j.fuproc.2012.04.005

28. Kim, H.-S., Matsushita, Y., Oomori, M., Harada, T., Miyawaki, J., Yoon, S.-H. and Mochida, I., "Fluidized bed drying of loy yang brown coal with variation of temperature, relative humidity, fluidization velocity and formulation of its drying rate", ***Fuel***, Vol. 105, (2013), 415-424. doi: 10.1016/j.fuel.2012.09.057

29. Tahmasebi, A., Yu, J. and Bhattacharya, S., "Chemical structure changes accompanying fluidized-bed drying of victorian brown coals in superheated steam, nitrogen, and hot air", ***Energy & Fuels***, Vol. 27, No. 1, (2012), 154-166. doi: 10.1021/ef3016443

30. Stokie, D., Woo, M.W. and Bhattacharya, S., "Attrition of victorian brown coal during drying in a fluidized bed", ***Drying Technology***, Vol. 34, No. 7, (2016), 793-801. doi: 10.1080/07373937.2015.1080723

31. Argimbaev, K.R. and Drebenstedt, C., "Korkinsk brown coal open pit as a case study of endogenous fires", ***International Journal of Engineering,TransactionsA: Basics***, Vol. 34, No. 1, (2021), 293-304. doi: 10.5829/ije.2021.34.01a.32

32. Dwari, R. and Rao, K.H., "Dry beneficiation of coal—a review", ***Mineral Processing and Extractive Metallurgy Review***, Vol. 28, No. 3, (2007), 177-234. doi: 10.1080/08827500601141271

33. Azimi, E., Karimipour, S., Xu, Z., Szymanski, J. and Gupta, R., "Statistical analysis of coal beneficiation performance in a continuous air dense medium fluidized bed separator", ***International Journal of Coal Preparation and Utilization***, Vol. 37, No. 1, (2017), 12-32. doi: 10.1080/19392699.2015.1123155

34. Ram, M. and Kumar, A., "Reliability measures improvement and sensitivity analysis of a coal handling unit for thermal power plant", ***International Journal of Engineering***, Vol. 26, No. 9, (2013), 1059-1066. doi: 10.5829/idosi.ije.2013.26.09c.11

35. Sahu, A., Tripathy, A., Biswal, S. and Parida, A., "Stability study of an air dense medium fluidized bed separator for beneficiation of high-ash indian coal", ***International Journal of Coal Preparation and Utilization***, Vol. 31, No. 3-4, (2011), 127-148. doi: 10.1080/19392699.2011.574936

36. He, Y., Zhao, Y. and Chen, Q., "Fine particle behavior in air fluidized bed dense medium dry separator", ***Coal Preparation***, Vol. 23, No. 1-2, (2003), 33-45. doi: 10.1080/07349340302268

37. Dave, P.C., "Dry cleaning of coal by a laboratory continuous air dense medium fluidised bed separator", (2012). doi: 10.7939/R3K339

38. Geldart, D., "Types of gas fluidization", ***Powder Technology***, Vol. 7, No. 5, (1973), 285-292. doi: 10.1016/0032-5910(73)80037-3

39. O'callaghan, J., Menzies, D. and Bailey, P., "Digital simulation of agricultural drier performance", ***Journal of Agricultural Engineering Research***, Vol. 16, No. 3, (1971), 223-244. doi: 10.1016/S0021-8634(71)80016-1

40. Midilli, A., Kucuk, H. and Yapar, Z., "A new model for single-layer drying", ***Drying Technology***, Vol. 20, No. 7, (2002), 1503-1513. doi: 10.1081/DRT-120005864

41. Diamante, L.M. and Munro, P.A., "Mathematical modelling of the thin layer solar drying of sweet potato slices", ***Solar energy***, Vol. 51, No. 4, (1993), 271-276. doi: 10.1016/0038-092X(93)90122-5

42. Chhinnan, M.S., "Evaluation of selected mathematical models for describing thin-layer drying of in-shell pecans", ***Transactions of the ASAE***, Vol. 27, No. 2, (1984), 610-0615. doi: 10.13031/2013.32837

43. Chandra, P.K. and Singh, R.P., "Applied numerical methods for food and agricultural engineers", (1994). doi: 10.1201/9781315137650

44. Wang, C. and Singh, R., *A single layer drying equation for rough rice*. 1978, ASAE paper. doi: 10.12691/ajfst-4-4-5

45. Coulson, J.M., Richardson, J.F., Backhurst, J.R. and Harker, J.H., "Particle technology and separation processes, Pergamon Press, Vol. 2, (1991). doi: 10.1016/C2009-0-25733-3

46. Zhang, K. and You, C., "Experimental and modeling investigation of lignite drying in a fluidized bed dryer", in Proceedings of the 20th international conference on fluidized bed combustion, Springer. (2009), 361-366. doi: 10.1007/978-3-642-02682-9_53

Persian Abstract

چکیده

ارزش حرارتی، بعنوان یک مولفه کلیدی در ارزیابی کیفیت سوخت، بطور مستقیم بر روی کارائی نیروگاه های حرارتی تاثیر می گذارد. زغالسنگ کیفیت بالا عموما بعنوان زغالسنگ متالورژیکی (کک شو) مورد استفاده قرار می گیرد، در حالی که کاربرد عمده زغالسنگ های کیفیت پایین در نیروگاههای تولید برق زغالی می باشد. رطوبت بالای زغال های حرارتی به شدت بر روی میزان انرژی قابل دستیابی از این مواد تاثیر می گذارد. در این مطالعه، عملکرد خشک کننده های بستر ثابت (Fixed bed) و بستر سیال کاذب (ADMFB) برای حذف رطوبت زغالسنگ در محدوده پارامتر های عملیاتی، سرعت ظاهری هوا ۱۵–۱۸ سانتی متر بر ثانیه، دمای هوای ورودی ۵۵–۷۵ درجه سانتیگراد در یک بازه ۸۰ دقیقه ای مورد بررسی قرار گرفت. مصرف کم هوا از خصوصیات ذاتی بسترهای سیال کاذب می باشد، درحالی که محدوده دمایی پایین برای هوای گرم، با توجه به دمای هوای باطله نهایی نیروگاههای حرارتی با سوخت زغال انتخاب شد. نتایج نشان داد که افزایش هر دو عامل (سرعت ظاهری هوا ۱۸ سانتی متر بر ثانیه، دمای هوای ورودی ۷۵ درجه سانتیگراد) منجر به افزایش میزان رطوبت حذف شده گشت، البته تاثیر افزایش دما بارز تر از افزایش دبی هوا بود. میزان رطوبت حذف شده در زمان های عملیاتی کوتاه تر برای سیستم بستر سیال کاذب بیشتر از بستر ثابت بود. بعنوان مثال برای کاهش ٪ ۱۰ رطوبت در دمای ۷۵ درجه سانتیگراد، خشک کننده بستر سیال کاذب ۵ دقیقه زمان کمتری نسبت به بستر ثابت نیاز داشت. کیفیت مدلسازی و میزان تطابق مدل های لایه نازک پرکاربرد در توصیف سینتیک فرآیند کاهش رطوبت به کمک سیستم های بستر سیال کاذب و بستر ثابت، با استفاده از پارامتر های معتبر آماری متعددی مورد بررسی و ارزیابی قرار گرفت. دیده شد که فرآیند خشک کردن در بستر ثابت به خوبی (R^2=0.999, RSE=0.001, RMSE=0.008) با استفاده از مدل Middilli & Kucuk و فرآیند خشک کنی با استفاده از بستر سیال کاذب به خوبی (R^2=0.998, RSE=0.002, RMSE=0.009) با استفاده از مدل Page قابل تصیف می باشد.

IJE TRANSACTIONS B: Applications Vol. 34, No. 05, (May 2021) 1371-1380

International Journal of Engineering

Journal Homepage: www.ije.ir

Kudryavy Volcano Crater Thick Rocks Electrical Breakdown Study in 50 Hz Electromagnetic Field

M. V. Rylnikova[a], K. R. Argimbaev*[b]

[a] Research Institute of Comprehensive Exploitation of Mineral Resources of the Russian Academy of Sciences, Moscow, Russia Federation
[b] Faculty of Mining, Saint Petersburg Mining University, St. Petersburg, Russia Federation

PAPER INFO

Paper history:
Received 19 February 2021
Received in revised form 17 March 2021
Accepted 26 March 2021

Keywords:
Current-Voltage Characteristics
Volcanic Deposit
Geothermal Field
Volcanic Breccia
Breakdown

ABSTRACT

Kudryavy volcano is the world's only deposit of rare elements in the form of pure rhenium mineralization. The development of the field is hampered by numerous factors: high temperatures of geothermal fields, strong winds, fumarolic activity, where the use of a drilling and blasting method to destroy rocks in a crater can lead to the closure of all fumarole channels, which will lead to the accumulation of enormous energy and further eruption. The article describes the existing electrical methods for the rock destruction, it was found that the current-voltage characteristic of volcanogenic breccia with an increase in the distance between the electrodes more than 50 cm turns into a *C*-shaped dependence, reducing the current strength from 0.85 A to 0.2 A, forming a full breakdown channel. In this case, the minimum breakdown strength of the electric field is 0.3±0.1 kV/cm, with an increase in this indicator to 3.7 kV/cm, the efficiency of channeling increases to 2%. Around the breakdown channel, a new substance is formed with new conductive properties, different from volcanic breccia, which prevents the formation of the channel along the old trajectory.

doi: *10.5829/ije.2021.34.05b.33*

1. INTRODUCTION

When evaluating various ways of rocks destruction, it can be stated that the development of a volcanogenic rhenium deposit in the crater of Kudryavy volcano showed the impossibility of using the traditional method of drilling and blasting to destroy rocks. This is caused by a number of factors, such as high temperature of the geothermal fields 300˚C, as well as non-interrupting fumarolic emissions.

The use of the electric method allows to destroy rocks safely without the risk of overlapping fumarole channels in the volcano depth.

The advantage of electrical approachs is a simple working medium supplying electrical energy to the rock. The development of these methods began in the 60s by number of scientists. In this research, the development trend analysis of this method was carried out, as well as the theories of dielectric breakdown of solids, in particular, the theory of thermal breakdown, were worked out, but the behavior of rocks with initial thermal stresses was not studied [1-6].

Many techniques of crushing rocks electrically developed up today [5-10] have not gone beyond laboratories; others have successfully passed industrial tests and can be recommended for commercial use.

Destroying rocks by electrical method was developed in various directions such as an electrothermal approach, an electrodynamic way, and a combined technology [1-4].

The electrothermal approach was used in the Iron Age, as oversized pieces of iron ore were splitted using the energy of fire. Currently, the source of such a way can be microwave radiation, high frequency current, industrial frequency current, or infrared radiation.

The electrothermal method of rock destruction is based on creation of an uneven distribution of temperature in the volume of the rock, as a result of which a solid working medium is formed that destroys the rock. The force generated by the working medium

*Corresponding Author Institutional Email: *diamond-arg@mail.ru* (K. R. Argimbaev)

Please cite this article as: M. V. Rylnikova, K. R. Argimbaev, Kudryavy Volcano Crater Thick Rocks Electrical Breakdown Study in 50 Hz Electromagnetic Field, International Journal of Engineering, Transactions B: Applications Vol. 34, No. 05, (2021) 1371-1380

must exceed the force of the disruptive strength of the rock.

$$F_{rt} \geq P, \tag{1}$$

where F_{rt} is the force generated by the working medium measured in N, and P is the force needed to destroy the rock measured in N

$$F_{rt} = \overline{\sigma_t} S_0, \tag{2}$$

where $\overline{\sigma_t} = \frac{\alpha E \overline{T}}{1-\nu}$ is the thermal stress created by the working medium at the average temperature of $\overline{T}$ measured in N/m^2; S_0 is the area, to which the force from the working medium is applied (the area of the loaded surface of the working medium) measured in m^2; α is the coefficient of volumetric expansion of the rock measured in 1/*deg*, and E is Young's modulus of the rock, N/m^2; and ν is Poisson's ratio of the rock. $\overline{T}$ is the average temperature of the working medium measured in ${}^0C$, and k is the coefficient that takes into account α decrease at working medium expansion in response to reaction from the rock surrounding the working medium ($k < 1$).

Since the working medium is located inside a piece of rock, it destroys the rock with tensile stresses. In this regard, using the theory of maximum stresses, we obtain:

$$P = \overline{[\sigma_r]} S_r, \tag{3}$$

where $\overline{[\sigma_r]}$ is the breakdown point of the tensile strength of the rock measured in N/m^2, and S_r is the area of the newly formed surface measured in m^2.

The temperature of the working medium is determined by the amount of energy supplied to it

$$\overline{T} = \frac{\omega\eta}{C_\nu V_0}, \tag{4}$$

where ω is the energy supplied from the source to the working medium, *J*; η is the efficiency of the input into the working medium; C_ν is the volumetric heat capacity of the rock, $J/m,^3 \cdot \deg$; and V_0 is the working medium volume, m^3.

Consequently, we get:

$$S_0 \frac{\alpha E k \omega\eta}{(1-\nu) C_\nu V_0} \geq \overline{[\sigma_r]} S_r, \tag{5}$$

That is the efficiency of electrothermal destruction is determined by the properties of the rock, the size of the destroyed piece, and the power of the current source [3, 7-10].

Energy ω can be imparted to the working medium by either electric current or electromagnetic radiation.

In contrast to the electrothermal method with a solid substance as a working medium and a low intensity of the energy input process, the electrodynamic method is a way with a gaseous working medium, and it is characterized by a high intensity of energy release, which gives a complete separation of the destroyed rock into several single pieces. The essence of this method is the use of an electrical impulse from a capacitor bank to destroy the rock [7-11].

Depending on the nature of preparing a piece for the supply of an energy pulse, there are two main versions of this method: with the preliminary formation of a breakdown path in the rock (high-frequency voltage or power-frequency voltage), and with the use of the electrohydraulic effect (with or without an exploding wire) [10, 11]. This method has not been widely applied in the mining industry. Installations for crushing oversized rocks have been manufactured and tested only based on the electrohydraulic effect [11-13].

In order to destroy a rock electrohydraulically, it is necessary to drill a hole, fill it with water, put into it a wire connected by a spark gap to the capacitor bank, or place in the water electrodes applying a high voltage to them to form a breakdown path and the subsequent discharge of the capacitor bank [10, 12, 13, 14].

To maximize the destruction effect, it is proposed to use the phenomenon of mechanical resonance, for which such parameters of the discharge circuit or such a medium are selected, in which the maximum energy of vibrations excited by each electrohydraulic shock falls on the spectrum that coincides with the natural vibration frequency of the rock particles.

The combined technique is a combination of the electrothermal way with either the mechanical or the electrodynamic one [6, 14-33].

The destruction of rocks with the lowest energy was carried out better in heated rocks [13-24]. Taking into account this fact, the use of the combined (electrical and mechanical) method for destroying a rock having an initial thermal stress is promising for use on a volcanogenic deposit of rare elements [14, 15].

In this regard, the Kudryavy volcano crater thick rocks electrical breakdown study in 50 Hz electromagnetic field remains relevant, since the development of the volcanogenic deposit of rare elements with high temperatures of geothermal fields is associated with the solution of this issue.

Thus, the aim of the study is to explore the current-voltage characteristic of the rock subjected to an initial thermo-stressed state under the temperature 300°C and to study the thick rocks electrical breakdown in order to increase the efficiency of its destruction by an electrical way.

The innovation of this research are studied the dependences of rock current-voltage characteristics on the electrode spacing and the electric field breakdown intensity as well as the dispersion of the resistance depending on the spacing.

Electric field breakdown intensity as a function of the rock resistance was examined as well as the path forming efficiency depending on the spacing and on the electric field intensity.

Interrelationship between temporal variation of current and that of voltage at breakdown path crystallization at *t* moment was traced.

The practical significance of this study lies in the fact that the object under study will make it possible to destroy the rocks of the geothermal fields of Kudryavy volcano safely without closing the fumarolic emission paths in the depth of the crater, which can provoke an eruption.

2. MATERIALS AND METHODS

The object of present study is to investigate the rock selected at the geothermal field of the volcanogenic deposit in the crater of Kudryavy volcano on the Kuril Islands (Russia).

The rocks have the following strength properties, determined by the method of coaxial counter-directed spherical indeters: the ultimate strength in uniaxial tension is 32 MPa, the ultimate strength of uniaxial compression is 133 MPa, and shear without normal stresses is 43 MPa [34-36].

Volcanic breccia are the complex multicomponent media, for which it is possible to determine the nature of the interaction with the electric field and reveal the type of the required dependencies in the laboratory conditions only [15-22]. For this purpose, an experimental plant was created, on which the whole complex of studies on rock breakdown in an electric field of industrial frequency was performed (Figure 1).

The electrodes were made of aluminum and in the experiments they were placed on the surface of the piece of rock ($l_{electrode gap}$ =length of the breakdown path $L_{surface}$) (Figure 1b).

Two types of the single-phased oil-cooled (IOM) transformers were used to supply power: IOM 100/25 with the rated power of 25 kVA and the other, more powerful, IOM 100/100, with the rated power of 100 kVA.

The studies were carried out on the volcanic breccia heated up to 300°C. The rocks of the geothermal fields represented by porous slag and tuff that could be destroyed mechanically did not study for the thick rock breakdown.

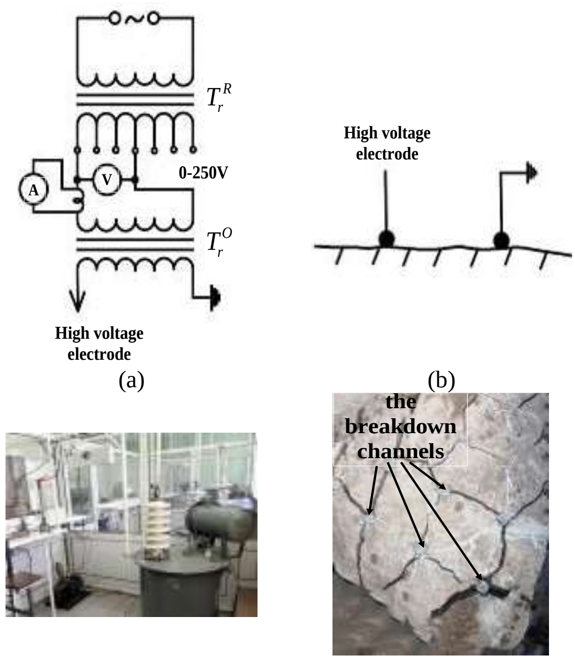

Figure 1. The diagram of the experimental plant for studying the breakdown of rocks in geothermal fields of Kudryavy volcano, heated to 300°C

T_r^R is the regulating transformer; T_r^O is the main transformer; a – is the power supply schematic drawing (split-winding transformer) is shown; b – is the arrangement schema of electrodes ($l_{electrode\ gap} = L_{surface}$); c – presents the I-V characteristics of the studying plant appearance; d – is the breakdown channels

The phenomenon of the thermal breakdown is described by the following differential equation system [1-4, 22]:

$$\left.\begin{aligned} &div(\lambda \cdot gradT) + \sigma \cdot (grad\varphi)^2 = 0 \\ &div(\sigma \cdot grad\varphi) = 0 \end{aligned}\right\} \qquad (6)$$

where φ is the potential; T is the temperature; σ is the specific electrical conductivity; and λ is the coefficient of the thermal conductivity of the dielectric.

The first equation shows that the amount of Joule heat released per unit time in the unit volume of the dielectric is equal to the of heat released amount by this volume per unit of time into its environment.

The second equation expresses the continuity of the streamlines in the dielectric.

This equation system solution is rather difficult mathematically. In addition, it is known that this system does not fully reflect the processes occurring in the rock when exposed to a strong field. In particular, this concerns the anomalous conductivity preceding the breakdown, which significantly changes the nature of the process [2, 6].

Equation (6) establishes the nature of the various rock properties influence on the breakdown process. It is impossible to obtain the quantitative values of electric field breakdown intensity and breakdown time for the rocks at different electrode spacings from the dependences; therefore, they have to be determined experimentally.

In practice, it is very difficult to determine the exact value of the breakdown voltage due to the imperfection of their structures. Therefore, some average value is determined according to the appropriate methodologies. [1-4, 13, 23-33] For rocks, which are complex heterogeneous multicomponent media, breakdown voltages depend on composition, rock structure, the occurrence conditions, the shape of the piece being destroyed, and the thermal stresses, etc. [2-5].

The methodology for determining the dependence of the electric field breakdown intensity on the electrode spacing included:

1) the current-voltage characteristics of volcanic breccia heated to 300°C in the non-uniform field for different electrode spacings were obtained;

2) the electric field breakdown intensity based on the current-voltage characteristics are determined at the following condition

$$\frac{dt}{dE} = tg\alpha, \text{ at } \alpha \to \frac{\pi}{2} \tag{7}$$

3) the breakdown intensity dependence on the electrode spacing from the obtained data were determined.

The experimental method for studying thick rocks electrical breakdown provides for gradually raising the voltage applied to the breakdown path, as well as lowering it gradually by fixing the current-voltage characteristics of the breakdown path.

3. RESULTS AND DISCUSSION

3. 1. Rocks Current-Voltage Characteristics Study

The nature of the heated volcanic breccia electrical conductivity can be determined only by the detailed study of the current-voltage characteristics.

Figure 2 shows the volcanogenic breccia current-voltage characteristics for the various electrode spacing $l_{electrode\ gap}$.

The transition of the current-voltage characteristic to an *C*-shaped one corresponds to the rock breakdown with formatting the complete breakdown path closing the electrodes.

To achieve it, it is necessary to ensure the minimum pre-breakdown current density, since for large thicknesses this factor determines the breakdown. It was

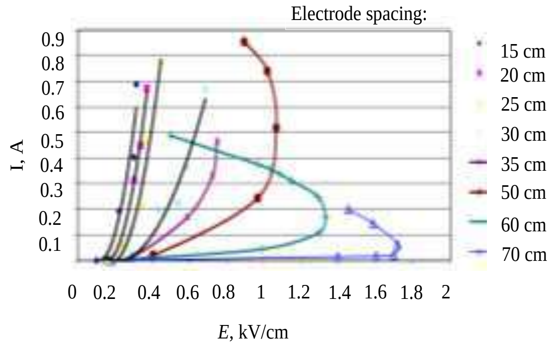

Figure 2. Current-voltage characteristic of the volcanic breccia heated up to 300˚C depending on the electrode spacing at $l_{electrodegap} = L_{surface}$

calculated from the experimental data that the current density in the rock required for the breakdown is constant and equal to $j \approx 0{,}3\times10^{-3}$ A/cm^2.

The decrease in *j* at $l_{electrode\ gap} > 50$ cm is associated with lack of power of the source, and not with the breakdown process.

If the power of the source is low, then there is a sharp drop in voltage at the output of the high-voltage transformer connected to the load, in comparison with its open circuit voltage

$$U_2 = \varepsilon - I_2 Z_2, \tag{8}$$

where U_2 is the voltage applied to the rock and ε is the transformer e.m.f., V; Z_2 is the transformer secondary winding resistance, Ω; I_2 is the secondary winding current (through the rock), *A*.
From expressions (8) and $I = jS_{T.C.}$ we get

$$U_2 = \varepsilon - jB_{T.C.}Z_2 \tag{9}$$

where $S_{T.C.}$ is the conducting section, m^2, i.e. the preservation of the required current density with an increase in the conducting section $S_{T.C.}$ is ensured only by the ε (e.m.f.) of the transformer.

It was found that, at a large electrode spacing, the current-voltage characteristics of the rock were stable. Therefore, there is a slight dispersion of the resistance.

The resistance dispersion studied as a function of the electrode spacing and that of the electric field intensity showed that the resistance dispersion decreases with increasing in both the spacing and intensity (Figure 3).

The small dispersion of the rock resistance for large distances between the electrodes and the uniformity of the current-voltage characteristics show that when the rock is destroyed, the operating parameters of the electrical installation will be quite stable.

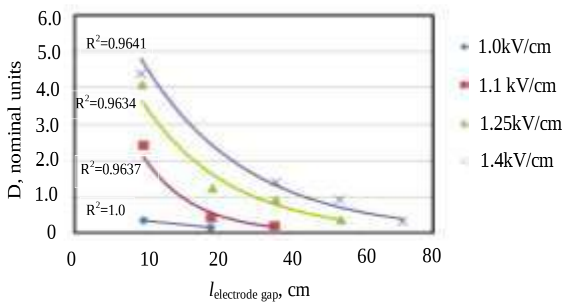

Figure 3. 300°C volcanic breccia resistance dispersion dependence on electric field intensity at $l_{electrodegap} = L_{surface}$

When placing the electrodes along the horizontal surface of the rock (half-space) (Figure 1b), the electric field intensity, *E*, which leads to anomalous conductivity and, as a consequence, to an electrical breakdown, decreases with increasing the spacing, tending to a certain constant at a larger spacing, $l_{electrode\ gap}$ (Figure 4).

Averaging the electric field breakdown intensity, $E_{el\ br}$, one can say that for a breakdown with the buried path, an electric field intensity not less than 0.3 ± 0.1 kV/cm is sufficient at an electrode spacing < 1 m.

The considered rock makes up the absolute majority among the rocky non-destructible rocks of the Kudryavy volcanic deposit, the rest of the rocks are the rocks that are amenable to mechanical destruction.

Having determined the average values, the electric field breakdown intensity of the rock under study, let us consider their relationship with the duration of staying of the sample under voltage before the breakdown. This is one of the most difficult questions, and it is possible to calculate an electrical breakdown time of a dielectric using a complex mathematical apparatus and for a one-dimensional case only [12-16, 25, 26]. Therefore, in each specific case, it is advisable to carry out experimental studies.

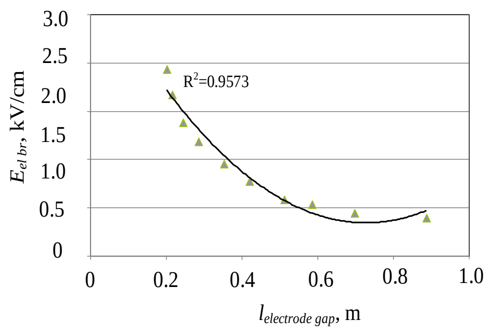

Figure 4. Electric field breakdown intensity dependence on the electrode spacing in volcanic breccia

The time to dielectric breakdown is determined by an intensity of the electric field in that it is located. The found values of the electric field breakdown intensity for the considered rock (Figures 4) are not limitation, that is, the values whose outreaching may lead to a surface breakdown.

As mentioned above, the more the exposure time, the less the electric field breakdown intensity. However, when a rock is destroyed, it is necessary, on the contrary, to minimize the exposure time before breakdown. This is achieved by increasing the electric field intensity to its limiting value, i.e., almost to the surface overlap intensity.

The more the field intensity, the less both the time to the dielectric breakdown and the dispersion of this time, which ultimately will make it possible to determine the performance of the plant or unit more accurately.

To estimate the breakdown time, we use the equation of the energy balance of the process.

The energy supplied to the rock is spent on heating the rock to the melting point, on the phase transition of matter in the volume of the path from the solid state to the liquid state, and on losses due to thermal conductivity.

The energy balance equation is as follows:

$$\int_0^t P dt = \int_0^{T_{melt.}} c m_{Path} dT + q + \int_0^t \lambda S_{Path\_Surf.} gradT dt, \tag{10}$$

where P is the incoming power; $m_{Path} = \pi r_{Path}^2 l \gamma k_2$ is the breakdown path mass; $S_{Path\_Surf.} = 2\pi r_{Path} l k_2$ is the breakdown path lateral surface area; $T_{melt.}$ is the rock melting temperature; c, λ are rock thermal properties; k_2 is the heat transfer coefficient; and q is the elektrische ladung.

The Equation (10) integration is as follows:

$$\bar{t} = \frac{\pi C_v r_{Path}^2 l k_2 \gamma T_{melt.} + q}{P - 2\pi r_{Path} l k_2 \overline{gradT}} \tag{11}$$

The power incoming to a rock

$$P = UI \tag{12}$$

can be expressed through the transformer e.m.f. from Equation (9) as follows:

$$P = I_2(\varepsilon - I_2 Z_2) \tag{13}$$

By substituting Equation (13) into Equation (11), we have:

$$\bar{t} = \frac{\pi C_v r_{Path}^2 l k_2 \gamma T_{melt.} + q}{I_2(\varepsilon - I_2 Z_2) - 2\pi r_{Path} l k_2 \overline{gradT}} \tag{14}$$

Figure 5 shows the results of a study of the average number of breakdowns *N* dependence on the time *t* of volcanic breccia being under stress at various electric field intensities.

The functions presented in the form of graphs in Figure 5, they have the properties of a gamma distribution, the density of which has presented in the following form [9-10]:

$$f(x) = \frac{\lambda_r}{G(\eta)} x^{\eta-1} e^{-\lambda x}, \tag{15}$$

where $G(\eta) = \int_0^\infty e^{\eta-1} x^{-x} dx$ is the gamma function; $\lambda_r > 0$ is a scale parameter; and η is a form parameter.

With an increase in λ_r parameter, which, in our case, is the increase in electric field intensity, the distribution shape remains constant, and the time to the breakdown decreases and is determined with a smaller scatters.

The $\bar{t}$ oscillations are associated with the dispersion of the resistance of the rock, which was indicated above, since the resistance of the dielectric determines the electric field breakdown intensity.
For volcanic breccia, this dependence is linear (Figure 6).

Due to the fact that when a rock is destroyed, breakdown path formation is a technological operation, it is necessary to determine the efficiency of energy use in this process. This is done by calculating the ratio of the energy required to form a breakdown path of a given diameter to the energy actually expended. When calculating the energy spent on the formation of the breakdown path itself, the diameter of the breakdown path was taken to be constant and equal to 3 mm, and the path length was 1.25 times larger than the electrode spacing. Thus, the energy during formation of the breakdown path 3 mm in diameter is spent on heating its volume to the melting temperature and on the phase transition from the solid to the liquid state. The actually expended energy was determined by device readings. The study results are shown in Figures 7 and 8.

As one can see, the breakdown path formation is an inefficient process. Its efficiency can be increased by using a high-intensive electric field.

However, it should be taken into account that while forming a breakdown path due to the high temperature gradient, a solid working medium is formed, which deforms the rock. Solid working medium formation in parallel with breakdown path formation significantly increases the efficiency of energy use.

3. 2. Thick Rocks Electrical Breakdown Study Results When the stationary mode of electrical conductivity is violated, thermal destruction of the dielectric occurs, which entails breakdown path

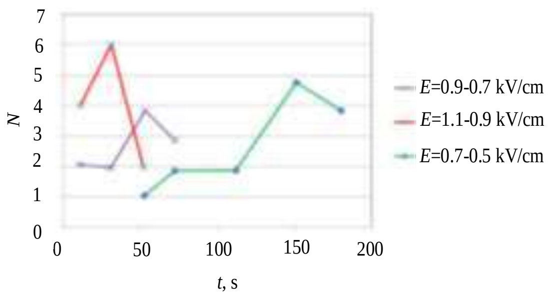

Figure 5. Specimen time to dielectric breakdown distribution at various electric field intensities (for volcanic breccia) at $l_{electrode\ gap}$=0.5m

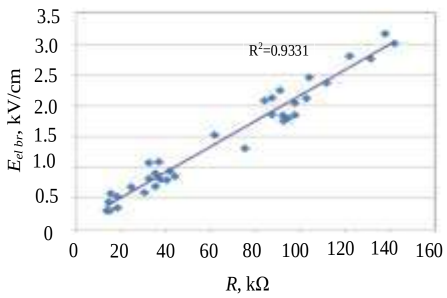

Figure 6. Electric field breakdown intensity dependence on rock resistance

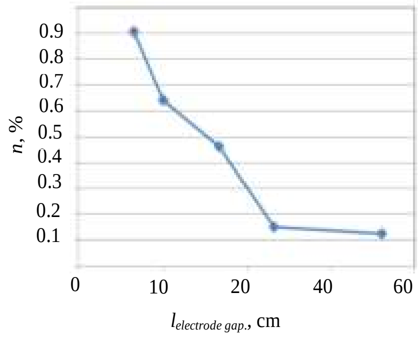

Figure 7. Path forming efficiency dependence on electrode spacing (IOM 100/100 single-phased oil-cooled transformer)

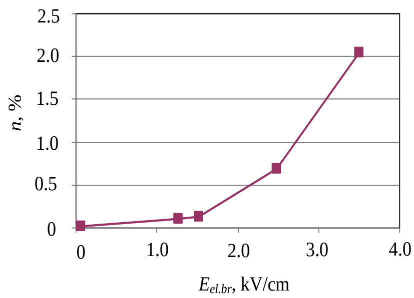

Figure 8. Path forming efficiency dependence on electric field intensity (IOM 100/100 single-phased oil-cooled transformer, $l_{electrode\ gap}$=50 cm, specific electrical resistance $R_{specific}$=1kΩ/cm (volcanic breccia)

formation. Such a path passes through the volume of the dielectric from one electrode to another. While the breakdown path is forming, the object destruction preparation is coming to its end, since the breakdown path is a circuit element in which the electrical energy is converted into mechanical work, accompanied by the destruction of the rock.

The supply of energy to the breakdown path, as is known, can be produced from a power transformer or a capacitor bank. In both cases, the efficiency of energy input is determined by resistance of the breakdown path formation, which depends on its length, electric field intensity, and mineral composition of the rock. The breakdown path resistance and its change in time determine the design parameters of the rock-cutting installation: the response time of the switching devices, the power, and operating voltage of the power current sources.

The thermal breakdown path in the rock consists of two phases: liquid (melt of mineral matter) and gaseous (vapor of mineral matter and air), which are in the condition of intense turbulent motion. The process of rock heating, formation, and growth of the path is accompanied by the ejection of the components that make up the path through its mouth. The intensity of their release is determined by the electric field intensity and the energy source power.

When the molten substance is released from the path, the resistance of the path increases, the energy is lost, and the efficiency of the process decreases.

Breakdown path resistance as a function of the effective voltage and the released power was studied with the experimental setup shown in Figure 1.

The voltage was reduced until the moment of regeneration of the dielectric properties of the sample caused by the melting crystallization. The change in current in the path with time at a constant voltage value was studied, as well as intensity of regeneration of dielectric properties in the sample. It was found that, for each voltage step, the value of the current passing by the path is stationary with respect to time (Figure 9).

The volcanic breccia breakdown path resistance established experimentally is 5.0 kΩ/cm. In the experiments, a high-voltage transformer of IOM 100/25 type with a rated power of 25 kVA was used. When operating the more powerful source, the transformer of IOM 100/100 type, the breakdown path resistance was 1 kΩ/cm.

The subsequent action of the current on the rock does not cause any breakdown path formation along the same trajectory, and its formation occurs in a new region of the dielectric. This is due to the fact that as a result of melting and subsequent crystallization, a new substance is formed, which has more ordered structure and, consequently, lower conductivity.

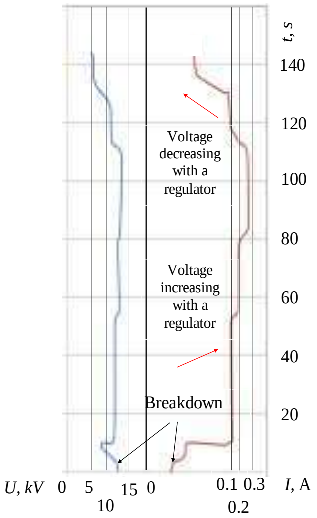

Figure 9. Current and voltage use in breakdown path diagram

The regenerating is a very intensive process determined by the amount of power released in the path. It was found that when it decreases to 0.4-0.6 kW, a phase transition occurs (Figure 10, point 1) and regeneration of the dielectric properties of the rock, and it can be seen that the resistance of the former path increases by 50% (which was obtained by comparing R_{Path} path resistance at points 1 and 2). Such an increase in the resistance of the circuit leads to a sharp decrease in the current in the rock and to an even greater cooling of the path. (Figure 10, from point 2 to point 3).

It should be noted here that when the closed breakdown path is formed, the reverse process with the same transition between phases occurs. This explains the fact that today it has not been possible to obtain a smooth current-voltage characteristic of the dielectric from its pre-breakdown state to its breakdown. The

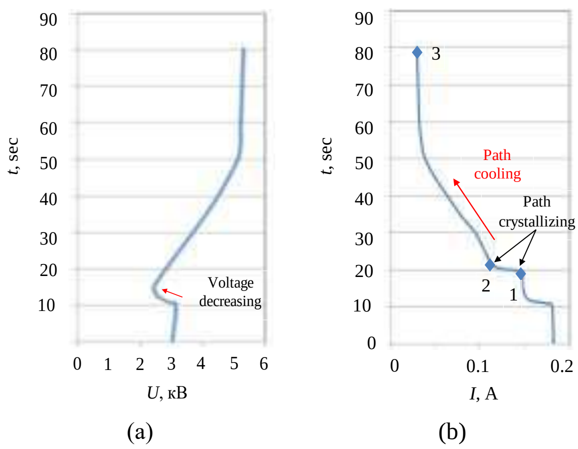

Figure 10. Temporal variation of voltage (a) and current (b) in crystalizing the breakdown path

transition from solid phase into liquid one reduces the resistance, which leads to a sharp increase in the current, the rate of which is determined by the dynamics of the phase transition, which gives a special point on the current-voltage characteristic of the dielectric, which undergoes breakdown (Figure 10).

Breakdown path temporal behavior study makes it possible to determine very important design parameter of the plant for an electrical destruction of rocks — the response time of switching devices, which switch power sources of current that load the path.

Crystallization of the breakdown path, the current-voltage characteristics of which are given in Figure 10, lasted for 1 second. With a higher released power, before removing the voltage, the crystallization process takes more time (Figure 11).

The trend of time of the path being in the melt state until the moment of its crystallization depending on the power released before removing the voltage is shown in Figure 12.

Thus, when using the high-voltage transformer of the greater power, the switches can operate in a relatively unstressed time mode, which allows the use of electromechanical drive.

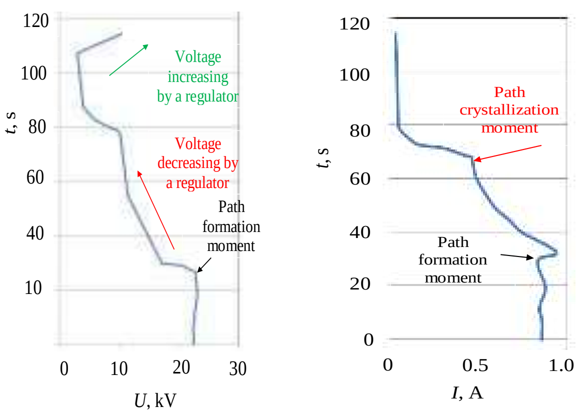

Figure 11. Temporal variation of voltage (a) and current (b) in crystalizing the breakdown path

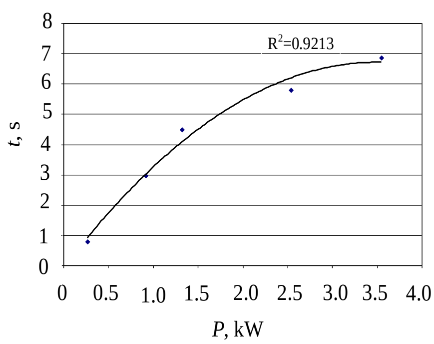

Figure 12. Time of the path being in the melt state until the moment of its crystallization, depending on the power released in the path at the moment of removing the voltage

4. CONCLUSIONS

Summing up, we can conclude that the study of thick rocks electrical breakdown in a 50 Hz electromagnetic field makes it possible to establish that the current-voltage characteristics of volcanogenic breccia, with an increase in the distance between the electrodes from $l_{эл}$ = 50 cm, transforms into a *C*-shaped curve, which corresponds to the breakdown of the rock with the formation of a complete breakdown channel closing the electrodes.

It was calculated that the current density required for breakdown in the rock is constant and equal to $j \approx 0{,}3\times10^{-3}$ A/cm^2. The decrease j at $l_{эл} > 50$ cm is associated with a lack of source power and not with the breakdown process. Given this feature, the studies were carried out with the distance between the electrodes up to 50 cm.

The study of the dispersion of resistance as a function of the distance between the electrodes and the electric field strength showed that it decreases with an increase in the distance between the electrodes and an increase in the electric field strength. A decrease in the dispersion of resistance in large gaps between the electrodes is associated with averaging the composition, and hence the properties of the rock.

Averaging the values of the breakdown strength $E_{el\,br}$ for volcanogenic breccias, one can conclude that the field strength of 0.3 ± 0.1 kV/cm is sufficient for the breakdown with the deepening of the channel at the distance between the electrodes <1 m.

The resistivity of the breakdown channel in volcanogenic breccia is 5.0 kOhm/cm when using the high-voltage transformer of the IOM 100/25 type with a rated power of 25 kVA, increasing the power of the transformer to 100 kVa (transformer of the IOM 100/100 type), the resistivity of the breakdown channel is 1 kΩ/cm.

In this case, the process of complete registration of the dielectric properties of the rock occurs after the stress is removed. The repeated action of the electric current on the rock forms the breakdown channel along the new trajectory. This is due to the formation of the new substance around the breakdown channel, which has new conductive properties.

The results obtained are of great importance in rocks electrothermal destruction theory development; namely, they show the behavior of current-voltage characteristics of the rock when electrode spacing is being increased. Besides, they can prove that rocks with initial thermal stress can be destroyed more easily and with minimal energy costs if the electrothermal method is used. The practical significance of the study is due to the way of destruction being applicable at the volcanogenic rhenium deposit of the Kudryavy active volcano crater.

5. REFERENCES

1. Sarapuu Erich, "Electro-energetic rock breaking systems", Mining Congress Institut, Vol. 59, (1973), 44-54.
2. Li Changping, Duan Longchen, Wu Laijie, Tan Songcheng, Zheng Jun, Chikhotkin Victor, "Experimental and numerical analyses of electro-pulse rock-breaking drilling", ***Journal of Natural Gas Science and Engineering***, Vol. 77, (2020), 103-263. doi: 10.1016/j.jngse.2020.103263
3. Rzhevskii V., Protasov Yu, Dobretsov V., "On the intensification of superhigh-frequency rock breaking", ***Journal of Mining Science - J MIN SCI-ENGL TR***, Vol. 5, (1969), 509-511. Doi: 10.1007/BF02501266
4. Yudin A. S., Kuznetsova N. S., Bakeev R. A. Zhgun D.V., Stefanov Yu. P. "Destruction of reinforced concrete by electric impulse discharges: Experiment and simulation", AIP Conference Proceedings 1909, Vol. 1, (2017), 15-39. doi:10.1063/1.5013915
5. O'Dwyer, J., "The Theory of Dielectric Breakdown of Solids", ***Journal of the Electrochemical Society***, Vol. 116, (1969), 239-242. Doi: 10.1149/1.2411805
6. Hassani, F., Nekoovaght, P. M., Radziszewski, P., & Waters, K. E., "Microwave assisted mechanical rock breaking", Harmonising Rock Engineering and the Environment - Proceedings of the 12th ISRM International Congress on Rock Mechanics, (2012), 2075-2080. doi: 10.1201/b11646-395
7. Zhou Huisheng, Xie Xinghua, Feng, Yuqing, "Rock breaking methods to replace blasting", IOP Conference Series: Materials Science and Engineering, Vol. 322, No. 2, (2018), 1-6. Doi: 10.1088/1757-899X/322/2/022014.
8. Ren F., Fang T., Cheng X., Chang Y., "Rock-breaking stress analysis and rock-breaking region under particle-waterjet impact", ***Shiyou Xuebao/Acta Petrolei Sinica***, Vol. 39, (2018). 1070-1080. doi: 10.7623/syxb201809011
9. Segsworth R., Kuhn K., "Electrical Rock Breaking", ***IEEE Transactions on Industry Applications,*** Vol. IA-13, (1977), 53-57. doi: 10.1109/TIA.1977.4503362
10. Moiseyenko Undina, Sokolova Liudmila, Istomin Vladimir, "Electrical and Thermal Properties of Rocks", (1970).
11. Segsworth R., Kuhn K., "Electrical Rock Breaking", ***IEEE Transactions on Industry Applications,*** Vol. IA-13, (1977), 53-57. doi: 10.1109/TIA.1977.4503362
12. Zhu Xiaohua, Dan Zhaowang, "Numerical simulation of rock breaking by PDC bit in hot dry rocks", ***Natural Gas Industry B,*** Vol. 6, No. 6, (2019), 619-628. doi 10.1016/j.ngib.2019.04.007
13. Mashchenko Volodymyr, Khomenko Oleh, Kvasnikov V., "Thermodynamic aspect of rock destruction", Naukovyi Visnyk Natsionalnoho Hirnychoho Universytetu, Vol. 6, (2020) 25-30. doi: 10.33271/nvngu/2020-1/025
14. Tretyak A. Ya, Popov V. V., Grossu A. N., Borisov K. A., "Innovative approaches to designing highly efficient rock-breaking tool", ***Mining Informational and Analytical Bulletin***, Vol. 8, (2017), 225-230. doi: 10.25018/0236-1493-2017-8-0-225-230
15. Wang M.S, Li Z.K., Geng Y.C., Tang H. L., "Laboratory study on rock breaking mechanism and its application", Vol. 29. (2008). 711-716.
16. Holman B.W., "Heat treatment as an agent in rock breaking". Vol. 36, (2020), 219-234.
17. Korostovenko, V. V., Sukhanova, A. V., "System analysis for estimating the opportunity of applying discharge-pulse methods in development of mineral resources", ***Successes of Modern Science,*** Vol. 11, (2017), 73-77
18. Rostovtsev, V. I., Kondrat'ev, S. A. and Baksheeva, I. I., "Improvement of Copper–Nickel Ore Concentration under Energy", ***Deposition Journal of Mining Science,*** Vol. 53, (2017), 907-914
19. Korzhenevsky S. R., Bessonova V. A., Komarsky A. A., Motovilov V. A. and Chepusov A. S., "Selection of electrohydraulic grinding parameters for quartz ore", ***Journal of Mining Science***, Vol. 52, (2016), 40-56
20. Korostovenko V. V., Korostovenko L. P., Stepanov A. G. and Sukhanova A. V., "Discharge-impulse methods application in technologies of mineral resources mastering", ***Journal of Physics: Conference Series***, Vol. 1399, No. 5, (2019), 493-496. doi: 10.1088/1742-6596/1399/5/055039 5 493-496
21. Lifshitz A. L., Otto M. S., "Pulse Electrical Engineering". Electroatomizdat, Moscow, (1983), 352
22. Yang, W., Li L. Zhao Y., "Preliminary inquiry of theory of resonance rock breaking", ***Energy Technology and Management***, Vol. 4, (2007), 7-9.
23. Belin V. A., Paramonov G. P., Jamiyan J., "Peculiarities of manufacturing and application of mixedexplosives of anfo type at mining enterprises of mongolia", ***Journal of Mining Institute,*** Vol. 232, (2018), 364-367 doi: 10.31897/PMI.2018.4.364
24. Salmi, A., Bousshine, L., Lahlou, K. A., "New Model of Equivalent Modulus Derived from Repeated Load CBR Test", ***International Journal of Engineering, Transactions A: Basics***, Vol. 33, No. 7, (2020), 1321-1330. doi: 10.5829/ije.2020.33.07a.19
25. AkbarpourShirazi, M., Adibee, N., Osanloo, M., Rahmanpour, M. An, "Approach to Locate an in Pit Crusher in Open Pit Mines», ***International Journal of Engineering, Transactions C: Aspects***, Vol. 27, No. 9, (2014), 1475-1484. doi: 10.5829/idosi.ije.2014.27.09c.18
26. Kovalevskyi V. N., Moldovan D. V., Chernobai V. I., "Determination of focal length for cumulative charges with various concavity shapes", ***International Journal of Mechanical Engineering and Technology***, Vol. 8, No. 11, (2017), 1119-1125
27. Mysin A. V., Kovalevskiy V. N., "Creation and Verification of Numerical Model of Explosive Charge Blast in the Ansys Software System, for the Purpose of Substantiating the Optimal Parameters of Drilling and Blasting Operations", E3S Web of Conferences, No. 174, (2020). 1046-1052. doi: 10.1051/e3sconf/202017401046
28. Marinin, M. A., Dolzhikov, V. V., "Blasting preparation for selective mining of complex structured ore deposition", IOP Conference Series: Earth and Environmental Science, Vol. 87, No. 5, (2017), 6-10. doi: 10.1088/1755-1315/87/5/052016
29. Dolzhikov, V. V., Marinin, M. A., "Quality preparation improvement of mined rock for mining extraction considering spatial temporary formation of field strain", IOP Conference Series: Earth and Environmental Science, Vol. 87, No. 5, (2017), 1-5. doi: 10.1088/1755-1315/87/5/052003
30. Afanasev, P. I., Sergey, K., Valentin, I., "The equation of state for explosive detonation products", International Journal of Mechanical Engineering and Technology, Vol. 9, No. 13, (2018), 865-868
31. Sidorov D. V., Ponomarenko T. V., "Estimation methodology for geodynamic behavior of nature-and-technology systems in implementation of mineral mining projects", Gornyi Zhurnal, No. 1, (2020), 40-53. doi: 10.17580/gzh.2020.01.09
32. Yastrebova K., Moldovan D., Chernobay V., "Influence of the nature of the outflow of explosion products from blast holes and boreholes on the efficiency of rock destruction", E3S Web of Conferences, Vol. 174, (2020), 1-6. doi: 10.1051/e3sconf/202017401017

33. Isheyskiy V. A., Yakubovskiy M. M., "Determination of strength reduction factor in blasted rocks versus the distance from the blast center", ***Gornyi Zhurnal***, Vol. 12, (2016), 55-59. doi: 10.17580/gzh.2016.12.12

34. Korshunov V. A., Kartashov Yu. M., Kozlov V. A., "Determination of indices of strength certificate of rocks using the method of specimens failire with spherical indentors", ***Journal of Mining Institute***, Vol. 185, (2010), 41-45

35. Beron A. I., Koifman M. I., Chirkov S. E., Solomina I. A., "The method for determination of strength of rocks using the specimens of irregular form", ***The Institute of mining named after A.A. Skochinski***, Moscow, 1976, 40

36. Korshunov V. A., "Determination of indices of volumetric strength of rocks under their loading with spherical indentors", ***Rock Geomechanics and Mining Surveying, Proc. VNIMI***, (1999), 70-75

Persian Abstract

چکیده

آتشفشان کودریاوی تنها رسوب عناصر کمیاب در جهان به صورت کانی سازی خالص رنیوم است. عوامل مختلفی مانع توسعه این میدان می شوند: دمای بالا در زمینه های زمین گرمایی ، وزش باد شدید ، فعالیت فومارولیک ، جایی که استفاده از روش حفاری و انفجار برای از بین بردن سنگ ها در یک دهانه می تواند منجر به بسته شدن تمام کانال های fumarole شود ، که منجر به تجمع انرژی عظیم و فوران بیشتر می شود. این مقاله روش های الکتریکی موجود برای تخریب سنگ را توصیف می کند ، مشخص شد که ولتاژ جریان مشخصه برش های آتشفشانی با افزایش فاصله بین الکترودها بیش از ۵۰ سانتی متر به یک وابستگی C شکل تبدیل می شود ، باعث کاهش قدرت جریان از A ۰.۸۵ تا A ۰.۲ ، تشکیل یک کانال شکست کامل. در این حالت ، حداقل مقاومت در برابر شکست میدان الکتریکی ۰.۳ ± ۰.۱ کیلو ولت بر سانتی متر است ، با افزایش این شاخص به ۳.۷ کیلو ولت بر سانتی متر ، بازده کانال سازی تا ۲٪ افزایش می یابد. در اطراف کانال تجزیه ، ماده جدیدی با خصوصیات رسانایی جدید ، متفاوت از برش آتشفشانی ، ایجاد می شود که از تشکیل کانال در امتداد مسیر قدیمی جلوگیری می کند.

International Journal of Engineering

Journal Homepage: www.ije.ir

New Model of Burden Thickness Estimation for Blasting of Open Pit Mines

E. Elahi*

Faculty of Mining Engineering, University of Sistan and Baluchestan, Zahedan, Iran

PAPER INFO

Paper history:
Received 07 January 2021
Received in revised form 26 February 2021
Accepted 27 February 2021

Keywords:
Blasting
Burden Thickness
Open Pit Mines
Specific Charge

ABSTRACT

Suitable pattern design of drilling and blasting is very important in open pit mines. Using of explosive energy for rock fragmentation with minimum cost of production is one of the blasting purposes in open pit mines. The most important parameters of blasting are including diameter of hole, specific charge, burden thickness and suitable dimensions of rock fragmentation. In this paper, specific charge is calculated based on quality of rock mass and then based on definition of specific charge, maximum and minimum thickness of burden in open pit mines is calculated. In this paper, a new models of burden estimation based on quadratic equations is presented. Therefore, based on this new equations, other parameters of blasting are corrected. Also, the validation results of the new equations in this article show the new burden thicknesses have slightly differences with the experimental results. The maximum error of calculated burden is equal 3% based on obtained data. Therefore, the output results of these new equations can be reliable and accurate for calculations of the burden thickness.

***doi**: 10.5829/ije.2021.34.05b.34*

1. INTRODUCTION

Over the past three decades, significant progress has been made in the development of new technology in an attempt to reduce costs and increase efficiencies and productivities of blasting activities [1].

Drilling and blasting process is not used for the production of rigid materials that is not economically and technically possible to excavate in open quarry industry. The production of aggregate starts with drilling and blasting and ends with loading, transportation, and size reduction. In quarry blasting, it is very important to estimate the average heap size distribution beforehand for creating blast designs resulting quarry operations with the least cost [2–8].

Drilling and blasting costs constitute up to 30% of the total operational costs in open pit mines, which will be increased up to 50% by adding more oversize parts and the requirement of secondary blasting. Hence, the specification of rock fragmentation after blasting such as shape and size is by far one of the most important parameters in product optimization in mineral industry [9].

Overall, mining production cycle could be divided into two groups main and auxiliary. The main production cycle is including drilling, blasting, loading and haulage. Accordingly, it is necessary to have a suitable pattern for drilling and blasting of mining, especially for open pit mines. Using of explosive energy for rock fragmentation with minimum cost of production is one of the blasting purposes in open pit mines. The other aims of blasting are reduction of resultant damages of ground vibration and air blast.

In blasting pattern of mines exist various parameters. The most important parameters are included specific charge and burden thickness. Therefore, the purpose of this paper is presentation new equations of burden thickness based on defining of specific charge.

Various theories were presented for designing of blasting pattern in open pit mines by many researchers. Some of the researchers are such as Anderson [10], Jimeno et al. [11], Ouchterlony [12], Ash [13], Rustan [14], Langfors and Kihlstrom [15], Sendlein et al. [16], Berta [17], Lilly [18], and Moomivand and Vandyousefi [19]. The most researchers believe that blasting pattern is calculated based on burden thickness because burden thickness is one of the most important parameters of blasting pattern in open pit mines. Burden thickness depends on various parameters. The most important parameters include characteristics of rock mass, diameter

*Corresponding Author Institutional Email: *elahi@eng.usb.ac.ir* (E. Elahi)

Please cite this article as: E. Elahi, New Model of Burden Thickness Estimation for Blasting of Open Pit Mines, International Journal of Engineering, B: Applications Vol. 34, No. 05, (2021) 1381-1389

of hole, diameter of charge, rock density, charge density, bench height, specific charge, spacing, hole length, charge length, stemming length, under drilling.

Some of researchers such Berta [17], Lilly [18], and Moomivand and Vandyousefi [19] believed that burden thickness depends on the specific charge. Specific charge is determined based on characteristics of the rock mass. Experimental results of blasting in open pit mines confirm the above information. Accordingly, this paper is presented quadratic equations for determining of burden thickness based on the specific charge. Then the final results of these new equations are controlled by the experimental results of blasting in open pit mines.

2. MATERIALS AND METHODS

2. 1. Hypotheses The most important of hypothesis for estimation of burden thickness of blasting in this paper is the concept of specific charge. The specific charge is one of the most important parameters in blasting mines. Accordingly, the amount of specific charge is better to calculate based on rock quality. For calculation of specific charge exists various methods. Three methods of energy transfer rule, blastability index and rock fragmentation index are more valuable of other methods because these three methods have been designed based on quality of rock mass.

2. 1. 1. Energy Transfer Rule Berta [17] presented his famous equation based on the energy transfer rule between explosive and rock. Berta [17] calculated specific charge of blasting based on Equation (1). This equation was defined based on requirement energy for rock fragmentation and released energy of the explosive. Berta [17] suggests that blasting burden thickness is calculated based on Equation (2). This equation has determined based on a full charge per hole for a square pattern.

$$q = \frac{s\,E_s}{\eta_1\,\eta_2\,\eta_3\,E_e} \tag{1}$$

$$B = \varphi_c \sqrt{\frac{\pi\,D_c}{4\,q}} \tag{2}$$

$$s = \frac{64}{D_{Max}} \tag{3}$$

$$\eta_1 = 1 - \frac{(I_2 - I_1)^2}{(I_2 + I_1)^2} \tag{4}$$

$$\eta_2 = \frac{1}{[e^{\frac{\varphi_h}{\varphi_c}}] - (e-1)} \tag{5}$$

$$I_1 = D_e\,V_e \tag{6}$$

$$I_2 = D_r\,V_r \tag{7}$$

where,

q : Specific charge (kg/m^3)

s : Desired degree of fragmentation (m^2/m^3)

E_s : Rock specific surface energy (MJ/m^2)

η_1 : Impedance efficiency

η_2 : Coupling efficiency

η_3 : Energetic fragmentation transfer efficiency (15%)

E_e : Explosive specific energy (MJ/kg)

B: Burden thickness (m)

φ_e : Charge diameter (m)

D_e : Explosive density (kg/m^3)

D_{Max} : Maximum fragmentation dimension (m)

I_1 : Explosive impedance

I_2 : Rock impedance

D_r : Rock density (kg/m^3)

V_r : Voice velocity in rock (m/s)

V_e : Explosive velocity (m/s)

φ_h : Hole diameter (m)

2. 1. 2. Blastability Index Lilly [18] presented his famous equation based on the blastability index. Lilly [18] calculated blastability index based on characteristics of the rock mass. The blastability index is calculated based on Equation (8) and so is specific charge based on Equation (9). The details of these parameters in blastability index have defined in Tables 1 to 5.

$$BI = \frac{1}{2}(RMD + JPS + JPO + SGI + HD) \tag{8}$$

$$q(\frac{kg}{ton}) = 0.004\ BI \rightarrow q(\frac{kg}{m^3}) = 0.004\,SG \times BI \tag{9}$$

TABLE 1. Rock Mass Description (RMD) [18]

Powdery/Friable	RMD = 10
Blocky	RMD = 20
Totally Massive	RMD = 50

TABLE 2. Joint Plane Space (JPS) [18]

Close (<0.1 m)	JPS = 10
Intermediate (0.1 to 1 m)	JPS = 20
Wide (>1 m)	JPS = 50

TABLE 3. Joint Plane Orientation (JPO) [18]

Horizontal	JPO = 10
Dip out of face	JPO = 20
Strike normal to face	JPO = 30
Dip into face	JPO = 40

TABLE 4. Specific Gravity Influence (SGI) [18]

SGI=25SG-50
SG is the density in (ton/m3)

TABLE 5. Hardness Description (HD) [18]

$E < 50$	$HD = \frac{1}{3}E$
$E > 50$	$HD = \frac{1}{5}C_0$
E : Young's modulus: GPa	C_0 : UCS : MPa

2. 1. 3. Rock Fragmentation Index Moomivand and Vandyousefi [19] presented his famous equation based on rock fragmentation index. They calculated rock fragmentation index based on characteristics of the rock mass [19]. The rock fragmentation index is calculated based on Equation (10) and so specific charge based on Equation (11) and so burden thickness on Equation (12). The details of these parameters in rock fragmentation index have defined in Tables 6 to 10.

$$RFI = DPA + DPS + DPO + RMD + UCS \tag{10}$$

$$q(\frac{kg}{m^3}) = 312.12\,SG \times RFI^{-2.082} \tag{11}$$

$$B = RFI \times \varphi_h \tag{12}$$

2. 2. The Proposed Method In this paper using of specific charge concept, useful tables of mines blasting and experimental valuable equations of blasting are used for mathematical analysis of burden thickness. Therefore, the proposed method for calculation of maximum and minimum burden thickness is a mathematical analytical method. In this method various models of blasting equations is investigated and then based on mathematical analysis method, optimum equation from among other equations is selected. This optimum equation is named as maximum and minimum burden thickness.

TABLE 6. Discontinuity Plane Aperture (DPA) [19]

Close(<1 mm)	DPA = 8
Intermediate (1 to 5 mm)	DPA = 7
Intermediate ((5 to 50 mm)/full)	DPA = 6
Intermediate ((5 to 50 mm)/empty)	DPA = 5
Wide ((>50 mm)/full)	DPA = 4
Wide ((>50 mm)/empty)	DPA = 3

TABLE 7. Discontinuity Plane Spacing (DPS) [19]

Close (<0.1 m)	DPS = 12
Intermediate (0.1 to 1 m)	DPS = 7
Wide (>1 m)	DPS = 4

TABLE 8. Discontinuity Plane Orientation (DPO) [19]

Horizontal	DPO = 6
Dip out of face	DPO = 5
Strike normal to face	DPO = 4
Dip into face	DPO = 3

TABLE 9. Rock Mass Description (RMD) [19]

Powdery/Friable	RMD = 10
Blocky	RMD = 6
Totally Massive	RMD = 4

TABLE 10. Unconfined Compressive Strength (UCS) [19]

Close (<25 MPa)	UCS = 6
Intermediate (25 to 50 MPa)	UCS = 5
Intermediate (50 to 100 MPa)	UCS = 4
Intermediate (100 to 200 MPa)	UCS = 3
Wide (>200 MPa)	UCS = 2

3. RESULTS

3. 1. The Maximum and Minimum Thickness of Burden Mining experiences in last decade showed that it is better to use characteristics of rock mass for estimating the amount of the specific charge. Therefore, the new thickness of burden according to specific charge based on Equations (13) to (21) is calculated. These equations are stated as follows:

$$q = \frac{Q}{V} = \frac{\frac{\pi}{4}\varphi_c{}^2 D_c L_c}{S\,B\,K} \tag{13}$$

$$L_c = H - S_t \tag{14}$$

$$H = \frac{K}{Sin\alpha} + U \tag{15}$$

$$S\,B = \frac{\pi\,\varphi_c{}^2 D_c}{4\,q\,K}(\frac{K}{Sin\alpha} + U - S_t) \tag{16}$$

$$a = \frac{\pi\,\varphi_c{}^2 D_c}{4\,q\,K} \tag{17}$$

$$S = k'\,B \tag{18}$$

$$k'\,B^2 = a\,(\frac{K}{Sin\alpha} + U - S_t) \tag{19}$$

$$U = (0.2 - 0.5)\,B \tag{20}$$

$$S_t = (0.7 - 1.3)\,B \tag{21}$$

where,

q : Specific charge (kg/m^3)

Q : Explosive weight (kg)

V : Blasting volume (m^3)

φ_c : Charge diameter (m)

D_c : Charge density (kg/m^3)

L_c : Charge length (m)

S : Spacing (m)

B : Burden (m)

K : Bench heights (m)

α : Hole slope in vertical direction (degree)

U : Under drilling (m)

S_t : Stemming (m)

H : Hole length (m)

Based on Equations (19) to (21) four various models for burden equations are obtained. These equations are stated as follows:

a. the first model

$$\left.\begin{array}{l} U = 0.2\,B \\ S_t = 0.7\,B \end{array}\right\} \rightarrow k'\,B^2 = a\,(\frac{K}{\operatorname{Sin}\alpha} - 0.5\,B) \tag{22}$$

b. the second model

$$\left.\begin{array}{l} U = 0.2\,B \\ S_t = 1.3\,B \end{array}\right\} \rightarrow k'\,B^2 = a\,(\frac{K}{\operatorname{Sin}\alpha} - 1.1\,B) \tag{23}$$

c. the third model

$$\left.\begin{array}{l} U = 0.5\,B \\ S_t = 0.7\,B \end{array}\right\} \rightarrow k'\,B^2 = a\,(\frac{K}{\operatorname{Sin}\alpha} - 0.2\,B) \tag{24}$$

d. the fourth model

$$\left.\begin{array}{l} U = 0.5\,B \\ S_t = 1.3\,B \end{array}\right\} \rightarrow k'\,B^2 = a\,(\frac{K}{\operatorname{Sin}\alpha} - 0.8\,B) \tag{25}$$

Based on Equations (22) to (25), two different models for burden equations are obtained. These equations are stated as follows:

a. the maximum thickness of burden

$$\begin{array}{l} k'\,B^2 = a\,(\frac{K}{\operatorname{Sin}\alpha} - 0.2\,B) \rightarrow \\ k'\,B^2 + 0.2\,a\,B - \frac{a\,K}{\operatorname{Sin}\alpha} = 0 \end{array} \tag{26}$$

b. the minimum thickness of burden

$$\begin{array}{l} k'\,B^2 = a\,(\frac{K}{\operatorname{Sin}\alpha} - 1.1\,B) \rightarrow \\ k'\,B^2 + 1.1\,a\,B - \frac{a\,K}{\operatorname{Sin}\alpha} = 0 \end{array} \tag{27}$$

The maximum and minimum thicknesses of burden based on Equations (26) and (27) are calculated. These equations are quadratic equations. Accordingly, the average thickness of burden based on Equation (28) can be calculated.

$$B_{ave} = \frac{B_{Max} + B_{Min}}{2} \tag{28}$$

Researchers believe to achieve optimum blasting pattern is necessary to the amount of K/B became between 3 till 4. Accordingly, the thicknesses of burden based on Equations (29) to (32) could be calculated.

$$\left.\begin{array}{l} K = 3B \\ a' = \frac{\pi\,\varphi_c{}^2\,D_c}{4\,q} \\ k'\,B^2 = a\,(\frac{K}{\operatorname{Sin}\alpha} - 0.2\,B) \\ k'\,B^2 = a\,(\frac{K}{\operatorname{Sin}\alpha} - 1.1\,B) \end{array}\right\} \rightarrow \left\{\begin{array}{l} 3k'\,B^2 = a'\,(\frac{3}{\operatorname{Sin}\alpha} - 0.2\,) \\ 3k'\,B^2 = a'\,(\frac{3}{\operatorname{Sin}\alpha} - 1.1\,) \end{array}\right. \tag{29}$$

$$\rightarrow \left\{\begin{array}{l} B_{Max} = \sqrt{\frac{a'}{3k'}\,(\frac{3}{\operatorname{Sin}\alpha} - 0.2\,)} \\ B_{Min} = \sqrt{\frac{a'}{3k'}\,(\frac{3}{\operatorname{Sin}\alpha} - 1.1\,)} \end{array}\right. \tag{30}$$

$$K = 4B \rightarrow \left\{\begin{array}{l} 4k'\,B^2 = a'\,(\frac{4}{\operatorname{Sin}\alpha} - 0.2\,) \\ 4k'\,B^2 = a'\,(\frac{4}{\operatorname{Sin}\alpha} - 1.1\,) \end{array}\right. \tag{31}$$

$$\rightarrow \left\{\begin{array}{l} B_{Max} = \sqrt{\frac{a'}{4k'}\,(\frac{4}{\operatorname{Sin}\alpha} - 0.2\,)} \\ B_{Min} = \sqrt{\frac{a'}{4k'}\,(\frac{4}{\operatorname{Sin}\alpha} - 1.1\,)} \end{array}\right. \tag{32}$$

Coefficient k' in Equations (26) and (27) is one of the important parameters in drilling pattern because this coefficient shows the angle amount of free face with spacing and burden. Usually the drilling pattern is displaying in various models such a square, rectangular or triangular. Accordingly, this factor is estimated as follows:

a. Square and Rectangular pattern

In this model, k' factor is estimated based on Figure 1 and Equation (33) as follows:

$$\left.\begin{array}{l} k' = \frac{S}{B} \\ \operatorname{Cot}\beta = \frac{S}{B}) \end{array}\right\} \rightarrow k' = \operatorname{Cot}\beta \tag{33}$$

b. Triangular pattern

In this model, this factor is estimated based on Figure 1 and Equation (34) as follows:

$$\left.\begin{array}{l} k' = \frac{S}{B} \\ \operatorname{Cot}\beta = \frac{S/2}{B}) \end{array}\right\} \rightarrow k' = 2\operatorname{Cot}\beta \tag{34}$$

β: The angle is between free face with spacing and burden

Other parameters of blasting in open pit mines are estimated based on Equations (35) to (42). These equations are stated as follows:

$$U = 0.3\,B_{ave} \tag{35}$$

$$H = \frac{K}{\sin\alpha} + U \tag{36}$$

$$L_c = \frac{4\,Q}{\pi\,\varphi_c^{\,2}\,D_c} \tag{37}$$

$$S_t = H - L_c \tag{38}$$

$$Q = q\,S\,B\,K \tag{39}$$

$$Q = \frac{s\,E_s}{\eta_1\,\eta_2\,\eta_3\,E_e}\,S\,B\,K \tag{40}$$

$$Q = 0.004\,SG\;BI\;S\,B\,K \tag{41}$$

$$Q = 312.12\,SG \times RFI^{-2.082}\,S\,B\,K \tag{42}$$

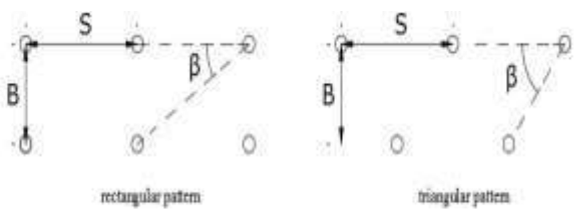

Figure 1. Various models of drilling pattern

3. 2. The Validation of the New Burden Thickness

For validation of the new burden thickness in Equations (26) to (28) is used optimum experimental data of blasting pattern in various open pit mines. Accordingly, this validation is performed in two different models such as the data of useful tables and optimum experimental data of blasting pattern in some open pit mines of Iran. They are discussed as follows:

3. 2. 1. The Data of Useful Tables This validation is performed based on the data of useful tables which published in the textbook of the blasting in mines by Hossaini and Poursaeed [20]. Accordingly, the summary of useful tables' data are presented in Table 11 and the results of new burden thickness and other blasting parameters have been presented in Table 12. Also, the comparison of these results has been presented in Table 13. Based on Table 13, difference of results are slight.

3. 2. 2. The Data of Some Open Pit Mines of Iran

This validation is performed based on optimum experimental data of blasting pattern in some open pit mines of Iran. Based on this, the summary of data of blasting in some open pit mines of Iran are presented in Table 14. The results of the new thickness of burden and other blasting parameters are summarized in Table 15. Based on Table 15, difference of results are slight.

TABLE 11. The pattern blasting of useful tables [20]

Num	φ_h (mm)	α (degree)	D_c (kg/m^3)	q (kg/m^3)	K (m)	B (m)	S (m)	H (m)	U (m)	S_t (m)
1	45	72	850	0.27	4	1.70	2.15	4.75	0.5	1.70
2	45	72	850	0.32	5	1.65	2.05	5.75	0.5	1.65
3	51	72	850	0.27	5	2.00	2.50	5.85	0.6	2.00
4	51	72	850	0.37	6	1.80	2.25	6.85	0.55	1.80
5	64	72	850	0.30	7	2.45	3.05	8.10	0.75	2.45
6	64	72	850	0.44	8	2.10	2.60	9.10	0.65	2.10
7	76	72	850	0.32	8	2.80	3.50	9.25	0.85	2.80
8	76	72	850	0.47	9	2.40	3.00	10.20	0.70	2.40
9	89	72	850	0.35	9	3.15	3.95	10.45	0.95	3.15
10	89	72	850	0.47	10	2.80	3.50	11.40	0.85	2.80
11	102	72	850	0.35	11	3.60	4.50	12.65	1.10	3.60
12	102	72	850	0.51	12	3.10	3.85	13.60	0.95	3.10
13	115	72	850	0.56	14	3.35	4.20	15.75	1.00	3.35
14	127	72	850	0.40	14	4.20	5.25	16.00	1.25	4.20
15	127	72	850	0.61	16	3.55	4.45	17.90	1.05	3.55
16	152	72	850	0.50	16	4.60	5.75	18.25	1.40	4.60
17	152	72	850	0.56	20	4.45	5.55	22.45	1.35	4.45

18	200	72	850	0.69	20	5.20	6.50	22.65	1.55	5.20
19	200	72	850	0.74	24	5.10	6.40	26.85	1.55	5.10

TABLE 12. The results of the new burden thickness in the first model

Num	φ_h (mm)	α (degree)	q (kg/m^3)	K (m)	B_{Min} (m)	B_{Max} (m)	B_{ave} (m)	$\frac{S}{B_{ave}}$	$\frac{U}{B_{ave}}$	$\frac{S_t}{B_{ave}}$
1	45	72	0.27	4	1.567	1.943	1.755	1.265	0.30	0.92
2	45	72	0.32	5	1.524	1.783	1.654	1.242	0.30	0.93
3	51	72	0.27	5	1.828	2.225	2.027	1.250	0.30	0.92
4	51	72	0.37	6	1.672	1.925	1.799	1.250	0.30	0.93
5	64	72	0.30	7	2.258	2.672	2.465	1.245	0.30	0.93
6	64	72	0.44	8	1.978	2.235	2.107	1.238	0.30	0.93
7	76	72	0.32	8	2.589	3.065	2.827	1.250	0.30	0.93
8	76	72	0.47	9	2.256	2.555	2.406	1.250	0.30	0.93
9	89	72	0.35	9	2.898	3.428	3.163	1.254	0.30	0.93
10	89	72	0.47	10	2.621	2.988	2.805	1.250	0.30	0.93
11	102	72	0.35	11	3.368	3.944	3.656	1.250	0.30	0.93
12	102	72	0.51	12	2.930	3.305	3.120	1.242	0.30	0.93
13	115	72	0.56	14	3.175	3.547	3.361	1.254	0.30	0.94
14	127	72	0.40	14	3.987	4.607	4.290	1.250	0.30	0.93
15	127	72	0.61	16	3.394	3.760	3.577	1.254	0.30	0.94
16	152	72	0.50	16	4.316	4.942	4.629	1.250	0.30	0.93
17	152	72	0.56	20	4.250	4.710	4.480	1.247	0.30	0.94
18	200	72	0.69	20	4.917	5.553	5.235	1.274	0.30	0.94
19	200	72	0.74	24	4.879	5.380	5.130	1.255	0.30	0.94

TABLE 13. The comparison of results in the first model

Num	φ_h (mm)	Δ_B (m)	Δ_B (%)	$\frac{S}{B}$	$\frac{\Delta S}{B}$	$\frac{U}{B}$	$\frac{\Delta U}{B}$	$\frac{S_t}{B}$	$\frac{\Delta S_t}{B}$
1	45	-0.055	3.24	1.265	0	0.294	-0.006	1	0.080
2	45	-0.004	0.24	1.242	0	0.303	0.003	1	0.070
3	51	-0.027	1.35	1.250	0	0.300	0.000	1	0.080
4	51	0.001	0.06	1.250	0	0.306	0.006	1	0.070
5	64	-0.015	0.61	1.245	0	0.306	0.006	1	0.070
6	64	-0.007	0.33	1.238	0	0.310	0.010	1	0.070
7	76	-0.027	0.96	1.250	0	0.304	0.004	1	0.070
8	76	-0.006	0.25	1.250	0	0.292	-0.008	1	0.070
9	89	-0.013	0.41	1.254	0	0.302	0.002	1	0.070
10	89	-0.005	0.18	1.250	0	0.304	0.004	1	0.070
11	102	-0.056	1.56	1.250	0	0.306	0.006	1	0.070
12	102	-0.02	0.65	1.242	0	0.306	0.006	1	0.070
13	115	-0.011	0.33	1.254	0	0.299	-0.001	1	0.060
14	127	-0.09	2.14	1.250	0	0.298	-0.002	1	0.070
15	127	-0.027	0.76	1.254	0	0.296	-0.004	1	0.060

16	152	-0.029	0.63	1.250	0	0.304	0.004	1	0.070
17	152	-0.03	0.67	1.247	0	0.303	0.003	1	0.060
18	200	-0.035	0.67	1.250	0	0.298	-0.002	1	0.060
19	200	-0.03	0.59	1.255	0	0.304	0.004	1	0.060

TABLE 14. The blasting pattern in some open pit mines of Iran [19]

Num	Mine name	φ_h (mm)	α (degree)	q (kg/m^3)	K (m)	B (m)	S (m)
1	Iron stone of Jalalabad	165	90	0.600	12	4.20	5.30
2	Iron stone of Choghart	165	90	1.300	12.5	3.00	4.00
3	Limestone of pirbakran	105	90	0.35	8	3.50	4.50
4	Limestone of Abelu	89	90	0.408	10	3.00	3.43
5	Limestone of Asgarabad	101.6	80	0.778	10	2.74	2.74
6	Limestone of Korehblagh	63.5	90	0.487	10	2.20	2.20
7	Chalk stone of Shireki	76.2	90	0.620	10	2.32	2.32
8	Chalk stone of Eivavgholi	64	90	1.030	10	1.50	1.50

TABLE 15. The results of the new burden thickness in the second model

Num	Mine name	q (kg/m^3)	K (m)	B_{Min} (m)	B_{Max} (m)	B_{ave} (m)	$\frac{S}{B_{ave}}$	$\frac{U}{B_{ave}}$	$\frac{S_t}{B_{ave}}$
1	Iron stone of Jalalabad	0.600	12	3.921	4.703	4.312	1.262	0.30	0.93
2	Iron stone of Choghart	1.300	12.5	2.810	3.156	2.983	1.333	0.30	0.94
3	Limestone of pirbakran	0.35	8	3.073	3.845	3.459	1.286	0.30	0.92
4	Limestone of Abelu	0.408	10	2.282	3.282	3.054	1.143	0.30	0.93
5	Limestone of Asgarabad	0.778	10	2.529	2.889	2.709	1	0.30	0.93
6	Limestone of Korehblagh	0.487	10	2.067	2.296	2.182	1	0.30	0.94
7	Chalk stone of Shireki	0.620	10	2.180	2.439	2.310	1	0.30	0.93
8	Chalk stone of Eivavgholi	1.030	10	1.490	1.603	1.547	1	0.30	0.94

TABLE 16. The comparison of results in the second model

Num	Mine name	Δ_B (m)	Δ_B (%)	$\frac{S}{B}$	$\frac{\Delta S}{B}$
1	Iron stone of Jalalabad	-0.112	2.67	1.262	0
2	Iron stone of Choghart	0.017	0.57	1.333	0
3	Limestone of pirbakran	0.041	1.14	1.286	0
4	Limestone of Abelu	-0.054	1.41	1.143	0
5	Limestone of Asgarabad	0.031	0.66	1	0
6	Limestone of Korehblagh	0.018	0.60	1	0
7	Chalk stone of Shireki	0.01	0.36	1	0
8	Chalk stone of Eivavgholi	-0.047	1.25	1	0

4. DISCUSSION

The amount of specific charge is one of the main parameters for determining the burden thickness in blasting of open pit mines. The estimation of specific charge is better to do base on characteristics of the rock mass. Therefore, using of energy transfer rule, blastability index and rock fragmentation index are suggested for estimating the amount of the specific charge. The experimental results of blasting in open pit mines are confirmed the above subject.

Various equations have been presented based on blasting experiences that some of they are valuable. These equations have been shown in Equations (13) to (21). Using of mathematical science and conflation of Equations (13) to (21) with together are obtained very useful of results. Mathematical analysis of these equations causes to presentation of Equations (22) to (32) for burden thickness. Accordingly, in this paper has been presented new equations for estimation the maximum and minimum thickness of burden. These equations have designed based on the amount of specific charge according to Equations (26) to (28). The arrangement of the drilling holes in most of the previous methods is not clear perfectly. Therefore, in this paper for more clarity of above subject was presented k' factor in Equations (26) to (28).

5. CONCLUSION

Tables 13 and 16 show the validation results of the new equations in this article. The results of the new equations of burden thickness have slight differences with the experimental results. Based on Tables 13 and 16, the maximum error of burden is calculated to be 3%.

In some previous methods for estimation of burden thickness requires solving nonlinear equations but solving of quadratic equations is easier. Also these new equations depend on rock quality that is the advantages the projected model. Accordingly in this paper quadratic equations are presented.

Blasting pattern in open pit mines can display in various models such a square, rectangular and triangular. Based on this, arrangement of drilling pattern is very important for estimation of burden thickness. Therefore, in this article the coefficient k' was defined. This coefficient considers effects of arrangement of drilling pattern in estimation of burden thickness. Therefore, using the definition of k' coefficient in these new equations, it can be claimed that these new equations are considered as the most reliable mathematical equation for the accurate calculation of the burden thickness.

6. REFERENCES

1. Ndibalema, A., and Mine, A. A. G. G., "Capturing economic benefits from blasting", The Southern African Institute of Mining and Metallurgy: Surface Mining Conference, (2008), 97–112.
2. Tosun, A., Konak, G., Toprak, T., Karakus, D., and Onur, A. H., "Development of the Kuz-Ram Model to Blasting in a Limestone Quarry ", ***Archives of Mining Sciences***, Vol. 59, No. 2, (2014), 477–488. doi:10.2478/amsc-2014-0034
3. Mishra, A. K., and Rout, M., "Flyrocks – Detection and Mitigation at Construction Site in Blasting Operation", ***World Environment***, Vol. 1, No. 1, (2012), 1–5. doi:10.5923/j.env.20110101.01
4. Elevli, B., and Arpaz, E., "Evaluation of parameters affected on the blast induced ground vibration (BIGV) by using relation diagram method (RDM)", ***Acta Montanistica Slovaca Ročník***, Vol. 15, No. 4, (2010), 261–268.
5. Choudhary, B. S., and Sonu, K., "Assessment of powder factor in surface bench blasting using schmidt rebound number of rock mass", ***International Journal of Research in Engineering and Technology***, Vol. 2, No. 12, (2013), 132–138.
6. Bakhshandeh Amnieh, H., Mohammadi, A., and Mozdianfard, M., "Predicting peak particle velocity by artificial neural networks and multivariate regression analysis-Sarcheshmeh copper mine, Kerman, Iran", ***Journal of Mining & Environment***, Vol. 4, No. 2, (2013), 125–132. doi:10.22044/JME.2013.209
7. Mandal, S. K., Bhagat, N. K., and Singh, M. M., "Magnitude of vibration triggering component determines safety of structures", ***Journal of Mining and Environment***, Vol. 5, No. 1, (2014), 35–46. doi:10.22044/jme.2014.269.
8. Neale, A. M., "Blast optimization at Kriel Colliery", ***Journal of the Southern African Institute of Mining and Metallurgy***, Vol. 110, No. 4, (2010), 161–168.
9. Oraee, K., and Asi, B., "Prediction of Rock Fragmentation in Open Pit Mines, using Neural Network Analysis", Fifteenth International Symposium on Mine Planning and Equipment Selection (MPES 2006), (2006), 1–15.
10. Anderson, O., "Blast hole burden design-introducing a new formula", ***Australian Institute of Mining and Metallurgy***, (1952), 115–130.
11. Jimeno, E., Jimino, C., and Carcedo, A., Drilling and Blasting of Rocks, Routledge, (1995).
12. Ouchterlony, F., "The Swebrec© function: linking fragmentation by blasting and crushing", ***Mining Technology***, Vol. 114, No. 1, (2005), 29–44. doi:10.1179/037178405X44539
13. Ash, R. L., "Design of Blasting Rounds", In: Surface Mining, AIME New York, (1990), 565–583.
14. Rustan, A. P., "Micro-sequential contour blasting—how does it influence the surrounding rock mass?", ***Engineering Geology***, Vol. 49, Nos. 3–4, (1998), 303–313. doi:10.1016/S0013-7952(97)00062-8
15. Langefors, U., and Kihlström, B., The Modern Technique of Rock Blasting, Wiley, (1978).
16. Sendlein, L., Yazicigil, H., and Carlson, C., Surface Mining Environmental Monitoring and Reclamation Handbook, (1983).
17. Berta, G., "Blasting-induced vibration in tunnelling", ***Tunnelling and Underground Space Technology***, Vol. 9, No. 2, (1994), 175–187. doi:10.1016/0886-7798(94)90029-9
18. Lilly P., "An empirical method of assessing rock mass blastability", Large Open Pit Mines Conference, Newman, Australia, (1986), 89–92.
19. Moomivand, H., and Vandyousefi, H., "Development of a new empirical fragmentation model using rock mass properties, blasthole parameters, and powder factor", ***Arabian Journal of Geosciences***, Vol. 13, No. 22, (2020), 1173. doi:10.1007/s12517-020-06110-2
20. Hossaini, M., and Poursaeed, H., "Modification of four-section cut model for drift blast design in Razi coal mine-North Iran", Proceedings of the 2010 Coal Operators' Conference, Mining Engineering, University of Wollongong, (2010), 180–186.

Persian Abstract

چکیده

داشتن الگوی مناسب برای چالزنی و انفجار از ضروریات علم معدن‌کاری و بالاخص معادن روباز است. یکی از اهداف آتشکاری در معادن روباز به خدمت گرفتن انرژی حاصل از انفجار مواد منفجره برای خرد کردن سنگ با حداقل هزینه تولید است. مهمترین پارامترهای آتشکاری شامل قطر چال، خرج ویژه، ضخامت بارسنگ و ابعاد خردشدگی مناسب سنگ است. مقادیر پارامترهای آتشکاری به کیفیت توده سنگ بستگی دارد. در این مقاله بر اساس امتیاز حاصل از کیفیت توده سنگ و مقدار خرج ویژه در آتشکاری، مقادیر حداکثر و حداقل ضخامت بارسنگ در آتشکاری معادن روباز بر اساس یک معادله درجه ۲ محاسبه می‌شود. براساس برآورد ضخامت جدید بارسنگ سایر پارامترهای آتشباری محاسبه می‌شوند. اعتبارسنجی انجام شده در این مقاله بیانگر این مطلب است که نتایج حاصل از این معادله جدید اختلاف ناچیزی با مقادیر واقعی ضخامت بارسنگ معادن مختلف ارائه شده در جداول ۱۳ و ۱۶ دارد. حداکثر خطای محاسبه شده در این اعتبارسنجی معادله جدید برابر ۳ درصد است که بیانگر قابلیت اطمینان بالای این ضخامت بارسنگ جدید است.

AIMS AND SCOPE

The objective of the International Journal of Engineering is to provide a forum for communication of information among the world's scientific and technological community and Iranian scientists and engineers. This journal intends to be of interest and utility to researchers and practitioners in the academic, industrial and governmental sectors. All original research contributions of significant value focused on basics, applications and aspects areas of engineering discipline are welcome.

This journal is published in three quarterly transactions: Transactions A (Basics) deal with the engineering fundamentals, Transactions B (Applications) are concerned with the application of the engineering knowledge in the daily life of the human being and Transactions C (Aspects) - starting from January 2012 - emphasize on the main engineering aspects whose elaboration can yield knowledge and expertise that can equally serve all branches of engineering discipline.

This journal will publish authoritative papers on theoretical and experimental researches and advanced applications embodying the results of extensive field, plant, laboratory or theoretical investigation or new interpretations of existing problems. It may also feature - when appropriate - research notes, technical notes, state-of-the-art survey type papers, short communications, letters to the editor, meeting schedules and conference announcements. The language of publication is English. Each paper should contain an abstract both in English and in Persian. However, for the authors who are not familiar with Persian, the publisher will prepare the latter. The abstracts should not exceed 250 words.

All manuscripts will be peer-reviewed by qualified reviewers. The material should be presented clearly and concisely:

- *Full papers* must be based on completed original works of significant novelty. The papers are not strictly limited in length. However, lengthy contributions may be delayed due to limited space. It is advised to keep papers limited to 7500 words.
- *Research* notes are considered as short items that include theoretical or experimental results of immediate current interest.
- *Technical notes* are also considered as short items of enough technical acceptability with more rapid publication appeal. The length of a research or technical note is recommended not to exceed 2500 words or 4 journal pages (including figures and tables).

Review papers are only considered from highly qualified well-known authors generally assigned by the editorial board or editor in chief. Short communications and letters to the editor should contain a text of about 1000 words and whatever figures and tables that may be required to support the text. They include discussion of full papers and short items and should contribute to the original article by providing confirmation or additional interpretation. Discussion of papers will be referred to author(s) for reply and will concurrently be published with reply of author(s).

INSTRUCTIONS FOR AUTHORS

Submission of a manuscript represents that it has neither been published nor submitted for publication elsewhere and is result of research carried out by author(s). Presentation in a conference and appearance in a symposium proceeding is not considered prior publication.

Authors are required to include a list describing all the symbols and abbreviations in the paper. Use of the international system of measurement units is mandatory.

- On-line submission of manuscripts results in faster publication process and is recommended. Instructions are given in the IJE web sites: www.ije.ir-www.ijeir.info
- Hardcopy submissions must include MS Word and jpg files.
- Manuscripts should be typewritten on one side of A4 paper, double-spaced, with adequate margins.
- References should be numbered in brackets and appear in sequence through the text. List of references should be given at the end of the paper.
- Figure captions are to be indicated under the illustrations. They should sufficiently explain the figures.
- Illustrations should appear in their appropriate places in the text.
- Tables and diagrams should be submitted in a form suitable for reproduction.
- Photographs should be of high quality saved as jpg files.
- Tables, Illustrations, Figures and Diagrams will be normally printed in single column width (8cm). Exceptionally large ones may be printed across two columns (17cm).

PAGE CHARGES AND REPRINTS

The papers are strictly limited in length, maximum 6 journal pages (including figures and tables). For the additional to 6 journal pages, there will be page charges. It is advised to keep papers limited to 3500 words.

Page Charges for Papers More Than 6 Pages (Including Abstract)	
For International Author ***	**$55 / per page**
For Local Author	**100,000 Toman / per page**

AUTHOR CHECKLIST

- Author(s), bio-data including affiliation(s) and mail and e-mail addresses).
- Manuscript including abstracts, key words, illustrations, tables, figures with figure captions and list of references.
- MS Word files of the paper.

International **J**ournal of **E**ngineering, P.O. Box 13145-1659, Tehran, I.R. Iran
Materials and Energy Research Center, 5 Ahuramazda St., Alvand Ave., Argentina Sq., Tehran, Islamic Republic of Iran
www.merc.ac.ir - www.emerc.ac.ir